DOCTOR OF PHILOSOPHY

Ferroelectric composites for pyro-and piezoelectric applications

Dias, Carlos Jorge Mariano Miranda

Award date:
1994

Awarding institution:
Bangor University

Ferroelectric composites for pyro- and piezoelectric applications

Thesis submitted in candidature for the degree of Doctor of Philosophy

January 1994

Carlos Jorge Mariano Miranda Dias

School of Electronic Engineering and Computer Systems

University of Wales

Bangor

United Kingdom

I - Abstract I

II - Acknowledgements II

III - List of symbols III

IV - Axis convention VI

1. - Introduction 1

1.1 - Background and motivation 1

1.2 - Ferroelectricity, piezoelectricity and pyroelectricity 4

1.2.1. - Ferroelectricity 4

1.2.2. - Piezoelectricity 6

1.2.3. - Pyroelectricity 9

1.3 - Ferroelectric ceramics 10

1.3.1. - PZT 15

1.3.2. - PLZT 17

1.3.3. - PT and PTCa 18

1.4 - Ferroelectric polymers: PVDF and P(VDF/TrFE) - structure and morphology 20

1.4.1. - PVDF 20

1.4.2. - P(VDF/TrFE) 26

1.5 - Fundamentals of ferroelectric composite materials 33

1.5.1.- 0-3 connectivity 36

1.5.2. - 1-3 connectivity 37

2 - Models of composites 42

2.1 - Short introduction 42

2.2 - Yamada model for 0-3 composites 42

2.3 - Furukawa model for 0-3 composites 45

2.4 - Connectivity approach 47

2.4.1 - Parallel connectivity properties 48

2.4.2 - Series connectivity properties 54

2.5 - 0-3 composites properties: cube models 61

2.6 - Other approaches 77

3 - Composite fabrication 79

3.1 - Introduction 79

3.2 - Review of preparation methods of 1-3, 3-3 and 0-3 composites 81

3.3 - Ceramic powder fabrication 85

3.4 - PVDF and P(VDF/TrFE) polymer fabrication 90

3.5 - 0-3 composite fabrication 92

4 - Polarization, dielectric and resistivity properties 105
4.1 - Introduction 105
4.2 - Polarization methods 106
4.2.1 - Conventional poling: dc and ac poling 106
4.2.2 - Corona poling 108
4.3 - Polarization efficiency in 0-3 composites 109
4.3.1 - Poling field across the ceramic 109
4.3.2 - Property dependence on the poling efficiency 113
4.4 - Resistivity properties in PTCa-1:P(VDF/TrFE) composites 114
4.5 - Dielectric properties of composites 117
4.5.1 - Temperature dependence of the dielectric properties 119
4.5.2 - Frequency dependence of the dielectric properties 123
4.5.3 - Volume fraction dependence 127
4.6 - Polarization hysteresis measurements 130
4.7 - Simulation of hysteresis 136

5 - Pyroelectricity in composites 143
5.1 - Introduction 143
5.2 - Measurement techniques 145
5.2.1 - The direct method 145
5.2.2 - Dynamic methods: radiative and heat excitation 146
5.3 - Composite pyroelectric properties review 151
5.4 - Pyroelectric measurements 154
5.4.1 - Pyroelectric coefficient in composites 154
5.4.2 - Temperature dependence in the composites 161
5.4.3 - Field and poling time dependence 163
5.4.4 - High temperature poling 164
5.4.5 - Corona versus conventional poling 165
5.4.6 - Milled and quenched ceramics 167
5.4.7 - Dynamic method 169
5.4.8 - Figure Of Merit FOMp 172
5.4.9 - Poling frequency 175
5.5 - Summary 176

6 - Piezoelectricity in composites and ultrasonic transducers 179
6.1 - Introduction and basic theory for a lossy piezoelectric resonator 179
6.2 - Measurements techniques 184
6.2.1 - kt measurement technique 184
6.2.2 - dh, gh, FOMh and d33 measurement techniques 187
6.3 - Literature review of composite piezoelectric properties 188
6.4 - Piezoelectric properties of composites (current work) 192

6.5 - Ultrasonic transducers 198
6.5.1 - Theory: ABCD matrices approach 198
Simulation of the time response 204
6.5.2 - Backing 206
6.5.3 - The influence of the front matching layer and of quality factor 207
6.5.4 - Testing of ultrasonic transducers 211

7 - Conclusions 215
7.1 - Concluding remarks 215
7.2 - Further work 217
7.3 - Papers and communications published in the course of this work 218
7.4 - References 220

Annex: Papers and Communications 235

I - Abstract

Composites made by dispersing a ferroelectric ceramic powder in a polymer host have been fabricated and evaluated for their pyroelectric and piezoelectric properties.

Lead zirconate titanate (PZT5A), calcium modified lead titanate (PTCa) and lanthanum doped lead zirconate titanate (PLZT) have been used as the electroactive dispersoid while the polymer polyvinylidene fluoride PVDF and its copolymer with trifluorethylene P(VDF/TrFE), have been used as hosts.

It has been found that the electro-active properties were highest in the composite using PTCa powder obtained through a quenching process dispersed in P(VDF/TrFE). The pyroelectric coefficient p, in this composite was 130 $\mu C/m^2K$, while its Figure Of Merit p/ε, where ε is the permittivity, had a value around 2 $\mu C/m^2K$ the latter value being comparable to that of the pure ceramic. The piezoelectric constant d_{33} in the same composite had a value of 48 pC/N, the thickness mode electromechanical coupling factor k_t was 0.24 and the acoustic impedance was equal to 16 MRayl. These piezo-properties are not so attractive for an ultrasonic transducer because PZT5A has better characteristics for an emitter while P(VDF/TrFE) on its own performs better as a receiver.

In this work a measurement technique has been developed which has been applied successfully to the measurement of the polarization hysteresis in composites. A value of 0.15 C/m^2 for the remnant polarization has been found for the composite mentioned above, while its coercive field was 18 MV/m.

A model, so-called mixed connectivity cube, has also been described which attempts to predict the properties of the composites based on the properties of the constituent materials with an emphasis on their connectivity.

II - Acknowledgements

My deepest of gratitudes goes to Dr. Dilip Das-Gupta for all the technical, financial and amicable support he has given me over the years. Thanks for everything Dilip.

I would like to acknowledge Marion Simon and R. Quad from Heiman GmbH and John Chilton, Rob Twinney and Geoff Garner from GEC Marconi and Dr. Lubitz from Siemens for all the help and assistance they have given over the years of collaboration. Cheers to everyone.

A warm appreciation and thankfulness goes also to my colleagues Zhang Shu-Ren which has helped me a great deal with the beginning of composite fabrication and Andrej Svatik a learned experimentalist whose enthusiasm seemed to grow with adversity. I would also like to acknowledge Vincent Mollard, Ülf Höpfner, Yvette Kaminorz and Paulo Scarpa for their contribution in the work that is now being presented. A warm cheers to everybody.

For that friendly helping hand in dealing with the practical details I am thankful to Albert and David Rees, Miles Woolfenden, Ivor Wynne and all the staff and porters from the school. Cheers again to everyone.

I thank also the crowd from the communications group (i.e. Paulo Moreira, Izzat Darwazeh...) for their expert help in dealing with the problems in the megahertz range and beyond. I thank also Henrique Gomes for all the enthusiastic discussions we had. Thank you mates.

I would like also to thank the Head of Department Prof. J. J. O'Reilly and Mr. Alwyn Owens for allowing me to use the facilities of the school.

The most warmest of appreciation goes to Maria Antónia and Henrique Salgado for their friendship cemented and welded over the years. It was(is) just like Port wine. To Luis Moura "meu camarada de armas e lapiseiras" goes a big hug for staying always tuned into a relaxing and joking atmosphere. To all the rest of the portuguese community goes also a big thank you for everything. Saravah companheiros.

I would like to acknowledge the Universidade Nova de Lisboa (Portugal) as well as Prof. Marat Mendes and my colleagues in the Applied Physics Section, for allowing and coping with, my extended period of leave from the normal academic duties.

Finally, I would like to express my particular gratitude to my family for their wise and loving advice and encouragement. It is to them that this thesis is dedicated.

III - List of symbols

SYMBOL	DESCRIPTION	UNITS
A	area	m^2
c	elastic stiffness; second rank tensor	GPa
C	Curie constant, capacitance	K^{-1};F
C_v	specific heat at constant volume	MJ/m^3K
d	piezoelectric charge constant (clamped free); third rank tensor	pC/N
D	dielectric displacement	C/m^2
D^*	pyroelectric detectivity	
e	piezoelectric charge constant (stress free); third rank tensor	C/m^2
E	electric field	V/m
E_a	activation field	MV/m
E_{ac}	activation energy	eV
E_c	coercive field	MV/m
f	frequency	Hz
f_o	resonance frequency	Hz
F	force	N
$FOM_h = d_h g_h$	hydrostatic piezoelectric Figure Of Merit	10^{-12} Pa^{-1}
$FOM_p = p/\varepsilon$	pyroelectric Figure Of Merit	$\mu C/m^2K$
g	piezoelectric voltage constant (clamped free); third rank tensor	mV·m/N
G	Yamada local field coefficient	
h	piezoelectric voltage constant (stress free); third rank tensor	GV/m
k	electromechanical coupling factor; third rank tensor	
k_t	thickness electromechanical coupling factor	
k_p	planar electromechanical coupling factor	
l	thickness	m
L	Furukawa local field coefficient	
m	dimension of the cube model	
n	dimension of the cube model	
p	pyroelectric coefficient; second rank tensor	$\mu C/m^2K$
P	polarization	mC/m^2
P_r	remnant polarization	mC/m^2
Q	charge	C
Q_m	mechanical quality factor	
r_V	pyroelectric voltage responsivity	V/W
R	resistance	Ω
s	elastic compliance; second rank tensor	TPa^{-1}
t	time	s
T	temperature	

T_c	Curie temperature	°C
U	particle velocity	m/s
v_s	velocity of sound	m/s
x	strain	
X	stress	Pa
w_{gs}	ceramic grain size	µm
Z	impedance	Ohms
Z_a	acoustic impedance	MRayl
α	κ/l^2	
α	sound wave loss factor(equation 6.22)	
α_a	sound attenuation constant	
α, α_x	linear expansion coefficient	10^{-6} K^{-1}
α_p	poling ratio	K^{-1}
$\alpha_P = \frac{1}{P}\frac{dP}{dT}$	temperature polarization coefficient	K^{-1}
$\alpha_\varepsilon = \frac{1}{\varepsilon}\frac{d\varepsilon}{dT}$	temperature permittivity coefficient	K^{-1}
β	inverse of the permittivity (second rank tensor)	
β	rate of change in temperature	°C/min
β_a	lossless wave number	
δ, δ_e	dielectric loss (angle)	°
ε	relative permittivity; first rank tensor	
ϕ	volume fraction	
γ	sound wave propagation number (complex)	
η	Yamada's shape factor	
κ	thermal diffusivity	mm^2/s
ν_o	rate of switching constant	Hz
θ_c	Curie temperature	K
ρ	density	kg/m^3
ρ	resistivity	$\Omega \cdot m$
ρ	volume charge	C/m^3
σ	conductivity	$(\Omega \cdot m)^{-1}$
σ	surface charge	C/m^2
$\psi=\delta_m$	mechanical losses (angle)	°
ω	angular frequency	rad/s
ω_a	adimensionalized frequency	

MATERIALS

PLZT	lanthanum doped PZT
PP	poly(propylene)

PT	lead titanate
PTCa	calcium modified (24 mol%) lead titanate
PVDF	poly(vinylidene fluoride)
P(VDF/TrFE)	poly(vinylidene fluoride/trifluorethylene) copolymer
PZ	lead zirconate
PZT	Lead Zirconate Titanate $Pb_xZr_{1-x}TiO_3$

SUPERSCRIPTS

c	ceramic property
D	differential taken at constant D
E	differential taken at constant E
p	polymer property
x	differential taken at constant x
X	differential taken at constant X

SUBSCRIPTS

e	electrical
h	hydrostatic
i	integer / Imaginary number
j	integer
m	mechanical

CONSTANTS

e	electron charge	$1.602 \cdot 10^{-19}$ C
k	Boltzman constant	$1.381 \cdot 10^{-23}$ J/K
ε_o	vacuum permittivity	$8.854 \cdot 10^{-12}$ F/m

IV - Axis convention

The following axis convention has been used throughout this thesis:

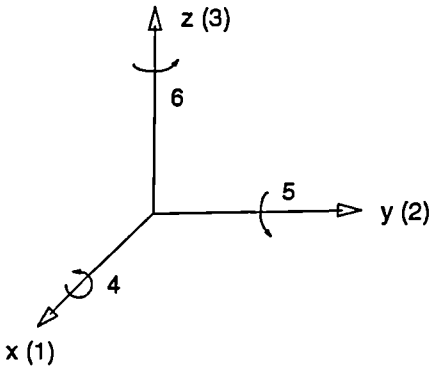

3 is the thickness direction
1 and 2 are the lateral directions
4, 5 and 6 are the rotational directions

PIEZOELECTRIC SAMPLE

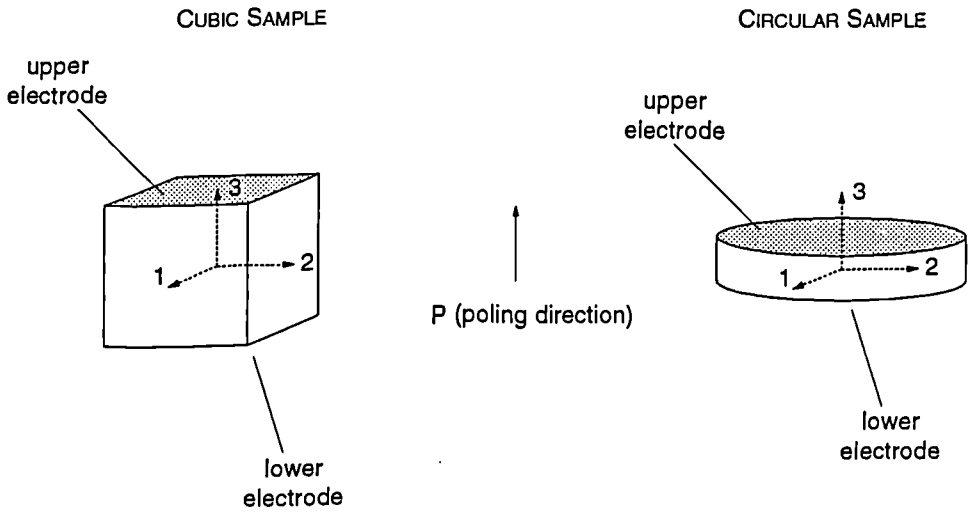

1. - Introduction

1.1 - Background and motivation

The work described here is the result of a three year BRITE-EURAM project designed for the fabrication of composite materials with improved electroactive properties over those materials currently available today (i.e. ferroelectric ceramics and polymers). The aim was to make a composite whose fabrication method is that of a ceramic dispersoid in a polymer host and whose properties would be comparable to those of the ceramics.

Combining a piezoelectric ceramic and a polymer host to form a flexible ferroelectric composite has been pursued in recent years in view of the greater flexibility allowed by these materials to suit particular properties, such as mechanical, electrical, thermal and/or a coupling between these properties.

Conventional piezoelectric materials, such as lead zirconate-titanate [Jaffe et al. 1955; Ouchi 1965], lead metaniobate and more recently modified lead titanates [Ueda et al. 1968; Yamashita et al. 1981; Jimenez et al. 1988] are nowadays the most popular choices in applications which use their piezo- and pyroelectric properties. These materials offer high electromechanical coupling ($k_t \approx$ 0.4-0.5), a wide selection of permittivities ($\varepsilon \approx$ 100-2400) and low dielectric and mechanical losses albeit with a large acoustic impedance resulting in a more difficult acoustic match to soft media such as tissues and water.

This range of electroactive materials has recently been enlarged with ferroelectric polymers such as polyvinylidene fluoride PVDF and its copolymer with trifluorethylene P(VDF/TrFE) [Lovinger 1983; Furukawa et al. 1988; Furukawa 1989] which have a low acoustic impedance ($\approx$ 4.5 MRayl) but also a low electromechanical coupling factor ($k_t \approx$ 0.2-0.3), high dielectric losses (0.15-0.25 at 1MHz) and low quality factors ($Q_m \approx$ 10-20) which make them useful for underwater operation and/or for broad band applications. These properties are coupled to a low permittivity, which can be advantageous in certain situations, such as in pyroelectric detectors.

Composites can be viewed as intermediate materials between these two extremes [Takeuchi et al. 1985] combining such attributes as flexibility and formability, to a whole range of piezoelectric and pyroelectric properties which depend both on the ceramic-polymer mixture and on the processing employed in its manufacture.

The comparison of properties is not always an easy assignment. To overcome some of the difficulties associated with this task Figures Of Merit (FOM) have been devised which evaluate the suitability of a material for a given application. Thus, there are FOM's for pyroelectric detectors and for piezoelectric transducers which will be used to compare the relative merits of these materials.

The identification of the relevant variables controlling the property behaviour is thus of utmost importance for the manufacture of a successful composite. The most obvious one

is that the ceramic material employed should exhibit high pyro- and piezoelectric properties. It was recognised, however, that the connectivity of the phases is also an important parameter [Newnham et al. 1978; Skinner et al. 1978] and this finding prompted research on composites consisting of embedding rods of a piezoelectric material in a polymer host, thus forming a 2D parallel network which exhibited better electro-active properties than the simpler powder dispersed composites. Other ceramic-polymer configurations have been tried such as using ceramic fibres and coral ceramic templates to make a 3D self connected ceramic phase. Nevertheless the powder in a matrix approach, which has been used throughout this work, was never quite abandoned mainly because of the attraction of mass production of cheap piezoelectric and pyroelectric materials that could impart in a reliable way special properties to various structures by a coating process. Large and thin film arrays of electroactive arrays for ultrasonic and infrared detection are also part of an agenda that still awaits for its fulfilment.

The phenomena of ferroelectricity, piezo- and pyroelectricity involved in ferroelectric materials have been reviewed in this first chapter. This is followed by a literature review of the properties of the most significant ceramics used for piezo- and pyroelectric applications with a special emphasis on the Lead Zirconate (PZT) and Calcium modified Lead Titanate (PTCa) which were used as ferroelectric dispersoids in the composites of the current work.

PVDF and P(VDF/TrFE) were used as hosts of the ceramic and their properties are also reviewed in this chapter. The main advantage for the composites of using such polymers as host materials does not come from an additional contribution to the electroactive properties of the composites besides that of the ceramic but rather from a better dielectric matching between the host and the dispersoid.

The matching of electrical [Chilton 1991] and mechanical properties [Smith 1993] is an area which should be given due consideration. The importance of electrically matching the ceramic to the polymer phase stems mainly from the difficulty of orienting the polarisation by means of an external field in randomly distributed ceramic grains of low resistivity and high permittivity embedded in a high resistivity, low permittivity polymer matrix without triggering an electrical breakdown.

This first chapter ends with a review of the fundamentals on composites pointing out the main variables involved. A classification of the composites according to their connectivity is described while the origin of their properties is outlined.

It is also an aim of this work to provide a theoretical framework in order to predict the dielectric pyroelectric, piezoelectric and elastic properties of composites. This theoretical model is based on the properties of the constituent materials and on their connectivity pattern. From this model features such as the electrical matching of the constituent phases will be prominent.

The origin of the properties is further dealt with in chapter 2 where models of composites of the type produced in this work are explained. These models include those of Yamada [Yamada et al. 1982], Furukawa [Furukawa et al. 1976; Furukawa et al. 1979] as well

as the cube models [Banno 1985]. Special reference is made to the latter ones and namely to the mixed connectivity cube model [Dias et al. 1993]. The main advantage of these cube models is their ability of predicting a range of composite properties which include the piezoelectric, pyroelectric, dielectric and elastic properties based on the properties of the constituent materials, their volume fraction and connectivity.

The fabrication methods of the composites made in this work are the subject of chapter 3. The morphology of the composites determined by Scanning Electron Microscopy (SEM) is also described in chapter 3.

The dielectric and resistive behaviour of the composites which is an important consideration for the electrical matching of the phases is dealt in chapter 4. Measurements of the dielectric behaviour with frequency and temperature are described, while the mixed connectivity cube model is used to explain the room temperature permittivity of composites loaded with different volume fraction of ceramic.

This chapter ends with the description of a technique for the measurement of the polarization hysteresis in conductive materials [Dias et al. 1993]. This technique has been applied for these composites to obtain values of the remnant polarization and coercive field.

The pyroelectric properties of composites are described in chapter 5. These include the measurement of the pyroelectric coefficient for a variety of composites as a function of the temperature. The value of this property at room temperature is subjected to theoretical modelling again using the mixed connectivity model. A measurement technique which uses a dynamic heat excitation to find the pyroelectric coefficient in composites is also described [Dias et al. 1993]. This method has the advantage of being an accurate and quicker alternative to the conventional technique of determining the pyroelectric coefficient [Byer et al. 1972].

The piezoelectric properties of these composites are described in chapter 6. These properties include the electromechanical coupling factor k_t, which is an important quantity for the performance of ultrasonic transducers. This has been achieved using an approach used for PVDF and P(VDF/TrFE) which in similarity with composites exhibit high mechanical losses. Other quantities such as the velocity of sound, the acoustic impedance and the d_{33} piezoelectric constant have been also measured and theoretically modelled. This chapter ends with the modelling of ultrasonic transducers where the k_t and the mechanical losses of the piezoelectric material are taking into account. The fabrication of ultrasonic transducers using the composites is also reported.

In chapter 7 the conclusions of this work are summed up with reference both to the composites which perform better regarding their electroactive properties and to the contributions of this work for the advancement of science.

1.2 - Ferroelectricity, piezoelectricity and pyroelectricity

1.2.1. - Ferroelectricity

Ferroelectricity is a term first used by Vasalek [Vasalek 1921] to stress the analogy between the non-linear hysteretic dielectric properties of Rochelle salt and the magnetic behaviour of ferromagnetic iron. The concept has nowadays been enlarged and the term ferroic has been used to cover materials which exhibit one or more phases in the form of a domain structure that can be oriented upon the application of a switching "field" whose nature can be magnetic, electric, elastic or a combination of these, conferring to these materials ferromagnetic, ferroelectric and/or ferroelastic properties respectively.

In analogy with ferromagnetism, in ferroelectric materials there exists a polarization (P) versus electric field (E) hysteresis loop characterised by electrical analogous quantities such as the saturation polarization (P_S), remnant polarization (P_r) and coercive field (E_C) as depicted in figure 1.1.

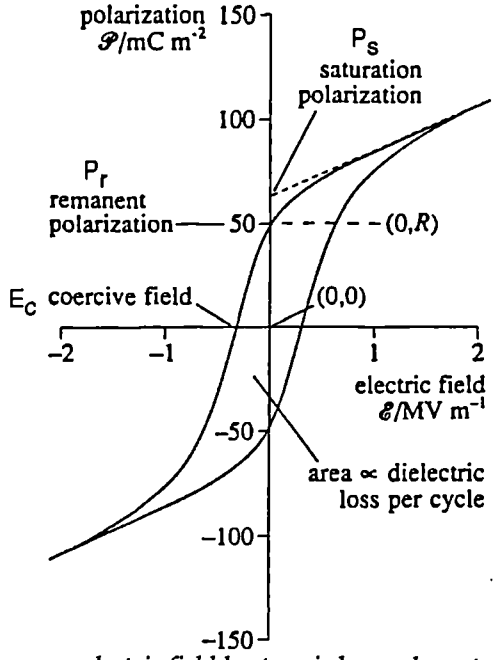

Figure 1.1 - Typical polarization versus electric field hysteresis loops characteristic from a ferroelectric material.

A feature of many ferroelectrics is that near a certain temperature known as the Curie temperature T_C, there is a high temperature dependence of the dielectric permittivity ε, such that above T_C it follows a relationship of the form:

$$\varepsilon = \frac{C}{T - \theta_c} \tag{1.1}$$

where T is the temperature, C is the Curie constant and θ_C is the Curie-Weiss temperature near but not necessarily equal to T_C. This law has again its counterpart in ferromagnetism although the dielectric Curie constant C, has a much higher value leading to a persistence of useful high permittivity values over a wider temperature range. By cooling the material through its Curie temperature, a phase transition in the domain state occurs at the Curie

temperature T_C from a paraelectric phase with zero polarization to a ferroelectric phase below which there exists a spontaneous non-zero polarization which increases as the temperature cools down until reaching a saturation value.

There is a distinction between the remnant (P_r) and spontaneous (P_s) polarization, i.e. P_r is the polarization generated by poling while P_s is rather a conceptual quantity referring to the polarization that a ferroelectric *crystal* possesses spontaneously [Furukawa 1989]. Experimentally, P_r is defined by the intersection of a hysteresis loop with the ordinate and P_s is evaluated from the linear extrapolation of the D-E curve in the high-field range to zero field (see figure 1.1). They largely coincide if a *single crystal* is used. When using semicrystalline samples however, P_r is the experimental remnant polarization of such samples and P_s is the hypothetical spontaneous polarization possessed by the crystalline regions.

In figure 1.2 is shown a rough sketch of the temperature dependence of the saturation polarization exhibited by various ferroelectric materials together with their respective Curie temperature where the spontaneous polarization vanishes. One should note the wide choice of both the saturation polarization and Curie temperature available amongst these materials.

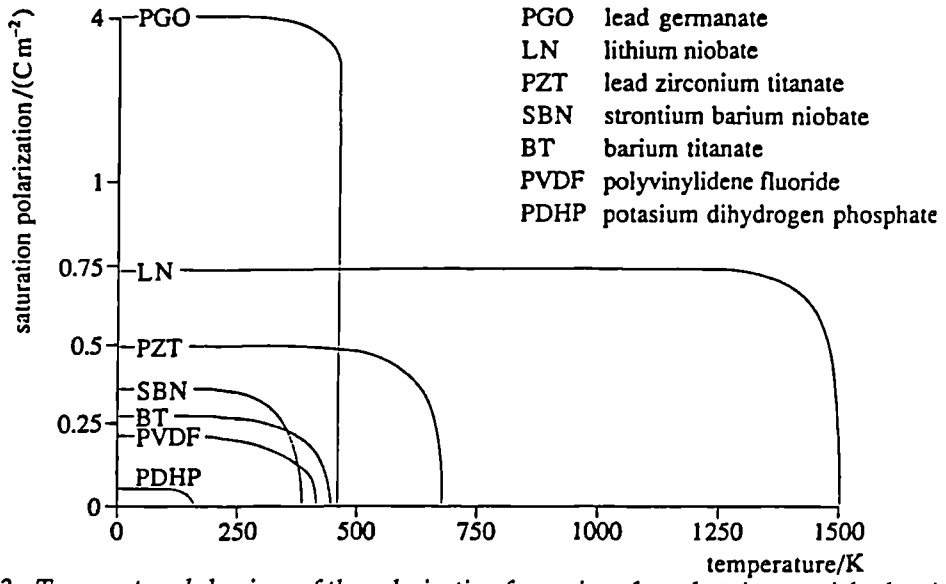

Figure 1.2 - Temperature behaviour of the polarization for various ferroelectric materials showing their respective Curie temperature beyond which these material cease to be ferroelectric. Note the logarithmic scale of the polarization axis [Braithwaite et al. 1990].

Ferroelectricity which requires the existence of a reversible spontaneous polarization, has up to now only been proved in relation to a change in the structure of crystals. The size of these crystals can vary widely as they can either be: single crystals as in lithium tantalate, polycrystalline as in ferroelectric ceramics such as $BaTiO_3$ and PZT, or spherulite crystals as in semi-crystalline materials such as PVDF which is a ferroelectric polymer. Recently, there has been however, some evidence of ferroelectric-like behaviour in an amorphous copolymer of vinylidene cyanide and vinyl acetate [Wang et al. 1987] which has shown a dielectric anomaly resembling the Curie Weiss law.

Associated with ferroelectricity one can always find the phenomena of piezoelectricity and pyroelectricity. Piezoelectricity in general terms describes the coupling between the polarization and the mechanical (stress/strain) state of a material while pyroelectricity is the coupling between the polarization and the thermal variables in a given sample. Although ferroelectricity always implies piezoelectricity and pyroelectricity the converse is not true. This leads to a relationship that exists between the structure of crystals and the properties of ferroelectricity, piezoelectricity and pyroelectricity.

Crystals are ordered structures of atoms or molecules arranged in a single pattern called the unit cell which repeats itself three-dimensionally. Depending on their symmetry crystals are classified in seven systems which are, starting from the highest symmetry: the cubic, hexagonal, trigonal, tetragonal, orthorhombic, monoclinic and triclinic systems. These systems are then further divided into 32 classes (or point groups) based again on symmetry considerations. By the use of the Neumann's principle which states that any macroscopic physical property of a crystal has at least the same symmetry as that of its own point group, a crystal can be proved piezoelectric if its point group lacks at least a centre of symmetry which of the 32 classes, 21 of them do [Burns 1990]. Of these 21 classes, 20 are piezoelectric, the only exception being for a point group in the cubic system which although lacking a centre of symmetry possesses other symmetry characteristics which combine to give no piezoelectric effect.

A crystal is pyroelectric if it possesses a net dipole moment per unit cell which means that the centre of mass of the positive charge is at a different position from that of the negative charge. This can be proved to imply a lower symmetry from the crystal point group than piezoelectricity does, and accordingly only 10 point groups of the above 20 are pyroelectric. Ferroelectricity is more restrictive than pyroelectricity because the net dipole moment should have a reversible nature and furthermore the spontaneous polarization should be switchable by means of an applied electric field. This latter consideration cannot directly be deduced from the crystal symmetry and must be experimentally checked.

1.2.2. - Piezoelectricity

Piezoelectricity and its converse electrostrictive effect are related either to a change of strain/stress due to an applied external electric field or conversely to a change of the polarization due to a mechanical excitation. For sufficiently small physical quantities the piezoelectric properties of ferroelectric materials can be conveniently described by the linear matrix equations [Smiths 1976; IEEE 1978]:

$$\begin{pmatrix} x \\ D \end{pmatrix} = \begin{pmatrix} s^E & d_t \\ d & \varepsilon_0 \varepsilon^X \end{pmatrix} \begin{pmatrix} X \\ E \end{pmatrix} \qquad (1.2)$$

in which the stress X and the electric field E have been chosen as the independent variables while the strain x and electric displacement D are the dependent variables; s, ε and d are the elastic compliance, the dielectric and the piezoelectric constant respectively while, superscripts of these variables denote the physical variable held constant during its

determination. Note that all variables are tensors and that the suffix t denotes a transposed tensor. These equations can be put in alternative forms by using either x and E, x and D or X and D as pairs of independent variables. The equations are then transformed into:

$$\begin{pmatrix} X \\ D \end{pmatrix} = \begin{pmatrix} c^E & -e_t \\ e & \varepsilon_o \varepsilon^x \end{pmatrix} \begin{pmatrix} x \\ E \end{pmatrix} \tag{1.3}$$

$$\begin{pmatrix} X \\ E \end{pmatrix} = \begin{pmatrix} c^D & -h_t \\ -h & \beta^x/\varepsilon_o \end{pmatrix} \begin{pmatrix} x \\ D \end{pmatrix} \tag{1.4}$$

$$\begin{pmatrix} x \\ E \end{pmatrix} = \begin{pmatrix} s^D & g_t \\ -g & \beta^X/\varepsilon_o \end{pmatrix} \begin{pmatrix} X \\ D \end{pmatrix} \tag{1.5}$$

where c is the stiffness elastic constant; e, h and g are the piezoelectric coefficients tensors, and finally β is defined as the inverse of the permittivity matrix. Each of the above equations 1.2-1.5 are used in view of a particular application and configuration in mind.

The piezoelectric constants are third rank tensors (e.g. a_{ijk}) as they couple a second rank tensor such as the strain x_{ij} or stress X_{ij} to an external electric field vector E_k or dielectric displacement vector D_k. Due to the symmetry of the mechanical tensor variables e.g. $x_{ij}=x_{ji}$ the strain tensor can be compacted into a first rank tensor as follows:

ij:	11	22	33	23	13	12
$x_i x_j$	x^2	y^2	z^2	yz	xz	xy
contracted index	1	2	3	4	5	6

so that the piezoelectric constants are converted into second rank tensors with the first index denoting the direction of the applied field specified from 1 to 3 while the second denotes the strain direction, denoted 1 to 6. For instance equation 1.2 can then be rewritten in a complete form for ferroelectric ceramics with a perovskite structure of symmetry ∞mm poled in the thickness or 3 direction as:

$$\begin{pmatrix} x_1 \\ x_2 \\ x_3 \\ x_4 \\ x_5 \\ x_6 \end{pmatrix} = \begin{pmatrix} s_{11}^E & s_{12}^E & s_{13}^E & . & . & . \\ s_{12}^E & s_{11}^E & s_{13}^E & . & . & . \\ s_{13}^E & s_{13}^E & s_{33}^E & . & . & . \\ . & . & . & s_{44}^E & . & . \\ . & . & . & . & s_{44}^E & . \\ . & . & . & . & . & s_{66}^E \end{pmatrix} \begin{pmatrix} X_1 \\ X_2 \\ X_3 \\ X_4 \\ X_5 \\ X_6 \end{pmatrix} + \begin{pmatrix} . & . & d_{31} \\ . & . & d_{31} \\ . & . & d_{33} \\ . & d_{15} & . \\ d_{15} & . & . \\ . & . & . \end{pmatrix} \begin{pmatrix} E_1 \\ E_2 \\ E_3 \end{pmatrix} \tag{1.6 a}$$

$$\begin{pmatrix} D_1 \\ D_2 \\ D_3 \end{pmatrix} = \begin{pmatrix} . & . & . & . & d_{15} & . \\ . & . & . & d_{15} & . & . \\ d_{31} & d_{31} & d_{33} & . & . & . \end{pmatrix} \begin{pmatrix} X_1 \\ X_2 \\ X_3 \\ X_4 \\ X_5 \\ X_6 \end{pmatrix} + \varepsilon_o \begin{pmatrix} \varepsilon_{11}^X & . & . \\ . & \varepsilon_{11}^X & . \\ . & . & \varepsilon_{33}^X \end{pmatrix} \begin{pmatrix} E_1 \\ E_2 \\ E_3 \end{pmatrix} \tag{1.6 b}$$

which can be grouped in one matrix equation as follows:

$$\begin{pmatrix} x_1 \\ x_2 \\ x_3 \\ x_4 \\ x_5 \\ x_6 \\ D_1 \\ D_2 \\ D_3 \end{pmatrix} = \begin{pmatrix} s_{11}^E & s_{12}^E & s_{13}^E & . & . & . & . & . & d_{31} \\ s_{12}^E & s_{11}^E & s_{13}^E & . & . & . & . & . & d_{31} \\ s_{13}^E & s_{13}^E & s_{33}^E & . & . & . & . & . & d_{33} \\ . & . & . & s_{44}^E & . & . & . & d_{15} & . \\ . & . & . & . & s_{44}^E & . & d_{15} & . & . \\ . & . & . & . & . & s_{66}^E & . & . & . \\ . & . & . & . & d_{15} & . & \varepsilon_o \varepsilon_{11}^X & . & . \\ . & . & . & d_{15} & . & . & . & \varepsilon_o \varepsilon_{11}^X & . \\ d_{31} & d_{31} & d_{33} & . & . & . & . & . & \varepsilon_o \varepsilon_{33}^X \end{pmatrix} \begin{pmatrix} X_1 \\ X_2 \\ X_3 \\ X_4 \\ X_5 \\ X_6 \\ E_1 \\ E_2 \\ E_3 \end{pmatrix} \tag{1.7}$$

where a dot represents a zero element and $s_{66}^E = 2\left(s_{11}^E - s_{12}^E\right)$. Thus in a ferroelectric ceramic there are five independent elastic compliances, two dielectric permittivities and three piezoelectric constants. Note further that there is no piezoelectric coupling in the shear plane perpendicular to the polarization direction (direction 6).

The piezoelectric constants appearing in equations 1.1 to 1.4 are not independent. For instance it is possible to prove that the following relations hold [Siemens 1981],

$$d = es^E = \varepsilon_o \varepsilon^X g; \quad g = hs^D = \left(\varepsilon_o \varepsilon^X\right)^{-1} d \tag{1.8}$$

$$e = dc^E = \varepsilon_o \varepsilon^x h; \quad h = gc^D = \left(\varepsilon_o \varepsilon^x\right)^{-1} e \tag{1.9}$$

$$c^{E,D} = \left(s^{E,D}\right)^{-1} \tag{1.10}$$

$$\varepsilon_o\left(\varepsilon^X - \varepsilon^x\right) = dc^E d_t; \quad s^E - s^D = d_t\left(\varepsilon_o \varepsilon^X\right)^{-1} d \tag{1.11}$$

where the variables are matrices and the operations are understood to be matrix operations. Hence, a piezoelectric material is fully characterised if its matrices s^E, ε^X and d involved in equation 1.2 or 1.6, for example, are known. In fact these are the most often set of variables used to characterise a piezoelectric material, because one can deduce all the other matrices from these and perhaps more importantly because the mechanical and electrical configuration necessary to accomplish their measurement are more readily applicable in practice. Thus, the elastic constant s^E and ε^X should be measured in an short-circuit and in stress-free configurations respectively while the d-constant should be determined in a no-clamping condition [Powers 1988].

An important parameter for a piezoelectric sample is the electromechanical coupling coefficient which can be loosely defined as a measure of the efficiency of the mechanical to electric energy conversion or the converse:

$$k^2 = \frac{\text{mechanical energy converted to electrical energy}}{\text{input of mechanical energy}} = \frac{\text{electrical energy converted to mechanical energy}}{\text{input of electrical energy}}$$

This physical quantity is a tensor and thus depends on the direction of the stress and electric field. An important variable for hydrophone design is the electromechanical coupling factor

k_t in the thickness direction whose experimental determination will be treated on chapter 8. This variable relates to the piezoelectric constants e and c^D through:

$$k_t = \frac{e_{33}}{\left(\varepsilon_o \varepsilon_3^x c_{33}^D\right)^{1/2}} \tag{1.12}$$

Due to the mechanisms of electrical and mechanical relaxation existing in all materials the electrical and mechanical constants have a frequency dependence and thus can be conveniently described by a complex number which varies with frequency. It follows then that the piezoelectric constants which represent the coupling between these two phenomena should also in general exhibit a frequency dependence e.g. [Furukawa et al. 1988],

$$\varepsilon = \varepsilon' - i\varepsilon'' = \varepsilon(1 - i\tan\delta) \tag{1.13 a}$$

$$s = s' - is'' \tag{1.13 b}$$

$$d = d' - id'' \tag{1.13 c}$$

This effect on the piezoelectric constant will however be considered negligible in this study. The dielectric losses and the mechanical losses ψ=tan δ_m=$(Q_m)^{-1}$ however will be included in the analysis. Thus the elastic stiffness constant $c^D{}_{33}$ is a complex quantity given by:

$$c_{33}^{*D} = c_{33}^D\left(1 + i\tan\delta_m\right) = c_{33}^D(1 + i\psi) \tag{1.14}$$

where Q_m is usually called the mechanical quality factor of the piezoelectric sample. The higher is this value the lower will the absorption of sound in the material. In transducer materials it is often required that this value should be low in order to improve its pulse response by preventing the "ringing" caused by the travelling of the sound wave back and forth along the thickness of the material.

In sonar low-frequency designs however, a more important feature is the hydrostatic performance of the piezoelectric properties. When a hydrostatic pressure p is applied, no shear stresses are present. Thus, the variation in polarization due solely to tensile stresses is given by,

$$\Delta P_3 = \left(d_{31} + d_{32} + d_{33}\right)p = d_h p \tag{1.15}$$

For perovskites and ferroelectric polymers, one can then define the hydrostatic piezo-constant as $d_h = d_{33} + 2d_{31}$ and $g_h = g_{33} + 2g_{31}$. A useful piezoelectric Figure Of Merit (FOM_h) in wide use for materials used in hydrophone design is,

$$FOM_h = d_h g_h \tag{1.16}$$

1.2.3. - Pyroelectricity

The pyroelectric coefficient is defined as the variation of the polarization when a sample is subjected to a uniform change of temperature. Thus, the clamped state (i.e. x=0) pyroelectric coefficient is defined as [Moulson et al. 1990]:

$$p_i^x = \left.\frac{dP_i}{dT}\right|_{x=0} \tag{1.17}$$

This effect can be understood with reference to figure 1.2 as being the slope of the curve of the polarization versus temperature. As the slope increases near the Curie temperature one expects that high pyroelectric coefficients can be found in this region a fact which has prompted some applications for pyroelectric detectors. The clamped state however is not used much, both in pyroelectric measurements or in detectors and a more practical arrangement is the stress-free (i.e. X=0) condition in which case there is an additional contribution to the pyroelectric coefficient due to the piezoelectric effect [Kepler et al. 1978; Furukawa 1989],

$$p^X = p^x + \alpha d / s^E \tag{1.18}$$

where α is the linear expansion coefficient. The two terms on the right hand side of equation 1.18 are commonly called the primary and secondary pyroelectric effects respectively. A third term, called the tertiary pyroelectricity, can also contribute to the pyroelectric current. This arises whenever there is a gradient of temperature in the sample. This effect has been used particularly in measurements of the thickness distribution of polarization using a thermal probe [Collins 1980; Lang et al. 1986].

In common ferroelectric materials due to their tetragonal (e.g. ceramics) or orthorhombic (e.g. polymers) symmetry it can be proved that the pyroelectric coefficient tensor has only one non-zero component [Furukawa 1989],

$$p = \begin{pmatrix} . & . & . \\ . & . & . \\ . & . & p_{33} \end{pmatrix} \tag{1.19}$$

which in the text below will thus be denoted simply by p.

A Figure Of Merit (FOM_p) for pyroelectric materials used in detectors is also commonly in use,

$$FOM_p = \frac{p}{\varepsilon} \tag{1.20}$$

and reflects the voltage responsivity of a pyroelectric material (please refer to Chapter 5 for more details).

1.3 - Ferroelectric ceramics

The most important ferroelectric ceramics are metal oxides having the perovskite structure and whose general formula is ABO_3. $BaTiO_3$ is the prototype of this kind of ferroelectric ceramics and thus some of its relevant features common to other perovskites will described. This structure is exhibited by barium titanate ($BaTiO_3$), lead titanate (PT) and lead zirconate titanate (PZT) and is shown in figure 1.3 for the case of $BaTiO_3$.

It comprises Ti^{4+} cations contained inside octahedral "cages" of O^{2-} ions joined corner-to-corner as shown in figure 1.3 (a). The large cuboctahedral "cage" in the middle of the Ti cube is occupied by the Ba^{2+} ion. To understand the ferroelectric properties of $BaTiO_3$ one must resort to the sizes of the cations relative to the cages in which they are enclosed. The

titanium ion with a radius of 68 pm has a size large enough to fill its octahedral cage so that the oxygen ions in the octahedral corners will not touch each other which is prevented anyway by electrostatic repulsion. The Ba^{2+} with a radius of 135 pm, though, is loosely fit into its cuboctahedral "cage". At high temperature due to the thermal agitation it tends to fill the empty space of the cubic crystal, but as the temperature decreases to 125 °C (its first Curie temperature) the octahedral cages distort and the positive ions move to off-centre positions resulting in a tetragonal form as shown in figure 1.3 (b).

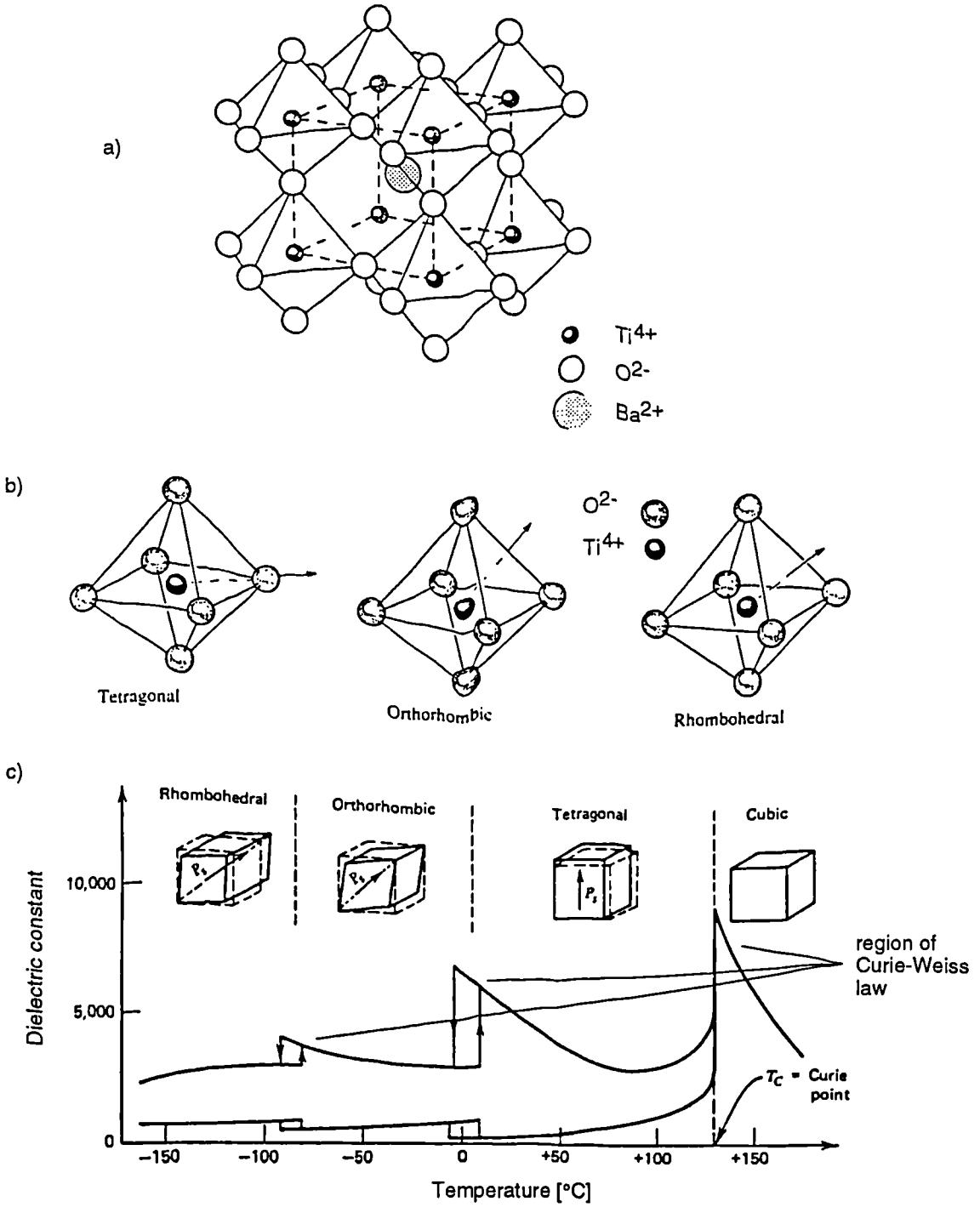

Figure 1.3 - Barium titanate (a) its perovskite structure (b) the crystal distortions (c) and the dielectric hysteretic behaviour near its Curie temperature [Braithwaite et al. 1990].

The positive and negative charges have no longer the same centre of mass and the material is found to be ferroelectric. It can be appreciated that slightly above the Curie

transition temperature the crystal is very susceptible to an external electric field which helps in the charge separation process and therefore high susceptibilities obeying the Curie-Weiss law are measured as depicted in figure 1.3 (c).

In the same graph other transitions at lower temperatures can be observed, which represent further distortions of the crystal lattice into the orthorhombic and the rhombohedral forms at 0 and -90 °C successively. In order to account for this behaviour a thermodynamic phenomenological approach has been outlined by Devonshire [Devonshire 1949; Devonshire 1951] which by expanding the free energy as a function of polarization and strain while making reasonable assumptions about its coefficients could account for the observed temperature transitions. This thermodynamic phenomenological approach has since been widely used by many authors for other ferroelectric materials [Haun et al. 1987].

A great deal of versatility in ferroelectric ceramics properties is imparted by suitably doping the material with various metal oxides so that conductivity, Curie temperature, coercivity and compliance can be manipulated in this way [Braithwaite et al. 1990]. This sort of property design although resembling to a kind of artistic activity can nevertheless be partly outlined by way of some manipulation mechanism. The basis for understanding this property modelling lies in the size and valence of the metal ions which are to be incorporated into the ceramic. Their size will, for instance, determine which sites in the perovskite structure (ABO_3) will they occupy, which can either be A or B type depending on whether Ba^{2+} or the Ti^{4+} ions are substituted. For instance, if alumina $Al^{3+}(O^{2-})_3$ is introduced into $BaTiO_3$ the aluminium being a small ion will occupy B-sites, substituting TiO_2 whilst bringing only 1 1/2 oxygen ions because of its lower valence. Hence, oxygen vacancies will be created, rendering the material ionically conductive although $BaTiO_3$ is an insulator if its stoichiometry Ba:Ti is kept 1:1 [Braithwaite et al. 1990].

In the tetragonal form the Ti^{4+} ion energy along the long axis of the tetragonal cell resembles that of figure 1.4. An applied field in the opposite direction in which the cell is polarised may enable it to pass the energy barrier switching the polarization to the opposite direction in a process called poling [Moulson et al. 1990]

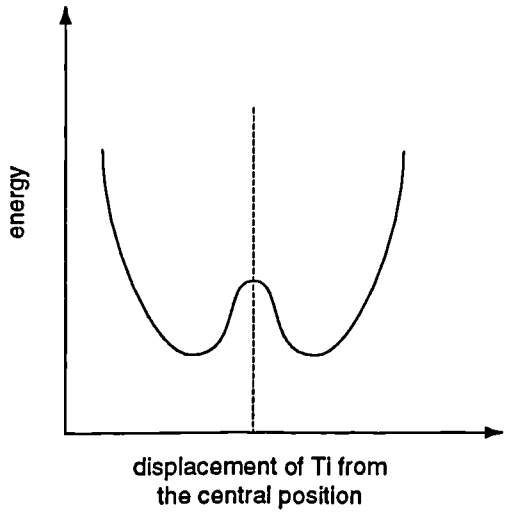

Figure 1.4 - Variation of the potential energy of Ti^{4+} along the long axis of the tetragonal cell

The ceramic morphology comprises grains separated by grain boundaries (see figure 3.7). Being a polycrystalline material in its usual form each of the grains will contain one or several crystals. When a paraelectric to ferroelectric phase transformation occurs, the polarization of the crystal lattice will grow starting from nuclei scattered in several places within a crystal. In the end there will be different regions within a crystal with different orientations called ferroelectric domains, separated by domain walls, whose relative orientations are correlated to the geometric crystal symmetry. For example, in a tetragonal crystal the domains with different orientations can only be at either 180° or at right angles 90° as shown in figure 1.5.

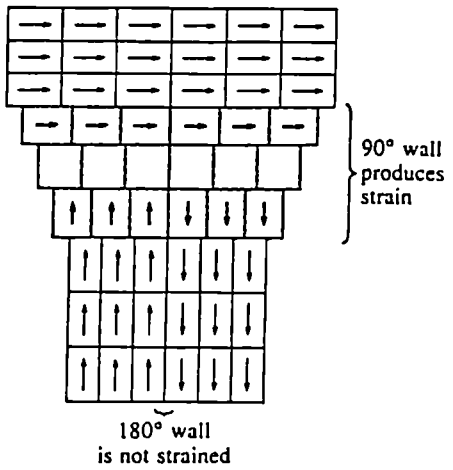

Figure 1.5 - Distortion of the crystal lattice due to the 90° domain walls.

The adjacent 180° walls as can be observed, fit conveniently parallel to each other but 90° walls do not, because in the latter the longer axis of one domain is contiguous with the shorter axis of the neighbouring cells. The result is that an internal stress is developed along the domain wall which is relieved by the transition taking place gradually along many crystal lattice cells.

During polarization switching the domain walls move co-operatively to enlarge the most favourably oriented domains with a concomitant decrease of those having an opposite component of the polarization vector. It is readily realised that the movement of 180° domain walls will be easy, very much like a wave sweeping through the crystal, whilst that of the 90° will be difficult as it has to travel across crystals of changing shape resulting thus in a higher coercivity of the material. The appearance of these types of walls is linked to stresses that exist in the grain boundaries as the ceramic during its formation cools through its Curie temperature. After removing the field there is a relaxation of the internal stresses and a correlated decrease in polarization to a lower value, which can take from minutes to days dependent on the coercivity of the material, in a phenomenon called ageing which follows roughly a logarithmic law [Moulson et al. 1990].

The saturation of the polarization can be reached in a single crystal sample when the polarization of each and all the unit cells point towards the opposite direction of the applied field. In polycrystalline materials such as ferroelectric ceramics that is not possible because each crystal after the phase transition will start having a random orientation in relation to

the later poling direction. Upon applying an electric field, the crystal will tend to orient so that it maximises the polarization in the direction of the field. As there are only a discrete number of these directions depending on the built-in crystal lattice a full orientation into a single direction will not be possible for the all crystals in the material. Obviously, other factors such as restricted 90° domain wall movement and the amorphous grain boundaries will also contribute to a decrease in the value of the saturation polarization in these types of materials. In a ferroelectric with a rhombohedral form the abutting angles between the domain walls can take on more values i.e. 180, 71 and 109° than in the tetragonal lattice [Moulson et al. 1990]

The grain size in the polycrystalline ceramics can have a strong influence in their properties. Measurements of the permittivity as a function of the grain size on $BaTiO_3$, have shown that the permittivity has a peak value at 0.4 μm as shown in figure 1.6 (a) [Shaikh et al. 1986; Shaikh et al. 1989] This was ascribed to opposing influencing factors as the size of the grains decreases. Grain boundaries with a low permittivity surrounding the ceramic grains make up an increased volume fraction as the grain size decreases, thus decreasing the overall permittivity. Opposing this effect, there is an increase of internal stress due to a clamping of domain walls which contribute to an increase in the permittivity as the grain size decreases. The internal electric field and the domain wall area have also the effect of increasing the permittivity with decreasing grain size [Shaikh et al. 1986; Shaikh et al. 1989].

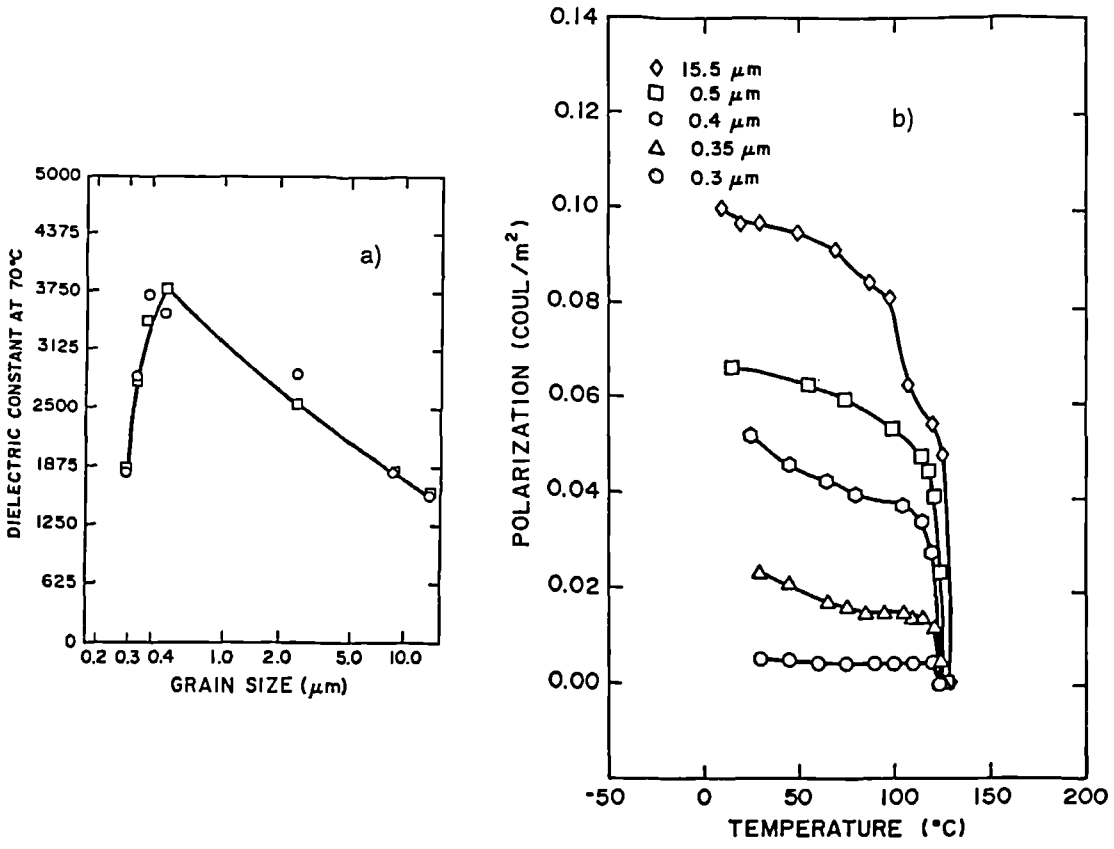

Figure 1.6 - Effect of the grain size on the (a) - permittivity and (b) - spontaneous polarization of $BaTiO_3$ [Shaikh et al. 1986]

The spontaneous polarization, however, decreases monotonously when the grain size

decreases (figure 1.6(b)) [Shaikh et al. 1986] due to a decrease in the crystallinity of the material as the grain boundary volume fraction rises. Furthermore, it is generally believed that a smaller grain size due to a higher stress concentration exhibit higher coercive fields than large grains [Durán et al. 1990].

1.3.1. - PZT

PZT was one of the ceramics used in our composite study. It has the same perovskite structure as $BaTiO_3$ and is an oxide alloy of PbO, ZrO_2 and TiO_2 where the number of divalent (Pb^{2+}) and tetravalent ions (Ti^{4+} and Zr^{4+}) are equal. It is thus an alloy of the binary system lead titanate/lead zirconate, i.e. $PbTiO_3$-$PbZrO_3$ whose general formula is $PbZr_xTi_{1-x}O_3$. The Ti ion and Zr thus compete for the same B-site of the ABO_3 perovskite structure.

In figure 1.7 is shown the phase diagram of $PbZr_xTi_{1-x}O_3$ binary alloy as functions of temperature and of the $PbZrO_3$ content. Lead titanate (i.e. $PbTiO_3$ or simply PT) in its pure form is a tetragonal ferroelectric material while lead zirconate (PZ) is an orthorhombic anti-ferroelectric material. In general, at sufficiently high temperatures the alloy in the whole composition range exhibits a cubic perovskite symmetry. As the temperature falls, a phase transition to a ferroelectric phase eventually happens. For intermediate zirconate content near 50%, there is a phase boundary where the ferroelectric crystals either take a rhombohedral or a tetragonal form [Jaffe et al. 1955]. This phase boundary results due to the differing ionic radius between the Ti^{4+} and the Zr^{4+} ion whose radii are 0.064 nm and 0.087 nm respectively and these have to be accommodated in the same octahedral B-site "cages" mentioned before (see figure 1.3 a).

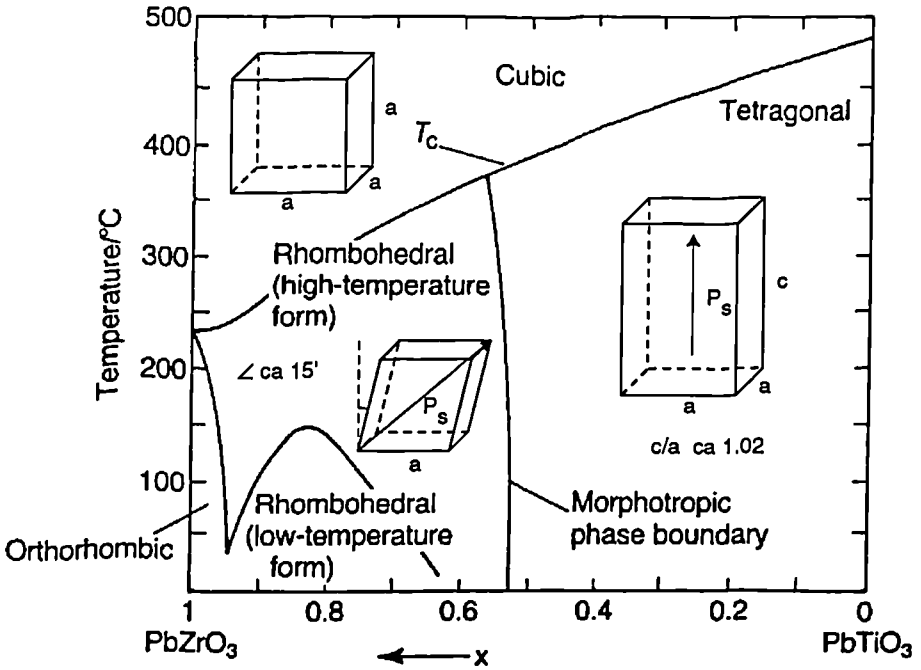

Figure 1.7 - $PbTiO_3$-$PbZrO_3$ binary system phase diagram [Cross et al. 1980].

It is near this morphotropic phase boundary (MPB) that large piezoelectric constant are

obtained [Jaffe et al. 1955; Jaffe 1968] as can be seen in figure 1.8, where the permittivity can reach a value of 1000; the planar electromechanical coupling factor reaches 0.6 and the remnant polarization peaks at 520 mC/m^2.

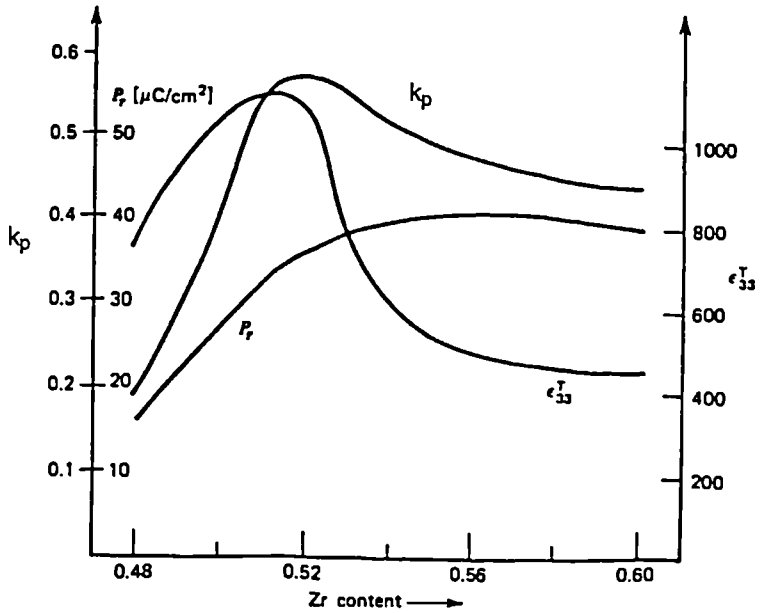

Figure 1.8 - PZT permittivity ε, remnant polarization P_r and electromechanical coupling factor k_p near the morphotropic phase boundary [Cross et al. 1980].

Typical values for piezoelectric *d*-constants are d_{33}≈400, d_{31}≈-170 and d_{15}≈500 pC/N. From X-ray diffraction data it has been found that around the MPB, the change in form is not abrupt but that both phases coexist within the material [Dass et al. 1986]. This has been suggested to be one of the reasons for the high remnant polarization as more choices are available for the crystals to orient themselves towards the electric poling field. This field has the effect of orienting the 180° and 90° domains of the tetragonal form as well as that of 180°, 71° and 109° domains of the rhombohedral form. A commonly used poling field is 1-4 MV/m applied for several minutes at around 100°C to ensure some mobility of the domain walls. At higher temperatures the alignment takes place faster although it always takes longer for the 90° domains to be oriented. The ageing of properties referred above for ferroelectric ceramics, is also a feature that can be observed in these ceramics.

PZT is a versatile material as through the addition of suitable dopings remarkably different properties can be obtained. Useful technological know-how in this field is proprietary to commercial companies which develop grades of PZT ceramic to suit particular applications. There are two major types of PZT modifications, designated as "hard" and "soft" respectively, which are distinguished by the piezoelectric constants they exhibit. Hard PZT's are doped with acceptor ions to create oxygen vacancies in the perovskite structure while the soft type PZT are usually doped with donor ions to create vacancies in A-sites. As a result, hard PZT's have typically a smaller grain size (≈2 μm), low permittivities, losses and piezoelectric coefficients whereas soft PZT have a larger grain (≈5 μm), higher permittivities, losses and piezoelectric constants but are easier to pole and depole (i.e. low coercivity). Isovalent ions can also be incorporated into PZT to modify other

properties.

Vernitron [Vernitron 1976], sells according to one of its catalogue five grades of PZT: PZT4, PZT-5A, PZT-5H, PZT-7A and PZT8. The PZT-4, a "hard" formulation, is recommended for electrical to mechanical energy conversion due to its low loss (ε= 1300, tan δ= 0.004), high Curie temperature (T_C=300°C) and high strain carrying capability while, PZT-5A known as a "soft" PZT, is more suitable for mechanical to electrical energy conversion on account of its high electro-mechanical coupling (k_t = 0.50) and high charge sensitivity (d_{33}= 374pC/N). In table 1.3 a complete list of the properties of PZT5A ceramics taken from a Vernitron catalog [Vernitron 1976] can be found.

Other modifications such as incorporation of La_2O_3 or Nb_2O_5 in PZT have led to the relationship of the dielectric with the mechanical loss mechanisms in PZT which were traced to the power losses occurring on 90° domain wall motion moving under the influence of an electric field or mechanical stress [Gerthsen et al. 1980]

1.3.2. - PLZT

One of the most commonly used dopings of PZT is lanthanum oxide La_2O_3. Its general formula is $Pb_{1-1.5y}La_yTi_{1-z}Zr_zO_3$ but a common notation is PLZT y/z/1-z. This ceramic has also been used in the present composite fabrication due to its high resistivity which is imparted by the La^{3+} substitution of Pb^{4+} in A-sites. In figure 1.9 is shown the phase diagram of PLZT system at room temperature as function of the lanthanum and zirconium molar fraction.

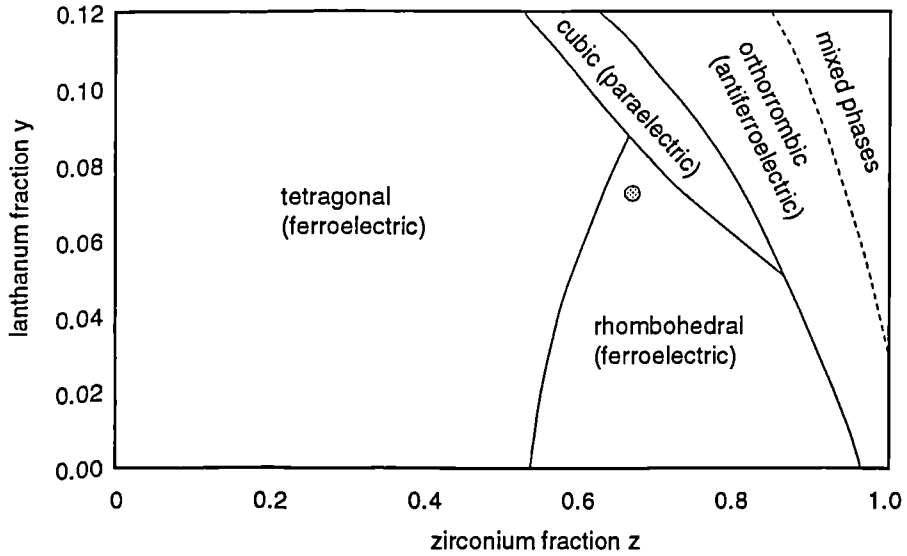

Figure 1.9 - Phase diagram of $Pb_{1-1.5y}La_yTi_{1-z}Zr_zO_3$ showing the stable phases at room temperature [Braithwaite et al. 1990].

Again it is near the morphotropic boundary point where the ferroelectric tetragonal and rhombohedral phases meet with the cubic paraelectric phase when higher piezoelectric activity is encountered. In fact we have used the PLZT 7/65/35 composition marked as a shaded circle in the PLZT phase diagram, for making composites.

Processing of samples can modify the properties of ceramics. For example, when

producing ceramics disks of PLZT, lapping and grinding operations have been found to decrease both the permittivity and the saturation polarization through the formation of a non-ferroelectric surface layer of low permittivity with surface stresses [Jiang et al. 1990]. These stresses are more important in thin samples and could be greatly relieved through an annealing procedure at 650 °C. Chemical etching on the other hand, was found to induce no effect on these properties of PLZT.

1.3.3. - PT and PTCa

As we have referred above $PbTiO_3$ in pure form is a room temperature ferroelectric material which crystallises in the perovskite tetragonal form. Its Curie temperature is around 490 °C while its calculated permittivity and spontaneous polarization are $\varepsilon_{33}\approx150$ and $P_s\approx0.6$ C/m^2 respectively [Wersing et al. 1989]. Its important feature is the high anisotropy between d_{33} and d_{31} which have been calculated to be 182 and -37 pC/N respectively [Wersing et al. 1989], which suppresses the parasitic coupling between the thickness and lateral modes of vibration, an important consideration for underwater hydrostatic transducers, hydrophones and NDT applications [Gallego-Juárez 1989] and array transducers [Wersing et al. 1989]. It is however a ceramic of difficult sinterability at it cools down through its Curie temperature. Due to the high tetragonal distortion in the ferroelectric phase (i.e. c/a 1.066 [Haun et al. 1987]) high internal stresses are induced during the phase transition which fractures and disintegrates the ceramic [Jaffe et al. 1955].

Attempts have been made to produce dense and hard $PbTiO_3$ by adding impurities or by forming solid solutions. Modifications of this ceramic with dopings of rare earths such as lanthanum and samarium [Takeuchi et al. 1982], bismuth and zinc [Ueda et al. 1968], alkaline earth materials [Yamashita et al. 1981] amongst others have been performed. One of the most successful effort was calcium doping which has found applications both in ultrasonic application [Yamashita et al. 1981] and pyroelectric detectors [Ichinose et al. 1985].

Yamashita et al. [Yamashita et al. 1981] first discovered that doping PT ceramics with calcium oxide CaO in varying amounts could improve the sinterability of the ceramic obtaining good densification and properties.

An optimum doping was found to be 24 mol% where the permittivity was in the 200 range while the electro mechanical coupling factors k_t and k_p showed a maximum and a minimum respectively and hence a maximum anisotropy ratio k_p/k_t (see figure 1.10). The spontaneous polarization can be seen in figure 1.11 to saturate at a level of 400 mC/m^2 beyond a calcium concentration of around 20 mol%. Furthermore, it has been also found that calcium doping requires a modification in the B-site with one of the following modifications pairs: Ni-Nb, Co-W or Fe-W to achieve optimum electromechanical anisotropy [Wersing et al. 1989].

The pyroelectric properties of calcium modified PT (PTCa) were investigated by Ichinose et al [Ichinose et al. 1985]. They have found that the pyroelectric coefficient increased monotonically with calcium content but that the pyroelectric $FOMp = p/\varepsilon$ saturated beyond 22 mol% at a value of 1.96 $\mu C/m^2K$ as can be observed in figure 1.11. This was due

to a sharp increase in the permittivity for calcium concentrations beyond 25 mol% (figure 1.10). At 24 mol% calcium content the pyroelectric coefficient p, and the FOM_p were 380μC/m^{2}K and 1.96μC/m^{2}K respectively. Due to this fact the 24 mol% composition has become a standard commercially available ceramic whose piezoelectric constants d_{33} and d_{31} are 68 and -3 pC/N respectively. Due to the small value of d_{31} the hydrostatic value $d_h \approx d_{33}$ provides a high hydrostatic Figure of Merit of around $FOM_h \approx 2220 \cdot 10^{-15}$ Pa^{-1}.

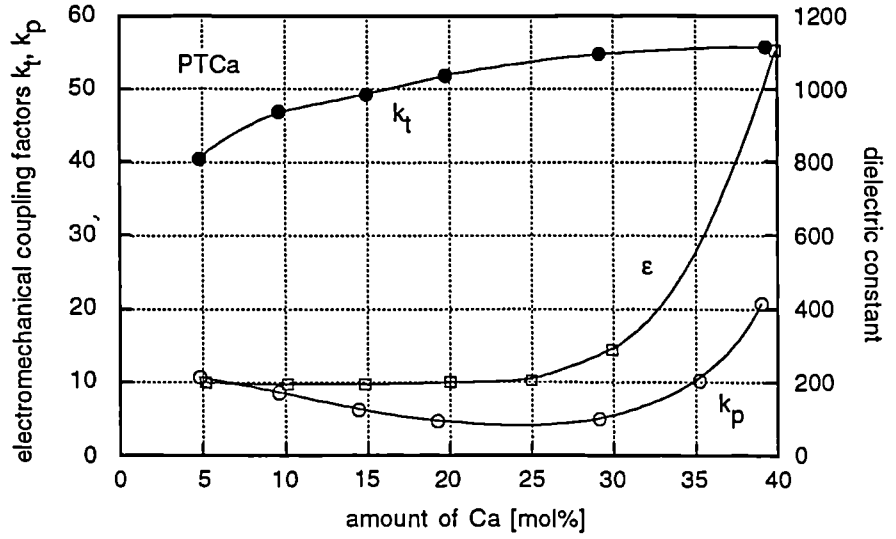

Figure 1.10 - Permittivity and the electromechanical coupling factors k_t and k_p as functions of calcium concentration doping on PT ceramics [Yamashita et al. 1981; Yamashita et al. 1983].

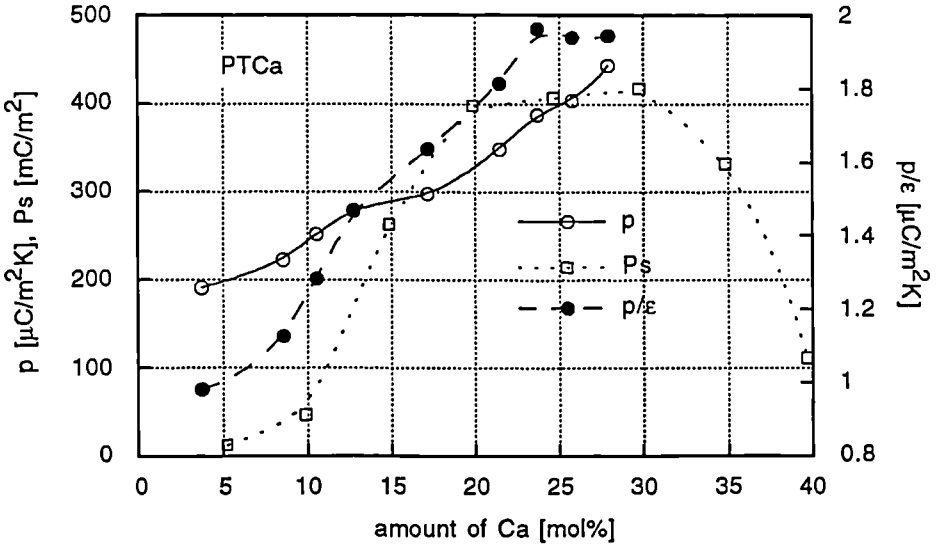

Figure 1.11 - Pyroelectric coefficient and FOM_p together with the spontaneous polarization as functions of the calcium concentration doping on PT ceramics [Ichinose et al. 1985].

Further doping with MnO have been suggested to improve the properties of these ceramics by increasing its resistivity [Yamashita et al. 1983] and decreasing the dielectric losses. An optimum doping value has been shown to be around 1% where the resistivity peaks at around $\rho \approx 5 \cdot 10^{13}$ Ω·m and tan $\delta \approx 0.011$.

A saturation in piezoelectric properties(k_t, k_p and d_{33}) has been achieved for poling fields higher than 3-3.5 MV/m for a period of 5 minutes and a temperature of 100 °C (see

figure 1.12) [Jimenez 1988; Jimenez et al. 1988]. An interesting point is that the planar electromechanical coupling factor k_p decreases at high poling fields. The mechanical quality factor which is the inverse of the mechanical losses ($Qm = \tan^{-1} \delta_m$) also decreases for higher poling fields probably due to the formation of micro-cracks in the grain boundaries which increase the mechanical losses [Jimenez 1988].

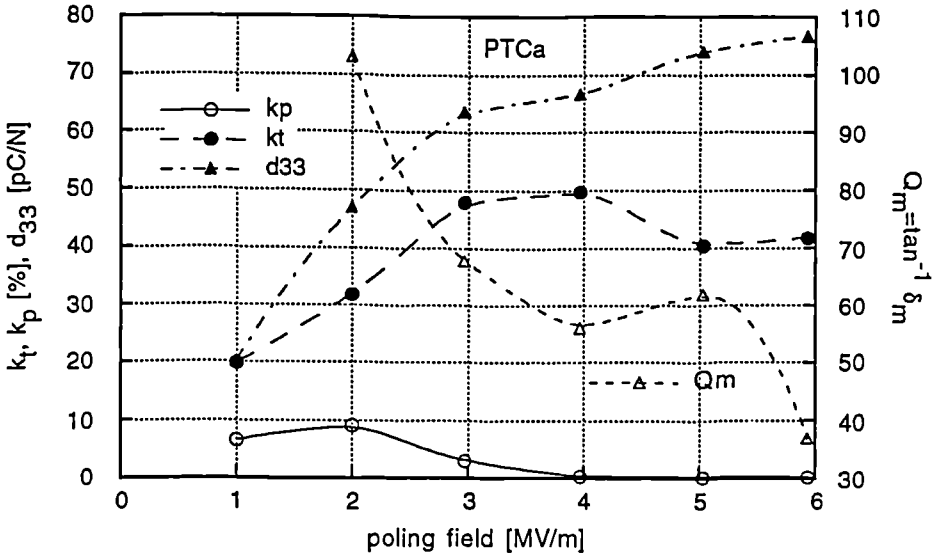

Figure 1.12 - Poling field dependence of piezoelectric properties for 24 mol% calcium modified lead titanate [Jimenez 1988].

Some controversy lies on the mechanisms which support this anisotropy. Wersing et al have demonstrated [Wersing et al. 1989] that the large anisotropy is caused by a combination of effects due to the statistical orientation of the crystallites in the polycrystalline ceramics together with the ratio of the electrostrictive coefficients and the ratio of the single-crystal permittivities $\varepsilon_{11}^x / \varepsilon_{33}^x$ in these ceramics. These have also implications in the temperature dependence of the anisotropy which could be predicted using the theory described by Wersing et al [Wersing et al. 1989].

At the end of this chapter in table 1.3 the representative properties of PTCa 24mol% have been listed. These values of properties of PTCa have been used throughout this thesis unless otherwise stated.

1.4 - Ferroelectric polymers: PVDF and P(VDF/TrFE) - structure and morphology

1.4.1. - PVDF

PVDF amongst the polymers known, exhibits the largest piezo- and pyroelectric effects [Sessler 1981]. There was some controversy in the beginning on the nature of its electro-activity whether it was due to space charge effects or to a true ferroelectric effect. This was compounded by evidence of space-charge injection during the poling procedure [Wada et al. 1976] as well as ionic charges introduced either during the formation of the polymer or through diffusion from atmospheric gases coupled to an absence of a Curie temperature

characteristic from ferroelectrics.

Mounting structural and morphological as well as electro-active evidence have now been put forward which demonstrates that this polymer is a true ferroelectric [Kepler et al. 1978] where space charges have a role in the stabilisation of the remnant polarization [Bihler et al. 1989; Legrand 1993].

PVDF is a semicrystalline polymer whose monomer unit is $-CH_2-CF_2-$ having thus two highly polar C-F bonds with a dipole moment of 1.9 D each (1 D $=3.34 \cdot 10^{-30}$ C·m) [Lovinger 1983]. Its macromolecule (or polymer chain) has a molecular weight of 10^5 corresponding to 2000 monomers or an extended length of 0.5 μm crossing various amorphous and crystalline regions. The material usually consists of 50% crystal lamellae embedded in an amorphous phase whose glass transition appears at -40°C.

It can crystallise in at least four different forms called polymorphs [Lovinger 1983] which are: the α, β, γ, δ phases represented in figure 1.13, differing from each other in the chain packing and sometimes also in the chain configuration. There are indications however, that a fifth polymorph ε-phase also exists. The most common polymorph is the non-polar α-phase (sometimes referred as Form II) represented in figure 1.13 (b) which is normally obtained from the melt. It may be seen that the unit cell consists of two chains in the tg^+tg^- (trans-gauche(+)-trans-gauche(-)) conformation whose dipole moments normal to the chain are anti-parallel thus neutralising each other thus resulting in a non-polar form.

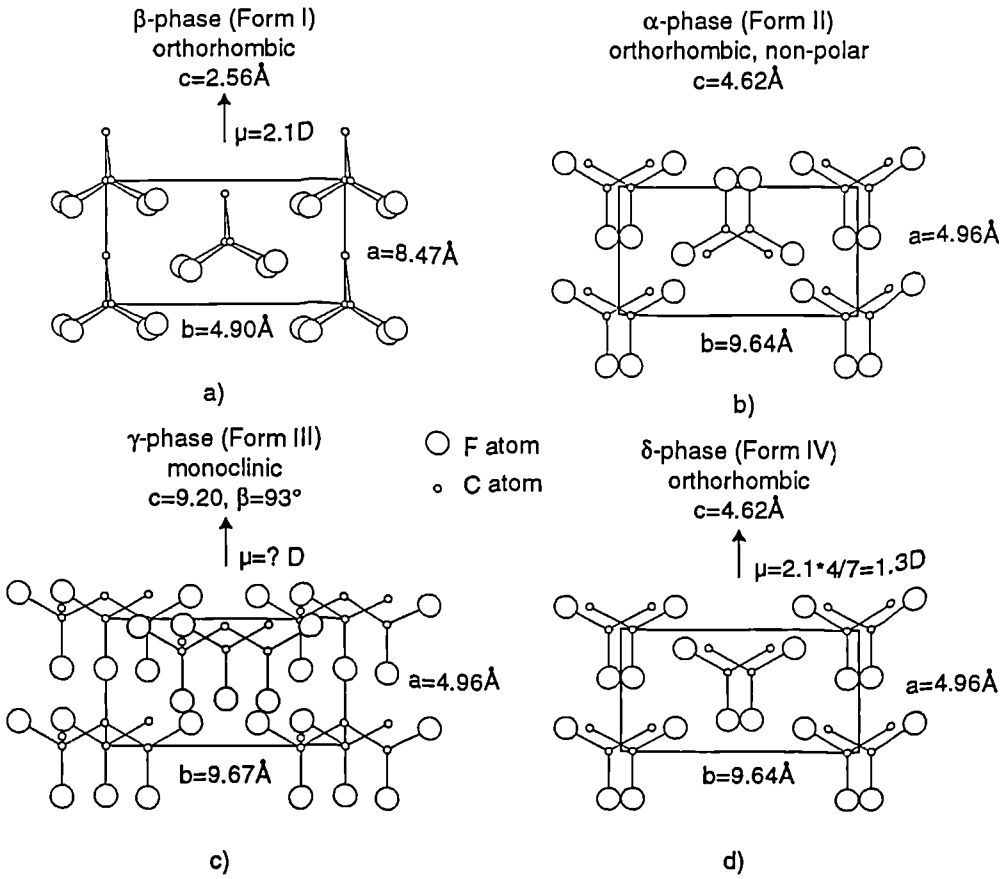

Figure 1.13 - Unit cells of four polymorphisms of PVDF projected onto the ab plane perpendicular to the polymer chain showing their dipole moments perpendicular to the chain [Tashiro et al. 1981].

A polar analogue of the α-phase is the δ-phase drawn in figure 1.13 (d) in which the two chains constituting the unit cell are parallel to each other and thus a dipole moment of 1.3D exists. This form can be obtained from the α-phase by poling at fields in excess of 100 MV/m [Davis et al. 1978].

The β-phase (or Form I) shown in figure 1.13 (a), consists of two chains in an all-trans conformation oriented in parallel to each other. This conformation and chain packing renders a dipole moment of 2.1 D per unit cell which is the highest of all the polymorphisms of PVDF and for this reason it is also the most electro-active of them. This form can be obtained from all the others by suitable conversion procedures as shown in figure 1.14. The most important route to obtain the β-phase is to stretch uniaxially or biaxially the α-phase polymer obtained from the melt to a 3-5:1 draw ratio, at a temperature not higher than 90° when the polymer is still sufficiently stiff to extend itself to its new conformation [Das-Gupta et al. 1978]. At higher temperatures the molecular chains just slide over each other and no change of phase is obtained.

The γ-phase is a less common polymorph of PVDF [Prest et al. 1978] whose structure is shown in figure 1.13, whose chain conformation is $tttg^+tttg^-$. Due to its chain packing it is also a non centro-symmetric polar form.

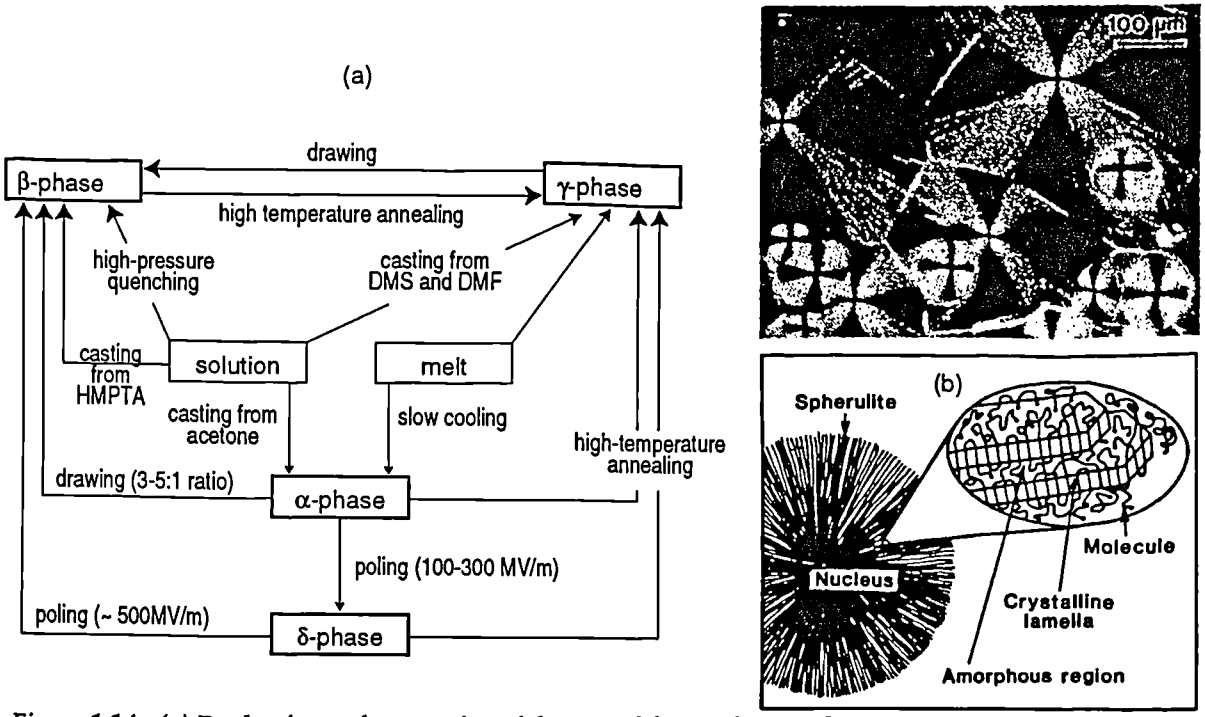

Figure 1.14 - (a) Production and conversion of the crystal forms of PVDF [Tashiro et al. 1981]; (b) Polymer crystals with a sperulite configuration

The morphology of PVDF consists of a crystalline part in spherullitic form embedded in an amorphous region [Lovinger 1983]. The spherulites starts at nuclei formed when the polymer is cooled down from the melt, and have at room temperature the approximate configuration shown in figure 1.14 (b). Radially from the nucleus of each spherulite grow several thin crystal lamellae around 10 μm thick and several microns long where the chains are packed in an ordered form. The ratio of the crystal to the amorphous part is around 0.5. Within the crystals molecular chains are disposed with their axes approximately

perpendicular to the lamellae surface and they may pass many times through the same or different crystal and amorphous layers. Upon drawing the α-phase the lamellae crystals, now converted into the β-form, have been found to orient themselves with the c-axis (or the chain axis) in the plane of the film towards the direction of the stretching and thus with the dipoles randomly oriented perpendicular to the surface of the film [Das-Gupta et al. 1978; Kupferberg 1988].

After obtaining the β-phase the polymer must undergo a poling process to orient the dipoles within the crystalline regions perpendicular to the surface of the film. This can be accomplished by conventional poling (see Chapter 5 for poling procedures) using an external field of 50-80 MV/m at a temperature of 90 to 110°C for about an hour. An alternative poling procedure is by corona poling [Das-Gupta et al. 1978; Das-Gupta et al. 1978] (see also Chapter 5) which additionally has been reported to transform the non-polar α-phase directly into the oriented β-phase without the need to stretch when very high poling fields are attained (~500MV/m). The orientation process is believed not to proceed through the crystallites domains but via a rotation of the chains around the carbon axis in discrete steps of 60° due to the close similarity of the β-phase to an hexagonal unit cell [Takahashi et al. 1981; Nakamura et al. 1984].

Ferroelectricity in PVDF was further proved when polarization [Furukawa et al. 1980], piezoelectric constant [Furukawa et al. 1980] and IR patterns [Guy et al. 1987] hysteresis loops were measured as a function of the applied electric field. A macroscopic polarization of *ca.* 60-80 mC/m^2 slightly increasing with decreasing temperature was measured while the coercive field was evaluated to be 180 MV/m at -100 °C decreasing to 30 MV/m at 100 °C. Compared with the traditional ceramics the polarization is almost 5-7 times lower while the coercive field is almost an order of magnitude higher.

Dielectric, piezo- and pyroelectric properties of PVDF have also been extensively studied. The temperature dependence of the complex permittivity at 10Hz, for drawn (i.e. mainly β-phase) and undrawn (i.e. mainly α-phase) PVDF can be observed in figure 1.15(a) [Furukawa 1989], showing that significant differences exist between them. Three relaxations processes can be identified as α, β and γ in order of descending temperature. The α-relaxation process which does not appear for drawn PVDF has been associated with molecular motions in the chain of the α-phase PVDF. The β-relaxation existing on both samples is identified with the glass transition occurring on the amorphous regions of PVDF while a higher value of the real part of the permittivity in drawn PVDF is ascribed to the higher polarity of the β-phase existing in this sample. Finally the γ-relaxation is believed to arise from the local twist motion of the main chains both in crystalline and amorphous regions. Dielectric properties as a function of frequency have also been measured [Das-Gupta et al. 1980] which show a corresponding behaviour in the time domain. In particular the β-relaxation shifts at 20°C to the frequency region around 1 MHz [Furukawa 1989].

Various models [Broadhurst et al. 1978; Tashiro et al. 1981; Purvis et al. 1983; Capron 1986] have been proposed to explain the electro-active properties of PVDF. They

fundamentally involve assigning to each of various mechanisms proposed a given percentage contribution for the property concerned: i.e. piezoelectricity or pyroelectricity. These mechanisms can be conveniently classified as:

electrostrictive contribution - the permittivity in the crystalline and amorphous phases are different and thus a change in strain or temperature in presence of polarization leads to a piezoelectric and a pyroelectric effect respectively,

dimensional contribution - due to the difference in the elastic constants in the crystalline and amorphous regions a strain dependence of the polarization exists,

crystalline contribution - an intrinsic piezoelectricity and pyroelectricity originates from the polar non-centro-symmetric crystalline regions.

In PVDF the dimensional effect has been found to be the larger contributor to the electro-active properties accounting according to one theory to as much as 70% and 50% of the piezoelectric and pyroelectric constants respectively [Broadhurst et al. 1978].

In figure 1.15 (b) is shown the temperature dependence of the complex piezoelectric constant d_{31} which has a relaxation around the glass transition temperature pointing to the direct coupling between the dielectric, the mechanical and piezoelectric properties. The real part of d_{31} increases with temperature which can be explained by the dimensional effect as the compliance decreases in the same range of temperature [Tasaka et al. 1981]. The k_{33} was found to be almost independent of temperature.

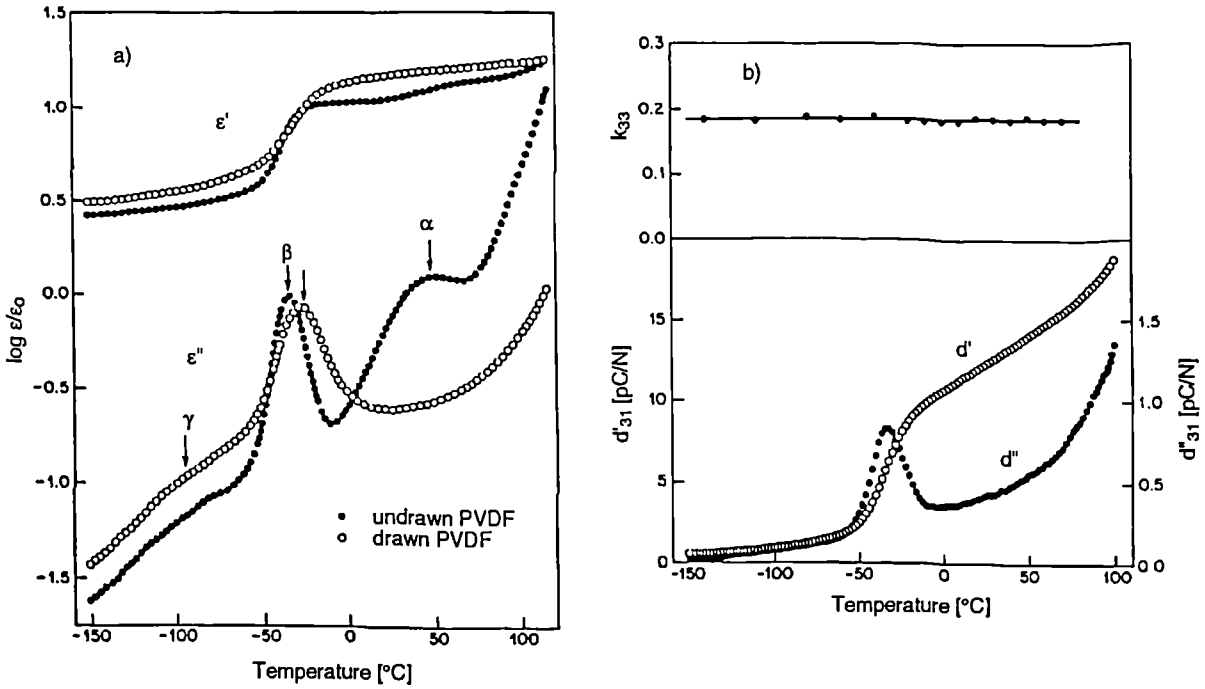

Figure 1.15 - Temperature dependence of a) the complex permittivity for drawn and undrawn PVDF and of b) the piezoelectric constant d31 and the electromechanical coupling constant k33 [Furukawa 1989].

The pyroelectric property in PVDF [Das-Gupta 1981; Das-Gupta et al. 1982; Das-Gupta 1991] can be appreciated from figure 1.16 [Kenney et al. 1979] where it is plotted as a function of the poling time and field. The maximum pyroelectric coefficient has been found to be 36 $\mu C/m^2K$ for room temperature poling at an external field in the range of 450-540

MV/m during 10 to 100 s. Although this is a low pyroelectric coefficient it leads to a high FOM_p=3 μC/m^{2}K due to the low permittivity of PVDF compared with traditional ferroelectric ceramics. An additional advantage of using PVDF is the low thermal diffusivity which is about κ=0.053·10^{-6} m^2/s compared for instance with that of $PbTiO_3$ ferroelectric ceramic which is 0.99·10^{-6} m^2/s. This is a great advantage for pyroelectric detector arrays as its reduces crosstalk between elements [Yamaka 1988].

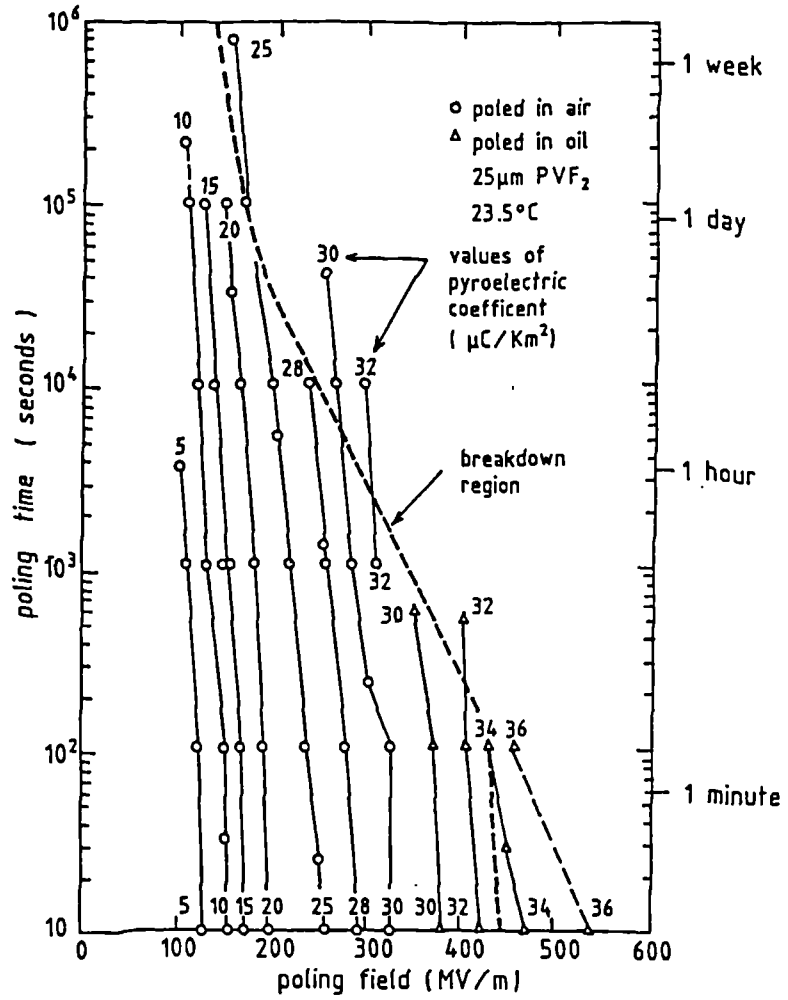

Figure 1.16 - Pyroelectric coefficient dependence on the poling time and field for PVDF [Kenney et al. 1979].

Although PVDF retains its piezoelectric and pyroelectric properties at room temperature, these rapidly degrade at temperatures higher than 70 °C [Bur et al. 1981] as can be observed from figure 1.17 [Das-Gupta et al. 1984] in which the normalised d_{31} and the remaining charge (i.e. a relative measure of the polarization decay) have been plotted as a function of the 24 h annealing temperature. Although the charge seems to decay faster due probably to some trapped charges one can observe a relationship between the decay of the two quantities leading to a reduction to 50% of their respective initial values after a 24 hour annealing at 120-140 °C. This decay which is a severe disadvantage, has been found to be minimised by cross-linking of the polymer after poling through γ-irradiation at a dose of 40 Mrad.

A list of the dielectric, piezoelectric and pyroelectric properties of PVDF has been listed

in table 1.3 at the end of this chapter [Schewe 1982; Varadan et al. 1989].

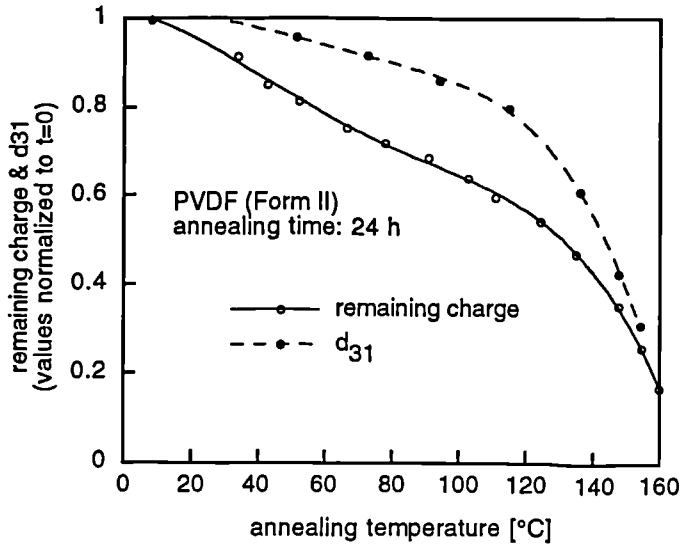

Figure 1.17 - Ageing characteristics of d_{31} and of retained charge in poled PVDF (Form II) [Das-Gupta et al. 1984].

1.4.2. - P(VDF/TrFE)

Lando and Doll [Lando et al. 1968] have suggested in their early work that the introduction of a small amount of trifluorethylene (TrFE, -CHF-CF_2-) or tetrafluorethylene (TeFE, -CF_2-CF_2-) monomers into a VDF chain would induce, through steric effects, a direct crystallisation from the melt into the β-form. Yagi et al. [Yagi et al. 1980] synthesised, later on, the VDF/TrFE copolymers across the entire range of composition with the VDF and TrFE monomers randomly distributed along the molecular chain to obtain a single crystalline phase analogous to β-form PVDF which exhibits in a certain range of composition a polarization hysteresis characteristic of a ferroelectric material (see figure 1.18).

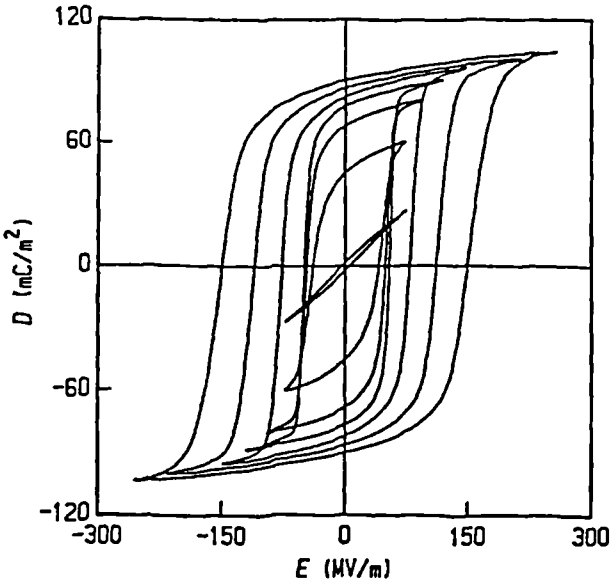

Figure 1.18 - Polarization hysteresis in P(VDF/TrFE) 65/35 mol% at various temperatures. From -70 °C (outermost curve) to 100 °C (innermost curve) [Furukawa 1989].

This latter fact renders P(VDF/TrFE) much more attractive than PVDF from a technological standpoint which needs, as seen before, an extra stretching operation. Moreover in P(VDF/TrFE), it is possible to impart greater crystallinity in the 80-90% range, if the material is heat treated between its Curie and melting temperatures [Ikeda et al. 1990]. An increase in the crystalline lamellae dimensions at the expense of the non-crystalline regions is then observed with the consequent increase in the remnant polarization, piezo- and pyroelectric properties [Koga et al. 1986].

Figure 1.19 shows the increase in crystallinity and remnant polarization for drawn and undrawn samples of P(VDF/TrFE) with a 73 mol% of VDF annealed in the 25 to 150 °C range of temperature [Furukawa 1989]. When the annealing temperature is over 120°C greater increases in the crystallinity and remnant polarization are observed reaching values around 80% and 100 mC/m^2 respectively. The rapid increase beyond the 120°C annealing temperature has been linked to the Curie phase transition temperature, which for this polymer, is around 120°C, suggesting that the crystallisation process in the amorphous regions correlates with the molecular motion in the crystal region at T_C [Ikeda et al. 1990].

In figure 1.19 is also shown for the same copolymer the remnant polarization as a function of the crystallinity. The curve for the drawn and undrawn samples follow the same pattern, and an extrapolation for the 100% crystallinity allows an estimate of the spontaneous polarization of 120 mC/m^2 for the P(VDF/TrFE) crystal of this composition.

Ferroelectric properties across the $P(VDF_X/TrFE_{1-X})$ composition have been studied by means of dielectric spectroscopy [Furukawa et al. 1981], Differential Scanning Calorimetry (DSC) [Yagi et al. 1980], piezoelectric and pyroelectric properties [Higashihata et al. 1981; Furukawa et al. 1984] and remnant polarization [Furukawa 1989].

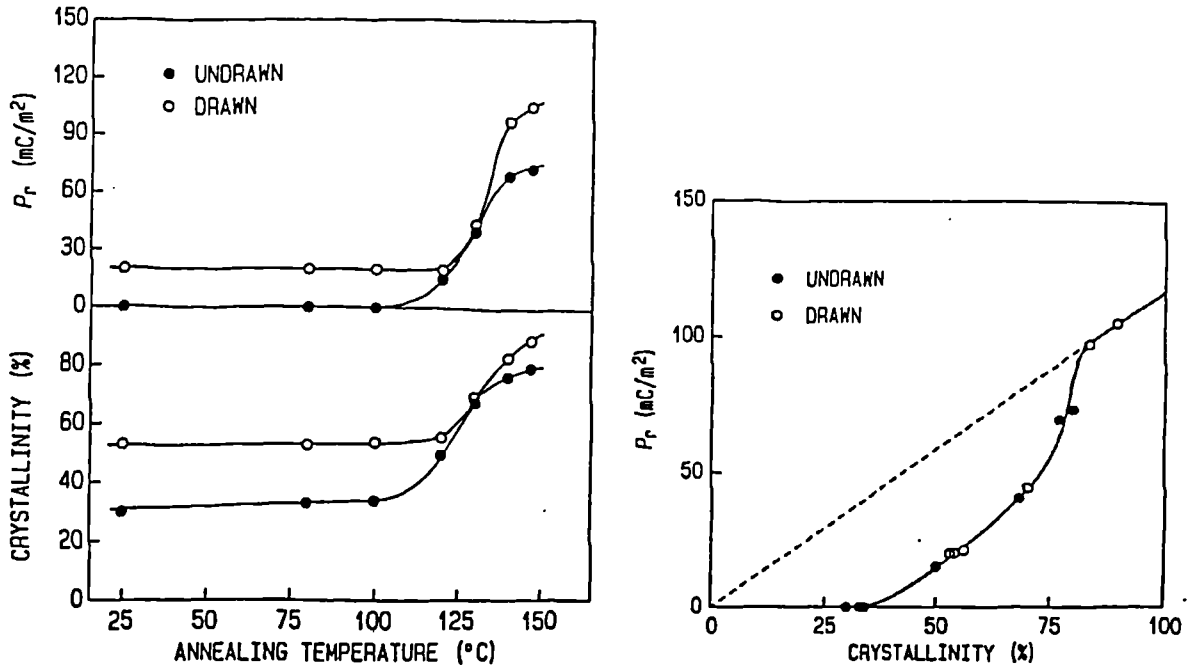

Figure 1.19 - Crystallinity and remnant polarization as functions of the annealing temperature for drawn and undrawn P(VDF/TrFE) 73/27 mol% copolymer [Furukawa 1989].

From these studies four distinct range of compositions have emerged which showed

different behaviour (see figure 1.20) [Ohigashi 1985; Koga et al. 1986].

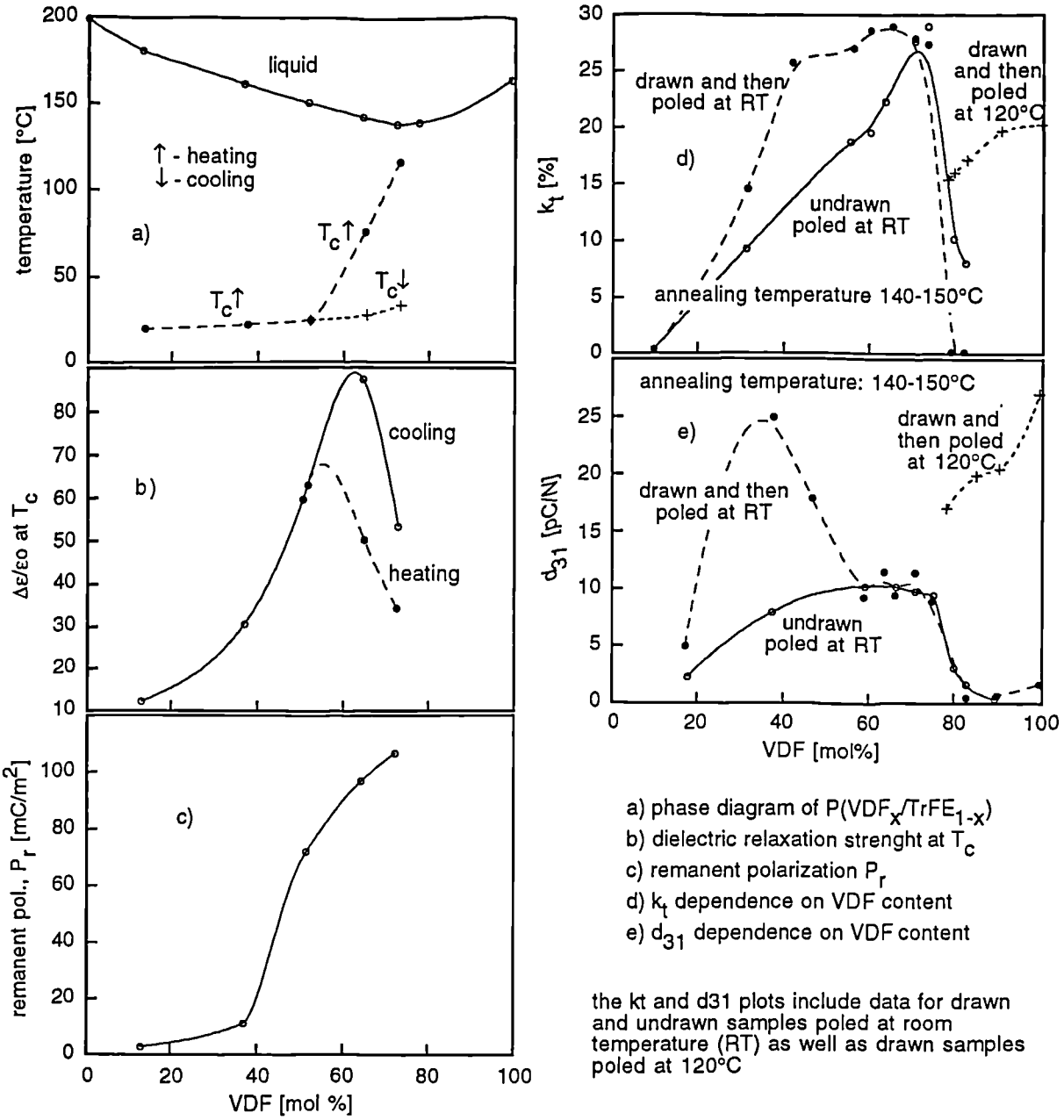

Figure 1.20 - Phase and property diagrams for the $P(VDF_x/TrFE_{1-x})$ (see text for references).

In the 0<x<0.4 range poor ferroelectric properties were observed even when additional operations like stretching were performed. The 0.4<x<0.6 range shows strong transverse piezoelectric activities (e.g. d_{31}) which increase if the sample is stretched. In the 0.6<x<0.8 the remnant polarization increases substantially and strong longitudinal coefficients are observed with k_t reaching a value of 0.3 in the 0.7<x<0.8 range. Stretching in this range of composition, does not improve the electro-activity substantially. Finally in the range from 0.8<x<1 the polymer composition and properties approach that of PVDF where a mixture of three phases α, β and γ are obtained from the melt. In this range the electro-active properties are enhanced by a stretching operation in analogy with PVDF. The continuos transition of properties in this range has allowed the extrapolation for a 100% VDF, of an analogous Curie temperature of 205°C. This would explain the reason for the absence of a Curie phase

transition in PVDF as it melts at a lower temperature of around 175 °C.

Due to the existence of a thermal hysteresis of the permittivity at the Curie temperature (see figure 1.20 (c)) it has been suggested that the phase transitions in the VDF/TrFE copolymers are basically of the first order [Furukawa 1989]. However, as the VDF content decreases to around 52 mol% the hysteresis diminishes and the transition tends to be second-order-type. The structural changes at the transition have been studied by IR and X-rays techniques. Tashiro et al. have shown by IR measurements [Tashiro et al. 1985] that during the transition from the ferro- to paraelectric phase the all-trans bands start to disappear with the simultaneous appearance of gauche bands. On the basis of these results it was concluded that the paraelectric phase of VDF/TrFE copolymers consists of random sequences of trans-trans, trans-gauche$^+$, trans-gauche$^-$ conformations. Thus in the ferroelectric state the chain adopts an all-trans conformation which is lost intramolecularly during the phase transition.

Based on the character of the phase transition, ferroelectrics are commonly separated into categories as being either displacive if a displacement of ions occurs or order-disorder when there is an ordering of dipoles. Based on the structural investigations the P(VDF/TrFE) copolymer can thus be described as an order-disorder ferroelectric.

The symmetry group of this copolymer in its undrawn ferroelectric state is ∞mm [Furukawa et al. 1988]. It is however, only of the statistical type due to the random substitution of monomers along the polymer chains [Legrand 1989]. The matrix relating the elastic and the electric quantities in the polymer has a cylindrical symmetry similar to that of the poled ferroelectric ceramics as given in equation 1.7. If the polymer is drawn perpendicular to the poling direction, the directions 1 and 2 cease to be equivalent and then the usual procedure is to identify the stretch with the 1-direction.

The copolymer used in the composite fabrication, has been chosen to be the P(VDF/TrFE) 75/25 mol% which according to the above classification lies in the third region i.e. $0.6<x<0.8$, where the ferroelectricity is evident below the melting temperature exhibiting a large temperature hysteresis.

In figure 1.21 is shown the permittivity on heating and cooling of a sample of P(VDF/TrFE) 70/30 mol% [Humphrey et al. 1987]. The Curie temperature on heating and cooling were measured to be 99 and 68.5 °C respectively. The P(VDF/TrFE) 75:25 mol% used in producing the present composites is thus expected to have a slightly higher Curie temperature as can be inferred from figure 1.20 (a). This is relevant because the higher the T_c is, the lower will be its effect on room temperature properties of the composite. Very unlike other polymers this material shows near its Curie temperature a high permittivity of the order of ε=40 on heating and ε=70 on cooling which can be very advantageous during composite poling as will be later demonstrated.

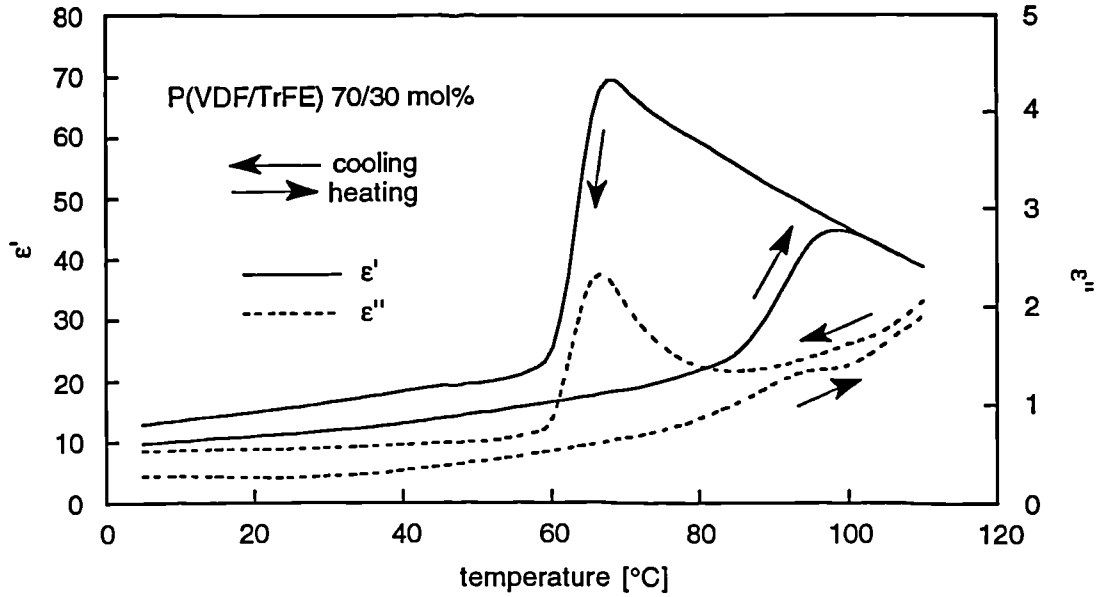

Figure 1.21 - Permittivity as function of the temperature near the Curie temperature for P(VDF/TrFE) 70/30 mol% showing the thermal hysteresis exhibited on heating and cooling the sample [Humphrey et al. 1987].

In figure 1.22 are shown the temperature spectra of various relevant quantities of P(VDF/TrFE) 75/25 mol% composition which were collected from the available literature. The remnant polarization and the coercive field for P(VDF/TrFE) 65/35 mol% are represented in figure 1.22 (a) where a thermal hysteresis can be observed on both cases.

A sharp increase below the Curie temperature is observed in the remnant polarization while the coercive field increases more steeply when the temperature approaches the glass transition temperature ($T_g \approx$ -40°C) which can be appreciated comparing it with figure 1.22 (b) for the permittivity [Humphrey et al. 1987; Schenk et al. 1992] The dielectric losses (i.e. tan δ) rise to about 0.05 around the glass transition then decrease at room temperature to 0.015 and finally increase again due to the onset of the phase transition.

Figure 1.22 (c) shows the behaviour of the electromechanical coupling factor k_t and the elastic stiffness c^D_{33}, both measured in the megahertz range on P(VDF/TRFE) 75/25 mol%. The elastic stiffness decreases as the temperature increases as is common in polymers; however, despite this k_t does not show a significant dependence on the temperature and it seems to be stable at a value of ≈0.27 up to about 100 °C. This value of k_t coupled to a low acoustic impedance of 4.5 MRayl renders this material attractive for hydrophone and biomedical applications.

The pyroelectric coefficient, shown in figure 1.22 (d), is around 10-15 $\mu C/m^2K$ at room temperature increasing by more than an order of magnitude as the temperature approaches T_c. The FOM_p shown in the same figure, has a similar behaviour to the pyroelectric coefficient in the temperature range from 20 to 70 °C.

The complex piezoelectric constants d_{33} and d_{31} are plotted in figure 1.22 (e). As was referred above, this composition renders materials with better longitudinal than transverse piezoelectric coefficients. The room temperature value for d_{33} of 30pC/N however, is still an order of magnitude lower than that of PZT. The imaginary part of the piezoelectric coefficients shows a relaxation near -40°C which is most probably due to the glass transition

of the polymer.

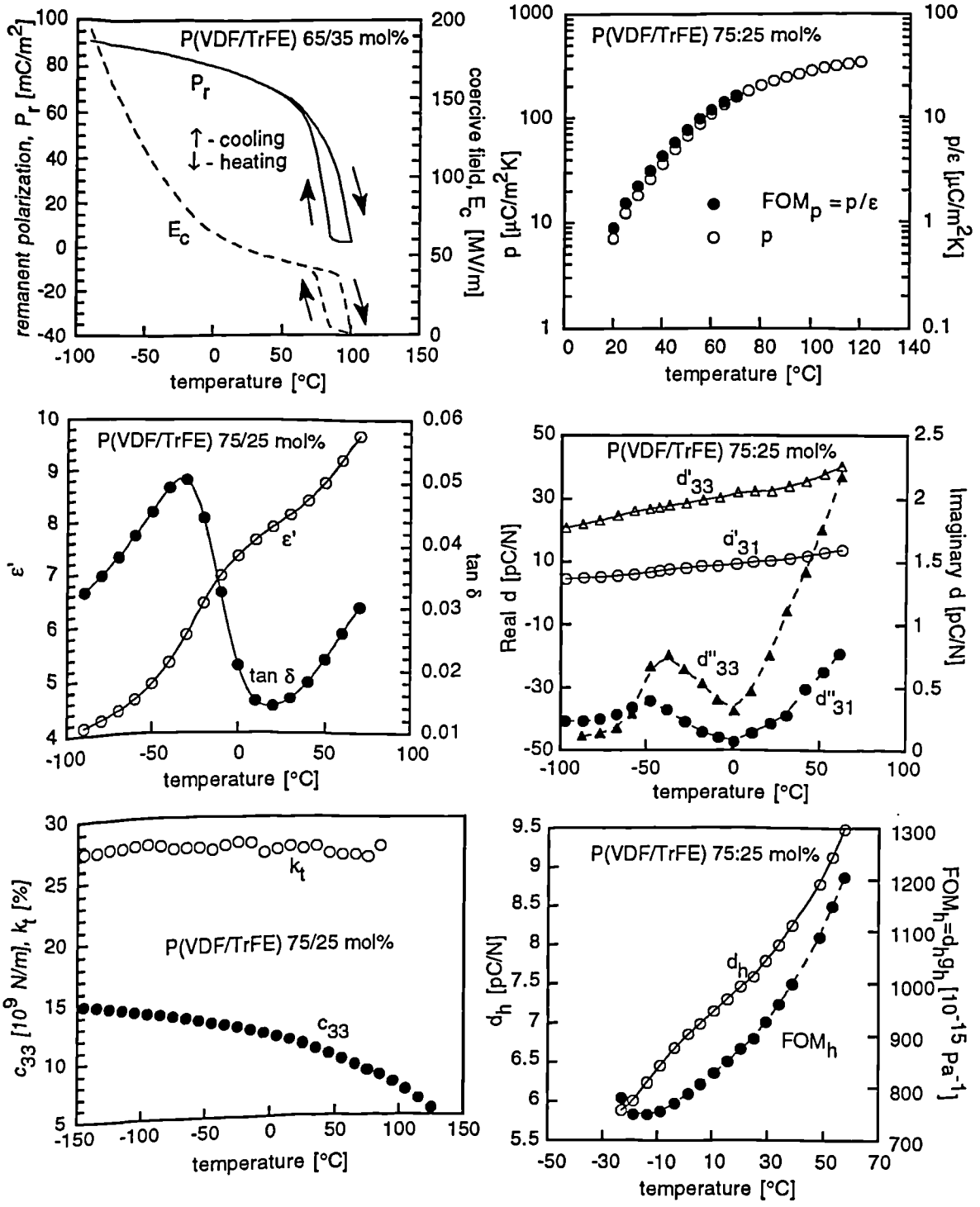

P(VDF/TrFE) properties temperature dependence

a) remanent polarization and coercive field
b) dielectric constant and tan δ; f=1.00kHz
c) k_t and c_{33}
d) pyroelectric constant and FOM_p
e) d_{33} and d_{31} complex piezo-constants
f) d_h and piezo- hydrostatic FOM_h

Figure 1.22 - Temperature spectra of various physical quantities in the P(VDF/TrFE) copolymer (see text for references).

The piezoelectric hydrostatic coefficient d_h increases from 6 to 9.5 pC/N in the temperature range of -30 to 50 °C as shown in figure 1.22 (f) [Stack et al. 1989] while the $FOM_h = d_h g_h$ increases from 750 to 1200 $\cdot 10^{-15}$ Pa^{-1}. The relatively high FOM_h compared to ferroelectric ceramics is brought about by the high voltage g_h coefficient which is 120

mV·m/N at room temperature.

The frequency dependence of the room temperature permittivity in P(VDF/TrFE) 70:30 mol% is shown in figure 1.23 [Schenk et al. 1992]. A relaxation process is clearly visible in the 1 MHz region while there may also be a presence of two others processes. One of them at frequencies lower than 10^{-2} Hz is denoted in the figure as α_1 and the other which is very small is in the 1 Hz region.

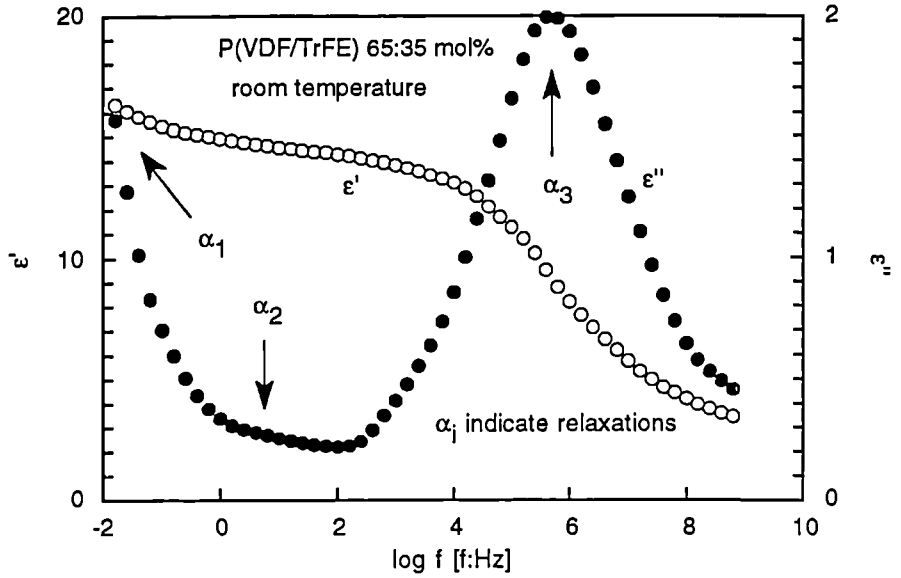

Figure 1.23 - Frequency dependence of the permittivity [Schenk et al. 1992].

The α_1 relaxation has been assigned to the a Debye type relaxation due to the movement of space charges, which perform a local compensation of the polarization. The α_3 relaxation was identified with motions associated with elementary trans-gauche transformations which become cooperative in the ferroelectric phase. Some ground exists however to presume that the relaxations of the non-crystalline motions attributed to the glass transition might coexist in this region due to the similarity with the PVDF frequency spectra.

As the temperature approaches the Curie temperature these polymers experience some reduction on their electro-active properties. In figure 1.24 is shown degradation for a 10 minutes ageing time at each plotted temperature for PVDF and two different P(VDF/TrFE) copolymers [Ohigashi 1985]. Although the Curie temperature of PVDF is estimated to be over its melting temperature a rapid decrease of k_t is observed for temperatures higher than 75 °C. The copolymers seem to maintain their properties closer to their respective T_c and consequently the copolymer with the higher VDF content (i.e. 86 mol%) retains its k_t value up to 125°C.

The nature of piezo- and pyroelectricity on P(VDF/TrFE) has been investigated by Furukawa et al [Furukawa et al. 1984; Furukawa et al. 1984]. The dimensional contribution to the piezoelectric effect was found to be given by,

$$d_{3i} = -P_r s_{ii} \qquad (1.21)$$

where the d, s and P_r are the piezoelectric constant, the compliance and the remnant

polarization of the sample respectively. By comparing the magnitude of the experimentally measured d_{31}/s_{11} with the magnitude of P_r they were able to demonstrate that 70% of the observed piezoelectricity originates from a dimensional contribution.

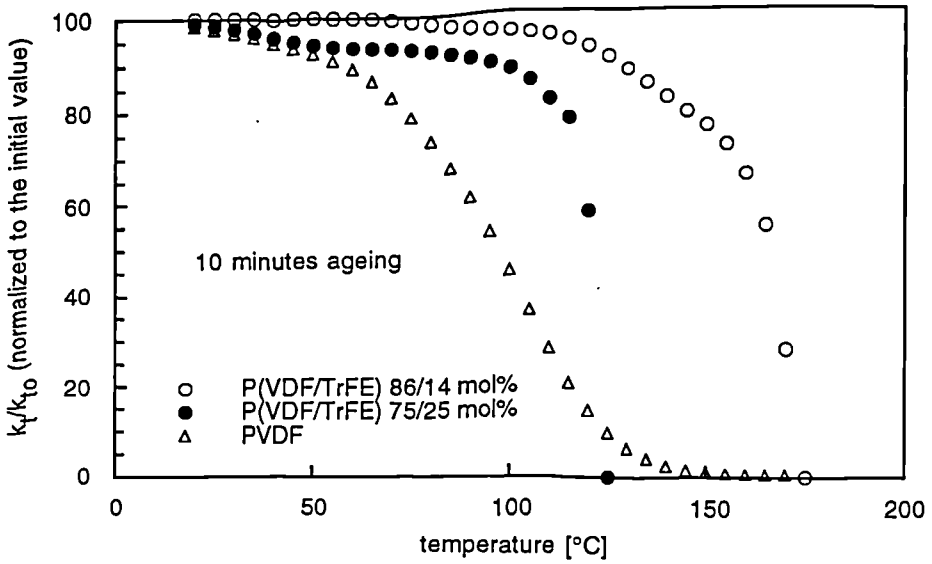

Figure 1.24 - Thermal stability of piezoelectric activity in PVDF and P(VDF/TrFE) [Ohigashi 1985].

Regarding pyroelectricity two effects were distinguished: the primary and the secondary dimensional pyroelectric effect respectively (see equation 5.31 and discussion), where the latter is given by,

$$p_3(\text{secondary}) = -P_r\alpha_3 \qquad (1.22)$$

where p and α_3 are the pyroelectric coefficient and the linear expansion coefficient in the thickness direction respectively.

Again, using the actual measured quantities of these variables it was concluded that the secondary contribution was small and thus pyroelectricity in P(VDF/TrFE) is dominated by the primary or intrinsic effect [Furukawa et al. 1984; Furukawa et al. 1984], which is due to a decrease of the spontaneous polarization as the temperature increases.

At the end of this chapter the properties of P(VDF/TrFE) available from the literature have been listed in table 1.3 [Ohigashi 1988; Yamaka 1988; Wang et al. 1993].

1.5 - Fundamentals of ferroelectric composite materials

In modern usage composite materials are made from a filler - either particles, flakes or fibres - embedded in a matrix made of polymer, metal or glass. Nevertheless, according to the broadest definition, a composite is any material consisting of two or more distinct *phases*. So, in this latter sense most of ferroelectrics may be included in the composite category.

Making composite materials, by a combination of a ferroelectric ceramic and a polymer of suitable properties, means not only choosing the right materials processed in a particular way, but also coupling them with the best possible design structure. This concept of connectivity, first established by Newnham et al [Newnham et al. 1978], to describe the

interspatial relationships in a multiphase material is of the utmost importance because it controls the mechanical, electrical and thermal fluxes between the phases.

In a composite each phase may be spatially self-connected in either one, two or three dimensions. In a diphasic or two phase system there are ten different combinations of phase connectivity which are usually indicated using two digits, denoting the connectivity of the filler and that of the matrix respectively in this order. These are the: 0-0, 0-1, 0-2, 0-3, 1-1, 1-2, 1-3, 2-2, 2-3, and 3-3 connectivities represented in figure 1.25 using a cube as a building block. For example, the commonly used composite of dispersed particles embedded in a matrix would then be indicated as a 0-3 composite while another common system consisting of fibres implanted on a matrix and oriented across one of the dimensions of the sample would be known as a 1-3 composite.

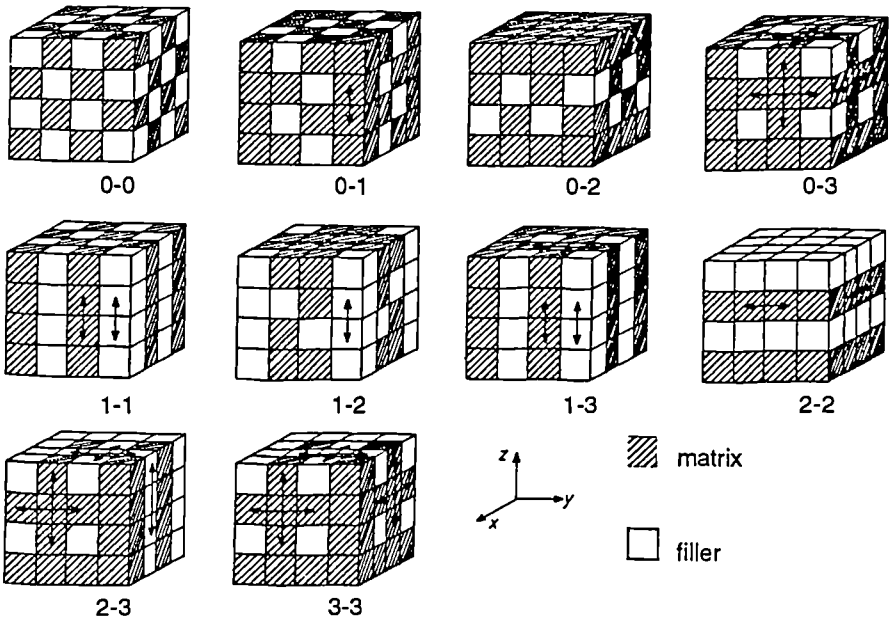

Figure 1.25 - Connectivity patterns in a diphasic composite system [Newnham et al. 1978].

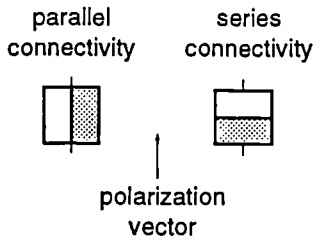

Figure 1.26 - Parallel and series connectivities with their usual respective orientation of the polarization vector.

This classification, however, does not specify the directions upon which the connectivity takes place nor does it say in what direction, in the case of a ferroelectric composite, the polarization vector points to. This information must obviously be asserted or be self-evident for the case in hand. For example, in the two dimensional case, both the so-called series and parallel connectivities shown in figure 1.26, would be categorised using this classification under the 2-2 connectivity pattern. They render obviously quite different properties in all respects as will be demonstrated later on in chapter 2.

The definition, in a diphasic system, of what is the filler and what is the matrix can be confusing when in the case of certain composites the volume fraction occupied by the filler is higher than that of the matrix. The connectivity criteria can be used in this case so that the matrix is the phase of highest connectivity in the composite.

Properties in composites can be advantageously classified in relation to those of the constituent phases as: sum, combination and product properties [Newnham et al. 1978]. A sum property, such as the case of the density, is one which derives its value from an equation which involves an averaging of properties of the phases so that the composite property value is bounded by those property values of the constituent phases.

A figure of merit for a given application often involves two or more material properties. This is an example of a combination property which requires an averaging of more than one property. The pyroelectric figure of merit p/ε depends both on the pyroelectric coefficient and on the permittivity and due to their different mixing rules the pyroelectric FOM_p can be higher or smaller than any of its constituent phases.

Product properties are the most complex ones as they originate due to a coupling between the two properties which do not match in the constituent phases and thus produce an entirely different property. As an example, the coupling of the piezoelectric effect with the linear expansion of a material produces a contribution to the pyroelectric effect.

More generally it is often the case that a property in the composite will have all these three different types of contributions.

The periodicity and scale in composites regarding both the filler and the matrix are important factors in determining, for instance, the upper frequency limit where resonance and interference occur. In order to get higher frequencies as well as other advantages such as miniaturisation, nanocomposites consisting of particles in the nanometer scale dispersed in a matrix, have been recently been experimented [Newnham et al. 1990]. These have been brought about by synergies in the production of fine ceramic powders using the sol-gel route coupled to the development of very high-temperature polyimides polymers. Concern however, must be exercised when using fine powders as properties vary with the ceramic grain. Presently however, common composites are around 5 to 10μm thick while the ceramic grains embedded in them are typically greater than 0.8-1 μm and thus acoustic frequencies up to around 500 MHz can be used without resonance effects.

Other effects such as interfacial, percolation and porosity effects can also play a role in composite properties [Newnham 1985]. Interfacial effects can occur between the ceramic grains and the polymer matrix leading to large dielectric relaxations normally at low frequencies otherwise known as Maxwell-Wagner relaxation, while in other cases interesting Schottky barrier phenomena can also occur. Space-charge compensation of dipolar polarization is also known to occur at the interface boundaries.

Percolation of ceramic grains inside a composite is an effect which can be of great help in aiding its polarization by establishing a continuos electrical flux through the ferroelectric grains.

Porosity, when not planned, can have adverse effects. However, it has been intentionally induced in PZT up to 70% in volume [Hikita et al. 1983] so that in this case, air was the filler material with very compliant properties. Decrease of the permittivity, the Young modulus, the transverse coefficients and of the mechanical Q_m were observed with increasing porosity whilst d_{33} remained stable and g_{33} increased. Such materials could be thus very attractive for longitudinal mode operation although some pressure dependence of properties would be expected.

1.5.1.- 0-3 connectivity

The most commonly studied composites are the 0-3 and 1-3 configurations, although for different reasons. The 0-3 connectivity owes its popularity to the easy fabrication procedure which allows for mass-production at a relatively low-cost. Thus it is not surprising that the first attempts in producing composites, used this type of connectivity [Pauer 1973; Furukawa et al. 1976]. The composite properties however, were quite low compared with ferroelectric ceramics. An improved version of the 0-3 composite was synthesised by Banno et al [Banno et al. 1983] where instead of using PZT, pure or modified lead titanate was the ceramic filler. The ceramic powder, in the 5μm range, was obtained by quenching the ceramic block thereby exploiting the high strain present in the lead titanate ceramic (see section on lead titanate).

Composites using PVDF as a matrix with a high content of PZT ceramic (<67%) were also fabricated by Yamada et al [Yamada et al. 1982] which were evaluated for their piezoelectric activity. Improved properties were found which for a 67% PZT content composite resulted in ε_{33}, d_{33} and Young modulus attaining values of 150, 50 pC/N and 3 GPa respectively. Yamazaki et al [Yamazaki et al. 1981] also experimented with PVDF but using lead titanate as the ceramic filler (see figure 1.27). Measurements of the 62% PT composite poled at 160°C with an electric field of 20 MV/m, gave a pyroelectric coefficient of 130 $\mu C/m^2K$ and a permittivity of 55.

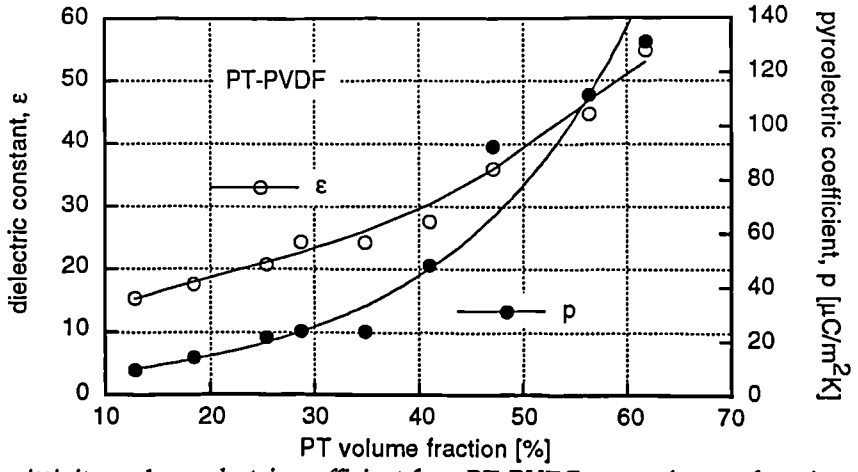

Figure 1.27 - Permittivity and pyroelectric coefficient for a PT-PVDF composite as a function of the PT content [Yamazaki et al. 1981].

Flexible 0-3 composites using a polyurethane matrix material and a ferroelectric filler

was produced by Zipfel at the Bell Laboratories [Zipfel 1983]. The liquid mixture was injected into a cylindrical chamber where during polymerisation a hydrostatic pressure and poling field were applied. The piezoelectric crystals suspended in the liquid copolymer rotate until they are electrically aligned and remained frozen in their position after polymerisation. The permittivity of this piezoelectric cable was 4.2 with a piezoelectric sensitivity "comparable to most ferroelectric materials".

The effect of the grain size used in the composite properties was investigated by a number of workers [Pardo et al. 1988; Lee et al. 1990; Reed et al. 1990; Slayton et al. 1990]. The general conclusion is that two variables can coexist. The dielectric and other properties of the ceramic grains are functions of the grain size and thus specially when very fine powders are used significant differences in properties can be obtained. The scale of the grain size relative to the composite dimensions is the other factor which can influence the ensuing property in composites. In general, a larger grain to thickness ratio increases both the permittivity and electro-active properties.

Poling is perhaps considered to be the biggest difficulty in 0-3 composites [Sa-Gong et al. 1986; Lee et al. 1988; Waller et al. 1988]. The reason is that the electric flux does not affect the ceramic grains efficiently because the ceramic resistivity and permittivity are in general lower and higher respectively than that of polymers. Thus when applying an external electric field to polarise a sample most part of it drops across the polymer matrix. This could be circumvented if the electrical field breakdown strength would increase. However, due to the statistical distribution of the grains there may exist a ceramic path across the sample which eventually limits the electric field breakdown strength.

1.5.2. - 1-3 connectivity

The 1-3 connectivity composites show in general a higher performance in terms of piezoelectric properties albeit at a higher manufacturing cost [Klicker 1980; Savakus et al. 1980]. This usually consists of pillars regularly spaced within a polymer matrix oriented with their long axis perpendicular to the surfaces of the film. In figure 1.28 are shown properties of PZT-polyurethane composites with a 25% ceramic loading [Takeuchi et al. 1985]. The impedance and phase characteristics due to the polymer damping effect plotted in the left hand-side of the figure, shows a single longitudinal resonance curve with no observable spurious response due to other coupling modes. The mechanical quality factor Q_m, determined from the resonant curves was in the range of 10-20.

The electromechanical coupling factor as a function of the PZT content, shown in the middle graph of figure 1.28, is fairly constant in 15-80 % range although a peak around 25% can be distinguished. The permittivity increases almost linearly in the same PZT content range. The pillar width-to-thickness (w/t) ratio also affects these quantities, as shown in the last graph of figure 1.28. The electromechanical coupling factor shows a higher sensitivity than the permittivity towards these variable exhibiting a peak value of 0.75 for a w/t ratio of 0.5. It is thus interesting to note that the volume fraction solely does not determine completely the permittivity or the electromechanical coupling factor.

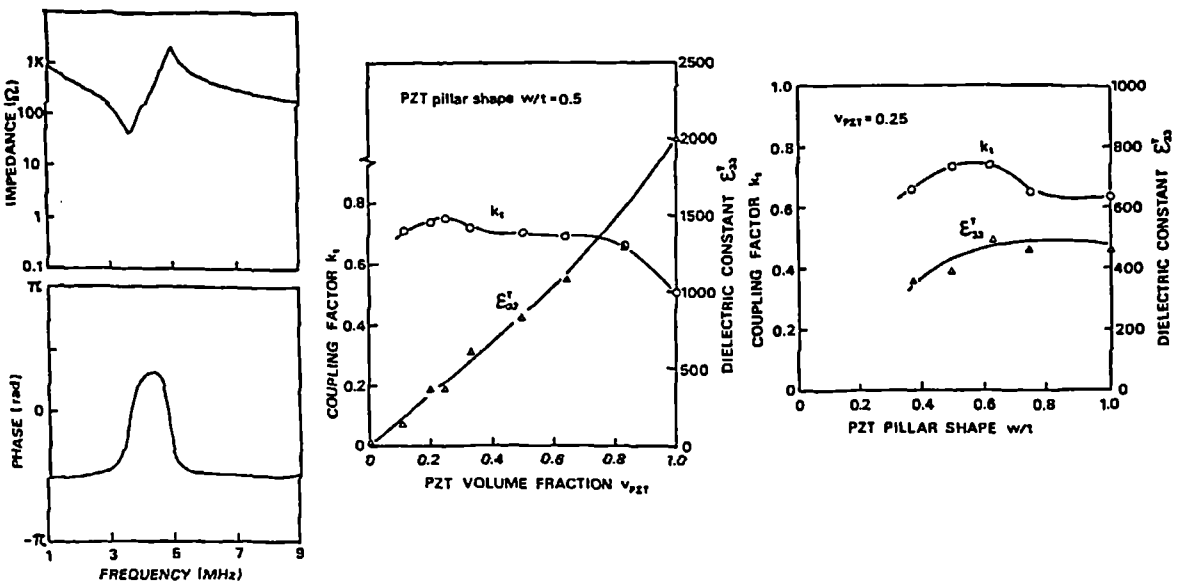

Figure 1.28 - Results for a 1-3 connectivity composite made of PZT in a polyurethane matrix [Takeuchi et al. 1985].

A problem in 1-3 composites arises as a result of the periodicity of the lattice rods which cause spurious resonances and degrades the performance of ultrasonic transducers [Auld et al. 1984; Smith 1989]. These resonances are caused by Bragg reflections of Lamb waves propagating laterally in a periodic array of rods. The frequency of these lateral modes are inversely proportional to the rod spacing while the thickness mode resonance depends on the plate thickness. Making thus the lateral scale finer pushes the lateral resonances to higher frequencies allowing the composite to behave as an effective homogeneous medium.

Very successful experiments have also been performed using composites of 3-3 connectivity [Skinner et al. 1978], which due to the existence of electrical ceramic paths across the thickness of the composite, has the ability of polarising very efficiently the grains even at low ceramic volume fractions and consequently with the advantage of a low permittivity and density.

In tables 1.1 and 1.2, typical values of properties of composites taken from the literature are listed [Safari et al. 1986; Gallego-Juárez 1989].

In the chapter 4 models for the composites will be described. These models will attempt to predict the dielectric, pyroelectric and piezoelectric properties of the composites from the properties of the constituent phases.

TABLE 1.1 - DIELECTRIC AND HYDROSTATIC PIEZOELECTRIC PROPERTIES OF COMPOSITES

COMPOSITE	density	ε	g_h	d_h	$d_h g_h$
	kg/m^3		mV·m/N	pC/N	10^{-12} Pa^{-1}
PZT 5A	7500	1700	2.2	32	0.07
PTCa 24 mol%	6890	209	33	62	2.07
PVDF	1750	12	100	10	1.00
0-3 PZT-polyurethane		26	8	2	0.01
0-3 PZT silicone (large particle)		100	32	28	0.90
0-3 0.5 PT-0.5Bi[$Fe_{0.98}Mn_{0.02}$]O_3		40	90	30	2.70
0-0-3 PZT-carbon-polymer		120	30	30	0.90
0-3 PT-chloroprene rubber		40	100	35	3.50
1-3 PZT rods-epoxy	1400	54	56	27	1.50
1-3 perforated composite	2600	650	30	170	5.10
2-3 perforated composite	2500	375	60	200	12.00
3-3 replamine PZT/silicone rubber	3300	40	45	180	8.10

TABLE 1.2 - PROPERTIES OF REGULAR AND IRREGULAR SHAPED 1-3 PZT RODS COMPOSITES

COMPOSITE	vol. fraction	rod diameter	thickness	density	k_t	Q_m	k_p	Z_a
	%	mm	mm	kg/m^3				MRayl
1-3 PZT-epoxy	5	0.45	0.6	1410	0.57	5	0.17	5.1
regular rods	10	0.45	0.6	1640	0.68	7	0.17	6.0
	20	0.45	0.6	2290	0.68	9	0.21	8.5
	30	0.45	0.6	3080	-	-	0.20	-
1-3 PZT-epoxy	60	≈0.6	0.7	4700	0.6	5	-	14.7
irregular rods	70	≈0.6	0.7	5800	0.58	5.5	0.24	19.2
	80	≈0.6	0.7	6600	0.52	5.8	0.3	24
	90	≈0.6	0.7	7000	0.52	6	0.3	27
PZT	100		0.7	7500	0.48	75	0.6	33.7

TABLE 1.3 - PROPERTIES OF THE COMPOSITES CONSTITUENT MATERIALS

PROPERTIES	PZT 5A	PTCa 24 mol%	PVDF *	P(VDF/TrFE) 75/25 mol%	UNITS
density	7500	6890	1780	1880	kg/m^3
d_{31}	-171	-3.1	28-21	10.7	pC/N
d_{33}	374	68	-33	-34	pC/N
d_h	32	62	-10	-13 ; 7.5	pC/N
g_{31}	-11.4	-2.2	312	153	mV·m/N
g_{33}	25	33	-482	-478	mV·m/N
g_h	2.2	33	-148	-180	mV·m/N
$d_h g_h$	0.07	2.07	1.48	2.1	10^{-12} Pa^{-1}
e_{31}	-5.4	1.6	≈0	≈0	C/m^2
e_{33}	15.8	8.5	-0.1 ; -0.08	-0.22 ; -0.11	C/m^2
h_{31}	-9.2	1.25	≈0	0.08	GV/m
h_{33}	2.17	6.6	-1.3 ; -2.6	-4.7 ; -1.7	GV/m
ε^T_{11}	1730	238	6.9	7.40	
ε^T_{33}	1700	209	7.6 ; 11	7.90	
tan δ	0.02	0.016	0.06	0.011	
s^E_{11}	16.4	7.35	365	332	TPa^{-1}
s^E_{33}	18.8	8.6	472	300	TPa^{-1}
s^E_{12}	-5.74	-1.5	-110	-144	TPa^{-1}
s^E_{13}	-7.22	-1.5	-209	-89	TPa^{-1}
c^D_{33}	147	183	9.1 ; 5.5	11.3 ; 4.8	GPa
k_{31}	-0.34	-0.04	0.16	0.08	
k_{33}	0.70	0.47	≈ 0.18	≈ 0.23	
k_t	0.48	0.47	0.20	0.30	
k_p	0.60	0.06	≈ 0.23	≈ 0.13	
Q_m	75	1200	10	20	
z_a	33.7	30	4.02	4.51	MRayl
p	420	380	20	17	$\mu C/m^2K$
p/ε	0.24	1.8	2.2	2.1	$\mu C/m^2K$
κ	0.26	0.99	0.053	(0.053)	mm^2/s
C_v	2.5	3.2	2.3	2.3	MJ/m^3K
α_3	7	10-36	≈120	≈100	10^{-6} K^{-1}
E_c	1.2	3-5	45	36	MV/m
T_c	365	255	>150	≈125	°C
P_r	380	400	55	85	mC/m^2
ρ	$\approx 10^{11}$	$\approx 10^{11}$	$1\text{-}10 \cdot 10^{14}$	$\approx 3 \cdot 10^{15}$	Ω·m

*uniaxially drawn

TABLE 1.4 - PROPERTIES OF ADDITIONAL POLYMERS USED IN THE PRESENT WORK

	PP	LDPE	STYCAST epoxy	SPURR epoxy	UNITS
density	900	900	1590	1100	
ε	2.2-2.6	2.5	4	3.5	
s_{11}		1370	108	330	TPa^{-1}
s_{12}		-630	-32	-122	TPa^{-1}
c_{11}	1.2	3.4	12.5	5.3	GPa
c_{12}		2.9	5.7	3.1	GPa
Poisson ratio		0.45	0.30	0.36	$-s_{12}/s_{11}$
α	100-180	100-200			$10^{-6}\ K^{-1}$
ρ	10^{14}-10^{16}	10^{13}-10^{16}			Ω·m

2 - Models of composites

2.1 - Short introduction

This chapter concerns with the prediction of composite properties made from electroactive ceramic powders embedded in a polymer host. This particular task is a small part of an ongoing work across the scientific community to model the performance behaviour of mixed phase materials. Various models have been proposed which deal specifically, for example with electrical properties such as the resistivity and the permittivity and a large amount of information in the literature exists on these subjects alone, while the same arises for the mechanical properties. However, this short review is concerned with predictions of the composite coupling coefficients between the electrical and the mechanical properties via the piezoelectric effect and with the coupling coefficient between the thermal and electrical properties through the pyroelectric effect.

In chapters 4, 5 and 6 which are devoted to the polarisation, pyroelectric and piezoelectric properties of composites respectively, the models described in this chapter will be used in order to explain their behaviour.

To calculate the properties of a composite a knowledge of the constituent phase properties is necessary. The properties for the materials used, PTCa, PZT5A and P(VDF/TrFE) are those listed at the end of chapter 1 in table 1.3. An epoxy with the commercial designation Stycast a stiff polymer, has also been used in this chapter for comparison purposes in the model calculations and its properties can be found in table 1.4 also at the end of chapter 1.

2.2 - Yamada model for 0-3 composites

Yamada and his co-workers [Yamada et al. 1982] have studied the binary system consisting of a PZT powder embedded in a polymer matrix of PVDF, with respect to their dielectric, piezoelectric and elastic properties. In the same work, a model has been proposed to explain the behaviour of composite properties using the properties of its constituent materials. Considering the binary system schematically shown in figure 2.1, composed of ellipsoidal particles dispersed in a continuos medium, the permittivity of the composite was shown to be:

$$\varepsilon = \varepsilon^p \left(1 + \frac{\eta \phi^c \left(\varepsilon^c - \varepsilon^p \right)}{\eta \varepsilon^p + \left(\varepsilon^c - \varepsilon^p \right) \left(1 - \phi^c \right)} \right) \tag{2.1}$$

where η is a parameter dependent on the shape of the ellipsoidal particles [Das-Gupta 1991] and their orientation in relation to the surface of the composite film, while ϕ is the volume fraction of the ceramic. The other symbols ε, ε^c, ε^p, refer to the magnitude of the composite, ceramic, and polymer permittivities respectively. Throughout the present chapter

superscripts c and p refer to the ceramic and polymer properties respectively while an absence of a superscript will usually denote a composite property.

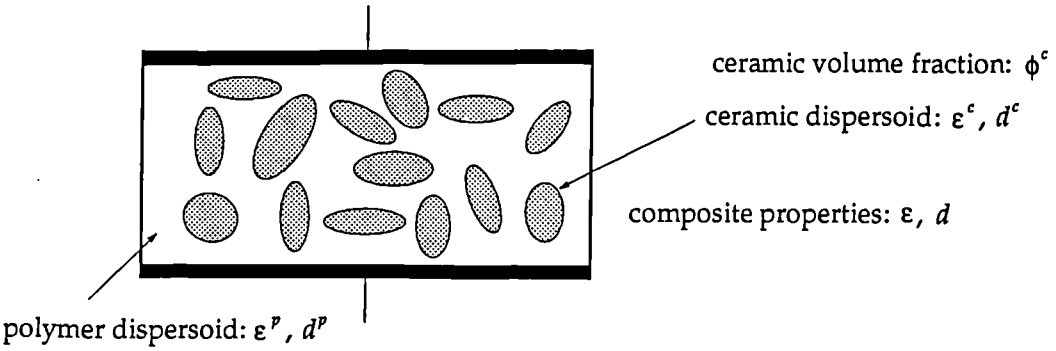

Figure 2.1 - Binary system consisting of piezoelectric ellipsoidal particles dispersed in a continuos medium

Assuming that the host polymer matrix does not show piezoelectric activity an expression for the piezoelectric constant d in this binary composite is given by:

$$d = \alpha_p \phi^c G d^c \tag{2.2}$$

where α_p is the ceramic poling efficiency ratio, G the local field coefficient acting on the ceramic grains and d^c the piezoelectric constant of the piezoelectric dispersoid (i.e. the ceramic). The local field coefficient G, using the shape parameter η is given by:

$$G = \frac{\eta\varepsilon}{\eta\varepsilon + (\varepsilon^c - \varepsilon)} \tag{2.3}$$

where the permittivity of the composite is given by equation 2.1. In this work [Yamada et al. 1982] a shape parameter η equal to 8.5 was found to fit these theoretical equations for the experimental results obtained for PZT:PVDF composites with different ceramic volume fractions (see figure 2.2 and 2.3).

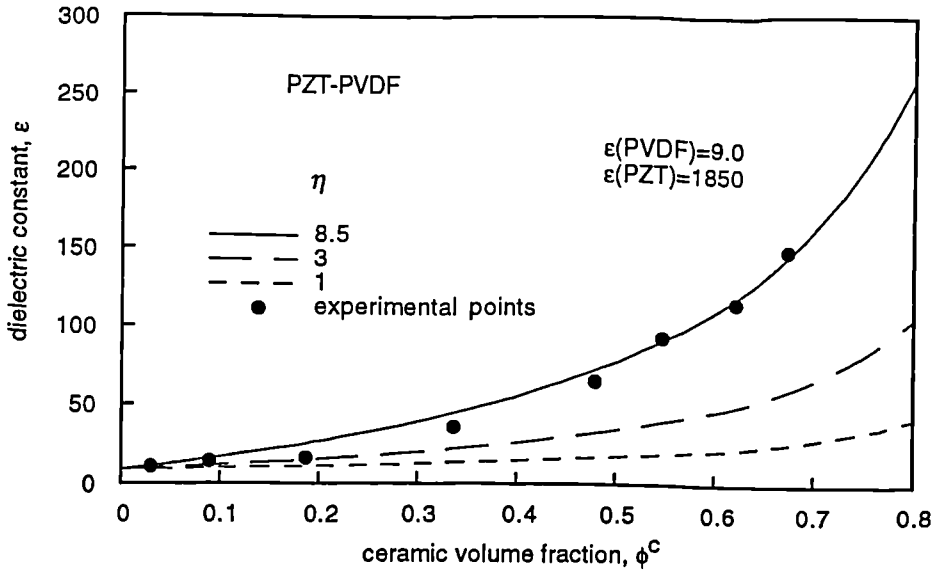

Figure 2.2 - Theoretical plot of the permittivity for three values of the shape factor in a PZT:PVDF composite together with the experimental data of this composite [Yamada et al. 1982]

This value of the shape parameter η, demanded that the ceramic ellipsoid axes ratio

was 2.8 with the long axis perpendicular to the surface of the composite film. This was difficult to accept in view of the procedure used to obtain the composite, which involved a high temperature mixing of the approximately ellipsoidal ceramic grains inside the polymer, followed by a pressing stage to obtain the composite films forcing thus, the longer axis of the ellipsoidal particles to be parallel to the surface of the film.

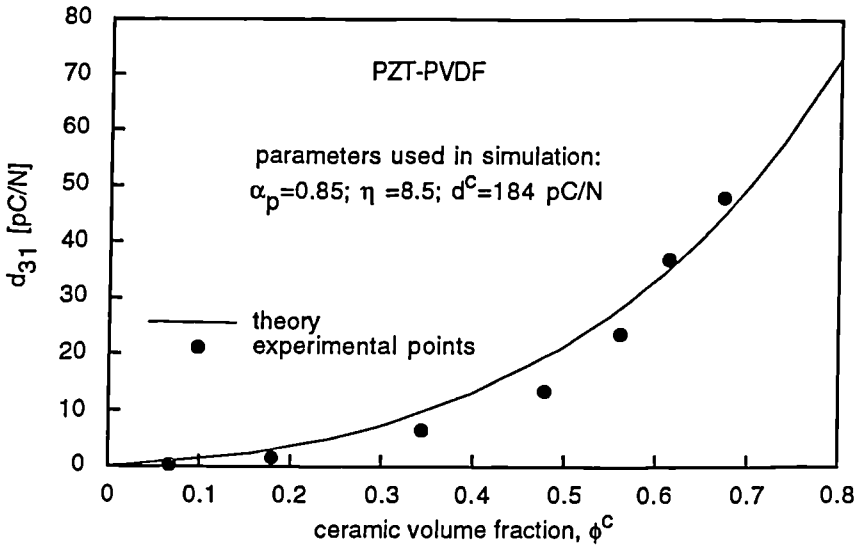

Figure 2.3 - Piezoelectric constant as a function of the ceramic loading. The experimental points were fitted using the Yamada model [Yamada et al. 1982].

An alternative interpretation put forward by Banno [Banno 1985] points out that the ceramic grains could be approximately spherical in shape but, if compared with the dimensions of the composite sample (i.e. thin film disks) in which they were embedded, they would appear to be larger in the thickness direction than in the other two perpendicular directions of the film. As a result, the shape factor η representing the spheres would appear to have been stretched in the thickness direction. In conclusion, the parameter η is not an absolute measure of shape of the ceramic grains, but takes also into account the dimensions of the films into which they are embedded.

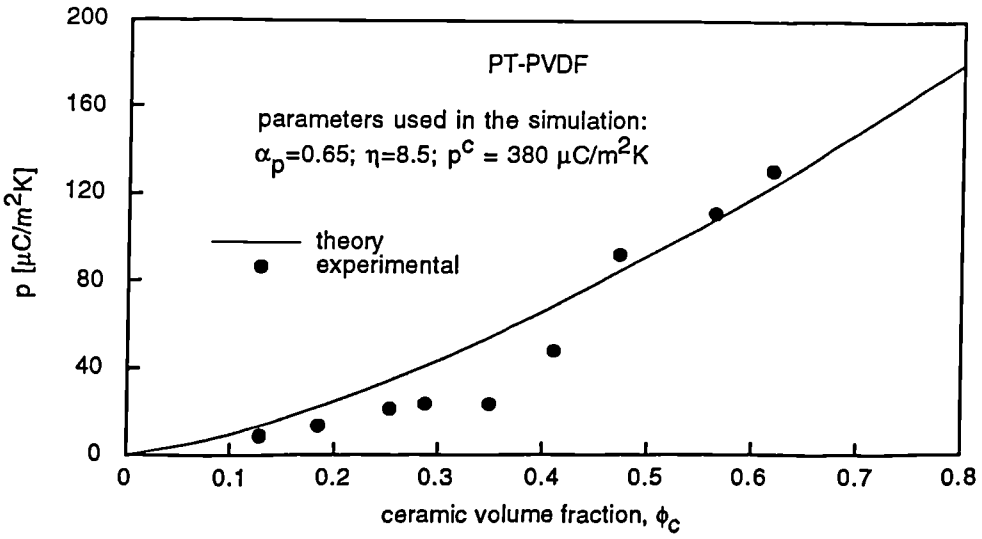

Figure 2.4 - Pyroelectric constant as a function of the ceramic content. The experimental points were calculated using equation 2.4 with the parameters as specified in the graph [Yamazaki et al. 1981].

Based on the same model and assuming the ceramic to be the only pyroelectric phase in the composite the magnitude of the pyroelectric coefficient p, may be expressed thus [Das-Gupta 1991; Wang et al. 1993],

$$p = \alpha_p \phi^c G p^c \tag{2.4}$$

where p^c is the pyroelectric coefficient of the ceramic whilst the other quantities have already been defined above. Using this expression a reasonable agreement could be found between the experimentally observed data and the calculated values in composites made of PT powder embedded in a PVDF matrix as plotted in figure 2.4 for the pyroelectric data of Yamazaki et al [Yamazaki et al. 1981].

2.3 - Furukawa model for 0-3 composites

Furukawa and co-workers [Furukawa et al. 1976; Furukawa et al. 1979] have also studied a two phase system composed of spherical inclusions (i.e. ceramic) embedded in a polymer matrix (see figure 2.5) which consists of a homogeneous medium whose properties approximate the average composite properties.

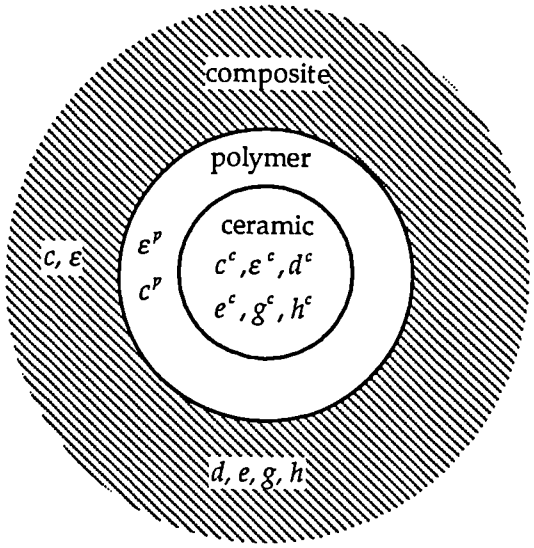

Figure 2.5 - Representation of a composite system consisting of spherical ceramic inclusions embedded in a polymer matrix sphere which in turn is covered with a homogeneous medium whose properties approximate the average composite properties.

In this work, expressions for the dielectric, elastic, and piezoelectric constants were given and compared with the experimental results. The permittivity of the composite is given, by the equation [Furukawa et al. 1976][and references therein]:

$$\varepsilon = \frac{2\varepsilon^p + \varepsilon^c - 2\phi^c\left(\varepsilon^p - \varepsilon^c\right)}{2\varepsilon^p + \varepsilon^c + \phi^c\left(\varepsilon^p - \varepsilon^c\right)}\varepsilon^p \tag{2.5}$$

while the elastic stiffness constant c, deduced on the assumption that the composite was incompressible, is given by:

$$c = \frac{3c^p + 2c^c - 3\phi^c\left(c^p - c^c\right)}{3c^p + 2c^c + 2\phi^c\left(c^p - c^c\right)}c^p \tag{2.6}$$

where the symbol c stands for the Young modulus of the material. Expressions for the piezoelectric constants d, e, g and h have also been derived and are given by:

$$d = \phi^c L_X L_E d^c \tag{2.7}$$

$$e = \phi^c L_x L_E e^c \tag{2.8}$$

$$g = \phi^c L_X L_D g^c \tag{2.9}$$

$$h = \phi^c L_x L_D h^c \tag{2.10}$$

where L_X, L_x, L_D and L_E are the local fields coefficients with respect to X (stress), x (strain), D (displacement) and E (field) respectively. The meaning of the local fields coefficients can be understood for example in relation to the case of L_E (local electric field coefficient) which is the ratio of the local electric field produced in the ceramic inclusion to the field applied to the composite as a whole.

It will be instructive to follow the derivation of one of the above equations for the piezoelectric properties, for instance, that of equation 2.7 for the d coefficient. By definition, d is given by:

$$d = \left(\frac{D}{X}\right)_E \tag{2.11}$$

When a stress X is applied to the composite, it produces the local stress X^c in the ceramic inclusions,

$$X^c = L_X X \tag{2.12}$$

Now, as the stress and the electric displacement in the ceramic inclusion are related by equation 2.11, we have:

$$D^c = d^c X^c = d^c L_X X \tag{2.13}$$

The apparent electric displacement D in the composite due to the local D^c is given by [Furukawa et al. 1976]:

$$D = \phi^c L_E D^c = \phi^c L_X L_E d^c X \tag{2.14}$$

Referring to equation 2.11 it may then be observed, that the composite behaves as a piezoelectric material whose piezoelectric d constant is given by equation 2.7. The local field coefficients derived by Furukawa in terms of the properties of the constituent materials of the two-phase system [Furukawa et al. 1979] are given by the following equations.

$$L_X = \frac{5c^c}{3(1-\phi^c)c^p + (2+3\phi^c)c^c} \tag{2.15}$$

$$L_x = \frac{5c^p}{(3+2\phi^c)c^p + 2(1-\phi^c)c^c} \tag{2.16}$$

$$L_E = \frac{3\varepsilon^p}{(2+\phi^c)\varepsilon^p + (1-\phi^c)\varepsilon^c} \tag{2.17}$$

$$L_D = \frac{3\varepsilon^c}{2(1-\phi^c)\varepsilon^p + (1+2\phi^c)\varepsilon^c} \qquad (2.18)$$

Using this formalism the ceramic/polymer composite systems of PZT-epoxy, PZT-PVDF, PZT-PE and PZT-PVA with ceramic volume fractions under 21% were analysed for their dielectric, elastic and piezoelectric properties [Furukawa et al. 1979]. The largest piezoelectric activity amongst these composites was obtained in the PZT-PVDF system in which case the expressions given above, only provide reasonable approximations for volume fractions of the ceramic under 10%. For a PZT volume fraction in the 20% range the measured values of d were found to be 2 to 3 times larger than predicted while similarly the experimental permittivity was found to be larger than that given by equation 2.5 by a factor of two. It was suggested that the reason for the discrepancy between observation and prediction was a consequence of some higher order composite effect like aggregation of the ceramic inclusions which was not accounted for in the derivation of the model.

In order to account for deviations of the 0-3 connectivity behaviour, an approach was conceived by Pardo and co-workers in which the composite was perceived as having a mixed connectivity pattern [Pardo et al. 1988]. Considering ϕ^c to be the total volume fraction of the ceramic in the composite, it was assumed that part of it say $\phi^c_{0\text{-}3}$, would have a 0-3 connectivity whilst the rest of the ceramic in the composite i.e. $\phi^c_{1\text{-}3} = \phi^c - \phi^c_{0\text{-}3}$, would connect to both surfaces of the composite film exhibiting thus 1-3 connectivity.

On measuring the ceramic grain size (w_{gs}) as well as the composite film thickness (t) their ratio (i.e. w_{gs}/t) was computed enabling then through a Monte Carlo simulation, the calculation of the magnitudes of the 0-3 and 1-3 volume fractions, $\phi^c_{0\text{-}3}$ and $\phi^c_{1\text{-}3}$ respectively. Using this approach the piezoelectric constant d_{33} was calculated from :

$$d_{33} = \left(\phi^c_{1\text{-}3} + \phi^c_{0\text{-}3}\alpha_p L_E\right) L_X d^c_{33} \qquad (2.19)$$

where α_p is the poling ratio for the fraction of the ceramic which has a 0-3 connectivity while the other symbols have the meaning stated above. A reasonable agreement was found between equation 2.19 and the experimental results in the transition region from the 0-3 to the 1-3 connectivity when the ceramic grain size was of the same order of magnitude as that of the thickness of the sample.

Zewdie and Brouers [Zewdie et al. 1990] have proposed a calculation procedure similar to that of Pardo and co-workers using modified local field coefficients which were claimed to include the shape of the dispersoid through an ellipsoid index. These local fields were found to be appropriate for intermediate ceramic concentrations.

2.4 - Connectivity approach

In the previous models assumptions were made that the composite is infinite and that the ceramic grains are sufficiently small so that a quasi-homogeneous medium is assumed to exist surrounding the ceramic grains. However, that can no longer be held true if a high concentration of the ceramic dispersoid is present and/or when the ceramic grains are of a

similar magnitude as the dimensions of the composite film (see figure 2.6). Moreover, it has been found experimentally that most of the useful ferroelectric composites fall in one of the latter cases which prompted the need to build up models that could take those facts into account.

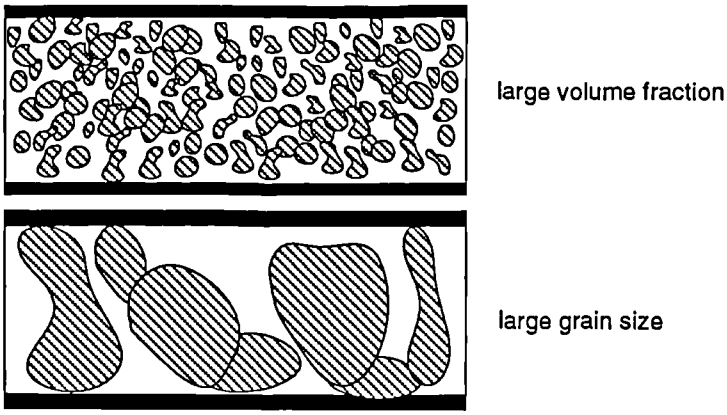

Figure 2.6 - The effect on the connectivity of large grain size and volume loading of the ceramic phase in a composite film

A central concept in the theoretical modelling of this type of composite behaviour is that of connectivity [Newnham et al. 1978] described in the previous chapter (see 1.5 - Fundamentals of ferroelectric composites).

For two phase structures, those in which we are interested, the simplest cases are the series and the parallel two-dimensional structures as represented in figure 2.7. According to Newnham et al. [Newnham et al. 1978] these structures are classified as having a 2-2 connectivity pattern and will form the building blocks of our understanding of 0-3 composites which have either a high concentration of ceramic or a large ceramic grain compared with the dimensions of the sample.

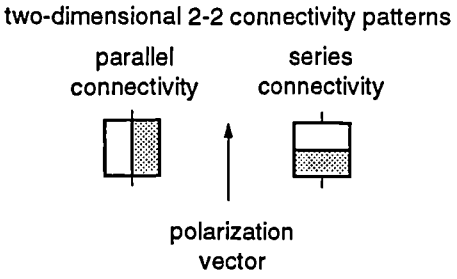

Figure 2.7 - Parallel and series connectivity patterns

The interest in these structures stems from the fact that an ordinary composite can be thought of as being an intermediate stage between these two limiting cases. Thus, in order to calculate the properties of a composite it is proposed here, to carry first the derivation of the elastic, dielectric, piezoelectric and pyroelectric properties for each of these two connectivities. Then using suitable mixing rules the properties of a diphasic composite dependent on the volume fraction of the filler and on the degree of parallel/series connectivity will be computed.

2.4.1 - Parallel connectivity properties

The evaluation of properties of the parallel structure have been the object of numerous

works notably by Newnham et al [Newnham et al. 1978], Smith [Smith 1991; Smith 1993] and others [Takeuchi et al. 1985].

The constitutive equations for each of the ferroelectric phases relate the stress, electric field, temperature, strain and dielectric displacement at every point in that phase. Thus, for the ceramic phase (superscript *c*) the following set of equations are valid:

$$\begin{pmatrix} x_1^c \\ x_2^c \\ x_3^c \\ x_4^c \\ x_5^c \\ x_6^c \\ D_1^c \\ D_2^c \\ D_3^c \end{pmatrix} = \begin{pmatrix} s_{11}^{E,c} & s_{12}^{E,c} & s_{13}^{E,c} & . & . & . & . & . & d_{31}^c & \alpha_1^c \\ s_{12}^{E,c} & s_{11}^{E,c} & s_{12}^{E,c} & . & . & . & . & . & d_{31}^c & \alpha_1^c \\ s_{13}^{E,c} & s_{12}^{E,c} & s_{33}^{E,c} & . & . & . & . & . & d_{33}^c & \alpha_3^c \\ . & . & . & s_{44}^{E,c} & . & . & . & d_{15}^c & . & . \\ . & . & . & . & s_{44}^{E,c} & . & d_{15}^c & . & . & . \\ . & . & . & . & . & 2\left(s_{11}^{E,c} - s_{12}^{E,c}\right) & . & . & . & . \\ . & . & . & . & d_{15}^c & . & \varepsilon_o \varepsilon_{11}^{X,c} & . & . & . \\ . & . & . & d_{15}^c & . & . & . & \varepsilon_o \varepsilon_{11}^{X,c} & . & . \\ d_{31}^c & d_{31}^c & d_{33}^c & . & . & . & . & . & \varepsilon_o \varepsilon_{33}^{X,c} & p_3^c \end{pmatrix} \begin{pmatrix} X_1^c \\ X_2^c \\ X_3^c \\ X_4^c \\ X_5^c \\ X_6^c \\ E_1^c \\ E_2^c \\ E_3^c \\ T^c \end{pmatrix} \tag{2.20}$$

while a similar set of equations (but with a *p* superscript) applies for the polymer phase which for now will be supposed to be ferroelectric as well, with a cylindrical symmetry identical to that of ceramic perovskites. It should be noted that this is true for an unstretched P(VDF/TrFE) ferroelectric polymer. Note that the matrix equation 2.20 is the same as equation 1.7 with an additional column variable to include the pyroelectric effect, in the stress-free condition, through the temperature variable.

In the low frequency range some assumptions can be made [Smith 1991; Smith 1993]. As our first approximation the stress and electric field will be assumed to be independent of the position in the composites phases and thus propagating uniformly throughout each of the phases. This is of course not true in detail but assumed to be so in an average sense.

As our interest lies on the composites with lateral dimensions much larger than its thickness and whose electroded surfaces are perpendicular to the 3-direction, it may be assumed that the electric field in a plane parallel to these electrodes are negligible, i.e.

$$\begin{aligned} E_1^c = E_2^c = E_1^p = E_2^p = 0 \\ D_1^c = D_2^c = D_1^p = D_2^p = 0 \end{aligned} \tag{2.21}$$

Furthermore, we assume that there is an isotropy of stress and strain in the same 1-2 plane, i.e. the 1 and 2 directions are equivalent due to the geometry of the problem coupled to the symmetry of the crystal. Thus,

$$\begin{aligned} X_1^c = X_2^c; \quad x_1^c = x_2^c \\ X_1^p = X_2^p; \quad x_1^p = x_2^p \end{aligned} \tag{2.22}$$

Moreover, as is common in hydrostatic and thickness mode oscillations, it will be assumed that there are no shear stresses or strains [Smith 1991; Smith 1993].

$$\begin{aligned} X_4^c = X_5^c = X_6^c = X_4^p = X_5^p = X_6^p = 0 \\ x_4^c = x_5^c = x_6^c = x_4^p = x_5^p = x_6^p = 0 \end{aligned} \tag{2.23}$$

The constitutive relations for the ceramic and polymer phases respectively embodied in

equation 2.20 now reduce to,

$$\begin{pmatrix} x_1^c \\ x_3^c \\ D_3^c \end{pmatrix} = \begin{pmatrix} s_{11}^c + s_{12}^c & s_{13}^c & d_{31}^c & \alpha^c \\ 2s_{13}^c & s_{33}^c & d_{33}^c & \alpha^c \\ 2d_{31}^c & d_{33}^c & \varepsilon_o \varepsilon_{33}^c & p^c \end{pmatrix} \begin{pmatrix} X_1^c \\ X_3^c \\ E_3^c \\ T^c \end{pmatrix} \qquad (2.24\text{ a})$$

and

$$\begin{pmatrix} x_1^p \\ x_3^p \\ D_3^p \end{pmatrix} = \begin{pmatrix} s_{11}^p + s_{12}^p & s_{13}^p & d_{31}^p & \alpha^p \\ 2s_{13}^p & s_{33}^p & d_{33}^p & \alpha^p \\ 2d_{31}^p & d_{33}^p & \varepsilon_o \varepsilon_{33}^p & p^p \end{pmatrix} \begin{pmatrix} X_1^p \\ X_3^p \\ E_3^p \\ T^p \end{pmatrix} \qquad (2.24\text{ b})$$

where the superscripts E and X for the s and ε properties were omitted.

In order to calculate the composite properties the constitutive relationships for the composite as a whole will have to be established. These relations are of a similar type as those of the equations 2.24 but with the superscripts in the variables being removed to denote average composite properties, i.e.

$$\begin{pmatrix} x_1 \\ x_3 \\ D_3 \end{pmatrix} = \begin{pmatrix} s_{11} + s_{12} & s_{13} & d_{31} & \alpha \\ 2s_{13} & s_{33} & d_{33} & \alpha \\ 2d_{31} & d_{33} & \varepsilon_o \varepsilon_{33} & p \end{pmatrix} \begin{pmatrix} X_1 \\ X_3 \\ E_3 \\ T \end{pmatrix} \qquad (2.25)$$

It was assumed in equations 2.24 and 2.25 that the linear expansion coefficient is isotropic which may be not strictly correct. It is often the case that there are no experimental values for the anisotropy of this property. Furthermore, the impact of the anisotropy would amounts to a second order effect in comparison with the difference between α^c and α^p.

It is our aim to calculate the elastic, dielectric, piezoelectric and pyroelectric properties of the composite as described in the matrix of equation 2.25 in terms of the properties of the phases as described in the matrices of equation 2.24.

With this objective in mind relationships must be established between the magnitudes of the stress, strain, electric field, electric displacement and temperature acting on the phases and on the composite [Smith 1993] These will be simplifying assumptions which take into account the parallel connectivity of the sample (see figure 2.8).

The first condition is that the composite sample is in a state of thermal equilibrium which means that the average composite temperature is the same as that of the ceramic and the polymer phase, i.e.

$$T = T^c = T^p \qquad (2.26)$$

The second and third conditions establish that due to the parallel connectivity it can be assumed that the strain (see figure 2.8) and the electric field in the 3-direction are approximately the same in both phases.

$$x_3 = x_3^c = x_3^p \qquad (2.27)$$

$$E_3 = E_3^c = E_3^p \tag{2.28}$$

The assumption embodied in equation 2.27 calls for a fine width on the part of the composite structure relative to the thickness of the composite while the equality of the electric fields in the 3-direction stems directly from the configuration of the electrodes.

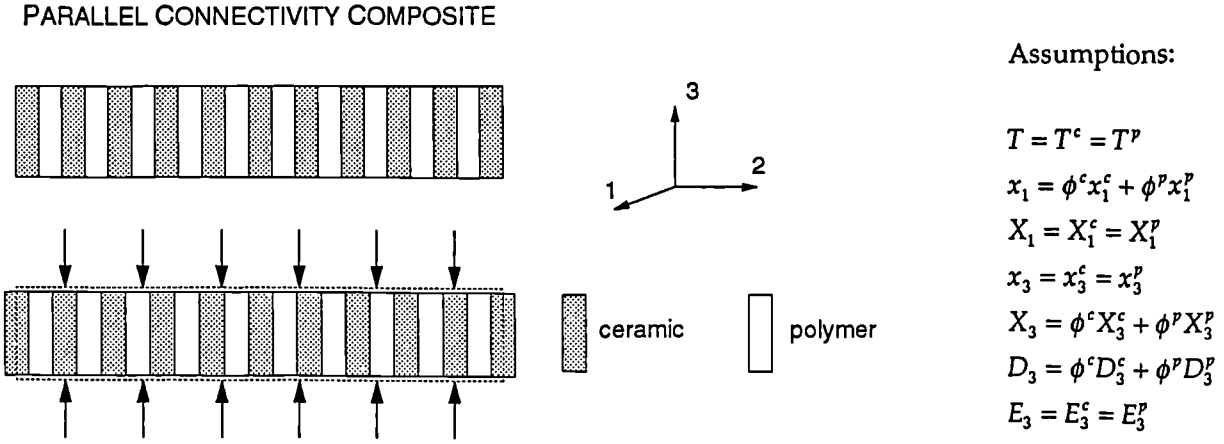

Figure 2.8 - The strain in the 3-direction on both phases are similar if the width of the ceramic rods are small compared with the thickness of the composite.

In the lateral dimension it is assumed that the stress in the phases are equal and thus,

$$X_1 = X_1^c = X_1^p \tag{2.29}$$

while the overall strain in the lateral dimension is a juxtaposition of the contribution from each phase,

$$x_1 = \phi^c x_1^c + \phi^p x_1^p \tag{2.30}$$

where ϕ^c and ϕ^p are the volume fractions of the ceramic and the polymer in the composite respectively.

Finally, the stress and electric displacement in the 3-direction are uniformly distributed between the phases and thus are also obtained by adding the weighted contributions of the ceramic and the polymer,

$$X_3 = \phi^c X_3^c + \phi^p X_3^p \tag{2.31}$$

$$D_3 = \phi^c D_3^c + \phi^p D_3^p \tag{2.32}$$

Using equations 2.26-32 and the matrix equations described in 2.24 the variables $X_1^c, X_3^c, x_1^c, x_3^c, D_3^c, E_3^c$ and $X_1^p, X_3^p, x_1^p, x_3^p, D_3^p, E_3^p$ are eliminated and a matrix equation similar to that of equation 2.25 is obtained with the composite variables x_1, x_3, D_3 as independent variables and X_1, X_3, E_3 and T as the dependent ones.

The property matrix thus obtained for the parallel connectivity composite is specified as a function of the properties of the constituent phases. Hence by identifying this matrix with that of equation 2.25, expressions relating the composite properties to those of the phases are obtained which are listed in table 2.1.

A useful way of looking into each of the properties of composites is to classify its contributing terms as either a sum, a combination or a product of the properties of its phases

as explained in section 1.5. Regarding the parallel connectivity composite, the first and second terms of the permittivity ε (equation 2.39) depend only on the permittivity of the constituent materials. A weighted average which takes into account the volume fractions of the two phases is used, and thus we classify this type as a sum contribution to the properties of the composite. This type of contribution, is characterised as being bound by the property values of the constituent phases. It is possible to identify a similar sum contribution in other properties as in the first and second terms of the equation for the pyroelectric constant (equation 2.40).

TABLE 2.1 - DETERMINATION OF PROPERTIES FOR A PARALLEL CONNECTIVITY COMPOSITE

		equation no.
$\frac{1}{s_{33}} = \frac{\phi^c}{s_{33}^c} + \frac{\phi^p}{s_{33}^p}$		(2.33)
$\frac{s_{13}}{s_{33}} = \frac{\phi^c s_{13}^c}{s_{33}^c} + \frac{\phi^p s_{13}^p}{s_{33}^p}$		(2.34)
$s_{11} = \phi^c s_{11}^c + \phi^p s_{11}^p + \Delta s_{11}$	$\Delta s_{11} = -\frac{\left(s_{13}^c - s_{13}^p\right)^2 s_{33}\phi^c\phi^p}{s_{33}^c s_{33}^p}$	(2.35)
$s_{12} = \phi^c s_{12}^c + \phi^p s_{12}^p + \Delta s_{12}$	$\Delta s_{12} = -\frac{\left(s_{13}^c - s_{13}^p\right)^2 s_{33}\phi^c\phi^p}{s_{33}^c s_{33}^p}$	(2.36)
$\frac{d_{33}}{s_{33}} = \frac{\phi^c d_{33}^c}{s_{33}^c} + \frac{\phi^p d_{33}^p}{s_{33}^p}$		(2.37)
$d_{31} = \phi^c d_{31}^c + \phi^p d_{31}^p + \Delta d_{31}$	$\Delta d_{31} = \frac{\left(d_{33}^c - d_{33}^p\right)\left(s_{13}^p - s_{13}^c\right)s_{33}\phi^c\phi^p}{s_{33}^c s_{33}^p}$	(2.38)
$\varepsilon = \phi^c\varepsilon^c + \phi^p\varepsilon^p + \Delta\varepsilon$	$\Delta\varepsilon = -\frac{\left(d_{33}^c - d_{33}^p\right)^2 s_{33}\phi^c\phi^p}{\varepsilon_o s_{33}^c s_{33}^p}$	(2.39)
$p = \phi^c p^c + \phi^p p^p + \Delta p$	$\Delta p = \frac{\left(d_{33}^c - d_{33}^p\right)\left(\alpha^p - \alpha^c\right)s_{33}\phi^c\phi^p}{s_{33}^c s_{33}^p}$	(2.40)
$\frac{\alpha}{s_{33}} = \frac{\phi^c\alpha^c}{s_{33}^c} + \frac{\phi^p\alpha^p}{s_{33}^p}$		(2.41)

Note: superscripts c and p represent properties of the ceramic and polymer phases respectively while an absence of superscript denotes composite properties. Some of the composite properties, such as d_{33} for example, are given using the properties of the constituent materials as well as the calculated elastic compliance for the composite s_{33}.

In a combination term the resulting property is calculated by taking some weighted average involving not only the same properties and volume fractions but other properties of the phases as in the calculation of d_{33} (equation 2.37) which takes the values of s_{33} of the raw materials also into account. Note that the calculation of s_{13} proceeds in a similar manner.

A third and more interesting contribution for a composite property occurs when there exists a mismatch of properties between the phases which interact to add an extra

contribution to an initially unrelated property. An example of these product type of contribution is the third term of the permittivity (equation 2.39) where the d_{33} mismatch between the phases, weighted by a suitable combination of their elastic compliances, gives rise to an extra contribution to the value of permittivity. The magnitude of this product contribution is sometimes small enough to be viewed as a modulation of the overall properties obtained when using just the sum and combination terms and as a result is not always a significant factor in the total value of a composite property. This is the case of the permittivity (see figure 2.9) where the product term contributes with less than 7% at low ceramic volume fraction to the total calculated permittivity in a composite of Calcium modified Lead Titanate (PTCa) embedded in a P(VDF/TrFE) polymer. This contribution decreases further to less than 1% for a ceramic content over 50%.

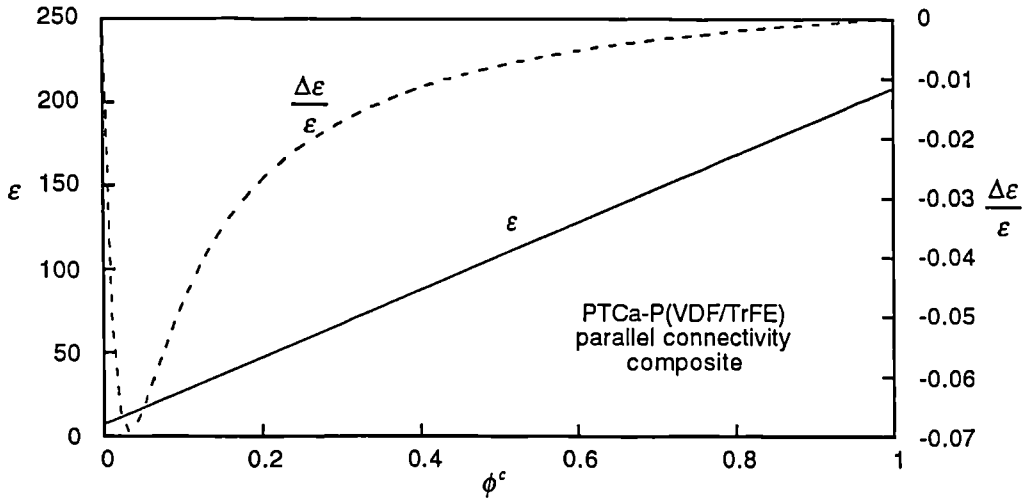

Figure 2.9 - Permittivity and the product property relative contribution resulting from piezoelectric coupling mismatch as function of the ceramic loading. It was assumed that the polymer had no electro-active properties.

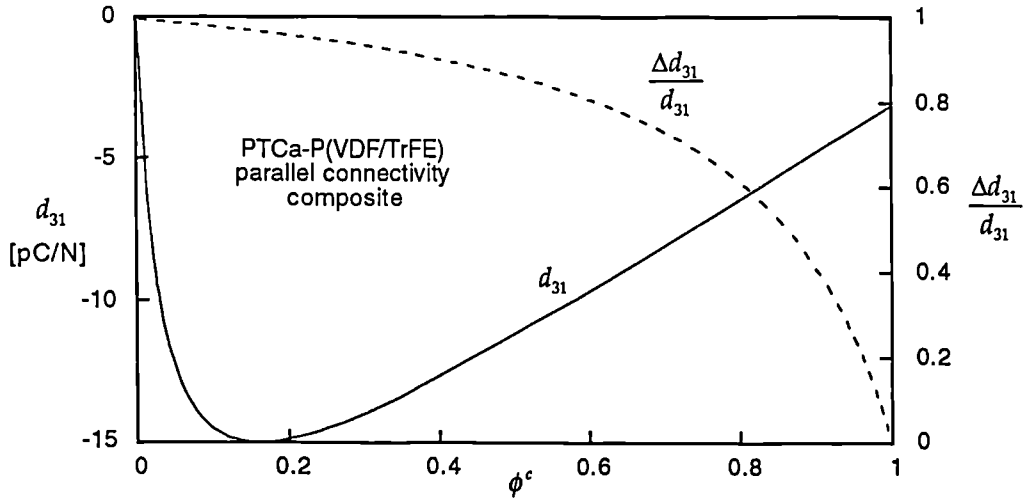

Figure 2.10 - d_{31} and its product property relative contribution resulting from the piezoelectric d_{33} and elastic s_{13} mismatch as function of the ceramic loading.

In other situations such as the d_{31} (equation 2.38) of the same composite as shown in figure 2.10, the product contribution can be as large as to be almost the sole contributor to its computed value in the composite material.

2.4.2 - Series connectivity properties

For a series connectivity composite shown in figure 2.11, the assumptions are the same as those for the parallel connectivity sample up to the discussion of equation 2.25, i.e., the electrical field parallel to the plane of the electrodes vanishes while there is an equivalence of the 1 and 2 directions regarding the mechanical stress and strain (equations 2.21 and 2.22). Moreover, the shear stress and strain are supposed to vanish as before (equations 2.23).

Furthermore, the sample is supposed to be in thermal equilibrium while the linear expansion coefficient is regarded to be an isotropic quantity.

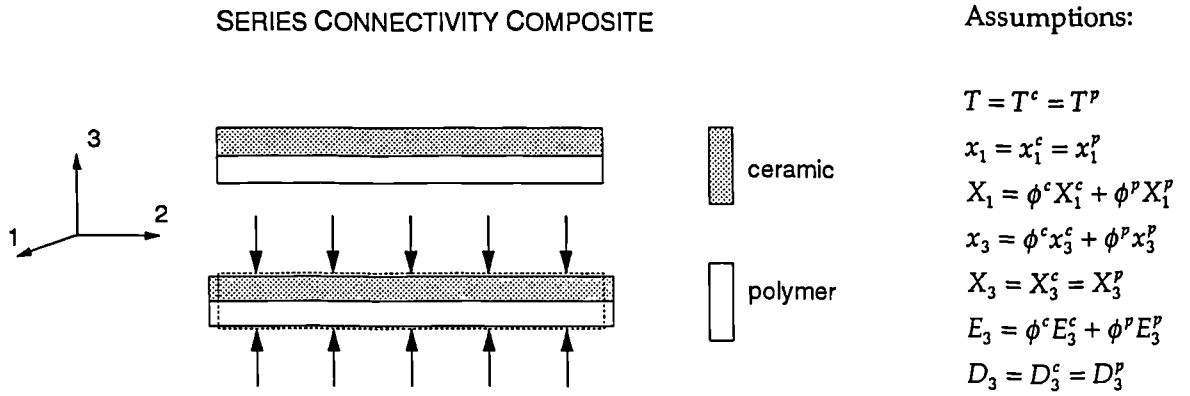

Figure 2.11 - The stress in the 3-direction for a series connectivity composite is equal in both phases.

Thus, equations 2.24 and 2.25 are also valid for the series instance, together with the statement of the problem ensuing the establishment of equation 2.25. The fact that it is a series connectivity problem emerges in the later assumptions.

For this connectivity case the stress in the 3-direction is equal in both phases while the strain is distributed between the phases (see figure 2.11), i.e.

$$X_3 = X_3^c = X_3^p \tag{2.42}$$

$$x_3 = \phi^c x_3^c + \phi^p x_3^p \tag{2.43}$$

while the converse happens in the 1,2-plane,

$$X_1 = \phi^c X_1^c + \phi^p X_1^p \tag{2.44}$$

$$x_1 = x_1^c = x_1^p \tag{2.45}$$

The electric field in the 3-direction is shared between the two phases and the dielectric displacement in the same direction is equal in both phases,

$$E_3 = \phi^c E_3^c + \phi^p E_3^p \tag{2.46}$$

$$D_3 = D_3^c = D_3^p \tag{2.47}$$

Using equations 2.42-2.47 together with those of 2.24 the properties for the series composite can be determined in a similar way as in the case of the parallel connectivity composite yielding the expressions listed in table 2.2.

TABLE 2.2 - DETERMINATION OF PROPERTIES FOR A SERIES CONNECTIVITY COMPOSITE

	equation no.
$s_{33} = \phi^c s_{33}^c + \phi^p s_{33}^p + \Delta s_{33}; \quad \Delta s_{33} = -\frac{\left(d_{33}^c - d_{33}^p\right)^2 \phi^c \phi^p}{a_1} - 2\frac{\left(\left[d_{33}^c - d_{33}^c\right]a_3 - \left[s_{13}^c - s_{13}^c\right]a_1\right)^2 \phi^c \phi^p}{\left(a_2 a_1 - 2a_3^2\right)a_1}$	(2.48)
$\frac{s_{13}}{\left(s_{11}+s_{12}\right)} = \frac{\phi^c s_{13}^c}{\left(s_{11}^c+s_{12}^c\right)} + \frac{\phi^p s_{13}^p}{\left(s_{11}^p+s_{12}^p\right)}$	(2.49)
$\frac{1}{\left(s_{11}+s_{12}\right)} = \frac{\phi^c}{\left(s_{11}^c+s_{12}^c\right)} + \frac{\phi^p}{\left(s_{11}^p+s_{12}^p\right)}$	(2.50)
$\frac{d_{33}}{\varepsilon} = \frac{\phi^c d_{33}^c}{\varepsilon^c} + \frac{\phi^p d_{33}^p}{\varepsilon^p}$	(2.51)
$d_{31} = \frac{d_{31}^p\left(s_{11}^c+s_{12}^c\right)\varepsilon_o \varepsilon^c \phi^p + d_{31}^c\left(s_{11}^p+s_{12}^p\right)\varepsilon_o \varepsilon^p \phi^c}{a_2 a_1 - 2a_3^2}$	(2.52)
$\frac{1}{\varepsilon} = \frac{\phi^c}{\varepsilon^c} + \frac{\phi^p}{\varepsilon^p}$	(2.53)
$\frac{p}{\varepsilon} = \frac{\phi^c p^c}{\varepsilon^c} + \frac{\phi^p p^p}{\varepsilon^p}$	(2.54)
$\alpha = \alpha^c \phi^c + \alpha^p \phi^p$	(2.55)

Auxiliary definitions:

$a_1 = \varepsilon_o\left(\phi^p \varepsilon^c + \phi^c \varepsilon^p\right)$

$a_2 = \phi^p\left(s_{11}^c + s_{12}^c\right) + \phi^c\left(s_{11}^p + s_{12}^p\right)$

$a_3 = \phi^p d_{31}^c + \phi^c d_{31}^p$

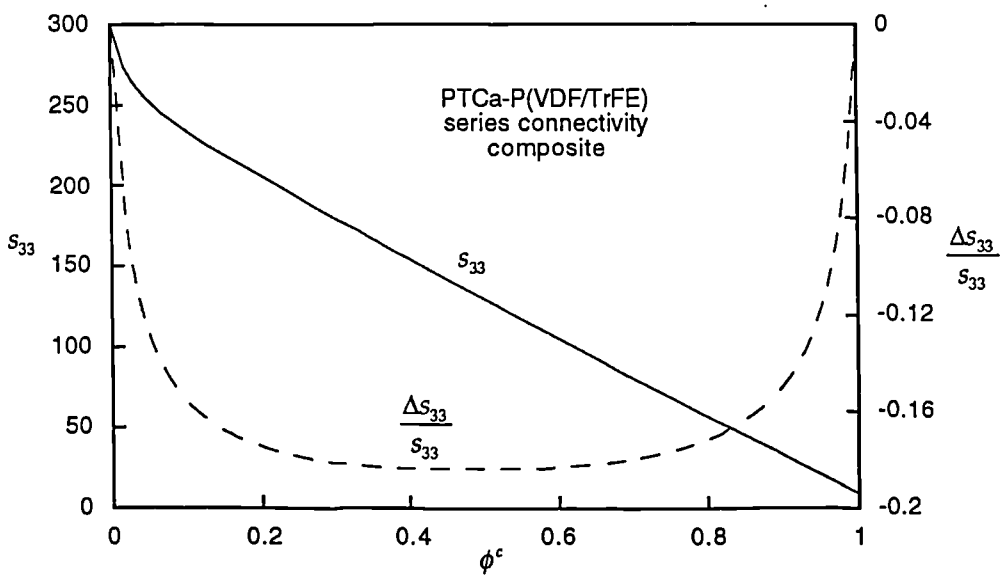

Figure 2.12 - Elastic stiffness constant s33 for which the product property makes a significant contribution.

These expressions do not include the product property terms except in the case of the s_{33} coefficient (equation 2.48) where the simulation of its contribution in a PTCa-P(VDF/TrFE) series composite was found to be significant (see figure 2.12). For the other properties the product property term was found to be small or negligible as for instance in the case of the permittivity where the additional term contributed with less than 0.0002% to

the total value of that property in the composite (see figure 2.13).

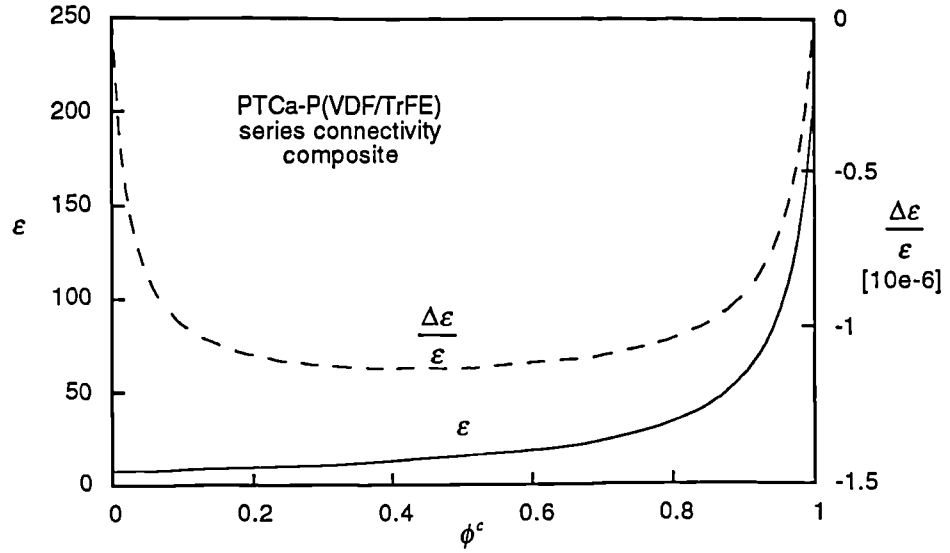

Figure 2.13 - Permittivity for a PTCa-P(VDF/TrFE) series connectivity composite

Comparing the expressions of the permittivity between the parallel and series connectivity diphasic structures it may be observed that their sum property contributions are nothing more than those obtained by using the rules for calculating the parallel and series capacitances respectively, applied to the permittivity of the composites. The same type of reasoning is applicable to the composite elastic constants whilst in the case of the piezoelectric and pyroelectric constants which involve a coupling between different sets of properties (i.e. charge/stress and charge/temperature respectively) that reasoning is not quite as straightforward.

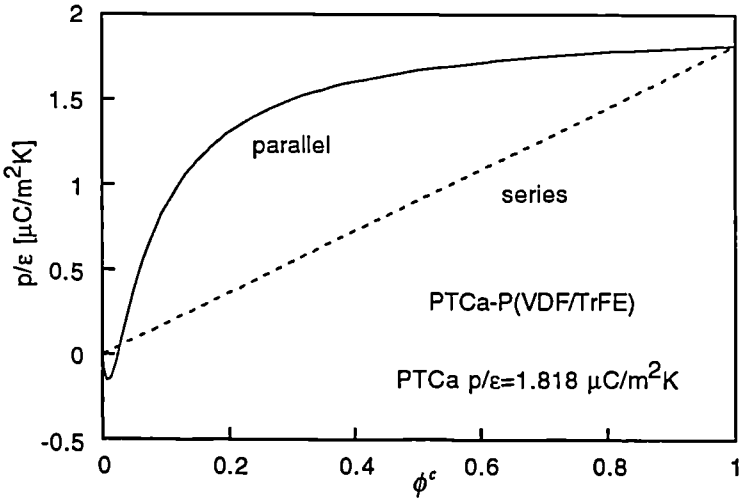

Figure 2.14 - Pyroelectric FOMp =(p/ε) for parallel and series connectivity PTCa-P(VDF/TrFE) composites.

It is useful to compare the piezoelectric and pyroelectric constants computed for a composite based on the parallel and series connectivities. In figures 2.14 and 2.15 we have calculated the pyroelectric Figure Of Merit (FOM_p) defined as p/ε and the hydrostatic piezoelectric $FOM_h = d_h g_h$, for both types of connectivities in a PTCa-P(VDF/TrFE) composite.

Comparing these graphs we can observe that the parallel connectivity structure shows

superior piezoelectric and pyroelectric properties than its series counterpart for the same ceramic volume fraction.

The pyroelectric FOM_p for the parallel connectivity composite can be approximated, if the product property contribution is small, by the ratio of equations 2.39 and 2.40 ,

$$\frac{p}{\varepsilon} \approx \frac{\phi^c p^c + \phi^p p^p}{\phi^c \varepsilon^c + \phi^p \varepsilon^p} \tag{2.56}$$

Now, if the polymer is not pyroelectric (p^p=0) and if its permittivity is small compared to that of the ceramic ($\varepsilon^p << \varepsilon^c$) as is usually the case, the pyroelectric coefficient for intermediate ceramic content will then be approximately given by,

$$\frac{p}{\varepsilon} \approx \frac{p^c}{\varepsilon^c} \tag{2.57}$$

Thus, the pyroelectric FOM_p for the parallel connectivity composite rapidly approaches that of the ceramic at intermediate concentrations as observed in figure 2.14. For the series composite and using the same arguments the FOM_p is given by the ratio of equations 2.54 to 2.53,

$$\frac{p}{\varepsilon} \approx \frac{\phi^c p^c \varepsilon^p + \phi^p p^p \varepsilon^c}{\varepsilon^c \varepsilon^p} = \phi^c \frac{p^c}{\varepsilon^c} + \phi^p \frac{p^p}{\varepsilon^p} \overset{\text{if } p^p=0}{=} \phi^c \frac{p^c}{\varepsilon^c} \tag{2.58}$$

which means that the pyroelectric coefficient in a series composite increases roughly linearly with the ceramic content as shown in figure 2.14.

We can try to understand the above consideration in a qualitative way through the following argument. The pyroelectric FOM_p is roughly proportional to the voltage responsivity of the material. In a parallel connectivity composite the charge generated by the ceramic through the pyroelectric coefficient , on heating the sample by one degree, has to charge both the ceramic and the polymer connected in parallel. But because the polymer phase has a low capacitance it will only need a small part of the total pyroelectric charge generated by the ceramic while the bulk of it will be used to charge the ceramic part. Thus the voltage responsivity will not degrade appreciably if a low permittivity material such as a polymer, is connected in parallel.

In the series connectivity case though, the pyroelectric response will charge the ceramic capacitor up to a certain voltage. Hence, the average voltage in the composite will be decreased by an amount proportional to the length of polymer in series with the ceramic.
It is interesting to note, that neither the series nor the parallel connectivity provides a more efficient composite, in pyroelectric terms, than the pure ceramic although in the case of the parallel connectivity a reasonable approximation can be achieved. Other considerations such as the flexibility of the composite, low manufacturing cost, large area availability or even the lower thermal diffusivity due to the polymer matrix must then come into play in choosing one alternative in detriment of the other.

The piezoelectric hydrostatic FOM_h for the series and parallel connectivity of a PTCa-P(VDF/TrFE composite is plotted in figure 2.15. It is again apparent that higher electro-active properties are obtained for the parallel than for the series connectivity. Similar

arguments as for the FOM_p, can be applicable in this case where the relevant variables are the compliance and the capacitance of the phases.

Other choices of the electro-active properties yield support for the view that a parallel connectivity composite is a better choice than a series connectivity as far as the electro-active properties are concerned.

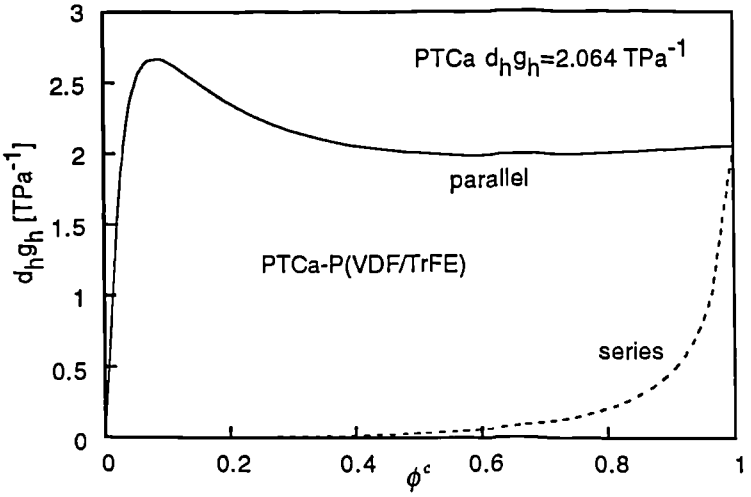

Figure 2.15 - Piezoelectric hydrostatic FOM_h for parallel and series connectivity PTCa-P(VDF/TrFE) composites.

The main feature of our particular choice of ceramic-polymer composite (i.e. PTCa-P(VDF/TrFE) is the high anisotropy of the piezoelectric constants in the ceramic, a feature inherited by this composite, together with the low permittivity mismatch of the ceramic relative to the polymer at temperatures approaching the T_C of the polymer. In other respects, such as the compliances and linear expansion, it exhibits typical properties of this class of materials.

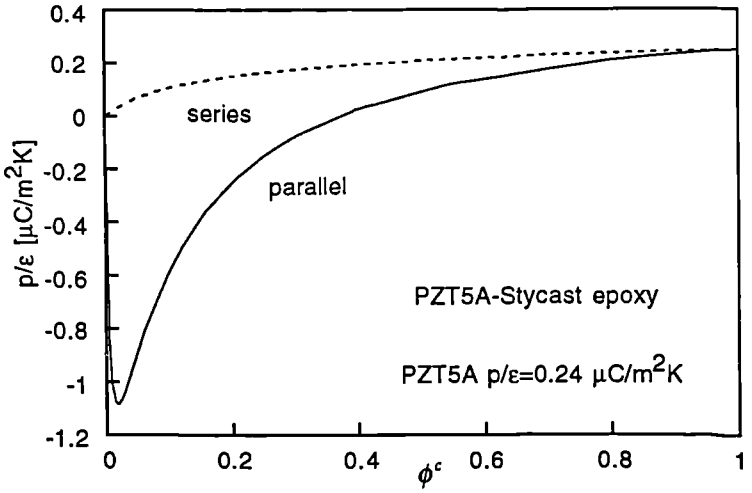

Figure 2.16 - FOM_p comparison between the series and parallel connectivities for a PZT5A-Stycast epoxy composite.

A popular choice among composites has been the PZT-epoxy combination. In figures 2.16 and 2.17 are shown the electro-active properties of the series and parallel connectivity composites made of PZT5A and Stycast a stiff polymer. PZT5A is not a good pyroelectric material and thus its composites do not show as high values for this property as the PTCa-

P(VDF/TrFE) combination.

There is an interesting phenomenon at low volume fractions of the ceramic for the pyroelectric coefficient of the parallel connectivity composite (figure 2.16). Due to the product property contribution to the pyroelectric coefficient through the piezoelectric effect and linear expansion mismatch between the phases, the pyroelectric coefficient changes its sign relative to that of the ceramic attaining a value of 1 $\mu C/m^2K$. This occurs, however, only at low ceramic volume fraction.

The FOM_h for the same composite and structures is plotted in figure 2.17. The series FOM_h does not exhibit a significant value in the whole range in agreement with that of the ceramic FOM_h. The parallel connectivity however shows a considerable increase in the FOM_h mainly due to a decrease of the d_{31} value relative to that of d_{33}.

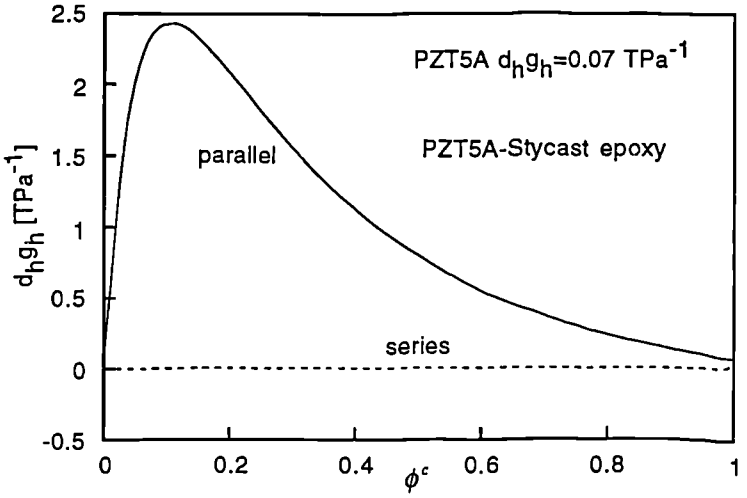

Figure 2.17 - FOM_h comparison between the series and parallel connectivities for a PZT5A-Stycast epoxy composite.

To determine the thickness electromechanical coupling factor k_t, using equation 1.12 it is necessary to know the e_{33}, c_{33}^D and ε_{33}^x properties of the composite. Although these values were not contemplated in the previous formalism by the use of the relationships [Moulson et al. 1990]

$$k_{33} = \frac{d_{33}}{\sqrt{\varepsilon_o \varepsilon_{33}^X s_{33}^E}} \tag{2.59}$$

$$k_p = -\frac{d_{31}}{\sqrt{\frac{\varepsilon_o \varepsilon_{33}^X}{2}\left(s_{11}^E + s_{12}^E\right)}} \tag{2.60}$$

and the approximate formula,

$$1 - k_t^2 \approx \frac{1 - k_{33}^2}{1 - k_p^2} \tag{2.61}$$

it is possible to calculate k_t using the present theory. In figure 2.18 is shown the k_t estimated for four different parallel connectivity composites. The ceramics used were PZT5A and PTCa while the polymers were Stycast epoxy and P(VDF/TrFE).

The difference in these two ceramics is seen more strikingly for intermediate ceramic

content. While the PZT5A loaded composite exhibits higher k_t than the ceramic in its pure form, in the PTCa composite, this does not occur. The PZT5A composite at intermediate concentrations seems to have a higher anisotropy than the pure ceramic while k_{33} is kept at a high value (see equation 2.61). Thus, the efficiency of converting mechanical vibrations in the thickness mode into electrical energy increases.

In PTCa the anisotropy is already built onto the ceramic and thus there is not a significant gain in an increase of anisotropy mechanism by using a polymer matrix. Hence for this ceramic k_t rapidly increases at low ceramic concentrations to a value near its pure value which is maintained throughout the rest of the concentration range.

The polymers do not exhibit such a striking difference between each other although it appears that P(VDF/TrFE) is a better choice probably due to its higher compliance.

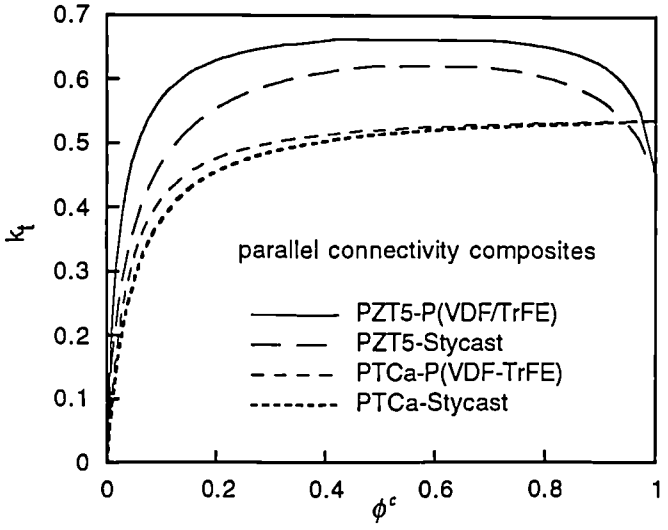

Figure 2.18 - Thickness electromechanical coupling factor k_t for various parallel connectivity composites.

These findings are in general agreement with Smith and Auld [Smith 1991] where the constitutive relations used, involved the set described by equation 1.3 (i.e. e, ε^x, c^E). A very interesting approach in that work was the plot of the composite k_t as a function of its acoustic impedance Z_a using the ceramic volume fraction as an parametric variable as shown in figure 2.18. In this figure the acoustic impedance was calculated using the relationship [Moulson et al. 1990],

$$Z_a = \sqrt{\rho c_{33}^D} \tag{2.62}$$

where ρ and $c^D{}_{33}$ are the density and the elastic stiffness constant respectively. The density of the composite is given by,

$$\rho = \phi^c \rho^c + \phi^p \rho^p \tag{2.63}$$

while $c^D{}_{33}$ is given in terms of the pre-calculated $s^E{}_{ij}$ values by [Moulson et al. 1990],

$$c_{33}^D = \frac{s_{11}^E + s_{12}^E}{s_{33}^E\left(s_{11}^E + s_{12}^E\right) - 2s_{13}^{E\,2}} \tag{2.64}$$

Using such a graph it is possible to target a specific transducer material with a desired

acoustic impedance and thickness electromechanical coupling factor.

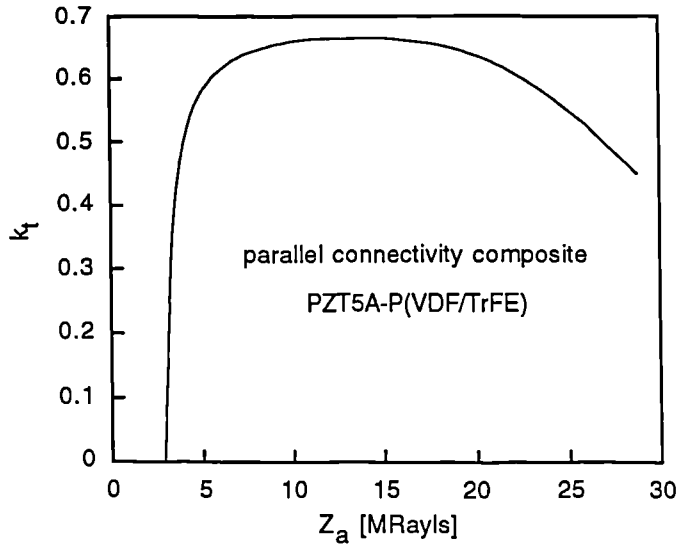

Figure 2.19 - Composite thickness electromechanical coupling factor k_t as a function of its acoustic impedance.

2.5 - 0-3 composites properties: cube models

In order to simulate theoretically the 0-3 type of composites an approach to the properties of diphasic materials known as cube model, was first proposed by Pauer [Pauer 1973]. This model consists of a cube with unit dimensions made of the host material (i.e. polymer) where another smaller cube made of the dispersoid (i.e. ceramic) is embedded (see figure 2.20a).

The aim of this model is then to find out the dimensions of the smaller cube such that the new-found equivalent cube has similar properties as those of the composite material.

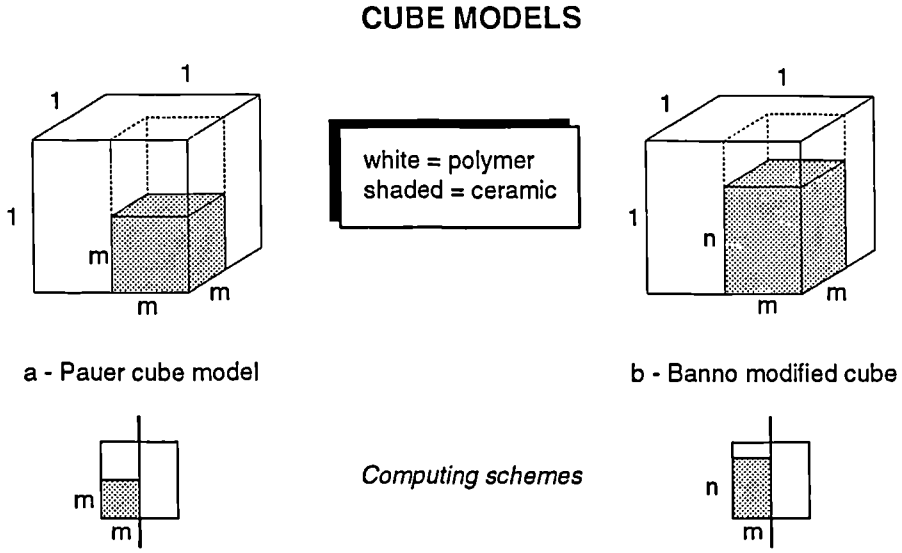

Fig. 2.20 - Schematic of the Pauer simple cube and (b) Banno's modified cube.

A way to calculate the properties of such cube is by the use of the computing scheme outlined under it, where each of the phases behaves as a series or a parallel component in analogy with an electrical circuit. For example in the Pauer cube a polymer part is connected in parallel with a branch comprising a polymer in series with a ceramic element.

Using the expressions for the series and parallel connectivities developed earlier it is a straightforward matter to calculate any property of this cube. First the properties of the series branch are calculated. In this case the volume fraction of the ceramic inside the volume of the series circuit branch is,

$$\phi^c(\text{series}) = \frac{m^3}{m^2} = m \tag{2.65}$$

while the polymer volume fraction in the same branch is $\phi^p = 1 - \phi^c = 1 - m$, allowing thus the calculation of the properties of the series branch. The properties of the cube can now be calculated by calculating the properties of the parallel connectivity circuit comprising the series circuit and the polymer part. The volume fraction of the series circuit and the polymer part to the total volume of the cube (i.e. unity) are given by,

$$\phi^{series} = m^2; \quad \phi^p(\text{parallel}) = 1 - m^2 \tag{2.66}$$

respectively. Although the expressions for the series and parallel connectivities defined above are general and symmetric in that they assume that both phases can be electro-active it should be pointed out that in the present parallel circuit only the series branch exhibits electro-active properties.

This model has thus one degree of freedom represented by the size of the ceramic cube embedded in the polymer and thus any property can be plotted against the m-parameter. Finally, as the m-parameter is related to the total ceramic volume fraction in the composite by,

$$\phi^c = m^3 \tag{2.67}$$

each of the composite properties can be plotted as a function of the ceramic volume fraction as shown in figure 2.21 for the permittivity and the pyroelectric FOM_p in a PTCa-P(VDF/TrFE) composite.

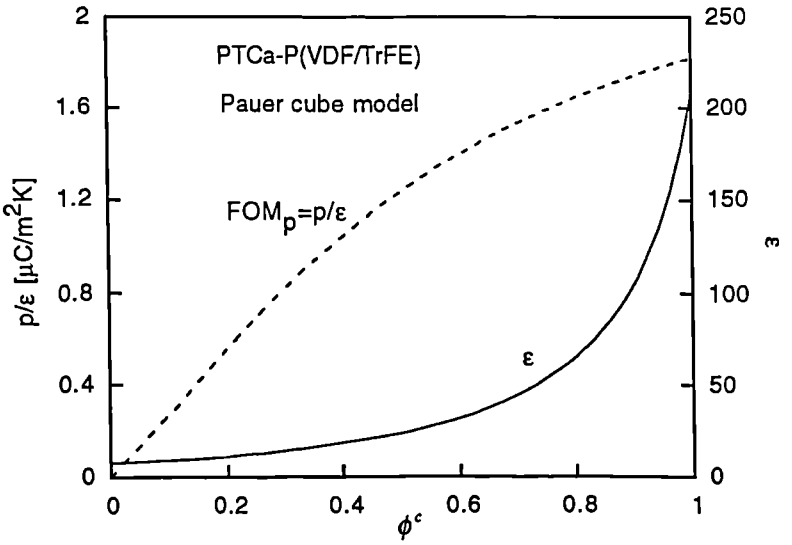

Figure 2.21 - Permittivity and pyroelectric FOM_p calculated for the Pauer cube model of a PTCa-P(VDF/TrFE) composite.

The dependence of these properties on volume fraction can be observed to obey

essentially that of a series composite. Thus, as we have seen before, for the series connectivity, the ceramic properties are not brought about until the composite is loaded with a high ceramic content, in contrast with the parallel connectivity as have been explained before.

The Pauer cube is adequate for true 0-3 composites composed primarily of small approximately spherical ceramic grains embedded in a matrix at low volume concentrations. This model, however, runs into difficulties either when large ellipsoidal grains compared to the thickness of the composites or at high ceramic volume fractions are employed.

The introduction of asymmetry into the ceramic cube was proposed by Banno [Banno et al. 1983; Banno 1985] by the so-called modified cubes model. As shown in figure 2.20 (b) the ceramic block inside the cube is given an additional degree of freedom with its height (i.e n) independent of its length and width which remain equal to each other (i.e. m). Thus, on varying the parameters n and m of the ceramic block either a pure series or parallel connectivity can be obtained. Other modifications [Lee et al. 1990] were proposed to this model notably by Garner et al [Garner et al. 1989] to improve on the isotropy of the modified cubes model. The approach to this model as will be described in this study, departs somewhat from the original work of Banno, viz., namely in the way the dimensions of the cube are defined as well as in the 2D approach that will be presented here.

According to this model each of the properties in the composite as well as the total ceramic volume fraction thus depend both on n and m. In particular

$$\phi^c = nm^2 \tag{2.68}$$

Thus a contour plot in the m-n plane can be drawn with lines of constant volume fraction as shown in figure 2.22.

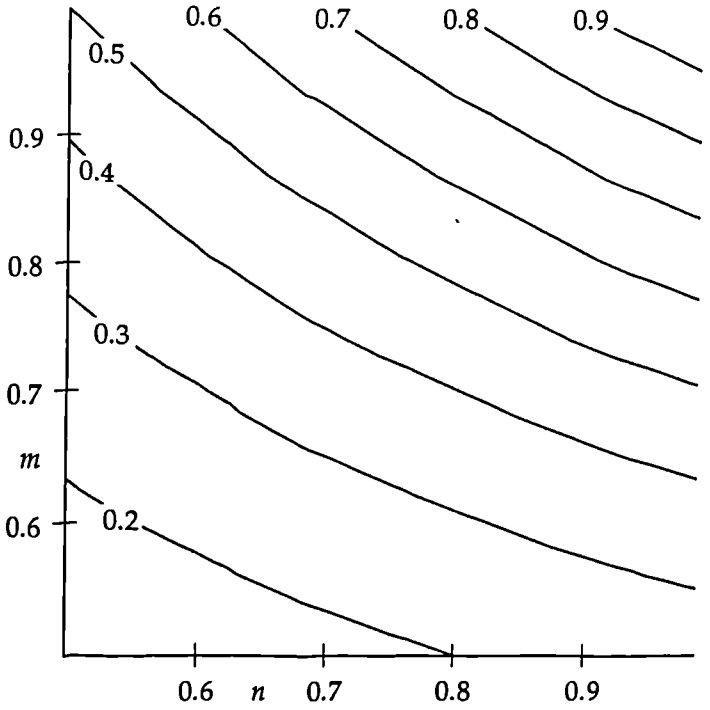

Figure 2.22 - Volume fraction contour plot as a function of the n *and* m *parameters.*

The calculation of the composite properties are accomplished using the composite equivalent circuit model drawn below the Banno cube of figure 2.20(b). A similar technique as that used in the computation of the Pauer cube model, is employed although with different expressions for the relevant volume fractions. In table 2.3 these quantities are listed.

TABLE 2.3 - VOLUME FRACTIONS USED IN THE SERIES AND PARALLEL CIRCUIT BRANCHES IN THE BANNO CUBE MODEL

	ϕ^c	ϕ^p	ϕ^s
SERIES	n	1-n	
PARALLEL		$1-m^2$	m^2
TOTAL	nm^2		

A difference from the previous cube model is that each composite property is now dependent on two variables (i.e. n and m) and thus in analogy with the ceramic volume fraction a contour graph can be plotted for each property in the n-m plane. In figures 2.23 and 2.24 contour plots of the permittivity and the pyroelectric FOM_p were drawn for a PTCa-P(VDF/TrFE) composite.

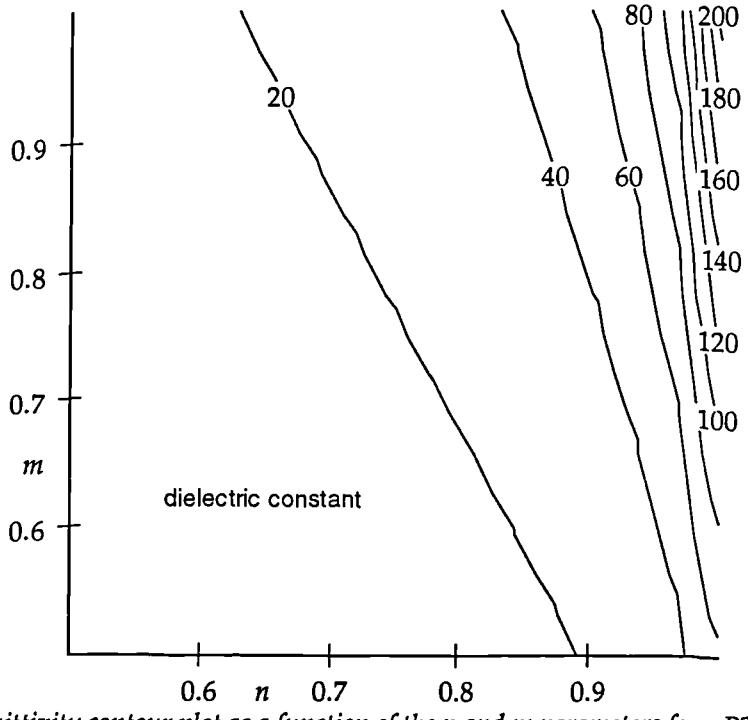

Figure 2.23 - Permittivity contour plot as a function of the n and m parameters for a PTCa-P(VDF/TrFE) composite.

In the n-m plane important lines can be identified. For example a pure series composite can be identified by referring to figure 2.20(b) with the m=1 line. Along this line, the composite behaves as being equivalent to a two layer composite whose ceramic thickness layer is equal to n and thus with a ceramic volume fraction also equal to n. This can be checked by comparing with the previous results for the permittivity of a series composite

made of the same raw materials plotted in figure 2.13. In that figure it was found that the permittivity for concentrations up to 80% of ceramic is small (i.e. 20-40), beyond which it increased steeply in agreement with the composite permittivity behaviour along the m=1 line of figure 2.23. A similar outcome is valid for other properties along this line.

Another important line is the parallel connectivity line n=1. Along this line the composite has a parallel connectivity whose volume fraction according to figure 2.20(b) is m^2. *This* can also be checked with the previous parallel property results.

Finally $n = m$ is the Pauer cube model line as can be confirmed from figure 2.21. The n-m plane can thus represent a blending of the series and parallel connectivity properties. It is thus clear that in order to get higher electroactive properties the composite should lie closer to the n=1 line where parallel connectivity properties are enhanced.

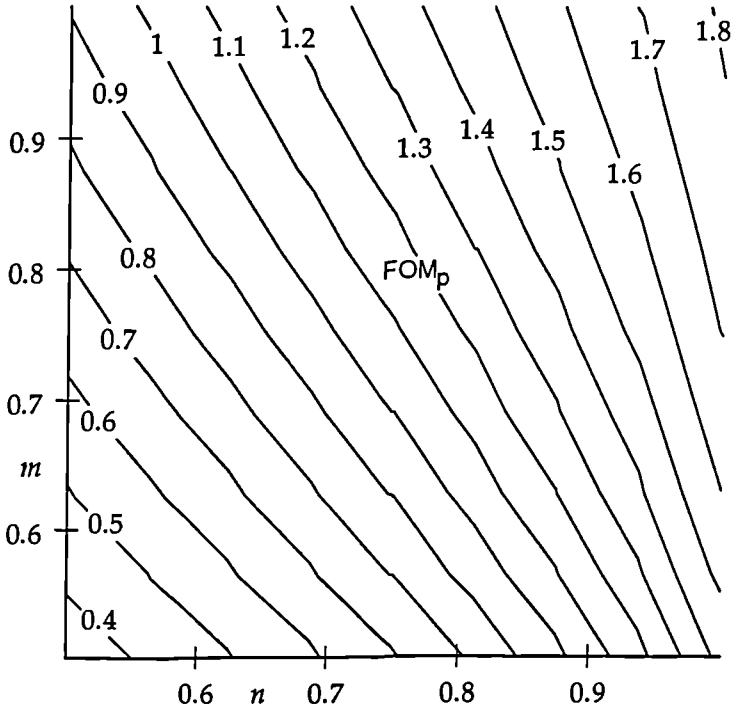

Figure 2.24 - Pyroelectric FOM_p contour plot as a function of the n and m parameters for a PTCa-P(VDF/TrFE) composite.

In practice, a situation arises where a particular composite is made with a certain volume fraction of ceramic and measured for its pyroelectric FOM_h. How do we relate this findings with the n-m charts?

A possible solution is to use the volume fraction chart (figure 2.22) superimposed on the FOM_p chart (figure 2.24) as is done in figure 2.25. In this figure, constant volume fraction have been traced with dashed lines with the values in plain style while constant FOM_p are traced as solid lines with its values in bold style.

If, for example, a composite PTCa-P(VDF/TrFE) sample has a 60% volume fraction and a $FOMp$ = 1.2μC/m^{2}K is measured, then it is possible to locate the point in the n-m plane to find the n (height) and m (i.e. width) dimensions of the cube which give rise to these property values. The experimental point lies at the intersection of the line with the 60% volume fraction (dashed lines) with the 1.2μC/m^{2}K line as is indicated in figure 2.25. Two

consequences can be derived, namely that the equivalent cube has a width larger than its height and thus an enhanced series than parallel connectivity exists. The second consequence, if this model is correct, is that it should predict the values of other properties (i.e. permittivity, piezoelectric constant and pyroelectric constant etc.) using the same values of n and m.

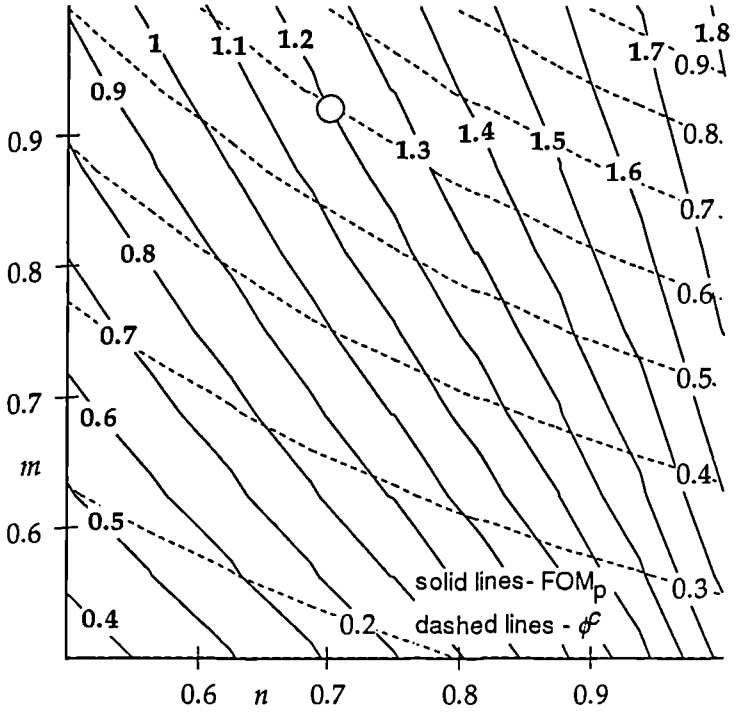

Figure 2.25 - Experimental point location using the combined data of volume fraction and pyroelectric FOM_p to determine n and m dimensions of the Banno cube model in a PTCa-P(VDF/TrFE) composite.

Figure 2.25 can also be used in the design of composites using the fact that for a fixed ceramic volume fraction a wide choice of FOM_p values are available depending on the dimensions of the ceramic cube. For instance in figure 2.25 a 60% PTCa-P(VDF/TrFE) composite can have a pyroelectric FOM_p ranging from 1.1 to 1.7μC/m^{2}K when going from a pure series to a pure parallel connectivity cube model.

A difficulty in the Banno's modified cubes model is encountered when the height of the ceramic block inside the equivalent cube approaches unity where the dielectric, piezoelectric and pyroelectric properties all change very fast for small increments of the height n of the ceramic thus making it difficult to find the proper equivalent cube as can be observed in the chart of figure 2.23 of the permittivity. Experimentally, this is the case when a large ceramic grain size is used in the composite causing a significant ceramic volume fraction to connect to both electrodes, and hence imparting an appreciable degree of parallel connectivity to the composite. This is reflected in the equivalent cube model through the fact that the embedded ceramic parallelepiped almost touches both electrodes in a region of n values where the gradient of the properties is very high.

In order to overcome this problem a different unit cell model is proposed, called mixed connectivity cube, as schematically shown in figure 2.26. It starts as the previous models with a host polymer unit cube, however, the ceramic part consists in this case of a cube of

size m in which a fraction of it n, in form of a parallelepiped, connects to both electrodes so that a part of the total ceramic fraction dispersed in the composite will be connected in series whilst the rest will be connected in parallel.

This is emphasised in the way of computing the properties of this mixed connectivity cube, outlined schematically in its equivalent circuit model. This consists of three parallel branches: a pure polymer, a pure ceramic together with a branch which has a series connection of a ceramic and a polymer parts. The n factor is thus a measure of the degree of 1-3 connectivity of the composite such that a value close to 1 means a pure 1-3 connectivity sample while lower values translate into a higher series character.

MIXED CONNECTIVITY CUBE MODEL

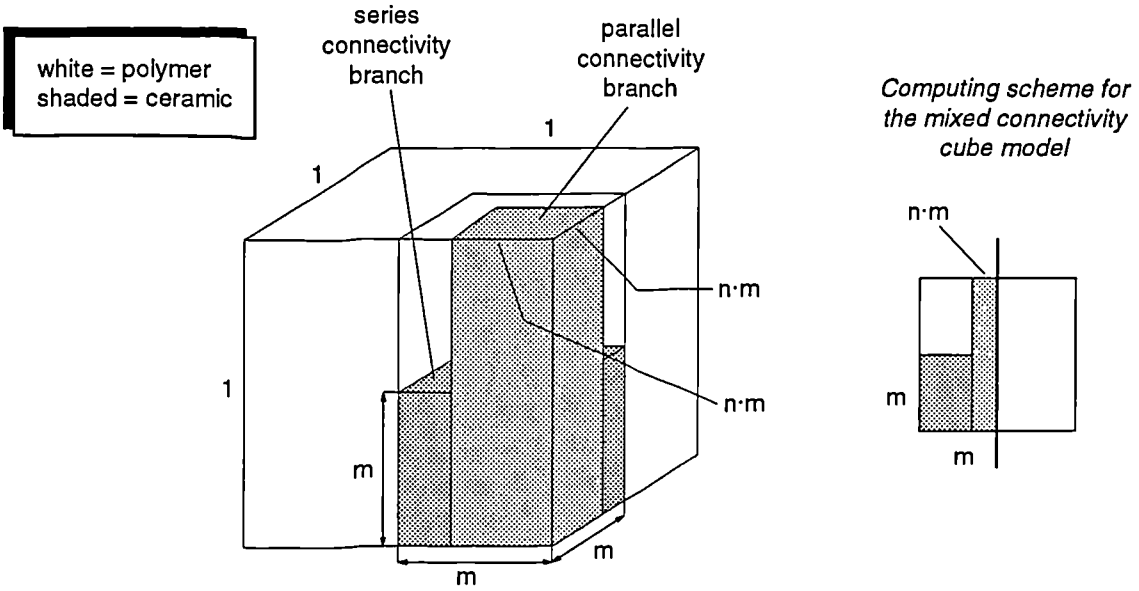

Figure 2.26 - Mixed connectivity model with its equivalent circuit diagram.

The calculation proceeds by determining first the properties of the series branch using the expressions given in table 2.2 for the series connectivity structure and then evaluating the total expressions for the properties of the cube using the parallel connectivity equations as given in table 2.1. The latter equations for a diphasic parallel configuration need yet be generalised for a triphasic parallel structure, which is easily done in the following way due to the inherent symmetry of those equations. In the case of the permittivity (the other properties generalise similarly) equation 2.39 transforms in a triphasic system into:

$$\varepsilon = \phi^c\varepsilon^c + \phi^p\varepsilon^p + \phi^s\varepsilon^s - \frac{\left(d^c_{33} - d^p_{33}\right)^2 s_{33}\phi^c\phi^p}{s^c_{33}s^p_{33}} - \frac{\left(d^c_{33} - d^s_{33}\right)^2 s_{33}\phi^c\phi^s}{s^c_{33}s^s_{33}} - \frac{\left(d^s_{33} - d^p_{33}\right)^2 s_{33}\phi^s\phi^p}{s^s_{33}s^p_{33}} \quad (2.69)$$

where the s superscript denotes properties of the third phase connected in parallel which in this case is the series circuit branch. As can be observed from this equation, the sum contribution for the permittivity contains an additional term arising from the series element whilst the product contribution has two extra terms to account for the interaction of the series branch with each of the other phases (i.e. the polymer and the ceramic phases). By inspection the same argument holds for the following properties: s_{11}, s_{12}, d_{31} and p. For the

piezoelectric constant d_{33} and the elastic constants s_{33} and s_{13} only one additional term is needed as no product contributions exist. Simplifications in the expressions could be carried out now to take into consideration the lack of intrinsic electro-activity in the polymer phase (i.e. $d_{ij}^{p}=0, p^{p}=0$).

In order to calculate the properties of the mixed connectivity model it is necessary to know as in the previous cube models, the volume fractions of each of the phases to be used in the expressions for the series and parallel connectivities. These are listed below in table 2.4. The calculation of the series branch requires the values of its ceramic and polymer volume fractions whilst, for the parallel calculation the volume ratios of the ceramic and polymer as well as that of the series branch in relation to the total volume (i.e. unity) need to be found. The total ceramic volume fraction inside the unit cube is found by summing up the ceramic volume in the series branch and that in the parallel one. In figure 2.27 is shown a 2D-graph of the ceramic volume fraction inside the mixed connectivity cube as a function of the m and n parameters.

TABLE 2.4 - VOLUME FRACTIONS OF THE PHASES USED IN THE MIXED CONNECTIVITY CUBE MODEL

	ϕ^{c}	ϕ^{p}	ϕ^{s}
SERIES	m	1-m	
PARALLEL	n^2m^2	$1-m^2$	$m^2(1-n^2)$
TOTAL	$m^3+n^2m^2(1-m)$		

There are important characteristic features in the n-m graphs as in the previous Banno cube. The line n=0 corresponds to the Pauer cube model when a simple cube lies inside the polymer cube. The line n=1 is the parallel connectivity line in similarity with the Banno cube model with a ceramic rod in parallel with the ceramic matrix.

The n-parameter can be thought to represent the degree of 1-3 connectivity in the 0-3 connectivity composite. This 1-3 connectivity can be imparted by the use of ceramic grains of the same order of magnitude as that of the thickness of the composite, connecting both the sample electrodes thus providing an equivalent cube with a high parallel connectivity. The same type of 1-3 character can be induced by a large ceramic volume fraction in the composite. In this case the likelihood of ceramic paths connecting both electroded faces will increase and thus the equivalent cube will tend to increase its n-parameter. On increasing the ceramic volume fraction from zero to one, a possible trajectory of the composite in the n-m plane can be represented with a bold line shown in figure 2.27. At low ceramic loading the n-parameter is small and the composite behaves as a series one. As the ceramic concentration increases and depending on the ceramic grain size the n-parameter increases so that the properties exhibited approach those obtained for a parallel connectivity composite.

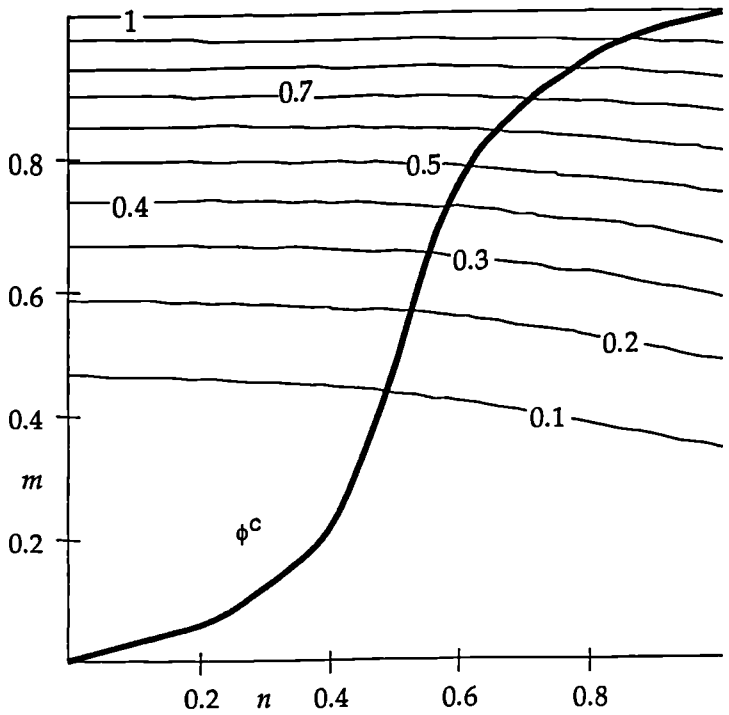

Figure 2.27 - Volume fraction as function of the m and n dimensions of the mixed connectivity model. The bold line represent an imaginary trajectory in the n-m plane for a composite of increasing ceramic volume fraction.

In figure 2.28 permittivity charts using the present model are shown. These values have been calculated for composites of all the different combinations of two ceramics (i.e. PTCa and PZT5A) and two polymers (i.e. Stycast epoxy and P(VDF/TrFE)). The major difference from the Banno cube model is that although there is still a region of a high gradient of properties, this region now lies in the ceramic volume fraction range of 80-90% and low *n*-values which as was concluded before is an unlikely situation. This high gradient region owes its existence to the way the properties vary along the line n=0 (series connectivity line).

In the more common range of 40-70% of ceramic content the permittivity of the composite seems to vary more smoothly making thus easier to assign *n* and *m* parameters to a particular composite.

The permittivity charts for the different composites reflect almost directly the raw materials from which the composites are made from. The general pattern of behaviour in the *n-m* plane however, for the different composites is quite similar. This is because little coupling exists between the permittivity and other properties and thus the transition from the series to the parallel connectivity takes place in a similar way in all the composites.

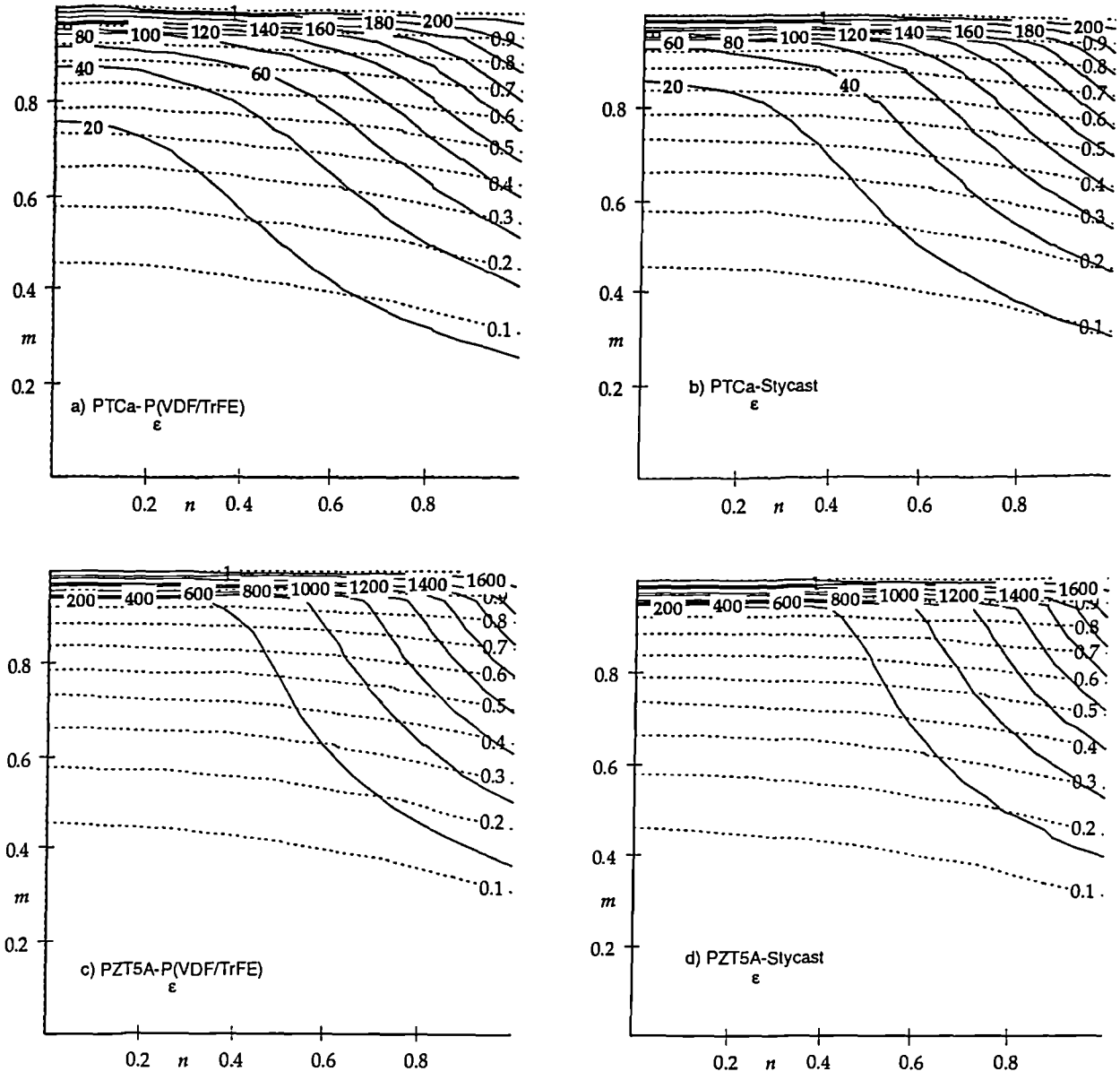

Figure 2.28 - Permittivity charts of a) PTCa-P(VDF/TrFE), b) PTCa-Stycast, c) PZT5A-P(VDF/TrFE) and d) PZT5A-Stycast composites shown as solid lines. In the background of these curves constant ceramic volume fraction curves have been drawn in dashed lines.

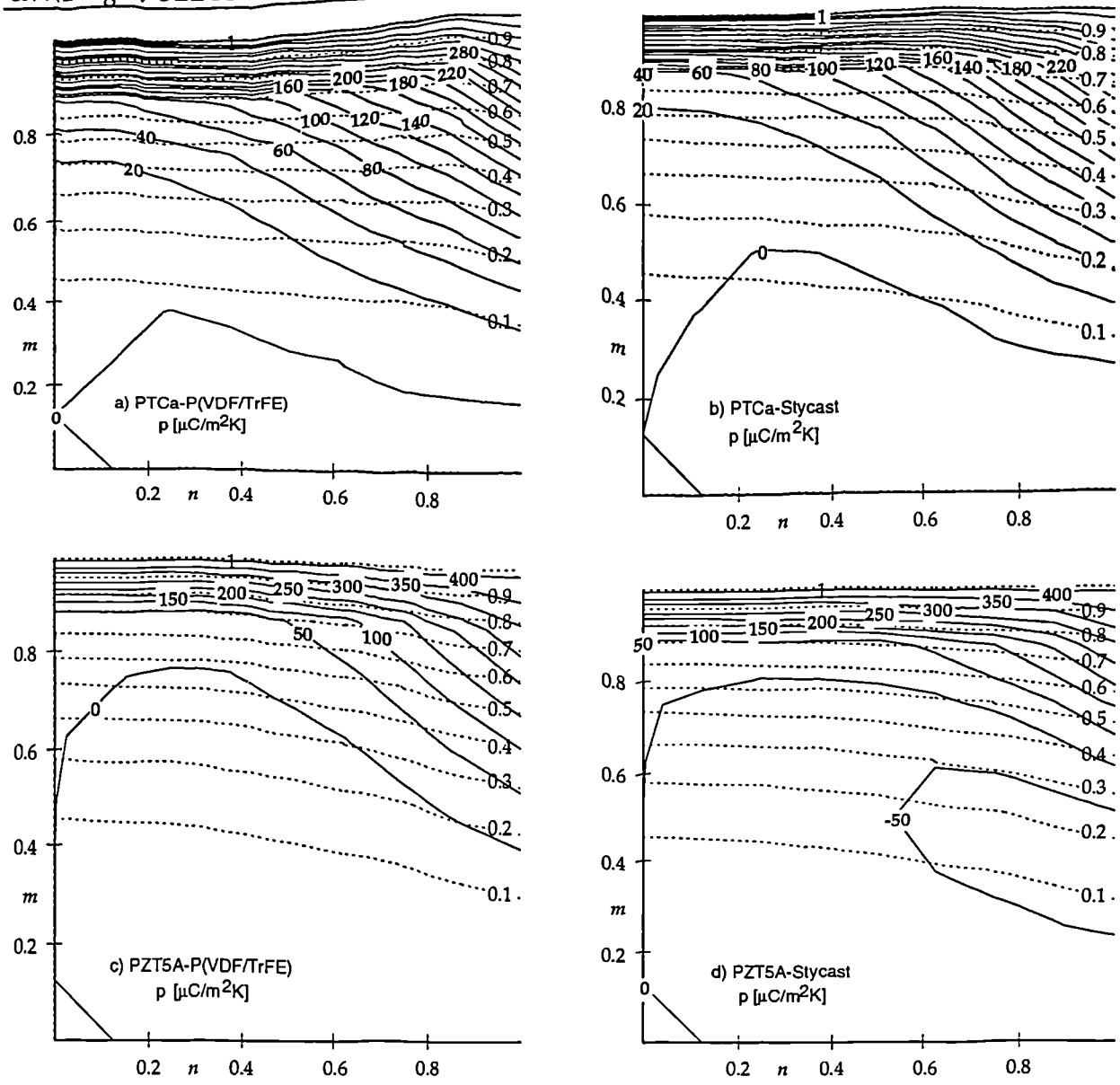

Figure 2.29 - Pyroelectric coefficient charts of a) PTCa-P(VDF/TrFE), b) PTCa-Stycast, c) PZT5A-P(VDF/TrFE) and d) PZT5A-Stycast composites shown as solid lines. In the background of these curves constant ceramic volume fraction curves have been drawn with dashed lines.

The pyroelectric coefficient charts for the same composites using the mixed connectivity cube model can be found in figure 2.29 in which, a large region in the *n-m* plane with a small pyroelectric coefficient can be observed. This region appears at low ceramic volume fractions and under certain conditions the composite (i.e. PZT5A-Stycast) can have an opposite pyroelectric coefficient to that of the ceramic.

This is a consequence of the non-zero pyroelectric product property generated by the piezoelectric and linear expansion coefficient mismatches (see Δp term in equation 2.40) in a region where the pyroelectric coefficient contribution generated by the intrinsic pyroelectric property of the ceramic is small. The useful pyroelectric coefficients can be found to lie at volume fractions above 40%. The best combination of materials regarding this property seem to be that of PTCa-P(VDF/TrFE) in which for the same ceramic volume fraction a higher pyroelectric coefficient is obtained.

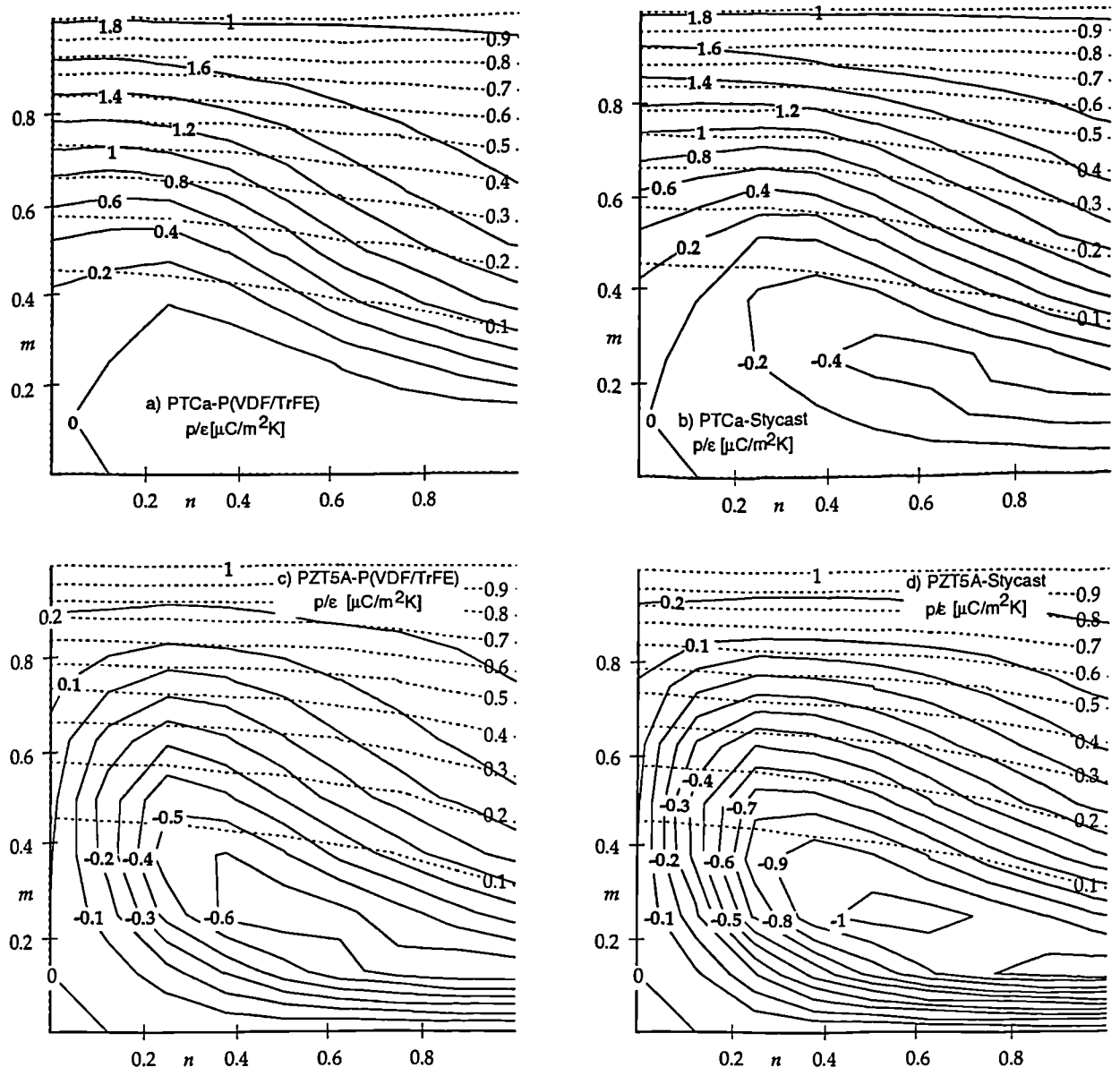

Figure 2.30 - Pyroelectric FOM_p charts of a) PTCa-P(VDF/TrFE), b) PTCa-Stycast, c) PZT5A-P(VDF/TrFE) and d) PZT5A-Stycast composites shown as solid lines. In the background of these curves constant ceramic volume fraction curves have been drawn with dashed lines.

Combining these two properties by taking the ratio p/ε the pyroelectric FOM_p charts are obtained and are shown in figure 2.30 for the same composites. It is apparent that the pyroelectric FOM_p does not exhibit, in general, values beyond that of the ceramic itself as was the case for the parallel connectivity composites discussed above. For the PZT-Stycast composite however, larger values of the FOM_p than that of the ceramic but of opposite sign are obtained. This is due to the very large piezoelectric coefficients of PZT5A coupled with large linear expansion mismatch between the phases of the composite which happens at low volume fractions. For intermediate PZT5A ceramic concentrations around 30-50% there is a region where the pyroelectric FOM_p can be very small and thus the PZT5A will not be a very useful material to use in a composite for this pyroelectric purposes.

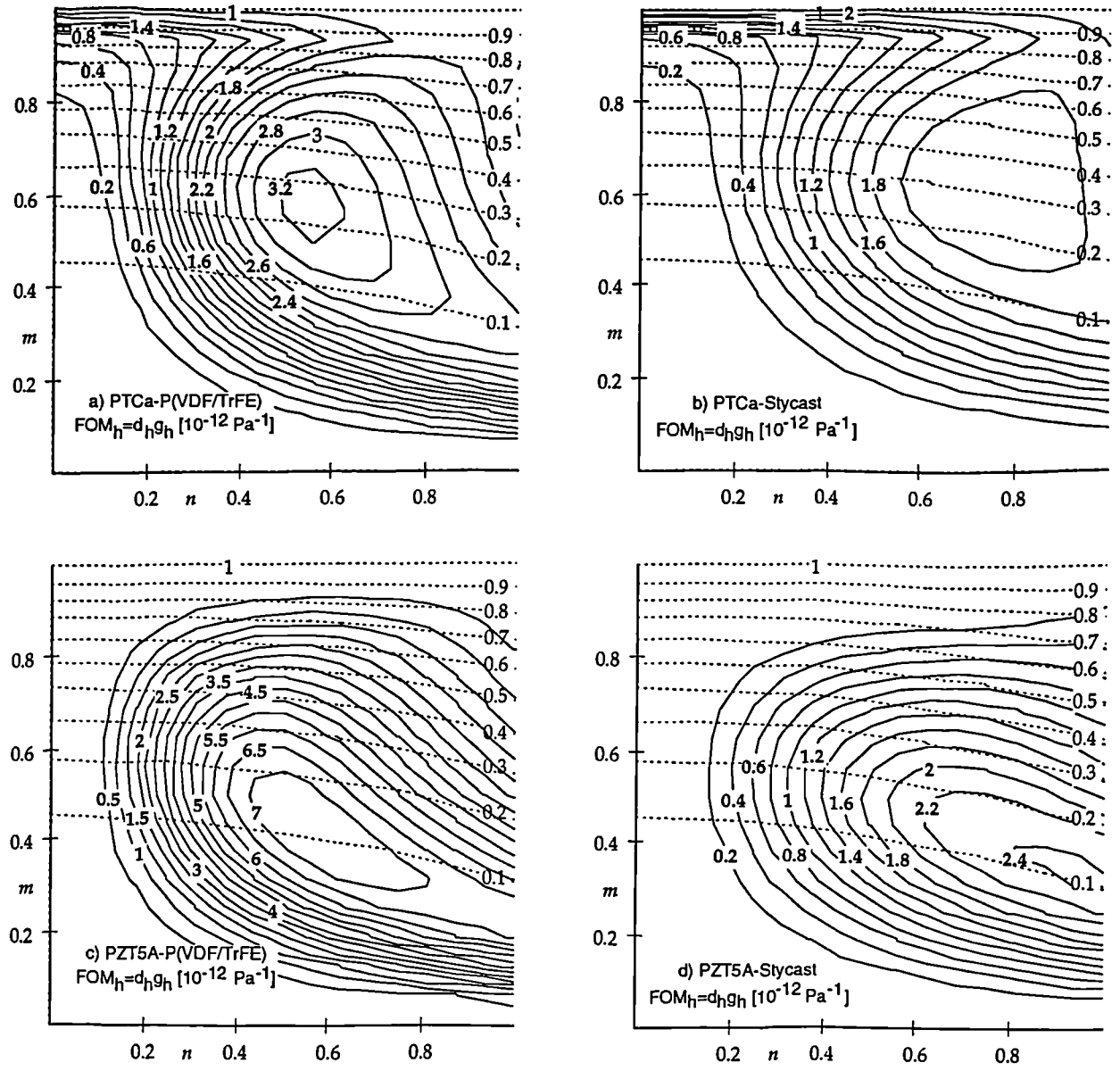

Figure 2.31 - Piezoelectric FOM_h charts of a) PTCa-P(VDF/TrFE), b) PTCa-Stycast, c) PZT5A-P(VDF/TrFE) and d) PZT5A-Stycast composites shown as solid lines. In the background of these curves constant ceramic volume fraction curves have been drawn with dashed lines.

In the graphs of figure 2.31 the FOM_h for these composites have been calculated. This property in the P(VDF/TrFE) composites shows an improvement over the pure ceramics. In the case of PZT5A-P(VDF/TrFE) a FOM_h as high as $7 \cdot 10^{-12}$ Pa^{-1} could be obtained for ceramic volume fractions around 10-20%. It can be observed that also at 60% ceramic loading the FOM_h value is much higher than that of the PZT5A which is $0.07 \cdot 10^{-12}$ Pa^{-1}.

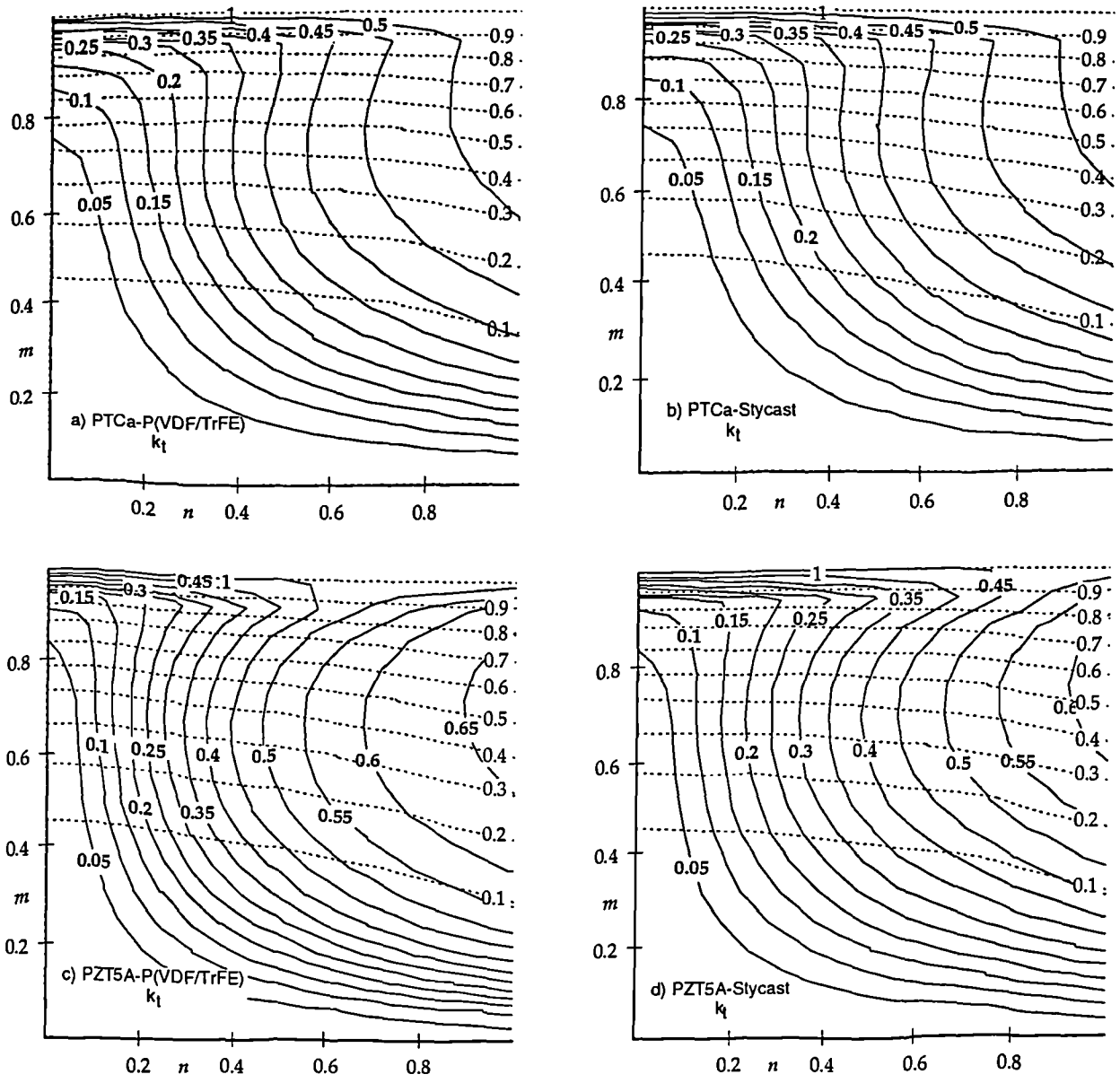

Figure 2.32 - Thickness electromechanical coupling factor k_t charts of a) PTCa-P(VDF/TrFE), b) PTCa-Stycast, c) PZT5A-P(VDF/TrFE) and d) PZT5A-Stycast composites shown as solid lines. In the background of these curves constant ceramic volume fraction curves have been drawn with dashed lines.

Figure 2.32 shows the calculated values for the thickness electromechanical coupling factor k_t for these same composites. The overall pattern behaviour in the *n-m* plane of this property seems to be similar for all the composites. It depends more strongly on the ceramic used than on the polymer. It also depends largely on the degree of 1-3 connectivity which is built into the composite.

The polymer matrix does not have a strong influence on the composite k_t. Comparing the PTCa-P(VDF/TRFE) and PTCa-Stycast composites a similar property pattern is obtained. The same is true for the PZT5A-P(VDF/TrFE) and PZT5A-Stycast composites.

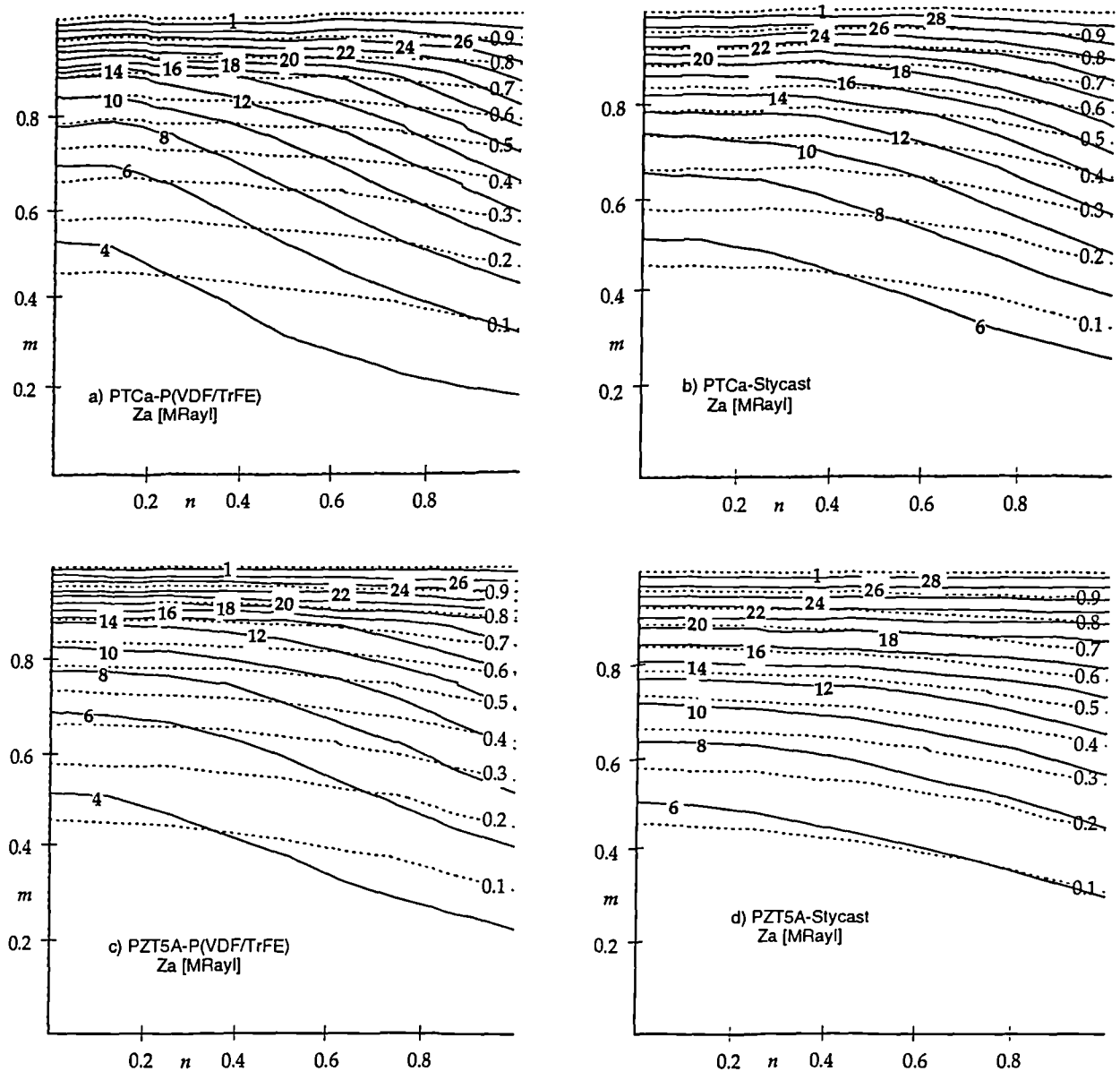

Figure 2.33 - Acoustic impedance charts of a) PTCa-P(VDF/TrFE), b) PTCa-Stycast, c) PZT5A-P(VDF/TrFE) and d) PZT5A-Stycast composites shown as solid lines. In the background of these curves constant ceramic volume fraction curves have been drawn with dashed lines.

In figure 2.33 the mechanical impedance for the composites have also been computed. This property has, as a rule, for the same volume fraction and 1-3 connectivity character higher values for the Stycast composites which is a stiffer polymer than P(VDF/TrFE). No big differences seem exists by changing the ceramic.

Depending on the degree of 1-3 connectivity a composite of a given volume fraction has a range of property values. A plot of the permittivity and pyroelectric constant for a PTCa-Stycast composite with a 65 % ceramic loading has been plotted in figure 2.34. These curves represent the properties values obtained in the *n-m* plane along the line 0.65 of the dielectric and pyroelectric properties charts for this composite.

The curves in this graph hence represent the manner in which this model achieves the property transition from a 65% series connectivity composite (i.e. n=0) to a parallel composite (i.e. n=1).

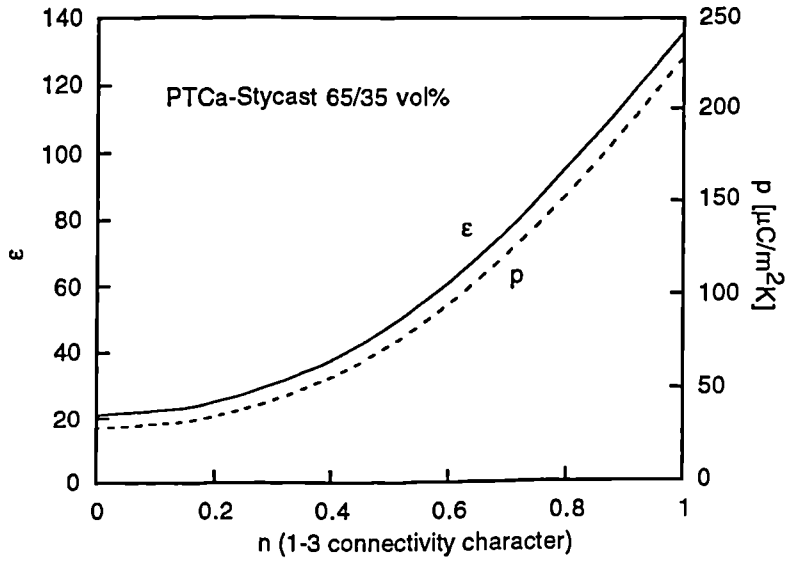

Figure 2.34 - Plot of the variation of the permittivity and pyroelectric coefficient as a function of the n-parameter (i.e. 1-3 connectivity character) for a PTCa-Stycast 65/35 vol%.

Thus, if a composite of 65% is made and its dielectric and pyroelectric properties are measured it is possible to find, by consulting this graph, its degree of 1-3 connectivity. A similar type of graph could be made using the Banno cube model, except that, in that model the same variable plot is steeper when n approaches unity. Obviously a graph such as that of figure 2.34 can be obtained for any property of a composite of a given volume fraction.

In figure 2.35 a 2D-graph with the electromechanical coupling factor k_t of a composite of PTCa-Stycast is shown with its acoustic impedance drawn in the background. This chart is the 2D analogue of the k_t versus Z_a graph of figure 2.19 drawn for a parallel connectivity PZT5A-P(VDF/TrFE) composite. In order to design a composite of a given k_t and mechanical acoustic impedance such graph can be usefully employed.

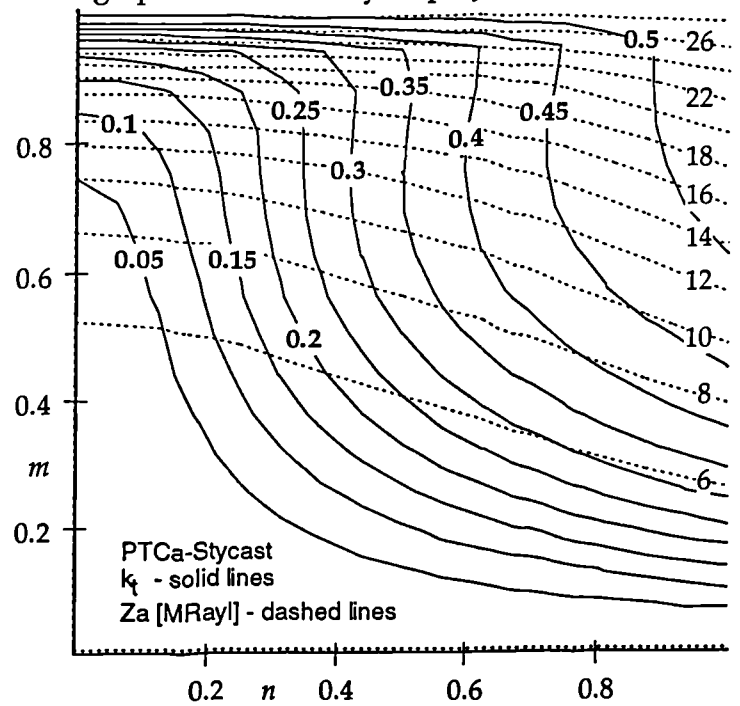

Figure 2.35 - Thickness electromechanical coupling factor k_t chart (solid lines) for a PTCa-Stycast composite with the acoustic impedance drawn in the background as dashed lines.

In order to gain a better insight over the resulting composite properties any other superposition of property charts as was performed in figure 2.35 can be examined.

Some criticism can be made of these charts. The values for the various properties are given in terms of the n and m parameters which characterise the equivalent mixed connectivity cube. These parameters are controlled in "real life" via the volume fraction and the grain size of the ceramic. Unfortunately, there is no simple rule to relate these variables. Thus, supposing that it is desirable to have a composite of n=0.5 and m=0.6 the ceramic volume fraction may be calculated from, $\phi^c=m^3+n^2m^2(1-m)=0.33$. It would not, however, be possible to determine the required ceramic grain size so that resort to an educated trial-and-error procedure would have to be made. A possible route is then to fix the volume fraction at 33% and then change the grain size gradually until the composite is located in the region of interest (i.e. has the right degree of 1-3 connectivity character).

The previous paragraph does not mean that the model cannot be checked. The test for this model is similar to that outlined for the Banno cube model. Using the property charts a consistency in the n and m values obtained for each property of a given composite, should be, obtained.

Another complication which may arise concerns the assumption that the ceramic inside the composite is fully polarised. This will not, in general, be true. Upon the application of an electric field to the composite to polarise the ceramic most of the field drops across the polymer phase because of its higher resistivity and lower permittivity relative to the ceramic. This problem will be specially acute for the ceramic part in the mixed connectivity cube which is in the series branch. The ceramic in parallel will sense the field fully and will thus be polarised with no difficulty. Hence, depending on the degree of polarisation of the series connectivity branch the composite can have a range of properties. The interplay of these considerations will be the subject of chapter 4. The permittivity and resistivity properties of the composites are also reported in the same chapter and their values compared with those calculated using the mixed cube connectivity model.

2.6 - Other approaches

Other theoretical models akin to the connectivity approach have been reported. Hashimoto and Yamaguchi [Hashimoto et al. 1986]have obtained similar results to those mentioned earlier for the two-dimensional series and parallel connectivity models using a matrix formulation of the piezoelectric equations. In their calculations it was assumed that for a parallel connectivity the equivalent composite properties of stiffness and permittivity are characterised by the corresponding ensemble average of raw material properties whilst for a series connectivity composite it is the equivalent compliance and the inverse of the permittivity of the composite are characterised by the weighted average of the compliances and of the inverse of permittivities of the constituents materials.

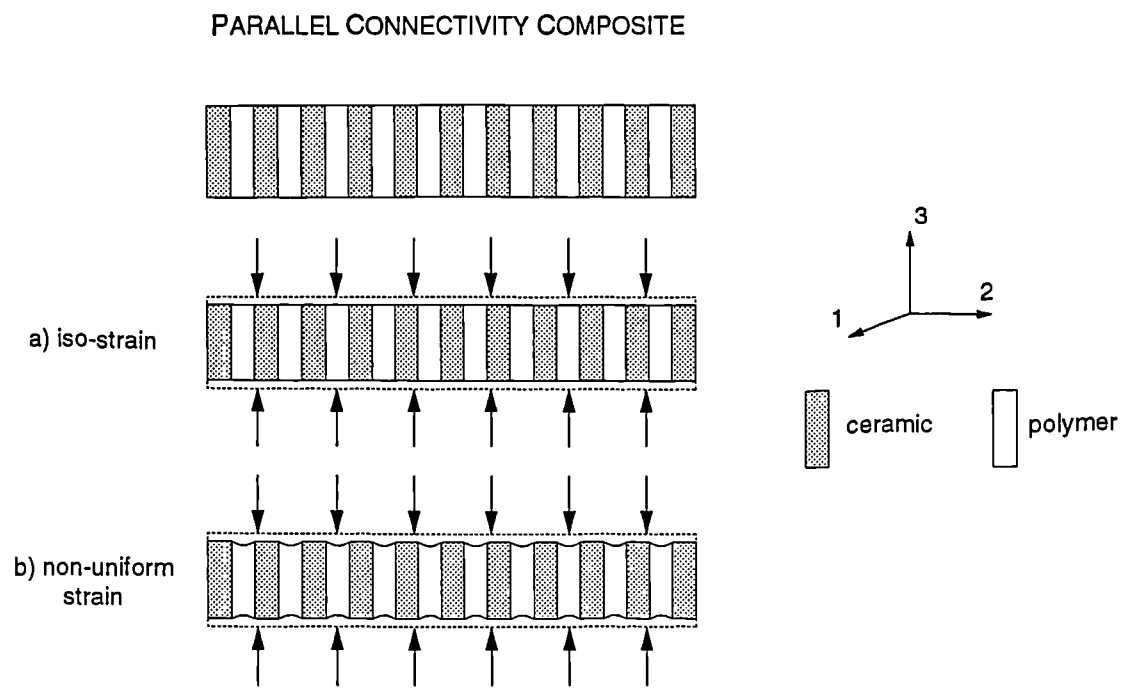

Figure 2.36 - Schematic plot of the deformation profiles (dashed lines) of a 2-2 composite under the assumptions (a) the strain is the same in both phases, (b) non-uniform deformation

A more rigorous treatment of the one dimensional parallel connectivity (i.e 2-2 connectivity composites) has been reported recently [Cao et al. 1993] where the longitudinal strain in the 3-direction is no longer assumed to be uniform (see figure 2.36 a) in contrast with Smith [Smith 1993] but continuos across the phases namely at the polymer/ceramic interface (see figure 2.36 b). In this case the interfacial bonding accounts for the continuos nature of the strain providing the mechanism for the stress transfer from the more compliant polymer to the stiffer ceramic. They have found that the iso-strain assumption is correct when the width of the structure is fine relative to the thickness of the sample as was stated before. If this is not true the iso-strain model in general overestimates the electro-active properties. When the width of the repetition unit has a similar magnitude as the thickness the error in the iso-strain model decreases for volume fractions higher than 40%. Thus, for the mixed connectivity model the charts discussed above will not be very reliable at low ceramic volume fractions and this point will have to be taken into account when we use this model in the subsequent chapters.

3 - Composite fabrication

3.1 - Introduction

In this chapter the fabrication procedures for obtaining binary mixtures of a ceramic and a polymer are described with special reference to those materials used, in making the composites studied in the course of this work.

The properties and connectivity of the phases constituting the composite, are the important factors in deciding the most appropriate way of fabricating a given composite. The influence of the properties in the composite fabrication can be seen particularly in the choice of polymer whether it is a thermoplastic, a thermoset or a rubber type of polymer. The thermoplastic type of polymer has two important properties which can be used in sample preparation: (1) in many instances is soluble in organic solvents and (2) softens in some temperature range in such a way that when cooled down the polymer regains its former properties before softening due to a low cross-linking of the polymer chains. The thermoset polymers [Ashby et al. 1986] commonly used in composites are of the epoxy type in which two components, a resin and the hardener, are mixed in some recommended proportion usually at room temperature. Upon mixing them, the components which initially form a liquid of low to medium viscosity react together to increase the viscosity up to a point where virtually a solid is formed. This process is called polymerisation setting and is influenced by the temperature of the mixture so that a higher temperature increases the rate of the setting reaction. In these polymers the resulting polymer main chains are usually heavily cross-linked; so thermosets are sometimes described as network polymers whose structure is almost always amorphous. These polymers have a softening temperature just as the thermoplastics do, and on heating the bonds between the main chains melt. However, the cross-links prevent true melting or viscous flow and thus the polymer cannot be hot-worked while further heating just causes the polymer to decompose. Rubber is another type of polymer used in composite manufacture. These are lightly cross-linked polymers which provide the memory function so that when stressed they retain the information about the position in which they were before the mechanical stress was applied. Rubbers have usually a low Young modulus of 3 MPa.

These differences in polymer behaviour have implications particularly at the temperature at which the composite is fabricated.

The connectivity of the constituent phases in the composites have probably the highest impact in the route employed in composite fabrication. It is evident that making a 0-3 connectivity composite which, in a simplified picture, is a mixture of a ceramic powder in a polymer host will be quite different and simpler than making 1-3 composites consisting of pillars of ceramic regularly spaced in a polymer matrix in a two dimensional network or even making 3-3 connectivity composites. Many manufacturing processes have been

proposed to obtain each type of the above connectivity structures (see figure 3.1) and as a result a wide range of properties and applications have also emerged which are often adapted to a certain combination of materials and/or applications.

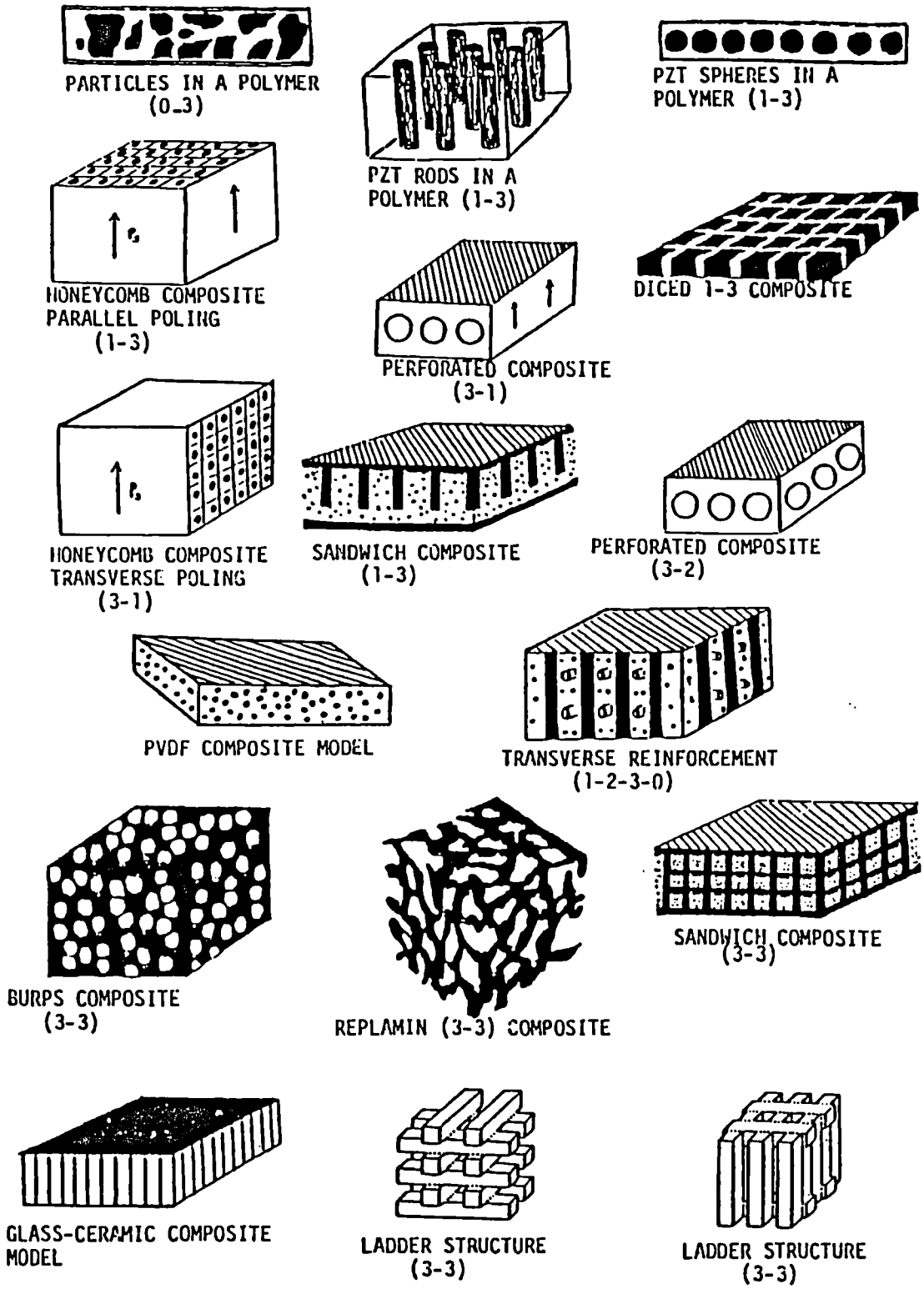

Figure 3.1 - Schematic diagrams of various types of piezo- and pyro-composites [Safari et al. 1986].

A review of the procedures for making composites of 0-3, 1-3 and 3-3 composites is now be given. It will be followed by a description on the production of the polymers and ceramics with special reference to P(VDF/TrFE) polymer and Calcium modified Lead

Titanate (PTCa) ceramic which has been used in the present study. The procedures used for the production of 0-3 composites will then be delineated as well as its morphological characterisation by SEM techniques.

3.2 - Review of preparation methods of 1-3, 3-3 and 0-3 composites

Composites of the 0-3, 1-3 and 3-3 connectivities are the most commonly made composites for piezo- and pyroelectric applications. Amongst these the 1-3 type is the most widely used and various procedures have been devised to make them. Here, a brief review of them will be given so that a comparison with composites of other connectivities and a proper evaluation of the work that is involved can be fully appreciated in making successful ferroelectric composites.

1-3 composite preparation - the original method [Klicker 1980; Smith 1989] illustrated in figure 3.2 involves an extrusion of fine piezoceramic pillars which are fired prior to their careful positioning in an mould. The complete assembly is then potted with a suitable epoxy polymer and a section of the required thickness sliced from the composite block thus obtained. Electroding and poling of the ceramic is then performed to obtain a workable piezoelectric composite sample. The method is effective for rod diameters of about 200 μm or more while being too cumbersome for finer spatial scales due to the fragility of the ceramic rods.

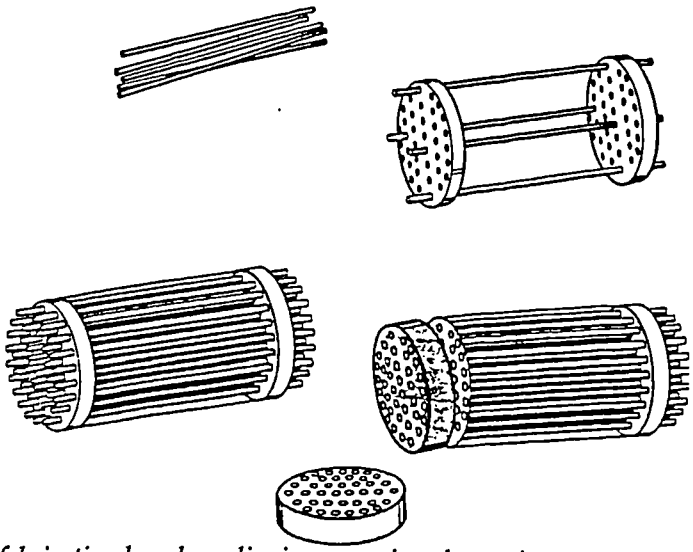

Figure 3.2 - Composite fabrication based on aligning ceramic rods, casting a polymer between them and slicing a composite disk [Smith 1989].

To overcome this limitation two approaches have been proposed which are as follows (1) a carbon fibre is woven into the desired structure by textile techniques and then the carbon structure replicated with a piezoelectric ceramic [Card 1988], (2) in another approach a "lost wax" method [Wersing 1986] is used to produce a complementary structure in plastic; a ceramic slip is injected into this mould and fired; the plastic mould burns away during the ceramic firing and a polymer is cast back into its place. Such methods allow for the production of large area and fine scales at relatively low cost.

An alternative and simpler procedure widely in use today, called the dice-and-fill technique, and shown in figure 3.3, was devised by Savakus et al [Savakus et al. 1980] where a pre-polarised ceramic disk, as commercially available from the manufacturers, is mounted on a diamond saw. A series of parallel grooves of a suitable thickness and pitch are made on the disk after which it is rotated by 90° and a second similar series of parallel cuts made. The grooves are then filled with a polymer and the resulting composite disk sliced off the ceramic base. Practical minimum spatial scale is in the 50 μm range as the ceramic rods become increasingly fragile and thinner saw blade wears off more rapidly when finer scales are attempted to fabricate. Finer scales can, however, be attained by using a laser to cut the grooves either by laser ablation or laser-induced chemical etching. A wide range of volume fractions and pillar thickness to length ratio can be achieved by changing either the saw cut thickness and/or the pitch.

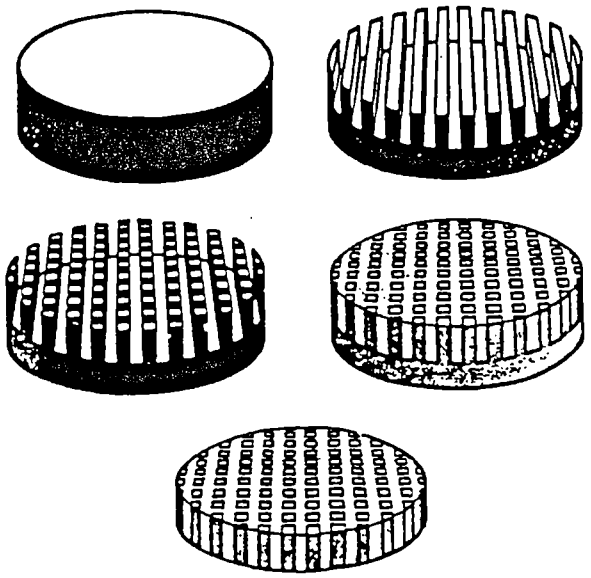

Figure 3.3 - Dice-and-fill composite fabrication. Deep grooves are cut in a ceramic disk in a mesh pattern leaving ceramic rods whose space is then filled with a polymer. The ceramic base is sliced off to obtain a composite disk [Smith 1989].

3-3 composite preparation - Skinner et al [Skinner et al. 1978] were the first to propose a method to obtain 3-3 connectivity ferroelectric composites by what was called the replamine form process (see figure 3.4). This consists of choosing a coral skeleton as a template for the ceramic material by the use of the following useful features of a coral (1) a narrow pore size distribution, (2) a pore volume approximately equal to the solid phase volume and (3) complete pore inter-connectivity making every pore accessible from all other pores. The making of the composite starts with shaping the coral to the proper dimensions desired for the composite followed by a vacuum impregnation with a casting wax after which the coral is leached away in hydrochloric acid leaving a wax negative of the coral template. The positive is then filled with a solution containing the ceramic and the wax is burnt off at 300 °C leaving only the ceramic structure which is sintered at high temperature (~1300 °C). The 3D structure thus formed is then impregnated with a polymer of a suitable viscosity to get a 3-3 composite. The spatial scales in this composites are determined by the

largest coral pore diameter which is about 600 μm. A further refinement can be introduced in that the composite after poling can be crushed to break the connectivity of the ceramic phase [Silk 1984]. This action will reduce the *d* piezoelectric charge coefficient and the permittivity ε while increasing the *g* piezoelectric voltage coefficient. This effect is mainly due to the interruption of the electric path through the ceramic.

Another method called BURPS or "fired composites" [Gururaja et al. 1986] requires the preparation of pellets by mixing the ceramic material with a solution containing a plastic binder. These pellets are then heated to different temperatures to fully burn the plastic. Upon cooling the pellets are vacuum impregnated with a suitable epoxy polymer, which fills the voids left over by the plastic binder, and cured for several hours. High ceramic loadings of 70% can be achieved with this method which is not easily attained with other techniques.

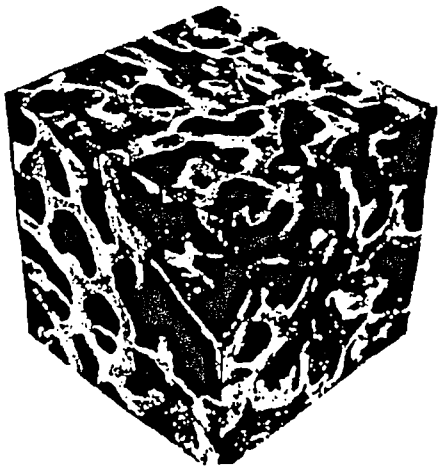

Figure 3.4 - Micrograph of a cube of a coral skeleton used as a template for making a 3-3 connectivity composite by the replamine form process [Skinner et al. 1978].

0-3 composite fabrication : the manufacturing processes of 0-3 connectivity composites are as a rule the simplest of the three connectivities which are dealt with in this review. Finer spatial scales and/or large areas are readily achieved in these composites although frequently, at the cost of lower electro-active properties.

When using epoxy polymers the procedure of fabricating the composite consists of mixing the two components at room temperature in an appropriate proportion, which is very often in 50 % volume parts, and then adding the ceramic gradually until the desired volume fraction is attained. The curing time of the epoxy will have to allow for the time which takes to incorporate the ceramic into the polymer. The curing of the epoxy can then proceed using the manufacturer's recommended temperature and time duration. Care should, however, be exercised in order to avoid the formation of air bubbles and the settling of the ceramic grains which can be helped to prevent by a suitable choice of the curing variables coupled to a curing in a vacuum environment. The thickness of the samples obtained using this technique is typically greater than 200 μm. However, in order to get films under 100 μm thick one has to choose a special very low viscosity epoxy and then use a paint brush to apply it over an extended surface [Egusa et al. 1993].

The hot-rolling technique is the oldest and most popular fabrication route when using a thermoplastic polymer as the host material [Furukawa et al. 1979; Yamazaki et al. 1981]. This involves as a first step, the softening of the polymer using a hot rolling mill kept near the polymer melting temperature which for PE (polyethylene) and PVDF (poly-vinylidene fluoride) are 140 and 175 °C respectively. Secondly, the ceramic which has been previously granulated, is gradually added to the viscous polymer mass, while the rolling action ensures that a thorough mixing is taking place, until the required volume fraction of ceramic has been incorporated. Usually just a visual examination of colour and texture, is used to control the uniformity and homogeneity of the composite mixture. The composite sheets made in this way have a thickness of typically 1-2 mm so that in order to obtain films of thickness in the range of 30-100 μm, a pressing operation is performed again at the polymer softening temperature.

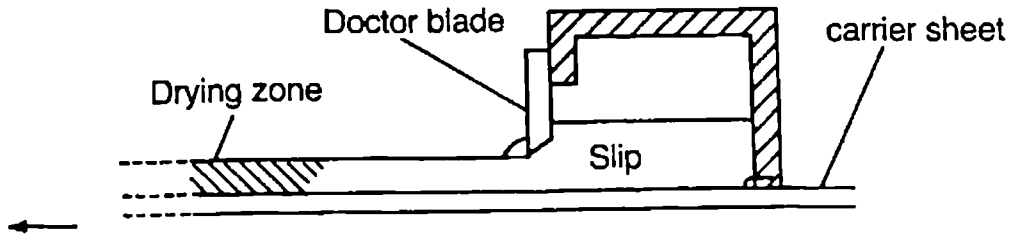

Figure 3.5 - Schematic diagram of the doctor-blade tape-casting process [Moulson et al. 1990].

Other techniques use the property that many polymers are dissolved in organic solvents such as ketones and toluenes. In this fabrication method a solution is made using the solvent and the polymer to which the ceramic grains are then added. Upon choosing the right quantities of the solvent to provide a suitable viscosity to the emulsion one can spread this slurry over an appropriate substrate using at least three different techniques which are: (1) spreading using a paint brush [Hanner et al. 1989], (2) tape-casting (see figure 3.5) where a strip of the emulsion is first laid over a substrate while a blade maintained at a constant distance from the substrate is then passed over to leave behind a constant thickness composite over the substrate and (3) spin coating whereby a substrate is spun at a constant frequency while the emulsion is dropped over it leaving a thin film composite coating. The resulting film can then be dried and aged in order to stabilise and remove the dissolving agents.

Other methods exists to make composites of various other connectivities and in this respect this review is by no means complete. Reference should however be made to research work which attempts to produce 1-3 connectivity composites using 0-3 connectivity methods of fabrication. This essentially consists of first making ceramic fibres or platelets which are then embedded in a polymer matrix with their long axis oriented parallel to the surface of the film through calendering (see figure 3.6) or "combing" techniques. The calendered sheets are then stacked parallel over each other and warm pressed into a block. In order to have the fibres oriented perpendicular to the surface of the film as in 1-3 composites it is necessary to cut the block into the appropriate direction. This method has shown very promising results

and lends itself to a mass production of 1-3 composites.

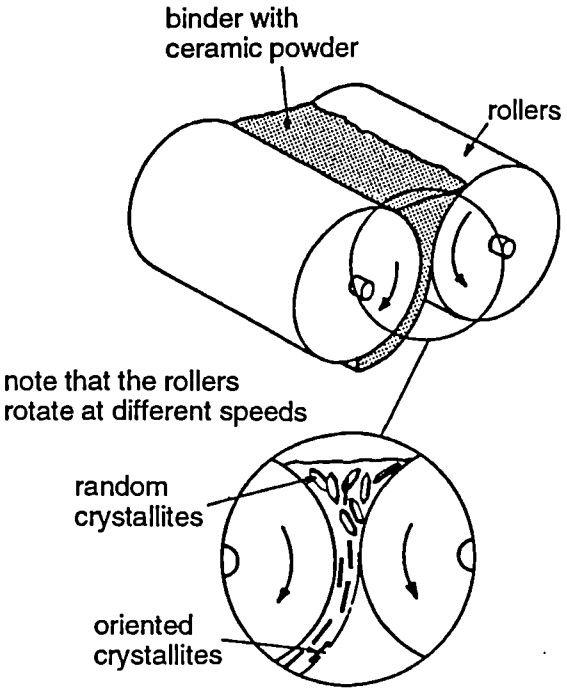

Figure 3.6 - Orientation of the ceramic powder during calendering [Moulson et al. 1990].

3.3 - Ceramic powder fabrication

There are many characteristics of the ceramics powders which can have a sizeable effect upon the electronic and physical properties of the ceramic material which is to be incorporated in a piezo- and pyroelectric composite. The main ones are listed in Table 3.1 and include chemical composition, purity, stoichiometry which relate to bulk properties, together with the particle size distribution and agglomeration/aggregation relating to the morphology of the ceramic grains.

TABLE 3.1 - IMPORTANT CHARACTERISTICS OF THE CERAMIC POWDERS

bulk oriented	*morphology oriented*
purity	particle size distribution
composition	agglomeration/aggregation
stoichiometry	residual surface coating
homogeneity	surface area

The most common route for ceramic powder preparation is that traditionally known as the mixed oxides technique in which component metal oxides or their acid salts are milled to achieve pulverisation and intimate mixing, and then calcined at high temperature to promote a solid state reaction, yielding the required compound. The specified particle size

distributions are achieved by further ball-milling.

The technical advantages of this type of process include fixing the batch composition and stoichiometry at the start of the process. Large scale homogeneity is usually excellent and some control over intra-particle heterogeneity and surface chemistry can be exercised during calcination [Bell 1990], the trade-offs being those of purity and particle size distribution. Other routes, namely the co-precipitation method and the sol-gel route, based on "chemically deriving" the ceramic material, can be pursued in order to provide a higher purity material by limiting the adventitious and intrinsic impurity levels. These processes, however, are often less economical than the mixed oxides route and should be used when improvements in the powder properties offset the cost in using them or when the cost of producing the powder does not have a major impact on the overall cost of the final product (i. e. ultrasonic transducer system)

Sol-gel processing to obtain $BaTiO_3$ and PZT first reported by Fukushima et al [Fukushima et al. 1984], is currently one of the most actively studied processing techniques of metal oxide based ferroelectric materials. This process starts with the preparation of a homogeneous solution containing the so-called liquid precursors for the ferroelectric material, which are usually metal-organics such as alkoxides acetates or inorganics such as metal hydroxides or nitrites. A "sol" is then prepared by dispersing the starting materials in an organic solvent (usually alcohols). Water and catalysts are added to the sol solution to initiate a series of hydrolysis and polycondensation reactions which produce a viscoelastic oxide gel network of suitable viscosity which can be either dip- or spin-coated on a substrate which on calcination gives a ferroelectric film or can be directly calcined from the gel to obtain a ferroelectric powder.

Pellets or other shapes can then be produced by shaping this so-called "green powder" using a suitable organic binder, for example PVA, as an agglomerating agent. A sintering process is then carried out to convert the compacted powder into a denser structure of crystallites joined to one another by grain boundaries (see figure 3.7).

The driving force behind sintering is a reduction in surface area of the compacted powder which contains a high free energy when compared with a more densified material with bigger size grains. Grain boundaries vary in thickness from about 10 Å to 1 μm and may consist of a disordered form of the major phase because of the differing lattice orientations in neighbouring grains. Grain boundaries are generally not as dense as the crystals grains and, in the early stages of sintering can allow free diffusion of gas in and out of the material. Grain growth also occurs in parallel with densification because it is energetically favoured by the reduction of the grain boundary area. The final grain size can vary from less than 0.1 μm to around 15 μm in $BaTiO_3$.

Two conflicting requirements often arise in relation to the sintering process. The need to optimise some characteristic parameters of the final product such as high densification, compositional and structural homogeneity, makes it necessary to use severe time and temperature sintering conditions. These can have, however, adverse effects due to the

volatility of lead oxide used in many piezo-ceramics at high temperatures. Thus, there is a need to find the best conditions of sintering which bring about the densification and stoichiometry best suited for a particular ceramic. For instance, in order to compensate for the lead oxide loss during sintering, the green ceramic is often enclosed with crucibles which contain a lead source powder.

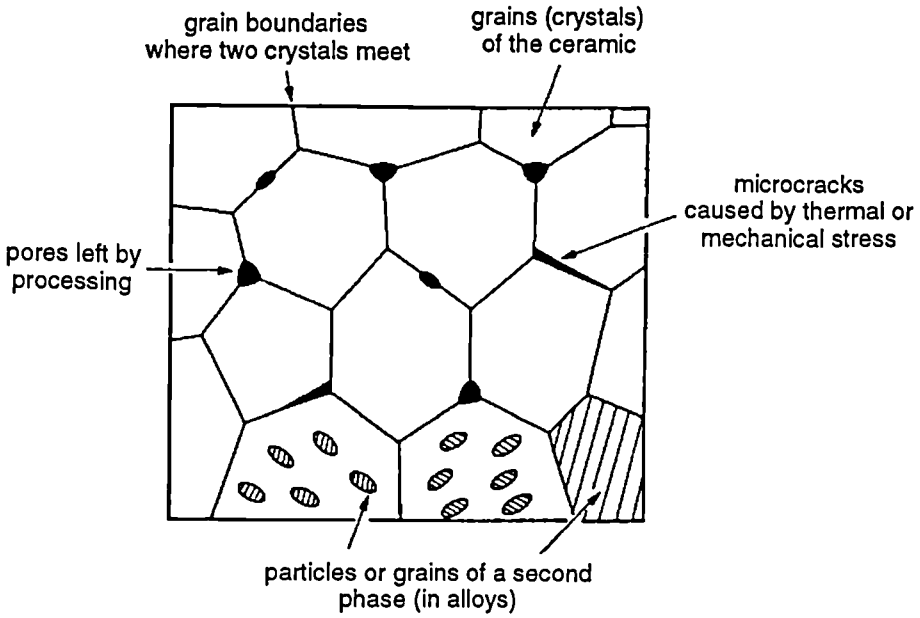

Figure 3.7 - Microstructural features of a crystalline ceramic: grains, grain boundaries, pores microcracks and second phases.

In the present work three different ceramics were used for composite fabrication, namely: lead zirconate titanate (PZT), lanthanum doped lead zirconate titanate (PLZT) and calcium modified lead titanate (PTCa). All three ceramics were used in a first stage in order to compare their relative merits regarding the composite properties. In a second stage, however, PTCa was chosen to be the most promising choice and a more thorough study was carried on composites made from this ceramic.

These ceramic powders were made in the course of a collaborative European project mentioned before, at the laboratories of our project partners. Thus, PTCa-1 and PZT ceramics were made at the Siemens (Münich -Germany) laboratory while PTCa-2 and PLZT were made at the GEC - Marconi Materials Research laboratory at Caswell (UK). An initial batch of PZT ceramic powder was also used which was bought from a commercial vendor (Morgan-Matroc). In the following we describe the route used to obtain these ceramic powders.

Two slightly different types of calcium modified lead titanate were used in this work both made according to the conventional mixed oxides technique used by Yamashita and co-workers [Yamashita et al. 1981; Yamashita et al. 1983] The chemical composition of these ceramics is listed in Table 3.2.

TABLE 3.2 - CERAMIC POWDER COMPOSITION

calcium modified lead titanate - 1	PTCa-1	$Pb_{0.75}Ca_{0.25}\left[\left(Ni_{1/3}Nb_{2/3}\right)_{0.08}Ti_{0.912}Mn_{0.008}\right]O_3$
calcium modified lead titanate - 2	PTCa-2	$Pb_{0.76}Ca_{0.24}\left[\left(Co_{1/2}W_{1/2}\right)_{0.04}Ti_{0.96}\right]O_3 + MnO_2$
lead zirconate titanate	PZT	$Pb(Zr,Ti)O_3$
lanthanum modified lead zirconate titanate	PLZT	$Pb_{0.895}La_{0.07}Ti_{0.35}Zr_{0.65}O_3$

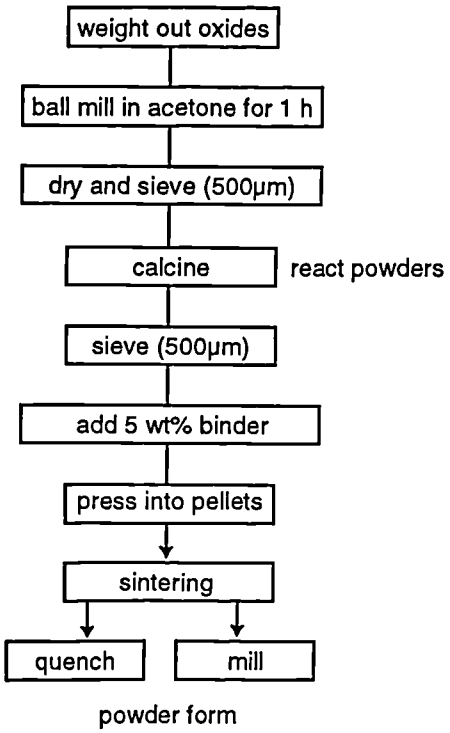

Figure 3.8 - Schematic diagram for the ceramic powder fabrication

In this method the starting materials are chemically pure metal oxides and carbonates: PbO, TiO_2, $CaCO_3$, CoO, WO_3, $MnCO_3$, and NiO [Garner et al. 1989; Wersing et al. 1989]. The desired ratios needed to make the powder were mixed, ground in ball mills, dried and calcined as shown schematically in figure 3.8.

MnO_2 doping was performed in order to control the resistivity and the dielectric loss of the ceramic which is of importance in the poling procedure. It is believed that this is achieved through the existence of the Mn cation acting as a trap of carriers [Moulson et al. 1990] p.247.

The ceramic powder obtained in this way was then pressed into disks and sintered at temperatures between 1150 and 1250 °C. It has been found previously [Wersing et al. 1989] that a sintering temperature optimum for the PTCa-1 was about 1210 °C while a temperature of 1100 °C was found to be appropriate for PTCa-2.

The PTCa-1 disks thus obtained were then milled to obtain fine powdered ceramic whose grain size distribution is depicted in figure 3.9. Its median grain size was found to be around 0.72 μm and the specific surface area was 2.29 m^2/g. An alternative procedure to

obtain a ceramic powder from the disks was to quench the ceramic block from the sintering temperature into water at room temperature. The use of quenching produces a coarser grain particles, from 7 to 60 μm, than those obtained from ball milling. Some quenched grains were however as large as 100 μm and had to be sieved prior to composite fabrication. The quenched material mainly consists of ceramic grains which have been fractured along the grain boundaries and thus these grains are expected to have less mechanical damage and residual stress than those obtained by mechanically grinding. The quenching technique has been performed both on PTCa-1 and PTCa-2 ceramics.

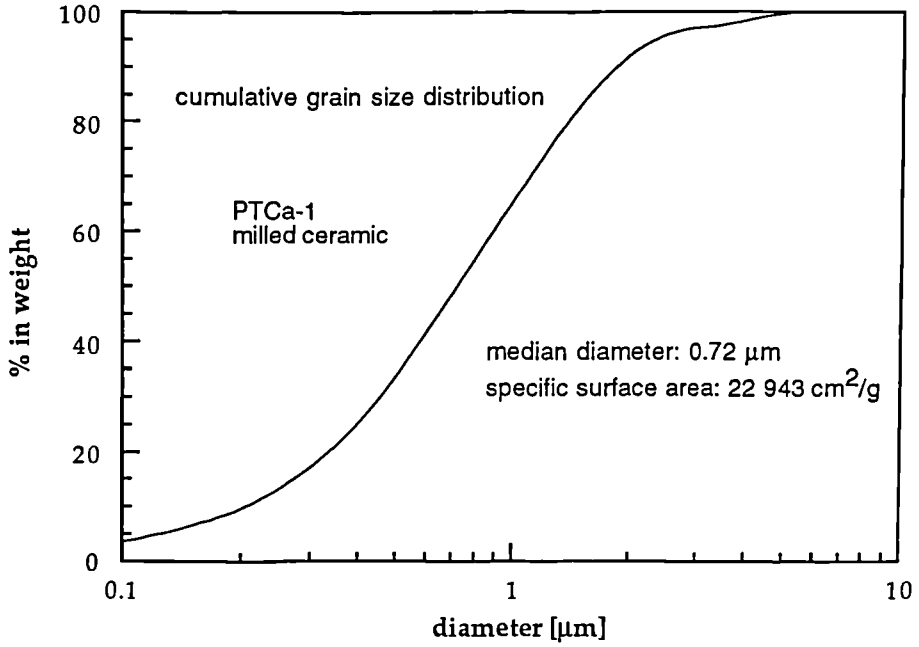

Figure 3.9 - Cumulative grain size distribution for the PTCa-1 obtained by milling the sintered ceramic blocks.

An experiment using PTCa-2 was designed to isolate the effect of larger grain size of the quenched powder from that due to their lower mechanical damage involved the separation of the quenched powder in two batches of powder one finer than the other. The separation was achieved through a sedimentation technique with the result that the finer batch had grains in the 7 to 20 μm range whilst the other had its grains in the 20 to 60 μm range.

By the use of X-ray diffraction the tetragonality of this ceramic was found to be c/a=1.036 which agrees well with the reported values for this parameter in the published literature [Yamashita et al. 1981; Olmo et al. 1988] giving a density of 6.89 g/cm^3.

PZT ceramics were also used in this study whose composition is shown in Table 3.2.. Two ways of preparing the ceramic were experimented. One method uses the conventional way schematically shown in figure 3.8, with the powder of an average grain size of 0.88 μm being obtained by milling the sintered block whose size distribution is shown in figure 3.10.

An alternative chemical route was also used where the ceramic powder was obtained by a "molten salt process" with no need of milling. The "as-grown" particles had a primary particle size of 1 μm; however, due to soft agglomeration, measurements of the grain size

distribution showed an apparent average diameter of 9.6 μm (see figure 3.10). The powder could however be easily dispersed during the composite preparation.

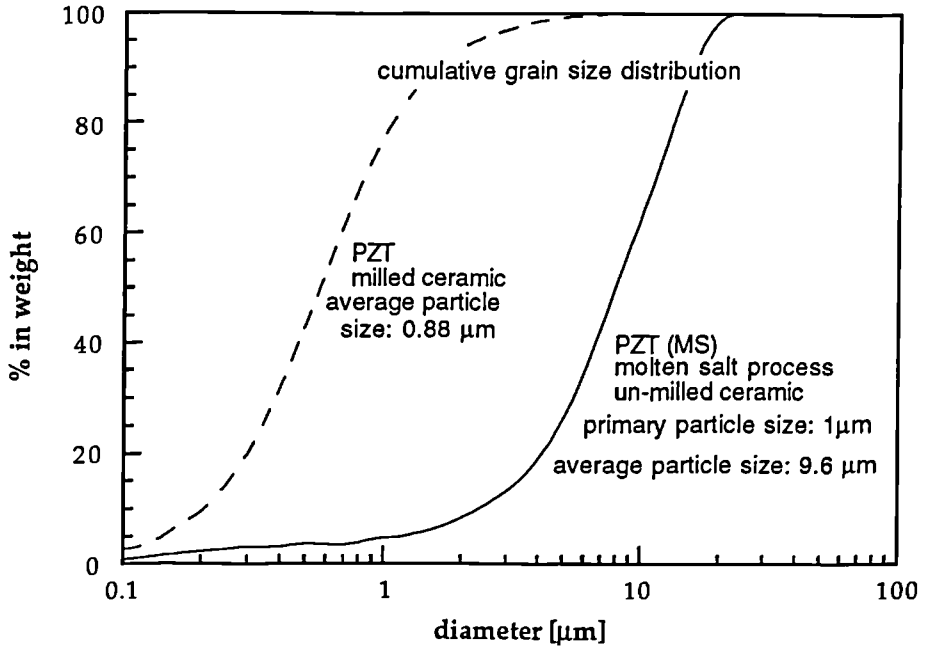

Figure 3.10 - Cumulative grain size distribution for the PZT used in the production of 0-3 composites

PLZT, a high resistivity ceramic was also used to make composites. Its composition shown in Table 3.2 was $Pb_{0.895}\,La_{0.07}Ti_{0.35}Zr_{0.65}O_3$ or PLZT 7/35/65 as customarily referenced in the literature which corresponded to a ferroelectric formulation of this ceramic material. The ceramic powder was obtained using the quenching process on the sintered blocks to obtain grains in the size range of 10 to 20 μm.

3.4 - PVDF and P(VDF/TrFE) polymer fabrication

In the present study an extensive use has been made of piezoelectric polymers as host of the ceramic powder in 0-3 composites. In this section a brief review is made of some of the techniques used to prepare polyvinylidene fluoride PVDF, and its copolymer with trifluorethylene P(VDF/TrFE).

PVDF is a polymer obtained by the consecutive addition of monomer units of vinylidene fluoride in a chain reaction called polymerisation. The monomer, vinylidene fluoride is a gas, member of the fluorocarbons or fluorinated series:

ethylene	$CH_2=CH_2$
fluoroethylene	$CHF=CH_2$
difluoroethylene (VDF)	$CH_2=CF_2$
trifluoroethylene (TrFE)	$CHF=CF_2$
tetrafluoroethylene (TeFE)	$CF_2=CF_2$

and can be obtained through gaseous pyrolysis reactions such as:

$$CF_3CH_3 \xrightarrow{\Delta} CH_2 = CF_2 + HF$$

The polymerisation of this monomer to form PVDF is usually performed by a liquid phase addition reaction where a free radical attaches to a monomer to initiate a propagation reaction which ends with a so-called chain transfer reaction that adds a hydrogen atom to the end of the polymer chain [Ferren 1988].

Polymer propagation normally occurs by the head of one monomer adding to the tail or head of another monomer of the growing chain. Commercial polymers have around 94 % of regular head-to-tail sequences.

-CH_2=CF_2-CH_2=CF_2-	head-to-tail addition
-CH_2=CF_2-CF_2=CH_2-	tail-to-tail addition

Various patent processes have been filed for the preparation of this polymer which specify such topics as catalysts, chain transfer agents, emulsifiers, suspending agents and the reaction medium. Some morphological differences between the polymer samples otherwise prepared under identical conditions, can be traced back to differences in molecular weight, molecular weight distribution, melting point, crystallinity, degree of regularity and spherulite size which are directly related to the polymerisation process.

Copolymers of VDF and particularly that with trifluorethylene TrFE, exhibit high piezo-and pyroelectric properties by forcing the crystallisation of the polymer into a polar form. By adding two or more different monomers to a chain one obtains a copolymer in a mixing at the molecular level. The manner in which a sequence of monomers are generated depends on the rates of reaction of the individual monomers to the growing polymer chain. Denoting the monomers by M_1 and M_2 the following reactions are possible:

$$M_1 + M_1 \xrightarrow{k_{11}} M_1M_1$$
$$M_1 + M_2 \xrightarrow{k_{12}} M_1M_2$$
$$M_2 + M_1 \xrightarrow{k_{21}} M_2M_1$$
$$M_2 + M_2 \xrightarrow{k_{22}} M_2M_2$$

The ratios of the reaction rates k_{11}/k_{12} and k_{22}/k_{21} have been defined as the reactivity ratios r_1 and r_2. When r_1 and r_2 are both equal to one; the copolymer has the same amount from both monomers whereas when they are less than one an alteration on the polymer chain continuation is likely to occur. The reactivity ratios of trifluorethylene (TrFE) with vinylidene (VDF) are 0.5 and 0.7 respectively. These ratios indicate that VDF and TrFE monomers react nearly as readily with each other as themselves. The monomer sequences should be randomly based on these ratios which was confirmed by NMR studies carried out by Japanese researchers from Daikin Kogyo Industries.

Some of the large producers have been withdrawing from the piezoelectric polymer market due to its exiguity when compared to other applications and currently PVDF and P(VDF/TrFE) are supplied by the producers listed below with proprietary names of the

resin in parentheses:

TABLE 3.3 - PVDF AND P(VDF/TRFE) SUPPLIERS

SUPPLIER	RESIN SUPPLIED
Pennwalt	PVDF (Kynar)
Kureha	PVDF (KF-polymer)
Piezotech	PVDF (Solef) and P(VDF/TrFE)
Dynamit Nobel	PVDF (Dyflor)
Daikin Industries	P(VDF/TrFE)

Both PVDF and P(VDF/TrFE) used in this study were bought from available producers. The PVDF in pellet form was obtained from Pennwalt while P(VDF/TrFE) was provided in powder form by Solvay which now is represented by Piezotech regarding its piezoelectric polymers product line. The P(VDF/TrFE) supplied had a nominal TrFE weight percentage of 24% being 19.8% in terms of the mole percentage. Other manufacturer quoted properties for the P(VDF/TrFE) powder are listed in table 3.4.

TABLE 3.4 - P(VDF/TRFE) COPOLYMER POWDER TYPE 2644 TECHNICAL DATA (SOLVAY)

% mol TrFE		19.8
% weight TrFE		24.0
intrinsic viscosity (DMF, 25°C)	l/g	0.096
melt index (5kg, 230°C)	g/10 min	14
apparent specific gravity	kg/l	0.29
melting temperature	°C	149.5
fusion enthalpy	J/g	67.6
Curie temperature	°C	134.5

The morphological and structural aspects of these piezoelectric polymers have been looked upon in the introduction chapter while other properties will be dealt with in the following appropriate chapters.

Polypropylene (PP), a non-polar polymer was also used in this study in order to asses its relative merit as a 0-3 composite host. This polymer is derived from the polymerisation of the (-CH_2=$CHCH_3$-) monomer and is part of the vinyl group of polymers whereby one H atom is replaced by a side-group or radical, which in this case is the -CH_3 radical.

3.5 - 0-3 composite fabrication

This section describes the actual procedures used in making the composites of the 0-3 connectivity which are the subject of the present study. The nomenclature used for referring to the home made composites is the following:

PTCa-1(q):P(VDF/TrFE) 60%
ceramic | powdering method | polymer | ceramic loading

The methods to produce ceramic powder can be either quenching (q) or milling (m). Most of the composites reported here have been fabricated by the hot-rolling milling technique and some have been made according to the solvent casting process. These composites were prepared so that a desired volume fraction of the ceramic into the polymer matrix would be achieved. To this end, the bulk densities of the materials to be mixed had to be known in advance. In table 3.5 are listed the densities of the materials used:

TABLE 3.5 - DENSITIES OF THE MATERIALS USED IN COMPOSITES

material	density [g/cm^3]	softening operating temperature [°C]
PVDF	1.80	170
P(VDF/TrFE)	1.85	170
PP	0.90	125
PTCa-1	6.9	
PTCa-2	6.9	
PZT	7.5	
PLZT	7.5	

Hot-roll milling technique - When using the hot-rolling and in order to determine the necessary quantities of the phases to be mixed, the ceramic volume fraction ϕ and the quantity in weight of ceramic to be used were set in advance. Then, knowing the densities of the materials a simple calculation (equation 3.1) was carried out to find the necessary weight of polymer to be used:

$$M^p = M^c \frac{\rho^p}{\rho^c} \frac{1-\phi}{\phi} \tag{3.1}$$

where M, ρ and ϕ are the mass, density, ceramic volume fraction and superscripts c and p denote ceramic and polymer properties respectively. The composite density ρ was then given by:

$$\rho = \phi\rho^c + (1-\phi)\rho^p \tag{3.2}$$

while the total composite volume V can be calculated from:

$$V = \frac{M^c}{\phi\rho^c} \tag{3.3}$$

In figure 3.11 is shown a schematic diagram of the roll-mill used to fabricate the composites. In this machine two rollers rotate at equal speeds but in opposite direction leaving a gap between them of one to two millimetres.

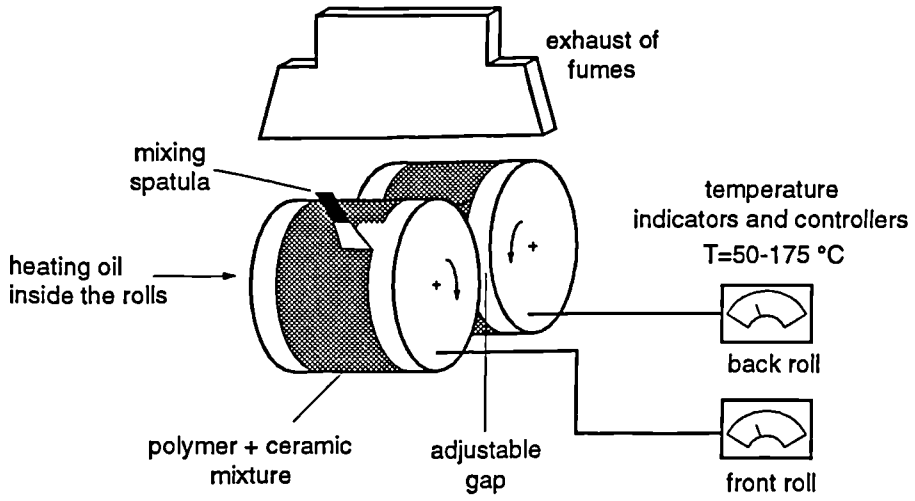

Figure 3.11 - Schematic of the hot-roll milling fabrication technique

A temperature controller set the temperature of each roller independently which is done by controlling the temperature of an high temperature oil circulating inside the rolls. This temperature was chosen to be near the melting point where the polymer is in workable viscous fluid form. In table 3.5 we have listed for the polymers their softening operating temperature used which is 170 °C for the PVDF and P(VDF/TrFE) and 125 °C for PP. The temperature of the rollers however, was not kept equal. Usually the front-roller was set to a lower temperature (i.e. around 5 °C less) so that the composite would stick preferentially to it and not distribute itself amongst the rolls.

Upon heating the rollers to the desired temperature the polymer powder or pellets would be gradually added to the mill until a uniform polymer film would cover them. The ceramic material would then be also gradually poured into the gap between the rollers while a thorough mixing would be ensured both by the action of the rotating rollers and by removing part of the film with a spatula in one region of the roller and placing it over another. After adding the required amount of ceramic the mixing action was carried out for around 30 to 60 minutes until a good uniformity had been achieved as observed by a visual inspection of colour and texture. The rolling action was then stopped and the film which at this stage was over just one of the rollers removed. The thickness of the films thus obtained were around 1.5 mm.

It must be stressed that a good mixing was only possible by judiciously choosing the various parameters involved namely: the temperature of the rollers, the gap between the rollers as well as the gradual addition of the ceramic. A fume extraction over the roll-mill was necessary to remove the smoke generated mainly by the decomposition of the grease used to lubricate the bearings of the rolls.

A disadvantage of this method regarding laboratory fabrication of composites was the large amount of ceramic necessary to operate the machine. In fact an absolute minimum ceramic quantity of around 150 g had to be used each time a composite was made so that around 30 cm^3 of composite were produced in each batch, a big part of which was not used. This also limited the number of composites made out of each type of ceramic. For instance in

certain cases where a limited amount of ceramic was available a smaller amount of ceramic employed would allow the study of the behaviour of some composites mixtures regarding its ceramic volume loading. At a later stage the solvent-casting method was undertaken at our laboratory with much added convenience whilst obtaining similar composite property-oriented results as the hot-rolling technique.

Later and in the case of the PTCa-1(q):P(VDF/TrFE) 60% quenched ceramic composite we have obtained lower volume fraction composites by successively remelting it and adding to it a suitable amount of polymer in the rolling mill to get 50, 40, 30 and 20% ceramic volume fraction composites.

Solvent casting technique - When making solvent-cast composites a slightly different procedure from the hot rolling technique was used, to calculate the necessary material quantities to obtain a given ceramic volume fraction ϕ in the composite. The total volume of the composite to be made would be set as V and then the mass of each of the component calculated according to:

$$M^c = \phi \rho^c V$$
$$M^p = (1-\phi)\rho^p V \qquad (3.4)$$

The composite density ρ is evidently given by the same formula as equation 3.2. Due to the typically smaller quantities of materials involved, the solvent casting requires a more accurate measurement of the mass of the materials to be mixed. Composite solvent casting was performed only with those made with P(VDF/TrFE).

The mixing was performed in a agate mortar were the weighed materials were placed. A suitable amount of methyl ethyl ketone (i.e. butanone), known to be a good solvent of P(VDF/TrFE), was then poured over the recipient until all the polymer powder was dissolved and an uniform slurry was formed. The procedure for obtaining composites then diverged from the usual one. The whole slurry was then mixed with the aid of a pestle until a solid was formed due to the evaporation of the solvent. Obviously not all the ketone was evaporated as the flexibility was still quite large indicating the presence of small amounts of the solvent still trapped in the bulk of the material. This solid mass was then formed into film sheets using the pressing facilities available and, during this process performed at high temperature, it was possible to note the expelling of the rest of the solvent as it boiled away from the composite mass. Spin-casting of the composite slurry has also been experimented. There were, however, problems in getting the right viscosity of the slurry throughout the casting process which was performed over a glass substrate. One other problem was the defects which appeared in the form of holes through the thickness of the samples.

In Table 3.6 are listed the composite materials made under this study. We have also listed important parameters such as the method of obtaining the powder and its grain size. The volume fraction of the composites and their method of fabrication are also cited in the same table. It is apparent from the table that the milled ceramic had all roughly the same grain size of around 1 μm while the quenched grains were in the tens of microns range.

TABLE 3.6 - 0-3 COMPOSITES FABRICATED

ceramic	powdering method	polymer	ceramic grain size [μm]	ceramic volume fraction [%]	fabrication method
PZT*	milled	PP	1	50	hot-roll
PZT	milled	PVDF	0.88	50	hot-roll
PZT	molten salt	P(VDF/TrFE)	9.6 (1**)	50	hot-roll
PLZT	milled	P(VDF/TrFE)	1	50	hot-roll
PTCa-1	milled	P(VDF/TrFE)	0.72	50, 60	hot-roll
PTCa-1	quenched	P(VDF/TrFE)	10-60	65, 60, 50, 40, 30, 20	hot-roll
PTCa-2	quenched	P(VDF/TrFE)	10-60	65, 60, 50	hot-roll
PTCa-2	quenched	P(VDF/TrFE)	7-20	50	hot-roll & solv.-cast
PTCa-2	quenched	P(VDF/TrFE)	20-60	50	hot-roll & solv.-cast

PZT from Morgan Matroc;primary particle size*

Pressing - To obtain films of these composites it was necessary to press at high pressure, near the softening temperature of the polymer as schematically shown in figure 3.12. This process was better achieved by pressing the composites in two stages and sometimes three. The first stage would bring the irregular thickness composite sheets down to a uniform thickness of 0.5 mm whilst the second would press the sample to around 50 to 80 μm. An optional stage in-between could be performed to press the samples to around 150 μm. The uniformity of thickness of the samples thus pressed was between 10 and 30%.

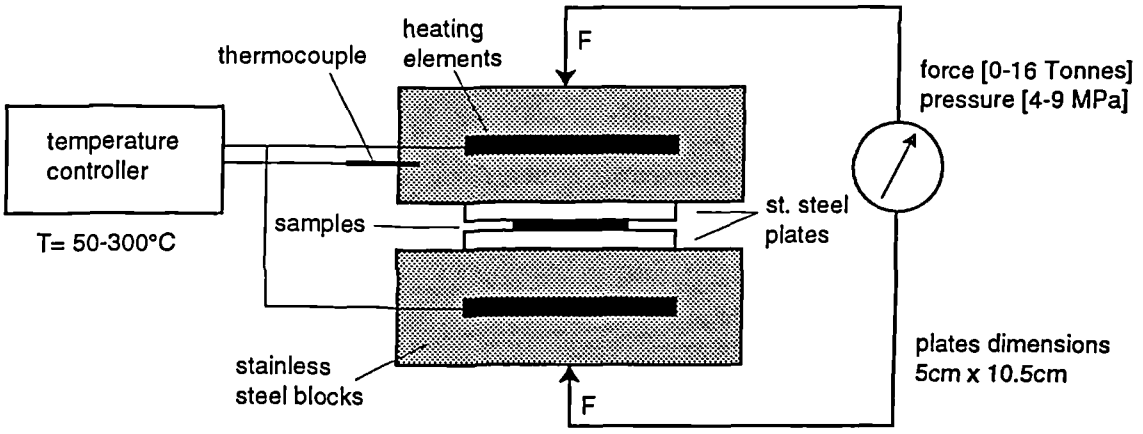

Figure 3.12 - Schematic of the pressing operation

A hydrostatic press with temperature control was used to press the samples. The temperature of the pressure steel blocks could be set up to 300 °C, while the pressure could be in the range of 4 to 9 MPa. Two chromium plated stainless steel plates were used to sandwich the samples to be pressed. In order to prevent sticking of the samples to the plates a releasing agent, consisting of a teflon dry-film from Radio Spares-RS 494-736, was sprayed over the plates prior to placing the samples.

Electroding - The electrodes were deposited by evaporation in vacuum of aluminium

(see figure 3.13). Upon heating a tungsten filament, containing an aluminium wire to be evaporated, to a temperature of around 1200 °C the vapour pressure of aluminium increases well above that of the vacuum pressure of the recipient and is forced to evaporate. The vacuum pressure had to be better than 10^{-4} Torr so that a good evaporation would take place while a clean vacuum system involving a diffusion and a rotary vacuum pumps was also necessary.

Circular masks were placed over the sample so that the aluminium electrode size was limited to a certain diameter. Samples used in pyro- and piezoelectric characterisation had an electrode diameter of 25 mm. For ultrasonic transducers a smaller electrode diameter of 10 mm was used.

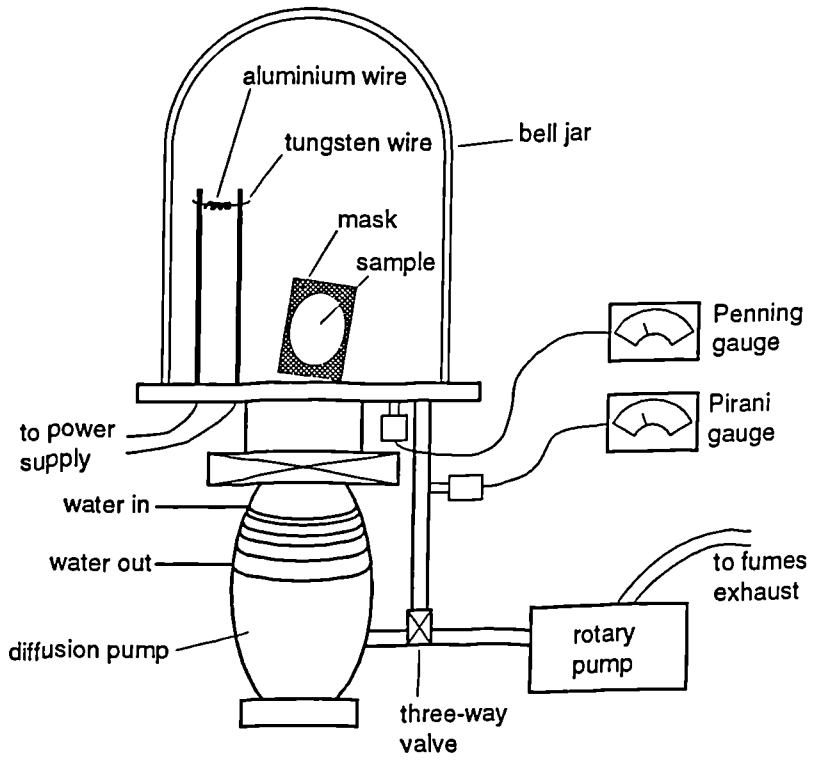

Figure 3.13 - Schematic of the aluminium evaporation process

Morphology - Scanning Electron Microscopy (SEM) was performed on composite samples in order to learn about the morphology of the composites made. These micrographs were all done on surfaces of damaged samples.

In figure 3.14 are shown micrographs of 50% loaded composite made with milled ceramic powder. The first micrograph labelled a) is from a PZT:PP composite; micrograph b) is from a PZT:PVDF composite, micrograph, c) from PLZT:P(VDF/TrFE) and d) from PZT:P(VDF/TrFE) composite. All of the micrographs shown in this figure were done at x3400 magnification so that the micrographs pictures are in real terms 29.4 long by 22 μm wide.

The milled ceramic powder were all of about the same grain size, that is in the 1 μm range, except for the PZT:P(VDF/TrFE) which in the cumulative grain size graph of figure 3.10 had shown, due to grain agglomeration, an average grain size of 9.6 μm although its primary particle size was also in the 1 μm range. Nevertheless these micrographs show a

similar morphology for all these composites with ceramic grains scattered in the polymer matrix. These grains appear either isolated but in certain cases they also show up in small clusters as indicated by the white circles in the micrographs. This means that the polymer during the composite process of fabrication was not able to wet sufficiently all the ceramic grains individually and hence the result of small pockets of ceramic appearing in the composite. As we have seen previously (i.e Chapter 2 - Models of composites) this is not detrimental in what concerns the electro-active properties because its effect is to increase in the 1-3 connectivity character of the composite. However, when using ceramic powder of 1 μm grain size to make composites it is desirable that each of the grains would be separated from the other and that a true 0-3 connectivity composite would be made. In this respect, and if further research into true 0-3 composites should be carried on, more work should be done to overcome this difficulty as some deleterious effects can appear for very thin samples, namely in relation to the brittleness and localisation of defects in the composite. One possible way to solve this clustering problem would be using a suitable surfactant agent to increase the wettability of the polymer taking into account that this incorporation in the composite matrix could also have an impact in the final properties of the composite itself.

Regarding the PZT:P(VDF/TrFE) composite, made of PZT obtained from the molten salt process it may be concluded, taking into account the similarity of the morphology scale with the other composites, that the PZT ceramic grains which were agglomerated prior to composite making, had been dispersed down to its primary size during the composite fabrication and in the end no more agglomeration could be observed for this composite than in the other ones.

In figure 3.15 are shown micrographs of PTCa-1 incorporated composites. These include a composite made with milled ceramic powder loaded at 50% in the case of the a) micrograph and with quenched powder at the same volume loading in the b) case. It can be observed a quite striking the difference in the grain size of the ceramic powder used. Moreover, while in the composite a) made with the milled powder, the ceramic grains are individualised entities covered with polymer in composite b) of the quenched ceramic powder the grains can be seen to touch one another creating a network of ceramic in the bulk of the material.

The other micrographs of figure 3.15, together with that of figure 3.16 show SEM pictures of composites made of the same PTCa-1 ceramic with quenched powder at different ceramic volume fractions. Thus, micrographs c) and d) of figure 3.15 are 30 and 60% while that of figure 3.16 is of 65% ceramic volume fractions respectively. It is not apparent from these pictures the ceramic loading used in these composites although in terms of their morphology they look quite similar. An interesting case is that of composite d) at 60% loading where the boundary of the film can be seen at the top of the micrograph. It is apparent from this photograph that the grains of the quenched powder are indeed quite large compared with the dimensions of the film which is emphasised by noting that the thickness of the pressed film which was around 60 μm is just about twice as large as the

length of the micrographs.

Quenching of a ceramic block can lead to some variation in the ceramic grain size. This can be seen by comparing again the composite d) with the other volume fraction composites made of PTCa-1 quenched powder. The grains in this composite are smaller than those of the rest of the composites. This means that obtaining a powder with a reproducible grain size using this process implies a better control of all the variables up to the quenching than when using the milling route.

Figure 3.16 shows a micrograph of a PTCa-1(q):P(VDF/TrFE) 65% composite at x5150 magnification where it is quite clear that there exist a ceramic path from the surface of the film into the bulk and very presumably traversing the whole thickness of the film. This particular composite turned out to be the best of the home-made composites in terms of its electro-active properties. One of the reasons for that is very likely to be this morphological effect which translates into a high 1-3 connectivity character for this composite.

SEM micrographs in figures 3.17 and 3.18 reveal the morphology of composites made of PTCa-2 quenched ceramic. They show a similar morphology as the other quenched ceramic composites. Micrographs 3.17 a) and b) should, however, reveal a more substantial difference between them regarding the ceramic grain size as these were the result of a separation method through a sedimentation technique as described above. The implication is that at least morphologically within the micrograph region the experiment designed to decouple the influence of quenching from that the size of the ceramic grain was not very successful. Results will be reported later on the respective macroscopic properties of these composites. In figure 3.18 which is an enlarged view of the 3.17 a) micrograph it may be observed clearly the similarity in the spatial scale of the film thickness and the ceramic grain size for these composites as well.

Voids and defects are other aspects which were also of looked for in these composites. Nevertheless, provided that the pressing operation was done carefully such features either did not occur or they did not show up in the course of our work. It must be pointed out however, that the polarization process would be a likely operation where such a problem would surface.

Brittleness, although not an acute problem, was more of a concern specially in handling the material. The higher the ceramic volume fraction the higher would be, as expected, the brittleness of the films.

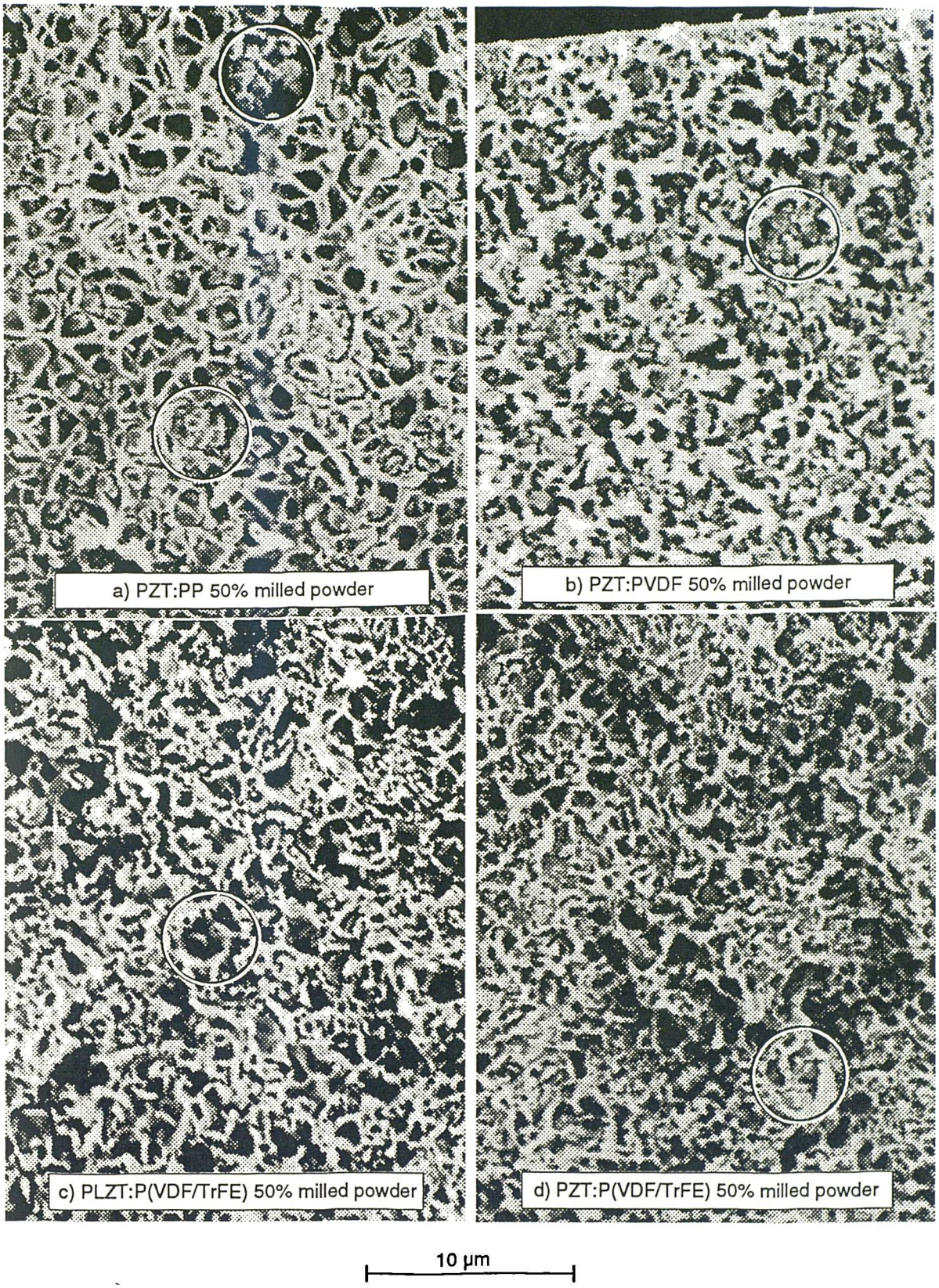

Figure 3.14 - Scanning Electron Microscopy (SEM) micrographs of composites made of PZT and PLZT milled powders dispersed on PP, PVDF and P(VDF/TrFE) polymers. Magnification: x3400.

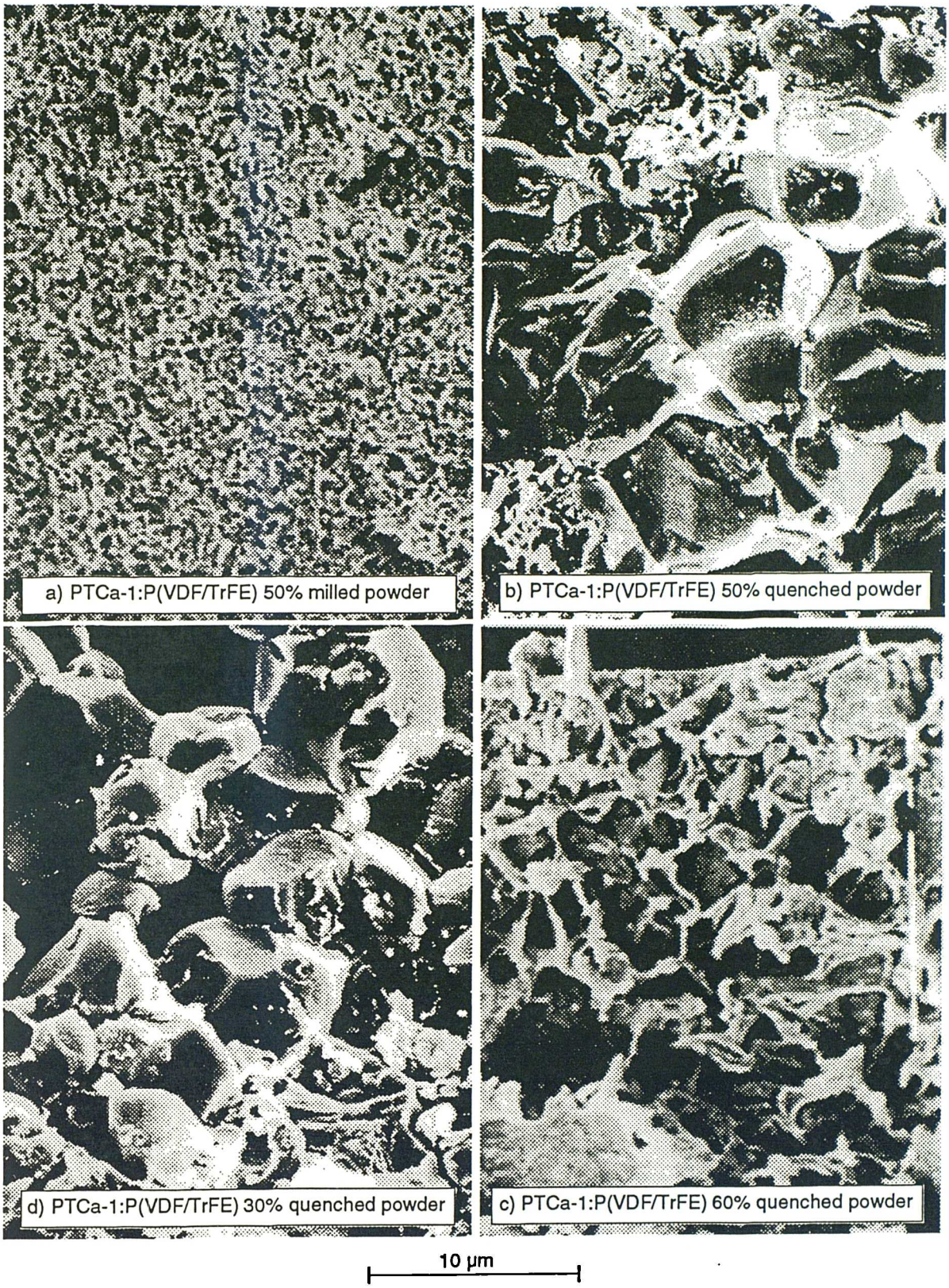

Figure 3.15 - SEM micrographs of PTCa-1 composites of milled and quenched powders. Magnification: x3400.

Figure 3.16 - SEM micrographs of a composite made from PTCa-1 quenched powder at 65% loading. Magnification: x5150.

Figure 3.17 - SEM micrographs of composites made of PTCa-2 quenched fine and coarse sedimented ceramic powders. Magnification: x3400.

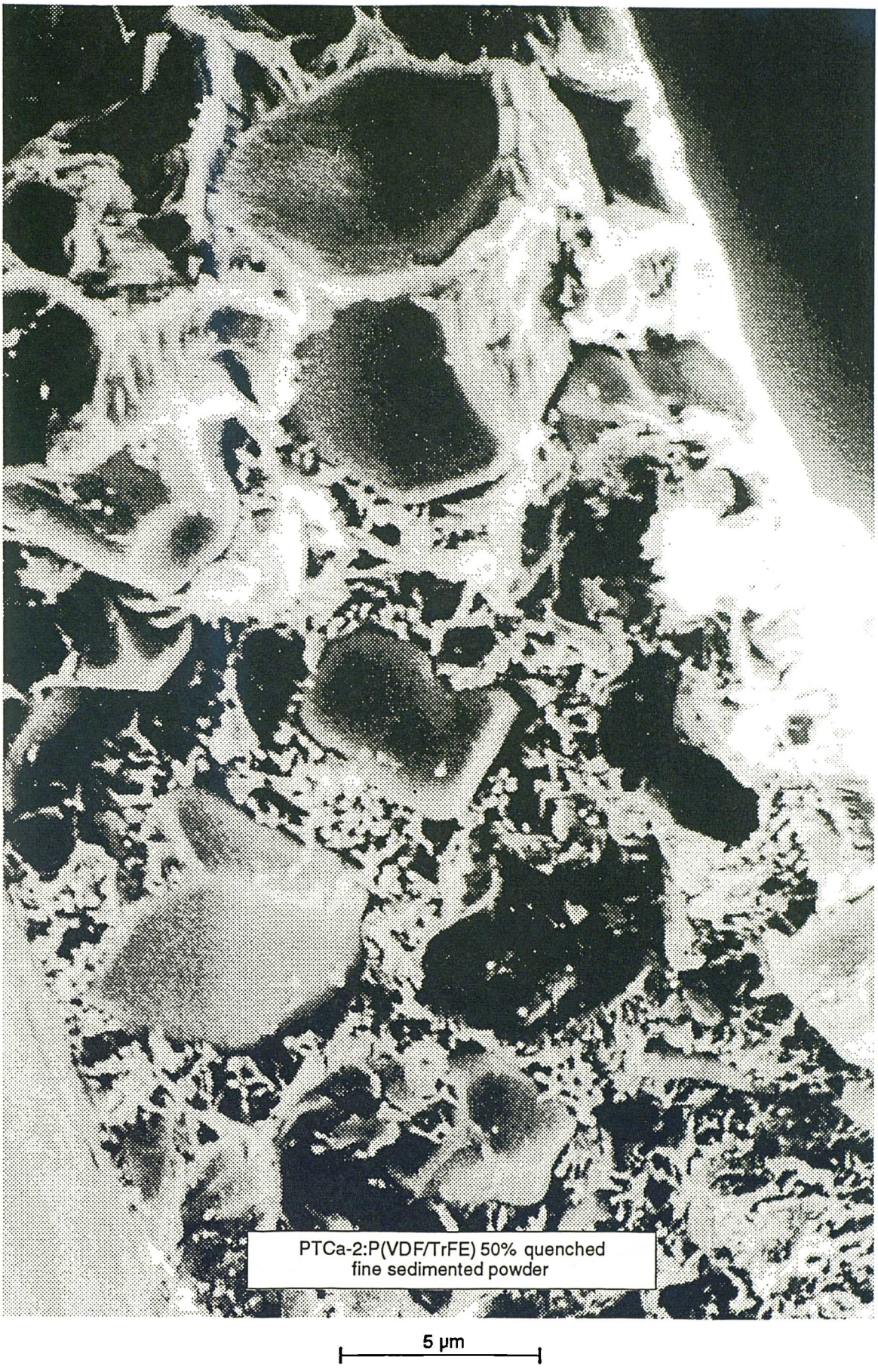

Figure 3.18 - Wider and enlarged view of the micrograph shown in figure 3.17 a). Magnification: x6800.

4 - Polarization, dielectric and resistivity properties

4.1 - Introduction

Polarization is the process a ferroelectric material undergoes when its dipole moment vector aligns irreversibly in the opposite direction to that of the applied field. The rate at which the polarization switches on $BaTiO_3$ has been modelled by Landauer [Landauer et al. 1956] as a field activated process described by the equation,

$$\frac{I_{pol}}{A} = \frac{dP}{dt} = v(P_s - P) \tag{4.1}$$

where I_{pol} is the current due to the switching polarization, A is the area of the sample, P_S is the saturation polarization, P is the polarization and v is a field dependent rate given by equation,

$$v = v_o \exp\left(-\frac{E_a}{E}\right) \tag{4.2}$$

where v_0 is a field independent rate constant, E_a the activation field and E the applied electric field.

Thus, the higher is the field the higher will be the rate at which the polarization switches. Because this process is field activated it means that the field E across a ferroelectric has to attain a minimum value, relative to its activation field E_a, in order that v reaches a sizeable order of magnitude and hence the polarization attains its saturation value during the lifetime of the experiment.

When applying a field to the composite the ceramic grains embedded in the polymer matrix will sense only part of the field applied to the composite. This quantity will depend on the connectivity of the ceramic and on its volume fraction as well as on the relative magnitudes of the dielectric and resistivity properties of the ceramic and polymer as will be described later in this chapter.

The dielectric and resistivity properties of the composites will also be dealt with in this chapter and attempts will be made to relate them to the constituent material properties.

The measurement of the switching of polarization is an usual method to evaluate the polarization and the coercivity of a ferroelectric material. Two main methods exist to this end which are (i) the ferroelectric switching method and (ii) the Sawyer-Tower method although other methods exist as well [Seggern et al. 1984; Guy et al. 1991].

The first technique, the ferroelectric switching method, consists of applying a voltage step to a ferroelectric material while measuring the current flow through the sample. Using this technique it is possible to measure the switching time of polarization as a function of the applied field as long as the polarization current is a large fraction of the total current or if it is possible to extract the polarization current from the total measured current. This method is thus appropriate for time related measurements.

The Sawyer-Tower method schematically shown in figure 4.1 consists in recording the polarization versus electric field hysteresis loop (see figure 1.1) obtained when an oscillating field is applied to a ferroelectric material. In this technique the x-channel of the oscilloscope monitors the voltage across the sample while the y-channel measures the current flowing through it. Using this technique quantities such as the saturation, remanent polarization and coercive field are obtained whose definitions can be seen in figure 1.1. In particular the coercive field is the electric field for which the polarization is zero while the remanent polarization is the polarization that remains when the electric poling field is removed.

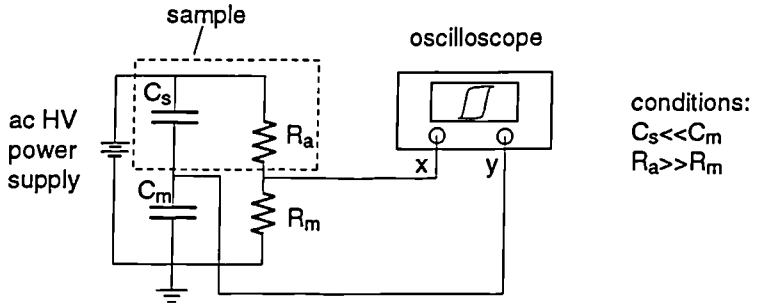

Figure 4.1 - Sawyer-Tower method for measuring polarization hysteresis.

These and other type of measurements rely on the fact that the total current generated in a ferroelectric material can be closely approximated by the polarization switching current or otherwise some means of extracting the polarization current from the total measured current has to be used. In this chapter a compensating technique is reported which allows for the determination of the polarization current in presence of resistive and capacitive contributions superimposed on the total current.

4.2 - Polarization methods

Two main methods exist to polarise a ferroelectric sample which are usually referred to as the conventional and the corona poling techniques. Both of them have been used in this work and will now be described.

4.2.1 - Conventional poling: dc and ac poling

The conventional poling technique schematically shown in figure 4.2, consists of metallising a sample in a film form on both sides. A high voltage is then applied to the sample which is kept at an appropriate temperature whilst the polarization is taking place. In order to prevent Paschen discharge and/or surface breakdown phenomena the sample is usually immersed in an insulating liquid which in our case was silicone oil. Alternative procedures are to evacuate the chamber where the sample is kept to a pressure below 10^{-5} Torr or to fill the chamber with an insulating gas such as SF_6.

The way in which the voltage is applied can take many forms. In order to prevent a breakdown it is better to increase the voltage gradually rather than rapidly until the desired field is attained. It is advisable to have some means of monitoring the current through the sample so that pre-breakdown phenomenon will show up as instabilities in the measured

current. A protection device which allows for short-circuits during the polarization process can also be used. This can simply be a resistor of a small value relative to the sample resistance which limits the current when there is a short-circuit condition.

In our studies two power supplies were used. One of them was a Brandenburg HV power supply which required an external ammeter and a protection device. Later on, a TREK 610C HV power supply was also used which had a built-in current ammeter and protection devices.

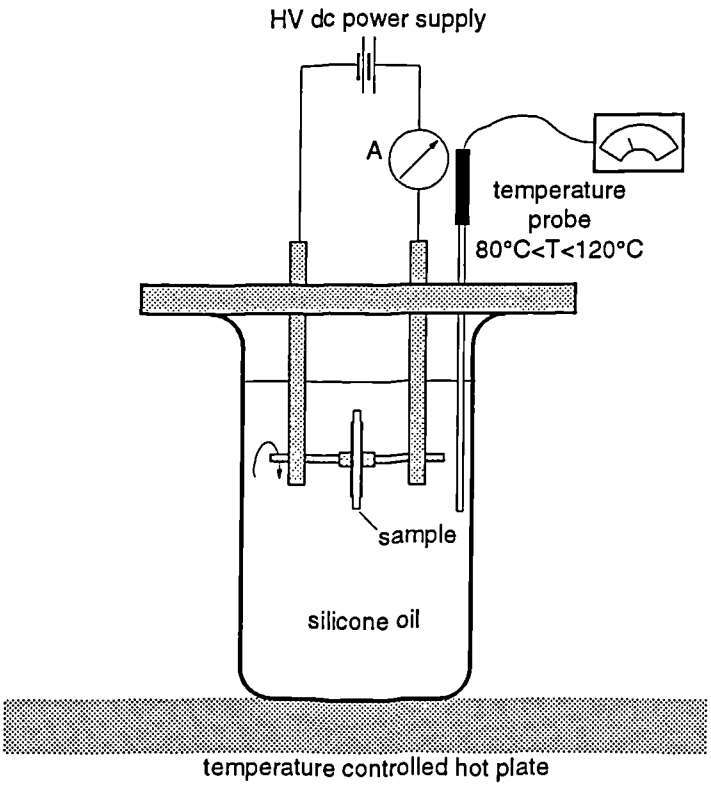

Figure 4.2 - Schematic set-up used for conventional poling of ferroelectric materials.

If different samples of a composite with different thicknesses but of the same area were to be polarised with the same field, it was found useful to measure for the first one the current flow during the polarization. Then, using this information the polarization of the remaining samples would be performed by applying a voltage such that the same current would be measured. The reason is that the flow of the resistive and capacitive current do not depend on the thickness of the sample but only on its area and on the electric field. In fact for the resistive current one can write,

$$I = \sigma AE \tag{4.3}$$

where A is the area and the other symbols have their usual meaning, while for the capacitive current in the composite sample,

$$I = \varepsilon\varepsilon_o A\frac{dE}{dt} \tag{4.4}$$

An ac poling voltage was also applied to the composite in certain cases. The TREK power supply worked in these experiments as an HV power amplifier driven be a low-

voltage function generator.

It should be pointed out that the majority of the breakdown events which occurred in the present composites had a self-healing character. Thus, when a breakdown occurred the short-circuit current was high enough to melt locally the sample and remove the aluminium metallization in the spot where the electrical breakdown initiated.

4.2.2 - Corona poling

Corona polarization is a technique which has been developed mainly in the field of electrets [Moreno et al. 1976]. The configuration set-up used in this study is called the corona triode for reasons that will be apparent shortly.

This set-up consists of a set of needles where a high voltage is applied, a grounded plate over which the one-sided metallized sample is placed (figure 4.3) and a metallic grid placed in-between them. The distance between the needles and the grid is 10 mm while that between the grid and the plate is around 15 mm.

Various operating modes exists in a needle-plate configuration depending on the high voltage applied to the needles and the distances involved such as the Geiger mode, the Townsend discharge (or corona regime), the pulseless glow and the spark or arc region [Gallo 1977]. For our purposes it suffices to say that for a negative polarity voltage a corona operating mode exists over which the current takes values between 1-100μA and the voltage varies from 2.5-10kV. For voltages beyond 10kV a glow discharge from the needle to the grid creeps in intermittently corresponding to the build-up of space-charge in the region near the tip of the needle.

Most of the current generated at the tip of the needle is then discharged into the grid. However depending on the optical and electrical transparency of the grid a small fraction of this current will be able to reach the front face of the sample [Oliveira et al. 1985; Giacometti 1987] where it is deposited as charge if the sample is a perfect insulator.

The voltage applied to the grid controls the electrical transparency of the grid. The higher (i.e. more negative) this voltage is, the higher will be the fraction of current reaching the sample which is of the order of micro-amperes (maximum). The current flow from the grid to a perfect insulator will then stop when the voltage of the front face of the sample roughly equals that of the grid.

In a dielectric material the deposited charge increases the surface potential of the non-metallized surface like the charging of a capacitor just as in a perfect insulator. When this voltage attains a sufficiently high value, however, there will be injection of charge into the material and a conduction current will start to flow through the sample. Thus the surface potential of the sample will stop to increase as soon as the conduction current equals that flowing from the grid to the sample [Giacometti et al. 1985].

A big advantage of this type of polarization is the lower probability of a complete destruction of the sample by an electrical breakdown relative to the conventional method. In the event of a weak spot and due to the absence of a metallization on the front side of the sample, there will only be a localised breakdown which will not spread to other parts of the

sample. A disadvantage is that this technique has a limited current delivering capability and thus if the sample is very conductive only a low poling voltage can be attained in the sample.

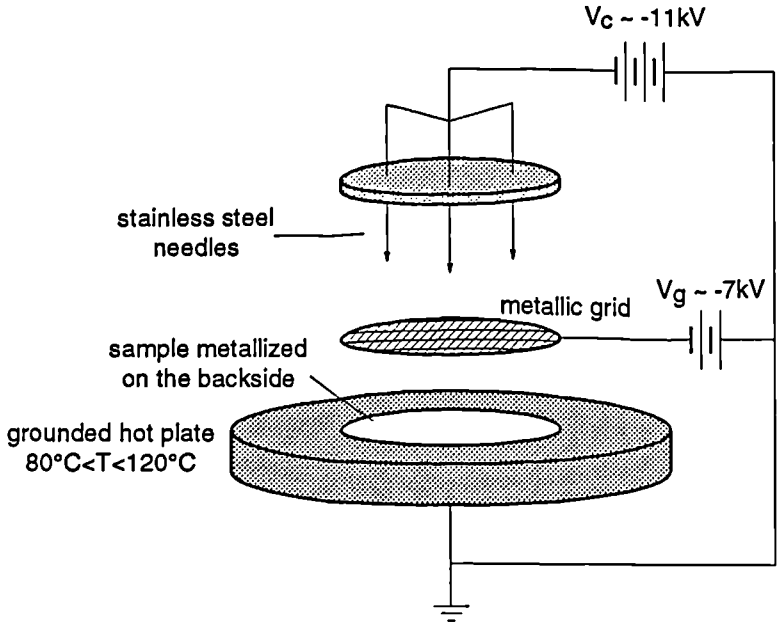

Figure 4.3 - Schematic set-up for corona poling of ferroelectric materials.

4.3 - Polarization efficiency in 0-3 composites

4.3.1 - Poling field across the ceramic

A major limitation in modelling 0-3 composite electro-active properties as mentioned in chapter 2 (i.e. 2 - Models of composites), arises from the dependence which exists between the efficiency of poling and the piezoelectric and pyroelectric properties of the ceramic powder. In chapter 2, for example, it was assumed that the ceramic grains embedded in the polymer matrix were fully polarised which, in 0-3 composites is not necessarily the case as will be demonstrated shortly.

The importance of the connectivity of phases in the efficiency of poling can now be appreciated. For the mixed connectivity cube model (figure 2.26) it is admitted that the ceramic in the parallel branch will certainly polarise if the applied voltage ensures the field along the rod to be higher than its coercive field (usually around a few MV/m).

In the series branch, however, the field across the ceramic depends on the electrical properties of the ceramic and polymer in that branch. The series branch of the mixed connectivity composite (figure 2.26) is a two layer composite as shown in figure 4.4 whose ceramic and polymer thicknesses are m and $1-m$ respectively. Each of these layers can be approximately modelled by a parallel circuit comprising a resistor and a capacitor representing the conductivity and the capacitance for the ceramic and the polymer respectively. The overall circuit for this two-layer composite can thus be described by the electrical equivalent circuit also drawn in figure 4.4.

The voltage V_c, across the ceramic part will thus vary depending on the frequency of the external applied voltage V, on the dielectric and resistive properties of the ceramic and

polymer as well as on the relative thickness of the layers. The general expression for the field across the ceramic V_c as a function of the frequency f of the applied voltage, is given below in equation 4.5 of table 4.1. The general expression has two regimes, namely, one at high frequency $f>>f_h$ (equation 4.6) and the other at low frequency $f<<f_l$ (equation 4.7).

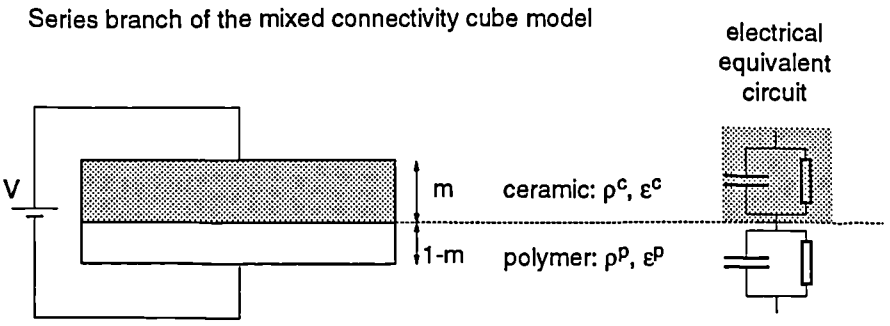

Figure 4.4 - Series connectivity branch of the mixed connectivity cube and its electrical equivalent cube.

TABLE 4.1 - VOLTAGE ACROSS THE CERAMIC IN A TWO-LAYER COMPOSITE

	Limit of validity	eq. no.
$V_c = \hat{V}\dfrac{1+2\pi i f \rho^p \varepsilon_0 \varepsilon^p}{1+2\pi i f \dfrac{\varepsilon_0\left(m\varepsilon^p+(1-m)\varepsilon^c\right)}{\left(\dfrac{m}{\rho^p}+\dfrac{1-m}{\rho^c}\right)}}\dfrac{m\rho^c}{m\rho^c+(1-m)\rho^p}$	All frequencies	(4.5)
$V_c = \hat{V}\dfrac{m\varepsilon^p}{m\varepsilon^p+(1-m)\varepsilon^c}$	$f >> f_h = \dfrac{1}{2\pi}\dfrac{m\rho^c+(1-m)\rho^p}{\left[m\varepsilon^p+(1-m)\varepsilon^c\right]\varepsilon_0\rho^c\rho^p}$	(4.6)
$V_c = \hat{V}\dfrac{m\rho^c}{m\rho^c+(1-m)\rho^p}$	$f << f_l = \dfrac{1}{2\pi\rho^p\varepsilon^p}$	(4.7)

At high frequency the voltage across the ceramic depends on the permittivities of the phases, and for the usual case where the ceramic has a much higher permittivity than the polymer, V_c will be approximately proportional to the ratio $\varepsilon^r = \varepsilon^p/\varepsilon^c$,which can be a quite small quantity when using a PZT5A ceramic and an epoxy for example where this ratio is 0.0024. For a typical ceramic thickness m equal to 0.7, in the short time just after the application of a typical external field of 25 MV/m, only around 0.06 MV/m will actually be applied to the ceramic layer which has a much higher coercive field of approximately 1-2MV/m. This magnitude of the field will not for this reason polarise the ceramic.

In the low frequency region the voltage drop across each of the phases will depend mainly on their resistance. For the usual situation where the ceramic is much more conductive than the polymer, the voltage V_c will be proportional to the ratio $\rho^r = \rho^c/\rho^p$ which is usually a small quantity due to the high resistivity of the polymer ($\approx 10^{12}$-10^{16} Ω·m) relative to the ceramic ($\approx 10^{9}$-10^{11} Ω·m). The voltage in the ceramic in the low frequency region is then of a similar or lower order of magnitude as that obtained in the high frequency

regime.

Various researchers have tried to improve the degree of poling by increasing the ceramic or decreasing the polymer resistivity. Some workers [Safari et al. 1986] obtained a decrease of the polymer resistivity by doping it with a conducting powder such as carbon, silver, silicon or germanium in PZT/polymer and PT/polymer composites and as a result they found that these materials could be effectively poled under a field of 3-4 MV/m for 5 minutes at 100°C. This approach can have, however, some adverse effects due to an increase in the dielectric loss of the composite and thus in its signal-to-noise (S/N) ratio. The decrease of the ceramic resistivity is usually not an option because the ceramics employed are in general optimised to have the highest electro-active properties with a low dielectric loss. Two other approaches [Chilton 1991] have been reported which are based on (i) the high temperature dependence of the resistivity of the polymer and (ii) the high diffusion coefficients of moisture on a polymer thus effectively decreasing the polymer resistivity relative to that of the ceramic. A successful exploitation of these routes requires the optimisation of poling conditions such as the temperature and the humidity of the environment in which case high piezoelectric sensitivities can be obtained.

Another approach is the use of host polar polymers which have a high permittivity together with the use of low dielectric loss ferroelectric ceramics such as modified Lead Titanates as dispersoids which was done in the present work. Polymers such as PVDF and its copolymer with TrFE can be useful alternatives as their permittivities are in the range of 5-12. Moreover, the copolymer P(VDF/TrFE) is a ferroelectric material whose Curie temperature (T_C) is in the 70-150 °C range depending on the molar content of VDF and as a consequence its permittivity can increase up to 60 [Furukawa et al. 1981] (see also 1.4 - Ferroelectric polymers) in the vicinity of its T_C, bringing the permittivity mismatch down to just a factor of 3 in a PTCa:P(VDF/TrFE) composite in that range of temperature.

Using the two-layer model of figure 4.4 we have calculated the magnitude and phase of the field sensed by the ceramic layer in the PTCa:P(VDF/TrFE) and PZT5A-P(VDF/TrFE) composites as a function of frequency, shown in figure 4.5 and 4.6 respectively. The applied field was 25 MV/m, a reasonable value usually below the electric field strength of 0-3 composites. A m value of 0.7 (see figure 4.4) was used, which using the Pauer cube model of figure 2.20, implies a 50% ceramic volume fraction in the composite. The values used for the material properties at 90°C are given in table 4.2.

TABLE 4.2 - PROPERTIES OF SOME COMPOSITE RAW MATERIALS AT 90°C

Material	ρ [Ω·m]	ε (f=10Hz)
P(VDF/TrFE)	$4.5 \cdot 10^{12}$	15.5
PTCa-1	$6.5 \cdot 10^{9}$	299
PZT5A	$3 \cdot 10^{-9}$	1700

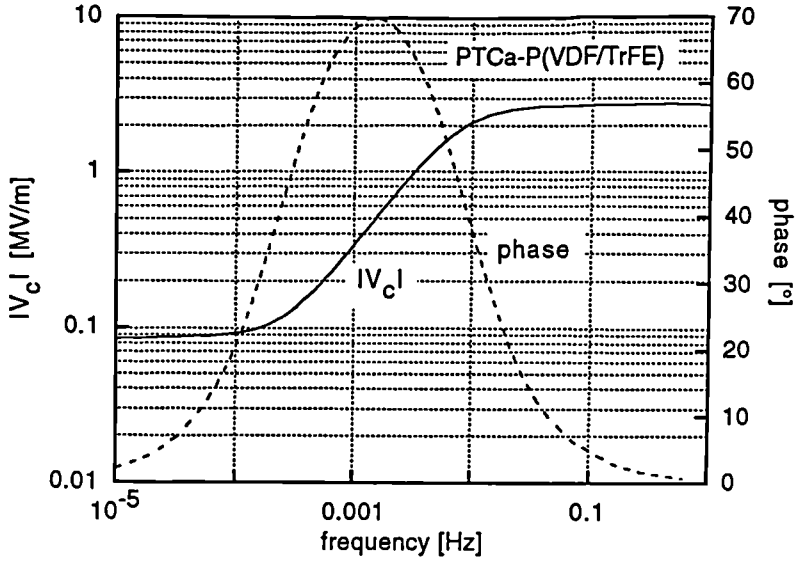

Figure 4.5 - Magnitude and phase of the field sensed on the ceramic in a two-layer composite of PTCa-1:P(VDF/TrFE) at 90℃. The ceramic thickness m is 0.7.

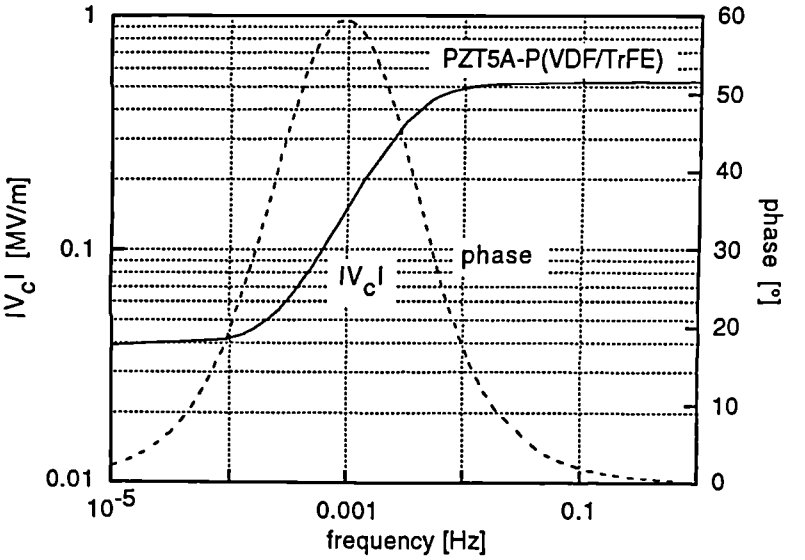

Figure 4.6 - Magnitude and phase of the field applied to the ceramic in a two layer composite of PZT5A-P(VDF/TrFE) at 90℃. The ceramic thickness m is 0.7.

Comparing the graphs of figure 4.5 and 4.6 it is observed that for both composites a higher fraction of the field is sensed by the ceramic at high than at low frequency. This implies that the permittivity mismatch is usually lower than that for the resistivity. As expected, the combination of PTCa-1:P(VDF/TrFE) which has the lowest permittivity mismatch is the one where the highest field is applied to the ceramic. It is obvious that using other material combinations with higher mismatches such as PZT5A-epoxy will decrease the poling efficiency even further.

It is acknowledged that the permittivities stated in table 4.2, which were measured at 10Hz will vary with frequency and thus the graphs of figures 4.5 and 4.6 are not strictly correct although these can be a reasonable approximation.

The f_h and f_l frequency limits that bound the transition region where V_c changes from a permittivity coupling to a resistivity one are not dissimilar for these two composites as can

be seen from table 4.3.

TABLE 4.3 - HIGH AND LOW FREQUENCY, REGIME BOUNDS FOR THE COMPOSITES OF FIGURES 4.2 AND 4.3

	f_l	f_h
PTCa-P(VDF/TrFE)	$2.5 \cdot 10^{-4}$	$8.3 \cdot 10^{-2}$
PZT5A-P(VDF/TrFE)	$2.5 \cdot 10^{-4}$	$3.4 \cdot 10^{-2}$

From figures 4.5 and 4.6 it can thus be concluded that to polarise those composites it is better to use an ac voltage with a frequency higher than 0.01 Hz. A point which should however be kept in mind, is that according to Jimenez [Jimenez 1988] and Chan [Chan et al. 1989] it takes around 5 minutes to polarise a PTCa ceramic whilst applying a step field of around 4 MV/m. Thus, when applying a 25 MV/m ac field to a PTCa-1:P(VDF/TrFE) composite at a frequency of say 0.01 Hz the field will oscillate between 0 and 2.6 MV/m (see figure 4.5). It is possible then, that although the ceramic has a higher field applied to it, the time for which the voltage is sufficiently high is not long enough to switch the polarization.

4.3.2 - Property dependence on the poling efficiency

Using the mixed connectivity model the properties of the composite can be found as a function of the degree of poling α, of the ceramic which is in the series branch while assuming that the parallel connectivity ceramic is always fully poled. This can be done by assuming that both the piezoelectric constant and the pyroelectric coefficient of the ceramic in the series branch are proportional to a parameter α measuring the efficiency of poling.

Figures 4.7 and 4.8 show both the pyroelectric FOM_p and k_t for a PTCa:PVDF 65% composite as function of n (i.e. the degree of 1-3 connectivity character) for various poling efficiencies.

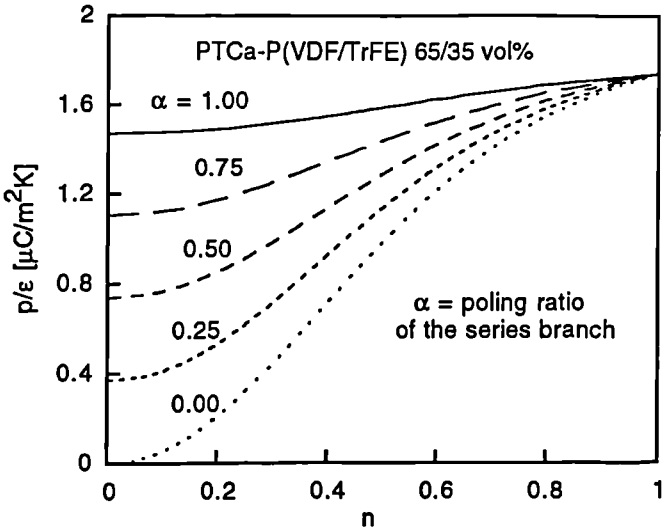

Figure 4.7 - Pyroelectric FOM=p/ε for the mixed connectivity model of a PTCa-P(VDF/TrFE) 65/35 vol% showing its dependence on the poling ratio α of the series branch.

It is apparent that the FOM_p is significantly dependent on the degree of poling contrary to k_t which is not affected as much. This implies that the series connectivity branch makes a higher contribution to the overall FOM_p than for the k_t, the latter being mostly dependent on the ceramic connected in parallel.

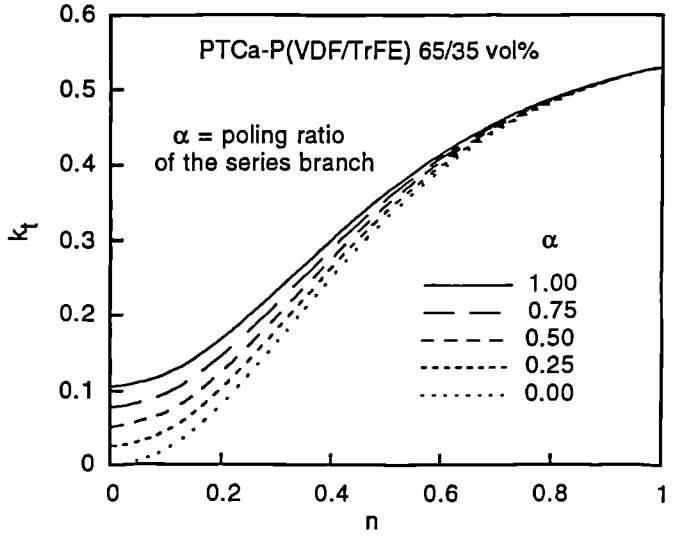

Figure 4.8 - Thickness electromechanical coupling factor k_t of the mixed connectivity model of a PTCa-P(VDF/TrFE) 65/35 vol% showing its dependence on the poling ratio α of the series branch.

4.4 - Resistivity properties in PTCa-1:P(VDF/TrFE) composites

The resistivity properties and the dielectric properties of the constituent materials of a composite influence to a great extent the electro-active properties of the composite as has been explained in chapter 2 (- Models of composites). In the previous section it was also acknowledged that these properties can be very important in the polarization process which is a critical step in obtaining a successful electro-active material.

For comparison and modelling purposes resistivity and dielectric measurements were performed on a ceramic sample of PTCa-1 provided by Siemens, who also provided the ceramic powder. The area of the ceramic disk was 1.1 cm^2 whilst its thickness was 1.04 mm.

Similar measurements were also done on P(VDF/TrFE) samples. The copolymer powder which was used to make the composites was placed between the stainless steel plates to press the composites. Then, using a hydraulic press at a similar pressure and temperature as for the composites, suitable copolymer films were obtained suitable for the intended measurements. The thickness of the copolymer samples was approximately 70 μm while the diameter of the electrodes were the same as that of the composites i.e. 25 mm.

As will be described in the following chapters on the composite pyroelectric and piezoelectric properties, PTCa:P(VDF/TrFE) has been found to the best electro-active material of the composites fabricated, in particular those at the 65% ceramic loading. In order to investigate the poling phenomenon explained above and due to a limitation of time the PTCa1-P(VDF/TrFE) composite was chosen as a suitable material for a more thorough study of resistivity and dielectric properties. The analysis which will be now described, can

certainly be extended to the other composites fabricated.

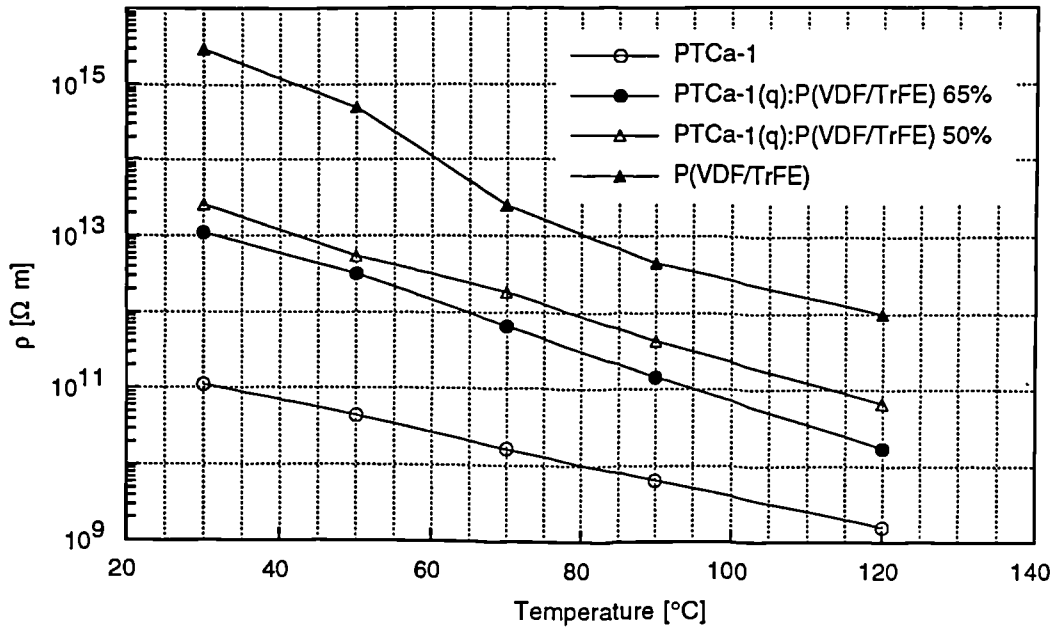

Figure 4.9 - Resistivity as a function of temperature for PTCa-1 ceramic, PTCa1(q):P(VDF/TrFE) 65 and 50% composites and P(VDF/TrFE) copolymer.

The resistivity data for PTCa1 and P(VDF/TrFE) together with those of its composites PTCa-1(q):P(VDF/TrFE), loaded with 65% and 50% ceramic, are shown in figure 4.9 which shows that the composites exhibit resistivity values between those of the polymer and the ceramic. Furthermore, it is noted that the composite loaded with 65% of ceramic has a lower resistivity than that of the 50% ceramic loading which should be anticipated just on the grounds of an increased ceramic volume fraction. An additional mechanism of increasing the resistivity resulting from an increased 1-3 degree of connectivity for the higher ceramic loading may also be present.

In figure 4.10 is shown a comparison of data for PTCa-1:P(VDF/TrFE) composites fabricated from milled and quenched ceramic powder loaded at 50%. It may be observed that although at room temperature they exhibit approximately the same resistivity, the milled ceramic exhibits a higher decrease in its resistivity with increasing temperature than the quenched ceramics. In fact the resistivity of the composite with 50% milled ceramic decreases beyond that of the composite loaded with 65% of quenched ceramic powder shown in figure 4.9 and approaches at 120°C that of the pure PTCa-1 ceramic. This behaviour is difficult to explain because the finer grain size of the milled ceramic should impart a lower degree of 1-3 connectivity to its composite. Consequently the milled ceramic composite should exhibit properties more akin to those of the polymer and hence a higher resistivity than the quenched ceramic composite loaded with the same volume fraction. Furthermore, it was also found that regarding other properties, the milled PTCa-1 ceramic composites behaviour could only be explained successfully if it was assumed that a milled ceramic powder exhibits different properties from the sintered bulk ceramic. This point will be brought up later in subsequent discussions of other properties.

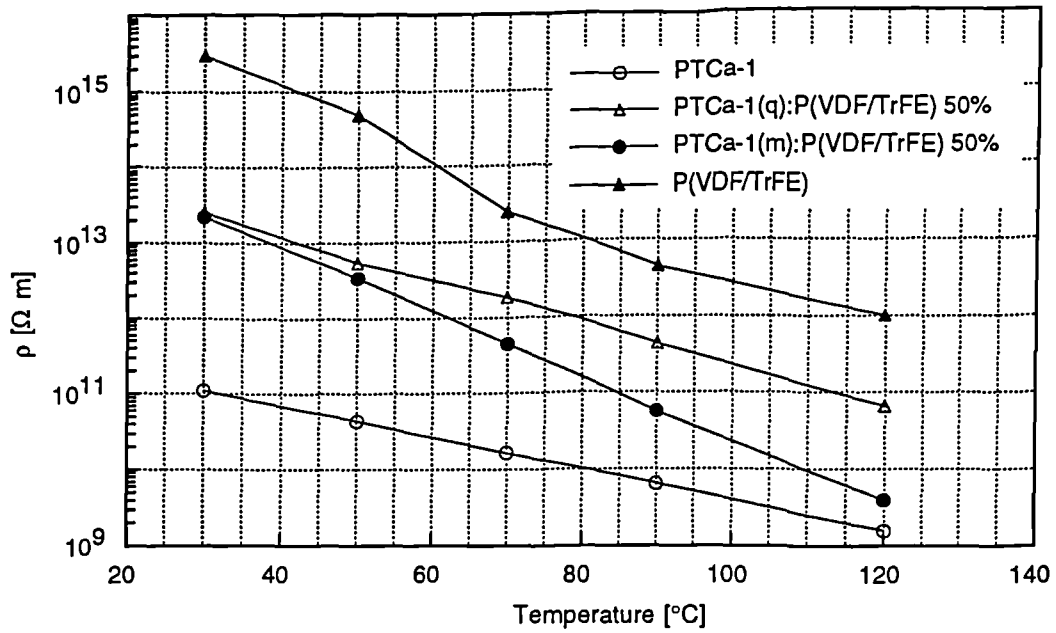

Figure 4.10 - Resistivity as a function of temperature for PTCa-1 ceramic, P(VDF/TrFE) copolymer and PTCa1:P(VDF/TrFE) 50% composites made with quenched and milled ceramic powders.

The temperature dependence of resistivity data, presented above, was modelled for each material using the equations

$$\sigma = \frac{1}{\rho} \quad \text{and} \tag{4.8}$$

$$\sigma = \sigma_o \exp\left(-\frac{E_{ac}}{kT}\right) \tag{4.9}$$

where σ is the conductivity of the material, σ_0 the extrapolated conductivity at zero temperature, E_{ac} activation energy, k the Boltzmann constant and T the absolute temperature. By fitting the data to these equations the values listed in table 4.4 were obtained.

TABLE 4.4 - CONDUCTIVITY ACTIVATION ENERGY FOR PTCA-1:P(VDF/TrFE) COMPOSITES AND ITS CONSTITUENT MATERIALS

	E_{ac} [eV]	σ_0 [Ω·m]$^{-1}$
PTCa-1	0.48	$8.74 \cdot 10^{-4}$
PTCa-1(q):P(VDF/TrFE) 65%	0.74	$1.575 \cdot 10^{-1}$
PTCa-1(q):P(VDF/TrFE) 50%	0.67	$5.547 \cdot 10^{-3}$
PTCa-1(m):P(VDF/TrFE) 50%	0.99	1158
P(VDF/TrFE)	0.96	3.124

From the table 4.4., it is observed that the activation energy, which is in fact a measure of its temperature dependence of the electrical conductivity, has a lower value in the pure ceramic than in the pure polymer. The 50% milled ceramic composite has an activation energy comparable to that of the polymer whilst the 65% and 50% quenched ceramic

composites have intermediate values of E_{ac} between the ceramic and the polymer.

Figure 4.11 shows a plot of the ratio of resistivity of PTCa-1 and P(VDF/TrFE) (i.e. $\rho^{PTCa-1}/\rho^{P(VDF/TrFE)}$) as a function of temperature. It can be noticed that this ratio increases with temperature, thus improving the poling conditions. However, the ratio ceases to increase beyond 90°C where the resistivity of the ceramic is roughly $1.5 \cdot 10^{-3}$ times that of the copolymer. Thus, one can conclude that although a higher temperature facilitates the poling process due to a better matching of resistivity, it may not be a sufficient factor to bring about an effective polarization of the ceramic grains.

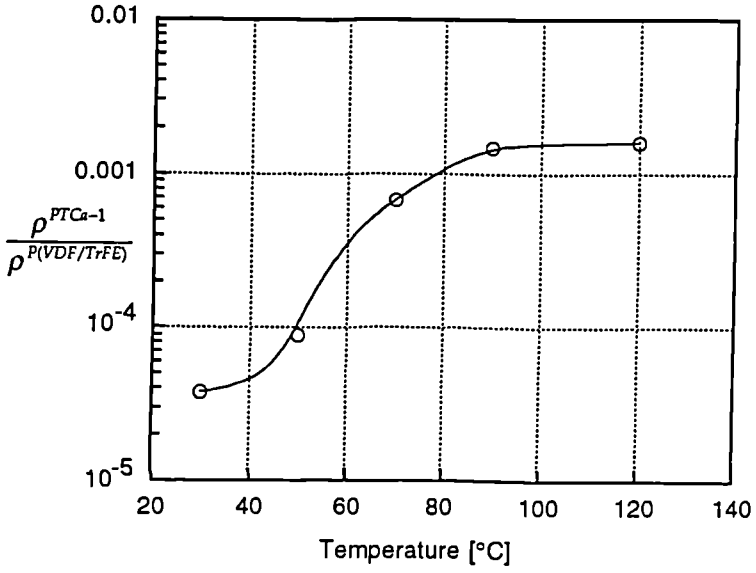

Figure 4.11 - Resistivity ratio between PTCa-1 and P(VDF/TrFE).

It is assumed that the other composites should not show strikingly different results from those shown here for the PTCa-1:P(VDF/TrFE) composites. The important point in our study is that the resistivity of the constituent phases bound the resistivity properties of the composites which are derived from them.

4.5 - Dielectric properties of composites

The permittivity and the loss measurements, at room temperature and at a frequency of 1kHz, were undertaken on the fabricated composites as well as on samples of PTCa-1 and P(VDF/TrFE). These values are listed in table 4.5.

The uncertainty of the measured values of the permittivity is around 15%. The permittivity is calculated from the measured capacitance C, the thickness l and the area A of the sample, using the relationship:

$$\varepsilon = \frac{Cl}{\varepsilon_o A} \qquad (4.10)$$

An uncertainty in the thickness l of the sample due to its non-uniformity, is reflected in the calculated value of the permittivity. There is also an error from a variation of the ceramic volume fraction in the composite from sample to sample as well as within batches which is assumed to be of the order of 5%.

TABLE 4.5 - DIELECTRIC PROPERTIES FOR THE COMPOSITES FABRICATED AND ITS CONSTITUENT MATERIALS (@ 30°C, 1kHz) AFTER POLING

material	ceramic vol. fraction	ε	tan δ
PP*		3.8	$3 \cdot 10^{-4}$
PVDF*		8	0.06
P(VDF/TrFE)		12	0.020
PZT5A:PP	40	13	<0.001
PZT:PVDF	50	63	0.018
PZT:P(VDF/TrFE)	50	118	0.020
PLZT:P(VDF/TrFE)	50	80	0.017
PTCa-2(q):P(VDF/TrFE)	50	40	0.013
"	60	49	0.012
"	65	51	0.011
PTCa-2(q fine):P(VDF/TrFE)	50	36	0.021
PTCa-2(q coarse):P(VDF/TrFE)	50	37	0.020
PTCa-1(q):P(VDF/TrFE)	20	21	0.018
"	30	28	0.015
"	40	34	0.013
"	50	40	0.013
"	60	49	0.013
"	65	67	0.013
PTCa-1(m):P(VDF/TrFE)	50	56	0.014
"	60	66	0.012
PTCa-1		230	0.006
PTCa-2		150	0.014
PLZT 7/65/35*		1860	0.018
PZT5A*		1700	0.020

* - the dielectric properties of these materials are those quoted from the available literature

From the data in the table 4.5, the permittivity and loss properties for each composite are seen to lie in-between those exhibited by the ceramic and the polymer which were used to fabricate the composite.

As a rule, it is also verified comparing for example the PZT:P(VDF/TrFE) and PZT:P(VDF/TrFE) composites that a higher permittivity of the ceramic will be reflected in a larger composite permittivity. The same argument applies for the polymer phase too.

For a given composite it is observed that an increasing ceramic volume fraction increases the permittivity of the composite. Regarding the dielectric loss of PTCa-1:P(VDF/TrFE) composites, a decrease with an increasing volume fraction is found.

The permittivity of the milled ceramic composite PTCa-1(m):P(VDF/TrFE) 50% is observed to be larger than that of the same composition material made with quenched

ceramic (i.e. PTCa-1(q):P(VDF/TrFE) 50%). This effect will be treated in more detail later on.

In order to get a better insight of the composite dielectric polarization mechanisms more detailed dielectric measurements were carried out on PTCa-1:P(VDF/TrFE) composites.

4.5.1 - Temperature dependence of the dielectric properties

In figures 4.12 and 4.13 are shown the temperature dependence of the permittivity and the loss tangent of PTCa-1(q):P(VDF/TrFE) composites of 65, 60, 50 40 and 30% together with the corresponding properties for the constituent materials. The measurements were taken at 1kHz. All the materials appear to show an increase in the permittivity with temperature. In relative terms P(VDF/TrFE) has the highest variation in its permittivity with temperature i.e. larger than a factor of 2 in the plotted temperature range.

This effect observed in all materials, is caused by the ferroelectric character of the constituent materials (i.e. PTCa-1 and P(VDF/TrFE)) so that when approaching their respective Curie temperature their permittivity increases.

From figure 4.12 it is verified that the composites with a higher ceramic volume fraction display a higher permittivity as it is expected.

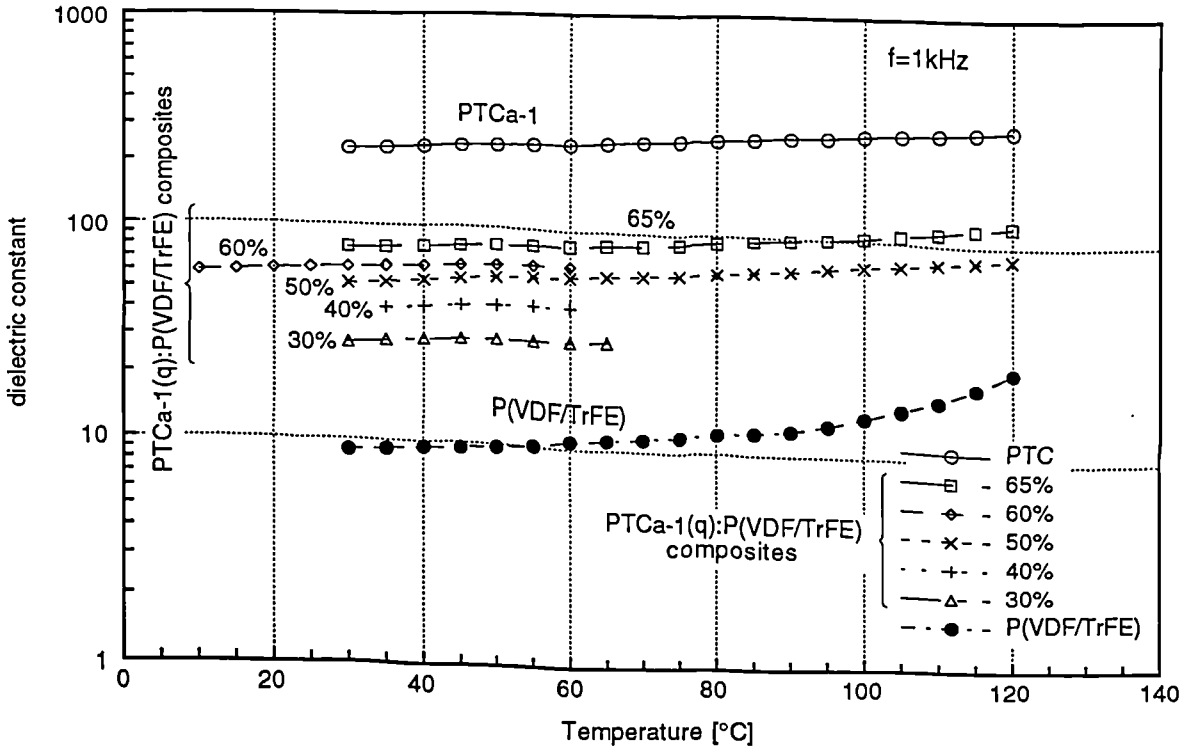

Figure 4.12 - Temperature dependence of the permittivity in PTCa-1(q):P(VDF/TrFE) composites and its constituent materials.

In figure 4.13 the dielectric loss or tan δ is displayed as a function of temperature for the same composites of figure 4.12. In general, similar values and temperature dependence of the dielectric loss can be noticed in these composites loaded with different volume fraction of the ceramic, although, a weak trend can be perceived, whereby a higher ceramic volume fraction composite displays a lower dielectric loss.

The dielectric loss values for the composites, however, are not bound by those of the constituent materials above 80 °C. It is not certain the reason for this behaviour but it is possible that some interfacial effects could be present. It should be pointed out nevertheless that the composites dielectric loss decreases in the low temperature range following an analogous behaviour to that of the polymer, while in the high temperature range the dielectric loss in the composites rises as in the case of PTCa-1 ceramic.

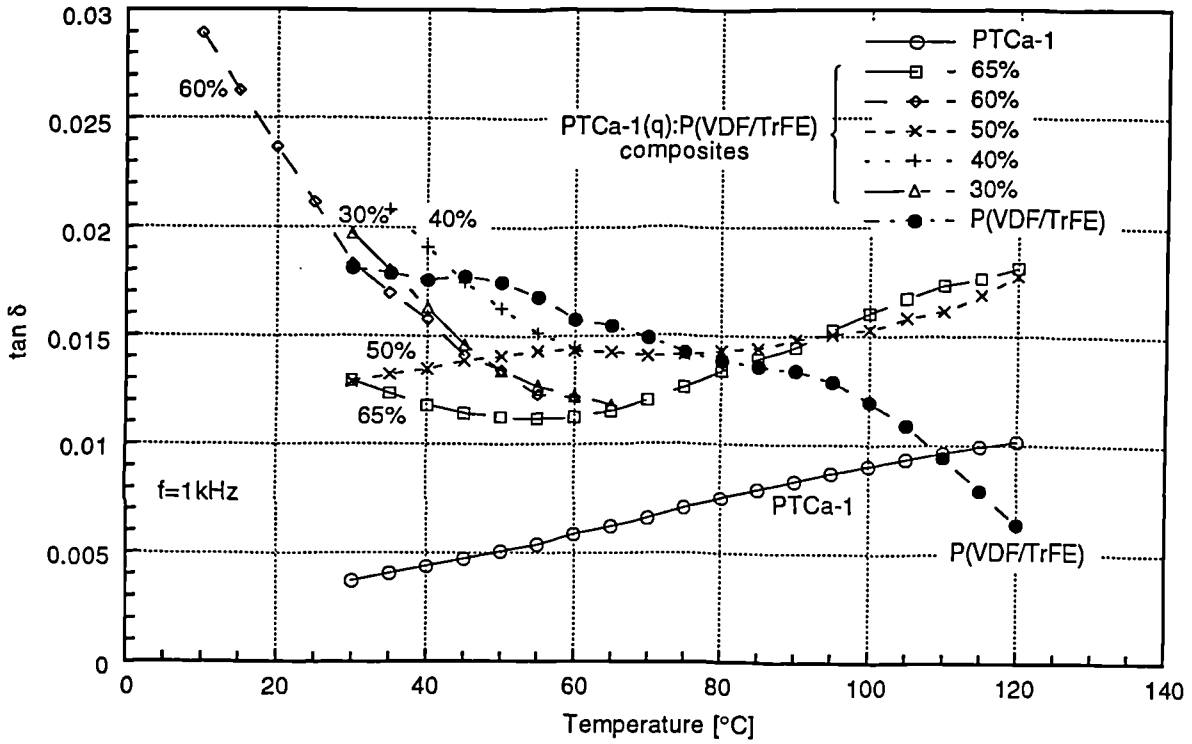

Figure 4.13 - Temperature dependence of the dielectric loss in PTCa-1(q):P(VDF/TrFE) composites and its constituent materials.

The temperature dependence data of figures 4.12 and 4.13 were taken during the heating of the samples. However, when recording the dielectric measurements during both the heating and cooling, a dielectric hysteresis was observed as shown in figures 4.14 and 4.15 for the PTCa-1(q):P(VDF/TrFE) 65% composite and P(VDF/TrFE). It is noticed that the dielectric hysteresis which characterises the polymer due to its ferroelectricity is reflected into the composite dielectric behaviour although in the case of the composite this happens at a higher value of the permittivity.

The imaginary part of the permittivity for this composite and for P(VDF/TrFE) plotted in figure 4.15 also exhibits a temperature hysteresis behaviour. The temperature hysteresis of the copolymer however is significantly larger than that of the composite which also emulates to a certain extent that of its constituent ceramic i.e. PTCa-1.

In the low temperature range at around 10°C a relaxation peak can be observed for PTCa-1(q):P(VDF/TrFE) 65% which can be identified with that of the β-relaxation peak of P(VDF) which relates to its glass-transition temperature.

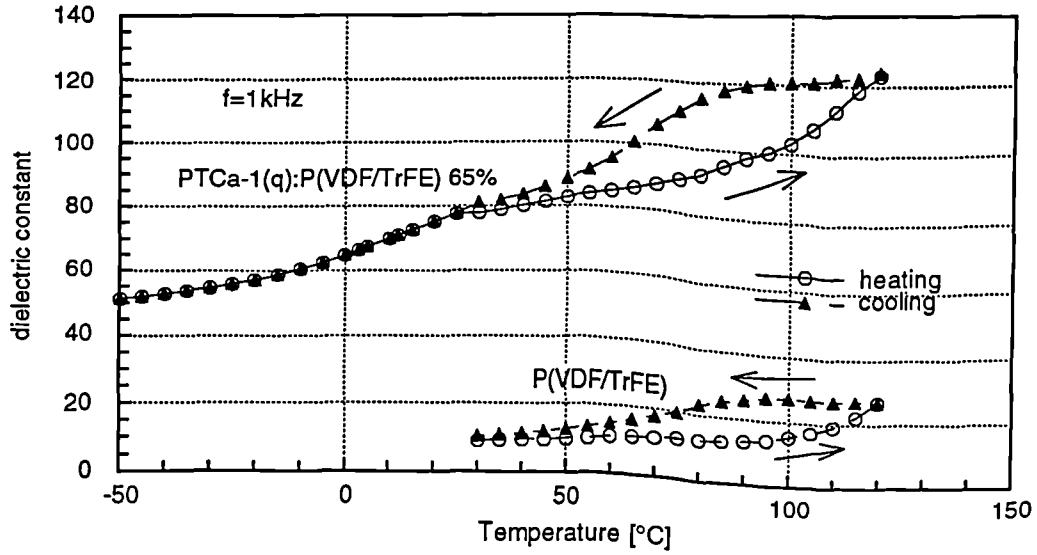

Figure 4.14 - Temperature hysteresis of the real part of the permittivity in the PTCa-1(q):P(VDF/TrFE) 65% composite and in P(VDF/TrFE) copolymer.

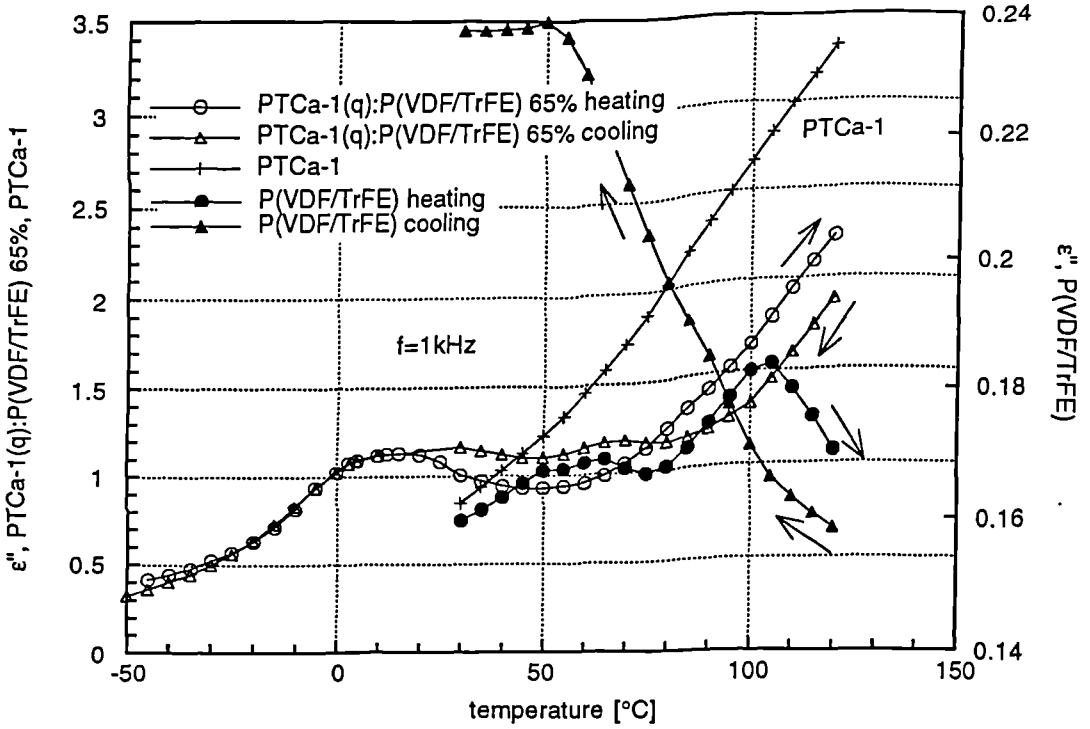

Figure 4.15 - Temperature hysteresis of the imaginary part of the permittivity in the PTCa-1(q):P(VDF/TrFE) 65% composite and in P(VDF/TrFE) copolymer. The temperature dependence of the imaginary part of the permittivity in PTCa-1 is also plotted in the same graph.

In order to check for the Curie temperature in the composites Differential Scanning Calorimetry (DSC) runs have been performed on PTCa-1 and PTCa2 composites made with P(VDF/TrFE) as the host polymer and the results are summarised in table 4.6.

Three endothermic peaks can be observed. The first peak is clearly identified with the ferroelectric transition of P(VDF/TrFE) phase. In fact it agrees quite reasonably well with the nominal value of T_C=134 °C, quoted by the Solvay which provided the copolymer. The small difference can be ascribed to a different cooling rate when the composite sample crystallises

from the melt after pressing. The second peak can be identified with the melting of the polymer which takes place roughly at 147°C and which also agrees with the value of 149°C quoted by copolymer manufacturer. The third peak is identified with the Curie temperature of the ceramic which for PTCa-1 and PTCa-2 are found roughly to be 271 and 256 °C respectively. An inconsistency can be found in the positive value of the third peak of the PTCa-1(q):P(VDF/TrFE) 60% indicating an exothermic peak. There is ground, however, to believe that this DSC peak is due to the ferroelectric character of PTCa-1.

TABLE 4.6 - DSC PEAKS IN COMPOSITES

	1st peak		2nd peak		3rd peak	
composite material	T[°C]	Area [J/g]	T[°C]	Area [J/g]	T[°C]	Area [J/g]
PTCa-2(q):P(VDF/TrFE) 65%	128.2	-1.9	148.3	-3.21	278.2	-0.89
PTCa-2(q):P(VDF/TrFE) 60%	127.7	-3.81	147	-4.55	272.1	-1.19
PTCa-2(q):P(VDF/TrFE) 50%	127.2	-1.27	145	-3.92	271	-0.95
PTCa-1(q):P(VDF/TrFE) 60%	127.7	-3.61	146.5	-3.78	257.9	+1.62

In figure 4.16 is shown the permittivity for the quenched and the milled ceramic composites of PTCa-1:P(VDF/TrFE) 50% composition. Contrary to the expectations the milled ceramic shows a higher permittivity throughout the temperature range than the quenched ceramic. In fact, due to the smaller grain size of the milled ceramic grains its composite should have a lower degree of 1-3 connectivity and hence a lower permittivity. This agrees, however, with the previous resistivity measurements of these composites which showed a lower resistivity for the milled ceramic composite.

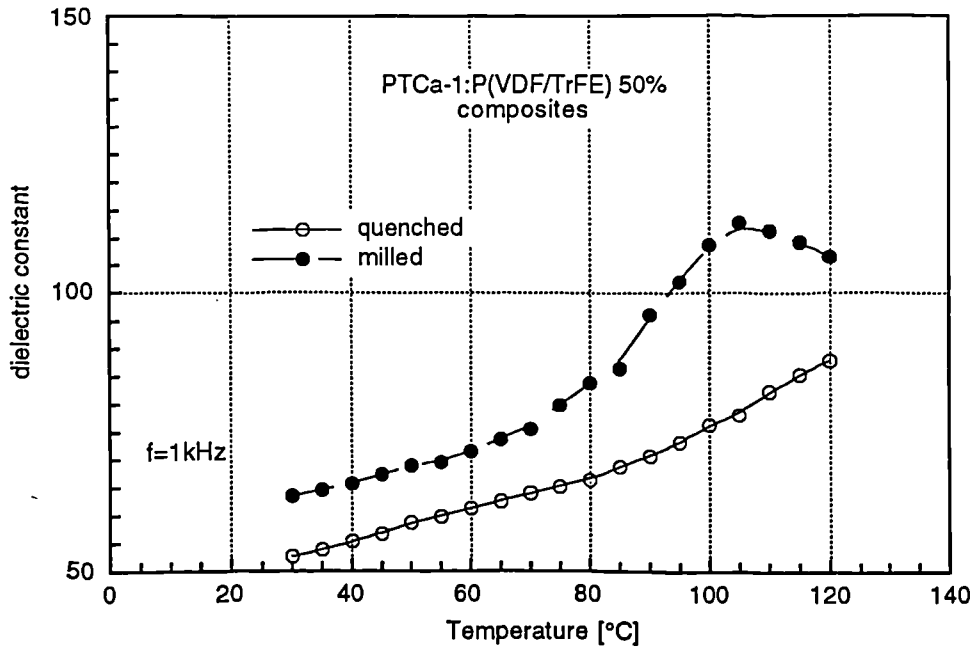

Figure 4.16 - Temperature dependence of the permittivity in PTCa-1:P(VDF/TrFE) 50% composite.

It is possible that during the ceramic grinding operation some surface stress could be

imparted to the grains, which may increase the permittivity of the powder relative to that of the bulk ceramic while lowering its surface resistivity. It is also possible that like $BaTiO_3$ (see section 1.3), in PTCa-1 and other ferroelectric ceramics there is a range where a decrease of the grain size increases the permittivity. These are speculations which could partly explain the behaviour of the milled composites and which obviously should be proven. The present reasoning, however, implies that the quenched ceramic powder retains in a greater measure the bulk properties of the ceramic. This is regarded as a reasonable assumption due to the way in which this kind of powder is obtained with little mechanical damage to the grains and with the natural cleavage planes determining the way in which the sintered ceramic breaks down.

4.5.2 - Frequency dependence of the dielectric properties

In figure 4.17 is plotted the frequency dependence of the permittivity at 30°C for PTCa-1:P(VDF/TrFE) composites and those of its constituent materials. Apart from a general expected decrease of the permittivity value with frequency nothing else relevant seems to be apparent in this graph. For example, the magnitudes of the permittivity of these different materials appear to maintain the same relative position they had in the previous temperature dependence measurements.

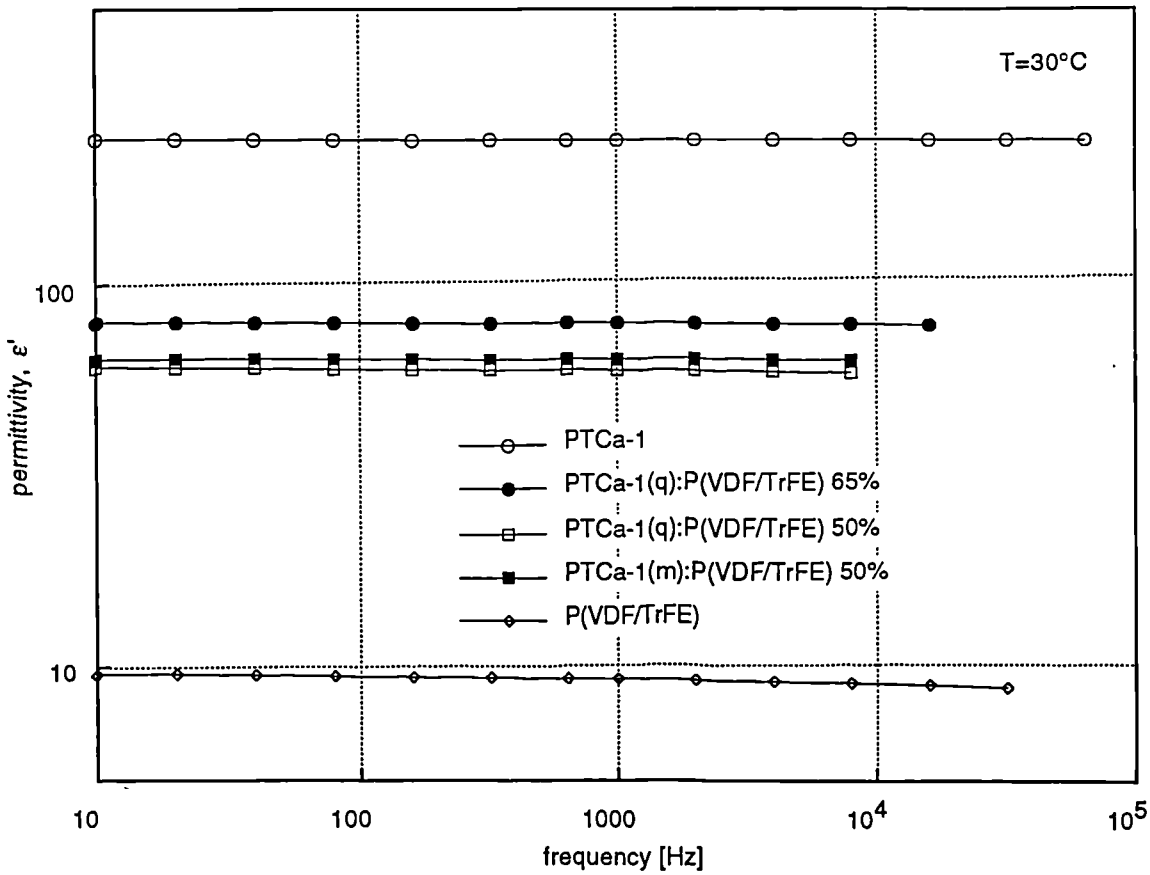

Figure 4.17 - Frequency dependence of the permittivity at 30°C for PTCa-1(q):P(VDF/TrFE) composites and its constituent materials.

In figure 4.18 is shown the frequency dependence of the imaginary part of the permittivity at 30°C. A similar frequency behaviour for all the composites which matches

that of the copolymer, is apparent from these measurements.

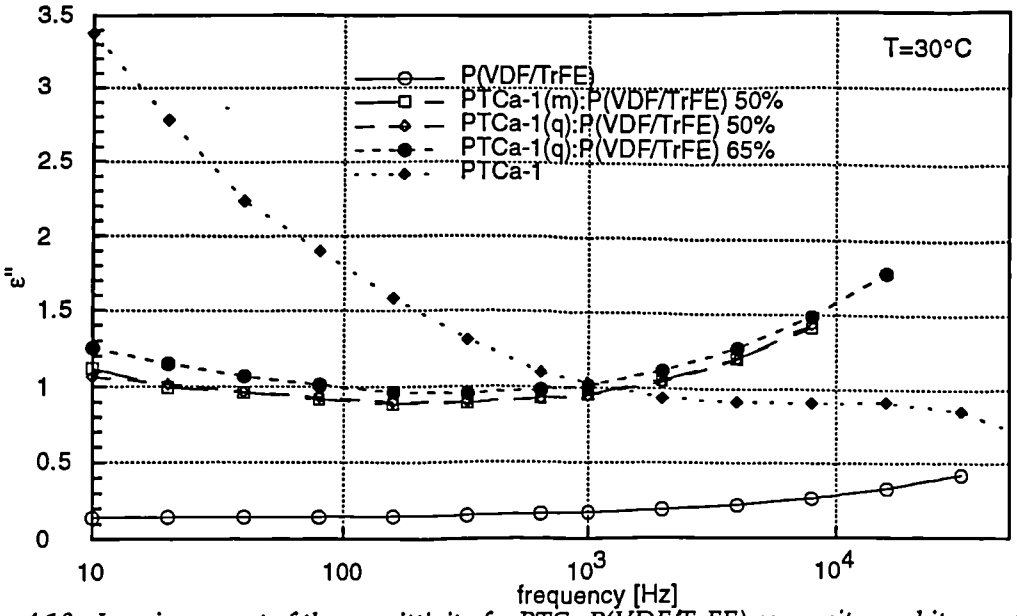

Figure 4.18 - Imaginary part of the permittivity for PTCa:P(VDF/TrFE) composites and its constituent materials.

For the 65% composite these measurements were done over a wide frequency range from 10^{-4} to 10^{5} Hz which are shown in figure 4.19. These measurements were done using a Solartron response analyser equipped with an interface developed at the Chelsea College. From this graph a relaxation peak can be presumed to exist in the megahertz region which coincides with that of P(VDF/TrFE) as shown in figure 1.23.

There is no explanation for the imaginary part of the permittivity of these composites to be larger than any of its constituent materials as displayed in figure 4.18 for frequencies beyond 1kHz.

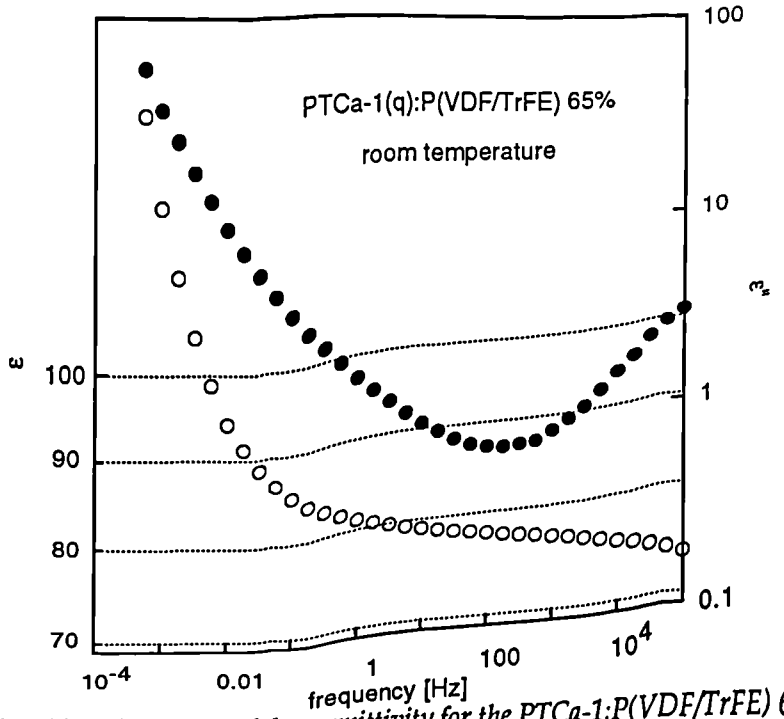

Figure 4.19 - Real and imaginary part of the permittivity for the PTCa-1:P(VDF/TrFE) 65% composite.

In figure 4.20 are shown the Cole-Cole plots for PTCa-1:P(VDF/TrFE) composites and its constituent materials taken at 30°C. In all of the graphs the range of frequency plotted is the same (i.e. 10Hz<f<16KHz) except for the graph 4.20(a) where the frequency range is the same as that of figure 4.19 (i.e. 5E-4<f<100KHz). For all plots the frequency increases from the right to the left.

In figure 4.20(a) for PTCa-1(q):P(VDF/TrFE) 65% the contribution of the resistivity at 30°C, to the imaginary part of the permittivity was calculated and also was plotted in the same Cole-Cole plot. Comparing its magnitude it is concluded that the resistivity contributes little to the dielectric loss even at $5 \cdot 10^{-4}$ Hz and hence a true low-frequency relaxation is present in the PTCa-1:P(VDF/TrFE) composites. This relaxation which can be due either to a Maxwell-Wagner or space-charge effect can only be resolved with further measurements at higher temperatures with the same frequency span.

In figure 4.20(e) for PTCa-1 it is observed that two relaxations seem to be present in the frequency range of measurement, while in graph 4.20(f) for P(VDF/TrFE) a relaxation seems to appear. Now, comparing graphs 4.20 b), c) and d) for the composites with those of the constituent materials i.e. graphs 4.20 e) and f), it can be concluded that in the low-frequency the relaxational behaviour of the composites seem to emulate that of the PTCa-1 while at high frequency the behaviour of P(VDF/TrFE) appears to be more prominent in the composites.

This type of analysis could lead us far into the dielectric behaviour of multiphase systems, and much work would be necessary in this respect.

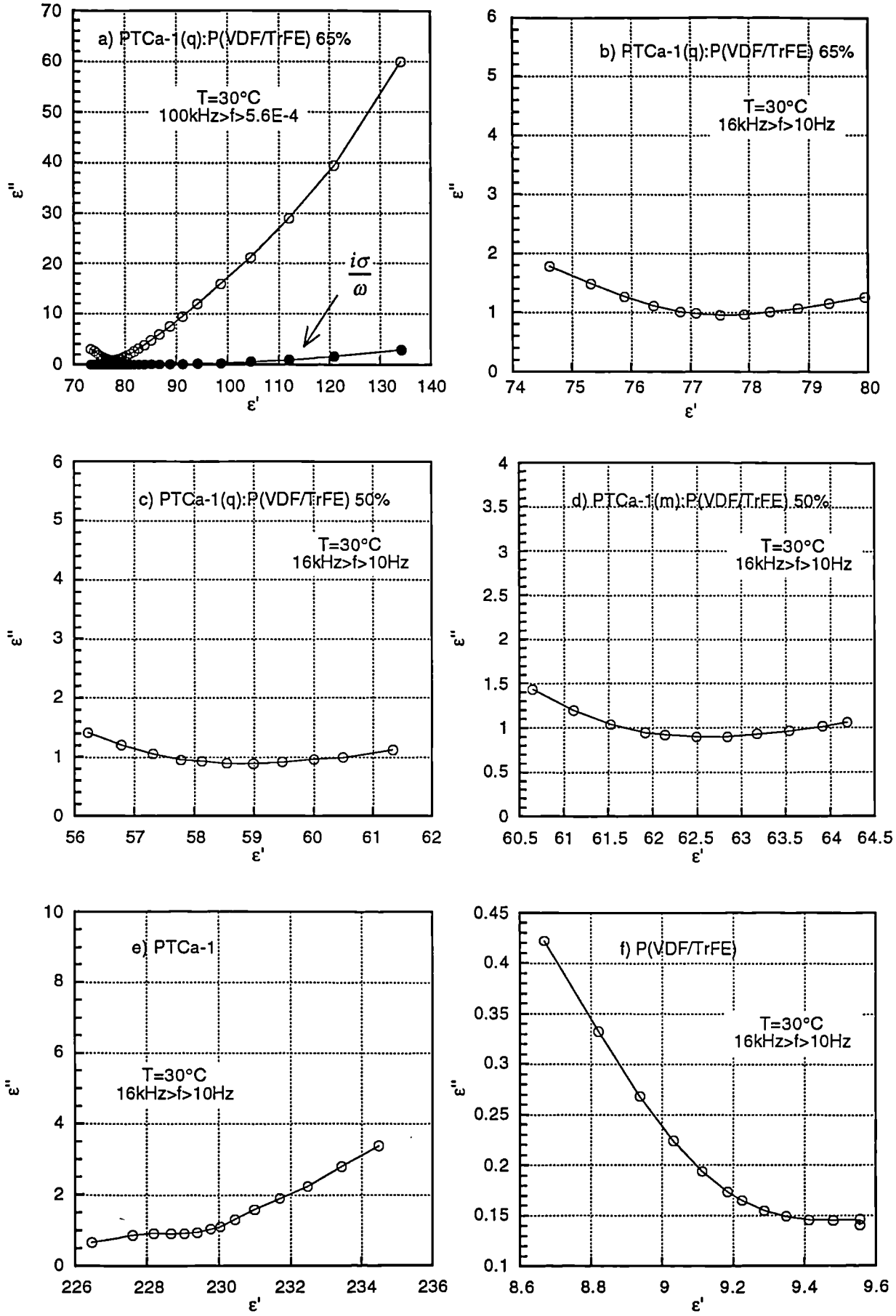

Figure 4.20 - Cole-Cole plots for PTCa-1:P(VDF./TrFE) composites and its constituent materials.

4.5.3 - Volume fraction dependence

In figure 4.21 is shown the behaviour of the permittivity measured at 1kHz and 30°C as a function of the ceramic volume fraction in PTCa-1(q):P(VDF/TrFE) composites. In the same figure are drawn the curves corresponding to a pure 2-2 parallel and series connectivity. It can be observed that the experimental points describe a curve that lies in-between these two limiting connectivity types.

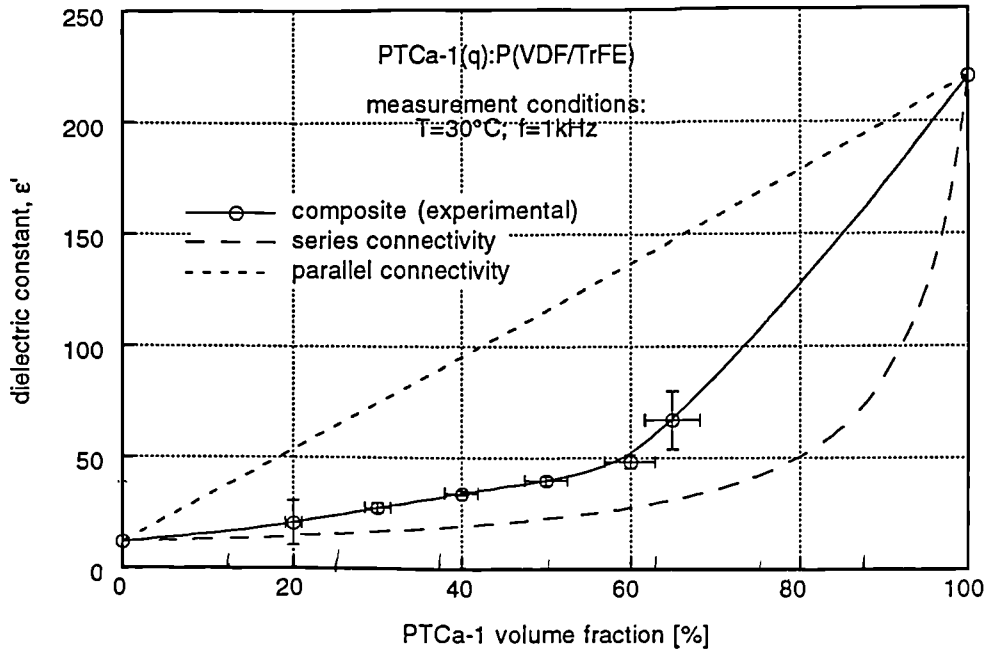

Figure 4.21 - Permittivity of PTCa-1(q):P(VDF/TrFE) composites as a function of the ceramic volume fraction.

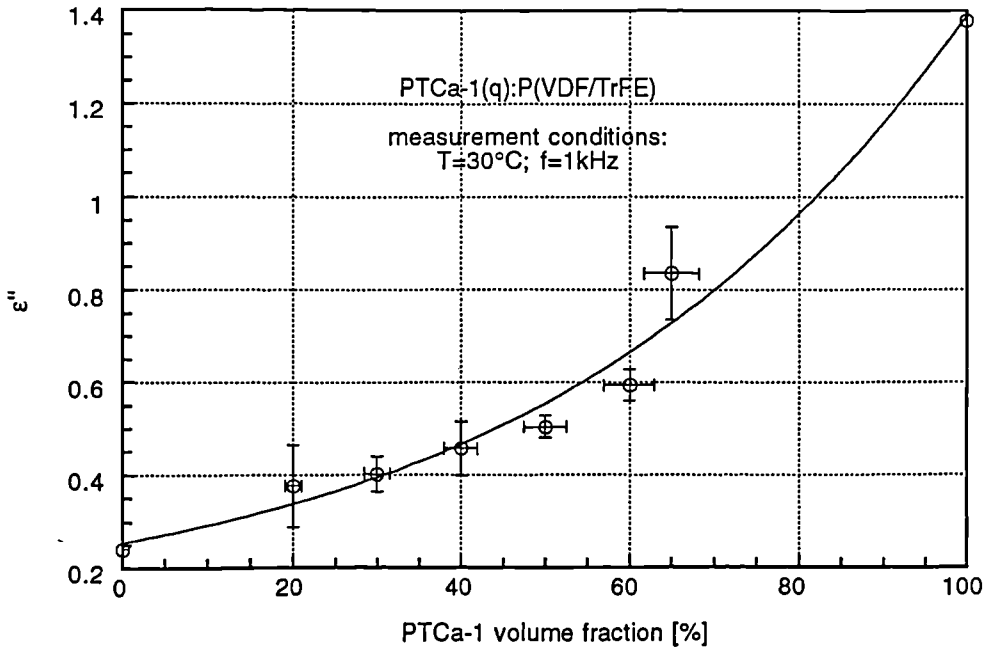

Figure 4.22 - Imaginary part of the permittivity for PTCa-1(q):P(VDF/TrFE) composites as a function of the ceramic volume fraction.

It is observed in figure 4.22 that the imaginary part of the permittivity also has a

similar variation as that of the real part. This is what should be expected because the rules to calculate the permittivity as described in chapter 2 (i.e. models of composites), should also apply to the complex permittivity and thus approximately to both the real and imaginary parts separately. This is an interesting point because the derivation of the formulae in chapter 2 are also valid if the properties are complex variables, and thus a prediction of the complex properties of composites (dielectric, piezoelectric and pyroelectric) should also be possible to obtain from these equations.

Figure 4.23 shows a contour chart for the permittivity of PTCa-1(q):P(VDF/TrFE) composite using the mixed connectivity cube model. For this chart the experimental values of the dielectric properties of the constituent materials at 30°C and 1kHz have been used. The constant volume fraction curves have also been drawn in the chart as dashed lines.

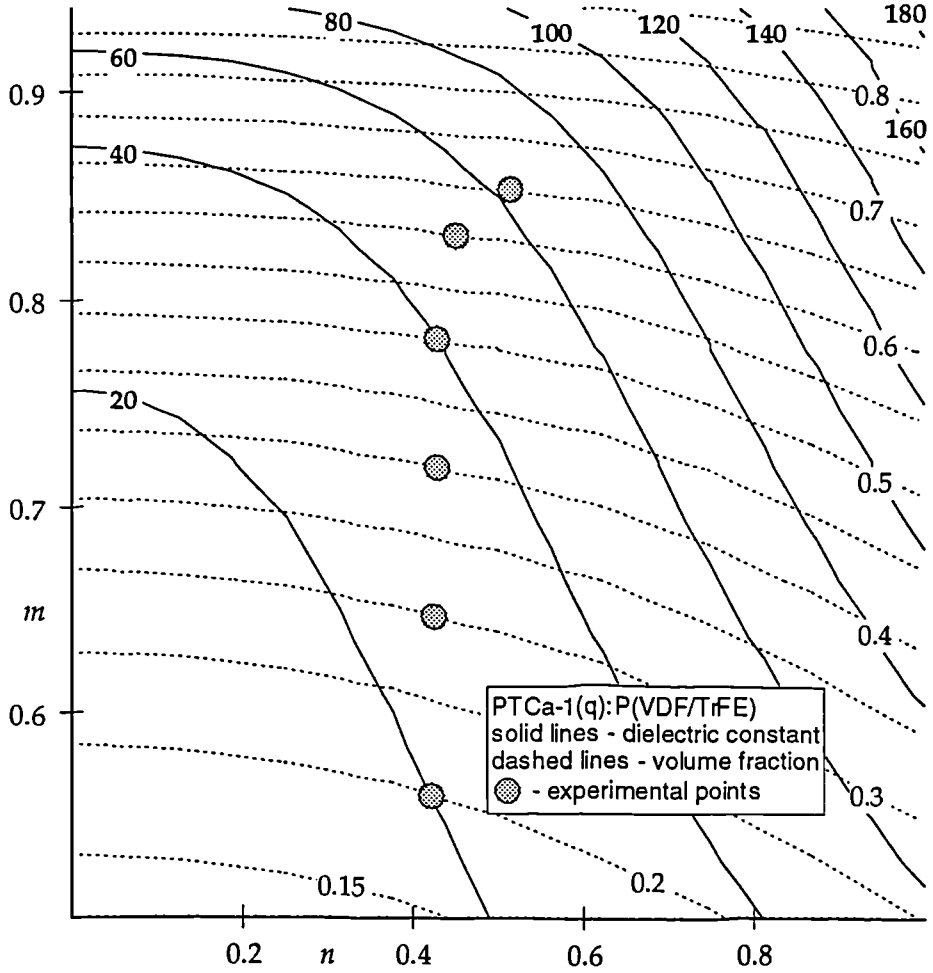

Figure 4.23 - Permittivity contour chart for the PTCa-1(q):P(VDF/TrFE) composite using the mixed connectivity cube model.

Following the procedure described in chapter 2 the experimental points, which were plotted in figure 4.21, have been located in the chart and are shown as grey circles.

In this chart it can be noticed that the experimental points have an n value which is in the range of 0.4-0.5 and thus about half of the ceramic cube touches both electrodes (see figure 2.26). This means that about a quarter of the ceramic cube exhibits an 1-3 connectivity.

Table 4.7 lists the values of n and m together with the value of the content of parallel connectivity ceramic relative to the total volume fraction in the composite. This latter

variable has been plotted in figure 4.24 as a function of ceramic loading.

TABLE 4.7 - n AND m PARAMETERS OF THE MIXED CONNECTIVITY CUBE MODEL FOR THE PTCa-1(q):P(VDF/TrFE) COMPOSITE

vol. fraction	ε	n	m	$\phi^{parallel}$
20	21	0.44	0.56	0.06
30	28	0.44	0.65	0.08
40	34	0.44	0.72	0.10
50	40	0.44	0.78	0.12
60	49	0.45	0.83	0.14
65	67	0.56	0.85	0.23

It appears that these composites exhibit a fairly constant degree of parallel connectivity of around n=0.44-0.56, irrespective of their volume fraction, which is probably due to the large size of the ceramic grains relative to the thickness of the composite (see figure 3.16). There is however a more than proportional increase in the ceramic part connected in parallel for the composite loaded with 65% ceramic as seen in figure 4.24. This can be an indication of a high ceramic loading effect described in chapter 2.

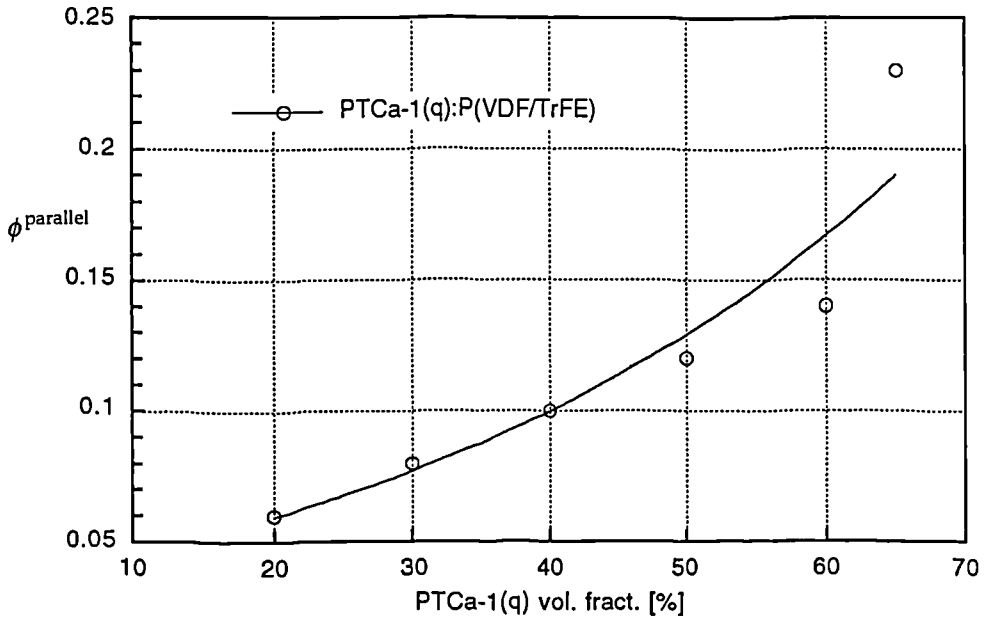

Figure 4.24 -Volume fraction of ceramic in parallel in the composite.

Figure 4.25 shows the permittivity ratio of P(VDF/TrFE) relative to PTCa-1 as a function of temperature both on heating and cooling. The permittivity has been measured at 1kHz. Obviously, the permittivity ratio will also depend on the frequency although it is assumed here that this dependence is much weaker than the temperature dependence.

The permittivity ratio increases on heating from a value of 0.04 at room temperature to 0.08 at 120°C. It also increases on cooling where it reaches a peak of 0.09 at around 90°C.

Thus an optimal procedure, applicable to these composites, is to heat the sample to 120°C and then cool down to 90°C before polarising the sample.

Comparing the figures 4.11 and 4.25 for the resistivity and the dielectric ratios respectively it is noticed that the permittivity ratio is in general one to two orders of magnitude higher than the ratio of resistivity. Thus, the polarization of the ceramic will proceed more effectively with an oscillating field than with a dc field. Of course a dc field can be applied to a sample in many ways, one of which is to apply a step of voltage. In this case the frequency content of the voltage which is the Fourier transform of an Heaviside function step will have a wide range of frequencies.

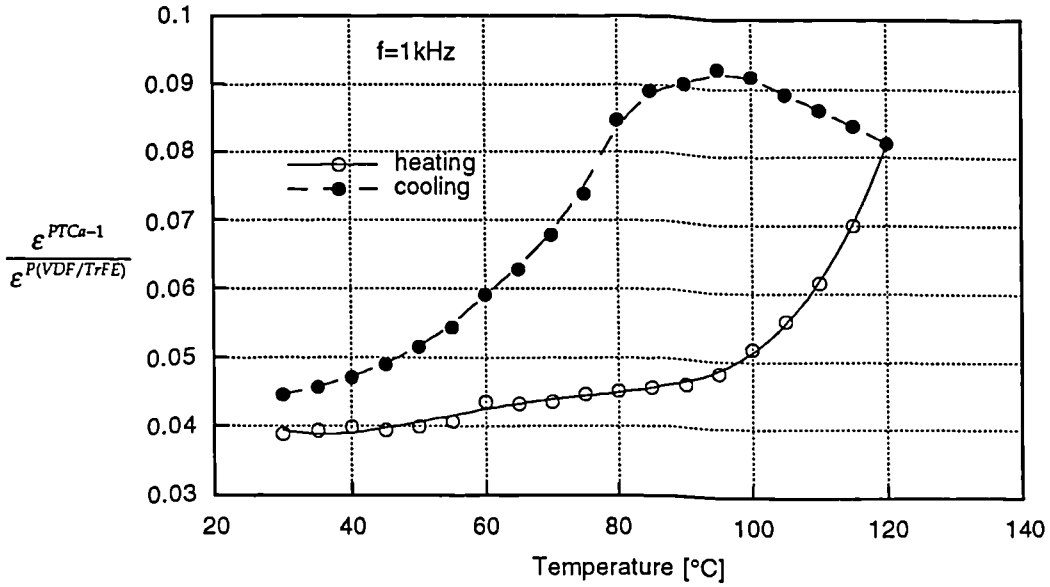

Figure 4.25 - Permittivity ratio of P(VDF/TrFE) relative to PTCa-1.

4.6 - Polarization hysteresis measurements

For the hysteresis measurements the sample was immersed in silicone oil, to reduce arcing, and its temperature could be controlled through a hot plate (see figure 4.2). A function generator was used to provide a small voltage signal with an appropriate shape, amplitude and frequency which was then amplified with a TREK 610C HV power supply in a 1:1000 ratio. This voltage was applied to the aluminium electrodes of the samples through spring contacts.

In the case of PZT:epoxy resin, mixed 1-3 and 0-3 connectivity composites [Pardo et al. 1988], the remanent polarization P_r has been found to lie in the range of 2.8-127 mC/m^2 while the coercive field E_c was found to be between 1.3 and 1.8 MV/m. It was further observed that the samples with higher 0-3 connectivity character had a lower remanent polarization and a higher coercive field because of the decrease of the local field in the ceramic particles, caused by the shielding action of its low permittivity and conductivity matrix.

The measurement of the hysteresis loop can be difficult in materials with low polarization and high permittivity and/or conductivity which are inherent with many

composites [Furukawa et al. 1986]. Various techniques have been devised to deal with this situation which include a method that measures the bipolar and the unipolar current measurement in succession to find the true polarization current [Dickens et al. 1992]. Another technique uses the value of the small signal resistivity and capacitance measurements to calculate the current which is subtracted from the total measured current [Dickens et al. 1992] while, in yet another technique known as the modified Sawyer-Tower circuit [Hicks et al. 1981; Ikeda et al. 1985], a resistance is connected in parallel with the measuring capacitor C_m (see figure 4.1) whose magnitude is such as to match the conductivity of the sample. A new technique reported here improves the observation of the polarization current based on the simultaneous measurement of the current of a sample to which a bipolar voltage is applied, and that of two other reference samples to which a unipolar field is applied (i.e. either positive or negative), whose values are used to find the true polarization current of the first sample. The present method should prove to be a more convenient way to measure readily the polarization of a ferroelectric material with a non-ideal capacitive and/or conductive behaviour.

The hysteresis measurements were performed by measuring the current while applying a high sinusoidal field to the sample. This current consists of the following three main components: (i) a capacitive current, (ii) a resistive contribution, both of them possibly non-linear at high fields and (iii) the polarization or switching current due to the orientation of the spontaneous polarization of the ceramic. The contribution due to the last component mentioned above, is of most interest in the measurement of the polarization hysteresis which features a memory effect after switching off the field.

In composite samples, a large resistive current is usually superimposed on the measured switching current which obscures its true value. In order to compensate for this effect, which is stronger at low frequencies of the applied field, three identical samples were used. On applying a full wave ac high voltage to the three samples (figure 4.26), samples *A* and *B* will be poled during the first positive half cycle while the sample *C* remains unpoled. During the first negative half cycle, the sample *C* is poled together with the sample *A* in which the polarization will now switch in the opposite direction. The polarization of the sample *A* undergoes repetitive switching in polarity with time while the samples *B* and *C* remain polarised in the positive and negative directions respectively with the progress of time. Thus, when an equilibrium is established only the resistive and capacitive components of the current will flow through the samples *B* and *C* while the sample *A* will have the polarization current as an additional component. As the current for all of three samples were measured with operational amplifiers in real time it was possible to subtract the reversible current from the switching current by the use of an appropriate electronic circuit (see figure 4.26).

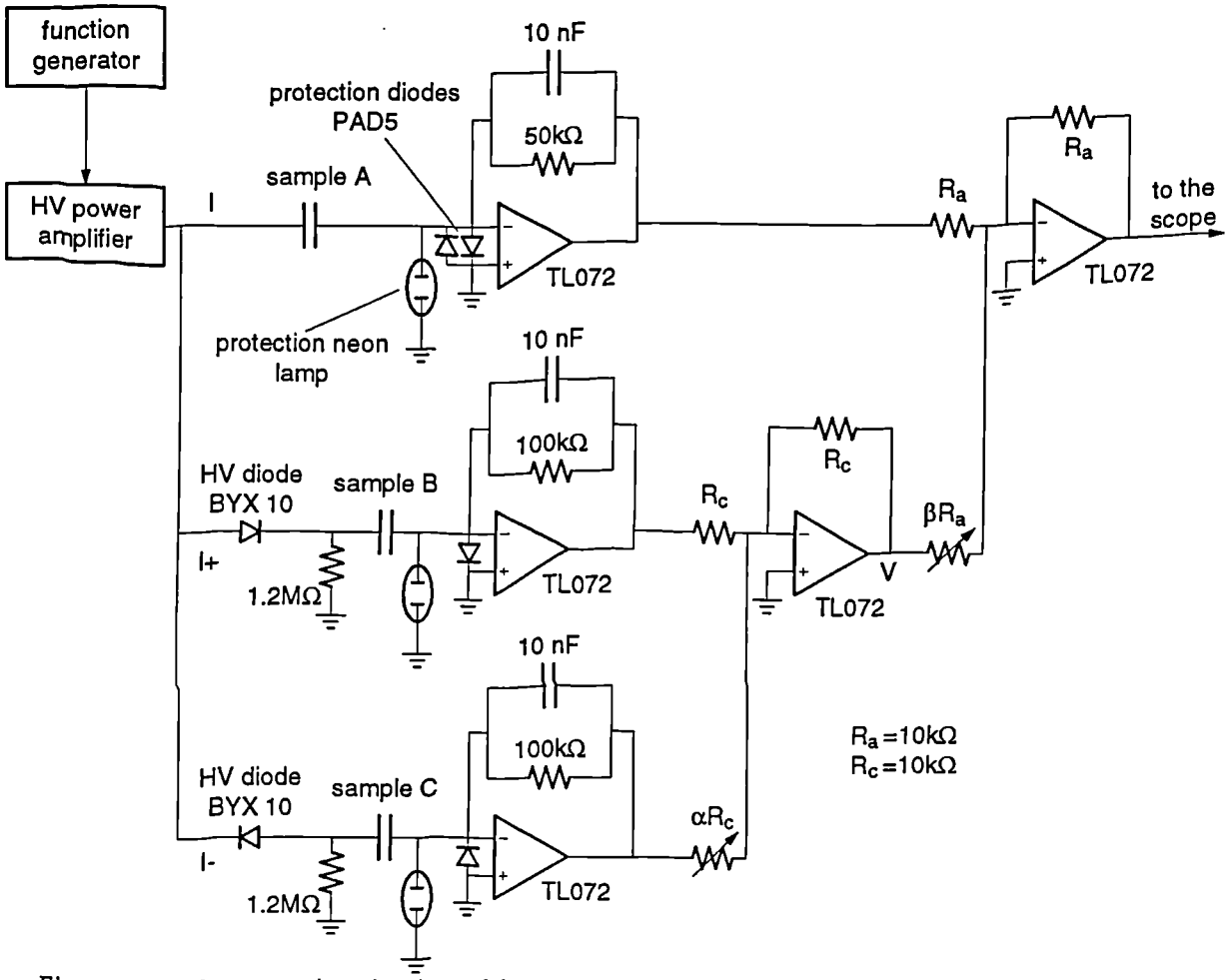

Figure 4.26 - Compensating circuit used for measuring polarization switching in ferroelectric composites.

The polarization current I_{pol} is given by:

$$I_{pol} = I - \beta(I_+ + \alpha I_-) \qquad (4.11)$$

where I_+ and I_- are the positive and negative half wave currents in samples B and C respectively and α and β the adjusting proportionality factors to allow for variations in the thickness and area of the samples respectively.

The latter parameters were implemented by means of potentiometers (see figure 4.26) and the procedures to determine their values were as follows. Initially a full wave ac (bipolar) voltage loop was applied to the three samples whilst monitoring the voltage at the point V of the electronic circuit (figure 4.26), which is proportional to the sum of the currents I_+ and I_-.The potentiometer $\alpha$was then set in such a way that the voltage at the point V was continuous when the applied voltage shifted from the negative to the positive polarity. After the correct adjustment of the potentiometer for the parameter α, a high oscillating field with a dc-offset (i.e. unipolar field) was applied to the three samples to allow for the determination of the β parameter. The unipolar field consisted of applying either an oscillating field with a positive or negative dc bias, thus implying that the measured current is only due to the capacitive and resistive components. Consequently the potentiometer was set in such a way that I_{pol} was as close to zero as possible.

It should be noted that in this procedure all the contributions to the current which have

no memory, are automatically subtracted including the capacitive current. The rectifier diodes (figure 4.26) were used to block either the positive or the negative voltage while a resistance was used in parallel with the sample to allow it to discharge when the voltage decreased from its maximum value to zero. The value of the resistance was chosen so that the inverse of the time constant of the discharge process was much greater than the frequency of the applied voltage. The polarization current was then digitised with an oscilloscope and transferred to a computer to calculate the polarization charge by integrating the measured current. A ferroelectric hysteresis loop was then drawn from which, the remanent polarization, the coercive field and other parameters were determined.

Figure 4.27 shows a comparison of the ferroelectric hysteresis loops obtained with and without using the above mentioned compensating circuit. These loops were obtained at 90°C, the frequency of the electric field excitation being 0.1 Hz while the thickness of the sample was 75μm. The hysteresis *loop 1* shows the nature of variation of the total current through the sample *A* whereas the *loop 2* represents the current through the same sample from which the resistive and capacitive components have been subtracted.

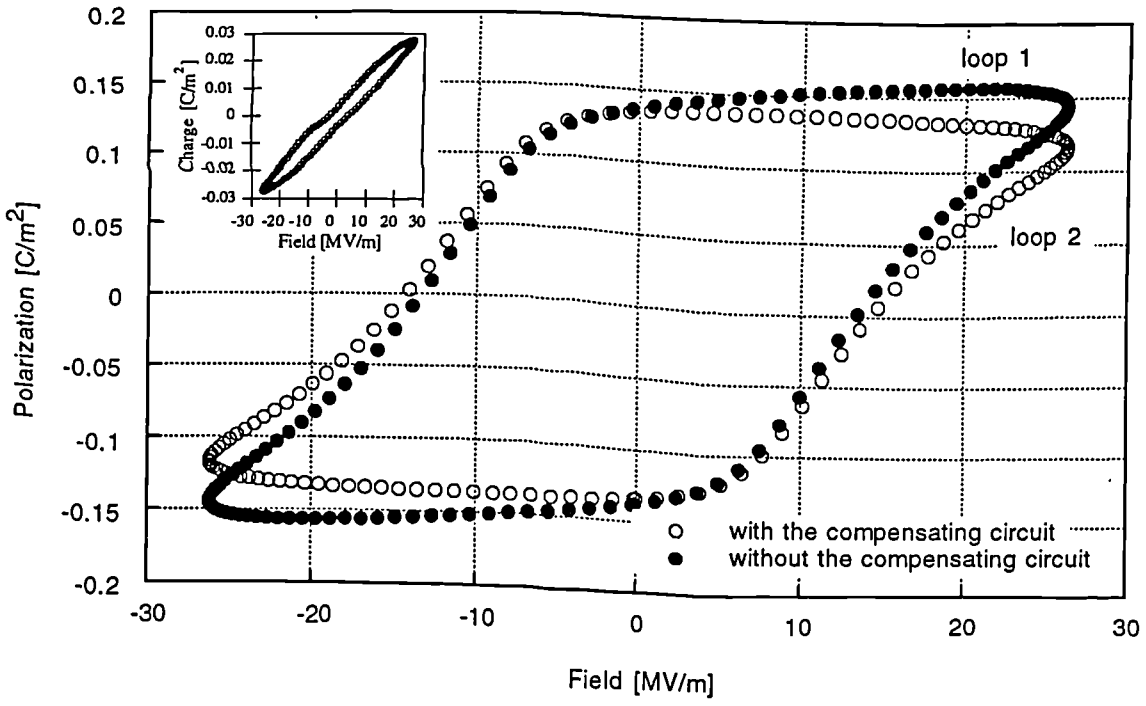

Figure 4.27 - Comparison of ferroelectric loops obtained with and without the compensating circuit. The temperature of the sample and the frequency of the field were 90°C and 0.1 Hz respectively.

The flatness of the polarization curve may be noticed when the field decreases from its maximum value in the compensated loop, when compared with the uncompensated case. It is evident, that no significant enhancement of polarization occurred when the field decreased below ±20 MV/m. This flatness also ensures that the resistive current component is not contributing to the polarization current. Figure 4.27 (insert) also shows the difference in polarization between the two loops 1 and 2 and this difference, i.e. the elliptical form of the polarization component, arises from the dielectric loss of the material and not from its

ferroelectricity. This curve has been fitted to a lossy dielectric model (figure 4.28) to obtain the permittivity of 119 and tan δ value of 0.16 at 0.1 Hz which are in good agreement with experimentally measured values. A discontinuity of slope near zero field is apparent in this curve because the positive conducting diode switches off at +1.5 Volts whilst the negative one is switched on only at -1.5 Volts. The subsequent polarization hysteresis results reported here, have been obtained from ferroelectric loops using the compensating technique.

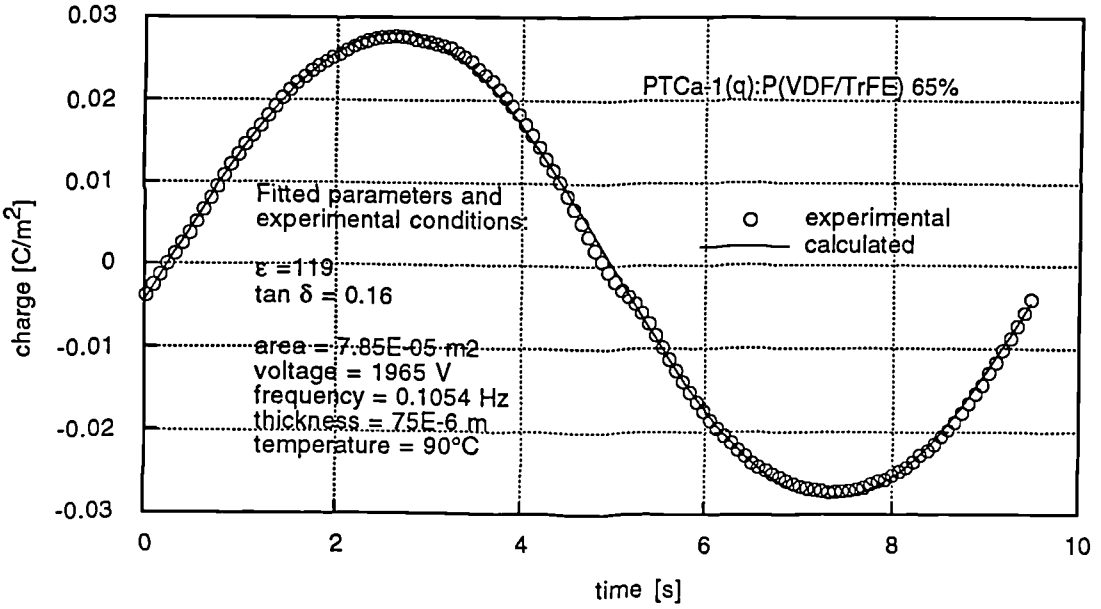

Figure 4.28 - Difference in current between loops 1 and 2 of figure 4.27 fitted to a sample whose permittivity and loss are 119 and 0.16 respectively.

After the unipolar voltage cycling, undertaken to determine the proportionality factors α and β mentioned above, it was observed that in the initial bipolar loops the polarization current was not symmetric for positive and negative fields suggesting that the polarization does not switch entirely to the opposite direction to which the unipolar field was previously applied. It is only after repeated cycles, that a symmetric behaviour is obtained. This effect of the waiting time on the polarization behaviour, has been attributed to space charge [Ikeda et al. 1988; Guy et al. 1991] or to a molecular reorientation kinetic effect [Dickens et al. 1992]. Our practice was to allow enough bipolar cycles (around 10) until a symmetric waveform was obtained before the measured values were recorded.

The hysteresis loops have been recorded as a function of the peak of the sinusoidal field for temperatures of 50, 90 and 120°C. The range of the applied field was between 5 and 26 MV/m, the latter value being close to the breakdown strength of the composite material. Due to the lower breakdown strength of the ceramic compared to the polymer, its magnitude for the composite material is very dependent on the size of ceramic grain in relation to the thickness of the sample. The temperature was not raised beyond 120°C to prevent the softening and melting of the composite. Figure 4.29 shows the nature of the remanent polarization at different fields from which it may be observed that a maximum polarization value of 170 mC/m^2 occurs at 120°C at a field of 26 MV/m which is close to its

breakdown field.

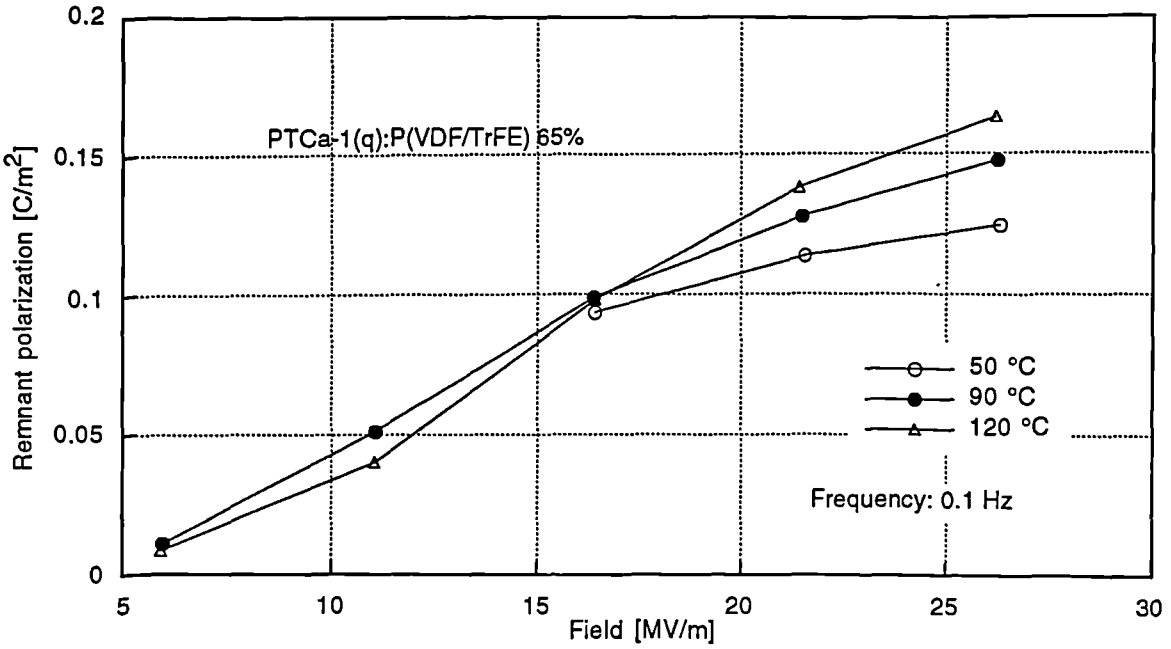

Figure 4.29 - Remanent polarization as a function of the peak of the sinusoidal field for temperatures of 50, 90 and 120°C.

Figure 4.30 shows the remanent polarization as a function of the frequency at 100 °C for 16 and 26 MV/m i.e. the peak values of the applied field, from which it may be observed that the polarization seems to increase with decreasing frequency with an indication of reaching a saturation level at frequencies below 0.1 Hz and at a field of 26 MV/m. However, such a saturation is not observed for the lower value of the oscillating field.

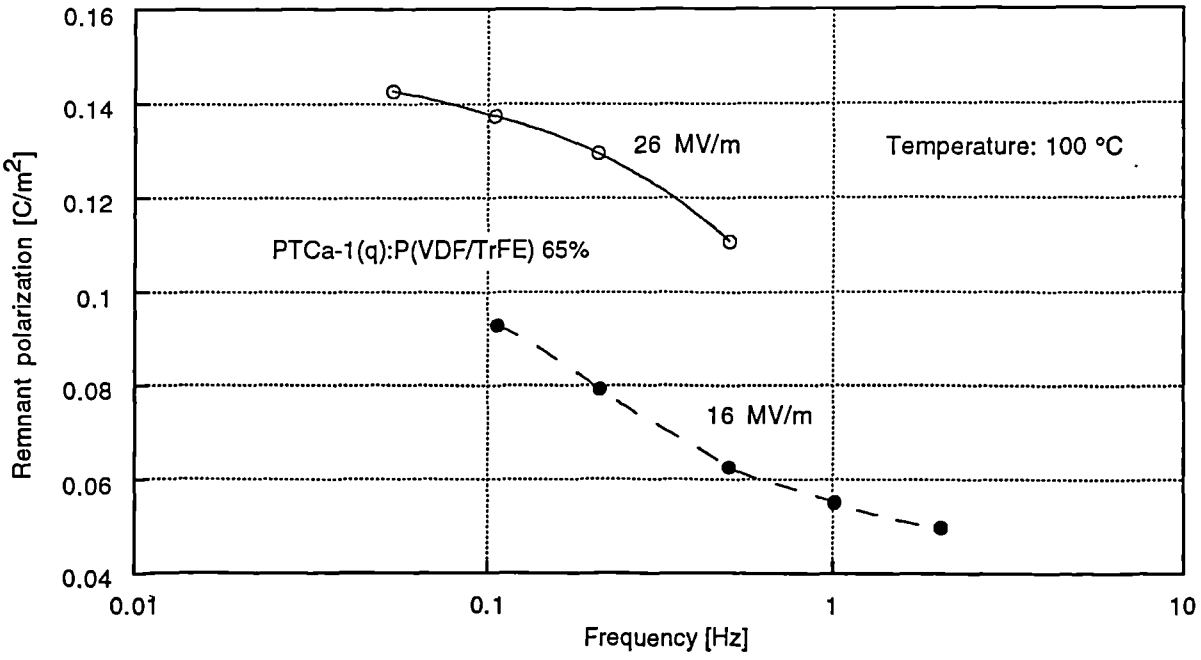

Figure 4.30 - Remanent polarization as a function of the frequency at 100°C for 16 and 26 MV/m peak values of the applied field.

The remanent polarization and the coercive field as a function of the temperature for an applied field of 30 MV/m and frequency of 0.1 Hz are shown in figures 4.31 and 4.32

respectively. A saturation of the remanent polarization was observed for temperatures approaching 120°C whilst the coercive field increased from 12.5 to 15.5 MV/m with increasing temperature.

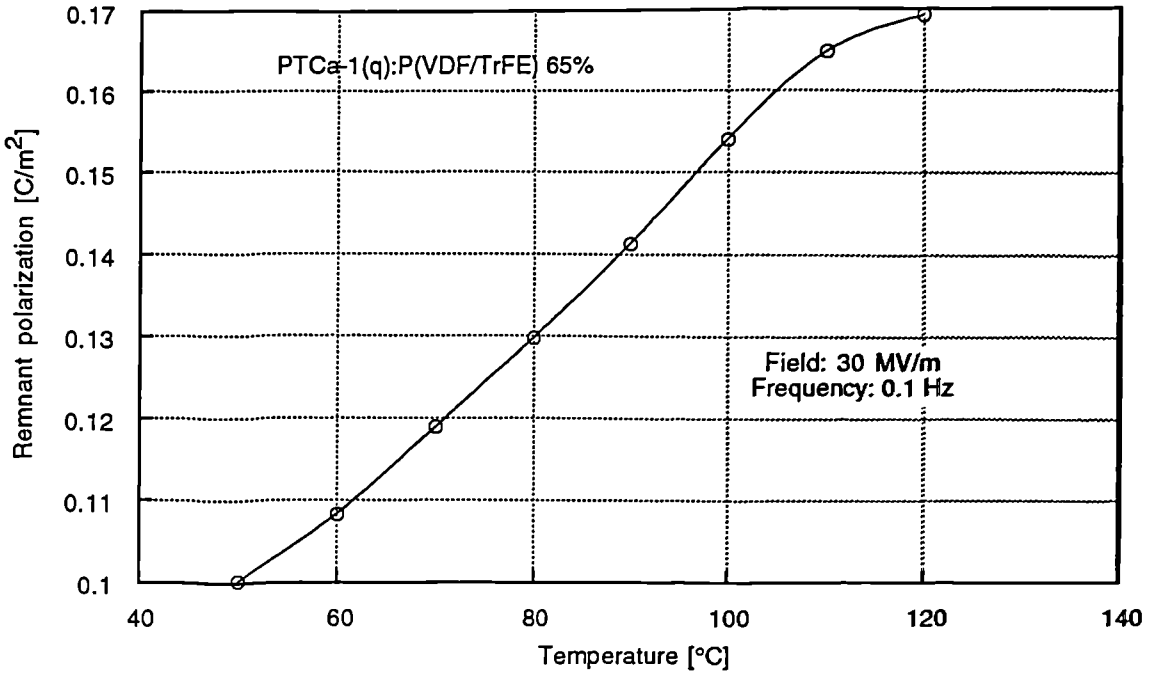

Figure 4.31 - Remanent polarization as a function of the temperature of the sample.

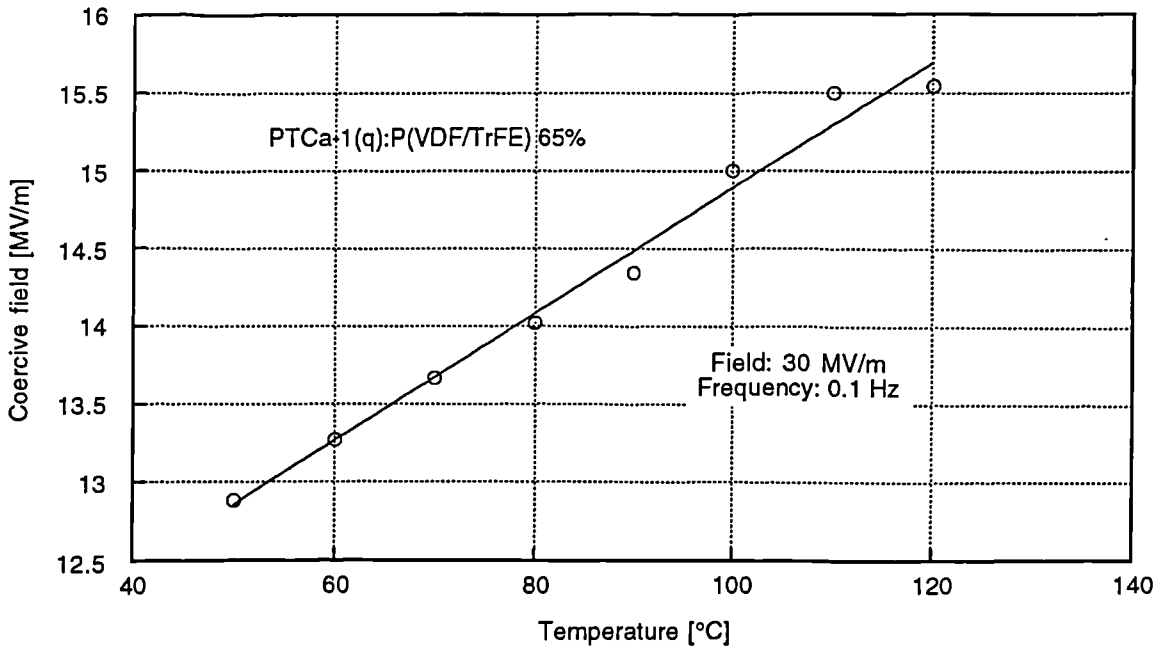

Figure 4.32 - Coercive field as a function of the temperature of the sample.

4.7 - Simulation of hysteresis

Landauer and his co-workers have proposed a simple relaxation equation for the polarization reversal given, combining equations 4.1 and 4.2, by

$$\frac{I_{pol}}{A} = \frac{dP}{dt} = v_o P_s \exp\left(-\frac{Ea}{E}\right)\left(1-\frac{P}{P_s}\right) \tag{4.12}$$

which states that the polarization P changes towards its equilibrium or saturation value P_S at a field activated rate. When the polarization switches from one direction to its opposite direction its value must go through zero and at that instant a simple relation holds for the polarization current I_0, which is given by the following equation:

$$\frac{I_o}{A} = v_o P_s \exp\left(-\frac{E_a}{E_c}\right) \tag{4.13}$$

where E_C is the coercive field. The value of E_a may be obtained from the slope of a plot of $\log(I_o/A)\,vs\,(1/E_c)$ while its ordinate on the vertical axis gives the magnitude of v_0P_S. To allow for the determination of these characteristics, various hysteresis loops were recorded in which the amplitude of the applied field was increased, which caused a corresponding increase in the coercive field as well as in the current I_0. Figure 4.33 shows such graphs at temperatures of 50, 70, 90 and 120°C while in table 4.8 we have listed the calculated values for the activation field and the product v_0P_S. Furthermore, by assuming that the saturation polarization is about P_S=0.17 C/m^2 which can be a valid assumption based on figure 4.31, an estimate for v_0 was also computed.

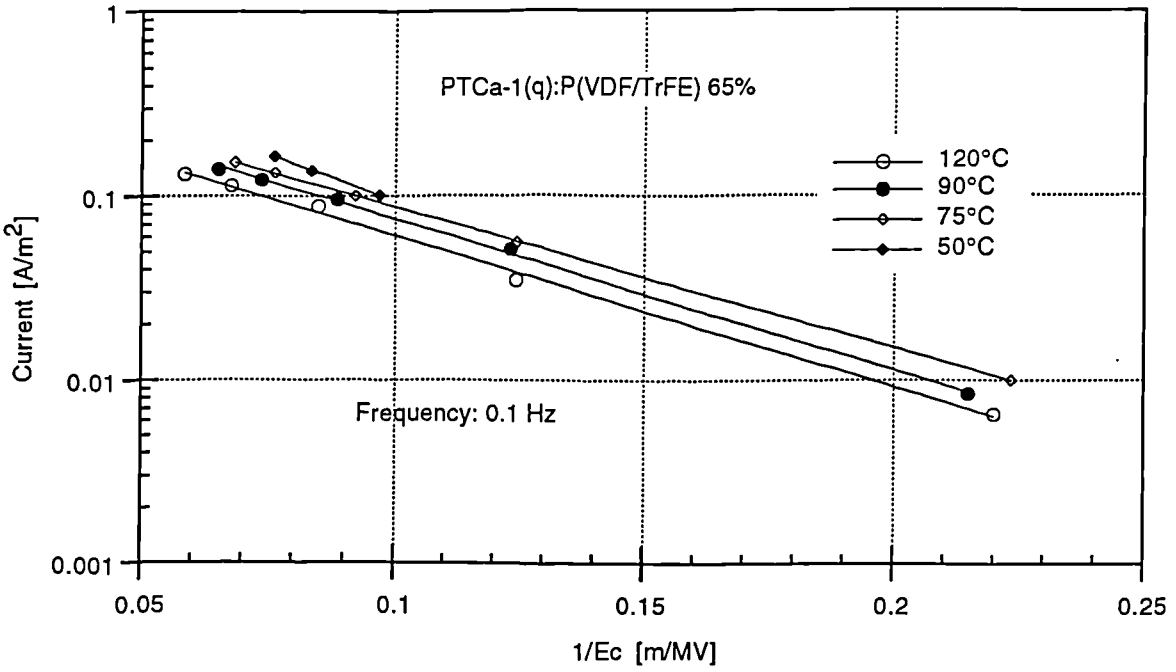

Figure 4.33 - Plot of the logarithm of the density of current when the polarization is zero versus the inverse of the coercive field. The slopes of these curves gives the activation field while its ordinate on the vertical axis is v_0P_S.

The activation field is thus seen to lie between 17 and 23 MV/m, whilst the rate constant v_0 is in the range of 8.8-16 Hz in the temperature range of 50 to 120 °C.

TABLE 4.8 - ACTIVATION FIELDS AND RATE CONSTANTS FOR PTCa-1(q):P(VDF/TRFE) 65% COMPOSITE

Temperature [°C]	E_a [MV/m]	v_0P_s	v_0 [Hz]
50	23	2.7	16
75	17.5	1.7	9.8
90	18	1.6	9.7
120	18	1.5	8.8

Using equation 4.12 a numerical solution was found for the experimental polarization current of the hysteresis loop of figure 4.27 (*loop2*) in the following manner. Equation 4.12 can be suitably formulated in the following form by dividing by P_S:

$$\frac{I_{pol}}{AP_s} = \frac{1}{P_s}\frac{dP}{dt} = v_o \exp\left(-\frac{Ea}{E}\right)\left(1-\frac{P}{P_s}\right) \tag{4.14}$$

Making the substitution $P' = P/P_s$ this equation transforms into:

$$\frac{dP'}{dt} = v_o \exp\left(-\frac{Ea}{E}\right)(1-P') \tag{4.15}$$

which is a differential equation that depends solely on the activation field E_a and on the rate constant v_0. Using the values of activation field E_a and rate constant v_0 at 90 °C from table 4.8 we have calculated the time dependence of both P' and its time derivative. This latter quantity relates to the density of the polarization current through:

$$\frac{I_{pol}}{A} = P_s\frac{dP'}{dt} \tag{4.16}$$

The density of the current obtained from equation 4.16 was then fitted to the experimental values using P_S as a fitting parameter. It should be noted that to perform the fiiting it is necessary to solve the differential equation 4.15 only once and that P_S acts only as a scaling factor of the time derivative of P'.

The experimental current and the calculated curve in which a saturation polarization P_S of 99 mC/m^2 was used are shown in figure 4.34. The discrepancy between the value used for the calculated curve (P_S=99 mC/m^2) and that of the experimentally observed saturation polarization ($P_{S(exp)}$=147mC/m^2) at 90°C can be understood if we assume that a distribution of activation fields exists in the composite as a result of an existence of a distribution in the grain size of the ceramic powder in the polymer matrix. It can be expected that the larger ceramic grains, comparable in size to the sample thickness will experience a greater field than the finer particles, as explained before. As the agreement between the experimental and the calculated values of current is better at the beginning of the switching phenomenon, it may be suggested that during this period the large ceramic grains are able to switch with an activation field of 18 MV/m providing a saturation polarization of 99 mC/m^2. However, the switching was still in progress at longer times for the smaller ceramic grains as can be

evidenced in the experimentally observed values of the current.

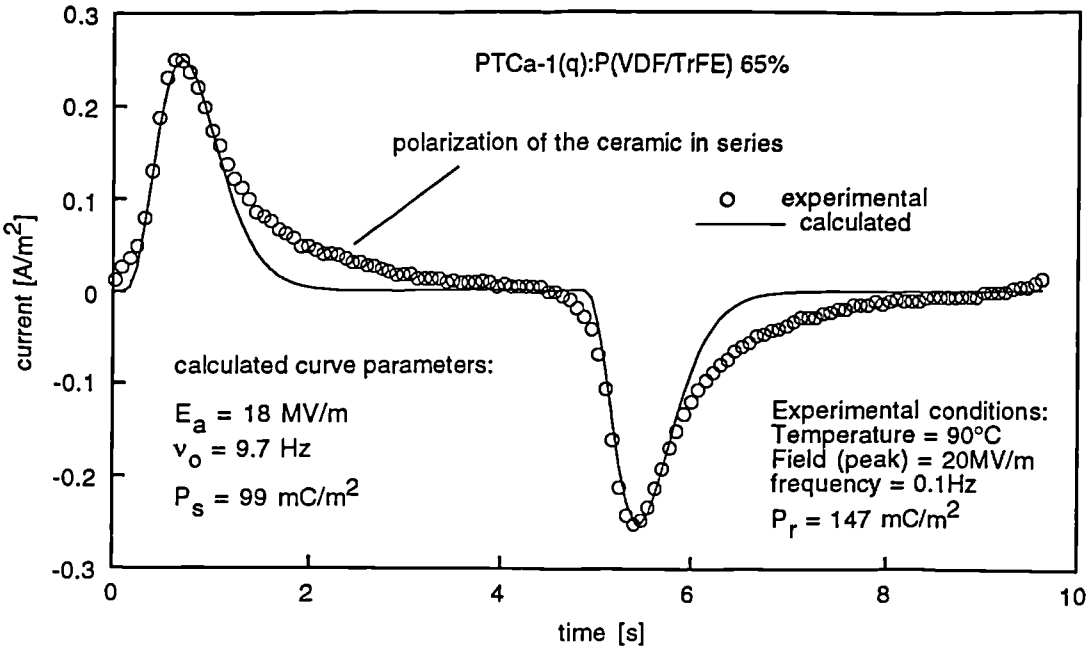

Figure 4.34 - Experimental and calculated curves for the hysteresis loop 2 of figure 4.27.

In fact, the activation field and the rate constants determined using equation 4.13 rely on the current at the moment when the polarization is zero. In the current versus time plot of figure 4.34 this happens near the peak value of the polarization current. If a distribution of activation fields exists the E_a and ν_0 values obtained using that procedure will reflect the polarization that switches faster and will thus give a better fit for the initial polarization current.

It may be assumed that two independent polarization processes exist in the composite, each characterised by its own saturation polarization P_S, activation field E_a and a rate constant ν_0. These two processes could be assigned, for example, to a ceramic in parallel and in series with the polymer host respectively. The total current is then the sum of the polarization current generated by each of the two processes. Optimised parameters for the two processes were obtained which are shown in figure 4.35 together with the calculated curve which fitted to the experimental current.

Comparing the figures 4.34 and 4.35 it is seen that a better fitting is obtained using two processes (i.e. in figure 4.35) instead of one (i.e. in figure 4.34). Moreover, using the two processes, the first one is observed to have an activation field of 15.1 MV/m which accounts for the current generated in the beginning of the switching whilst the second process has an activation field of 20.5 MV/m accounting for the current generated in the later stage of switching. It should be noted that these values enclose the 18MV/m value previously found. The saturation of polarization for each of these processes is 80 and 71 mC/m^2 respectively so that the total saturation polarization is 151 mC/m^2 which is in agreement with the experimental value of 147 mC/m^2.

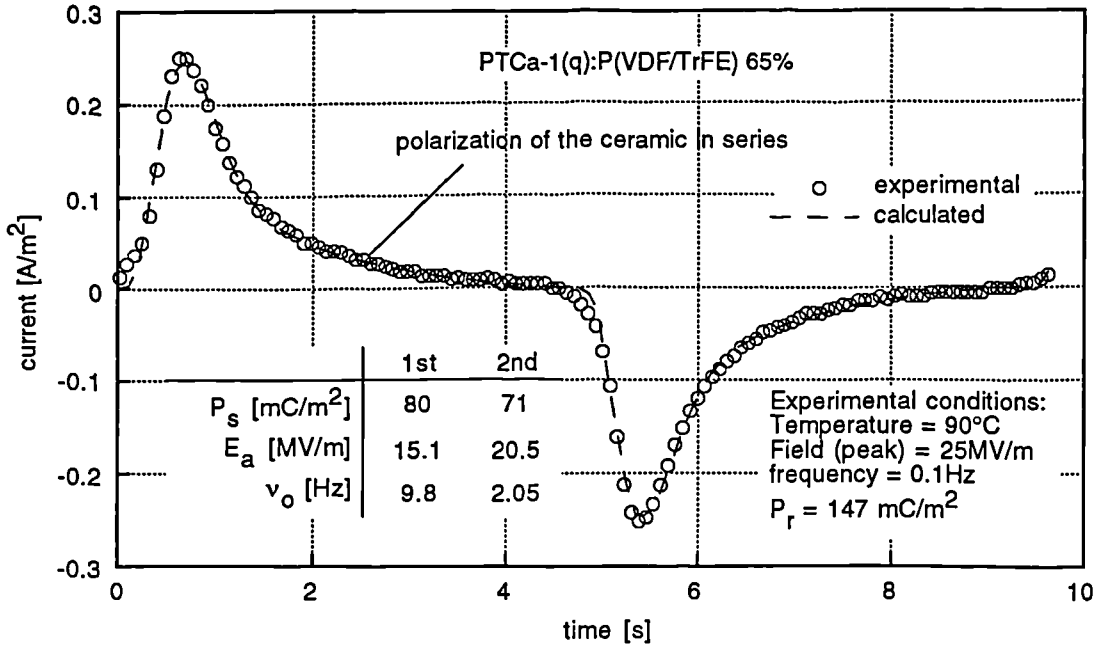

Figure 4.35 - Simulation curve assuming two polarization processes.

It can thus be concluded that the composite can be modelled by the two switching components which can be thought to be represented by the parallel and the series connectivity ceramic. The parallel connectivity ceramic due to the higher proportion of the applied field the activation field is lower than in the ceramic in series.

In a real composite it is possible that the ceramic grains have varying amounts of polymer in series and thus there can be activation fields higher than the 20.5 MV/m value found in the fitting of figure 4.34 . A proper treatment of this general case would involve calculating the total polarization current using a distribution of activation fields, rate constants and saturation polarization.

An alternative and simpler procedure would be the use of the mixed connectivity model (see figure 2.26) with three parallel branches (i.e. the polymer, the ceramic and the series of a ceramic and polymer branches). This line of work was not fully undertaken here because there were no available experimental values for the saturation polarization, activation field and rate constant for the PTCa-1 ceramic as a function of the field and frequency.

The procedure to carry the evaluation of the composite polarization can nevertheless be described here briefly. The overall circuit of the mixed connectivity model composite can be modelled as shown in figure 4.36. Basically, at a given frequency where the simulation is to be carried out, each of the ceramic and polymer parts can be simulated by a resistance and a complex capacitance. In addition, each of the ceramic elements generates a polarization current modelled by equation 4.12.

The capacitance and resistance of all elements can be calculated from the n and m values together with the experimental values of the permittivity and resistivity of the constituent phases at the desired frequency according to the formulae listed in table 4.9. The saturation of polarization of the ceramic elements also listed in table 4.9, can also be

calculated from the saturation polarization of the ceramic P_s together with the n and m values. The activation and rate constant in the ceramic elements could be as those of the pure ceramic.

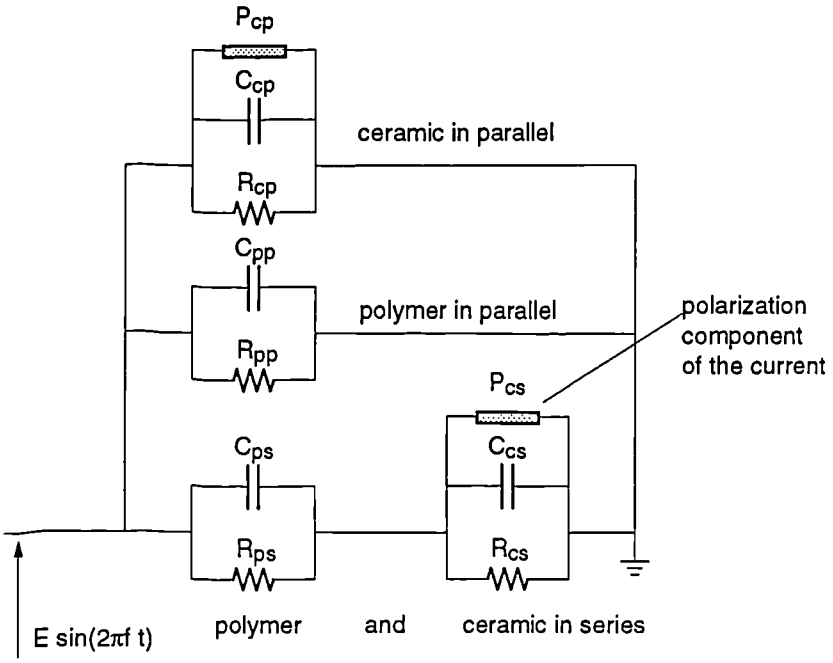

Figure 4.36 - Electrical equaivalent circuit for polarization switching in a mixed connectivity cube model.

TABLE 4.9 - LIST OF THE FORMULAS TO CALCULATE THE CIRCUIT PROPERTIES OF THE ELEMENTS IN THE MIXED CONNECTIVITY MODEL

	R	C	P
polymer in parallel (pp)	$\frac{\rho^p}{(1-m^2)}$	$\varepsilon^p\varepsilon_o(1-m^2)$	
ceramic in parallel (cp)	$\frac{\rho^c}{(nm)^2}$	$\varepsilon^c\varepsilon_o(nm)^2$	$P_s(nm)^2$
polymer in series (ps)	$\rho^p\frac{1-m}{m^2(1-n^2)}$	$\varepsilon^p\varepsilon_o\frac{m^2(1-n^2)}{1-m}$	
ceramic in series (cs)	$\frac{\rho^c}{m(1-n^2)}$	$\varepsilon^p\varepsilon_o m(1-n^2)$	$P_s m^2(1-n^2)$

A preliminary hysteresis polarization loop, shown in figure 4.36, was calculated using the properties of the constituent materials at 10Hz and 90°C as described in table 4.2. The saturation polarization of the ceramic was assumed to be 600 mC/m^2 whilst the activation field and the switching rate were the same as those found in the composite i.e., 18MV and 9.8 Hz respectively. The n and m values used were those obtained for the permittivity of PTCa-1(q):P(VDF/TrFE) 65% (see table 4.7) i.e. n=0.56 and m=0.85. In the calculation of this hysteresis loop it was found that all the ceramic had switched resulting in a contribution to

the composite polarization of 140 mC/m^2 while the ceramic in series contributed with a polarization of only 10 mC/m^2. It was apparent from this preliminary work that although the dielectric matching helped the polarization process of the ceramic connected in series the whole picture is more complex than described here. In fact, during the switching process the ceramic acts as possessing a permittivity much higher than that of the small signal permittivity which makes the permittivity matching more difficult. There are also phase shifts in the applied field to the ceramic which makes the polarization switching in the ceramic in series to lag behind that of the ceramic in parallel. This line of work, which is still unexplored, could represent a possible way towards a better understanding of the polarization mechanisms in the composites.

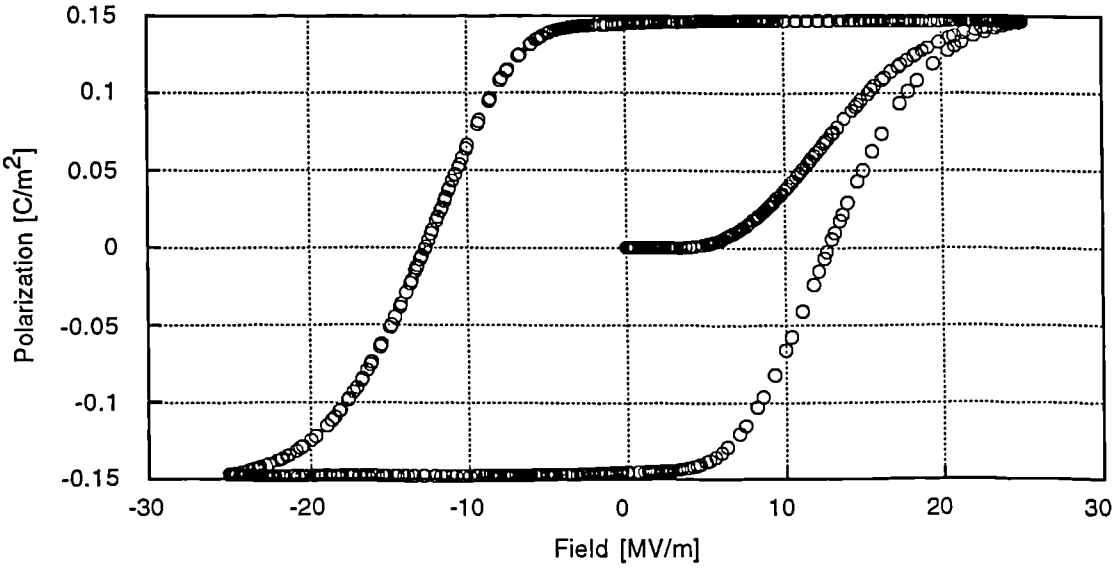

Figure 4.37 - Simulation of polarization hysteresis loop using the mixed connectivity model.

It can be summarised that this work has demonstrated that PTCa-1(q):P(VDF/TrFE) showed a maximum polarization of 170 mC/m^2 at 0.1Hz while applying a field of 30 MV/m. This value of polarization is about 30-40% of that of PTCa-1. The coercive field for this composite which was 15.5 MV/m at 120°C, was found to be much higher than that of pure PTCa-1 which should be around 3-4 MV/m. This is clearly linked to the lower conductivity and resistivity properties of the host material. The activation field of 18MV/m found for this composite lie in-between those of the $BaTiO_3$ and P(VDF/TrFE) whose values are typically 1 MV/m and 75MV/m respectively.

This work on hysteresis measurement has been carried only on PTCa-1(q):P(VDF/TrFE) 65% composite. Although there were reasons for choosing this composite namely due to its large pyro- and piezoelectric coefficients (see chapters 5 and 6) it is acknowledge here that further work should be carried on the other composites. These measurements together with the simulation of the switching of polarization using the mixed connectivity model could then provide a sounder knowledge for an efficient polarization process in these materials.

5 - Pyroelectricity in composites

5.1 - Introduction

In this chapter the pyroelectric properties of the composites are discussed. A literature review of the work on pyroelectricity in composites is first undertaken. The measurement techniques used in this work will then be discussed which include the direct method and the dynamic radiative and heat excitation methods.

The pyroelectric properties of the composites fabricated are then outlined. This description includes a comparison of the pyroelectric coefficient and FOM_p at 30°C for all the composites. The temperature dependence of the pyroelectric coefficient is then considered. Other factors affecting the pyroelectric coefficient of composites, the process of obtaining the ceramic powder and the parameters of the poling procedure are also discussed.

No unique way exists to evaluate the suitability of a pyroelectric material which is to be used in a pyroelectric detector. That is to say that the Figure Of Merit (FOM) has been defined in many different ways in the literature [Byer et al. 1972; Garn et al. 1974; Liu et al. 1978; Porter 1981; Moulson et al. 1990] depending mainly on the configuration of the detector.

The voltage responsivity r_V [V/W] of a single element detector (see figure 5.1) for an incident radiation of power density W_{in} [W] is given by [Liu et al. 1978],

$$r_V = \left|\frac{V_{out}}{W_{in}}\right| = \frac{p}{C_V \varepsilon \varepsilon_o \omega A} \frac{\eta T'}{m} \tag{5.1}$$

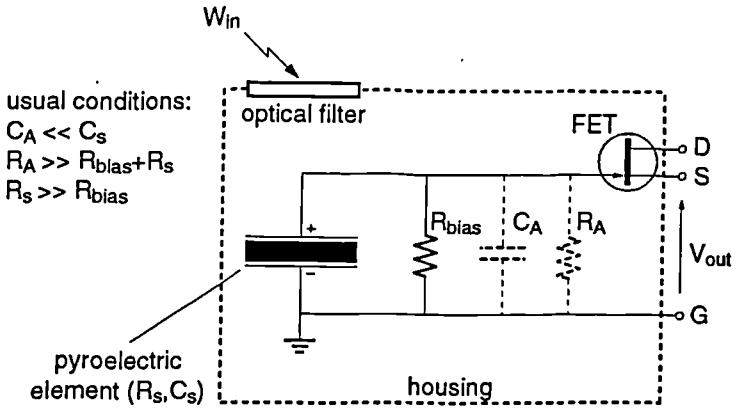

Figure 5.1 - Schematic of a single element pyroelectric detector

where η is the emissivity coefficient of the absorptive surface layer over the pyroelectric material, p is the pyroelectric coefficient of the sample, A the area of the element, C_V the volume specific heat, T' the normalised time derivative of the average temperature of the sample and m is related to the admittance Y of the circuit of figure 5.1 viewed from the FET amplifier as thus: the admittance Y is equal to,

$$Y = g + \omega C_s \tan\delta + i\omega(C_s + C_A) \quad \text{and} \tag{5.2}$$

$$|Y| = m\omega C_s \quad \text{so that} \quad m = \sqrt{\left(1+\frac{C_s}{C_A}\right)^2 + \left(\tan\delta + \frac{g}{\omega C_s}\right)^2} \tag{5.3}$$

where g is the conductance of the circuit of figure 5.1, given by the parallel combination of the resistances,

$$g = \frac{1}{R_{bias}} + \frac{1}{R_s} + \frac{1}{R_A} \approx \frac{1}{R_{bias}} \tag{5.4}$$

which has a typical value of 10^{-12} mho and tan δ is the dielectric loss in the pyroelectric sample. The subscripts s and A for the resistors and capacitor elements in figure 5.1 stand for the sample and amplifier parameters respectively.

Using equation 5.1 for the voltage responsivity some conclusions can be drawn. In normal operation m has a value close to unity, because the capacitance of the amplifier C_A is much lower than that of the pyroelectric material while both tanδ and $g/\omega C_S$ are quantities close to zero. Thus, by extracting the material properties involved in equation 5.1 an expression for the Figure Of Merit (FOM) of a pyroelectric material is obtained, i.e.,

$$FOM_V = \frac{p}{C_V \varepsilon}$$

Taking into account that the volume specific heat is a fairly constant property for the customary pyroelectric materials whose value approximates 2.3 MJ/m^{3}K we arrive at the FOM_p expression proposed earlier in chapter 1 (equation 1.20),

$$FOM_p = \frac{p}{\varepsilon} \tag{5.5}$$

It should be pointed out, however, that the case for an ever decreasing permittivity as suggested by this FOM_p does not remain always valid. When it was assumed that m is close to unity it was implied that $C_s >> C_A$ as well as that $C_s >> g/\omega$. If for example, the latter assumption (i.e. $C_s >> g/\omega$) is not valid, which can happen at low-frequency and for a low permittivity pyroelectric material, a different FOM is obtained such that

$$FOM = \frac{p}{C_V} \tag{5.6}$$

and in this case, the higher the pyroelectric coefficient of the material the better is the FOM. This may be one of the reasons why PVDF does not perform as well as its high FOM_p would suggest.

Equation 5.5 means that a material with higher FOM_p will exhibit a larger responsivity when used in the detector as shown in figure 5.1. However, the voltage response of the pyro-detector must be equated against the noise generated in the detector, in a parameter designated detectivity. The sources of noise and their expressions as a function of frequency have been discussed in detail by Liu [Liu et al. 1978]. These include the noise due to (i) the dielectric loss, (ii) the thermal noise from R_{bias}, (iii) an open-circuit input amplifier noise and (iv) the short-circuit voltage noise. When the intrinsic noise due to the dielectric loss of the

pyroelectric material is the dominant source of noise a slightly different expression for the figure of merit designated FOM_D is obtained,

$$FOM_D = \frac{p}{\sqrt{\varepsilon \tan \delta}} \tag{5.7}$$

Hence, equation 5.5 for FOM_p is linked to the responsivity, while equation 5.7 for FOM_D has implications to the detectivity of the pyroelectric detector.

5.2 - Measurement techniques

5.2.1 - The direct method

The experimental determination of the pyroelectric constant p^X of a material of area A is obtained from the change of the charge Q at the electrodes due to a change in sample temperature T,

$$p^X = \left.\frac{dP}{dT}\right|_{E,X} = \frac{d}{dT}\left(\frac{Q}{A}\right) = \frac{1}{A}\frac{dQ}{dT} + \frac{1}{Q}\frac{dA}{dT} \approx \frac{1}{A}\frac{dQ}{dT} \tag{5.8}$$

In the above equation the approximation is valid only when the area A of the sample does not vary significantly in the temperature range of measurement.

In order to measure this coefficient the most commonly used way, so-called the direct method [Byer et al. 1972], is to heat and/or cool the sample at a constant rate β in a cryostat while the current $I = dQ/dt$ is monitored. The pyroelectric coefficient, after suitable manipulation of equation 5.8, is then obtained from,

$$p = \frac{I}{\beta A} \tag{5.9}$$

Because this procedure is the same as for the Thermally Stimulated Discharge Current (TSDC) measurement, it is necessary to ensure that the latter contribution to the total current is negligible. Using the property that the pyroelectric current is a reversible current while the TSDC is an irreversible one, this is accomplished by heating the sample several times until a reproducible current is measured or by performing an annealing of the sample at a temperature higher than the highest temperature of measurement for an extended period of time until the level of current subsides to a negligible level relative to that which is to be measured.

In figure 5.2 is shown a schematic of experimental set-up used to measure the pyroelectric coefficient in the composite samples. The sample was heated using a series of heating elements embedded in a copper block, whose power was controlled in such a way that the thermocouple temperature rises at the rate of β=1°C/min. The cooling of the sample was accomplished via the introduction of liquid nitrogen in a reservoir which can be performed either in a quench-like operation or at controlled rate by the use of the heating elements to restrain the cooling process. The current during heating and cooling was monitored using a Keitley model 616 electrometer. The whole process was controlled by computer which also recorded the temperature and the current of the sample at a predefined

rate. The upper electrode consisted of a hollow copper parallelepiped which was gently pressed against the sample in order to ensure a good contact of the sample to both electrodes. The whole set-up was enclosed in a stainless steel chamber which was evacuated to a pressure of about 10^{-2}Torr to prevent the formation of moisture below the dew point temperature.

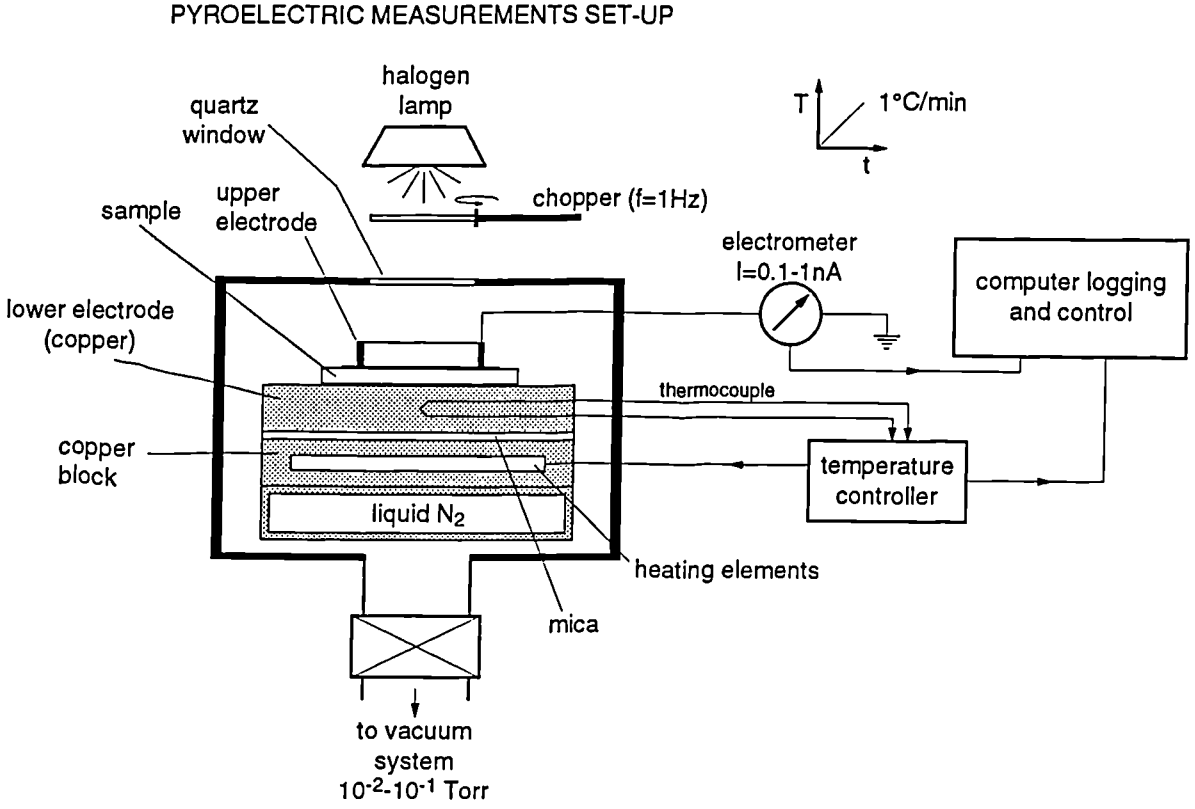

Figure 5.2 - Schematic set-up for pyroelectric measurements using the direct and the dynamic radiative methods.

5.2.2 - Dynamic methods: radiative and heat excitation

Dynamic methods which use either a sinusoidal or a step excitation are other types of measurement of the pyroelectric coefficient.

In the radiative dynamic method of determining the pyroelectric coefficient a radiant heat source is used to deliver an ac thermal power W_{in} [W]. Assuming that, the sample heats up uniformly and that a negligible amount of heat is lost to the surroundings within one cycle, the pyroelectric coefficient is given by:

$$p = C_V l \frac{I}{\eta W_{in}} \qquad (5.10)$$

where l is the thickness of the sample and the other quantities have the same meaning as stated earlier in this chapter. When the incident radiation is chopped, a lock-in amplifier must be used to monitor the current generated at the modulation frequency. A comparison of pyroelectric coefficients between various samples is still possible to obtain if the two above assumptions cannot be met, provided that the samples have similar thickness, area and surface emissivity. This procedure was often used during the course of this work to

obtain a quick estimate of the pyroelectric activity.

Another method based on oscillating the temperature of the sample, uses Peltier elements whose current is controlled in order to generate a low-frequency temperature oscillation at both surfaces of a sample of thickness *l* and area *A* [Dias et al. 1993] as shown schematically in figure 5.3.

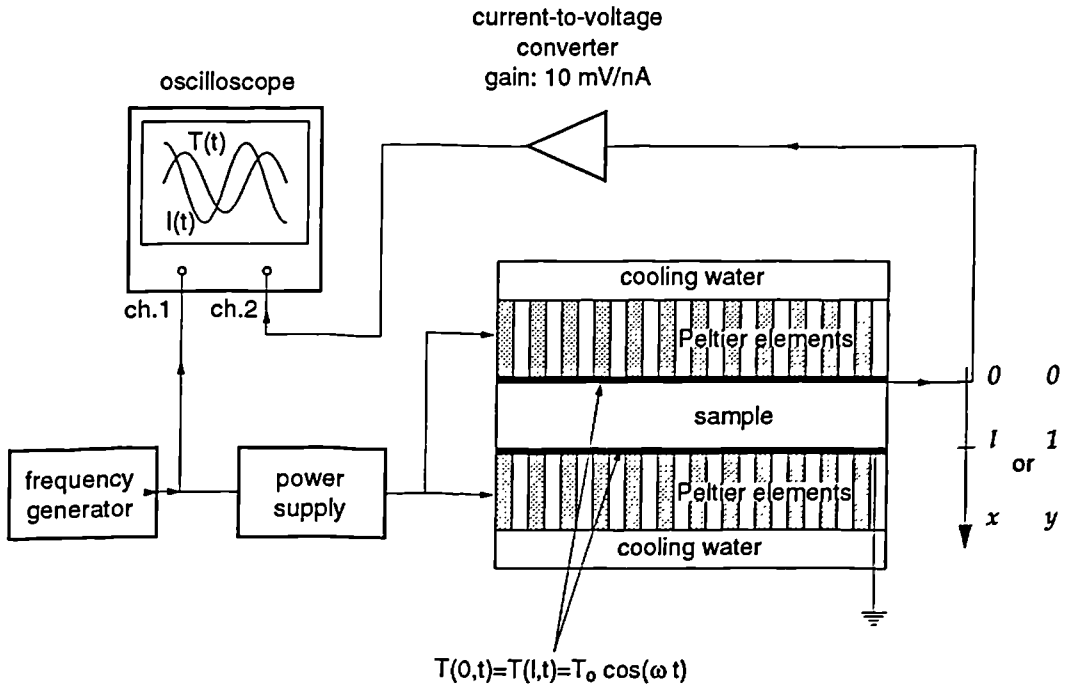

Figure 5.3 - Schematic set-up for pyroelectric measurements using the heat excitation dynamic method.

If the diameter of the sample is much greater than its thickness the equation for the diffusion of heat is one-dimensional,

$$\frac{\partial T}{\partial t} = \kappa \frac{\partial^2 T}{\partial x^2} \tag{5.11}$$

where T(K) is the difference between actual temperature and room temperature and κ (m^2/s) the thermal diffusivity. Because the sample is in-between two Peltier elements driven by the same power supply, the boundary conditions are:

$$T(0,t) = T(l,t) = T_0 \cos(\omega t) \tag{5.12}$$

A similar type of problem has been solved by Carslaw [Carslaw et al. 1959]. The solution consists of the sum of a transient and a periodic term. The transient term decays with a time constant of 10 ms for the typical conditions used and thus, does not contribute to the experimentally measured quantities. The periodic term which is a solution of equation 5.11 can be expressed in normalised form as [Holeman 1972]:

$$T(y,t) = T_\omega(y,\omega_a)e^{i\omega t} = \left[B_1 \cosh(\omega_a y) + B_2 \sinh(\omega_a y)\right]e^{i\omega t} \tag{5.13}$$

where $y = \frac{x}{l}$ (5.14),

$$\alpha = \frac{\kappa}{l^2} \tag{5.15}$$

$$\omega_a = (1+i)\sqrt{\frac{\omega}{2\alpha}} \tag{5.16}$$

Substituting equation 5.13 and equations 5.12 into equation 5.11 we obtain for the temperature phasor inside the sample:

$$T_\omega(y,\omega_a) = T_o[\cosh(\omega_a y) - \sinh(\omega_a y)\tanh(\omega_a/2)] \tag{5.17}$$

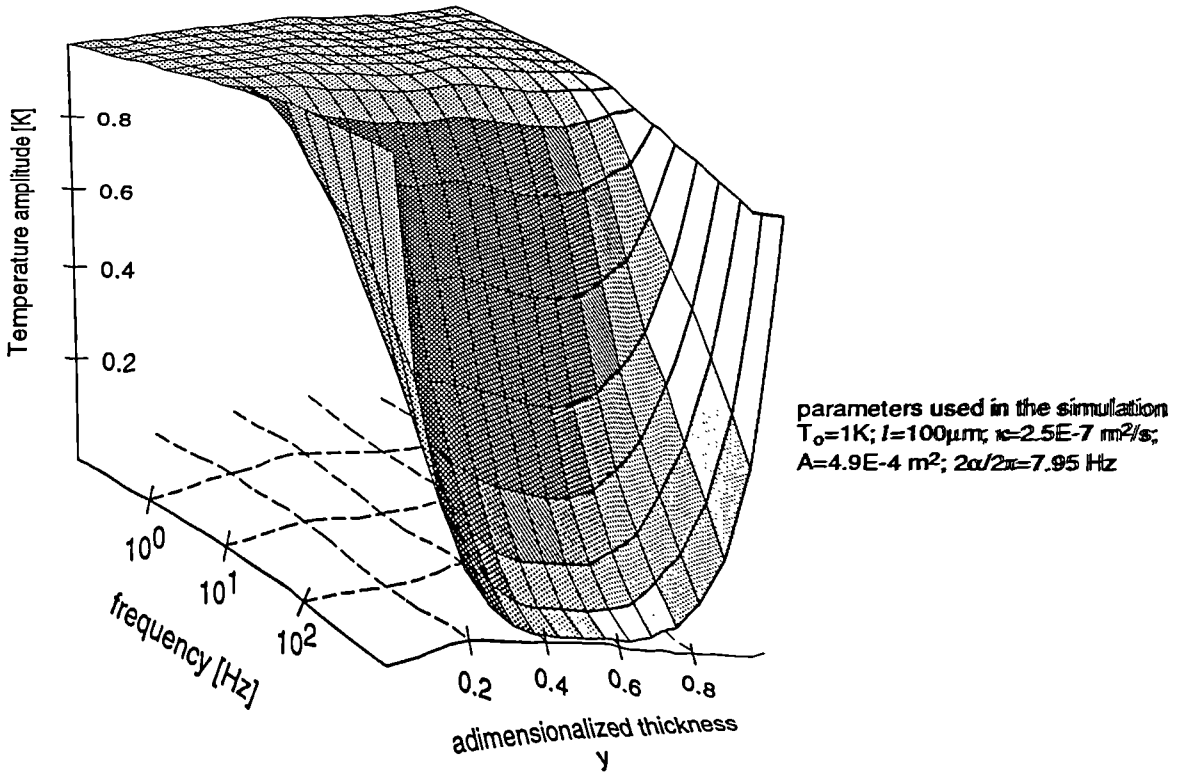

Figure 5.4 - Amplitude of the temperature oscillation both as a function of the position inside the sample and the excitation frequency. The parameters used in the simulation are quoted in the figure.

The magnitude of the temperature oscillation inside the sample, as described by equation 5.17, is shown in figure 5.4 both as a function of frequency and the position y inside the sample.

It may be observed that for lower frequencies (i.e. $\omega/2\alpha \ll 1$) the temperature oscillation inside the sample is rather uniform, while at high frequencies (i.e. $\omega/2\alpha \gg 1$) there is an attenuation of temperature oscillation in the bulk thus creating at higher frequencies a distributed non-uniform thermal force which has been used before in the Laser Intensity Modulation Method (LIMM) to measure the spatial distribution of polarization in polymer electrets [Lang et al. 1986].

The expression for the short-circuit pyroelectric current I, measured for a sample subjected to a non-uniform distribution of temperature, containing a polarization and a surface charge density distribution $P(y)$ and $\sigma(y)$ respectively, has been deduced by Mopsik [Mopsik et al. 1982], which after suitable manipulations is given by:

$$\frac{I}{A} = \alpha_p \int_0^1 P(y)\frac{\partial T}{\partial t}\,dy + (\alpha_x - \alpha_\varepsilon)\int_0^1 \left[\left(P(y)-\overline{P}\right)-\left(\sigma(y)-\overline{\sigma}\right)\right]\frac{\partial T}{\partial t}\,dy \tag{5.18}$$

where α_p, α_x and α_ε are the polarization, the permittivity and the linear temperature coefficients respectively and A is the area of the sample. The surface charge density $\sigma(y)$, is related to the volume space charge density $\rho(y)$, through,

$$\sigma(y) = \int_0^y \rho(y)\, dy \tag{5.19}$$

Case 1: Uniform temperature - From equation 5.18 it may be observed that when the temperature distribution is uniform across the sample, the second term of the current density, due to the local spatial deviation from the mean of both the polarization and space charge, vanishes and thus does not contribute to the measured current.

Hence, we can derive a constraint for the exciting thermal modulation frequency ω, which is $\omega << 2\alpha$, in which case we get the usual expression for the pyroelectric current as:

$$I = A\alpha_p \int_0^1 P(y)\frac{\partial T}{\partial t}\, dy = \alpha_p \overline{P} A \frac{\partial T}{\partial t} = pA\frac{dT}{dt} = i\omega p A T_o \tag{5.20}$$

where $p = \alpha_p \overline{P}$ is the pyroelectric coefficient. It should be emphasised that for all dynamic methods for the determination of the pyroelectric coefficient, including the step input of thermal radiation, the temperature distribution in the specimen will not be uniform unless the condition $\omega << 2\alpha$ is satisfied. The second term in the equation 5.18, which is usually called the tertiary pyroelectric coefficient, will thus make a contribution to the pyroelectric current if the above condition is not met.

Case 2: Uniform polarization and uniform space charge - We now assume that the polarization and space charge spatial distributions are uniform across the sample. The time derivative of temperature in equation 5.18 should then be taken from the average temperature of the sample which is equal to,

$$\frac{d\overline{T}}{dt} = \frac{d}{dt}\left[\int_0^1 T(y, w_a)dy\right] = i\omega T_o\left[\frac{2}{\omega_a}\tanh\left(\frac{\omega_a}{2}\right)\right]e^{i\omega t} \tag{5.21}$$

It should be noted that the average temperature inside the sample is calculated from its time derivative by dividing the second member of equation 5.21 by $i\omega$ which is justified by the Fourier transformation integration property. Substituting equation 5.21 into equation 5.18 it may be shown that,

$$I = I_\omega\, e^{i\omega t} = pA\frac{d\overline{T}}{dt} = i\omega p A T_o\left[\frac{2}{\omega_a}\tanh\left(\frac{\omega_a}{2}\right)\right]e^{i\omega t} \tag{5.22}$$

If the frequency of excitation is low enough, the phasor of the current I_ω will be given by,

$$I_\omega = i\omega p A T_o\left[\frac{2}{\omega_a}\tanh\left(\frac{\omega_a}{2}\right)\right] \overset{\omega << 2\alpha}{\approx} i\omega p A T_o \tag{5.23}$$

This equation describes the current phasor in terms of the pyroelectric coefficient, the sample area, the frequency of excitation and the temperature amplitude. It further shows that the current will be leading the temperature excitation by 90° provided that $\omega << 2\alpha$.

As was pointed out by Garn and Sharp [Garn et al. 1982], when the depolarisation

current varies a great deal within the amplitude of the temperature oscillation there will be a significant current, in phase with temperature, which should be discarded from the total current by taking into account that in the case of a low frequency excitation the true pyroelectric current is 90° out of phase relative to the temperature.

In figure 5.5 we have simulated the current which may be measured using typical values for the sample properties and assuming a temperature amplitude T_0=1°C. The value used for the thermal diffusivity (i.e. 2.5 10^{-7} m^2/s), is an estimate taking into account that the composite we are trying to emulate, has a 60% ceramic volume fraction. Furthermore, we have assumed a uniform polarization distribution such that the sample has a pyroelectric coefficient ≈$10^{-5}C/m^2K$. In this simulated case the thermal cut-off frequency (i.e. α/π) is 7.95 Hz.

From figure 5.5 we observe that in the low frequency range the current rises proportionally with the frequency while above the thermal cut-off it rises as the square root of the frequency. This is possibly due to the fact that the current is proportional to the time derivative of the average temperature oscillation which in turn is equal to the product of the frequency and the average temperature oscillation. At low frequency the temperature is uniform across the sample and so the current rises proportionally with the frequency but as a thermal gradient starts to build-up inside the sample (i.e. for frequencies above 7.95 Hz) the average temperature oscillation begins to drop and the increase of the current will not be so steep. The phase plot shows that at low frequency the current leads the temperature wave by 90° and that this reduces to 45° in the high frequency region.

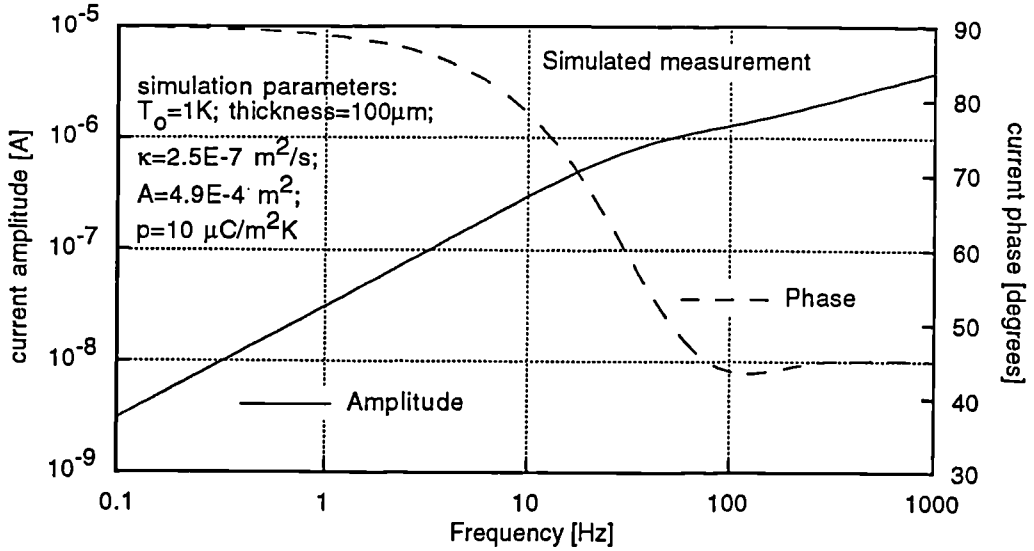

Figure 5.5 - Simulation of the current and phase when heating the sample sinusoidally.

The inverse problem of calculating the pyroelectric coefficient from the measured current is, however, more common in laboratory situations. Solving the simplified equation 5.23, the pyroelectric coefficient will normally be given by the simple expression,

$$p = \frac{I}{A\omega T_o} \qquad (5.24)$$

where I is the amplitude of the measured current, provided the temperature is uniform inside the sample. However, when the frequency increases so that the temperature is no longer uniform inside the sample the pyroelectric coefficient given by equation 5.24 will no longer give correct results. In this case, the measured current will be lower than if entire sample was oscillating at the temperature T_0 and, therefore, the measured or apparent pyroelectric coefficient of the sample given by equation 5.24 will be lower than the real pyroelectric coefficient of the sample. The relationship between the apparent (p_{app}) and the real pyroelectric coefficient (p) is then

$$p_{app} = p\,\frac{2\sqrt{i}}{\omega_a}\left|\tanh\left(\frac{1}{2}\omega_a\right)\right| \qquad (5.25)$$

In figure 5.6 is a simulation of the apparent pyroelectric coefficient, obtained when using equation 5.24, for a sample whose pyroelectric coefficient is assumed to be uniform and equal to 10μC/m^{2}K. The other properties used in this simulation are also the same as those of figure 5.5.

In figure 5.6 it may be observed that at low frequency the apparent pyroelectric coefficient coincides with the real value, but as the frequency increases its value starts to decrease as explained above.

In section 5.4.5 experimental results using this technique will be described. The experimental set-up was built by at Heiman GmbH and the experimental data reported here using this technique are the result of a collaboration between our two laboratories.

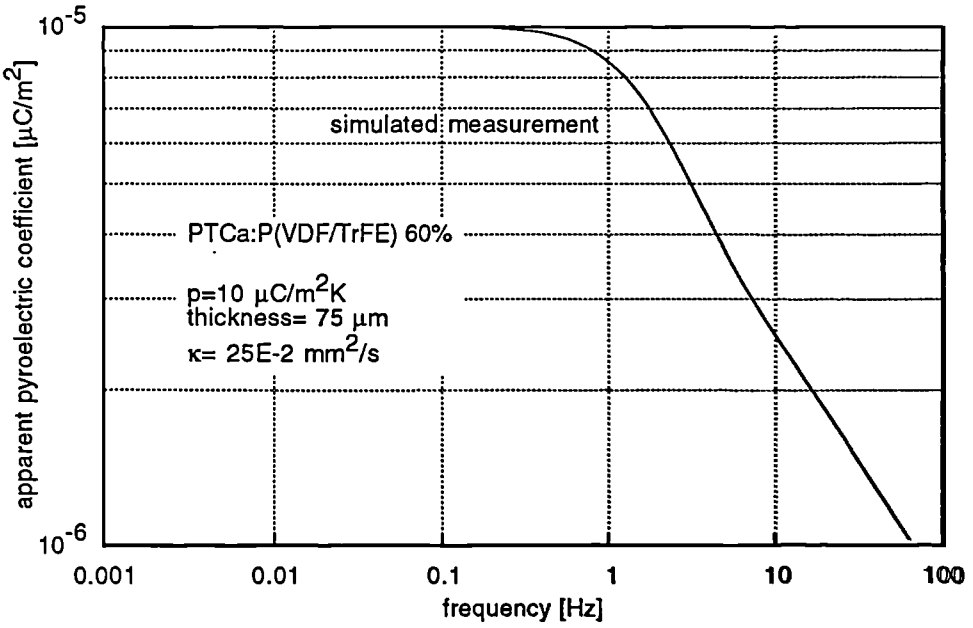

Figure 5.6 - Simulation of the apparent pyroelectric coefficient obtained using equation 5.24 as a function of frequency, for a sample having a uniform polarization of 10μC/m^{2}K

5.3 - Composite pyroelectric properties review

Various combinations of ceramic/polymer 0-3 composites have been reported in view of optimising the pyroelectric coefficient and/or the pyroelectric FOM$p = p/\varepsilon$ [Wang et al.

1993]. These reports have also included studies of the effect of the volume loading and in some cases of the ceramic grain size effect. Although the amount of publications on this subject does not compare with that performed on composite piezoelectric properties there is ground to believe that successful commercial devices can be made out of these materials. Here, we try to review some of this work.

Bhalla and co-workers [Bhalla et al. 1981] have reported on the pyroelectric coefficient of PZT:epoxy composites of both 0-3 and 3-3 connectivity. It was anticipated that improved pyroelectric properties would be brought about as a result of the enhancement of the secondary pyroelectric effect arising from the thermal expansion mismatch (see section 2.4 on the composite models) of the component phases. The ferroelectric PZT material used, was of a formulation designed to give high piezoelectric *d* coefficients and thus was not the best one suited for pyroelectric applications. However, it had the advantage of being able to reproduce consistent electrical properties. The epoxy material used with the commercial designation of *SPURRS*, was a multicomponent system designed for casting and replication due to its very low viscosity and, therefore, suited for the preparation of the 3-3 connectivity composites. The ceramic loading used was approximately of 40%. Pyroelectric and dielectric measurements demonstrated that the pure 0-3 composite behaved as a dilute PZT system whose pyroelectric coefficient and permittivity were both reduced by a factor of ten in such a way that its ratio p/ε (i.e. composite $p/\varepsilon=0.35\mu C/m^2K$) was roughly equal to that of the pure ceramic (PZT FOM = $0.27\mu C/m^2K$). In the 3-3 composites made, whose structural unit size was 100-150μm, it was observed that critical size effects appeared for thicknesses smaller than 6-10 structural units (>1mm). The pyroelectric coefficient exhibited under 45°C a sign opposite (i.e. positive) to that of the ceramic changing to the same sign for higher temperatures. This effect was related to a change of the relative contributions of the primary pyroelectricity, which is due to the intrinsic pyroelectric properties of the ceramic, and secondary pyroelectricity, the latter showing a stronger contribution for thicker samples and at lower temperatures due to the stiffer nature of the polymer host in these conditions.

$BaTiO_3$-rubber 0-3 composites have been synthesised by Amin and co-workers [Amin et al. 1988; Amin et al. 1988]. The powdered ceramic was introduced in a butadiene acrylonitrile rubber after which the whole mixture was vulcanised in stainless steel moulds to obtain thin films. The poling of the composites was performed at 130°C and 170°C (i.e above the Curie temperature of the ceramic) under poling fields ranging from 0.1-5 MV/m. A peculiar behaviour was found as the pyroelectric coefficient was found to decrease with increasing poling field when poling at 130°C. This effect was ascribed to space charge formation which also contributed to the pyroelectric current measured by the direct method. At 170°C, however, the sample was found to be free of the space charge and the true pyroelectric coefficient was found to be approximately equal to $60\mu C/m^2K$ for a 30% $BaTiO_3$ volume loading. The permittivity was found to be around 17 and thus the pyroelectric FOM was 3.5 $\mu C/m^2K$ which is quite a high value.

Tripathi et al. [Tripathi et al. 1991] have produced 0-3 composites of $BaTiO_3$-PVDF in

which the $BaTiO_3$ powder, 1μm in size, was obtained by means of the sol-gel route. The permittivity of the composites was around 20 and good pyroelectric properties relative to the pure $BaTiO_3$ were observed; however, no absolute values for the pyroelectric coefficients were reported

TGS-PVDF 0-3 composites have also been evaluated for their pyroelectric properties [Fang et al. 1991; Wang et al. 1993]. TGS crystals ground to particle sizes of 45 to 75 μm were mixed in different proportions up to 80% volume loading with PVDF dissolved in an organic solvent and then poured over glass plates to obtain films 50 to 100 μm thick. The polarisation procedure was performed at 70-80°C for 2-3 hours whilst applying a field of 0.4-0.6MV/m. The pyroelectric properties increased with the ceramic loading and at 80% the pyroelectric coefficient was around 90 $\mu C/m^2K$ with a FOM_p of 3.3 $\mu C/m^2K$.

Experiments with PVDF and PE (polyethylene) as hosts polymers have been performed by Yamazaki et al [Yamazaki et al. 1981] using as dispersoids ceramic grains of PZT and PT in the 0.5 to 3 μm size range. The 0-3 composites produced utilising the hot-rolling technique described above, were then pressed to obtain thin films in the 30-70 μm thickness range. Pyroelectric measurements were then performed using the radiative dynamic method. It was found that for a similar ceramic volume fraction of 62% the highest pyroelectric voltage responsivity was that of PT-PVDF which was six times higher than PZT-PVDF and about 50 times higher than PE-PT. The pyroelectric coefficient for the PT-PVDF 62% volume fraction composite was found to be $130\mu C/m^2K$ whilst its permittivity was around 54 resulting in pyroelectric FOM equal to 2.4 $\mu C/m^2K$. This value compares well with that of the pure ceramic which was reported to have a p/ε of $3\mu C/m^2K$.

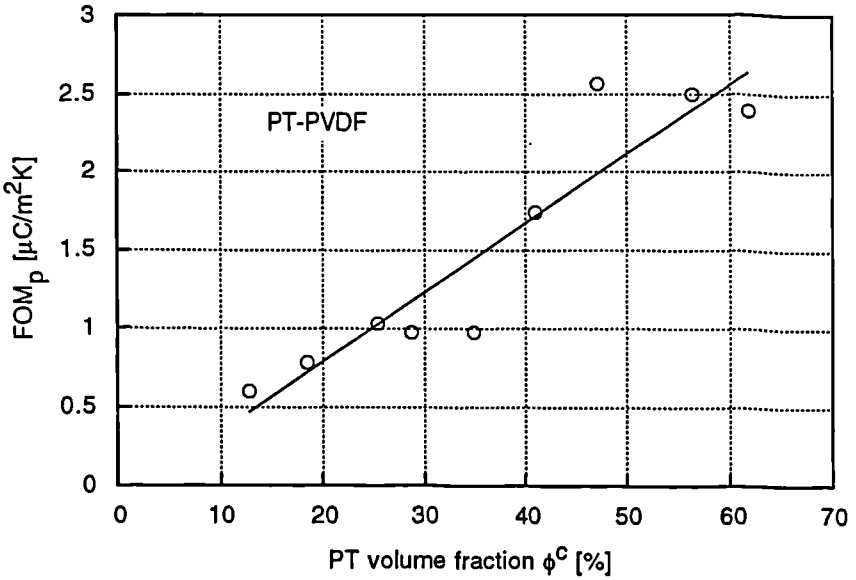

Figure 5.7 - Pyroelectric Figure Of Merit (FOM) as a function of the content of the ferroelectric powder [Yamazaki et al. 1981].

In figure 5.7 is shown the pyroelectric coefficient as a function of the PT content where it may be observed that the slope of the curve increases for ceramic loading over 35% and thus no optimum volume fraction may exist. In their work it was suggested, according to a

composite model developed therein, that polymer hosts with higher permittivities would be desirable in order to improve on the magnitude of the pyroelectric coefficient.

PZT-PVDF and PZT-P(VDF/TrFE) together with a composite Piezel (Daikin Industries of Japan) made of PZT and a polymer matrix were evaluated by Abdullah and Das-Gupta [Abdullah 1989; Abdullah et al. 1990]. The composites were manufactured by means of the hot-rolling technique using a fine powdered ceramic using a 50% volume loading. The pyroelectric coefficient at room temperature was found, using the direct method to be 10μC/m^{2}K increasing to 140 μC/m^{2}K at 70°C. The corresponding ratio p/ε was 0.35 μC/m^{2}K and 1.5 μC/m^{2}K respectively at room temperature and 70°C demonstrating a high dependence of the pyroelectric properties on the temperature as was also found by Bhalla et al [Bhalla et al. 1981], thus at 70°C their *FOM* was higher than that of the pure ceramic. The nature of the dependence of the pyroelectric coefficient on the poling time, field and temperature was also undertaken (see figure 5.8) for these composites where it can be observed that saturation of polarisation is attained for poling times in excess of 5 hours [Abdullah et al. 1990]. However, increasing the poling temperature and field results in a monotonous increase of the pyroelectric coefficient and no saturation pattern is apparent.

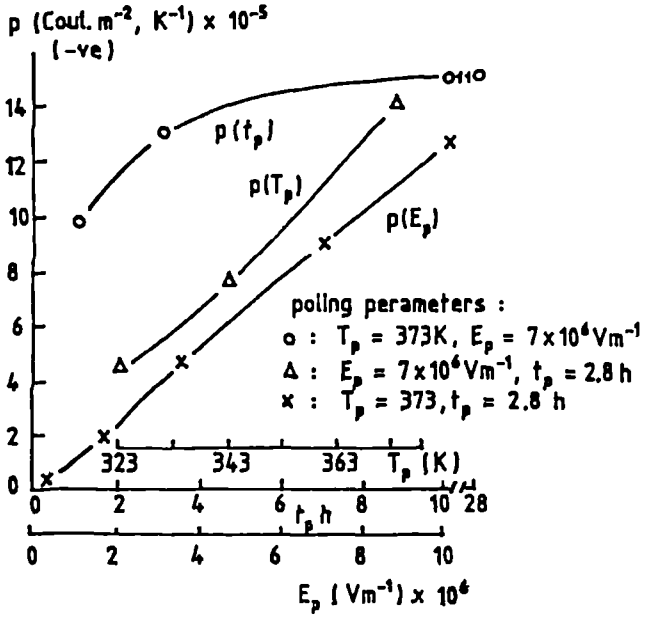

Figure 5.8 - The dependence of pyroelectric coefficient on poling parameters at 343 K in a PZT-P(VDF/TrFE) 50% composite [Abdullah 1989; Abdullah et al. 1990].

5.4 - Pyroelectric measurements

5.4.1 - Pyroelectric coefficient in composites

In table 5.1 are listed the pyroelectric coefficients for the composites fabricated. The quoted values have been obtained using the direct method of measurement and taking the value of the pyroelectric coefficient at 30°C. For comparison, the values of the pyroelectric coefficient of the composites reviewed in the last section have also been included in the same table as well as those of the constituent materials of the fabricated composites.

TABLE 5.1- PYROELECTRIC COEFFICIENT OF SELECTED COMPOSITES (@RT)

composite ceramic	cer. vol. fraction [%]	composite polymer	relative permittivity ε	diel. loss tan δ	pyro. coeff. p (@RT) μC/m²K	pyro. FOM$_p$ p/ε (@RT) μC/m²K	Ref.
PZT	40	epoxy SPURRS	110		40	0.35	[1]
$BaTiO_3$	30	rubber	17		60	3.5	[2]
$BaTiO_3$	20	PVDF	20				[3]
TGS	80	PVDF	12		90	3.3	[4]
PT	62	PVDF	54		130	2.4	[5]
PZT	50	PVDF	90		10	0.11	[6]
		PVDF	7.6-11	0.060	20	2.2	
		P(VDF/TrFE)	7.9	0.011	17	2.1	
PZT5A	40	PP	13	<0.001	2	0.15	
PZT	50	PVDF	50	63	10	0.2	
PZT	50	P(VDF/TrFE)	118	0.020	39(cor.)	0.33	
PLZT	50	P(VDF/TrFE)	80	0.017	17(cor.)	0.21	
PTCa-2(q)	50	P(VDF/TrFE)	40	0.013	25(90)	0.63(2.25)	
PTCa-2(q)	60	P(VDF/TrFE)	49	0.012	30(100)	0.61(2.04)	
PTCa-2(q)	65	P(VDF/TrFE)	51	0.011	45(120)	0.88(2.35)	
PTCa-2(q c.)	50	P(VDF/TrFE)	36	0.021	30(65)	0.83(1.8)	
PTCa-2(q f.)	50	P(VDF/TrFE)	37	0.020	35(80)	0.95(2.16)	
PTCa-1(q)	20	P(VDF/TrFE)	21	0.018	25	1.2	
PTCa-1(q)	30	P(VDF/TrFE)	28	0.015	34	1.21	
PTCa-1(q)	40	P(VDF/TrFE)	34	0.013	55	1.61	
PTCa-1(q)	50	P(VDF/TrFE)	40	0.013	79	1.97	
PTCa-1(q)	60	P(VDF/TrFE)	49	0.013	95	1.93	
PTCa-1(q)	65	P(VDF/TrFE)	67	0.013	130	1.94	
PTCa-1(m)	50	P(VDF/TrFE)	56	0.014	54(cor.)	0.7	
PTCa-1(m)	60	P(VDF/TrFE)	66	0.012	60	0.9	
PTCa-1			220	0.006	380	1.73	
PTCa-2			235	0.014	410	1.74	
PZT5A			1700	0.020	420	0.24	[7]
PLZT 7/65/35			1860	0.018	1300	0.69	[8]
$LiTaO_3$			45	2E-4	170	3.77	

Notes: (i) for PTCa-2 and between parentheses are the pyroelectric properties using the dynamic method; (ii) f. and c. stand for fine and coarse sedimented PTCa-2 powders; (iii) typical error Δp/p=10%; (iv) cor. means corona poling

References: [1] - [Bhalla et al. 1981]; [2] - [Amin et al. 1988]; [3] - [Tripathi et al. 1991]; [4] - [Fang et al. 1991]; [5] - [Yamazaki et al. 1981]; [6] - [Abdullah et al. 1990]; [7] - [Matroc 1992]; 8 - [Liu et al. 1972]

The relative permittivity and the loss at 1 kHz and room temperature for all these materials, are also listed in table 5.1. From these data one can calculate the figure of merit

$FOMp = p/\varepsilon$, which is roughly proportional to the responsivity of a detector made with that particular sample as explained in the first section of this chapter. This parameter stresses the fact that it is important to have a high pyroelectric coefficient while keeping the permittivity low.

The values listed, represent the highest pyroelectric coefficient obtained for the material concerned. Thus, it is possible that, for example, in one material the best procedure to polarise the sample was corona poling whilst in another the conventional procedure could be proved to be a better one. These effects will be dealt with later on.

The quoted values for the pyroelectric coefficient in table 5.1 have an estimated error of 10%. There are various sources for this error of which the more important are: the variation in the volume fraction, the non-uniformity of thickness and the pyroelectric current measurement error due to the contribution of the discharge current to the pyroelectric current. A variation in the volume fraction can appear if during the pressing operation the sample does not spread uniformly in the radial direction. This could lead to a weak gradient of concentration from the centre to the edges of the sample. The pressing operation can also lead to a non-uniformity of thickness in the radial direction, so that the applied field is lower in the centre of the sample where the sample is thicker in comparison with that of the edges.

It should be noted that the listed values of the FOM_p should then have a relative error which is the sum of relative errors both of the permittivity and pyroelectric coefficient i.e.,

$$\frac{\Delta FOM_p}{FOM_p} = \frac{\Delta \varepsilon}{\varepsilon} + \frac{\Delta p}{p} \tag{5.26}$$

which amounts to about 20%. Thus, its listed values should be regarded with caution.

Because of the restrictions due to electrical breakdown the maximum poling field was usually in the range of 15-25 MV/m. As a result, the polymer does not contribute to the overall pyroelectricity of the composite as its coercive field is in the 50-80 MV/m range. Furthermore, the annealing procedure which consisted of the short-circuit ageing at 90°C for 12 hours, also reduces any pyroelectric contribution of the polymer that might be present. Thus, the polymer although of a ferroelectric nature, does not contribute to the electroactive properties of the composite and acts only has a low stiffness host to the electroactive ceramic powder.

For the composites made in our laboratories it is observed that PTCa incorporated composites exhibit in general a higher pyroelectric coefficient than PZT and PLZT incorporated composites. This could be due to the lower dielectric matching which, as was explained before, has negative implications both in the properties and in the poling. The negative influence can be appreciated from the analysis of equation 2.54 (chapter 2) for the pyroelectric coefficient of the series connectivity composite which can be approximated for a high permittivity ceramic thus,

$$p \overset{\text{if } \varepsilon^c >> \varepsilon^p}{\approx} \frac{\phi^c}{\phi^p}\frac{\varepsilon^p}{\varepsilon^c}p^c \overset{\phi^c=50\%}{\approx} \frac{\varepsilon^p}{\varepsilon^c}p^c \tag{5.27}$$

Hence, the lower the permittivity match is the lower will be the pyroelectric constant of the composite.

The PLZT ceramic was also used in view of its higher resistivity (10^{11} Ω·m) than any of the other ceramics which have resistivity values of the order of 10^{9}-10^{10} Ω·m. This should improve the poling efficiency by having a higher fraction of the poling voltage across the ceramic grains for long poling times. As can be seen in the table 5.1 the pyroelectric coefficient for the PLZT/P(VDF/TrFE) is not as large as that of PTCa composites and is even lower than that of the PZT:P(VDF/TrFE) composite. Thus, we conclude that the resistivity matching is not a critical factor in determining the final pyroelectric response and, furthermore, it appears that the permittivity matching is a more important factor as explained above.

It can be observed also from this table that of the polymers used i.e. polypropylene (PP), PVDF and P(VDF/TrFE) the last one appears to be the best to use in composite fabrication. P(VDF/TrFE) has a high permittivity which increases as much as three times near its Curie temperature and, therefore, this also indicates that dielectric matching between the ceramic and the polymer is a significant factor in obtaining composites with improved pyroelectric properties

An effort was thus more strongly directed in studying in detail the properties of composites made of PTCa ceramic embedded in a P(VDF/TrFE) matrix.

For the PTCa-1 and PTCa-2 composites, the pyroelectric coefficient increases with the volume fraction of ceramic incorporated into the polymer as can be seen in table 5.1 and in figure 5.9. This happens both because the pyroelectric response monotonically increases with the amount of ceramic and as the volume fraction increases, the likelihood of having a path of ceramic grains traversing continuously from one to the other electrode also increases thus assigning the composite a higher degree of 1-3 connectivity.

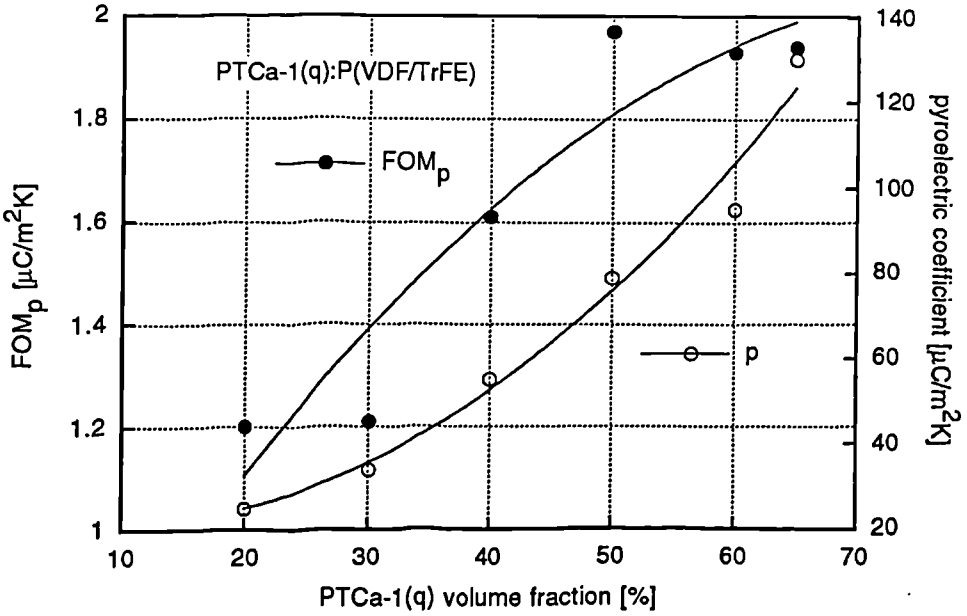

Figure 5.9 - Pyroelectric coefficient and FOM_p as a function of the ceramic volume fraction in the PTCa-1(q):P(VDF/TrFE) composite.

In PTCa-2 composites an abnormal pyroelectric phenomenon occurred. The pyroelectric coefficient measured by the direct method, was substantially lower than that obtained using the heat excitation dynamic method. Furthermore, there was a dependence of the pyroelectric coefficient on the frequency using the dynamic technique, such that its value decreased with decreasing frequency. The quoted values were taken at about 0.1 Hz where a stabilisation of the pyroelectric coefficient appeared to exist. As yet there is no quantitative explanation for this behaviour although a possible answer could be as follows. If a pyroelectric ceramic of a low resistivity as is the case of this particular ceramic composition, is incorporated in a high resistivity matrix it is possible, that the pyroelectric charge generated when heating the sample discharges through the resistance of the ceramic (see figure 5.10) and therefore does not contribute to the measured pyroelectric current. This phenomenon would be more pronounced at a low frequency of temperature excitation. At a high frequency compared to the inverse of electrical time constant RC of the ceramic, the pyroelectric current would then approximate to a saturation value as the discharge process through the ceramic would no longer take place. Assuming a permittivity of 235 and a resistivity of the ceramic of $10^9\Omega$·m the frequency of measurement has to be higher than 0.5 Hz to prevent this discharge process. It should be noted, however, that this phenomenon is not detrimental in a pyroelectric detector which normally works in the ac mode detecting changes in the pyroelectric charge in the frequency region of 1Hz.

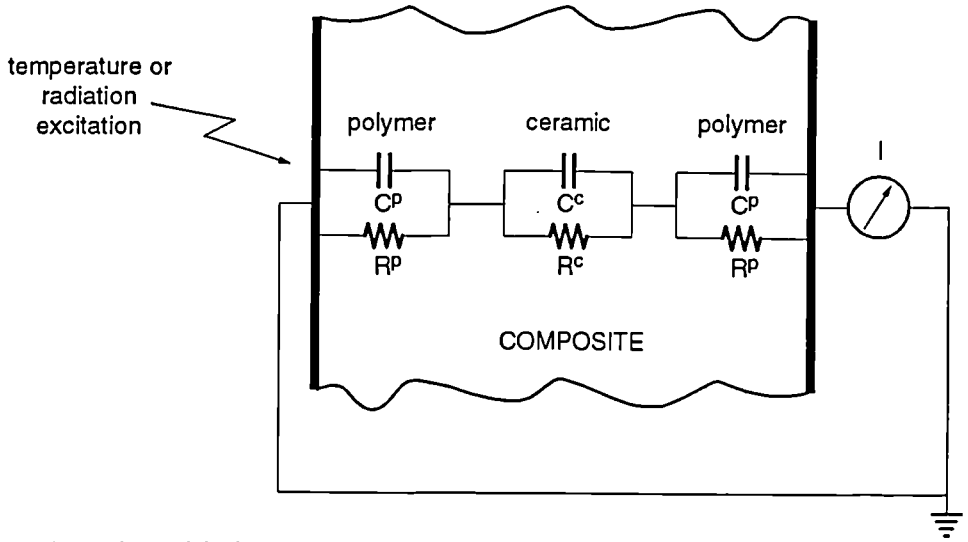

Figure 5.10 - Schematic model of a composite which could explain the frequency dependence of its pyroelectric coefficient.

We have nevertheless used the direct method to measure the pyroelectric coefficient by heating and cooling the PTCa-2 composite samples at the rate of 1°C/min. Although this is not a true measure of pyroelectricity it gives a relative indication of pyroelectricity between samples of similar composition.

It is noted from the table 5.1 that the 65% loaded PTCa composites exhibit the highest pyroelectric coefficients with FOM_p closer to that of the ceramic, making these composites attractive to use in pyroelectric detectors.

The behaviour of the pyroelectric FOM_p in the composites however, is not clear-cut as

can be observed in figure 5.9. Values closer and surpassing that of the ceramic (i.e. $FOM_p^{(PTCa\text{-}1)}$=1.73 μC/m^{2}K) have for example, been obtained for the PTCa-1(q) composites of 50, 60 and 65% loadings while for 20, 30 and 40% its value is clearly lower than that of the ceramic. A closer examination of this quantity will be treated in section 5.4.8.

In order to test the mixed connectivity model, the experimental points taken from the quenched PTCa-1(q) composite, shown in gray circles, were plotted in the mixed connectivity cubes charts of figure 5.11 assuming a 100% poling of the ceramic. The location of each of the points in the pyroelectric chart of figure 5.11 is found by using simultaneously the volume fraction of the composite and the experimental value of that property as explained before in the chapter 2 - models of composites. For example, in the case of the 65 vol% PTCa-1(q) composite with a pyroelectric coefficient of 130 μC/m^{2}K one locates first the line of 65% volume fraction in the pyroelectric coefficient chart and then find the property line closer to the value of 130 μC/m^{2}K. This locates the point in the chart giving an estimate for the values m and n characterising the equivalent mixed connectivity cube of the composite. In the present case m~0.85 and n~0.62 and thus 27% of the composite is constituted by ceramic touching both the upper and lower electrodes while the rest of the ceramic (i.e. 65-27=38%) is connected in series with the polymer. This procedure has been carried out for the 20, 30, 40, 50, 60 and the 65 % PTCa-1(q):P(VDF/TrFE) composites from which the values listed in table 5.2 were obtained.

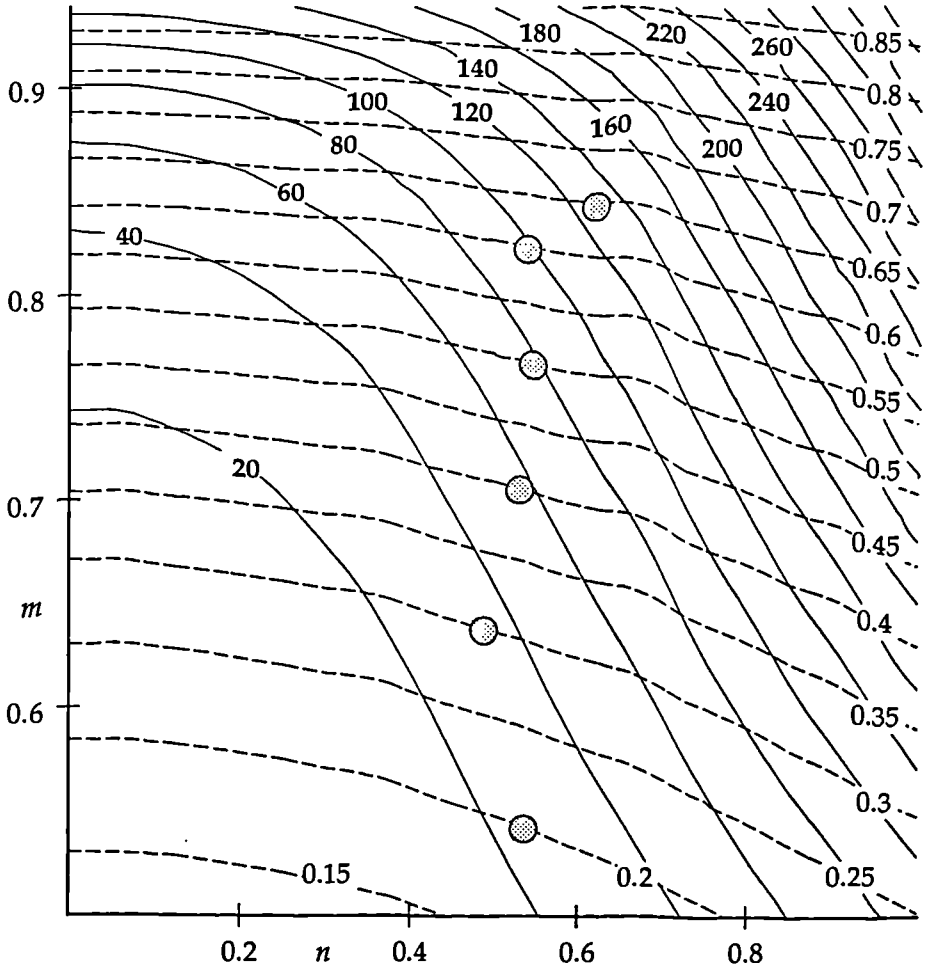

Figure 5.11 - Mixed connectivity chart for the pyroelectric constant in PTCa-1(q):P(VDF/TrFE) composites.

TABLE 5.2 - n AND m PARAMETERS OF THE MIXED CONNECTIVITY CUBE MODEL FOR THE PTCa-1(q):P(VDF/TrFE) COMPOSITE USING THE PYROELECTRIC COEFFICIENT

vol. fraction	p	n	m	$\phi^{parallel}$
20	25	0.54	0.54	0.086
30	34	0.48	0.64	0.096
40	55	0.52	0.71	0.136
50	79	0.55	0.77	0.18
60	91	0.52	0.82	0.19
65	130	0.62	0.85	0.27

In figure 5.11 it can be noticed that the experimental points have a *n* value which is in the range of 0.48-0.62 and thus about more than half of the ceramic cube touches both electrodes (see figure 2.26). The volume fraction connected in parallel for the same composites rises from about 9% for the 20% loaded composite to about 27% in the 65% composite (see figure 5.12).

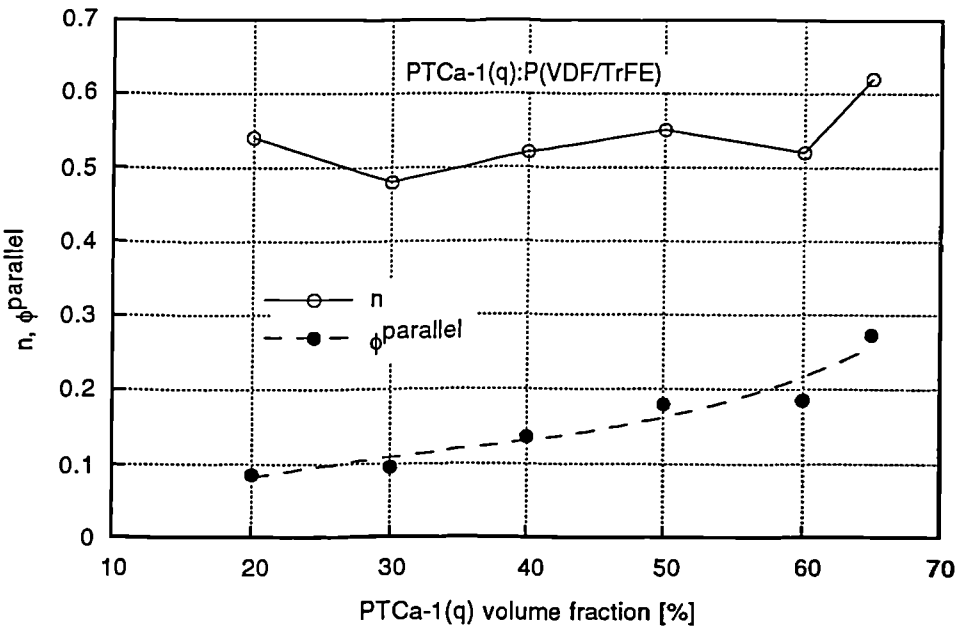

Figure 5.12 - Dependence of the n parameter and of the percentage of ceramic connected in parallel upon the ceramic volume fraction.

It appears thus that these composites exhibit a fairly constant degree of parallel connectivity defined by the *n* parameter, irrespective of their volume fraction, which is probably due to the large size of the ceramic grains relative to the thickness of the composite (see figure 5.12). For the composite loaded with 65% ceramic however, a visible increase in the parallel connectivity of the ceramic is observed. This can be an evidence of a high ceramic loading effect described in chapter 2.

The pyroelectric chart of figure 5.11 was drawn assuming that the ceramic in series was fully poled. If a value of less than unity was assumed, the points would have to be located in

a region of the chart with higher n values. This would not be reasonable because then the n values in the pyroelectric chart would be higher than those of the permittivity chart. This may indicate that the assumption of a 100% poling for all the composites is justified.

In conclusion it may be said that the model seems to help to portray the general behaviour of a composite for certain conditions, but care should be taken in ensuring that the premises such as a 100% poling and consistent raw material properties are met.

5.4.2 - Temperature dependence in the composites

The direct method was used to measure the pyroelectric coefficient in composites made with PZT, PLZT and PTCa-1(m) and the results are shown in figure 5.13. These are 50% ceramic volume fraction composites poled by the conventional method at 100°C for about 3 hours while applying an electric field of 20 MV/m. It may be observed that the pyroelectric coefficient of Lead Titanate ceramics composites are about 50 and 150 % higher than PZT and PLZT composites respectively at room temperature. However, as the temperature increases, the PZT and PLZT composites perform better relative to the PT composites due to the low temperature dependence of the latter. We note however, that a low dependence on the temperature is a useful feature to assure a steady working performance of a pyroelectric detector system.

The PLZT composite has the lowest pyroelectric coefficient amongst these composites which indicates that the resistivity matching of the ceramic to the polymer is not a crucial factor in determining the final pyroelectric coefficient of the composite.

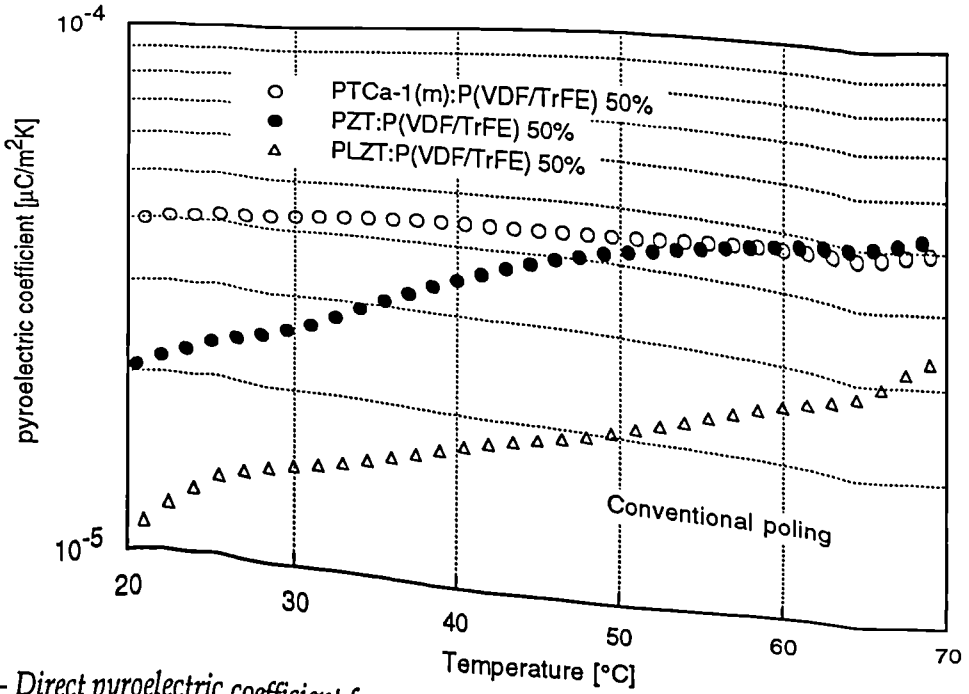

Figure 5.13 - Direct pyroelectric coefficient for various 50% volume fraction composites conventionally poled at 100 °C with a field of 20MV/m.

The temperature dependence of the pyroelectric coefficient in the composites was quantified as follows. The percentage of variation α of the pyroelectric coefficient p per unit of rise in temperature T can be defined as,

$$\alpha = \frac{1}{p}\frac{dp}{dT} \tag{5.28}$$

which leads to an equation of the type,

$$p = p_o \exp(\alpha T) \tag{5.29}$$

which can be fitted to the direct method of measurement curves to find the experimental value of the α parameter of the different composites. After finding these values and in order to give a more meaningful insight we have calculated the percentage increase in the pyroelectric coefficient for a ΔT=50°C increase in temperature (for instance from 20° to 70°C). This quantity is related to α by,

$$\frac{\Delta p}{p} = 1 - \frac{p_o}{p} = 1 - \exp(\alpha \cdot \Delta T) = 1 - \exp(50\alpha) \tag{5.30}$$

The values obtained for $\Delta p/p$ in these composites are listed in table 5.3. From these data it is interesting to note that for PZT and PLZT composites a similar value of 158% variation in the pyroelectric coefficient is obtained for a 50°C temperature rise, which can be due to a similar ceramic composition. In the case of the PTCa-1(m) composite however, the pyroelectric coefficient only changes by 20% for the same increase in temperature, which is beneficial to the production of pyro-detectors.

TABLE 5.3 - PERCENTAGE INCREASE IN THE PYROELECTRIC COEFFICIENT FOR A 50°C INCREASE IN TEMPERATURE FOR CERAMIC:P(VDF/TRFE) COMPOSITES

ceramic	PTCa-1(m)	PZT	PLZT	PTCa-1(q) composites						PTCa-1
ϕ^c	50%	50%	50%	20%	30%	40%	50%	60%	65%	
$\Delta p/p$[%]	20	158	158	158	110	145	69	101	42	35

In figure 5.14 is shown the pyroelectric coefficient for six PTCa-1(q):P(VDF/TrFE) composites with different volume fraction (i.e. 20, 30, 40, 50 60 and 65%) all of which are conventionally poled with a field of 25 MV/m during 15 minutes at 90°C. In addition the pyroelectric coefficient of a PTCa ceramic is shown in the same graph for comparison.

It appears (figure 5.14) that the p-coefficient increases more than 4 times when the ceramic volume fraction rises from 20 to 65%, which is well in excess of a linear increment.

The temperature variation of the pyroelectric coefficient has also been calculated for these composites as well as for the ceramic and is listed in table 5.3. It can be observed from table 5.3 that for a 50°C temperature rise the amount of variation in the pyroelectric coefficient decreases for increasing ceramic loadings. This means that this property also approximates to that of the pure ceramic, which shows a 35% variation (see table 5.3).

From the data measured for the PTCa-1(q) and PTCa-1(m) composites it is possible to say that it is beneficial in pyroelectric terms that a ceramic which is introduced into a polymer matrix should not have a very high permittivity. In terms of the volume fraction a substantial increase in the pyroelectric coefficient was observed between the 60% and 65%

ceramic loaded composites which indicates that a higher degree of parallel connectivity is being achieved at this level of ceramic concentration.

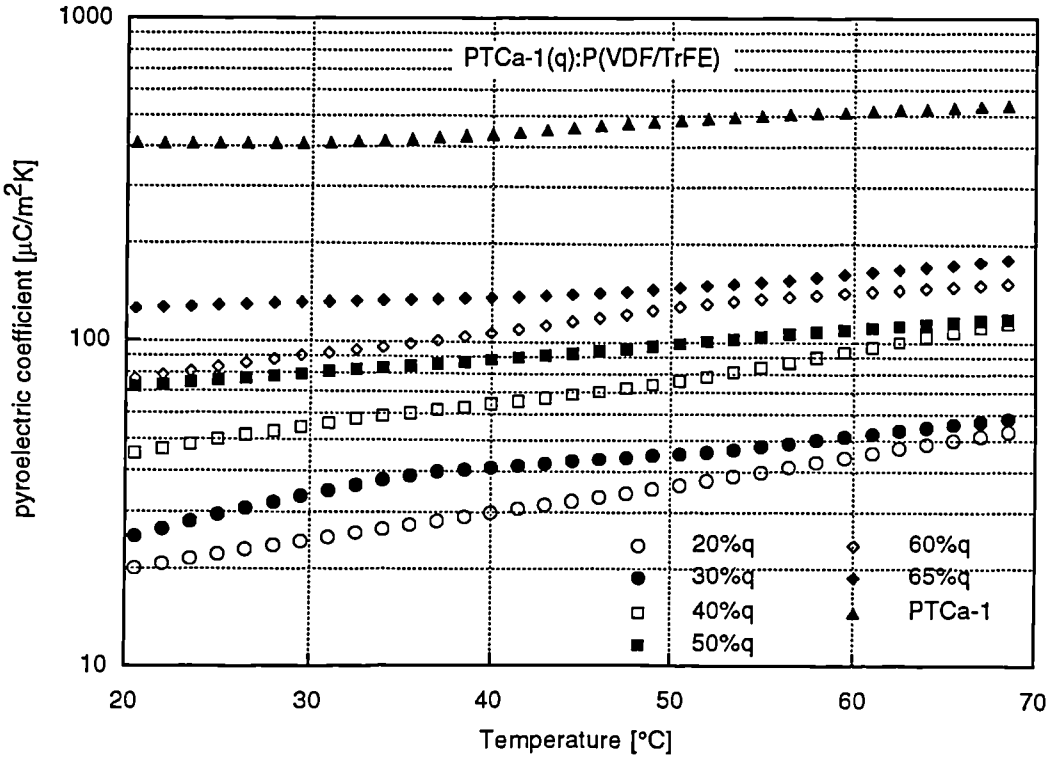

Figure 5.14 - Direct pyroelectric coefficient for PTCa-1(q):P(VDF/TrFE) conventionally poled samples at 95℃ with a field of 25MV/m for 15 min.

5.4.3 - Field and poling time dependence

In figure 5.15 are shown the direct pyroelectric coefficients in a PTCa-1(m):P(VDF/TrFE) 50% composite polarised with an increasing field of 5, 10, 15 and 20 MV/m.

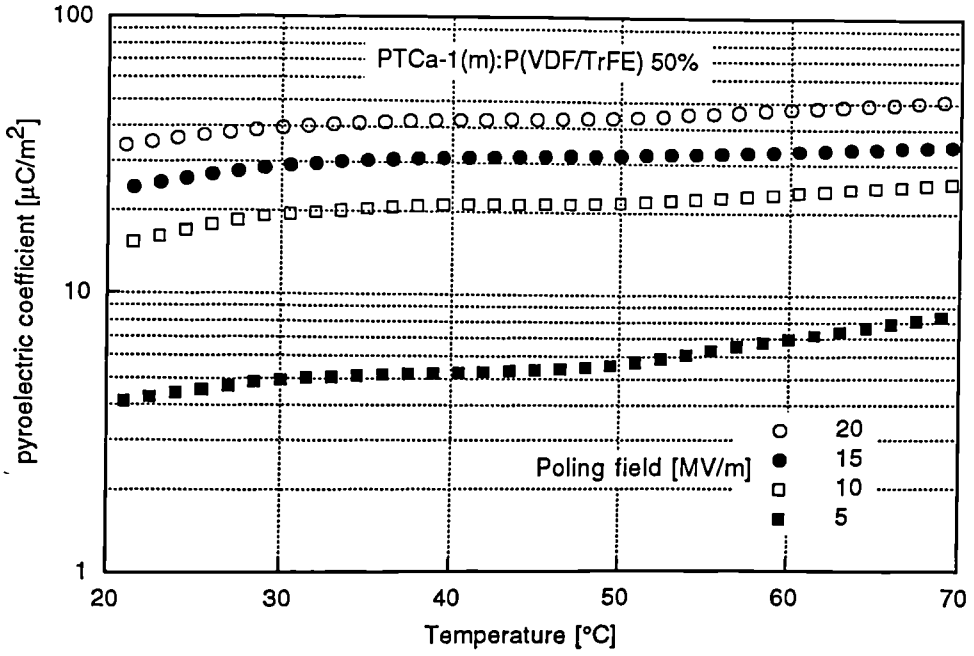

Figure 5.15 - Direct pyroelectric coefficient showing the effect of the poling field on a PTCa-1(m):P(VDF/TrFE) 50% composite.

A significant increase in the pyroelectric coefficient can be expected when the field increases from 5 to 10MV/m.

This increase is proportionally lower for further increases in the poling field. It is not, however, possible to distinguish a saturation of the pyroelectric coefficient in these composite as is shown in figure 5.16.

No experiments of a similar kind have been performed on the other composites although a similar pattern of behaviour is to be expected.

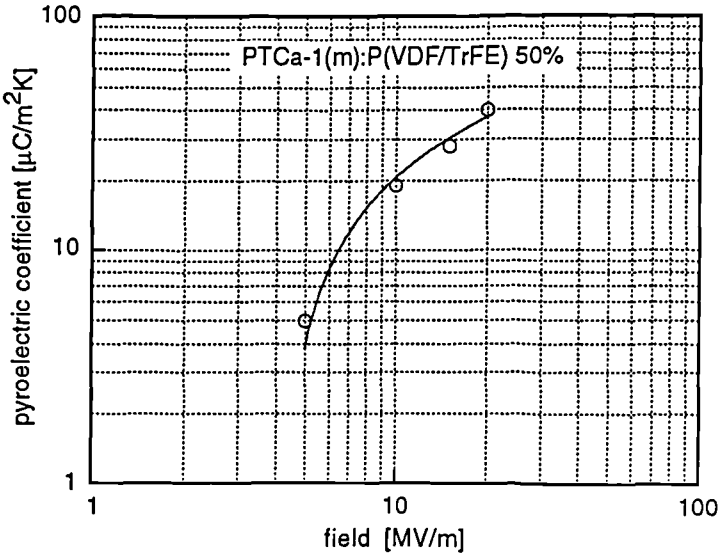

Figure 5.16 - Poling field dependence of the pyroelectric coefficient in the PTCa-1(m) P(VDF/TrFE) composite.

5.4.4 - High temperature poling

The PTCa ceramic has a Curie temperature which is in the region of $T_C \approx 250\text{-}260$ °C. At that temperature it is easier to polarise the ceramic due to the enhanced mobility of the ferroelectric structure so that a lower poling field would be able to polarise the ceramic lattice in a desired direction. Although the polymer melts at 175°C it does not burn until much higher temperature. Thus an experimental set-up was devised to polarise the sample at a temperature approaching 250°C as shown in figure 5.17.

A metallized sample with aluminium strips on both sides was placed in-between two Teflon sheets about 500μm thick and the latter enclosed by two stainless steel plates (figure 5.17). This arrangement was placed in the hot-press at a pressure of 1 Tonne force while the temperature increased slowly up to 175°C. A field of 6MV/m was then applied for 30 minutes after which the sample was allowed to cool down with the field. It was observed in the course of this experiment that a higher poling field caused severe breakdown problems.

As can be observed in figure 5.18 the pyroelectric coefficient for this composite does not improve on poling at 90 °C at a field of 20 MV/m which have been the normal poling promoters in the present work. It should be commented, however, that for such a weak poling field of 6 MV/m applied at a high temperature, a substantial amount of polarization was achieved which probably would not be obtained if the poling temperature were 90°C. This idea of high temperature poling was not explored further although, it is believed that a

more thorough investigation of this poling procedure could be fruitful.

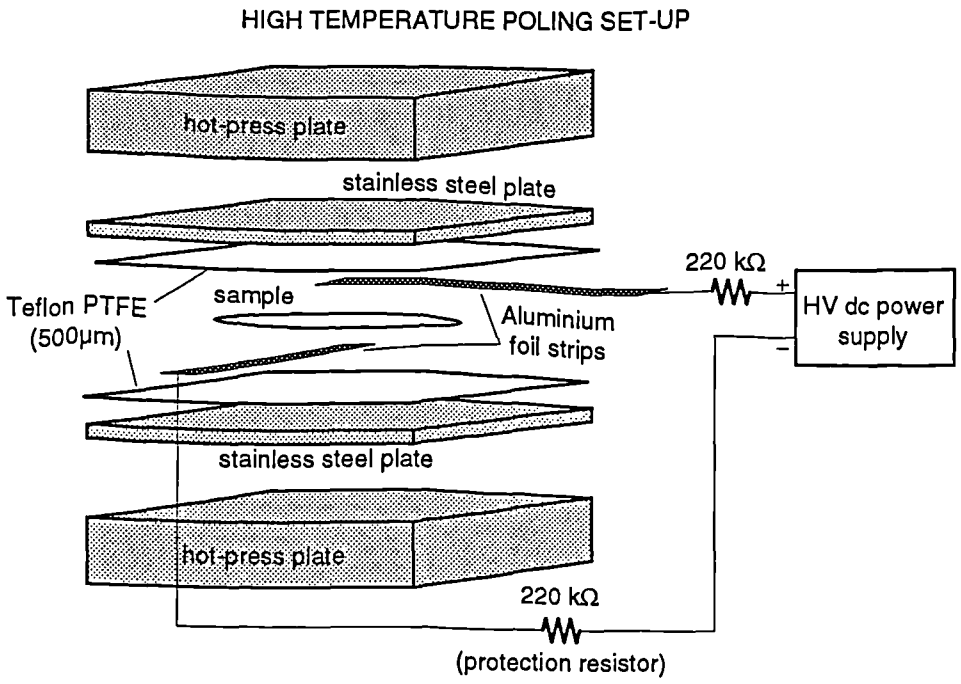

Figure 5.17 - Schematic for high-temperature poling set-up.

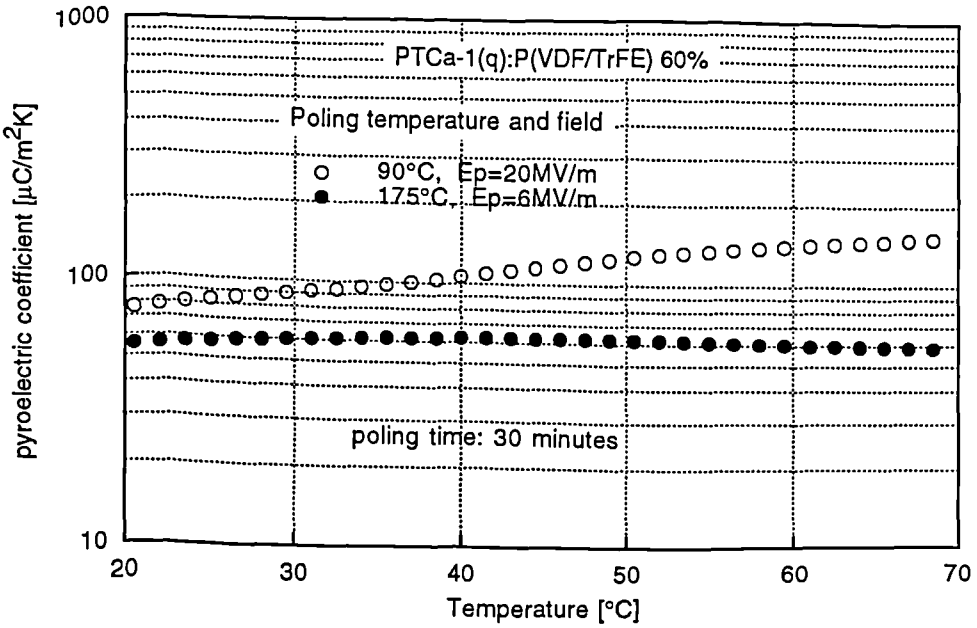

Figure 5.18 - Comparison of pyroelectric coefficient of composites polarised below and above the Curie temperature of the ceramic.

5.4.5 - Corona versus conventional poling

Figure 5.19 shows the direct pyroelectric coefficient for corona poled composites using PTCa-1(m), PZT and PLZT ceramics at 50% loading in a P(VDF/TrFE) matrix. These are the same composites which were conventionally poled and whose pyroelectric coefficients are plotted in figure 5.13. The results from that figure have been replotted in figure 5.19 for comparison between the corona and conventional poling procedures.

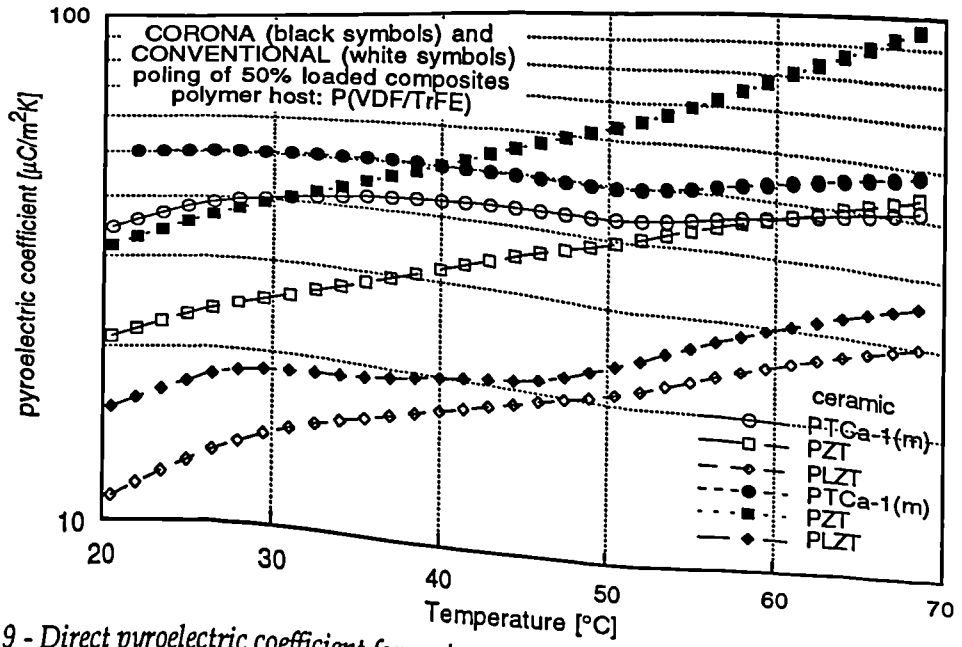

Figure 5.19 - Direct pyroelectric coefficient for various 50% volume fraction composites polarised using the corona and the conventional techniques.

It is observed again that amongst the corona poled composites the PTCa-1(m) composites have a higher pyroelectric coefficient at room temperature than the other ceramic composites. It is 30 and 70% higher than the corresponding PZT and PLZT composites respectively. However, at temperatures higher than 40°C the PZT:P(VDF/TrFE) composite has a higher pyroelectric coefficient than that for the PTCa-1(m) ceramic. The temperature dependence of these composites is the same as that exhibited by the conventionally poled samples, the PTCa-1(m) composite showing the lowest dependence whereas the PZT and PLZT have a similar variation with temperature.

It is apparent from a comparison between the conventional and corona poled samples that these 50% volume fraction composites are more efficiently poled by the corona poling method than by the conventional one. This can be due to a higher poling field applied in the corona poling than in the conventional method without serious breakdown problems. From the comparison of both poling methods it is seen that the improvement in the pyroelectric response in relative terms is greater for the PZT and PLZT composites than for the PTCa-1(m) which is an indication of a higher degree of poling for the PTCa-1(m) composites when using the conventional poling method.

It is usually assumed that the surface voltage of the sample during corona poling is the same as the voltage applied to the grid, which for a low resistivity sample may not be the case. For instance, in the case of the 60% volume fraction PTCa-1(q) composites (i.e. lower resistivity materials) we measured lower pyroelectric coefficients for the corona poled samples than for the conventional poled ones as shown in figure 5.20. This can only be explained if the conduction current through the composite sample restricts the surface voltage to a much lower value than that of the corona grid (see section 4.2).

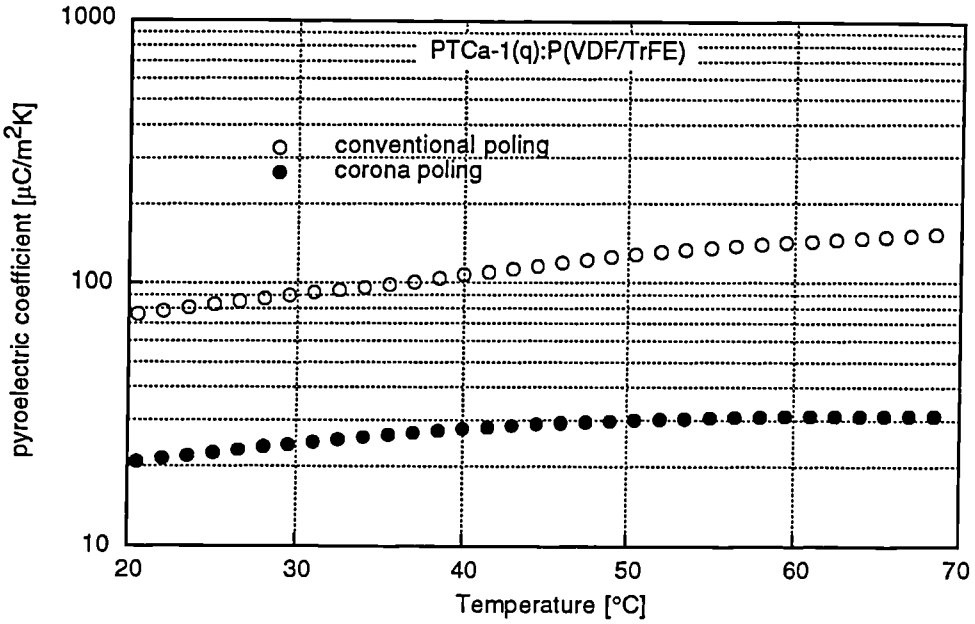

Figure 5.20 - Direct pyroelectric coefficient for PTCa-1(q):P(VDF/TrFE) 60% composite poled using the corona and the conventional techniques.

5.4.6 - Milled and quenched ceramics

In figure 5.21 is shown the pyroelectric coefficient of four PTCa-1(q) conventionally poled composites using two different volume fractions i.e., 50 and 60% and two different powder processing methods either milled and quenched whose ceramic grain sizes are in the range of 1μm and greater than 20μm respectively. From these plots the pyroelectric coefficient seems to increase both with the volume fraction and the ceramic grain size.

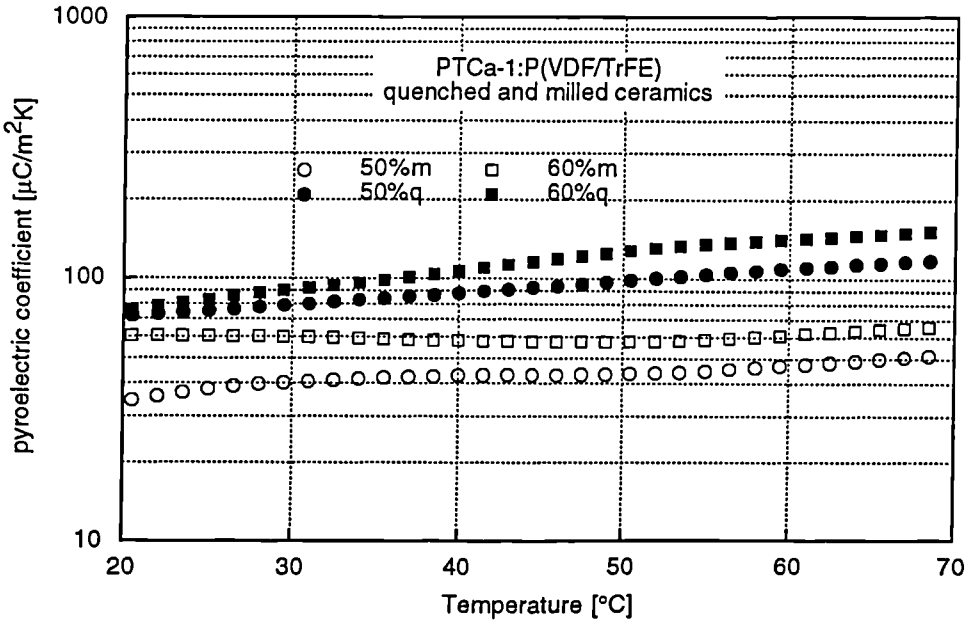

Figure 5.21 - Direct pyroelectric coefficient for conventionally poled composites made with milled and quenched powders of calcium modified lead titanate.

A large grain size of the ceramic powder seems to provide an increasing pyroelectric coefficient at least when its size becomes comparable to that of the thickness of the sample. This has been observed before [Bhalla et al. 1981] and is easily explained by the mixed

connectivity model as stated in chapter 2.

The difference in the behaviour between the quenched and milled composites can thus be explained partly by the larger grain sizes produced by the quenching procedure. It should be noted however, that the grain size effect does not explain certain features of the behaviour such as the slightly higher permittivity found in the milled ceramic composites compared with the quenched ones. This contradicts the 1-3 connectivity argument, which predicts a simultaneous rise in the permittivity and pyroelectric coefficient for an increase in the 1-3 connectivity, and thus forces one to admit that the grains obtained through the milling procedure are in some way altered by the mechanical forces impressed upon them during the processing stage.

Assuming a similar behaviour of PTCa with the grain size as that for $BaTiO_3$ [Shaikh et al. 1986; Shaikh et al. 1989] the permittivity increases with decreasing grain size, reaching a peak value at 1 μm and decreasing subsequently with any further reduction of the grain size (see chapter 1, figure 1.6a). It is possible that a similar behaviour arising from the considerations of the effects of grain boundaries, internal stress and field and domain wall area, may also be expected for PTCa thus helping to explain the increase in the permittivity of the milled ceramic composites. It was also found in the same work [Shaikh et al. 1986; Shaikh et al. 1989] that the polarization monotonically decreases with a decreasing grain size. This could explain why with a simultaneous increase in the permittivity the pyroelectric constant decreases for the milled ceramic composites compared with the quenched ceramic ones.

It has also been reported that a higher coercivity exists for smaller ceramic grains [Durán et al. 1990]. This would have the adverse effect in making it more difficult to polarise composites made with smaller ceramic grains.

In addition with these grain size effects the way in which the ceramic powders are obtained, also affect their properties [Jiang et al. 1990; Lee et al. 1990]. Lapping and polishing operations have the effect of further reducing the ferroelectric properties of the ceramic through the formation of an inactive layer of low permittivity over the ceramic grain. As the milled ceramic grains are obtained using a mechanical operation in contrast with the quenched ceramics, a decrease in the pyroelectric properties in the milled ceramic composites should be expected.

To distinguish between the grain size and the mechanical effects two batches of PTCa-2(q) both of quenched ceramics one with a fine grain size (7.5-20μm) and the other with a larger grain size(w_{gs}> 20μm) have been reported earlier in chapter 3. The latter batch was passed through a 62 μm sieve to remove the very large grains in order to obtain thin films. Although no direct measurement was made, the difference between the two average grain sizes was small as evidenced from the SEM micrographs (see figures 3.17 a and b). Our attention has also been drawn by the supplier of the ceramic powder to the fact that the quenching produced unusually fine size grains on this occasion. Nevertheless, due to the grain size difference one should expect that the pyroelectric coefficient improves for the

same volume fraction and sample thickness for samples with the larger ceramic grain size, if the 1-3 connectivity argument was to be correct. Composites, 50% in volume of ceramic, were made with these batches so that a comparison with previous composites could also be made. These were then pressed to a thickness of 45-55 μm .

In figure 5.22 we have plotted the direct pyroelectric coefficient of the PTCa-2(q):P(VDF/TrFE) 50% sedimented ceramic composites, together with a composite with the same composition, in which no sedimentation of the ceramic grains was performed. From the figure 5.22 it may be observed that the fine grain composite seems to have a slightly higher pyroelectric coefficient than the other composites. In view of what was stated above regarding the pyroelectric coefficient of these composites, we also have checked the comparative dynamic response of these composites and in this respect an opposite pattern emerged. As listed in the table 5.2 the average dynamic pyroelectric coefficient for three samples poled, under the same conditions, of the coarse and fine grain ceramic was 80 and 60 $\mu C/m^2K$ respectively. We thus believe that the grain size to be a significant parameter in the pyroelectric performance of a composite. The small difference in the pyroelectricity between the samples can be due to a corresponding small difference in the average grain size of the coarse and fine batches of the ceramic powder used. In fact, we can see the same trend in the PZT:PVDF and PZT:P(VDF/TrFE) 50% composites in which the grain size of the ceramic was 1 and 10μm respectively. Although PVDF and P(VDF/TrFE) polymers are not very different from each other, a very significant improvement on the pyroelectric coefficient was observed in the case where a larger grain size ceramic (i.e. PZT:P(VDF/TrFE)) was used.

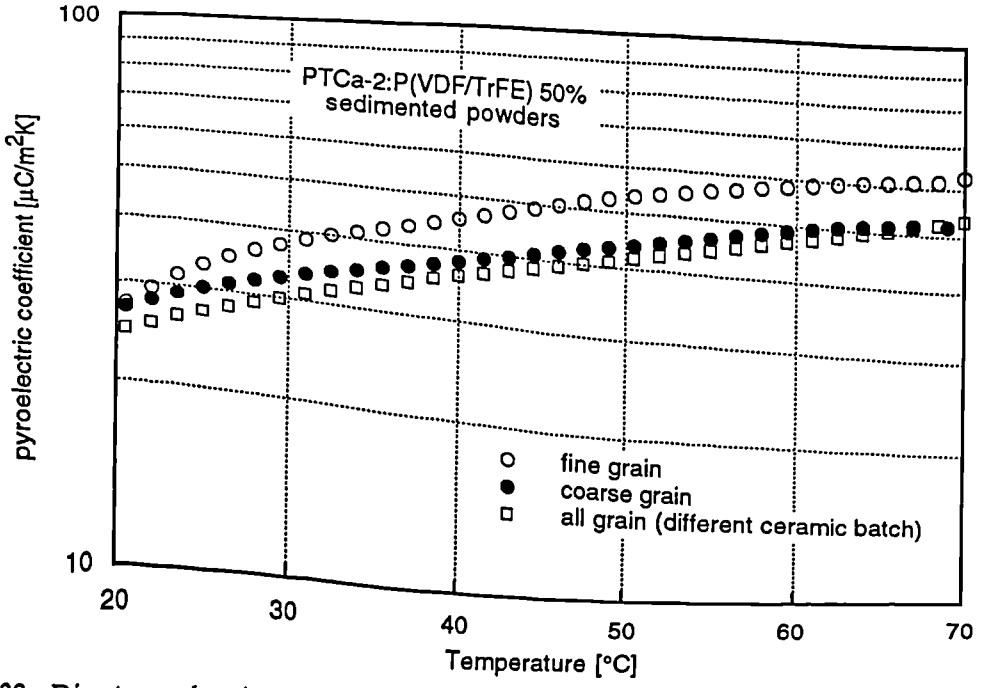

Figure 5.22 - Direct pyroelectric coefficient of PTCa-2 composites made with quenched sedimented powder.

5.4.7 - Dynamic method

An outline of the experimental method is shown in figure 5.3 and is as follows. The

sample is mounted in-between two sets of Peltier elements, whose temperature is kept oscillating with an amplitude T_0(K) at a frequency ω(rad/s). A good thermal contact between the Peltier elements and the sample was ensured whilst keeping the pressure on the sample to a minimum. In this work, we have not found a variation of the pyroelectric measurements within the range of pressure applied due to the mounting. The output current was fed into a current-to-voltage converter and the voltage was monitored together with the driving voltage of the Peltier elements in an oscilloscope. The temperature amplitude and phase T_0 was measured and calibrated both as a function of frequency and the average (background) temperature of the sample, with the aid of a $LiTaO_3$ sample with documented properties. $LiTaO_3$ was used, because it shows a truly pyroelectric response [Garn et al. 1982]. Within the frequency range 0.02-0.6 Hz, T_0 varies proportional to 1/f and we chose as a suitable measuring frequency 0.1 Hz based on our estimation of the thermal cut-off frequency which is about 8Hz for the PTCa(q):P(VDF/TrFE) composites. The driving voltage represents the power supplied to the Peltier elements, and at 0.1 Hz there is a 90° phase shift relative to the temperature wave. As the true pyroelectric current is also 90°C phase shifted to the temperature wave, the two signals (i.e. the driving voltage and the pyroelectric current) have a phase shift of 0° or 180°, depending on the poling direction of the sample. Typical values for the temperature oscillation obtained in our experimental set-up and measured at 0.1Hz are T_0=1.51 K and T_0=1.67 K when the background temperature is 14°C and 40°C respectively.

We have checked the validity of the present technique for a composite sample of PTCa-1(q):P(VDF/TrFE) 60% 80μm thick. After metallising on both sides with Cr/Au electrodes (A=6.85 cm^2) the film was DC poled for 2.6 hours at T=102°C while applying a poling field of 30MV/m. In figure 5.23 we show the pyroelectric coefficient measured with the static and with the dynamic method before and after poling.

Three runs were performed for the determination of the pyroelectric coefficient before we annealed the sample. The first run with the static set-up shows very large irreversible contributions as the measurement took place immediately after the poling process. The second run was performed with the dynamic set-up. During the measurement of the current amplitude we observed a high DC component yet the phase shift with respect to the driving voltage remained 0°. Therefore, we concluded that in this case the contribution of the depolarisation current to the oscillating current is small enough to be neglected. The third run with the static set-up still displays a large depolarisation current. After these measurements the sample was annealed at 55° for 17 hours under short-circuit. Annealing is not only a time consuming step, there is also the risk of depoling the components with low T_C. The fourth and fifth run show the static and dynamic pyroelectric measurement data after the annealing, which agree very well. This ensures the fitness of the technique for the pyroelectric coefficient measurements in the present case. Nevertheless, if phase shifts between the two measuring signals should be observed, a phase analysis would be necessary, to determine the true pyroelectric current.

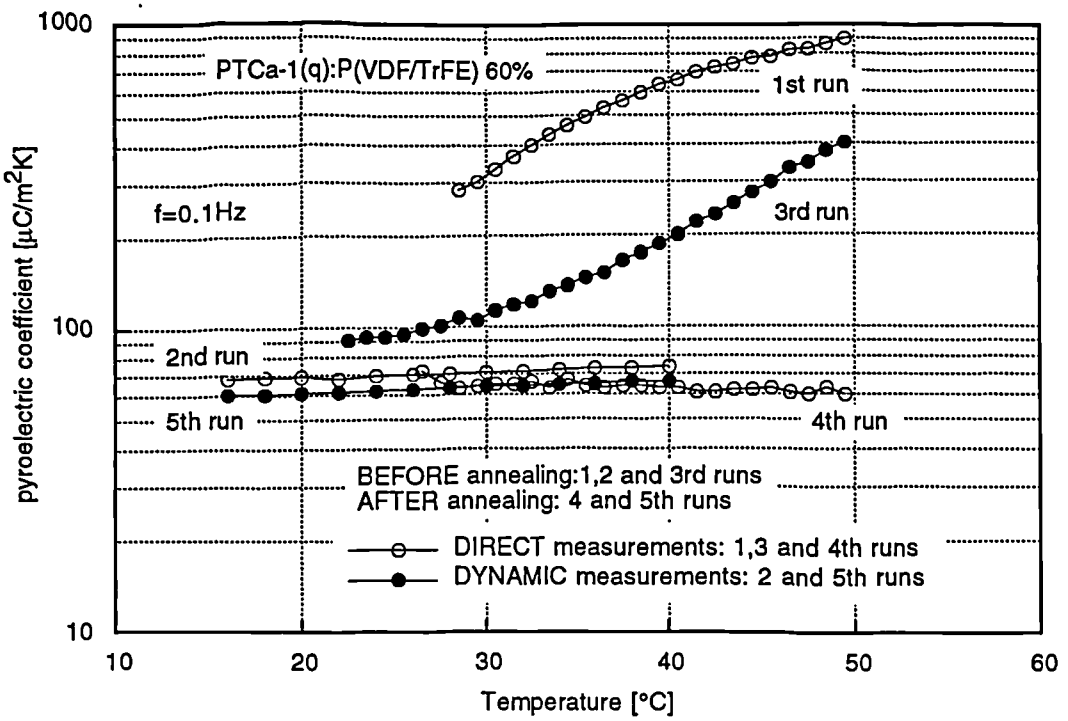

Figure 5.23 - Heat excitation dynamic and direct pyroelectric measurement of a PTCa-1(q):P(VDF/TrFE) 60% composite.

It is well established that an injection of charge carriers from the electrodes into the bulk of a dielectric becomes dominant when a sample is poled at high field and temperatures. These injected carriers may remain localised at grain boundaries, dislocation sites and other interfaces (*viz.*, crystalline-amorphous boundaries in semicrystalline polymers). For such a case a true reversible pyroelectric current may not be obtained, particularly at temperatures approaching that of the poling, unless an annealing process is undertaken to remove such trapped charges. However, at sufficiently high annealing temperatures one can promote not only the detrapping of charges but even the decaying of the frozen-in polarization. The slight difference between the dynamic measurements, before and after annealing, can thus be due to a depoling or ageing caused by the annealing process.

In measuring pyroelectric coefficients one must always induce a temperature change in the sample, which is to be measured. The methods, which use a small temperature change of only one sign (e.g. only heating) cannot distinguish between the true pyroelectric currents and other thermally stimulated currents. One method to overcome this drawback is to use a sinusoidally modulated temperature wave. A theory was given in this chapter to calculate an upper frequency below which, the temperature distribution inside the sample is uniform and how the cut-off frequency depends on the thickness and thermal properties of the sample (i.e. if one uses a sample of the same material composition but thickness L=500μm the cut-off frequency will be as low as 0.3 Hz). An experimental set-up is described and a comparison between quasi-static and dynamic results given. The method proved to be suitable to measure the pyroelectric coefficient of ceramic/polymer composites, which would otherwise need extensive annealing.

The dynamic technique can indeed be an accurate method for the measurement of the pyroelectric coefficient even in the presence of other sources of current such as those of depolarisation currents. However, one has to take into account only the portion of the oscillating current which is 90°C out of phase with the temperature in order to get a true value of pyroelectric activity.

In figure 5.24 is shown the pyroelectric coefficient of a composite sample of PTCa-1(q):P(VDF/TrFE) 490μm. A decay is observed in the apparent pyroelectric coefficient at frequencies above 0.1 Hz. Because the sample is sufficiently thick, at this frequency the temperature inside the sample is no longer uniform. In this case the apparent pyroelectric coefficient p_{app} relates to the true pyroelectric coefficient p as a function of the frequency of temperature oscillation through equation 5.25. A fitting of the experimental points of figure 5.24 to the expression given by equation 5.25 was carried out. A good fitting curve could be calculated using a value for the thermal diffusivity of $\kappa=4.3\cdot10^{-2}$ mm^2/s and a uniform polarization of $p=115\mu C/m^2$. This value of thermal diffusivity is close to that of the polymer which is around $5.3\cdot10^{-2}$ mm^2/s.

This low value of the thermal diffusivity indicates a potential use of these composites in imaging array devices as they will exhibit a low smearing of the thermal image with the elapsed time due to a low diffusion of heat across nearby elements. More work should, however, be carried in this respect to check this property in these composites.

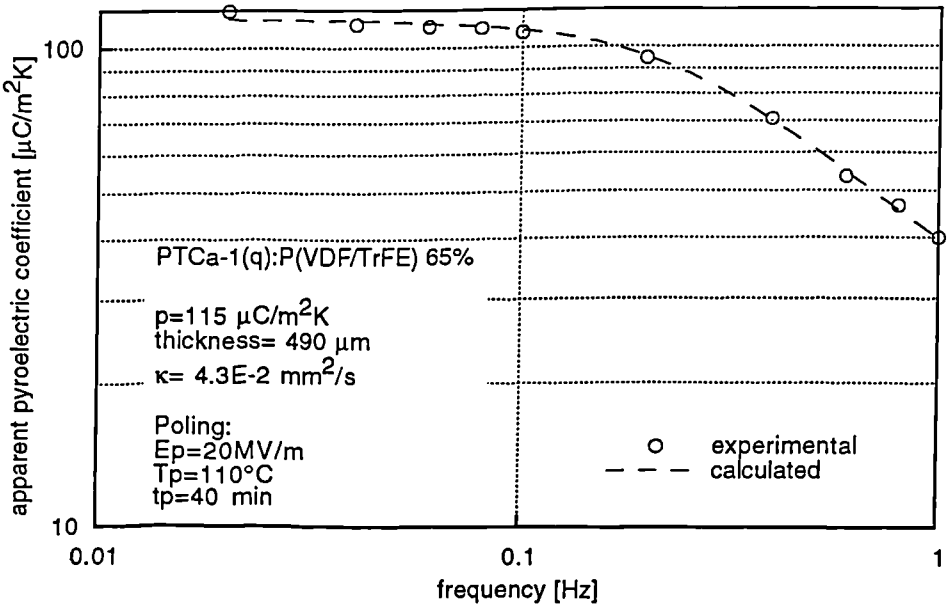

Figure 5.24 - Experimental results and calculated values for the apparent pyroelectric coefficient of a PTCa-1(q):P(VDF/TrFE) 65% composite 490μm thick.

5.4.8 - Figure Of Merit FOM_p

The experimental values of the temperature dependence of both the pyroelectric coefficient and permittivity have been used to compute the value of the pyroelectric FOM_p of PTCa-1:P(VDF/TrFE) composites as a function of temperature. In figure 5.25 this quantity is shown for composites loaded with 65, 50 and 30% of quenched PTCa-1 as well as for the 50%

loaded composite with milled PTCa-1.

Two main conclusions can be drawn from the graph, i.e., (i) the milled ceramic has a much lower FOM_p than the quenched ceramic composite with the same volume fraction and that (ii) the FOM_p increases with the ceramic volume fraction although for the composites with higher ceramic loading this increase does not seem very significant.

The first point has been implicitly dealt with in section 5.4.6, concerning the pyroelectric coefficient in quenched and milled ceramic composites. In that section it was suggested that the milled ceramics due to the small grain size and way of processing could exhibit a higher permittivity, a lower polarization and higher coercivity. All these factors contribute to a lower FOM_p by decreasing the numerator and increasing the denominator in the ratio p/ε.

The increase of the FOM_p with increasing volume fraction is in general to be expected from a higher proportion of ferroelectric material incorporated in the matrix. A closer examination can, however, be performed using the mixed connectivity model.

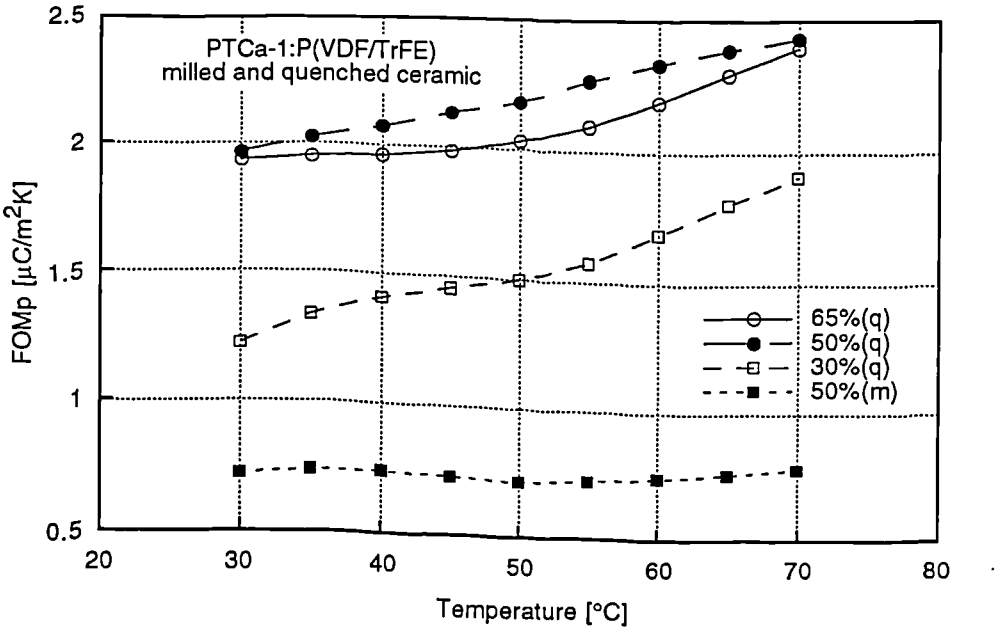

Figure 5.25 - Temperature dependence of the Figure Of Merit in PTCa-1(q):P(VDF/TrFE) composites.

The mixed connectivity charts for FOM_p should, in principle, give a location for the experimental points similar to that of the pyroelectric charts. In figure 5.26 such a chart is shown from which it can be verified that the PTCa:P(VDF/TrFE) composites according to this model cannot exhibit a higher value of the pyroelectric FOM_p than that of the ceramic which is around 1.7 $\mu C/m^2K$. It is thus not possible to locate the experimental points given in table 5.1 in such a chart so that the model does not seem to be completely correct in this respect.

In figure 5.26 we have plotted the n and m parameters determined in the pyroelectric chart of figure 5.11 in the same location in the FOM_p chart. Thus, for example for the 65% ceramic loaded composite which shows a FOM_p of 2 $\mu C/m^2K$, was expected to exhibit a FOM_p of only 1.6$\mu C/m^2K$ if it were located in the same point as in the pyroelectric chart

(figure 5.11). This is a deviation of +25% which cannot be accountable a measurement error and thus some effect must be present which has been not been included in the theory.

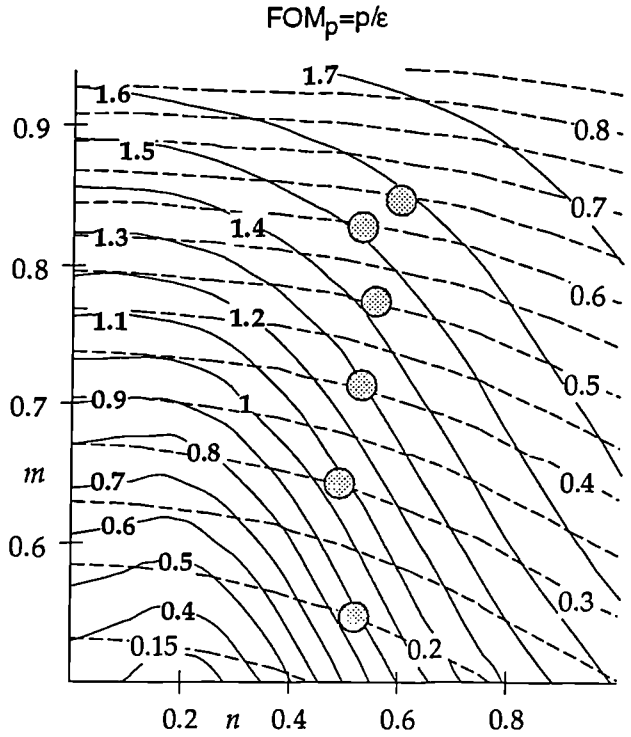

Figure 5.26 - FOM_p contour chart for the PTCa-1(q):P(VDF/TrFE) composite.

As the FOM_p is the ratio of the pyroelectric coefficient to the permittivity an under-estimation of its value implies that either the pyroelectric coefficient is being under-estimated or the permittivity is being over-estimated. At the moment it is not possible to say for certain where the error is.

Nevertheless, it should be pointed out that in the derivation of the pyroelectric coefficient in the composites it was not taken into account the contribution of the variation in the area of the sample to the pyroelectric coefficient (see section 5.2.1). This effect has been studied by Kepler and Anderson as well as by Ward and co-workers [Kepler et al. 1978; Anderson et al. 1981; Ward et al. 1986]. If one assumes that the sample of area A and thickness l, has a remanent polarization P which corresponds to a total dipole moment M these are related through,

$$Q = PA = \frac{M}{l} \tag{5.32}$$

where Q is the charge on the electrodes. The measured pyroelectric coefficient is given by,

$$p^X = \frac{1}{A}\left(\frac{dQ}{dT}\right)_X = \frac{1}{Al}\left(\frac{dM}{dT}\right)_X - \frac{M}{Al^2}\left(\frac{dl}{dT}\right)_X \tag{5.33}$$

so that if we define,

$$p_d^X = \frac{1}{Al}\left(\frac{dM}{dT}\right)_X \quad \text{and} \quad \alpha_3 = \frac{1}{l}\left(\frac{dl}{dT}\right)_X \tag{5.34}$$

we obtain for the measured pyroelectric coefficient p^X, at constant stress

$$p^X = p_d^X - \alpha_3 P \tag{5.31}$$

in which the first term p_d^X of the right hand-side, identifies the part of the pyroelectric response which arises from a change in the total dipole moment of the sample (i.e., as that which would arise from a temperature dependent amplitude of vibration of the dipoles or a change in crystallinity) and is identified with the dipolar contribution and is thus the sum of the primary pyroelectric coefficient and the piezoelectric contribution. This term usually has a negative value as the total dipole density tends to decrease with an increasing temperature. It is this part of the pyroelectric coefficient response which is estimated in the mixed connectivity model.

The last term of equation 5.31 relates to the contribution to pyroelectricity due to a change in area of sample with temperature. Dividing both members of equation 5.31 by the permittivity we get,

$$\left(FOM_p\right)_{\text{measured}} = \left(FOM_p\right)_{\text{dipolar}} - \frac{\alpha_3 P}{\varepsilon} \qquad (5.32)$$

The last term of the right hand-side of equation 5.32 can be estimated for a PTCa-1(q):P(VDF/TrFE) 65% composite if we assume that the polarization of the sample is equal to 0.15C/m^2 (see chapter 4), ε=67 and $\alpha_3 \approx 10^{-4}$ K^{-1} so that $\alpha_3 P/\varepsilon \approx 0.23$ μC/m^{2}K. This value has to be subtracted from the FOM_p calculated using the mixed connectivity model to obtain a correct estimation of the experimental value of the FOM_p. It should be noted first that the algebraic value of the calculated FOM_p in the mixed connectivity model has a negative value so that the corrected calculated figure is then -(1.6+0.23)=-1.83 μC/m^{2}K.

The modulus of the calculated value for the FOM_p is now closer in agreement to the experimental value of 1.94 μC/m^{2}K. Furthermore and perhaps more important, the present argument allows the composite to exhibit higher FOM_p values than that of the ceramic via the contribution from a change of area of the sample to the pyroelectric coefficient.

The next step in the prediction of the pyroelectric coefficient and FOM_p can thus be the inclusion of this change of area effect through the measurement of the values for the remanent polarization and linear expansion coefficients in the composites.

Finally, it is acknowledged that the cube representation of the composite is a crude analogue of the composite and thus only the approximate properties can be evaluated. Perhaps, more information on the morphology of the composite should be incorporated into a composite model to make it a more exact model.

5.4.9 - Poling frequency

As pointed out in chapter 4, the field applied to the composite film is not uniform across the thickness of the film (see section 4.3.1). The worst situation in terms of the field applied on the ceramic is that of a two layer ceramic/polymer structure. In that case the field in ceramic is given by equation 4.5 from which it was concluded that at frequencies lower than f_l the field on the ceramic is low because it is determined by the resistivity ratio of the two phases whilst for frequencies higher than f_h it depends on the ratio of the permittivities.

There is a frequency transition region where both ratios can affect the field across the

ceramic (see figures 4.5 and 4.6). In the case of the series branch of the mixed connectivity model of PTCa:P(VDF/TrFE) 65% *m* is approximately equal to 0.85 as found in the dielectric and pyroelectric charts. Using the properties of the constituent phases at 90°C of table 4.2 we have calculated that f_l= 2.5·10^{-4}Hz and the voltage across the ceramic is 0.15% of the total voltage while f_h=0.007 Hz and the voltage increases to 0.16% of the total voltage which for a field of 25MV/m represents a field of 4 MV/m across the ceramic.

In order to investigate the influence of the frequency of the poling field in the pyroelectric properties of the composites a sample was first polarised with a +25 MV/m dc step voltage for one hour after which the pyroelectric coefficient was measured. Then the sample was turned round and a 0.05 Hz ac field oscillating between 0 and 25 MV was used to switch the polarization to the opposite direction. Again after one hour of poling, the field was switched off and pyroelectric measurements were performed. Then a similar procedure was undertaken for a frequency of 0.001Hz.

The pyroelectric coefficient at the various stages of the experimental procedure is plotted in figure 5.27. It is observed that although the difference is not very large, the pyroelectric coefficient is higher when the poling field frequency is 0.05 Hz and is the lowest at 0.001 Hz whilst the step voltage poling lies in between. This is in agreement with the theory put forward that the series connectivity branch would be better poled at higher frequencies where a better dielectric matching is achieved.

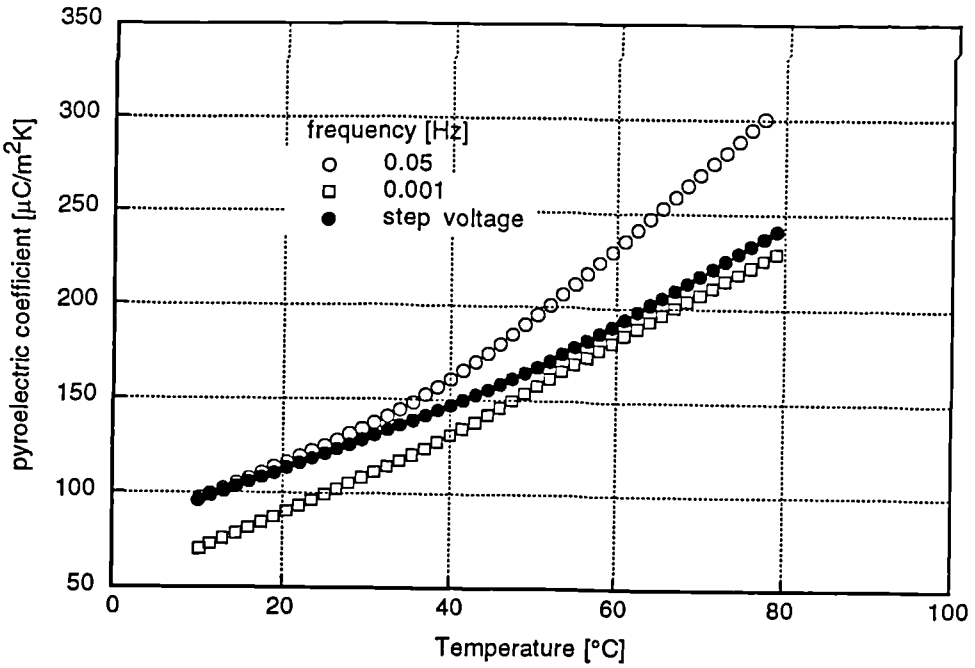

Figure 5.27 - Pyroelectric coefficient for one hour poling using two different frequencies and a DC step field of 25 MV/m. Note the linear scale of the pyroelectric coefficient.

5.5 - Summary

It has been shown in this chapter that the PTCa(q) composites and in particular those made with P(VDF)/TrFE seem to be the most suitable material for making pyroelectric detectors as they have both the highest room temperature pyroelectric coefficient and lowest

permittivity (see figure5.28). In particular the figure of merit of the PTCa(q):P(VDF/TrFE) 65% composite (p/ε=1.94μC/m^{2}K) is comparable to that of PVDF which has a high figure of merit of 2.2 μC/m^{2}K due to the very low permittivity of the polymer material. The composite however has the advantage of being easier to pole in thicker self-supporting samples, preventing thus the need for a substrate which will act as a heat sink.

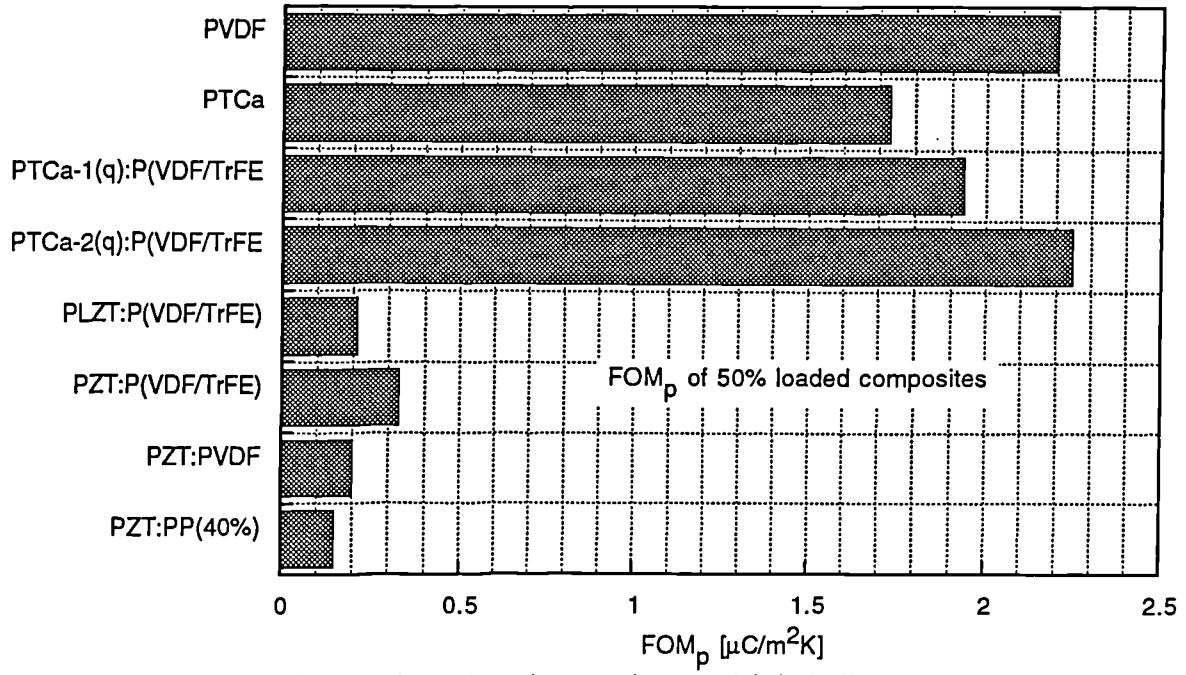

Figure 5.28 - Comparison of FOM_p for various electro-active materials including some of the composites made in the current work.

From the data measured for these composites it is possible to say that it is beneficial in pyroelectric terms that the ceramic should not have a very high permittivity. The permittivity of the composite will be consequently low, whilst the pyroelectric coefficient will be high thus improving its figure of merit. The poling may also be more efficient through the matching of the permittivity as pointed out above.

Figure 5.29 shows a comparison of the responsivity of single element pyroelectric detectors built by a commercial organisation. In these detectors, some of the composites prepared in the current work were used, as well as some competitive materials for pyroelectric applications such as PVDF 25 and 40 μm thick, $LiTaO_3$ and PTCa. The values of responsivity are given relative to the value of the responsivity of the $LiTaO_3$ detector.

The $LiTaO_3$ and PZT:P(VDF/TrFE) composite detectors show the highest and the lowest responsivity respectively, while the PTCa(q):P(VDF/TrFE) composites show a sensitivity which is higher than that of the PTCa ceramic. This is in agreement with their respective values of FOM_p. The only discrepancy is that of the responsivity of PVDF detectors which should exhibit a higher value due to its high FOM_p (see figure 5.28). Due to the high compliance of PVDF thin films a mounting arrangement to support the film had to be used. This caused some heat conduction through the substrate which decreased the expected value of responsivity for PVDF detectors.

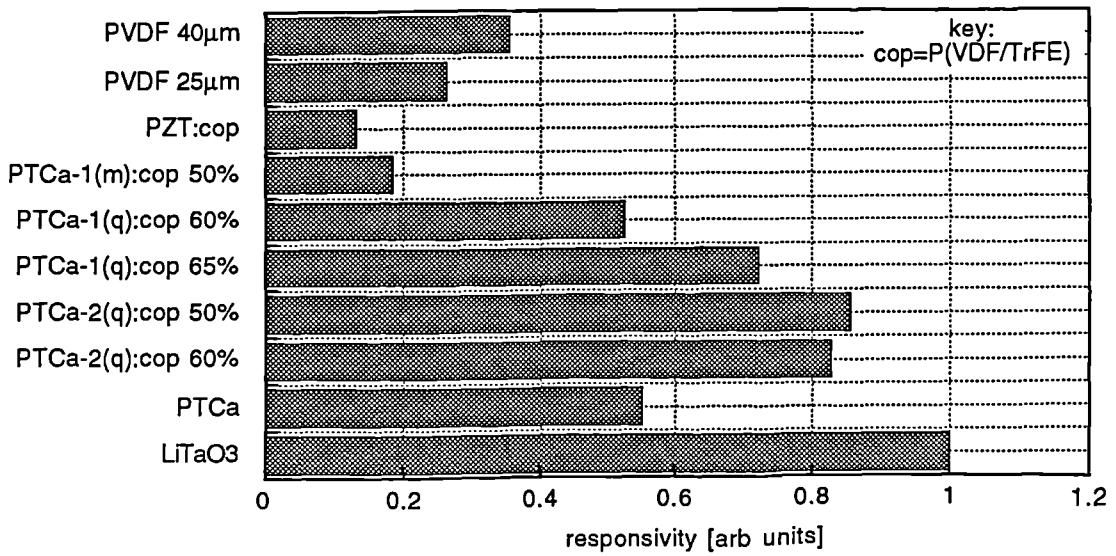

Figure 5.29 - Comparison of the sensitivity of pyroelectric single element detectors in arbitrary units.

6 - Piezoelectricity in composites and ultrasonic transducers

6.1 - Introduction and basic theory for a lossy piezoelectric resonator

In this chapter the piezoelectric properties in composites are described. These properties include the thickness mode electromechanical coupling factor k_t, the d_{33} and g_{33} piezoelectric constants and the hydrostatic piezoelectric constants d_h, g_h and the hydrostatic Figure Of Merit $FOM_h=d_h g_h$.

Properties such as the mechanical loss (tan δ_m) and the mechanical specific acoustic impedance (z_a) in composites have also been dealt with in this chapter. These latter properties are very relevant in the ferroelectric ceramic-polymer composite research for reasons which were explained in the introduction.

The theory used for analysing the piezoelectric response in the high frequency region will now be outlined. This theory has implications both on the determination of the k_t and the quality factor Q_m as well as on the design of hydrophones which work in the frequency region around the first mechanical resonance of the piezoelectric sample. When a mechanical wave characterised by a stress (X(z,t)) and a displacement velocity (U(z,t)), exists in a disk there will be a resonance when the frequency (f_o) of oscillation corresponds to a wavelength (λ_o) equal to half of the sample thickness (see figure 6.1). These quantities are related with the velocity of sound in the material v_s through,

$$\lambda_o f_o = v_s \tag{6.1}$$

so that if the thickness of the sample is l, it follows that $\lambda_o = 2l$ and,

$$f_o = \frac{v_s}{2l} \tag{6.2}$$

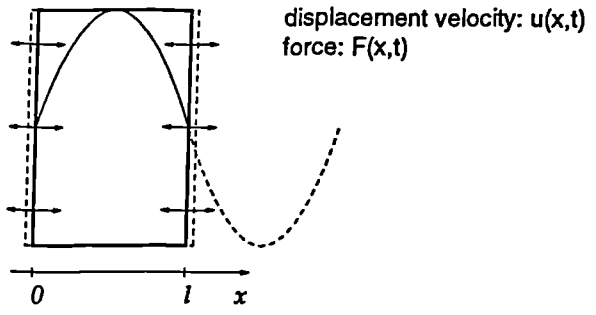

Figure 6.1 - First mechanical resonance in a piezoelectric material.

Various procedures to analyse the impedance spectra of lossy materials have been proposed, amongst others by Bui and co-workers [Bui et al. 1977], Ohigashi [Ohigashi 1976; Ohigashi 1988], Saitoh and co-workers [Saitoh et al. 1985] and Brown and Carlson [Brown et al. 1989]. Our analysis of a lossy piezoelectric material will follow those of Bui et al and of Ohigashi.

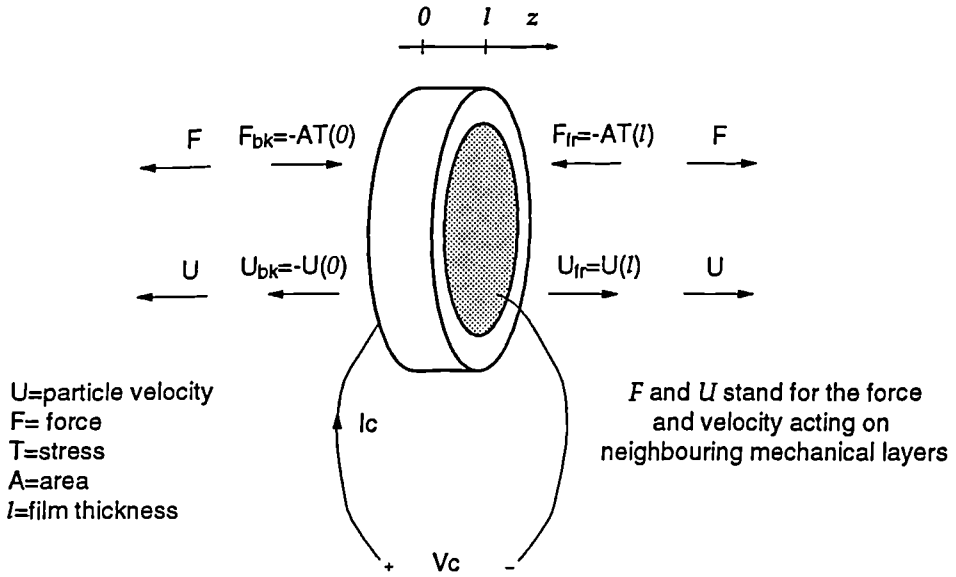

Figure 6.2 - Piezoelectric sample as a free resonator

Assuming that the lateral dimensions of a sample of area A are large compared to its thickness l, a one-dimensional analysis can be made. For the high frequencies which we are interested in, the piezoelectric sample is laterally clamped because the wavelength of the mechanical wave is assumed to be much shorter than the lateral dimensions of the sample and is of the order of the thickness of the sample.

The constitutive equations, in the 3-direction, relating the stress X, strain x, electric displacement D and electric field E then can be written as,

$$X = c^E x - eE \tag{6.3}$$

$$D = \varepsilon_0 \varepsilon^x E + ex \tag{6.4}$$

Figure 6.2 shows the one-dimensional resonator together with its associated electrical and mechanical variables. A special mention should be made in relation to the force variable at the piezoelectric boundaries. According to Newton's third law, the force acting on one side of the piezoelectric resonator has the same value and the opposite direction as that acting on the contiguous medium. It should be noted that a positive stress is extensional while a negative one is compressional and thus, the force on the front face, for example, has the opposite sign of that of the stress X at that boundary. The boundary conditions can now be written as,

$$F_{fr} = -AX(l) \tag{6.5}$$

$$F_{bk} = -AX(0) \tag{6.6}$$

$$U_{fr} = U(l) \tag{6.7}$$

$$U_{bk} = -U(0) \tag{6.8}$$

The total current through the transducers is,

$$I_c = i\omega AD \tag{6.9}$$

We assume that the electrical wavelength is much larger than that of the thickness of the sample so that in a first approximation D is uniform in the thickness direction (i.e. $\partial D/\partial z = 0$). The voltage across the transducer is,.

$$V_c = \int_0^l E dz \tag{6.10}$$

The acoustic equations describing the mechanical wave in the sample are the following:

$$\frac{\partial X}{\partial z} = \rho \frac{\partial U}{\partial t} \tag{6.11}$$

$$\frac{\partial U}{\partial z} = \frac{\partial x}{\partial t} \tag{6.12}$$

We assume that each of the relevant quantities namely the stress $X(z,t)$, strain $x(z,t)$ and particle velocity $U(z,t)$ are a product of two functions: a z-function i.e. $X_z(z)$, $x_z(z)$, and $U_z(z)$ and an oscillatory time function exp(iωt), so that the equations 6.9 and 6.10 simplify to

$$\frac{dX_z}{dz} = i\omega\rho U_z \tag{6.13}$$

$$\frac{dU_z}{dz} = i\omega x_z \tag{6.14}$$

while in equations 6.3 to 6.8 the variables X, x, and U should be understood to involve only the z-function of these variables. As the electrical quantities do not change with z, the symbols D, E and V represent just the amplitude of these quantities in the material.

We include the internal acoustic and dielectric losses in the constitutive equations 6.3 and 6.4. The acoustic losses can be accounted for by adding a term to equation 6.3 as,

$$X_z = \left(c^E + i\omega\eta\right)x_z - eE \tag{6.15}$$

where $i\omega\eta x$ [Bui et al. 1977; Ravinet et al. 1980] represents the acoustic damping which increases proportionally with the frequency. Multiplying both members of equation 6.14 by η we find that,

$$i\omega\eta x_z = \eta \frac{dU_z}{dz} \tag{6.16}$$

from which it may be concluded that the acoustic loss is proportional to the gradient of particle velocity inside the material.

The dielectric loss can be included in the constitutive equations by equating the dielectric constant to

$$\varepsilon^x = \varepsilon'^x\left(1 - i\tan\delta_e\right) \tag{6.17}$$

where ε'^x is the real part of the dielectric constant and $\tan\delta_e$ represents the dielectric losses.

From equation 6.4 we express E in terms of D and x and substitute the result into 6.15 to obtain,

$$X_z = \left(c^D + i\omega\eta\right)x_z - hD \tag{6.18}$$

where h is the piezoelectric constant related to the piezoelectric constant e by,

$$h = \frac{e}{\varepsilon_o \varepsilon'^x} \tag{6.19}$$

and c^D is the short-circuit elastic coefficient related to the open-circuit elastic constant c^E through,

$$c^D = c^E + eh \tag{6.20}$$

We now define the "effective" elastic constant of the material as $\alpha^2 c^D$ so that equation 6.18 becomes,

$$X_z = \alpha^2 c^D x_z - hD \tag{6.21}$$

where α is given by,

$$\alpha = \sqrt{1 + i\psi\frac{f}{f_o}} \tag{6.22}$$

f is the frequency, f_0 is the resonance frequency and ψ is related to η through

$$\psi = 2\pi f_o \frac{\eta}{c^D} \tag{6.23}$$

The "effective" elastic constant of the material at the resonance frequency f_0 reduces to,

$$\alpha^2 c^D_{f=f_o} = c^D(1 + i\psi) \tag{6.24}$$

so that ψ represents the mechanical loss of the material at the resonance frequency.

Solving equation 6.21 in order to x_Z and substituting in the acoustic equation 6.12 we obtain after differentiating with respect to z,

$$\frac{d^2U_z}{dz^2} = -\gamma^2 U_z \tag{6.25}$$

where γ is given by,

$$\gamma = \frac{1}{\alpha}\frac{\omega}{v_s} \tag{6.26}$$

v_S is the sound velocity of equation 6.1 which equals

$$v_s = \sqrt{\frac{\rho}{c^D}} \tag{6.27}$$

Equation 6.25 is a differential equation called the wave-equation whose general solution is given by,

$$U_z = A\cos(\gamma z) + B\sin(\gamma z) \tag{6.28}$$

This represents a linear combination of two waves one travelling in the positive and the other in the negative 3-direction. This point is more clearly acknowledged if the general solution of equation 6.28 is expressed in the alternative form,

$$U_z = U_z^+ + U_z^- = Ae^{-i\gamma z} + Be^{i\gamma z} \tag{6.29}$$

where it can be noted that γ represents the complex wave number of the oscillatory solution. This wave number γ at the frequency f_o and for values of $\psi<<1$ is given by,

$$\gamma \approx \frac{\omega}{v_s}\left(1 - i\frac{\psi}{2}\right) \tag{6.30}$$

which if substituted in equation 6.28 gives for the positive travelling wave,

$$U_z^+ = Ae^{-i\frac{\omega}{v_s}\left(1-i\frac{\psi}{2}\right)z} = \left(Ae^{-\frac{\omega}{v_s}\frac{\psi}{2}z}\right)e^{-i\frac{\omega}{v_s}z} \tag{6.31}$$

where it can be appreciated that it consists of an oscillating wave whose amplitude decays exponentially as it travels along the positive direction of the material. A similar argument applies to the negative travelling wave provided that attention is given to the sign convention. An attenuation constant α_a is then defined as,

$$\alpha_a = \frac{\omega}{v_s}\frac{\psi}{2} \tag{6.32}$$

while the acoustic quality factor Q_m is the ratio of the lossless wave number i.e. $\beta_a = \omega/v_s$ to twice the attenuation constant α_a [Bui et al. 1977; Ohigashi 1988],

$$Q_m = \frac{\beta_a}{2\alpha_a} = \frac{1}{\psi} \tag{6.33}$$

Using the boundary conditions of equations 6.7 and 6.8 the particle velocity in the sample is found to be,

$$U_z = \frac{U_{fr}\sin\gamma z - U_{bk}\sin\gamma(l-z)}{\sin\gamma l} \tag{6.34}$$

which using equation 6.14 enables the calculation of x_Z.

$$x_z = -\frac{i\sin\gamma(l-z)}{\alpha v_s \sin(\gamma l)}U_{fr} - \frac{i\cos\gamma(l-z)}{\alpha v_s \sin(\gamma l)}U_{bk} \tag{6.35}$$

Using x_Z, the voltage across the sample can be calculated from equations 6.10, 6.9 and 6.4 as,

$$V_c = \frac{ih}{\omega}U_{fr} + \frac{ih}{\omega}U_{bk} + \frac{1}{i\omega C_s} \tag{6.36}$$

where C_S is the capacitance of the sample (i.e. $C_s = \varepsilon^x \varepsilon_o A/l = \varepsilon'^x(1 - i\tan\delta_e)\varepsilon_o A/l$).

The force at the front and at back, F_{fr} and F_{bk} respectively, can now be calculated from equations 6.35, 6.21 and 6.4 together with the boundary conditions 6.5 and 6.6 , in terms of U_{fr}, U_{bk} and I_C.

The characterisation of the acoustic resonator as a three-port network is performed by expressing the two acoustic port variables F_{fr} and F_{bk} and the electrical voltage V_C in terms of U_{fr}, U_{bk} and I_C. The electroacoustic properties of the piezoelectric transducer can then be described by the following 3X3 matrix:

$$\begin{bmatrix} F_{bk} \\ F_{fr} \\ V_c \end{bmatrix} = \begin{bmatrix} \dfrac{iZ_a}{\tan\left(\dfrac{\pi f}{\alpha f_o}\right)} & \dfrac{iZ_a}{\sin\left(\dfrac{\pi f}{\alpha f_o}\right)} & -\dfrac{ih}{\omega} \\ \dfrac{iZ_a}{\sin\left(\dfrac{\pi f}{\alpha f_o}\right)} & \dfrac{iZ_a}{\tan\left(\dfrac{\pi f}{\alpha f_o}\right)} & -\dfrac{ih}{\omega} \\ \dfrac{ih}{\omega} & \dfrac{ih}{\omega} & \dfrac{1}{i\omega C_s} \end{bmatrix} \begin{bmatrix} U_{bk} \\ U_{fr} \\ I_c \end{bmatrix} \tag{6.37}$$

where Z_a is the acoustic impedance of the piezoelectric material given by,

$$Z_a = A\rho v_s \alpha = Az_a \alpha \tag{6.38}$$

where z_a is the specific acoustic impedance equal to ρv_S. In deducing the matrix equation 6.37 use was made of the equality

$$\gamma l = \frac{\pi f}{\alpha f_o} \tag{6.39}$$

This, so-called, impedance matrix of equation 6.37 will be the basis for the determination of the electromechanical coupling factor k_t as well as of the modelling and the simulation of ultrasonic hydrophones in the megahertz range.

It should be pointed out that this impedance matrix is formally identical to that of a lossless piezoelectric resonator apart from the factor α. When the sample has no loss α is equal to one (see equation 6.22) and the matrix reduces to that of the lossless case.

6.2 - Measurements techniques

6.2.1 - k_t measurement technique

The determination of the piezoelectric properties such as the electromechanical coupling factor k_t can be achieved from the measurement of the electrical impedance of a sample vibrating as a free resonator. This involves the measurement of the electrical impedance of a piezoelectric material standing free in air in the frequency range around the first resonance peak f_0.

With the piezoelectric sample standing free in air we can assume that the forces acting on its faces are close to zero, i.e. $F_{fr} \approx F_{bk} \approx 0$. If this assumption is substituted in the impedance equation 6.37 it can be shown that the electrical impedance Z of a piezoelectric sample resonating in its thickness mode is equal to a sum of two terms: the electric impedance $Z_C(\omega)$ of the sample capacitance and an acoustic term $Z_{ac}(\omega)$ [Ohigashi 1988].

$$\frac{V_c}{I_c} = Z = Z_c(\omega) + Z_{ac}(\omega) = \frac{1}{i\omega C_s} + i\frac{2}{Z_a}\left(\frac{h}{\omega}\right)^2 \tan\left(\frac{1}{2}\frac{\pi f}{\alpha f_o}\right) \tag{6.40}$$

The experimentally determined impedance can thus be fitted by this equation to yield values of the piezoelectric constant h, mechanical loss ψ, resonant frequency f_0 and capacitance of the material C_S which optimise that fitting.

The equation 6.40 is not in the proper form to ensure an easy fitting process because the characteristics of the real part of resonance peak such as its height and width are controlled by a combination of the above parameters. As an example, the piezoelectric constant h does not determine the peak height nor does ψ determine its width.

The value of the real part of the acoustic impedance $\mathrm{Re}(Z_{ac})=R_{max}$ at resonance can be shown to be related to the piezoelectric constant h through,

$$h^2 = 2\pi^2 R_{\max} A z_a f_o^2 \tanh\left(\frac{1}{4}\pi\psi\right) \tag{6.41}$$

where it was assumed that the value of ψ is small. The piezoelectric constant h is related to k_t through [Ohigashi 1988],

$$k_t^2 = \frac{h^2 \varepsilon'^x}{c^D} \tag{6.42}$$

Substituting equation 6.41 into equation 6.40 we obtain

$$Z = \frac{1}{i\omega C_s} + \frac{iR_{\max}}{\alpha}\left(\frac{f_o}{f}\right)^2 \tanh\left(\frac{1}{4}\pi\psi\right)\tanh\left(\frac{\pi}{2\alpha}\frac{f}{f_o}\right) \tag{6.43}$$

The electrical impedance due to the capacitance $C_s = C(1 - i\tan\delta_e)$ of a lossy sample which is represented by the first term of equation 6.43 has both a real part and an imaginary part,

$$Z_c = -\frac{i}{\left(1+\tan\delta_e{}^2\right)\omega C} + \frac{\tan\delta_e}{\left(1+\tan\delta_e{}^2\right)\omega C} \overset{\tan\delta_e<<1}{\approx} -\frac{i}{\omega C} + \frac{\tan\delta_e}{\omega C} \tag{6.44}$$

where C is the real part of the capacitance of the sample and tan δ_e is the dielectric loss. The first and the imaginary term of the electrical impedance represents the capacitance of the sample while the second and resistive term accounts for the dielectric losses.

In order to account for a dielectric dispersion in the wide frequency range where the impedance measurements are made, and as well for a possible series resistance R at high frequencies, a modified but similar expression as that of equation 6.44 has been used to model the electrical impedance $Z_C(\omega)$, i.e.,

$$Z_c = R + \frac{A}{f^a} - i\frac{B}{f^b} \tag{6.45}$$

where A, B, a, b and R are adjustable parameters. The whole expression for the impedance can now be expressed thus,

$$Z = R + \frac{A}{f^a} - i\frac{B}{f^b} + \frac{iR_{\max}}{\alpha}\left(\frac{f_o}{f}\right)^2 \tanh\left(\frac{1}{4}\pi\psi\right)\tan\left(\frac{\pi}{2\alpha}\frac{f}{f_o}\right) \tag{6.46}$$

Upon measuring the real and imaginary parts of the impedance, the real part is fitted first with the above equation 6.46 to find the optimum values of the parameters A, a, R, R_{max}, ψ and f_0. The fitting process requires a prior estimation of these parameters after which the optimisation process undertakes a finer tuning to minimise the error between the calculated and the experimental curves. A rough estimation of some of these parameters can be

performed from the plot of the logarithm of the real part of the impedance versus the logarithm of the frequency as shown in figure 6.3. The general slope and the ordinate at the origin of the curve can for example give the starting values for the parameters A and a. The resonance frequency f_0 can be estimated from the frequency where there is a peak in the real impedance while R_{max} is the amount of increase of the impedance around resonance over the general impedance curve (see figure 6.3). The resistance R can be set either to zero or to the constant value the real part of the impedance tends at high frequency (see figure 6.3). Finally, there is no simple way of estimating ψ although a safe starting value can be around 0.1.

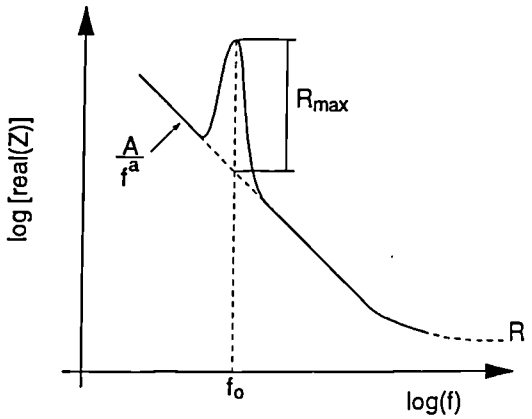

Figure 6.3 - Schematic plot of the real part of the impedance of a free resonating piezoelectric.

The imaginary part of the impedance is then fitted by using the values for R_{max}, ψ and f_0 obtained from the real part fitting, in order to find the optimum values for B and b whose starting values can be estimated in the same way as the parameters A and a.

If the thickness l and area A of the sample are known and if we estimate the density of the composite to be

$$\rho = \phi^c \rho^c + \phi^p \rho^p \tag{6.47}$$

various other quantities besides those found in the fitting procedure can be calculated. These include the velocity of sound $v_s = 2f_o l$, the specific acoustic impedance $z_a = \rho v_s$, the elastic constant $c^D = z_a v_s$ and the piezoelectric constant h (equation 6.41)

The dielectric constant (ε^x) and loss ($\tan\delta_e$) at the resonance frequency f_0 can be calculated in the following manner. We denote RZ_C and $-IZc$ as the real and imaginary parts of Z_C respectively (equation 6.44) at $f=f_0$. The dielectric loss $\tan\delta_e$ and the dielectric constant ε^x are then given by,

$$\tan\delta_e = \frac{RZc}{IZc} \tag{6.48}$$

$$\varepsilon'^x = \frac{l}{2\pi f_o \varepsilon_o A} \frac{IZc}{\left(IZc^2 + RZc^2\right)} \tag{6.49}$$

Upon calculating these quantities the electromechanical coupling factor k_t can be calculated using equation 6.42.

The electrical impedance was measured in the range from 300kHz to 50MHz using the

set-up of figure 6.4 . A network analyser model HP 8702A was used to make the impedance measurements. Prior to the measurement a calibration procedure had to be undertaken to ensure that the true impedance of the sample was measured with no contribution from the capacitance of the cables or connectors. The data collected by the network was then transferred to a computer in order to perform the mathematical computation of the piezo properties.

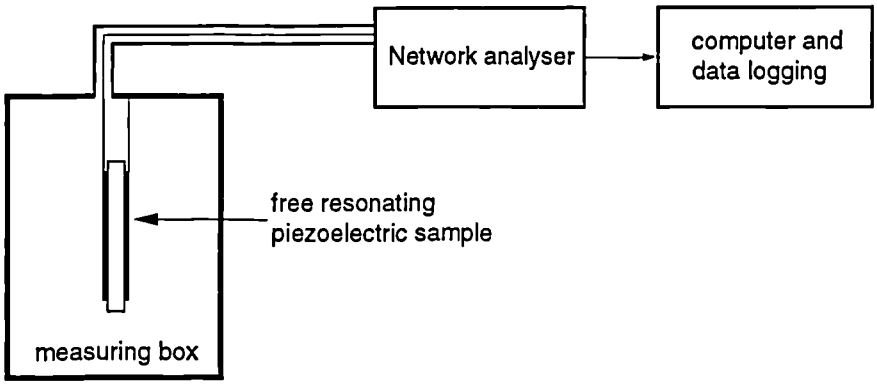

Figure 6.4 - Schematic set-up for the measurement of the electrical impedance in the megahertz range.

6.2.2 - d_h, g_h, FOM_h and d_{33} measurement techniques

The g_h and d_h hydrostatic piezo-coefficients can be measured using a low frequency acoustic method (see figure 6.5).

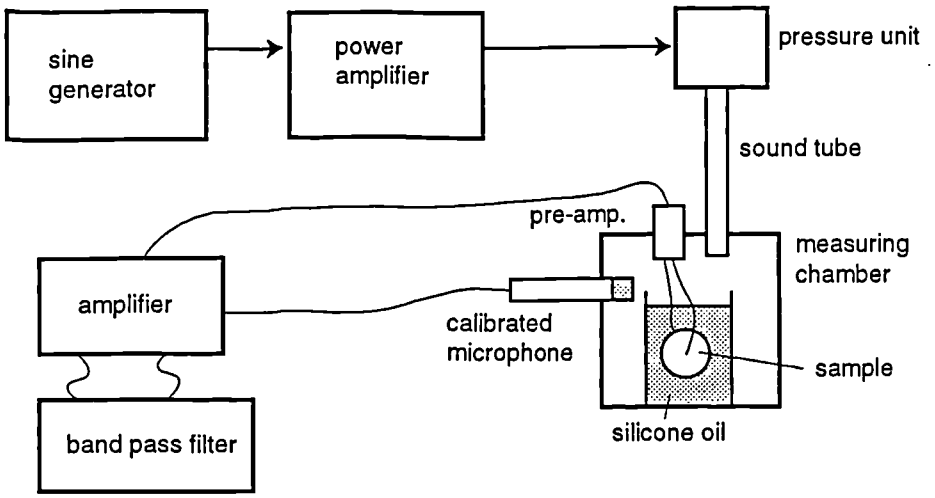

Figure 6.5 - Schematic set-up for measuring the piezoelectric g_h coefficient.

The sample is placed in a sealed box where a low-frequency (f=80 Hz) sound pressure is generated and the resulting output voltage compared with that of a calibrated microphone with a sensitivity of -39 dB re 1V/Pa (i.e. s_{mic}=11.2 mV/Pa). If the voltage output from the microphone after the band pass filter is V_{mic} and that of the sample is V_s then, the piezoelectric constant g_h is equal to,

$$g_h = s_{mic} \frac{1}{l} \frac{V_s}{V_{mic}} \tag{6.50}$$

The d_h coefficient can then be computed by multiplying the g_h constant by the constant stress

dielectric constant,

$$d_h = \varepsilon_o \varepsilon^x g_h \tag{6.51}$$

while the hydrostatic Figure Of Merit (FOM_h) is just the product $FOM_h = d_h g_h$.

The d_{33} stress coefficient was measured using a Pennebaker 8000 d_{33} tester from American Piezo Ceramics Inc.

6.3 - Literature review of composite piezoelectric properties

Good review papers have been published on the piezoelectric composites for ultrasonic applications by Gururaja [Gururaja et al. 1985], Smith [Smith 1989] and Ting [Ting 1990]. Here we will review some of the results reported for 0-3 composites.

PZT- epoxy composites are amongst the earliest reported composites for piezoelectric applications [Pauer 1973; Chilton 1991], and by Furukawa and co-workers [Furukawa et al. 1979] who prepared films 200μm in thickness, using ceramic grains with the diameter range between 0.2 and 2 μm up to a volume loading of 23%. Figure 6.6 shows the piezoelectric stress coefficient d_{31} as a function of the poling field. Using the Furukawa model, described in section 2.3 it was found that the experimental d-constants were about 3/4 of the predicted values which lead to the conclusion that the composites were imperfectly poled.

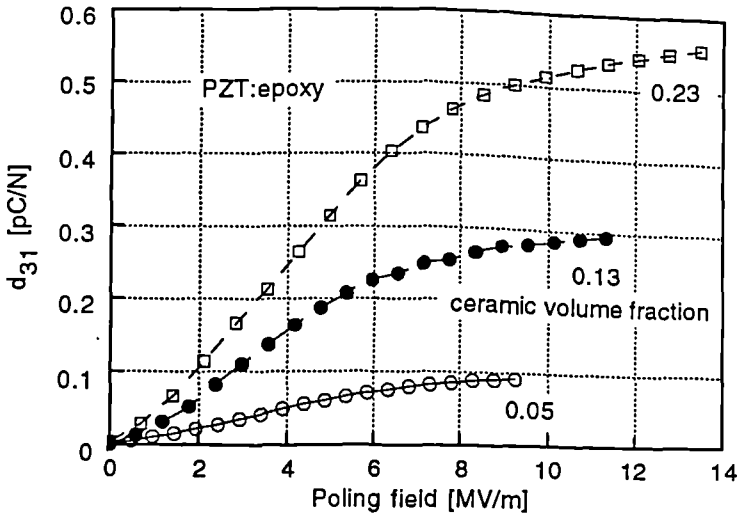

Figure 6.6 - Poling characteristics of PZT-epoxy composites [Furukawa et al. 1976].

Pardo and co-workers [Pardo et al. 1988] have also reported on these composites in which the grain size to thickness ratio (w_{gs}/l)was varied from 0.5 to 3.8. They found that a mixed connectivity composite was obtained if the grain size employed was comparable to the sample thickness regardless of the volume fraction of the ceramic. The d_{33} coefficient was found to be higher for the greatest ceramic volume fraction and grain to thickness ratio used (i.e ϕ^c=43% and w_{gs}/l=3.44) and equal to 165 pC/N whilst the g_{33} coefficient was maximum at a lower volume fraction of 27% and w_{gs}/l ratio of 0.8. Espinosa et al. [Espinosa et al. 1986] have reported on a manufacturing procedure which consists in multi-fracturing a commercial piezo-ceramic plate by using different techniques and then pouring a plastic phase between the ceramic elements with the result that the mechanical losses were

increased whilst the sensitivity based on the electromechanical coupling factor (around 50-60%) was similar to that of 1-3 composites with the advantage of being easier to fabricate.

A series of 0-3 type composites called Piezo-Rubbers (PR-303/PR-307) have been more recently developed by NTK Technical Ceramics Division of the NGK Spark Plugs Corporation in Japan which consist essentially of fine lead titanate particles dispersed in a chloroprene polymer matrix and whose main characteristic was that high $d_h g_h$ products in the range of $1\text{-}5 \cdot 10^{-12}$ Pa^{-1} were achieved and good transmitter/receiver pulse responses were obtained without ringing [Banno et al. 1983; Gururaja et al. 1986; Banno et al. 1987].

A new method of preparing 3-3 connectivity composites was reported by Gururaja [Gururaja et al. 1986] which consisted of preparing a ceramic ($PbTiO_3$) using a co-precipitation method, and then forming pellets using a PVA binder which was burnt out during a firing operation. The voids were subsequently filled with an epoxy to form the composites whose ceramic loading was around 70%. The composites were poled both conventionally and by the corona method which provided similar results. The piezoelectric hydrostatic FOM_h was $1.75 \cdot 10^{-12}$ Pa^{-1} whilst the electromechanical coupling factor was 8%.A measurement of the 002 and 200 x-ray diffraction peaks before and after poling showed an apparent saturation of the poling.

A more uniform composite was claimed to have been prepared by Han and co-workers [Han et al. 1990; Han et al. 1991] using a colloidal processing. for the production of composites of $(Pb_{0.5},Bi_{0.5})$ $(Ti_{0.5},(Fe_{1-x}Mn_x)_{0.5})$ O_3 (x=0.00 to 0.02) in an epoxy matrix so that a poling field equal to 15 MV/m was possible to be sustained without breakdown of the sample. The values of the piezoelectric coefficients d_{33}, d_h and g_h were as high as 65, 41 pC/N and 145 mV·m/N respectively and thus the $d_h g_h$ product equalled $5.95 \cdot 10^{-12}$ Pa^{-1}.

Calcium modified Lead Titanate composites in an epoxy matrix have been extensively studied by Pardo [Pardo et al. 1989], Chilton [Chilton et al. 1990], Garner [Garner et al. 1989] and Shaulov [Shaulov et al. 1989]. Pardo has reported on the dependence of the piezoelectric activity on the grain size of the ceramic particles relative to the thickness of the sample where he found that similar to the PZT ceramic composite case, a higher grain size to thickness ratio was beneficial to its properties. Garner and co-workers [Garner et al. 1989] reported on the effect of obtaining the ceramic powders through two different routes namely by ball-milling and quenching with the result that the quenched material was found to perform better. Investigations into the appropriate volume loading showed that 50% was a good compromise when optimising the $d_h g_h$ product. The piezoelectric constants d_h, g_h and $d_h g_h$, obtained using a poling field of 20 MV/m was 22.5 pC/N, 80mV·m/N and $1.8 \cdot 10^{-12}$ Pa^{-1} respectively. Shaulov et al [Shaulov et al. 1989], have also reported good results on a 1-3 composite made of the same ceramic and two different polymer hosts, one being stiffer (Stycast epoxy $s_{11}= 108 \cdot 10^{-12}$ Pa^{-1}) than the other (Spurrs epoxy $s_{11}= 332 \cdot 10^{-12}$ Pa^{-1}). Better piezo-properties were obtained for the composite using the stiffer host where d_h, g_h and the $d_h g_h$ product were equal to 32 pC/N, 66 mV·m/N and $2.1 \cdot 10^{-12}$ Pa^{-1} respectively.

A practical way of preparing a piezoelectric paint has been reported by Hanner and co-

workers [Hanner et al. 1989]. Two polymers, an acrylic and a polyurethane were utilised in their study and loaded with 60-70% of PZT or co-precipitated Lead Titanate (PT) ceramic. Both polyurethane and the acrylic polymer were dissolved in a suitable dispersing agent to which the powder was then added. The films were prepared by casting the mixtures onto brass plates and cured in a vacuum oven. Air dry silver paint was used as an electrode for the final dry films while the brass plate acted as the second electrode, for the composite thickness in the range of 200-500 μm. Composites of the combination of PT and acrylic gave the best results in terms of their piezoelectric properties while the lowest value was that of the PZT/polyurethane composite. The piezoelectric properties of the PT-acrylic composite d_h, g_h and the $d_h g_h$ product were equal to 32 pC/N, 67 mV·m/N and $2.15 \cdot 10^{-12}$ Pa^{-1} respectively.

Ferroelectric polymers such as PVDF and its copolymer P(VDF/TrFE) have also been used to make composites. Their main features, apart of being pyro and piezoelectric, are their high dielectric constant due to their polar nature and high stiffness relative to other thermoplastics. The composites, loaded with PZT up to 21% [Furukawa et al. 1979], were obtained through the hot-rolling technique and pressed to 200μm in thickness and gold evaporated on both sides. The properties of poling at 120°C for 30 minutes was studied for the dependence of the electric field (figure 6.7) which shows that a poor piezoelectric activity is obtained probably due to the insufficient poling field together with a low ceramic loading. It is clear that with the low poling fields applied, it is not possible to orient the polymer phase whose coercive field is in excess of 80 MV/m.

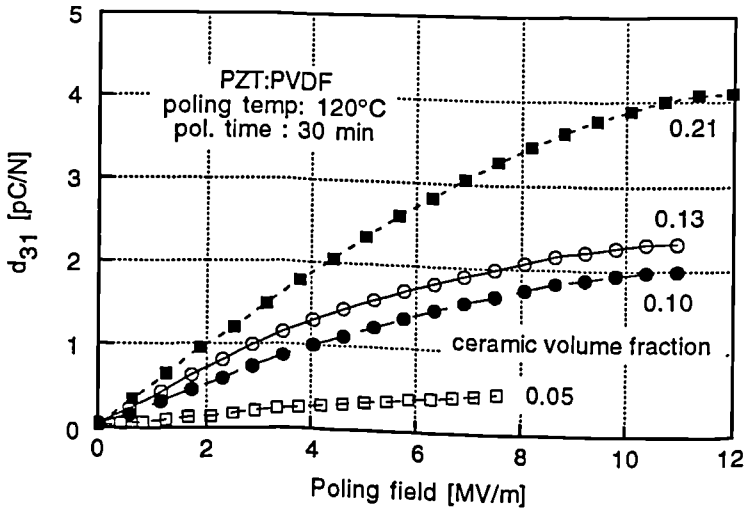

Figure 6.7 - Poling behaviour of a PZT-PVDF composite.[Furukawa et al. 1979].

Yamada [Yamada et al. 1982] have also reported on PZT-PVDF composites with concentrations of ceramic up to 70%. The dependence of the dielectric constant and the piezoelectric constant d_{33} on the PZT volume fraction is shown in figure 6.8 in which the simulated curves are those obtained according to equations 2.1 and 2.2 where the parameter η used in the calculation equals 8.5 representing a ceramic elongated ellipsoid particle with its long axis arranged perpendicular to the surface of the film (see discussion of the Yamada model in chapter 2.2).

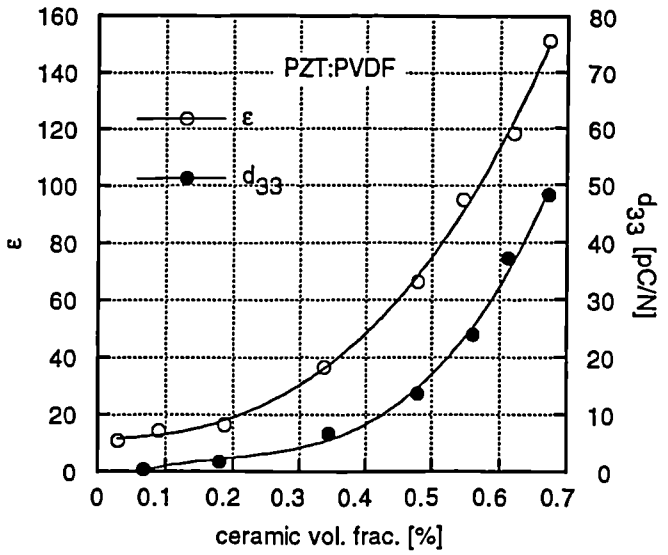

Figure 6.8 - Dependence of the dielectric piezoelectric constants on the PZT volume fraction [Yamada et al. 1982].

The ceramic particle dependence has also been investigated by Lee et al [Lee et al. 1990] with a Barium Titanate-phenolic resin composite. The ceramic particles size range was 2-130μm while the ceramic volume fraction was kept constant at 60%. They were able to explain the experimental results based on the existence of a surface layer on the $BaTiO_3$ grains [Merz 1956] approximately, 1.59 μm thick, whose dimensions become significant for the smaller grains of the ceramic and whose characteristics are their low dielectric constant (around 105) and non-ferroelectric behaviour. This effect disappeared when the ceramic grains were larger than 100 μm. It was pointed out, however, that the thickness and properties of the surface layer may depend on the previous processing of the ceramic powders.

PT-P(VDF/TrFE) composites were investigated by Ngoma et al [Ngoma et al. 1990]. They found that the ceramic inclusions do not modify the nature of copolymer crystalline phase with respect to its dielectric and the DSC behaviour. Due to the low fields applied, which were in the range of 9 MV/m, they also found that a poor piezoelectric activity was present in these composites.

Poling studies have been evaluated by changing the poling conditions and measuring the resulting piezoelectric properties and XRD diffractograms on a composite of 70% volume fraction co-precipitated PT in a gel polymer (Eccogel 1365-0) [Waller et al. 1988] In these studies, which used ceramic grains in the 12-1100 nm size range, a saturation of poling was found for poling fields of 8 MV/m at 85 °C and 15 min of poling where a remanent polarisation of 0.13-0.14 C/m^2 was measured while the coercive field was about 0.6 MV/m. It should be pointed, however, that a saturation of poling does not imply 100% poling of the ceramic but rather that a plateau in the target property has been reached such that increasing the poling field, time or temperature any further, does not lead to an improvement in that property. Measurements of the properties against the grain size showed a sharp increase of the piezoelectric constant d_{33} for grain sizes larger than 20 μm which was ascribed to a transition from single domain to multi-domain behaviour for ceramic grains larger than

200μm.

The piezoelectric properties of the composites reviewed in this section have been listed in table 6.1.

TABLE 6.1 - PIEZOELECTRIC PROPERTIES OF SOME OF THE COMPOSITES REVIEWED

material	vol. fraction [%]	host	k_t	Q_m	z_a MRayl	d_{33} pC/N	d_h pC/N	$d_h g_h$ pPa^{-1}	Ref.
PZT	57	epoxy				140			[1]
PZT	50-90	araldite	0.6-0.5	5-9	15-26				[2]
PT	?	rubber					17-44	1-5	[3]
PT	70	epoxy	0.08				25	1.8	[4]
$(Pb,Bi)TiO_3$	35	epoxy					41	6.0	[5]
PTCa	50	epoxy					22	1.8	[6]
PTCa	55	epoxy				45			[7]
PTCa	25	Stycast					32	2.1	[8]
PT coprec.	70	acrylic					32	2.2	[9]
PZT	67	PVDF				48			[10]
PTCa	30	P(VDF/TrFE)				25			[11]

References: [1] - [Pardo et al. 1988]; [2] - [Espinosa et al. 1986]; [3] - [Banno et al. 1987]; [4] - [Gururaja et al. 1986]; [5] - [Han et al. 1991]; [6] - [Garner et al. 1989]; [7] - [Pardo et al. 1989]; [8] - [Shaulov et al. 1989]; [9] - [Hanner et al. 1989]; [10] - [Yamada et al. 1982];[11] - [Ngoma et al. 1990]

6.4 - Piezoelectric properties of composites (current work)

Measurements of the electromechanical coupling factor were performed by the resonance method whilst the hydrostatic measurements were performed using the set-up of figure 6.5. The measurements of the piezoelectric coefficients were always done at room temperature and pressure.

These piezoelectric properties, determined at room temperature and pressure are strictly valid in the frequency region around the resonant frequency of the sample. Regarding the ageing of the composites with temperature, measurements were done on annealed samples at 90°C for over 12 hours and the results showed that at least in the PTCa composites the polarization does not exhibit a decay phenomenon. This latter observation further indicates that although the host polymer is of a ferroelectric nature it behaves in this composite as a passive carrier of the electroactive (i.e. ceramic) material.

Figure 6.9 shows a plot of the impedance measurements made on a PTCa-2(q):P(VDF/TrFE) 50% composite. The experimental curves were fitted with equation

6.45 as described in section 6.2. Using the relevant parameters from this graph a k_t value of 0.19 was found which provided a good agreement between the experimental values and the theoretical curve (equation 6.49). When the value of the electromechanical coupling factor is small i.e. $k_t \leq 0.1$, however, the resonance feature in the impedance curve is no longer prominent and a larger uncertainty will exist regarding the exact value of the k_t and mechanical loss ψ.

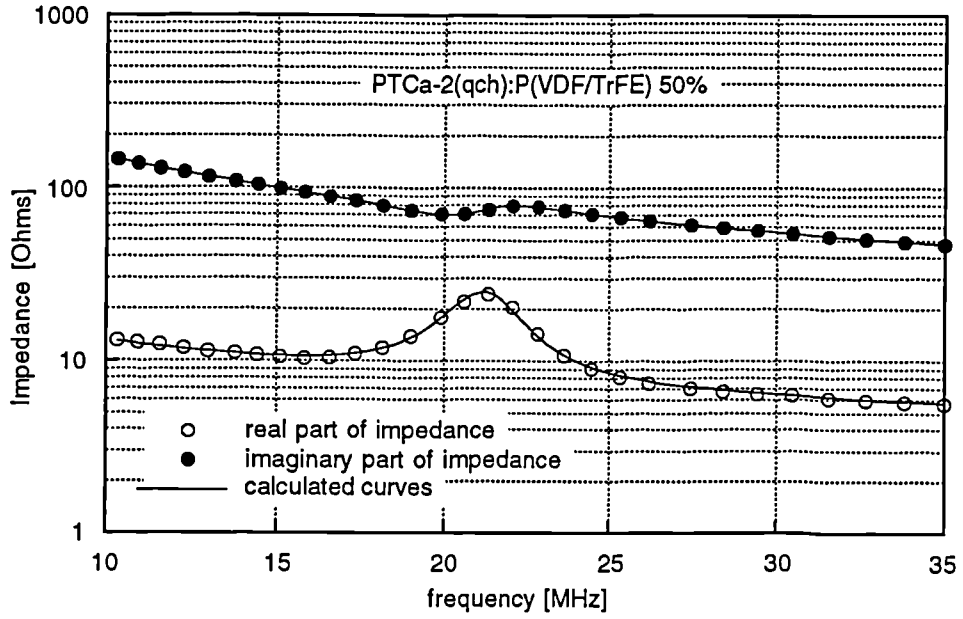

Figure 6.9 - Plot of the experimental impedance of a 50% PTCa-P(VDF/TrFE) composite together with the fitted theoretical curves to its real and imaginary parts using equation 6.46.

Table 6.2 gives a list of the piezoelectric properties found for the composites. These properties include the electromechanical coupling factor (k_t), the quality factor (Q_m), the specific acoustic impedance (z_a) the velocity of sound (v_s), the elastic constant (c^D)and the piezoelectric constant h. We have listed in the same table the properties of PTCa PZT5A PVDF and P(VDF/TrFE).

No results for the PZT-P(VDF/TrFE) composite regarding its electromechanical coupling factor and its related properties were reported as it was not possible to detect any resonance peak in the impedance spectra in any of its polarised samples. This fact together with the low d_h and FOM_h coefficients which will be reported later leads us to suggest that this material has a low piezoelectric activity.

From the table 6.2 it can be appreciated that the PTCa-1(q) and PTCa-2(q) composites exhibit comparable electromechanical coupling factors, the largest being that for the PTCa-1(q):P(VDF/TrFE) 65% composite, where a value of 0.24 is observed. In this composite, however the acoustic impedance is also the largest i.e., 16.5 MRayl.

TABLE 6.2 - PIEZOELECTRIC PROPERTIES OF SELECTED MATERIALS

electroact. material	vol. fraction [%]	host	k_t	Q_m	z_a MRayl	ε @ 1MHz	ρ kg/m^3	v_s km/s	c^D GPa	h GV/m	Ref
PVDF			0.20	10	4.0	6.2	1780	2.26	9.1	-2.6	
P(VDF/TrFE)			0.30	20	4.5	5.3	1.880	2.4	11	-4.7	[1]
PTCa-2(q)	50	P(VDF/TrFE)	0.19	7.9	12.5	30	4400	2.9	36	2.2	
PTCa-2(q)	60	P(VDF/TrFE)	0.18	5.1	15.2	31	4900	3.1	48	2.3	
PTCa-2(q)	65	P(VDF/TrFE)	0.21	6.2	13.5	39	5100	2.6	35	2.1	
PTCa-2(q c.)	50	P(VDF/TrFE)	0.12	6	11.8	19	4400	2.7	32	1.6	
PTCa-2(q f.)	50	P(VDF/TrFE)	0.06	6.7	9.6	19	4400	2.2	21	0.7	
PTCa-1(q)	20	P(VDF/TrFE)	0.11	2.4	9.0	12	2900	3.1	29	1.8	
PTCa-1(q)	30	P(VDF/TrFE)	0.13	2.3	11	17	3400	3.3	37	2.1	
PTCa-1(q)	40	P(VDF/TrFE)	0.14	3.7	11	19	3900	2.8	31	1.8	
PTCa-1(q)	50	P(VDF/TrFE)	0.09	4.1	13.8	25	4400	3.1	44	1.3	
PTCa-1(q)	60	P(VDF/TrFE)	0.11	7.4	14	37	4900	2.9	41	1.3	
PTCa-1(q)	65	P(VDF/TrFE)	0.24	4.3	16.5	43	5100	3.2	53	2.8	
PTCa-1(m)	60	P(VDF/TrFE)	0.06	12	14.7	39	4900				
PTCa			0.47	1200	30		6890	4.35	183	6.6	[2]
PZT5A			0.48	75	34		7500	4.35	147	2.1	[2]

References: [1] - [Ohigashi 1988]; [2] - [Matroc 1992];

In figure 6.10 is shown a mixed connectivity chart for the electromechanical coupling factor for a PTCa-1(q):P(VDF/TrFE) composite where the experimental points have also been plotted. The determination of the location of the points was achieved through a similar procedure as that used for the dielectric constant chart. The *n* parameter which measures the degree of 1-3 connectivity in the mixed connectivity cube model found for the different loadings of this composite lies between 0.2 and 0.35. This is a lower range of values when compared with those obtained for the dielectric constant (see figure 4.23) and pyroelectric coefficient (see figure 5.11) charts. The reason for this discrepancy could be the following. A 0-3 composite is composed of piezoelectric ceramic grains embedded in a polymer matrix. The resonance frequency as was explained before, in equation 6.1 depends on the thickness of the piezoelectric material and thus, in the present case, on the size of the ceramic grain. If a distribution in the size of the ceramic grains exists in the composite they will start resonating at slightly different frequencies and as a consequence, a broad and low resonant peak will be obtained which lowers both the mechanical quality and the electromechanical coupling factors. In the calculation of the electromechanical coupling factor using the mixed connectivity cube model the wave nature of the sound was not taken into account and thus the model estimation should be more appropriate in the low-frequency region where the wavelength of the sound wave is much larger than the thickness of the sample.

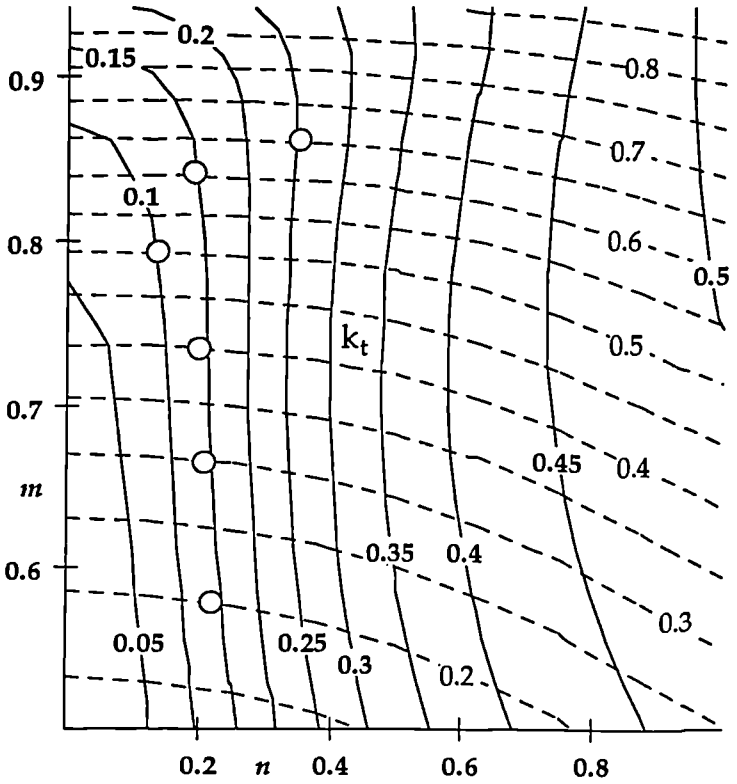

Figure 6.10 - Electromechanical coupling factor chart for the PTCa-1(q):P(VDF/TrFE) composite using the mixed connectivity cube model.

Regarding these composites a low mechanical quality factor was observed. The quantity has a low value between 5.5 and 8 both because of a distribution of ceramic grain size as explained above and probably also due to the very dispersive nature of the composite media in which the ceramic grains act as scatters leading to an attenuation of sound waves. There is no clear dependence of this property either on the volume fraction or on the size of the grains. One should use some caution as the thickness variation which is about 5%, could also lead to a smoothing of the resonant peak which in turn, would artificially decrease the estimated quality factor.

The acoustic impedance of these composites seems to follow roughly the Reuss model [Pelmore 1979], which assumes a constant stress throughout the solid like a series connectivity composite, giving in the case of the PTCa-1 composite a value of 12.5 MRayl at 60% volume fraction. This model has been used before with some success on the prediction of the acoustic impedance of other composites [Grewe et al. 1990]. The acoustic impedance increases from 14.2 to 16.5 MRayl in the case of the quenched PTCa-1(q) composite when the ceramic volume fraction rises from 60 to 65%, which is reasonable when one considers that the ceramic has a higher acoustic impedance than the polymer.

In table 6.3 are listed the hydrostatic and 3-direction piezoelectric d and g constants of the composites fabricated.

TABLE 6.3 - PIEZOELECTRIC CONSTANTS d, g AND FOM$_h$ FOR THE COMPOSITES FABRICATED

electroact. material	vol. fraction [%]	host	ε @ 1 kHz	d_{33} pC/N	g_{33} mV·m/N	d_h pC/N	g_h mV·m/N	$d_h g_h$ pPa^{-1}	Ref.
PVDF			8	-33	-482	-10	-148	1.5	
P(VDF/TrFE)			12	-34	-478	-13	-180	2.3	[1]
PZT5A	40	PP	13	20	174				
PZT	50	PVDF	63	20	34	3.1	3.1	0.03	
PZT	50	P(VDF/TrFE)	118	22	21	30*	39*	0.12*	
PLZT	50	P(VDF/TrFE)	80	21	30	13	19	0.23	
PTCa-2(q)	50	P(VDF/TrFE)	40	35	99	21	42	0.86	
PTCa-2(q)	60	P(VDF/TrFE)	49	50	115	28	49	1.36	
PTCa-2(q)	65	P(VDF/TrFE)	51	43	95	35	57	2.01	
PTCa-2(q c.)	50	P(VDF/TrFE)	36	27	84	8.5	27	0.23	
PTCa-2(q f.)	50	P(VDF/TrFE)	37	25	76	8.1	24	0.19	
PTCa-1(q)	20	P(VDF/TrFE)	21	30	161				
PTCa-1(q)	30	P(VDF/TrFE)	28	31	125				
PTCa-1(q)	40	P(VDF/TrFE)	34	35	116				
PTCa-1(q)	50	P(VDF/TrFE)	40	43	121				
PTCa-1(q)	60	P(VDF/TrFE)	49	46	106	12	18	0.22	
PTCa-1(q)	65	P(VDF/TrFE)	67	48	81	28	45	1.26	
PTCa-1(m)	50	P(VDF/TrFE)	56	31	62	9.4	18	0.17	
PTCa-1(m)	60	P(VDF/TrFE)	66	21	36	8.5	13	0.11	
PTCa			230	68	33	62	33	2.1	[2]
PZT5A			1860	374	25	32	2.2	0.07	[3]

References: [1] - [Ohigashi 1988]; [2] - [Matroc 1992]; [3] - [Matroc 1992]

From the table 6.3 it can be appreciated that the PTCa-1(q) and PTCa-2(q) composites show a better agreement with previous results of electro-active properties than those of the PZT and PLZT composites. This is also true from the comparison between the quenched and milled ceramic composites of PTCa-1. We thus believe that the arguments for the explanation of the pyroelectric properties in these composites can also be applied to a certain extent in the case of this piezoelectric properties, namely, the grain size and the dielectric matching effects.

Figure 6.11 shows the behaviour of the d_{33} as function of the volume fraction of the ceramic in the PTCa-1(q):P(VDF/TrFE) composite. As expected there is a monotonic increase in its value as the ceramic content increases. In figure 6.12 is shown a d_{33} mixed connectivity chart for the same PTCa-1(q):P(VDF/TrFE) composite. The values of the n-parameter which are in the range of 0.3 and 0.5 seem to be more in accordance with those values obtained for

the dielectric and pyroelectric coefficient charts obtained before than those of the k_t.

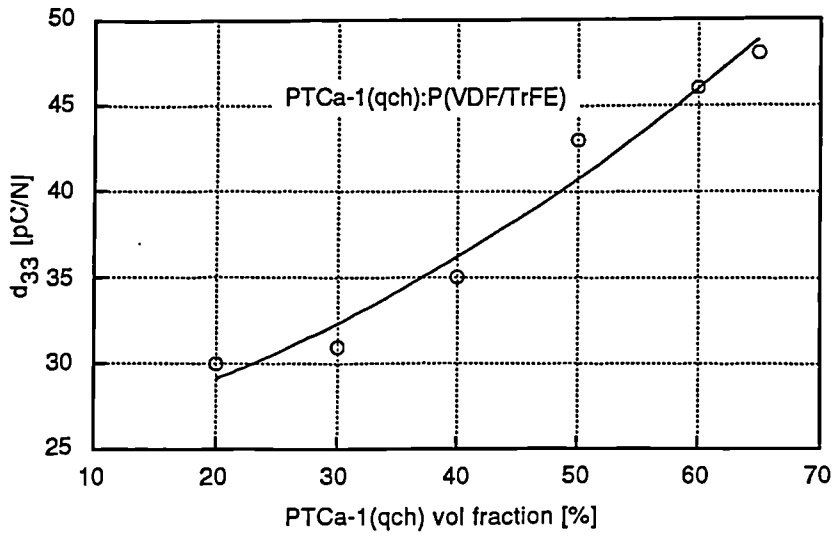

Figure 6.11 - Piezoelectric d_{33} constant as a function of the volume fraction of the ceramic in the PTCa-1(q):P(VDF/TrFE) composite

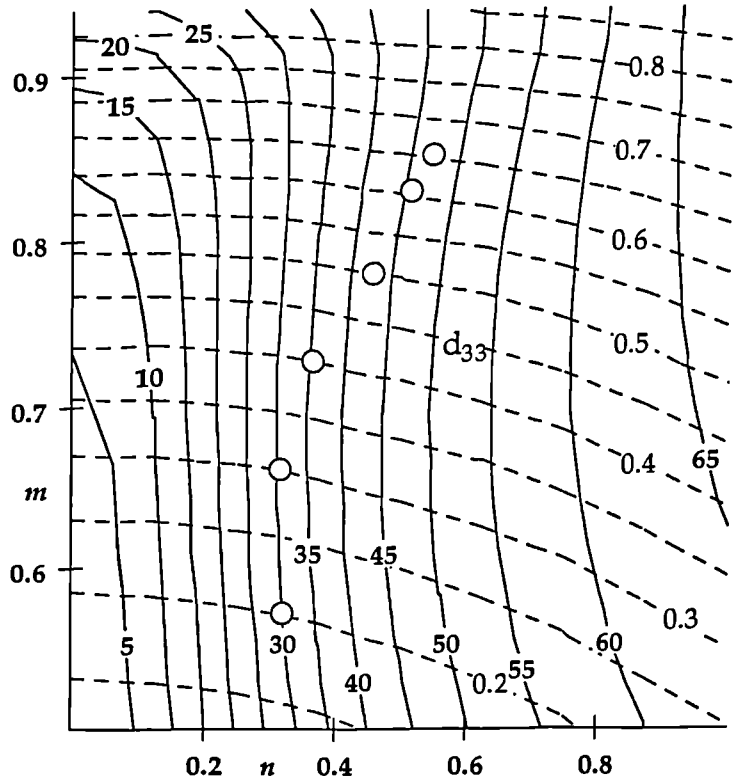

Figure 6.12 - Piezoelectric d_{33} constant chart for the PTCa-1(q):P(VDF/TrFE) composite.

In figure 6.13 is shown the poling field characteristics of the quenched PTCa-1(q):P(VDF/TrFE) 65%composite for the d_{33} coefficient. An alternating poling field with 0.05 Hz frequency with a variable amplitude was applied to the sample and the d_{33} was measured after a complete poling cycle. Although an indication of a saturation seems to appear for poling field amplitudes approaching 25 MV/m, it is not certain what the saturation polarization is in this experiment as the maximum electrical breakdown strength of the composite did not allow for higher values of the field. However, for a polarisation method which involved applying a step field of 25 MV/m during one hour we found a value

of d_{33}=55pC/N which can thus be estimated to be the saturation value for this property using this poling field.

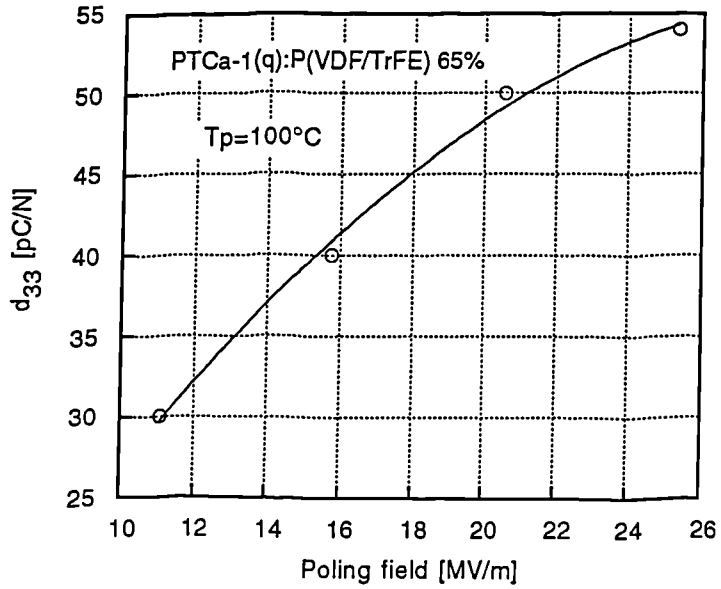

Figure 6.13 - Poling field characteristics of the PTCa-P(VDF/TrFE) composite

The hydrostatic properties of these composites listed in table 6.3 are directly related to the ceramic materials properties from which they are produced. In this respect the PTCa ceramic has a much higher g_h than the PZT ceramic and this is in agreement with experimentally observed value of g_h for the PTCa composite which is greater than that of the PZT composite. Composites with ceramic volume fraction increasing from 60 to 65% produced twice as much increase in the g_h value, the exact reason for this excessive increase is yet to be determined. However, it is suggested that as the g_h is equal to $g_{33}+2g_{31}$ it is possible that g_{33} increases with the volume fraction, while g_{31} due to the ceramic grains connectivity does not increase proportionately causing g_h to increase much more than in the case of an homogeneous ceramic material. In relation to the piezoelectric Figure Of Merit ($FOMh = dh\,g_h$) the same type of argument seems to apply. This is even more so because when the volume fraction of the ceramic increases, the dielectric constant of the composite also rises, causing the FOM_h also to rise through an increase of the hydrostatic charge coefficient d_h ($= \varepsilon\varepsilon_0 g_h$).

6.5 - Ultrasonic transducers

6.5.1 - Theory: ABCD matrices approach

In order to simulate the behaviour of the thickness mode ultrasonic transducers various types of analysis have been proposed which can be conveniently classified either as frequency or time domain methods. The frequency domain analysis is the older type of approach and was first formulated by Mason [Mason 1942]. The Mason model consists of an electrical analogue which behaves in the frequency domain as the piezoelectric transducer. In his model the electrical analogue has three ports: two of them mechanical in origin,

representing the front and the back face of the transducer and one electrical port where the voltage is either applied as in a transmitter or measured as in a receiver.

In a transmitter the voltage applied to the sample generates a sound wave which propagates in the material much like in an electrical transmission line, part of it travelling backwards and the other forward. At the interfaces part of the sound wave is transmitted into the nearby medium whilst the rest is reflected back into the sample in a proportion that depends on the acoustic impedance of the interfacing media. The travelling of the wave inside the material goes on until all the sound wave energy is transmitted out of the sample. There is an additional way for the sound wave to lose its energy which is by generating heat due to the acoustic losses. This process was not accounted for in the work of Mason and will be dealt with in the section.

Other models improving or modifying the Mason model, have been proposed which include the widely used KLM model [Krimholtz et al. 1970] while a more systematic approach, more suitable for the simulation of acousto-electric systems has been proposed by Sittig [Sittig 1967; Sittig 1969; Sittig 1971]. This latter approach is based in the so-called ABCD matrices which will be undertaken here.

The time domain methods have been proposed more recently and these include a systems approach based on the z-transform proposed by Hayward [Hayward et al. 1984] and the simulation on a computer of the time behaviour of ultrasonic transducers using a SPICE program [Morris et al. 1986].

The ABCD matrices are commonly applicable to two-port networks and are based on the following idea. We relate the input voltage and current V_{in} and I_{in} respectively to the output voltage and current V_2 and I_2, of two port network, in the following matrix form,

$$\begin{bmatrix} V_{in} \\ I_{in} \end{bmatrix} = \begin{bmatrix} A_1 & B_1 \\ C_1 & D_1 \end{bmatrix} \begin{bmatrix} V_2 \\ I_2 \end{bmatrix} \tag{6.52}$$

Thus, if another two port network whose output voltage and current are V_{out} and I_{out} is cascaded with the previous one, we have,

$$\begin{bmatrix} V_2 \\ I_2 \end{bmatrix} = \begin{bmatrix} A_2 & B_2 \\ C_2 & D_2 \end{bmatrix} \begin{bmatrix} V_{out} \\ I_{out} \end{bmatrix} \tag{6.53}$$

so that if this equation for V_2 and I_2 is substituted in equation 6. we obtain

$$\begin{bmatrix} V_{in} \\ I_{in} \end{bmatrix} = \begin{bmatrix} A_1 & B_1 \\ C_1 & D_1 \end{bmatrix} \begin{bmatrix} A_2 & B_2 \\ C_2 & D_2 \end{bmatrix} \begin{bmatrix} V_{out} \\ I_{out} \end{bmatrix} = \begin{bmatrix} A & B \\ C & D \end{bmatrix} \begin{bmatrix} V_{out} \\ I_{out} \end{bmatrix}$$

relating the input to the output quantities. Thus, a cascade of two-port electrical networks is simply translated into a product of matrices.

Table 6.4 gives a list of ABCD matrices of various types of electrical circuits namely for an impedance Z in series, an admittance Y in parallel and a lossy transmission line.

TABLE 6.4 - ABCD MATRIX ELEMENTS FOR SOME BASIC TWO-PORT PASSIVE ELECTRICAL NETWORKS

description	port 1(input) port 2(output)	A	B	C	D
series element	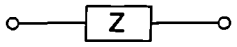	1	Z	0	1
shunt element	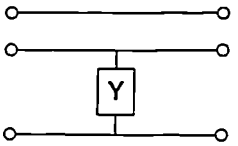	1	0	Y	1
lossy transmission line	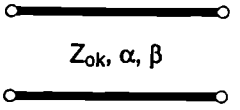 γ = iα+β (complex wave number)	cos(γl)	i Zok sin(γl)	i sin(γl)/Zok	cos(γl)

Once all the matrices have been defined and multiplied to obtain the overall ABCD matrix various quantities can be calculated assuming that the load impedance to the circuit is Z_l (i.e. $V_{out} = Z_l I_{out}$).

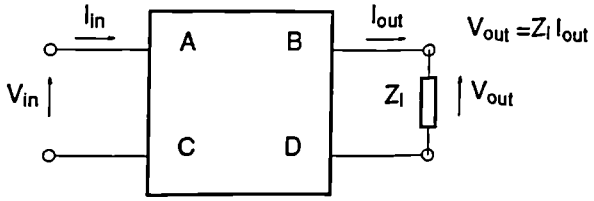

The ratio of the output voltage to the input voltage $Vout/Vin$ usually called the transfer function of the system $T(\omega)$ is given by,

$$T(\omega) = \frac{V_{out}}{V_{in}} = \frac{Z_l}{B + AZ_l} \tag{6.54}$$

The input impedance of the circuit V_{in}/I_{in},

$$Z_{in} = \frac{V_{in}}{I_{in}} = \frac{B + AZ_l}{D + CZ_l} \tag{6.55}$$

and the ratio of the power output to the power input P_{out}/Pin is,

$$\frac{P_{out}}{P_{in}} = \frac{V_{out} I_{out}}{V_{in} I_{in}} = \frac{Z_l}{BD + (BC + AD)Z_l + ACZ_l^2} \tag{6.56}$$

It should be pointed out that for a passive network which means a network which has no input of energy other that through its input port the determinant of the ABCD matrix is equal to unity. This is the case of the ABCD matrices listed in table 6.4 and will also be the case for the piezoelectric ABCD matrix. In the latter case although a conversion of energy exists from electrical to acoustic form and vice-versa there is no production of energy in the material. In this case of a passive network, it can be shown that if we were to reverse the circuit described by an ABCD matrix so that the input port would now be the output port

the new reversed ABCD matrix would read as,

$$\begin{bmatrix} V_{in} \\ I_{in} \end{bmatrix} = \begin{bmatrix} D & B \\ C & A \end{bmatrix} \begin{bmatrix} V_{out} \\ I_{out} \end{bmatrix} \tag{6.57}$$

In order to simulate the behaviour of an ultrasonic transducer we have thus to find the ABCD matrix of a lossy piezoelectric transducer acting, as say, a transmitter (the receiver matrix relates to the transmitter one through equation 6.57). It will be necessary also to find what is the ABCD matrix of a mechanical layer which is intermediate between the piezoelectric transmitter and the receiver.

Figure 6.14 shows an schematic diagram of an ultrasonic transmitter. It includes the piezoelectric material to which a voltage V_C is applied so that a current I_C flows through it. This voltage and current are generated by a voltage (or pulse) power supply with an output impedance R_{out} passing through a cascade network of impedance Z and admittance Y.

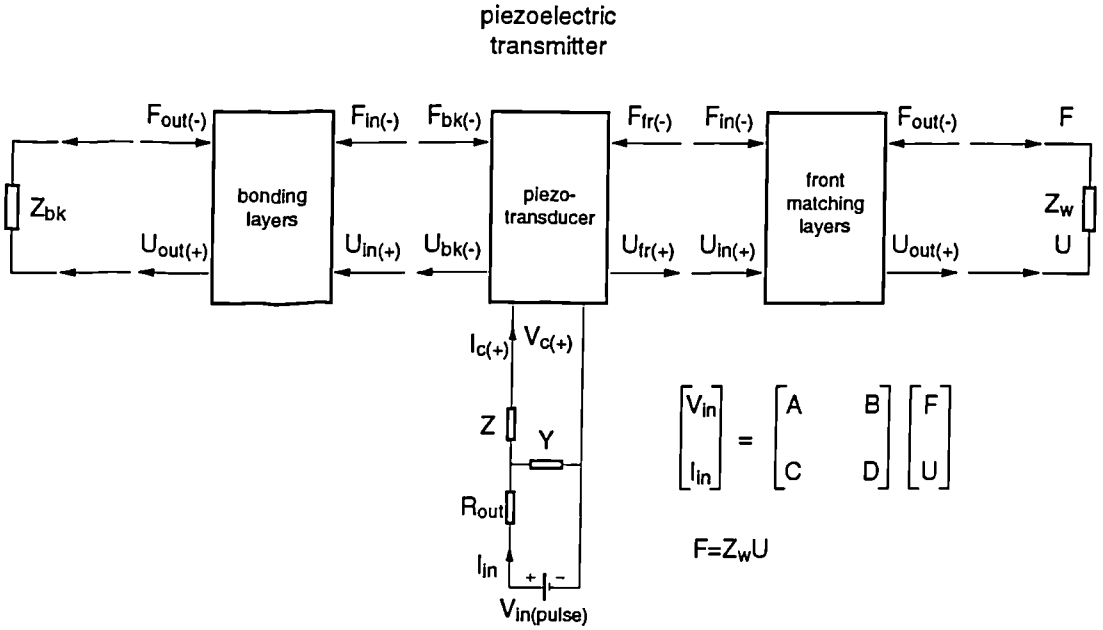

Figure 6.14 - Schematic of an ultrasonic transmitter.

At the back of the transducer we have a bonding (mechanical) layer and a backing load whose specific acoustic impedance is Z_{bk}. At the front of the transmitter there can be front matching layers to help the acoustic match between the piezoelectric impedance and that of the water into which the transducer radiates.

In order to relate the voltage V_C and current I_C to the front force F_{fr} and the particle velocity U_{fr} we can make use of equation 6.37 in the following way. Assuming that the bonding layer at the back did not exist, the relationship between the force and the velocity in the backing would be

$$F_{bk} = Az_{bk}U_{bk} = Z_{bk}U_{bk} \tag{6.58}$$

where the z_{bk} is the specific acoustic impedance of the backing and A the area of the transducer.

Substituting equation 6.58 into equation 6.37 and solving for the voltage V_C and current

I_C we obtain an equation in the ABCD form

$$\begin{bmatrix} V_c \\ I_c \end{bmatrix} = \frac{1}{\phi Q}\begin{bmatrix} 1 & i\frac{\phi^2}{\omega C_s} \\ i\omega C_s & 0 \end{bmatrix}\begin{bmatrix} \cos\gamma l + iz_b \sin\gamma l & Z_a[z_b \cos\gamma l + i\sin\gamma l] \\ \frac{i}{Z_a}\sin\gamma l & 2(\cos\gamma l - 1) + iz_b \sin\gamma l \end{bmatrix}\begin{bmatrix} F_{fr} \\ U_{fr} \end{bmatrix} \quad (6.59)$$

where ϕ is hC_S, Z_a is the acoustic impedance of the piezoelectric material given by equation 6.38 and z_b is the ratio of the acoustic impedance $z_b = Z_{bk}/Z_a$. The factor Q is equal to,

$$Q = \cos\gamma l - 1 + iz_b \sin\gamma l \quad (6.60)$$

It should now be pointed out that the *ABCD* equation 6.59 is identical to that which we obtain for a lossless piezoelectric transducer using the Mason model [Sittig 1969] the only differences being in the value of γl which is now given by (see equation 6.39)

$$\gamma l = \frac{\pi f}{\alpha f_o} \overset{\psi=0}{\approx} \frac{\pi f}{f_o} \quad (6.61)$$

which reduces to the lossless case when ψ is zero. In addition the value of the acoustic impedance Z_a which is given by equation 6.38 is now,

$$Z_a = A\alpha z_a \overset{\psi=0}{\approx} Az_a = A\rho v_s \quad (6.62)$$

which also reduces to the lossless case when there are no mechanical losses.

To find the *ABCD* matrix for a mechanical layer we have to return to the deduction of the piezoelectric equations but with no voltage or current through it (see section 6.1). If in the constitutive equation 6.3 we set *E* equal to zero while setting the boundary conditions to be (see figure 6.14 for the front matching layer),

$$F_{out} = -AX(l) \quad (6.63)$$

$$F_{in} = -AX(0) \quad (6.64)$$

$$U_{out} = U(l) \quad (6.65)$$

$$U_{in} = U(0) \quad (6.66)$$

it is possible to prove that the *ABCD* matrix equation is given by

$$\begin{bmatrix} F_{in} \\ U_{in} \end{bmatrix} = \begin{bmatrix} \cos\gamma l & iZ_a \sin\gamma l \\ \frac{i\sin\gamma l}{Z_a} & \cos\gamma l \end{bmatrix}\begin{bmatrix} F_{out} \\ U_{out} \end{bmatrix} \quad (6.67)$$

where γl and Z_a have the same meaning as for the piezoelectric equations and are given by equations 6.61 and 6.62 respectively. This *ABCD* matrix is formally equivalent to that of a lossy electrical transmission line listed in table 6.4.

When there are acoustic layers between the piezoelectric and the backing load, the impedance Z_{bk} to be used in the *ABCD* equation 6.59 has to be calculated in the following manner. The ABCD matrix of the circuit of figure 6.15 has first to be calculated using equation 6.67. The input impedance of this circuit which is equal to the effective backing

impedance $Z_{bk(eff)}$ placed at the back of the piezoelectric, can then be found using equation 6.55.

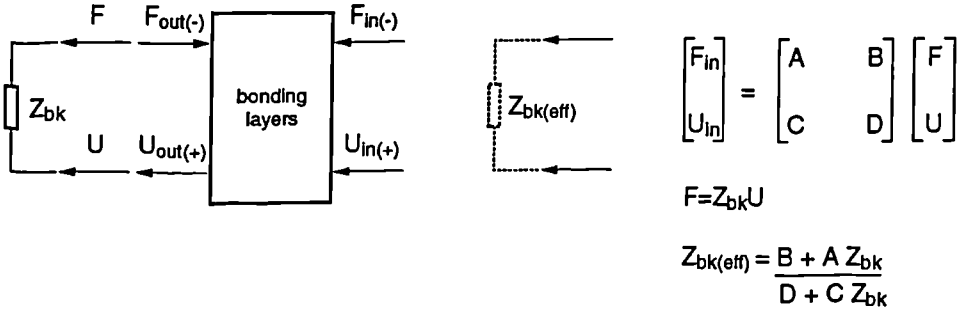

Figure 6.15 - Determination of the backing impedance to the piezoelectric transducer.

Figure 6.16 shows an ultrasonic receiver where the output voltage and current appear across the resistance of an oscilloscope R_{osc}. Here the ABCD matrix is related to the transmitter ABCD matrix through equation 6.57. In a system consisting of a transmitter and a receiver the medium (i.e. water in the hydrophone case) in-between can be regarded as a two-port network of impedance $Z_w=Az_w$ where z_w is the specific acoustic impedance of water which is equal to 1.5 MRayl.

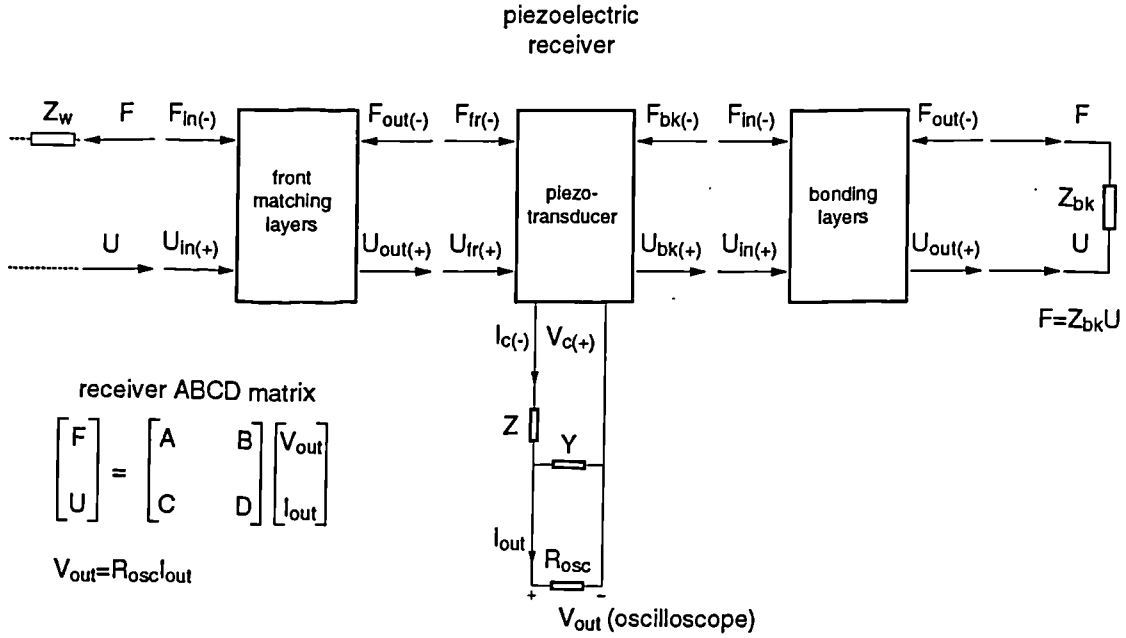

Figure 6.16 - Two-port representation for a piezoelectric receiver circuit.

This type of approach to the modelling of an ultrasonic transducer is most suitable to be carried out with a computer.

The ABCD matrix in a computer program was defined as a four column matrix where column 1 2 3 and 4 are identified with A, B, C and D elements of the matrix as shown in equation 6.68. Each row in the matrix gives the A, B, C and D values at a particular frequency, so that the number of rows is equal to the number of frequency points N for which the *ABCD* matrix is calculated.

$$\begin{bmatrix} A & B & C & D \end{bmatrix}$$
$$\begin{bmatrix} A_1 & B_1 & C_1 & D_1 \\ A_2 & B_2 & C_2 & D_2 \\ A_3 & B_3 & C_3 & D_3 \\ & & & \\ & & & \\ A_N & B_N & C_N & D_N \end{bmatrix} \qquad (6.68)$$

After determining the ABCD matrix of each element of the circuit the overall ABCD matrix is obtained by multiplying all the matrices in the appropriate order. From this matrix quantities such as the ratio of the output voltage to the input voltage V_{out}/V_{in} (equation 6.54), the input impedance of the circuit V_{in}/I_{in} (equation 6.55) and the ratio of the power output to the power input P_{out}/P_{in} (equation 6.56) can be obtained.

To find the time-response of the circuit we use the following procedure. The output voltage V_{out} is given, using equation 6.54 by,

$$V_{out} = \frac{R_{osc}}{B + R_{osc}A} V_{in} = T(f) V_{in} \qquad (6.69)$$

where all the quantities are frequency dependent.

In the context of circuit theory *Vout* and V_{in} are the Fourier transforms of the output and input voltage respectively while *T(f)* is the transfer function of the circuit. Thus, to find the time response of the circuit one has to find the Fourier transform of the input voltage, multiply it by the transfer function in the frequency domain and then perform a inverse Fourier transform to obtain the time behaviour of the output voltage.

It should be noted that for an impulse excitation of the type of a Dirac delta function $\delta(t)$, the Fourier transform of the input voltage V_{in} is equal to unity so implying that the transfer function *T(f)* is the Fourier transform of the so-called impulse response of the circuit.

Simulation of the time response

Figure 6.17 shows a simulation of the output force with time of a PZT5A 1 MHz ultrasonic transmitter. The electrical circuit to excite this transducer was assumed to be that of figure 6.18. It consists of a voltage pulse generator whose voltage peak is 300 V with a rise time of 15 ns and a decay time of 100 ns. This has been a test case which was first described by Hayward and Jackson [Hayward et al. 1984] and dealt again by Morris and Hutchens [Morris et al. 1986] to evaluate a simulation by a circuit analysis program using SPICE. The properties of the PZT5A material used in the simulation have been listed in table 6.5 while the backing material has an acoustic impedance of 9.1 MRayl. A comparison of the two simulations shows that the decay of the force in the present simulation is much faster than that of the simulations done by either of the above workers. This can be attributed to a lack of knowledge in the pulse width of excitation. The value of 100 ns pulse width is the most commonly used in the ultrasonic work while a resistance of 1.3 Ω in series with the power supply was quoted in the initial simulation of Hayward (see figure 6.18). We have simulated

the same transducer under larger pulse width of 500 ns and up to a 50Ω series resistance of the power supply and found that a better agreement could be found for these larger values of the pulse width and series resistance.

It should be noted that the output response shown in figure 6.17 is acceptable. The initial spike has the approximate form of the voltage pulse excitation while the other peaks are just the reflections of the sound wave bouncing back and forth inside the piezoelectric material. In fact the time between the die-out of the first positive peak and the onset of the first negative peak corresponds to the time the sound wave takes to travel from the back to the front face of the piezoelectric crystal which is around 0.5 μs.

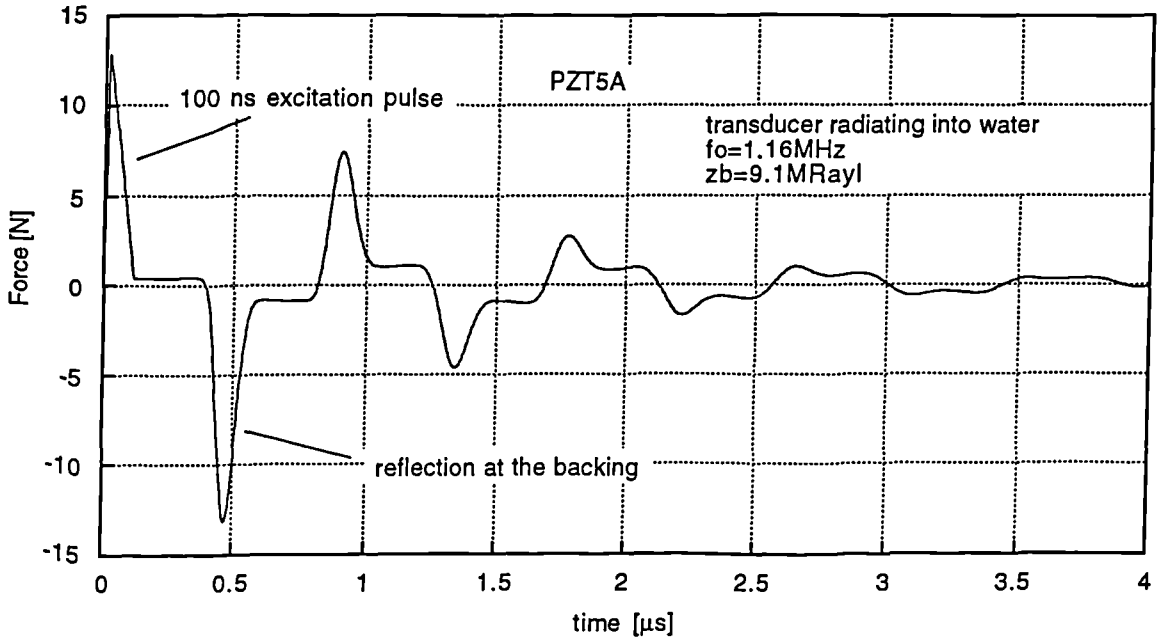

Figure 6.17 - Simulation of the time response of a PZT5A transmitter

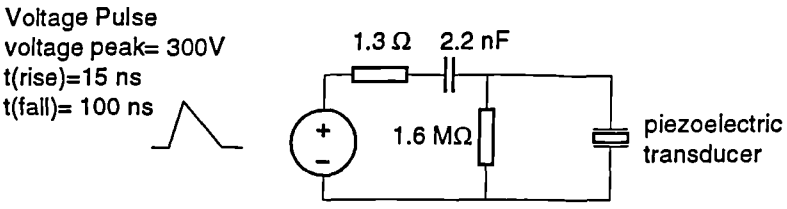

Figure 6.18 - Voltage pulse generator and electrical components assumed to be in series with the piezoelectric transmitter

TABLE 6.5 - PROPERTIES OF MATERIALS USED IN ULTRASONIC TRANSDUCERS

Material	ε^x @ 1MHz	tan δ_e @ 1MHz	k_t	Q_m	z_a MRayl	ρ kg/m^3
PZT5A	830	0.02	0.48	100	33	7750
PTCa	220	0.02	0.47	1200	30	6890
P(VDF/TrFE)	5.3	0.15	0.30	20	4.5	1880
PTCa(q):P(VDF/TrFE) 65%	43	0.10	0.24	4.3	16.5	5130

6.5.2 - Backing

Two main criteria exist in the design of ultrasonic transducers. Those are the sensitivity which should be as high as possible and the "compactness" of the time response. This latter criterion means that upon being excited with a voltage or force pulse depending on whether it is a transmitter or a receiver its response should be as short as possible in time with no "ringing". The desire for this property stems from the fact that clean signals reflected from objects are needed to achieve a high resolution image from ultrasonic probes.

With regard to this response property the backing to the piezoelectric material plays perhaps the most important role in the design of a transducer. When the backing of the transducer has the same impedance as that of the piezoelectric material, all the sound wave will propagate into the backing with no reflection at the interface. As a result only two pulses should be measured for a properly backed transducer: one resulting from the expansion of the front face and the other representing a contraction.

In figure 6.19 shows the simulation for the force output of transducers made from PZT5A, PTCa, P(VDF/TrFE) and PTCa-1(q):P(VDF/TrFE) whose properties are listed in table 6.5.

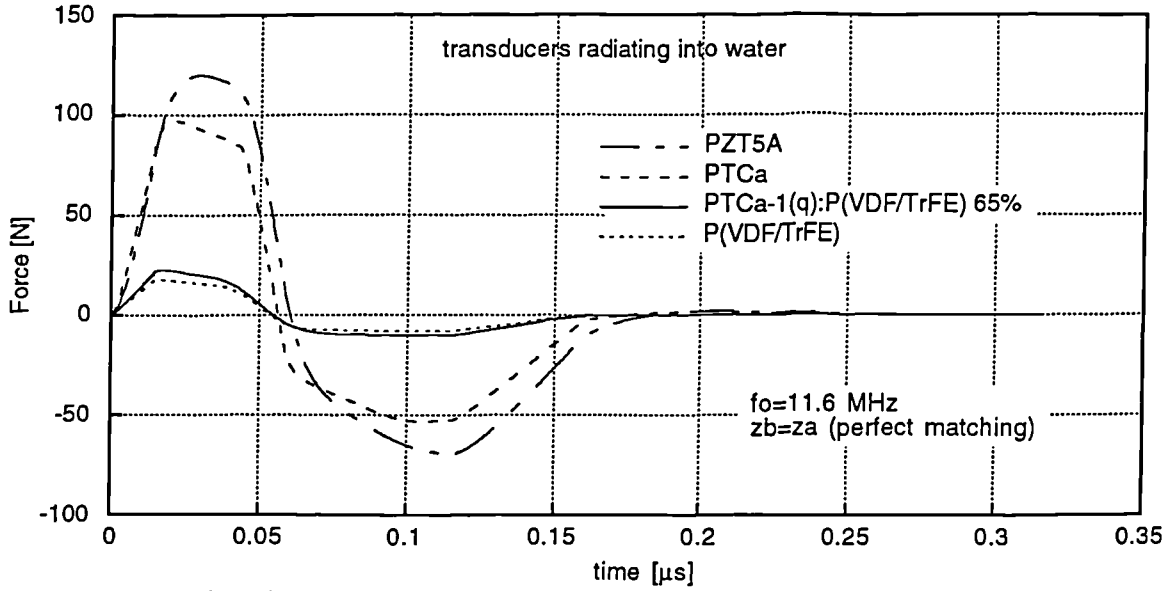

Figure 6.19 - Output force from ultrasonic transmitters made from PZT5A, PTCa, PTCa(q):P(VDF/TrFE) and P(VDF/TrFE) which have an ideal backing.

It is observed from this figure that if a proper backing is made to the transducers the force output does not exhibit the ringing observed in figure 6.17 for a PZT5A transducer whose backing had a specific acoustic impedance of 9.1 MRayl. From figure 6.19 it can be observed that both PZTa and PTCa produce the highest force output while the composite and the polymer seem to perform quite similarly in this respect.

Using a backing whose acoustic impedance is the same as that of the piezoelectric material seems quite straightforward; however, in practice it is not always very easy to obtain such a backing. This is specially true for ceramics which have a high acoustic impedance.

A property which is desirable for the backing is that it should exhibit high losses so

that the sound wave is attenuated to a negligible value before the reflected wave from the back of the backing reaches the piezoelectric material. This rules out metallic material which have low mechanical losses and a more suitable solution lies in making a composite of tungsten in an epoxy matrix in such a proportion as to give the right value of the acoustic impedance. Because it is a composite such a type of backing will exhibit high losses.

In figure 6.20 is shown the acoustic impedance obtained with such a mixture. We have plotted both the experimental points and two boundary models, namely the Reuss and logarithmic models [Grewe et al. 1990], between which the experimental values are believed to lie. It can thus be appreciated that it is not easy to make a backing whose acoustic impedance matches that of the piezoelectric ceramic.

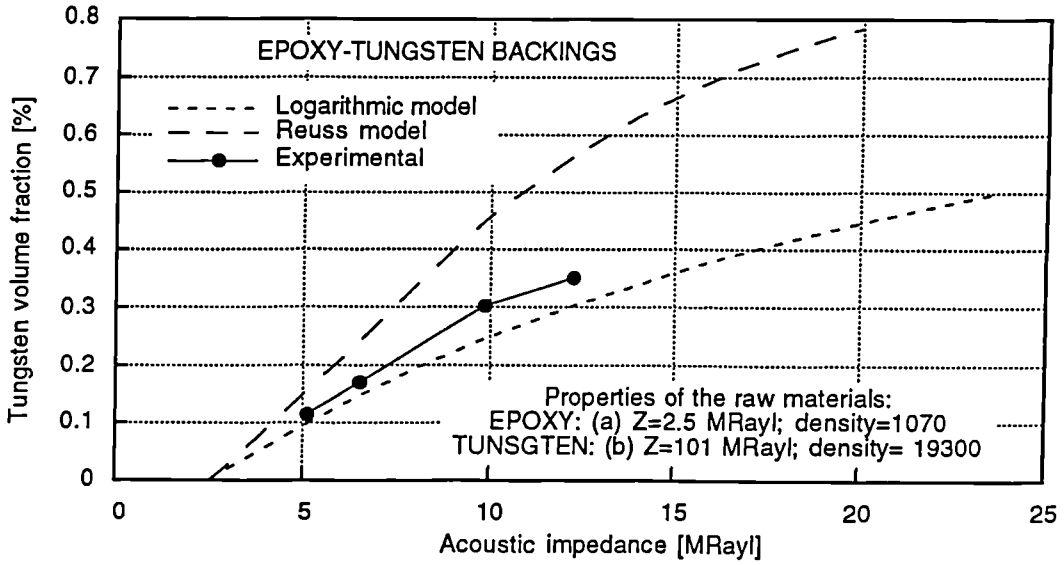

Figure 6.20 - Acoustic impedance of epoxy-tungsten mixtures.

A very acute problem is that of the bonding of the piezoelectric material to the backing. A high regularity in the interface has to exist while the bond line must be kept to a minimum. This minimum is set by the wavelength of the sound wave which for a piezoelectric material in the 10 MHz range, is in the range of 100 μm. In order to be transparent an Araldite bond line must be kept under 2.8 μm, which corresponds to one hundredth of the wavelength at 10 MHz [Silk 1984]. This range of thickness can only be accomplished with the utmost care

6.5.3 - The influence of the front matching layer and of quality factor

In similarity with the electrical transmission lines the transmission of energy from one mechanical layer to the other is a function of their relative impedances and in general, the closer they are in value the better is the transmission.

Because the sound wave is generated inside a piezoelectric material which has in general, a higher impedance than that of the water, techniques used in electrical transmission line theory can be readily applied to this case. One of the techniques, the so-called quarter wavelength matching, consists of placing in front of the piezoelectric material a layer whose acoustic impedance is the geometric mean of the acoustic impedances of water

and the piezoelectric respectively and whose thickness is a quarter of the wavelength at the resonance frequency f_0 of the piezoelectric material.

In figure 6.21 is shown a simulation of the time response on a ultrasonic system consisting of a transmitter and a receiver made with PTCa:P(VDF/TrFE) composite where this technique was applied. It is observed that the sensitivity of the signal increases considerably almost doubling with the front matching.

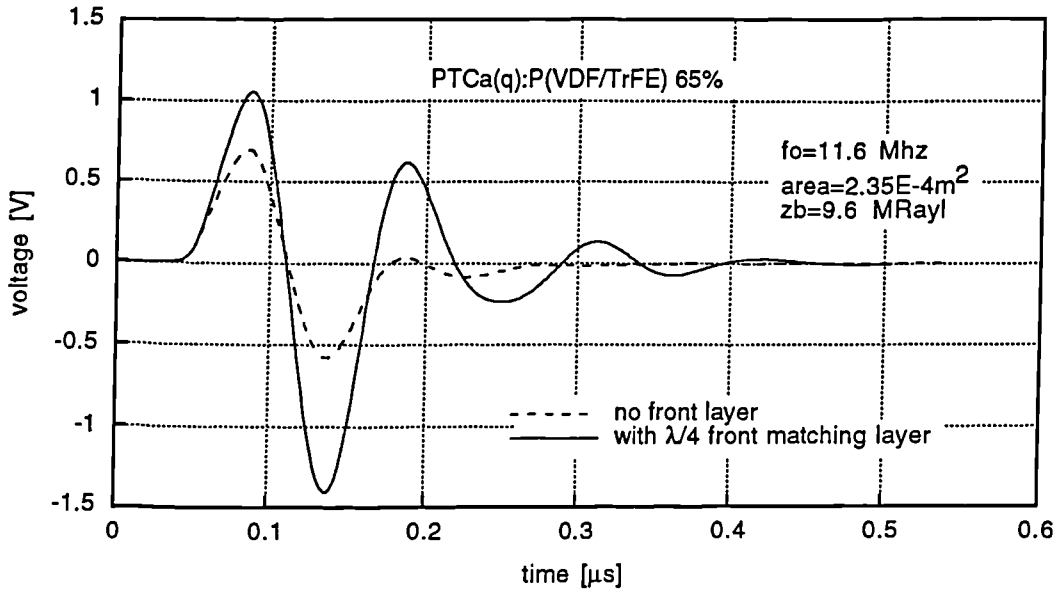

Figure 6.21 - The effect of the front matching layer on a transmitter receiver system

Other schemes have been proposed [Silk 1984] which take this point further by increasing the number of layers placed in front of the piezoelectric.

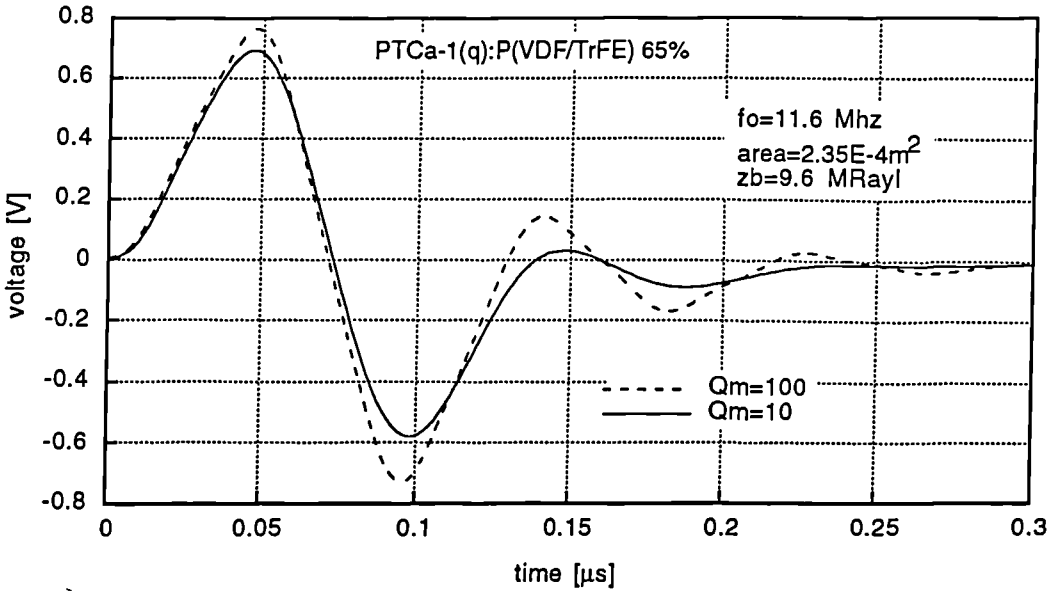

Figure 6.22 - The effect of the quality factor on the response of a transmitter-receiver ultrasonic system

It is a desired feature of a piezoelectric material that it should exhibit to a certain extent mechanical losses which help in the process of turning the response signal more compact. In figure 6.22 we have simulated the time response of a transmitter-receiver system made with PTCa:P(VDF/TrFE) having a quality factor Q_m of 10 and 100 respectively. The value of 10 is

typical from ferroelectric polymer and composites while Q_m=100 is a characteristic value for ceramics. It can be observed that the curve for the higher quality factor exhibits higher response and ringing than that of the lower Q_m. There does not seem to exist, a large difference between these two curves to justify the fabrication of new materials based on this quantity.

The simulation of a transmitter/receiver which was shown in figures 6.21 and 6.22, was calculated as follows [Sittig 1969]. The transmitter ABCD matrix was computed and the transfer function between the output voltage and the input force was calculated assuming that the load is water (see figure 6.23).

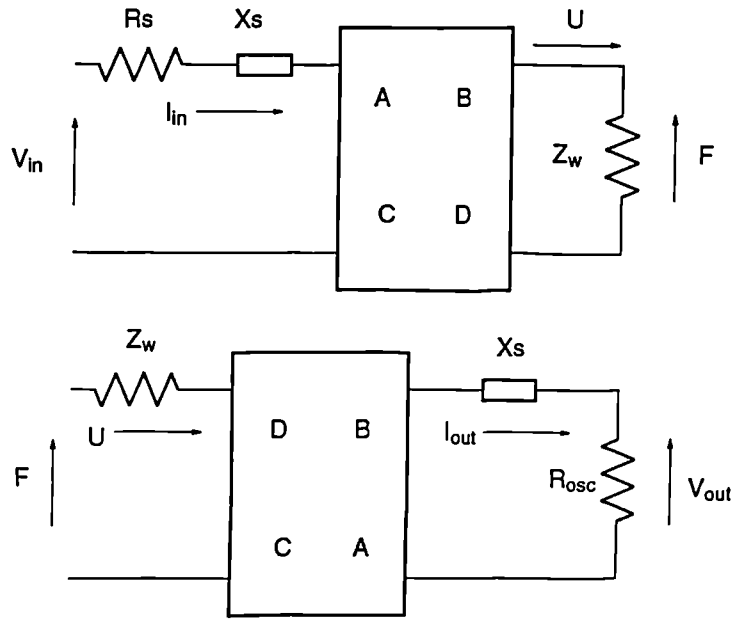

Figure 6.23 - Calculation scheme for the transfer function of a transmitter/receiver ultrasonic system [Sittig 1971].

Then, the transfer function of the receiver relating the output voltage to the input force, was calculated from the reversed ABCD matrix of a transmitter matrix.. Finally assuming that the receiver and the transmitter are decoupled (i.e. that the water medium acts simply as a delay medium) the overall transfer function is just the product of the transmitter and the receiver transfer functions.

PZT5A can be considered the most suitable material to use as a transmitter as can be observed in figure 6.19 as it generates the largest output force for the same voltage excitation. This is not true, however, from a receiver point of view. In figure 6.24 is shown the simulation of the output voltage of receivers made of PZT5A, PTCa, P(VDF/TrFE) and PTCa(q):P(VDF/TrFE) 65%. A PZT5A transmitter was kept constant in this simulation to provide the source of sound pressure. It can be appreciated from figure 6.24 that P(VDF/TrFE) due to its low acoustic impedance (i.e. closer to that of water) seems to be the better receiver material in these conditions. The composite and the ceramics seem to have a comparable performance in this respect.

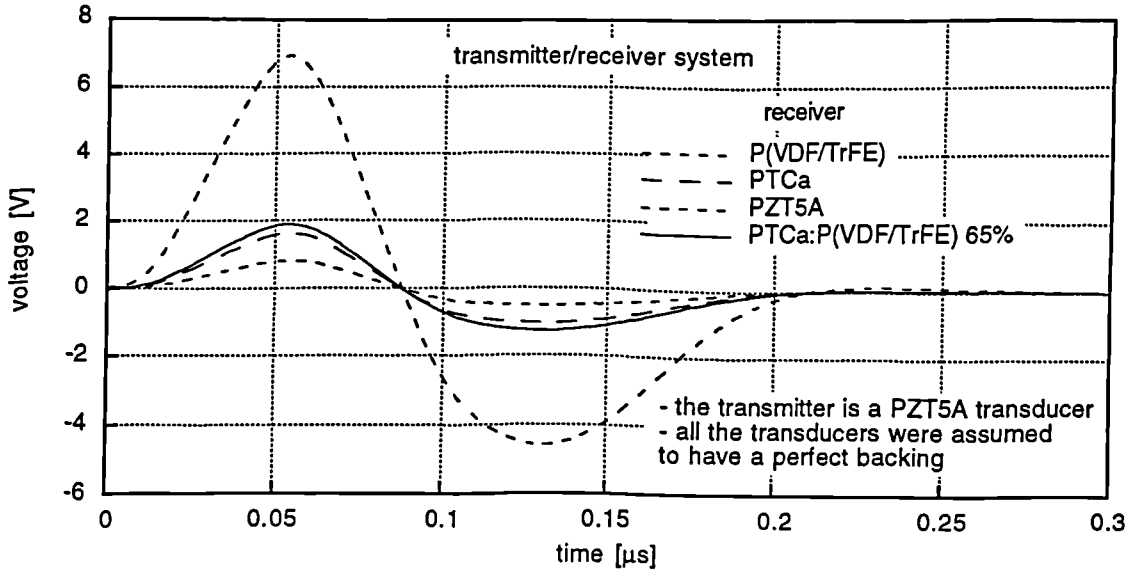

Figure 6.24 - Response of the transducers as ultrasonic receivers. The transmitter is a PZT5A transducer.

Silk [Silk 1984] has reported on indices of efficiency applicable to transducers working at frequencies lower than the resonance frequency. The transmitter efficiency parameter Y_T has been quoted as,

$$Y_T = \frac{k_t}{1-k_t^2}\sqrt{\frac{\varepsilon_{33}^x}{c_{33}^D}} \tag{6.70}$$

while the receiver efficiency parameter Y_R is,

$$Y_R = \frac{k_t v_s}{\sqrt{c_{33}^D \varepsilon_{33}^x}} \tag{6.71}$$

and the product $Y_T Y_R$ represents the performance of a single probe in a transmitter-receiver mode of operation. In table 6.6 these indices have been calculated for PZT5A, PTCa, PVDF, P(VDF/TrFE and PTCa(q):P(VDF/TrFE) 65%, the best of the composite in terms of piezoelectric properties.

TABLE 6.6 - TRANSMITTER ND RECEIVER EFFICIENCY INDICES FOR TRANSDUCER MATERIALS

material	Y_T	Y_R	$Y_T Y_R$
PZT5A	1.491e-10	66.17	9.864e-09
PTCa	6.653e-11	112.9	7.514e-09
PVDF	1.618e-11	639.5	1.035e-08
P(VDF/TrFE)	2.124e-11	988.7	2.101e-08
PTCa:P(VDF/TrFE) 65%	2.158e-11	171.0	3.690e-09

These indices do not represent an actual physical quantity and serve just as a relative Figure Of Merit of these materials regarding ultrasonic generation or detection. From the table a good agreement between the simulation of figure 6.19 and 6.24 and those indices can be found. Thus P(VDF/TrFE) is found to be the best material to use as a receiver while

PZT5A is shown to be the best one in the transmitter mode.

6.5.4 - Testing of ultrasonic transducers

Tests on the performance of ultrasonic transducers working as transmitters were performed using the set-up of figure 6.25.

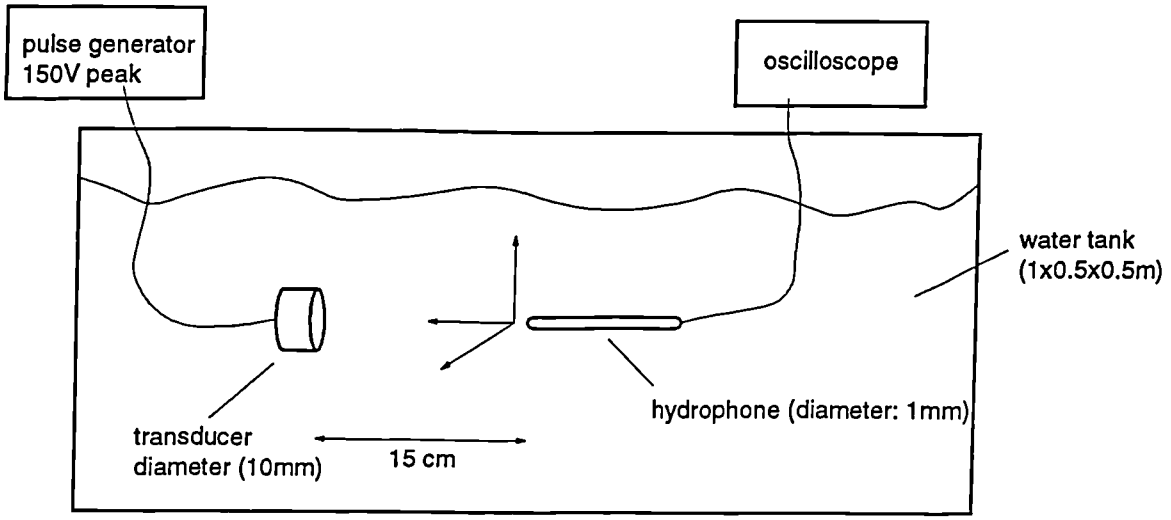

Figure 6.25 - Schematic set-up for the measurement of the transmitter characteristics of ultrasonic transducers.

This set-up consists of a water tank where the ultrasonic transmitter and a needle hydrophone are immersed. The needle hydrophone whose bandwidth is essentially flat in the 1-10 MHz range acts as a probe of the sound pressure. The diameter of the probe is 1 mm and its sensitivity is 112 nV/Pa for a load of 1 MΩ in parallel with a 30 pF capacitance. It should be pointed out that this type of load is that of a common oscilloscope which in our case (see figure 6.25) had a 1MΩ input impedance in parallel with 47 pF. The probe was provided with a three degrees of freedom movement to adjust its position.

The voltage generated by the pulse generator SPIKE 150PR from PAR Scientific Instruments is shown in figure 6.26. The pulse has a rise time of about 20 ns to 90V and a decay time of around 100 ns. Its output impedance is unknown although a value of 50Ω could be assumed.

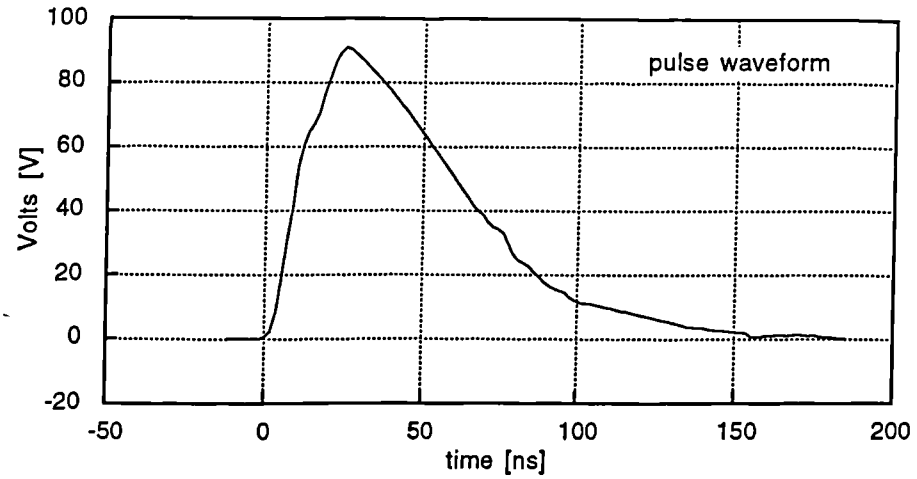

Figure 6.26 - Voltage waveform at the output of the pulse generator.

The oscilloscope used to measure the voltage from the hydrophone is a digital storage

GOULD 420 oscilloscope with 35MHz sampling rate. This bandwidth limited the frequency of the transducers to around 10 MHz.

Three piezoelectric materials have been used for evaluation which are: PTCa, P(VDF/TrFE) and PTCa(q):P(VDF/TrFE) 65%. The design of these transducers is schematically outlined in figure 6.27. It consists of a grounded stainless steel case, an epoxy-tungsten backing for the composite or other electroactive material and a protective or front matching layer at the top. The live electrode was connected to the back face of the piezoelectric film by means of a conductive epoxy (Electrodag 938, Acheson Colloids Company) while the upper face of the piezoelectric was gold evaporated in order to make contact to the grounded case.

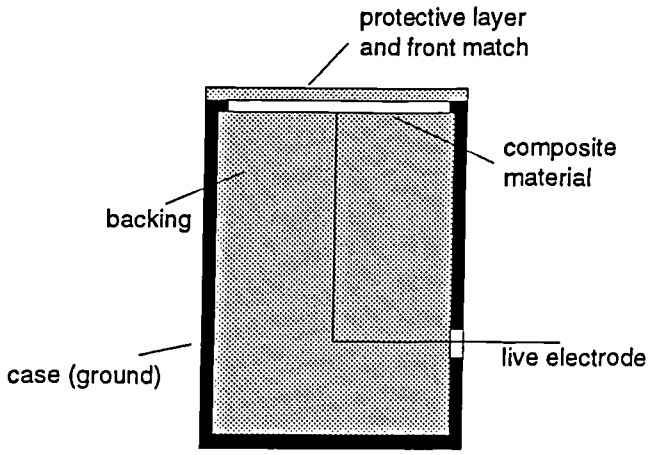

Figure 6.27 - Schematic of an ultrasonic transducer

In the case of the composite and PTCa the backing had a 35% tungsten loading so that it corresponded to around 12 MRayl of specific acoustic impedance. This was close to the maximum load permitted by this mixture in which the tungsten powder had a grain size in the 25-250 μm range.

In figure 6.28 is shown the time response measured by the hydrophone of these transducers which had a resonant frequency of around 10 MHz. Due to the flat response of the hydrophone in this frequency region these waveforms approximate the pressure generated by these transducers on their front face. It can be observed that as expected the PTCa transducer generates the highest pressure while the composite show a similar response. In the case of PTCa probably due to the poor backing some ringing can be observed.

Figures 6.29 and 6.30 show the time response of composite transducers which had a resonant frequency of 25 and 2.39 MHz respectively. From these graphs it can be appreciated that the time waveform for the 25MHz transducer is much smoother than that of the 2.39 MHz. This is attributable to the fact that in the low frequency transducer the pulse can be seen more clearly as in the case of the simulated 1 MHz PZT5A transducer of figure 6.17.

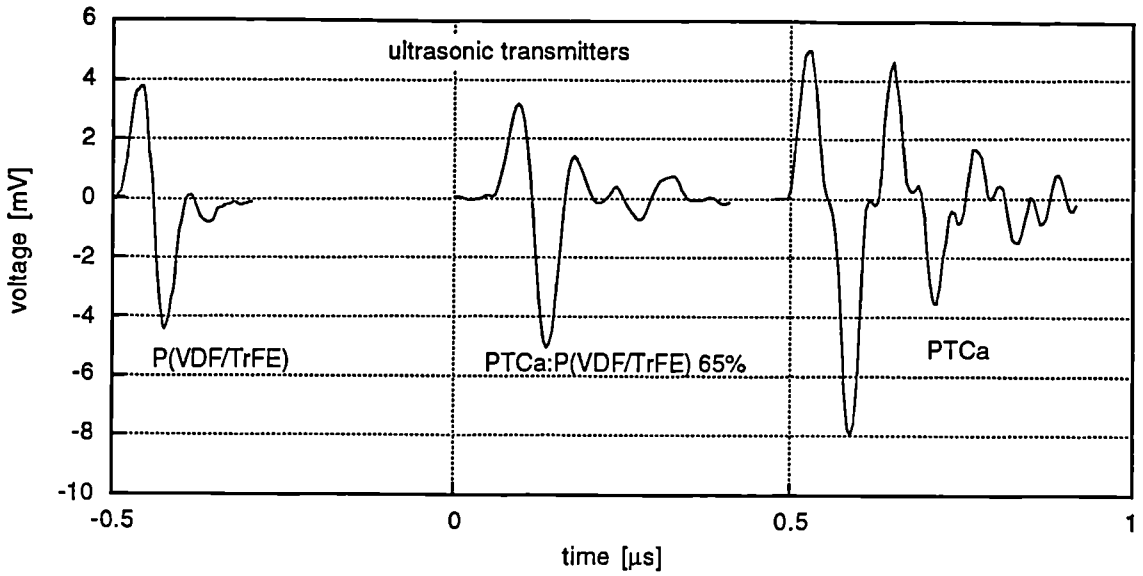

Figure 6.28 - Time response of PTCa, PTCa:(q):P(VDF/TrFE) 65% and P(VDF/TrFE ultrasonic transmitters.

No simulation of these waveforms were performed however due to the lack of knowledge of various parameters the most important of which are the electrical characteristics of the pulse generator and the influence of the bonding, at the back of the piezoelectric material, both to the backing and to the live electrode. It was recognised in the course of the work that the significance of the bond thickness for these high frequency transducers is extremely important, as was pointed out earlier. Thus only a qualitative comparison is being made.

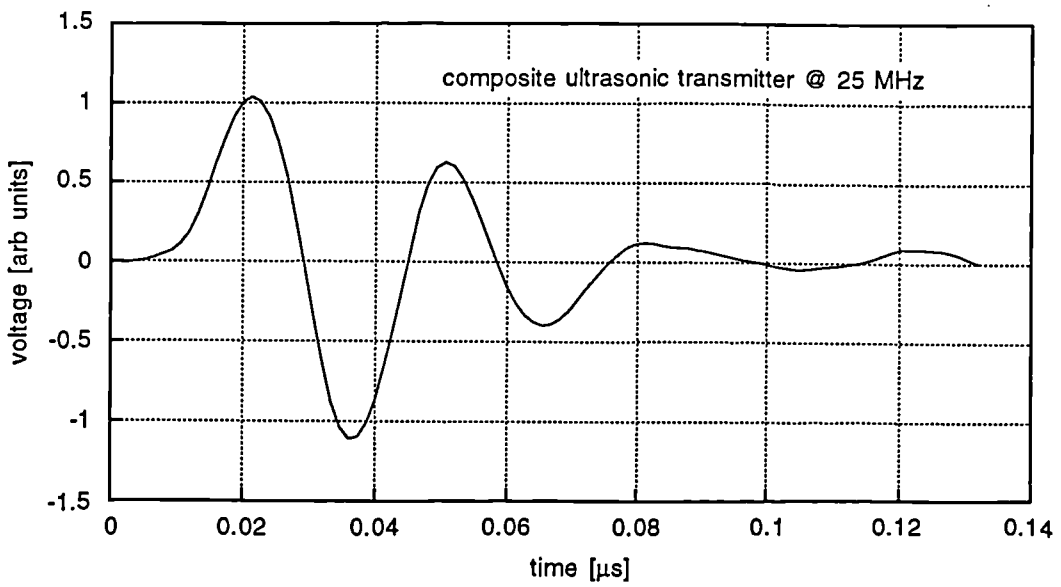

Figure 6.29 - Time response measured by a needle hydrophone of a 25MHz composite transducer

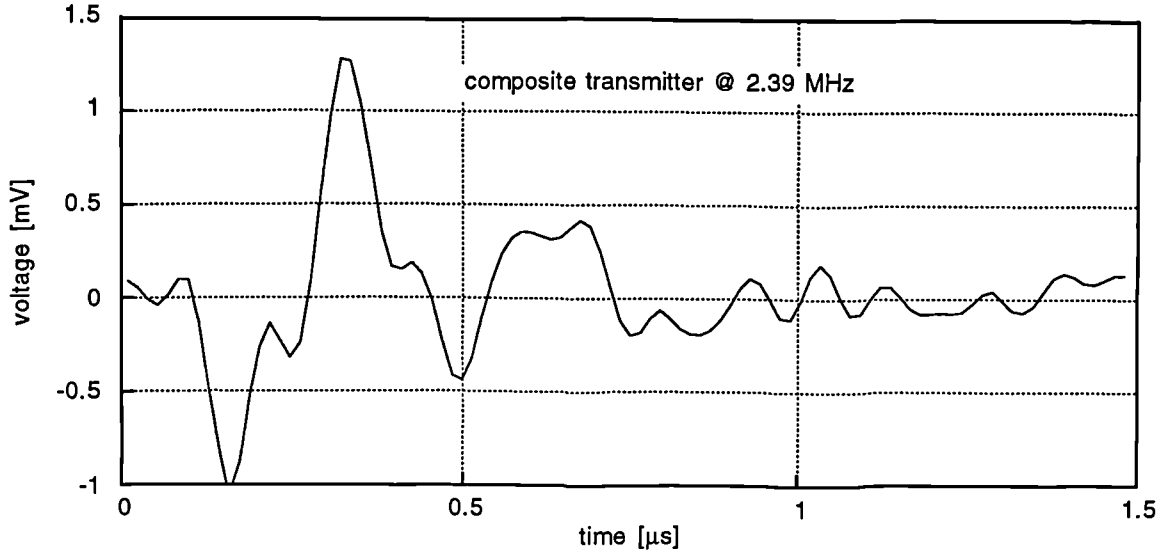

Figure 6.30 - Time response measured by a needle hydrophone of a 2.39 MHz composite transducer

It can thus be concluded that although these composites do show piezoelectric activity their magnitude does not render them sufficiently attractive for piezoelectric applications.

Addendum: In the course of producing this thesis it was realised that the calculation of both the electromechanical coupling factor k_t and the piezoelectric constant h_{33} using a computer program has been affected by an extra factor equal to the square root of π. Thus, in the following papers the correct value of these quantities are given by,

$$(k,h)_{corrected} = \frac{(k,h)_{quoted}}{\sqrt{\pi}}$$

Papers to be corrected:

Dias, C. and D.K. Das-Gupta (1992). *"Piezoelectric properties of 0-3 ceramic-polar polymer composites"* Materials Research Society, Symposium Proc. vol. 276, Smart Materials Fabrication and Materials for Micro-Electro-Mechanical Systems, pp. 25-29.

Dias, C.J. and D.K. Das-Gupta (1993). *"Polymer/ceramic composites for piezoelectric sensors"*, Sensors and Actuators A **37-38**, pp. 343-347.

7 - Conclusions

7.1 - Concluding remarks

Composites made of various polymers and ceramics have been fabricated. Furthermore, those with the highest promise have been more thoroughly investigated for their pyroelectric and piezoelectric properties. We have found that the composite made of quenched powder of calcium modified lead titanate ceramic embedded in the copolymer of polyvinylidene fluoride and trifluorethylene to be the most electroactive of them.

Two main reasons seem to justify this fact. One of them is that the better dielectric matching between these two materials allows the ceramic to be better poled which was pointed out in chapter 4. A higher dielectric matching also increases the electro-active properties of the composites assuming that the ceramic is fully poled as shown in chapter 2 (figures 2.28-2.33).

The other main reason for the higher electro-activity in this composite is linked to the morphology of the ceramic grains. It was found that the ceramic grains obtained through quenching were a better choice than those obtained from milling. The difference in these grains are both in size (i.e. the quenched grains are larger) and in the mechanical processing. Indications are that a combination of these factors plays a role in explaining this differing behaviour. The grain size effect is easily understood from the standpoint of the cube model. The higher the degree of 1-3 connectivity imparted either by a large grain size relative to the thickness of the sample and/or by a large ceramic volume fraction, the greater will be the electro-active properties. The contribution of a variation of the ceramic grain properties with its size or mechanical damage thus differing from the properties of the bulk ceramic, is a matter for speculation although, as was pointed out in chapter 1 and 5 some work has been reported in the literature in this respect concerning $BaTiO_3$ ceramic.

As was naturally expected, the electro-activity increases with increasing volume fraction of the ceramic. Furthermore, the pyroelectric Figure Of Merit, given by the ratio p/ε, seems also to increase in the volume fraction range of the ceramic used (i.e. up to 65%). The composite with the highest loading shows a $FOM_p \approx 2\mu C/m^2K$ which is in excess of that of the *PTCa* ceramic which is $1.8\mu C/m^2K$, but still short of that of $LiTaO_3$ which has a value of $3.77\mu C/m^2K$. It can thus be concluded that the composite PTCa(q):P(VDF/TrFE) 65% is an attractive material for pyroelectric applications where low-cost is an important consideration where the sensitivity is not of critical importance.

The piezoelectric properties of the PTCa(q):P(VDF/TrFE) composites also increase with the ceramic volume fraction Thus, maximum values for the k_t of 0.24 and d_{33} of 48 pC/N were found for the PTCa:P(VDF/TrFE) 65% composite together with a specific acoustic impedance of 16 MRayl. This increase in the piezoelectric constant, however, does not render this material an attractive one for piezoelectric applications such as for high

frequency ultrasonic transducers. In fact, as a transmitter it is not a better material than the piezoelectric ceramics while as a receiver it does not surpass the performance of ferroelectric polymers. It appears moreover, that a better alternative is the use of 1-3 connectivity composites whose k_t is comparable to that of the piezoceramics while exhibiting lower acoustic impedance values (see table 1.2).

The modelling of these composites using a mixed connectivity cube model was proposed in this work and undertaken in chapter 2. One of the main advantages of this model it that it allows the prediction of a whole range of properties of the composites which validate each other. The model is by no means an accurate predictor of all these properties but it serves, nevertheless, the useful purpose of setting a range of property values that in normal circumstances would be expected from a composite. The range of values is set by the parameter n which characterises the degree of 1-3 connectivity of a 0-3 connectivity composite. Of course, it is assumed in the model that the properties of the ceramic grains are the same as that of the bulk ceramic which, as was pointed out earlier, may not always be strictly correct.

The ferroelectricity in these composites was verified by measuring the polarization hysteresis loops as described in chapter 4 where a value of 0.17 C/m^2 of remanent polarization and a coercive field of 18 MV/m was found for the PTCa(q):P(VDF/TrFE) 65% composite. The technique used to measure these loops is useful for samples whose polarization switching can be masked by resistive currents and was first established in the course of this work. Using this technique a linear relationship was found between the remanent polarization and both the pyroelectric coefficient and the d33 piezoelectric constant (see figure 7.1) [Dias et al. 1993].

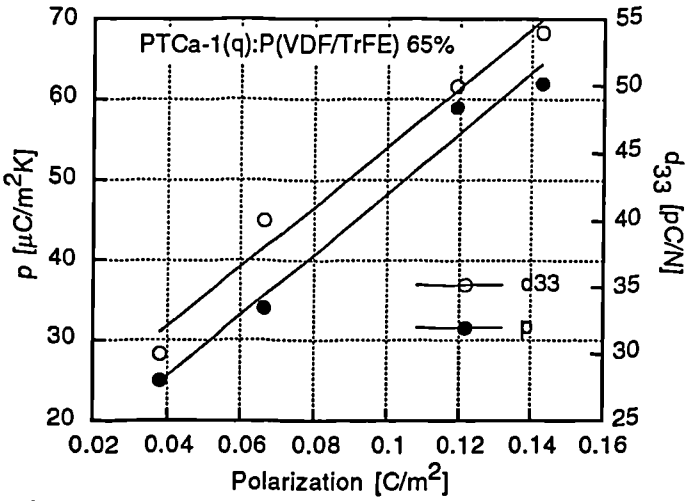

Figure 7.1 - The relationship between the remanent polarization both the pyroelectric coefficient and the d_{33} piezoelectric constant.

On the basis of the better dielectric dielectric matching, than resistive matching between the phases the studies have extended to include the frequency dependence of the electroactive properties using an ac poling field. The conclusion was that the electroactive properties for a fixed poling time decreased for frequencies below 0.05 Hz where the

operative mechanism of field distribution between the composite phases is the resistive matching.

The measurement of the pyroelectric coefficient using a dynamic heat excitation technique is also one of the contributions of this work. Although no extensive work was carried out using this technique in the work reported here, a good agreement between the values the dynamic and the quasi-static method was found. Furthermore, the modelling of the frequency dependence of the apparent pyroelectric coefficient in PTCa-1(q):P(VDF/TrFE) 65% has enabled the estimation of a value for the thermal diffusivity of $0.043 \cdot 10^{-6}$ m^2/s.

The measurement of k_t using the formalism of Bui and Ohigashi [Bui et al. 1977; Ohigashi 1988] for lossy materials such as PVDF and P(VDF/TrFE) has been applied in this work. There has seldom been a report on this piezoelectric constant for composites in the literature probably due to the low resonance peaks of the majority of the 0-3 connectivity composites quite unlike those of piezoceramics. In this context, it should be noted that the value of 0.24 is the highest reported value for the 0-3 composites.

Finally the expected performance of lossy transducers was calculated using a simulation model. It was found that when a lossy piezoelectric material was employed in transducers, the Mason model for the lossless case could still be used provided that, an appropriate modification was carried on the definition of the acoustic impedance and the wave number of the sound wave (equations 6.61 and 6.62).

7.2 - Further work

- The most natural question now is:

Are these the highest values for the electroactive properties in 0-3 composites one can obtain?

One would be tempted to say that, yes, most probably. In fact, for the best composite i.e. PTCa(q):P(VDF/TrFE), the grains of the ceramic used were comparable to the thickness of the sample while the dielectric matching between the constituent phases was about the best one could hope for between a piezoceramic and a polymer.

Large values of the $d_h g_h$ product have been reported recently for example. These have been assigned to the way in which the ceramic powder was prepared (i.e. through a co-precipitation method). Is this an indication that high electromechanical coupling factors can be achieved? It should be pointed out again that the mixed connectivity model requires that the properties of the ceramic grains to be known or otherwise one has to resort to those of the bulk ceramic.

- The estimation of composite properties using the mixed connectivity model should however be improved. In fact for the k_t the mixed connectivity cube model predicted a higher value than that of the experimental values. The exact reason for this discrepancy is

not known at the moment. Is it because in the model the acoustic losses were not taken into account? These losses in a composite material are very high so that according to equation 6.32 the sound wave attenuates around 20% when travelling 100 μm in the megahertz frequency range. This would involve extending the prediction of properties of composites to include both the real and the imaginary parts (i.e. acoustic and dielectric losses).

The mixed connectivity cube model can also be improved with respect to the estimation of the pyroelectric constant and its FOM_p to take into account the change in area of the composite sample as pointed in chapter 4. The exploitation of product properties in composites would be enhanced if a complete set of properties could be measured. This would include the elastic, linear expansion and the d_{31} piezoelectric constants.

A tentative modelling was made of the polarization switching using the cube model. This work could be extended to cover a variety of polarization hysteresis conditions thus extending the model to predict the remanent polarization in a composite.

- High temperature poling was an idea which should probably be tried again, perhaps with a different composite. It showed some promising results although the problem of electrical breakdown appeared to be a great impediment.
- The explanation of the low-frequency behaviour of the pyroelectric coefficient in PTCa-2 composites seems to be a phenomenon which should be given due consideration possibly along the lines pointed out in chapter 4.
- The increase of the volume fraction of the ceramic could also be a possible way of improving some of the electro-active properties although it seems that the advantages of low acoustic impedance high mechanical losses and low relative permittivity would degrade with such an approach.

7.3 - Papers and communications published in the course of this work

Dias, C. and D.K. Das-Gupta (1991). *"Electroactive and dielectric properties of corona and thermally poled polymer-ceramic composites"* International Symposium on Electrets (ISE 7), pp. 495-500, Berlin.

Dias, C. and D.K. Das-Gupta (1992). *"Piezoelectric properties of 0-3 ceramic-polar polymer composites"* Materials Research Society, Symposium Proc. vol. 276, Smart Materials Fabrication and Materials for Micro-Electro-Mechanical Systems, pp. 25-29.

Dias, C. and D.K. Das-Gupta (1992). *"Ferroelectric ceramic/polar polymer composite films for pyroelectric sensors"* 6th Int. Conf. on Dielectric Materials, Measurements and Applications, DMMA6, pp. 393-396, Manchester.

Dias, C. and D.K. Das-Gupta (1993). *"Electro-active polymer-ceramic composites for piezoelectric and pyroelectric applications"* Materials Research Society Symposium (Spring 1993), to be published.

Dias, C., M. Simon, R. Quad and D.K. Das-Gupta (1993). *"Measurement of the pyroelectric coefficient in composites using a temperature-modulated excitation"*, J. Phys. D: Appl. Phys. **26**, pp. 106-110.

Dias, C.J. and D.K. Das-Gupta (1993). *"Hysteresis measurements on ferroelectric composites"*, J. Appl. Phys. **74**(10), pp. 6317-6321.

Dias, C.J. and D.K. Das-Gupta (1993). *"Polymer/ceramic composites for piezoelectric sensors"*, Sensors and Actuators A **37-38**, pp. 343-347.

Dias, C.J. and D.K. Das-Gupta (1994). *"Piezo- and pyroelectricity in ferroelectric polymer/ceramic composites"*, ed. by D. K. Das-Gupta, Trans Tech Pub. to be published

Dias, C.J. and D.K. Das-Gupta (1994). *"Poling behaviour of ceramic/polymer ferroelectric composites"*, Ferroelectrics, to be published

7.4 - References

Abdullah, M.J. (1989). A study of electro-active properties of polymer/ceramic composites, PhD, University of Wales - SEECS (Bangor).

Abdullah, M.J. and D.K. Das-Gupta (1990). *"Electrical properties of ceramic/polymer composites"*, IEEE Trans. Electr. Insul. **25**(3), pp. 605-610.

Amin, M., L.S. Balloomal, K.A. Darwish, H. Osman and B. Kamal (1988). *"Pyroelectricity in rubber composite films"*, Ferroelectrics **81**, pp. 381-386.

Amin, M., H. Osman, L. Balloomal, K.A. Darwish and B. Kamal (1988). *"Electrical properties of acrylonitrile-butadiene rubber-barium titanate composites"*, Ferroelectrics **81**, pp. 387-392.

Anderson, R.A. and R.G. Kepler (1981). *"Inequality of direct and converse piezoelectric coefficients"*, Ferroelectrics **32**, pp. 13-15.

Ashby, M.F. and D.R.H. Jones (1986). Engineering materials 2: an introduction to microstructures, processing and design, Oxford Pergamon Press.

Auld, B.A. and Y. Wang (1984). *"Acoustic wave vibrations in periodic composites plates"* IEEE Ultrasonics Symposium, pp. 528-532, Texas (USA).

Banno, H. (1985). *"Theoretical equations for the dielectric and piezoelectric properties of ferroelectric composites based on modified cubes model"*, Jap. J. Appl. Phys. **24**(Suppl. 2), pp. 445-447.

Banno, H., K. Ogura, H. Sobue and K. Ohya (1987). *"Piezoelectric and acoustic properties of piezoelectric flexible composites"*, Jap. J. Appl. Phys. **26 (Suppl. 1)**, pp. 153-155.

Banno, H. and S. Saito (1983). *"Piezoelectric and dielectric properties of sinthetic rubber and $PbTiO_3$ or PZT"*, Jap. J. Appl. Phys. **22 (Suppl. 2)**, pp. 67-69.

Bell, A.J. (1990). *"Powders for electrical ceramics- an industrial view"*, Ceramic Transactions 8: Ceramic Dielectrics: composition, processing and properties pp. 41-48.

Bhalla, A.S., R.E. Newnham, L.E. Cross and W.A. Schulze (1981). *"Pyroelectric PZT-Polymer composites"*, Ferroelectrics **33**, pp. 139-146.

Bihler, E., K. Holdik and W. Eisenmenger (1989). *"Polarization distributions in isotropic, stretched or annealed PVDF films"*, IEEE Trans. Electr. Insul. **24**(3), pp. 541-545.

Braithwaite, N. and G. Weaver (1990). *"Electronic Materials"*, in Materials in Action, London, Butterworths, pp. 177.

Broadhurst, M.G., G.T. Davis, J.E. McKinney and R.E. Collins (1978). *"Piezoelectricity and pyroelectricity in polyvinylidene fluoride - a model"*, J. Appl. Phys. **49**(10), pp. 4992-4997.

Brown, L. and D.L. Carlson (1989). *"Ultrasound transducer models for piezoelectric polymer films"*, IEEE Transactions on Ultrasonics Ferroelectrics and Frequency Control **36**(3), pp. 313-318.

Bui, L.N., H.J. Shaw and L.T. Zitelli (1977). *"Study of acoustic wave resonance in piezoelectric PVF2 film"*, **SU-24**(5), pp. 331-336.

Bur, A.J. and A.K. Tsao (1981). *"Depolarization of poled PVF2 samples with "thick" electrodes"*, Ferroelectrics **32**, pp. 185-189.

Burns, G. (1990). Solid State Physics, Academic Press.

Byer, R.L. and C.B. Roundy (1972). *"Pyroelectric coefficient direct measurement technique and application to a nsec response time detector"*, Ferroelectrics **3**, pp. 333-38.

Cao, W., Q.M. Zhang and L.E. Cross (1993). *"Theoretical study on the static performance of piezoelectric ceramic/polymer composites with 2-2 connectivity"*, IEEE Ultrason. Ferroelec. Freq. Contr. **40**(2), pp. 103-109.

Capron, B.A. (1986). *"Microscopic models of piezoelectric polymers"*, IEEE Transactions on Ultrasonics Ferroelectrics and Frequency Control **UFFC-33**(1), pp. 33-40.

Card, R.J. (1988). *"Preparation of hollow ceramic fibers"*, Advanced Ceramic Materials **3**, pp. 29-31.

Carslaw, H.S. and J.C. Jaeger (1959). Conduction of Heat in Solids, Oxford Clarendon.

Chan, H.L.W. and J. Unsworth (1989). *"Mode coupling in modified Lead Titanate/polymer 1-3 composite"*, J. Appl. Phys. **65**(4), pp. 1754-1758.

Chilton, J.A. (1991). *"Electroactive composites"*, GEC Review **6**(3), pp. 156-164.

Chilton, J.A., G.M. Garner, R.W. Whatmore and F.W. Ainger (1990). *"0-3 composite sensitivity"*, Ferroelectrics **109**, pp. 217-222.

Collins, R.E. (1980). *"Practical application of the thermal pulsing technique to the study of electrets"*, J. Appl. Phys. **51**(6), pp. 2973-2986.

Cross, L.E. and K.H. Härdtl (1980). *"Ferroelectrics"*, in Encyclopedia of Chemical Technology, Jonh Wiley & Sons, pp. 1-30.

Das-Gupta, D.K. (1981). *"On the nature of pyroelectricity in polyvinylidene fluoride"*, Ferroelectrics **33**, pp. 75-89.

Das-Gupta, D.K. (1991). *"Pyroelectricity in polymers"*, Ferroelectrics **118**, pp. 165-189.

Das-Gupta, D.K. and K. Doughty (1978). *"Corona charging and the piezoelectric effect in polyvinylidene fluoride"*, Ferroelectrics **49**(8), pp. 4601-4603.

Das-Gupta, D.K. and K. Doughty (1978). *"Piezo- and pyroelectric behaviour of corona charged polyvinylidene fluoride"*, J. Phys. D: Appl. Phys. **11**, pp. 2415-2423.

Das-Gupta, D.K. and K. Doughty (1980). *"Dielectric relaxation spectra of poled polyvinylidene fluoride"*, Ferroelectrics **28**, pp. 307-310.

Das-Gupta, D.K. and K. Doughty (1982). *"Piezoelectricity and pyroelectricity in thin polymer films"*, Thin Sol. Films **90**, pp. 247-252.

Das-Gupta, D.K. and K. Doughty (1984). *"The stability and ageing of poled polyvinylidene fluoride (PVF_2) electrets"*, Ferroelectrics **60**, pp. 51-59.

Das-Gupta, D.K. and D.B. Shier (1978). *"Small-angle light scattering (SALS) from uniaxially streched polyvinylidene fluoride"*, J. Appl. Phys. **49**(11), pp. 5685-5687.

Dass, M.L.A., U. Dahmen and G. Thomas (1986). *"Electron microscopy characterization of lead zirconate titanate ceramics at the morphotropic phase boundary composition"* IEEE 1986 6th Int. Symposium on Applications of Ferroelectrics, pp. 146-149, Pennsylvania (USA).

Davis, G.T., J.E. McKinney, M.G. Broadhurst and S.C. Roth (1978). *"Electric field induced phase changes in poly (vinylidene fluoride)"*, J. Appl. Phys. **49**(10), pp. 4998-5002.

Devonshire, A.F. (1949). *"Theory of Barium Titanate (part I)"*, Philos. Mag. **40**, pp. 1040-1063.

Devonshire, A.F. (1951). *"Theory of Barium Titanate (part II)"*, Philos. Mag. **42**, pp. 1065-1079.

Dias, C., M. Simon, R. Quad and D.K. Das-Gupta (1993). *"Measurement of the pyroelectric coefficient in composites using a temperature-modulated excitation"*, J. Phys. D: Appl. Phys. **26**, pp. 106-110.

Dias, C.J. and D.K. Das-Gupta (1993). *"Hysteresis measurements on ferroelectric composites"*, J. Appl. Phys. **74**(10), pp. 6317-6321.

Dias, C.J. and D.K. Das-Gupta (1993). *"Piezo- and pyroelectricity in ferroelectric polymer/ceramic composites"*, ed. by D. K. Das-Gupta,

Dias, C.J. and D.K. Das-Gupta (1993). *"Poling behaviour of ceramic/polymer ferroelectric composites"*, Ferroelectrics **to be published**, pp.

Dickens, B., E. Balizer, A.S. DeReggi and S.C. Roth (1992). *"Hysteresis measurements of the remanent and coercive field in polymers"*, J. Appl. Phys. **72**(9), pp. 4258-4264.

Durán, P., J.F. Fernández, P. Recio and C. Moure (1990). *"Processing and properties of modified-Lead Titanate ceramics"*, Mat. and Manuf. Processes **5**(3), pp. 427-443.

Egusa, S. and N. Iwasawa (1993). *"Piezoelectric paints: preparation and applications as built-in vibration sensors of structural materials"*, J. Mater. Sci. **28**, pp. 1667-1672.

Espinosa, F.R.M., V. Pavia, J.A. Gallego-Juárez and M. Pappalardo (1986). *"Fractured piezoelectric ceramics for broadband ultrasonic composite transducers"* IEEE Ultrasonics Symposium, pp. 691-696.

Fang, C., M. Wang and H. Zhou (1991). *"Pyroelectric properties of a new composite material PVDF-TGS film"* 7th Intern. Symp. on Electrets, Berlin.

Ferren, R.A. (1988). *"Synthesis of poly(vinylidene) fluoride and its copolymers"*, in The applications of ferroelectric polymers, ed. by T. T. Wang, J. M. Herbert and A. M. Glass, Glasgow & London, Blackie, pp. 6-20.

Fukushima, J., K. Kodaira and T. Matsushita (1984). J. Mater. Sci. **19**, pp. 595.

Furukawa, T. (1989). *"Ferroelectric properties of vinylidene fluoride copolymers"*, Phase Transitions, Sect. B **18**(3-4), pp. 143-212.

Furukawa, T., M. Date and E. Fukada (1980). *"Hysteresis phenomena in polyvinylidene fluoride under high electric field"*, J. Appl. Phys. **51**(2), pp. 1135-1141.

Furukawa, T., K. Fujino and E. Fukada (1976). *"Electromechanical properties in the composites of epoxy resin and PZT ceramics"*, Jap. J. Appl. Phys. **15**(11), pp. 2119-2129.

Furukawa, T., K. Ishida and E. Fukada (1979). *"Piezoelectric properties in the composite systems of polymer and PZT ceramics"*, J. Appl. Phys. **50**(7), pp. 4904-4912.

Furukawa, T. and G.E. Johnson (1981). *"Dielectric relaxations in a copolymer of vinylidene flouride and triflourethylene"*, J. Appl. Phys. **52**(2), pp. 940-943.

Furukawa, T., K. Suzuki and M. Date (1986). *"Switching process in composite systems of PZT ceramics and polymers"*, Ferroelectrics **68**, pp. 33-44.

Furukawa, T. and T.T. Wang (1988). *"Measurements and properties of ferroelectric properties of ferroelectric polymers"*, in The applications of ferroelectric polymers, ed. by T. T. Wang, J. M. Herbert and A. M. Glass, Glasgow & London, Blackie & Son, pp. 6-20.

Furukawa, T. and J.X. Wen (1984). *"Electrostriction and piezoelectricity in ferroelectric polymers"*, Jpn. J. Appl. Phys. **23**(9), pp. L677-679.

Furukawa, T., J.X. Xen, K. Suzuki, Y. Takashina and M. Date (1984). *"Piezoelectricity and pyroelectricity in vinylidene flouride/triflourethylene copolymers"*, J. Appl. Phys. **56**(3), pp. 829-834.

Gallego-Juárez, J.A. (1989). *"Piezoelectric ceramics and ultrasonics transducers"*, J. Phys. E: Sci. Instrum. **22**, pp. 804-816.

Gallo, C.F. (1977). *"Corona - a brief status report"*, IEEE Trans. Industry Appl. **IA-13**(6), pp. 550-557.

Garn, L.E. and E.J. Sharp (1974). *"Pyroelectric vidicon target materials"*, IEEE Trans. Parts, Hybrids, Packaging **PHP-10**(4), pp. 208-221.

Garn, L.E. and E.J. Sharp (1982). *"Use of low-frequency sinusoidal temperature waves to*

separate pyroelectric currents from non-pyroelectric currents. Part I. Theory", J. Appl. Phys. **53**(12), pp. 8974-8979.

Garner, G.M., N.M. Shorrocks, et al. (1989). "*0-3 piezoelectric composites for large area hydrophones*", Ferroelectrics **93**, pp. 169-176.

Gerthsen, P., K.H. Härdtl and N.A. Schmidt (1980). "*Correlation of mechanical and electrical losses in ferroelectric ceramics*", J. Appl. Phys. **51**(2), pp. 1131-1134.

Giacometti, J.A. (1987). "*Radial current-density distributions and sample charge uniformity in a corona triode*", J. Phys. D: Appl. Phys. **20**, pp. 675-682.

Giacometti, J.A., G.F.L. Ferreira and B. Gross (1985). "*Negative charge transport in fluorethylene propylene by the constant current method*", Phys. Stat. Sol. (a) **88**, pp. 297-307.

Grewe, M.G., T.R. Gururaja, T.R. Shrout and R. Newnham (1990). "*Acoustic properties of particle/polymer composites for ultrasonics transducer backing applications*", IEEE Trans. Ultrason. Ferroelec. Freq. Control **37**(6), pp. 506-514.

Gururaja, T.R., W.A. Schulze, et al. (1985). "*Piezoelectric composite materials for ultrasonic transducer applications. Part I: Resonant modes of vibration of PZT rod-polymer composites*", IEEE Trans. Son. Ultrason. **SU-32**(4), pp. 481-498.

Gururaja, T.R., Q.C. Xu, A.R. Ramachandran, A. Halliyal and R.E. Newnham (1986). "*Preparation and piezoelectric properties of fired 0-3 composites*" IEEE Ultrasonics Symposium, pp. 703-708.

Guy, I.L. and D.K. Das-Gupta (1991). "*Polarization reversal and thermally stimulated discharge current in a vinylidene fluoride trifluorethylene copolymer*", J. Appl. Phys. **70**(10), pp. 5691-5693.

Guy, I.L. and J. Unsworth (1987). "*Conformational and crystallographic changes occurring in polyvinyledene flouride during the production of D-E hysteresis loops*", J. Appl. Phys. **61**(12), pp. 5374-.

Han, K., A. Safari and R.E. Riman (1991). "*Colloidal processing for improved piezoelectric properties of flexible 0-3 ceramic-polymer composites*", J. Am. Ceram. Soc. **74**(7), pp. 1699-1702.

Han, K.H., R.E. Riman and A. Safari (1990). "$(Pb_{0.5},Bi_{0.5})(Ti_{0.5},Fe_{0.5})O_3$ *powder prepared by chemically precipitated method for 0-3 ceramic/polymer composites*", Ceramic

Transactions 8: Ceramic Dielectrics: composition, processing and properties pp. 227-232.

Hanner, K.A., A. Safari, R.E. Newnham and J. Runt (1989). *"Thin film 0-3 polymer/piezoelectric ceramic composites: piezoelectric paints"*, Ferroelectrics **100**, pp. 255-260.

Hashimoto, K.Y. and M. Yamaguchi (1986). *"Elastic, piezoelectric and dielectric properties of composite materials"* IEEE Ultrasonics Symposium, pp. 697-702.

Haun, M.J., E. Furman, S.J. Jang, H.A. McKinstry and L.E. Cross (1987). *"Thermodynamic theory of PbTiO3"*, J. Appl. Phys. **62**(8), pp. 3331-3338.

Hayward, G. and M. Jackson (1984). *"Discretetime modelling of the thickness mode piezoelectric transducer"*, IEEE Trans. Sonics and Ultrasonics **SU-31**(3), pp.

Hicks, J.C. and T.E. Jones (1981). *"Frequency dependence of remanent polarization and the correlation of piezoelectric coefficients with remanent polarization in polyvinyledene flouride"*, Ferroelectrics **32**, pp. 119-126.

Higashihata, Y., J. Sako and T. Yagi (1981). *"Piezoelectricity of vinylidene fluoride trifluorethylene copolymers"*, Ferroelectrics **32**, pp. 85-92.

Hikita, K., K. Yamada, M. Nishioka and M. Ono (1983). *"Effect of porous structure to piezoelectric properties of PZT ceramics"*, Jap. J. Appl. Phys. **22 (Suppl. 2)**, pp. 64-66.

Holeman, B.R. (1972). *"Sinusoidally modulated heat flow and the pyroelectric effect"*, Infrared Phys. **12**, pp. 125-35.

Humphrey, K.J., G.M. Garner and R.W. Whatmore (1987). *"The dielectric and piezoelectric properties of vinylidene fluoride-trifluorethylene copolymers"*, Ferroelectrics **76**, pp. 383-391.

Ichinose, N., Y. Hirao, M. Nakamoto and Y. Yamashita (1985). *"Pyroelectric infrared sensor using modified PbTiO3 and its applications"*, Jap. J. Appl. Phys. **24 (Suppl. 3)**, pp. 178-180.

IEEE, S.o.P. (1978). ANSI/IEEE Std 176-1978. American National Standards Institute.

Ikeda, S., T. Fukada and Y. Wada (1988). *"Effect of space charge on polarization reversal in a copolymer of vinylidene flouride and triflourethylene"*, J. Appl. Phys. **64**(4), pp. 2026-2030.

Ikeda, S., S. Kobayashi and Y. Wada (1985). *"Analysis of the effect of electric conductance of*

ferroelectric polymers on D-E hysteresis curves measured by the Sawyer-Tower method", J. Polym. Sci.: Polym. Phys. **23**, pp. 1513-1521.

Ikeda, S., Z. Shimojima and M. Kutani (1990). "*Correlation between ferroelectric phase transition and crystallization behaviour of ferroelectric polymers*", Ferroelectrics **109**, pp. 297-301.

Jaffe, B., R.S. Roth and S. Marzullo (1955). "*Properties of piezoelectric ceramics in the solid solution series lead titanate-lead zirconate -lead oxide: tin oxide and lead titanate-lead hafnate*", J. Res. National Bureau of Standards **55**, pp. 239-254.

Jaffe, H. (1968). "*Piezoelectric applications of ferroelectrics*", IEEE Trans. Electron. Devices **ED-16**, pp. 557-561.

Jiang, Q.Y., S.B. Krupanidhi and L.E. Cross (1990). "*Effects of the lapped surface layer and surface stress on the dielectric properties of PLZT ceramics*", Ceramic Transactions 8: Ceramic Dielectrics: composition, processing and properties pp. 375-383.

Jimenez, B. (1988). "*90° domain reorientation in lead-calcium titanate ceramics*", Ferroelectrics **81**, pp. 265-268.

Jimenez, B., J. Mendiola, et al. (1988). "*Contributions to the knowledge of Calcium modified Lead Titanate ceramics*", Ferroelectrics **87**, pp. 97-108.

Kenney, J.M. and S.C. Roth (1979). J. Res. Nat. Bur. Std. **84**, pp. 447.

Kepler, R.G. and R.A. Anderson (1978). "*Piezoelectricity and pyroelectricity in polyvinylidene fluoride*", J. Appl. Phys. **49**(8), pp. 4490-4494.

Klicker, K.A. (1980). Piezoelectric composites with 3-1 connectivity for transducer applications, PhD thesis, The Pennsylvania State University.

Koga, K.K. and H. Ohigashi (1986). "*Piezoelectricity and related properties of vinylidene fluoride and trifluorethylene copolymers*", J. Appl. Phys. **59**(6), pp. 2142-2150.

Krimholtz, Leedom and Matthaei (1970). "*New equivalent circuit for elementary piezoelectric transducers*", Electron. Lett. **6**(13), pp. 338-339.

Kupferberg, L.C. (1988). "*Orientation of crystallites in piezoelectric poly (vinylidene fluoride)*", J. Appl. Phys. **64**(5), pp. 2316-2323.

Landauer, R., D.R. Young and M.E. Drougard (1956). *"Polarization reversal in the barium titanate hysteresis loop"*, J. Appl. Phys. **27**(7), pp. 752-758.

Lando, J.B. and W.W. Doll (1968). *"The polymorphism of poly(vinylidene) fluoride. 1. the effect of head-to-head structure"*, J. Macromolec. Sci., Phys. **B2**, pp. 205-218.

Lang, S.B. and D.K. Das-Gupta (1986). *"Laser-Intensity-modulation method: A technique for determination of spatial distributions of polarization and space charge in polymer electrets"*, J. Appl. Phys. **59**(6), pp. 2151-60.

Lee, H.-G. and H.-G. Kim (1990). *"Ceramic particle size dependence of dielectric and piezoelectric properties of piezoelectric ceramic-polymer composites"*, J. Appl. Phys. **67**(4), pp. 2024-2028.

Lee, M.-H., A. Halliyal and R.E. Newnham (1988). *"Poling studies of piezoelectric composites prepared by coprecipitated PbTiO3 powder"*, Ferroelectrics **87**, pp. 71-80.

Legrand, J.F. (1989). *"Structure and ferroelectric properties of P(VDF/TrFE) copolymers"*, Ferroelectrics **91**, pp. 303-317.

Legrand, J.F. (1993). *"Morphology and structure of polymer electrets"*, IEEE Trans. on Electr. Insul. **28**(3), pp. 336-343.

Liu, S.T. and D. Long (1978). *"Pyroelectric detectors and materials"*, Proc. IEEE **66**, pp. 14-26.

Liu, S.T. and O.N. Tufte (1972). *"The pyroelectric properties of the lanthanum-doped ferroelectric PLZT ceramics"*, Ferroelectrics **3**, pp. 281-285.

Lovinger, A. (1983). *"Ferroelectric polymers"*, Science **220**, pp. 1115-1121.

Mason, W.P. (1942). Electromechanical transducers and wave filters, New York Van Nostrand.

Morgan Matroc Ltd. (1992). "Piezoelectric ceramics", Vauxhall Industrial Estate Ruabon, Wrexham Clwyd LL14 6HY, UK.

Merz, W.J. (1956). *"Switching time in ferroelectric BaTiO3 and its dependence on crystal thickness"*, J. Appl. Phys. **27**(8), pp. 938-943.

Mopsik, F.I. and A.S. DeReggi (1982). *"Numerical evaluation of the dielectric polarization distribution from thermal pulse data"*, J. Appl. Phys. 53(6), pp. 4333-39.

Moreno, R.A. and B. Gross (1976). *"Measurement of potential build-up and decay, surface charge density and charging currents of corona-charged polymer foil electrets"*, J. Appl. Phys. **47**(8), pp. 3397-3402.

Morris, S.A. and C.G. Hutchens (1986). *"Implementation of Mason's model on circuit analysis programs"*, IEEE Trans. Ultrasonics, Ferroelectrics and Freq. Control **UFFC-33**(3), pp. 295-298.

Moulson, A.J. and J.M. Herbert (1990). Electroceramics: materials, properties and applications, Cambridge Chapman & Hall.

Nakamura, K., Y. Teramoto and N. Murayama (1984). *"Rotation of polar axis of b-form poly (vinylidene fluoride) under high electric field"*, Ferroelectrics **57**, pp. 139-149.

Newnham, R.E. (1985). *"Ferroelectric composites"*, Jap. J. Appl. Phys. **24 (Suppl. 2)**, pp. 16-17.

Newnham, R.E., D.P. Skinner and L.E. Cross (1978). *"Connectivity and piezoelectric-pyroelectric composites"*, Mat. Res. Bull. **13**, pp. 525-36.

Newnham, R.E. and S.E. Trolier-McKinstry (1990). *"Structure-property relationships in ferroic nanocomposites"*, Ceramic Transactions 8: Ceramic Dielectrics: compostion, processing and properties pp. 235-252.

Ngoma, J.B., J.Y. Cavaille, J. Paletto and J. Perez (1990). *"Dielectric and piezoelectric properties of copolymer-ferroelectric composite"*, Ferroelectrics **109**, pp. 205-210.

Ohigashi, H. (1976). *"Electromechanical properties of polarized polyvinylidene flouride films as studied by the piezoelectric resonance method"*, J. Appl. Phys. **47**(3), pp. 949-955.

Ohigashi, H. (1985). *"Piezoelectric polymers - materials and manufacture"*, Jpn. J. Appl. Phys. **24 (Suppl. 2)**, pp. 23-27.

Ohigashi, H. (1988). *"Ultrasonic transducers in the megahertz range"*, in The applications of ferroelectric polymers, ed. by T. T. Wang, Glasgow, Blackie, pp. 237-273.

Oliveira, O.N. and G.F.L. Ferreira (1985). *"Grid-to-plate current-voltage characteristics of a*

corona triode", Rev. Sci. Instrum. **56**(10), pp. 1957-1961.

Olmo, L.d., L. Pardo, B. Jimenez and J. Mendíola (1988). "*Piezoelectric behaviour of* $Pb_{1-x}Ca_xTiO_3$ *ceramics obtained by reactive processes*", Ferroelectrics **81**, pp. 293-296.

Ouchi, H. (1965). J. Am. Ceram. Soc. **48**, pp. 630.

Pardo, L., J. Mendiola and C. Alemany (1988). "*Theoretical treatment of ferroelectric composites using Monte Carlo calculations*", J. Appl. Phys. **64**(10), pp. 5092-5097.

Pardo, L., J. Mendiola and C. Alemany (1989). "*Theoretical study of ferroelectric composites from Ca-modified Lead Titanate ceramics*", Ferroelectrics **93**, pp. 183-188.

Pauer, L.A. (1973). IEEE Intern. Conf. Rec., pp. 1.

Pelmore, J.M. (1979). "*Acoustic impedance of composite materials*", Acoust. Lett. **3**(3), pp. 65-68.

Porter, S.G. (1981). "*A brief guide to pyroelectric detectors*", Ferroelectrics **33**, pp. 193-206.

Powers, J.M. (1988). "*Long range hydrophones*", in The application of ferroelectric polymers, ed. by T. T. Wang, J. M. Herbert and A. M. Glass, Glasgow, Blackie & Son Ltd., pp. 118-161.

Prest, W.M. and D.J. Luca (1978). "*The formation of the* γ *phase from the* α *and* β *polymorphs of polyvinylidene fluoride*", J. Appl. Phys. **49**(10), pp. 5042-5047.

Purvis, C.K. and P.L. Taylor (1983). "*Piezoelectricity and pyroelectricity in poly (vinylidene fluoride) influences in the lattice structure*", J. Appl. Phys. **54**(2), pp. 1021-1028.

Ravinet, P., J. Hue, et al. (1980). "*Acoustic and dielectric losses processes in* PVF_2" IEEE Ultrasonics Symposium, pp. 1017-1022.

Reed, D.M., T.T. Srinivasan, Q.C. Xu and R.E. Newnham (1990). "*Effect of particle size on the dielectric and piezoelectric properties of PbTiO3-polymer composites*" IEEE 7th Int. Symposium on Applications of Ferroelectrics, pp. 324-327, Urbana (USA).

Sa-Gong, G., A. Safari and R.E. Newnham (1986). "*Poling study of* $PbTiO_3$*-polymer composites*" IEEE 6th Int. Symp. on Appl. Ferroelectrics (ISAF'86), pp. 281-284, Pennsylvannia (USA).

Safari, A., G. Sa-Gong, J. Giniewicz and R.E. Newnham (1986). *"Composite piezoelectric sensors"* Proc. of the 21st University Conf. on Ceramic Science, pp. 445-454.

Saitoh, S., H. Honda, N. Kaneko, M. Izumi and S. Suzuki (1985). *"The method of determining k_t and Q_m for low Q piezoelectric materials"* IEEE Ultrasonic Symposium, pp. 620-623.

Savakus, H.P., K.A. Klicker and R.E. Newnham (1980). *"PZT-epoxy piezoelectric transducers: a simplified fabrication process"*, Mater. Res. Bull. **16**, pp. 677-680.

Schenk, M., S. Bauer, T. Lessle and B. Ploss (1992). *"Dielectric spectroscopy on ferroelectric P(VDF/TrFE)"*, Ferroelectrics **127**, pp. 215-220.

Schewe, H. (1982). *"Piezoelectricity of uniaxially oriented polyvinylidene fluoride"* IEEE Ultrasonics Symposium, pp. 519-524.

Seggern, H. and T.T. Wang (1984). *"Polarization behaviour during high field poling of poly (vinylidene fluoride)"*, J. Appl. Phys. 56(9), pp. 2448-2452.

Sessler, G.M. (1981). *"Piezoelectricity in polyvinylidene"*, J. Acoust. Soc. Am. **70**(6), pp. 1596-1608.

Shaikh, A., R.W. Vest and G.M. Vest (1989). *"Dielectric properties of ultrafine grined BaTiO3"*, IEEE Trans. Ultrasonics, Ferroelectrics and Freq. Control **36**(4), pp. 407-413.

Shaikh, A.A., R.W. Vest and G.M. Vest (1986). *"Dielectric properties of ultrafine grained $BaTiO_3$"* IEEE 1986 6th Int. Symposium on Applications of Ferroelectrics, pp. 126-129, Pennsylvania (USA).

Shaulov, A.A., W.A. Smith and R. Ting (1989). *"Modified-Lead-Titanate/polymer composites for hydrophone applications"*, Ferroelectrics **93**, pp. 177-182.

Siemens (1981). "Vibrit - piezoelectric ceramics from Siemens", Spezialkeramik PS 12, Postfach 60, D 8627 Redwitz, Germany.

Silk, M.G. (1984). Ultrasonic transducers for non-destructive testing, Bristol Adam Hilger Ltd.

Sittig, E.K. (1967). *"Transmission parameters of thickness driven piezoelectric transducers*

arranged in multilayered configurations", IEEE Trans. Sonic and Ultrasonics **SU-14**(4), pp. 167-174.

Sittig, E.K. (1969). "*Effects of bonding and electrode layers on the transmission parameters of piezoelectric transducers used in ultrasonic digital delay lines*", IEEE Trans. Sonics and Ultrasonics **SU-16**(1), pp. 2-10.

Sittig, E.K. (1971). "*Definitions relating to conversion losses in piezoelectric transducers*", IEEE Trans. Sonics and Ultrasonics **SU-18**(14), pp. 231-234.

Skinner, D.P., R.E. Newnham and L.E. Cross (1978). "*Flexible composites transducers*", Mat. Res. Bull. **13**, pp. 599-607.

Slayton, M.H. and H.S.N. Setty (1990). "*Single layer piezoelectric-layer composite*" IEEE 7th Int. Symposium on Applications of Ferroelectrics, pp. 90-92, Urbana (USA).

Smith, W.A. (1989). "*The role of piezocomposites in ultrasonic transducers*" IEEE Ultrasonics Symposium, pp. 755-766.

Smith, W.A. (1991). "*Modelling 1-3 composite piezoelectrics: thickness-mode oscillations*", IEEE Ultrason. Ferroelec. Freq. Contr. 38(1), pp. 40-47.

Smith, W.A. (1993). "*Modelling 1-3 composite piezoelectrics: hydrostatic response*", IEEE Ultrason. Ferroelec. Freq. Contr. **40**(1), pp. 41-48.

Smiths, J.G. (1976). "*Iterative method for accurate determination of the real and imaginary parts of the materials coefficients of piezoelectric ceramics*", IEEE Trans. Sonics and Ultrasonics **SU-23**(6), pp. 393-402.

Stack, G.M. and R.Y. Ting (1989). "*Piezoelectric properties and temperature stability of poly (vinylidene fluoride - trifluorethylene) copolymers*", IEEE Trans. Ultrason. Ferroelec. Freq. Control **UFFC-36**(4), pp. 417-423.

Takahashi, N. and A. Odajima (1981). "*Ferroelectric reorientation of crystallites in polyvinylidene fluoride*", Ferroelectrics **32**, pp. 49-59.

Takeuchi, H., S. Jyomura and C. Nakaya (1985). "*New piezoelectric materials for ultrasonic transducers*", Jap. J. Appl. Phys. **24 (Suppl. 2)**, pp. 36-40.

Takeuchi, H., S. Jyomura, E. Yamamoto and Y. Ito (1982). "*Electromechanical properties of*

(Pb,Ln)(Ti,Mn)O3 ceramics (Ln=rare earths)", J. Acoust. Soc. Am. **72**(4), pp. 1114-1120.

Tasaka, S. and S. Miyata (1981). *"The origin of piezoelectricity in poly (vinylidene fluoride)"*, Ferroelectrics **32**, pp. 17-23.

Tashiro, K. and M. Kobayashi (1985). *"Structural phase transition in ferroelectric vinylidene fluoride trifluorethylene copolymers"*, Jpn. J. Appl. Phys. **24 (Suppl. 2)**, pp. 873-875.

Tashiro, K., H. Tadokoro and M. Kobayashi (1981). *"Structure and piezoelectricity of poly (vinylidene fluoride)"*, Ferroelectrics **32**, pp. 167-175.

Ting, R. (1990). *"The hydroacoustic behaviour of piezoelectric composite materials"*, Ferroelectrics **102**, pp. 215-224.

Tripathi, A.K., T.C. Goel and P.K.C. Pillai (1991). *"Pyroelectric and piezoelectric properties of sol-gel derived BaTiO3 polymer composites"* 7th Int. Symp. on Electrets, Berlin.

Ueda, I. and S. Ikegami (1968). *"Piezoelectric properties of modified PbTiO3 ceramics"*, J. Jap. Appl. Phys. **7**, pp. 236-242.

Varadan, V.V., Y.R. Roh, V.K. Varadan and R.H. Tancrell (1989). *"Measurement of all the elastic and dielectric constants of poled PVDF"* IEEE Ultrasonic Symposium, pp. 727-730.

Vasalek, J. (1921). Phys. Rev. **17**, pp. 475.

Vernitron Ltd. (1976). "Five modern piezoelectric ceramics", USA.

Wada, Y. and R. Hayakawa (1976). *"Piezoelectricity and pyroelectricity of polymers"*, Jpn. J. Appl. Phys. **15**(11), pp. 2041-2057.

Waller, D. and A. Safari (1988). *"Corona poling of PZT ceramics and flexible piezoelectric composites"*, Ferroelectrics **87**, pp. 187-95.

Wang, H., Q.M. Zhang and L.E. Cross (1993). *"Piezoelectric, dielectric and elastic properties of poly(vinylidene fluoride/trifluorethylene)"*, J. Appl. Phys. **74**(5), pp. 3394-3398.

Wang, T.T. and Y. Takase (1987). *"Ferroelectriclike dielectric behaviour in the piezoelectric amorphous copolymer of vinylidene cyanide and vinyl acetate"*, J. Appl. Phys. **62**(8), pp. 3466-3469.

Wang, Y., W. Zhong and P. Zhang (1993). *"Pyroelectric properties of ferroelectric-polymer*

composites", J. Appl. Phys. **74**(1), pp. 512-524.

Ward, I.M., G.R. Davies, et al. (1986). "*Primary and secondary pyroelectricity in highly oriented polyvinylidene fluoride*" IEEE 1986 6th Int. Symposium on Applications of Ferroelectrics, pp. 182-187, Pennsylvania (USA).

Wersing, W. (1986). "*Composite piezoelectric for ultrasonic transducers*" IEEE 6th Int. Symp. on Appl. Ferroelectrics (ISAF'86), pp. 212-223, Pennsylvannia (USA).

Wersing, W., K. Lubitz and J. Mohaupt (1989). "*Anisotropic piezoelectric effect in modified $PbTiO_3$ ceramics*", IEEE Ultrason. Ferroelec. Freq. Contr. **36**(4), pp. 424-433.

Yagi, T., M. Tatemoto and J. Sako (1980). "*Transition behaviour and dielectric properties in trifluorethylene and vinylidene fluoride copolymers*", Polym. J. **12**(4), pp. 209-223.

Yamada, T., T. Ueda and T. Kitayama (1982). "*Piezoelectricity of a high content lead zirconate titanate/polymer composite*", J. Phys. Phys. **53**(4), pp. 4328-4332.

Yamaka, E. (1988). "*Pyroelectric devices*", in The applications of ferroelectric polymers, ed. by T. T. Wang, Glasgow, Blackie & Son, pp. 329-48.

Yamashita, Y., K. Yokoyama, H. Honda and T. Takahashi (1981). "*$(Pb, Ca)((Co_{1/2}W_{1/2}),Ti)O_3$ piezoelectric ceramics and their applications*", Proc. of the FMA-3, Jap. J. Appl. Phys. **20 (Suppl. 4)**, pp. 183-187.

Yamashita, Y., S. Yoshida and T. Takahashi (1983). "*Effect of MnO additive on piezoelectric properties in modified $(Pb,Ca)TiO_3$ ferroelectric ceramics*", Jap. J. Appl. Phys. **22 (Suppl. 2)**, pp. 40-42.

Yamazaki, H. and T. Kitayama (1981). "*Pyroelectric properties of polymer-ferroelectric composites*", Ferroelectrics **33**, pp. 147-153.

Zewdie, H. and F. Brouers (1990). "*Theory of ferroelectric polymer-ceramic composites*", J. Appl. Phys. **68**(2), pp. 713-718.

Zipfel, G.G. (1983). 0-3 piezocomposite. Bell Labs Record. **April 83:** 11-13.

Annex - Papers published during the course of this work

Hysteresis measurements on ferroelectric composites

C. J. Dias[a] and D. K. Das-Gupta
School of Electronic Engineering Science, University College of North Wales, Dean Street, Bangor, Gwynedd LL57 1UT, United Kingdom

(Received 15 June 1993; accepted for publication 3 August 1993)

Ceramic/polymer composites made of calcium-modified lead titanate grains in the matrix of a copolymer of vinylidene fluoride and trifluorethylene, in a 65:35 volume fraction percentage, respectively, were produced in order to obtain mechanically strong ferroelectric films with improved piezo- and pyroelectric properties. Their poling behavior was studied using a modified ferroelectric hysteresis measurement setup that allowed for the measurement of the remanent polarization P_r and coercive field E_c, as a function of the peak of the sinusoidal applied field, the frequency of the excitation, and the poling temperature. The ranges of variation of the electric field, frequency, and temperature were from 5 to 25 MV/m, from 0.04 to 2 Hz, and from 50 to 120 °C, respectively. Estimates of the activation field and saturation polarization were calculated based on these measurements. The observed properties in the ferroelectric composites were then compared and correlated with the properties of the ceramic material.

I. INTRODUCTION

Ferroelectric composites are usually a mixture of a ferroelectric material embedded in a polymer matrix. The aim of these materials is to exhibit the high piezoelectric and pyroelectric coefficients of the dispersoid while retaining some of the properties of the polymer such as the ease of manufacture and flexibility which could allow for a lower manufacturing cost of the related sensors/related devices. Various approaches have been successfully tried in which both the constituent materials and their connectivity have been varied. While the impact of the constituents materials on the resulting properties may be obvious, the connectivity pattern can be as well an important factor in determining the final properties of the composite.[1] The connectivity is usually denoted by two digits in which the first digit specifies the dimensions in which the ceramic is self-connected while the second digit describes the same quantity for the polymer phase. There are ten possible combinations of connectivity for a diphasic material of which the most important configurations are the 0-3 and the 1-3 connectivity patterns. The composites described in this article are of the 0-3 connectivity type as they have grains of ceramic powder dispersed in a polymer matrix. However, the large grain size of the ceramic dispersoid compared with the thickness of the sample may approximate to a certain 1-3 connectivity character to these composites.[2]

To induce piezoelectric and pyroelectric activities, a ferroelectric composite must undergo a poling procedure in order to orient the spontaneous polarization of the ceramic phase. A common method to observe this process is through a hysteresis loop where a sinusoidal field is applied to the sample while the polarization reversal current and/or charge is continuously monitored. These measurements allow a determination of the remanent polarization (the amount of polarization after the poling field is removed) and the coercive field (the field required to switch back the previous polarization to make the sample net polarization zero) which are characteristic features of the ferroelectric materials. In the case of PZT:epoxy resin (where PZT is lead zirconic titanate), mixed 1-3 and 0-3 connectivity composites,[2] the remanent polarization P_r has been found to lie in the range of 127–2.8 mC/m^2 while the coercive field E_c was found to be between 1.3 and 1.8 MV/m. It was further observed that samples with higher 0-3 connectivity character had a lower remanent polarization and a higher coercive field because of the decrease of the local field in the ceramic particles, caused by the shielding action of its low permittivity and conductivity matrix.

The measurement of the hysteresis loop can be difficult in materials with low polarization and high permittivity and/or conductivity which are inherent with many composites.[3] Various techniques have been devised to deal with this situation which include a method that measures the bipolar and the unipolar current measurement in succession to find the true polarization current.[4] Another technique uses the value of the small signal resistivity and capacitance measurements to calculate the current which is subtracted from the total measured current[4] while, in yet another technique known as the modified Sawyer–Tower circuit,[5,6] a parallel resistance is connected in parallel with the measuring capacitor whose magnitude is such as to match the conductivity of the sample. A new technique is reported here which improves the observation of the polarization current based on the simultaneous measurement of the current of a sample to which a bipolar voltage is applied, and that of two other reference samples to which a unipolar field is applied (i.e., either positive or negative), whose values are used to find the true polarization current of the first sample. The present method should prove to be a more convenient way to measure readily the polarization of a ferroelectric material with nonideal capacitive and/or conductive behavior.

[a]Permanent address: Universidade Nova de Lisboa, SGAAF-FCT, Quinta da Torre, 2825 Monte da Caparica, Portugal.

 0021-8979/93/74(10)/6317/5/$6.00

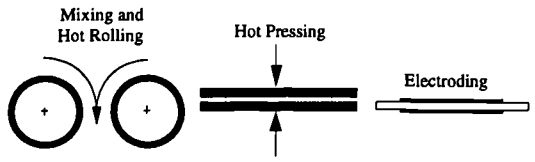

FIG. 1. Schematic procedure for the preparation of the composite films.

II. EXPERIMENTAL PROCEDURE

A. Materials preparation

The composite material was obtained through the following procedure (see Fig. 1): The host polymer [i.e., P(VDF/TrFE) 75:25 mol %] was melted in a hot rolling mill at approximately 170 °C. The ceramic grains of calcium-modified lead titanate (PTCa), were then gradually introduced into the polymer melt, up to the required volume fraction, while mixing until all the ceramic was evenly distributed in the composite when a uniform color and texture were observed. The ceramic grains were previously obtained by quenching a ceramic block from a high temperature which produced a coarse grain size of about 10–60 μm and probably with a small mechanical damage inflicted in the ferroelectric domains. This composite sheet was then pressed at 165 °C temperature and 4 kPa pressure to produce films in the thickness range of 50–100 μm. Aluminum electrodes of $\sim$1000 Å thickness were then evaporated on both sides of these films.

The resistivity of this material as well as that of PTCa and P(VDF/TrFE) were measured by applying an electric field of 3, 0.3, and 6 MV/m, respectively, at temperatures ranging from 50 to 120 °C, while recording the steady-state current with a Keithley electrometer model 616. In each case a field was chosen such that a negligible polarization of the sample would occur. The dielectric constant was also measured in the same temperature range at 1 kHz with a Wayne–Kerr capacitance bridge.

B. Hysteresis measurement

For the hysteresis measurements the sample was immersed in silicone oil, to reduce arcing, whose temperature could be controlled through a hot plate. A function generator was used to provide a small voltage signal with the suitable shape, amplitude, and frequency which was then amplified with a TREK 610C HV power supply in a 1:1000 ratio. This voltage was applied to the aluminum electrodes of the samples through spring contacts.

The hysteresis measurements were performed by measuring the current while applying a high-voltage sinusoidal field to the sample. This current consists of the following three main components: (i) a capacitive current; (ii) a resistive contribution, possibly nonlinear at high fields; and (iii) the polarization or switching current due to the orientation of the spontaneous polarization of the ceramic. The contribution due to the last component mentioned above is of most interest in this experiment which features a memory effect after switching off the field. In composite samples, a large resistive current is usually superimposed over the measured switching current which obscures its true value. In order to compensate for this effect, which is stronger at low frequencies of the applied field, three identical samples were used. On applying a full wave ac high voltage to the three samples (Fig. 2), samples A and B will be poled during the first positive half-cycle while the sample C remains unpoled. During the first negative half-cycle sample C is poled together with sample A in which the polarization is now reversed (i.e., switching). The polarization of sample A undergoes repetitive switching in polarity with time while samples B and C remain polarized in the positive and negative directions, respectively, with the progress of time. Thus, when an equilibrium is established only the resistive and capacitive components of the current will flow through samples B and C while sample A will have the polarization current as an additional component (see Fig. 2). Since the current for all three samples was measured with operational amplifiers in real time it was

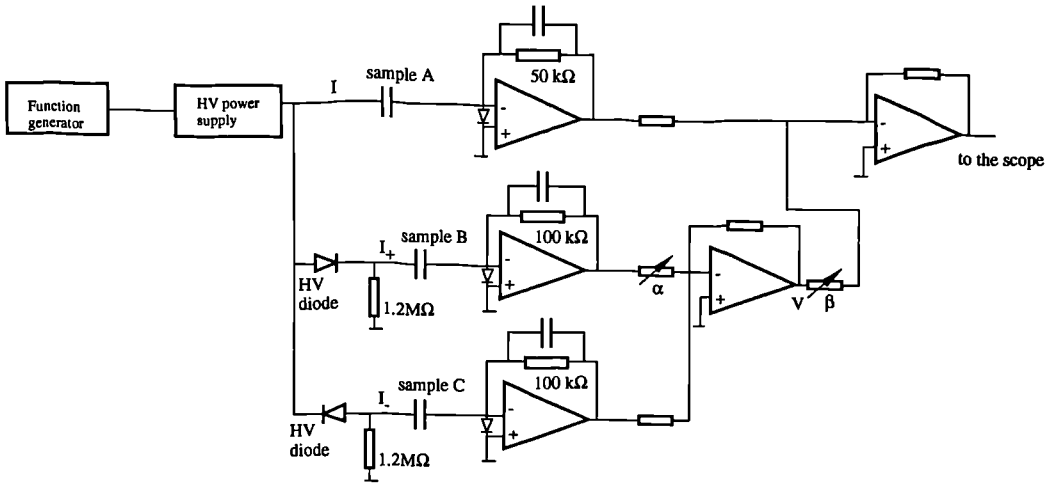

FIG. 2. Schematic setup for the hysteresis loop measurement.

possible to subtract the reversible current from the switching current by the use of an appropriate electronic circuit (see Fig. 2). The polarization current I_{pol} is given by

$$I_{pol}=I-\beta(I_{+}+\alpha I_{-}), \quad (1)$$

where I_{+} and I_{-} are the positive and negative half-wave currents in samples B and C, respectively, and α and β the adjusting proportionality factors to allow for variations in the thickness and area of the samples.

The latter parameters were implemented by means of potentiometers (see Fig. 2) and the procedures to determine their values were as follows. Initially a full-wave ac (bipolar) voltage loop was applied to the three samples while monitoring the voltage at point V of the electronic circuit (Fig. 2), which is proportional to the sum of currents I_{+} and I_{-}. The potentiometer α was then set in such a way that the voltage at the point V was continuous when the applied voltage went from the negative to the positive polarity. After the correct adjustment of the potentiometer for the parameter α, a high-voltage oscillating field with a dc offset (i.e., unipolar field) was applied to the three samples to allow for the determination of the β parameter. The unipolar field consisted of applying either an oscillating field with a positive or negative dc bias, thus implying that the measured current is only due to the capacitive and resistive components. Consequently the potentiometer was set in such a way that I_{pol} was as close to zero as possible.

It should be noted that in this procedure all the contributions to the current which have no memory are automatically subtracted, including the capacitive current. The rectifier diodes (Fig. 2) were used to block either the positive or the negative voltage while a resistance was used in parallel with the sample to allow it to discharge when the voltage decreased from its maximum value to zero. The value of the resistance was chosen so that the inverse of the time constant of the discharge process was much greater than the frequency of the applied voltage. The polarization current was then digitized with an oscilloscope and transferred to a computer to calculate the polarization charge by integrating the measured current. A ferroelectric hysteresis loop was then drawn, from which the remanent polarization, the coercive field, and other parameters were determined.

III. RESULTS AND DISCUSSION

Figure 3 shows a comparison of ferroelectric hysteresis loops obtained with and without using the above-mentioned compensating circuit. These loops were obtained at 90 °C, the frequency of the electric field excitation being 0.1 Hz while the thickness of the sample was 75 μm. Hysteresis loop 1 shows the nature of variation of the total current through sample A whereas loop 2 represents the current through the same sample from which the resistive and capacitive components have been subtracted.

The flatness of the polarization curve may be noticed when the field decreases from its maximum value in the compensated loop, when compared with the uncompensated case. It is evident that no further enhancement of

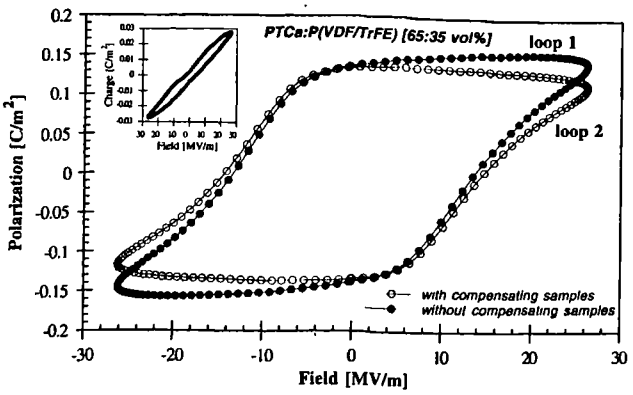

FIG. 3. Comparison of ferroelectric loops obtained with and without the compensating circuit. The temperature of the sample and the frequency of the field were 90 °C and 0.1 Hz, respectively.

polarization occurred when the field decreased below ±20 MV/m. This flatness also ensures that the resistive current component is not contributing to the polarization current. Figure 3 (insert) shows the difference in polarization between the two loops 1 and 2 and this difference, i.e., the elliptical form of the polarization component arises from the dielectric loss of the material and not from its ferroelectricity. This curve has been fitted to a lossy dielectric model to obtain the dielectric constant of 119 and tan δ value of 0.15 at 0.1 Hz, which are in good agreement with the experimentally measured values. A discontinuity of slope near zero field is apparent in this curve because the positive conducting diode switches off at +1.5 V while the negative one is switched on only at −1.5 V. The subsequent results reported in this article have been obtained from ferroelectric loops using the compensating technique.

After the unipolar voltage cycling, undertaken to determine the proportionality factors α and β mentioned above, it was observed that in the initial bipolar loops the polarization current was not symmetric for positive and negative fields, suggesting that the polarization does not switch entirely to the opposite direction to which the unipolar field was previously applied. It is only after repeated cycles that a symmetric behavior is obtained. This effect of the waiting time on the polarization behavior has been attributed to space charge[7,8] or to a molecular reorientation kinetic effect.[4] Our practice was to allow enough bipolar cycles (around 10) until a symmetric wave form was obtained before actual measurements were recorded.

Hysteresis loops have been recorded as a function of the peak of the sinusoidal field for temperatures of 50, 90, and 120 °C. The range of the applied field was between 5 and 26 MV/m, the latter value being close to the breakdown strength of the composite material. Due to the lower breakdown strength of the ceramic compared to the polymer its magnitude for the composite material is very dependent on the size of ceramic grain in relation to the thickness of the sample. The difficulty in poling this composite, which has a mixed-type connectivity, lies in the fact that the field limitation prevents the poling of the smaller grains which are isolated in the polymer matrix. The tem-

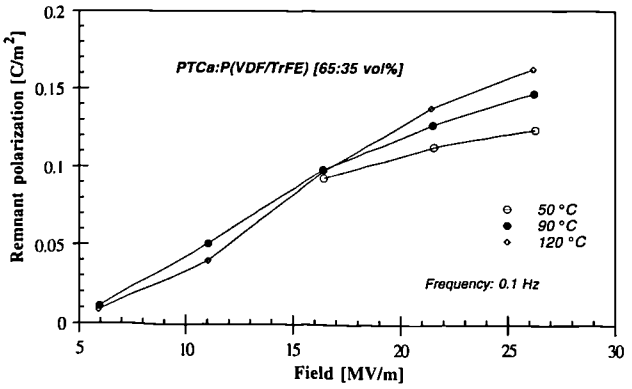

FIG. 4. Hysteresis loops as a function of the peak of the sinusoidal field for temperatures of 50, 90, and 120 °C.

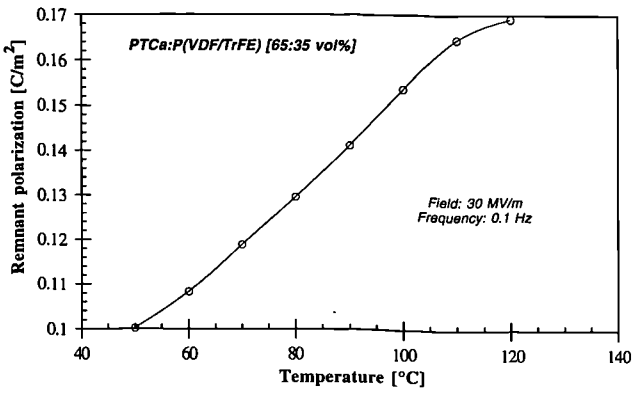

FIG. 6. Remanent polarization as a function of the temperature of the sample.

perature was not raised beyond 120 °C to prevent the softening and melting of the composite. Figure 4 shows the nature of the remanent polarization at different temperatures from which it may be observed that a maximum polarization value of 170 mC/m^2 occurs at 120 °C at a field of 26 MV/m which is close to its breakdown field.

Figure 5 shows the remanent polarization as a function of the frequency at 100 °C for 16 and 26 MV/m, i.e., the peak values of the applied field, from which it may be observed that the polarization seems to increase with decreasing frequency with an indication of reaching a saturation level at frequencies below 0.1 Hz and at a field of 26 MV/m. However, such a saturation is not observed for the lower value of the oscillating field.

The remanent polarization and the coercive field as a function of the temperature for an applied field of 30 MV/m and frequency of 0.1 Hz are shown in Figs. 6 and 7, respectively. A saturation of the remanent polarization was observed for temperatures approaching 120 °C while the coercive field increased from 12.5 to 15.5 MV/m with increasing temperature.

Landauer, Young, and Drougard[9] have proposed a simple relaxation equation for the polarization reversal which is given by

$$I_{\rm pol}=\frac{dP}{dt}=\nu(P_s-P)=\nu_0\exp\left(-\frac{E_a}{E}\right)(P_s-P), \qquad (2)$$

which states that the polarization P changes toward its equilibrium or saturation value P_s at a field activated rate ν. In Eq. (2), ν_0 is a rate constant independent of the field, E_a is the activation field, and E is the applied field. When the polarization switches from one direction to the other its value must go through zero and at that instant a simple relation holds for the polarization current I_0, which is given by the following equation:

$$I_0=\nu_0 P_s\exp\left(-\frac{E_a}{E_c}\right), \qquad (3)$$

where E_c is the coercive field. The value of E_a may be obtained from the slope of a plot of $\log(I_0)/(1/E_c)$ while its ordinate on the vertical axis gives the magnitude of $\nu_0 P_s$. To allow for the determination of these characteristics, various hysteresis loops were recorded in which the amplitude of the applied field was increased, which caused a corresponding increase in the coercive field as well as in the current I_0. Figure 8 shows such graphs at temperatures of 50, 70, 90, and 120 °C while in Table I we have listed the calculated values for the activation field and the product $\nu_0 P_s$. Furthermore, by assuming that the saturation polar-

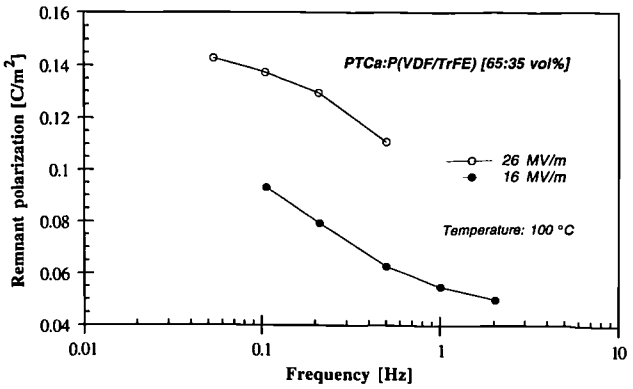

FIG. 5. Remanent polarization as a function of the frequency at 100 °C for 16 and 26 MV/m peak values of the applied field.

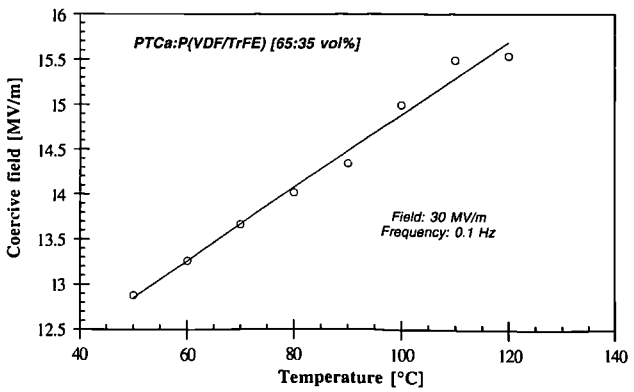

FIG. 7. Coercive field as a function of the temperature of the sample.

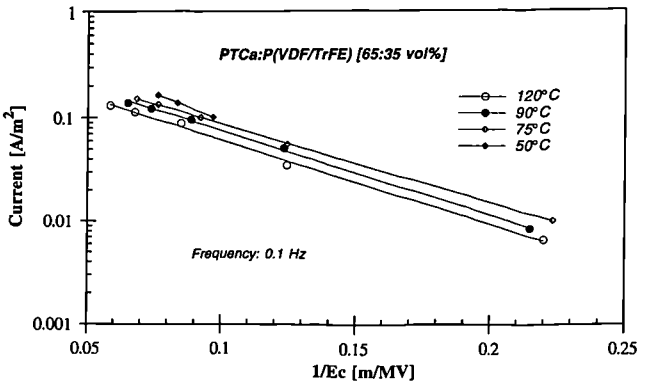

FIG. 8. Plot of the logarithm of I_0 (i.e., current when the polarization is zero) vs the inverse of the coercive field. The slope of these curves gives the activation field while its ordinate on the vertical axis is $\nu_0 P_s$.

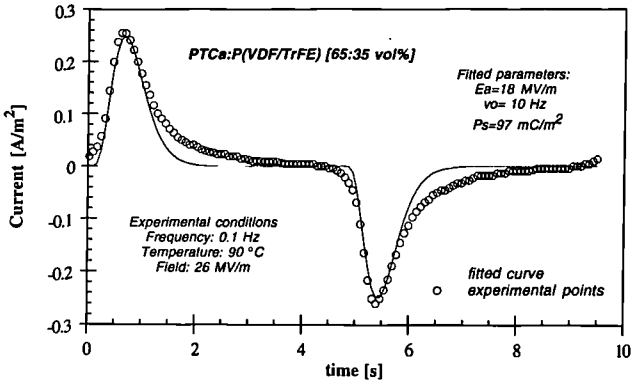

FIG. 9. Simulation of the current measured during the measurement of the hysteresis loop shown in Fig. 3.

ization is about P_s=0.17 C/m^2, which can be a valid assumption based on Fig. 6, an estimate for ν_0 was also computed.

The activation field is thus seen to lie between 17 and 23 MV/m while the rate constant is in the range of 8.8–16 Hz in the temperature range of 50–120 °C.

Using the values of activation field E_a and rate constant ν_0 at 90 °C we have simulated the current (see Fig. 9), measured in the hysteresis loop of Fig. 3. The calculation of the current involved the numerical solution of Eq. (2) using the saturation polarization P_s as a fitting parameter. The experimental current and the calculated curve in which a saturation polarization P_s of 97 mC/m^2 was used are shown in Fig. 9. The discrepancy between the value used for the calculated curve (P_s=97 mC/m^2) and that of the experimentally observed saturation polarization ($P_{s(\text{expt})}$ = 170 mC/m^2) can be understood if we assume that a distribution of activation fields exists in the composite as a result of the existence of a distribution in the grain size of the ceramic powder in the polymer matrix. It can be expected that the larger ceramic grains, comparable in size to the sample thickness, will experience a greater field than the finer particles, as explained before. As the agreement between the experimental and the calculated values of current is better at the beginning of the switching phenomenon, it may be suggested that during this period the large ceramic grains were able to switch with an activation field of 18 MV/m providing a saturation polarization of 97 mC/m^2. However, the switching was still in progress at longer times for the smaller ceramic grains as can be evidenced in the experimentally observed values of the current.

TABLE I. Activation fields and rate constants for PTCa:P(VDF/TrFE) (65:35 vol %) composite.

Temperature (°C)	E_a (MV/m)	$\nu_0 P_s$	ν_0 (Hz)
50	23.0	2.7	16.0
75	17.5	1.7	9.8
90	18.0	1.6	9.7
120	18.0	1.5	8.8

IV. CONCLUSIONS

An experimental procedure to measure the true polarization of a composite has been outlined and used to determine the remanent polarization and coercive field in a material made with calcium-modified lead titanate powder dispersed in the matrix of a copolymer of vinylidene fluoride and trifluoethylene. It was observed that the magnitude of the composite was greater than that of the ceramic by a factor of 2 while its coercive field was higher than that of the ceramic by the same amount. These effects are to be expected because of the presence of the shielding effect of the ceramic by the polymer matrix. The experimental hysteresis loops allowed also a determination of a value for the activation field of 18 MV/m which may be identified with that of the larger ceramic grains in the composite.

ACKNOWLEDGMENTS

The authors express their appreciation to the management of GEC-Marconi (Caswell) and Siemens (Munich, Germany) for a generous supply of the ceramic material for this work. One of the authors (C.J.D.) also expresses his gratitude to Professor Marat-Mendes of the Applied Physics Section and to the Science and Technology Faculty of the New University of Lisbon for granting him a study leave for 3 years.

[1] R. E. Newnham, D. P. Skinner, and L. E. Cross, Mater. Res. Bull. **13**, 525 (1978).
[2] L. Pardo, J. Mendiola, and C. Alemany, J. Appl. Phys. **64**, 5092 (1988).
[3] T. Furukawa, K. Suzuki, and M. Date, Ferroelectrics **68**, 33 (1986).
[4] B. Dickens, E. Balizer, A. S. DeReggi, and S. C. Roth, J. Appl. Phys. **72**, 4258 (1992).
[5] J. C. Hicks and T. E. Jones, Ferroelectrics **32**, 119 (1981).
[6] S. Ikeda, S. Kobayashi, and Y. Wada, J. Polym. Sci. Polym. Phys. **23**, 1513 (1985).
[7] S. Ikeda, T. Fukada, and Y. Wada, J. Appl. Phys. **64**, 2026 (1988).
[8] I. L. Guy and D. K. Das-Gupta, J. Appl. Phys. **70**, 5691 (1991).
[9] R. Landauer, D. R. Young, and M. E. Drougard, J. Appl. Phys. **27**, 752 (1956).

J. Phys. D: Appl. Phys. 26 (1993) 106–110. Printed in the UK

Measurement of the pyroelectric coefficient in composites using a temperature-modulated excitation

C Dias†, M Simon‡, R Quad‡ and D K Das-Gupta†

† School of Electronic Engineering Science, University College of North Wales, Dean Street, Bangor LL57 1UT, UK
‡ Heiman Optoelectronics GmbH, Weher Köppel 6, Wiesbaden, D-6200 Federal Republic of Germany

Received 20 July 1992

Abstract. Ferroelectric polymers such as PVDF and its copolymer P(VDF/TrFE) as well as ferroelectric ceramic-polymer composites have to be annealed at a high temperature for an extended period of time after poling, before the measurement of the pyroelectric coefficient by the direct method can be performed, in order to eliminate the high depolarization current which hinders the determination of the true pyroelectric current. Here it is suggested that a periodic temperature oscillation of a ceramic–polymer composite sample would permit measurement of its true pyroelectric coefficient without the need to anneal the sample.

The temperature distribution inside the composite sample, the magnitude of the pyroelectric current and their variation with the frequency of temperature oscillation have been simulated with the present theory. Pyroelectric measurements using this technique have been made on a poled composite of calcium-modified lead titanate ($PbTiO_3$) and a copolymer of vinylidene fluoride and trifluorethylene P(VDF/TrFE) and compared with the results of the direct measurements before and after annealing, in order to test the validity of the method.

1. Introduction and outline of method

Ferroelectric polymers such as PVDF and its copolymers P(VDF/TrFE) and P(VDF/TeFE) are now widely used in pyroelectric devices and applications [1]. Composite polymer–ceramic ferroelectric films are currently under investigation, because in these materials the mechanical strength, flexibility and low dielectric constant of the polymers can combine with the high pyroelectric coefficients of ferroelectric ceramics [2, 3]. It is thus assumed that polymer-based pyroelectric materials will have, in the future, a growing impact on pyroelectric devices and applications.

The most usual way to measure the pyroelectric coefficient is by the so-called quasi-static direct method [4]. In this method the temperature of the sample is increased at a constant rate while recording the short-circuited pyroelectric current. However, for polymeric materials the total current is usually made up of two non-distinguishable contributions, namely: (1) the irreversible depolarization current due to space charge relaxation and (2) the true reversible pyroelectric current [2]. Thus, in order to find the true pyroelectric current, it has to be ensured that the depolarization current decays to negligible values either by performing several heating runs until the measured current stabilizes or by annealing the sample for an extended period of time at a high temperature, usually above the temperature range in which the pyroelectric measurements are to be performed.

A measurement method that permits determination of the true pyroelectric current is to sinusoidally modulate the temperature of the sample while recording the current (or voltage) at the same frequency as that of the temperature oscillation [5, 6]. A practical approach to this method is to place the sample in-between two Peltier elements in which the supply current is controlled in such a way as to oscillate its temperature at a suitable frequency while recording the output current both in amplitude and phase. Any DC current present is thus spurious and can be assigned to the depolarization current at the average temperature of the sample and consequently neglected for the purpose of the pyroelectric measurement. However, if the depolarization current, which is a temperature-dependent variable, varies a great deal in the temperature range of oscillation, when compared with the true pyroelectric current, it is necessary to take into account the phase shift between the temperature and the current oscillation as suggested by Garn and Sharp [6] in order to

0022-3727/93/010106+05$07.50

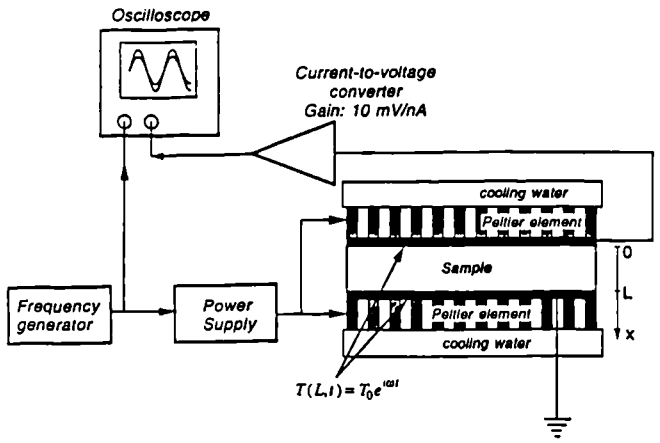

Figure 1. Schema of experimental set-up. The sample is enclosed in-between two Peltier elements which are driven at a certain frequency by a power supply. An oscilloscope is used to measure the voltage amplitude (after current–voltage conversion) and monitor the phase shift between the control voltage and signal voltage.

find the true pyroelectric coefficient. The reason is that the oscillating current in a pyroelectric material should have a 90° phase shift relative to the temperature oscillation, provided that a low enough frequency is used, whilst the oscillating depolarization current is in phase with the temperature.

There is a similarity between this type of measurement and the radiative dynamic method for the pyroelectric coefficient determination [7] as the excitation is a periodic one for both cases, thus ensuring the measurement of the true pyroelectric coefficient of a sample. However, while in the radiative method [7] the heat input is applied through a radiation source, in the present method the temperature of the sample is controlled directly. This means that no radiation absorption or heat capacity coefficients are needed and a direct measurement of the pyroelectric coefficient is possible.

In this paper a model has been developed that simulates the current output of a pyroelectric sample in which a temperature-modulated excitation is applied. The frequency response of this current for a uniformly polarized material has been determined in terms of the thickness, thermal diffusivity and pyroelectric coefficient of the sample under test. From this model an upper limit for the frequency of excitation can be deduced so that a 90° phase shift between the current and the temperature is verified. This model can also, with suitable modifications, be applied to the dynamic measurement method.

2. Theory of method: temperature distribution and pyroelectric current

An outline of the experimental method is shown schematically in figure 1, and is as follows. The sample with thickness L and area A is mounted in-between two Peltier elements, whose temperature is kept oscillating with an amplitude T_0 (K), at a frequency ω_0 (rad s^{-1}).

The temperature distribution inside the sample will be now calculated in order to find the suitable frequency of temperature excitation. It is understood that at low frequencies the temperature will be uniform across the sample, whereas at higher frequencies the heat will not propagate through the entire sample and the magnitude of the temperature oscillation will be attenuated towards the bulk of the material.

If the diameter of the sample is much greater than the thickness of the sample the equation for the diffusion of heat is one-dimensional:

$$\frac{\partial T}{\partial t} = K\frac{\partial^2 T}{\partial x^2} \tag{1}$$

where T (K) is the difference between actual temperature and room temperature and K ($m^2\ s^{-1}$) the thermal diffusivity. Because the sample is in-between two Peltier elements driven by the same power supply, the boundary conditions are:

$$T(0,t) = T(L,t) = T_0 e^{i\omega_0 t}. \tag{2}$$

A similar type of problem has been solved before [8]. The solution consists of the sum of a transient and a periodic term. The transient term decays with a time constant of 10 ms for the typical conditions used and so does not contribute to the experimentally measured quantities. The periodic term which is a solution of equation (1) can be expressed in non-dimensionalized form as [9]:

$$\begin{aligned} T(y,t) &= T_\omega(y,\omega)e^{i\omega_0 t} \\ &= [A\cosh(\omega y) + B\sinh(\omega y)]e^{i\omega_0 t} \end{aligned} \tag{3}$$

where

$$y = \frac{x}{L} \tag{4}$$

$$\alpha = \frac{K}{L^2} \tag{5}$$

and

$$\omega = (1+i)\sqrt{\frac{\omega_0}{2\alpha}}. \tag{6}$$

Substituting equation (3) into equation (2) we obtain for the temperature phasor inside the sample:

$$T_\omega(y,\omega) = T_0[\cosh(\omega y) - \sinh(\omega y)\tanh(\omega/2)]. \tag{7}$$

The magnitude of the temperature oscillation inside the sample, as described by equation (7), is shown in figure 2 both as a function of frequency and the position y inside the sample. It may be observed that for lower frequencies (i.e. $\omega_0/2\alpha \ll 1$) the temperature oscillation inside the sample is rather uniform, while at high frequencies (i.e. $\omega_0/2\alpha \gg 1$) there is an attenuation of temperature oscillation in the bulk, thus creating at higher frequencies a distributed non-uniform thermal

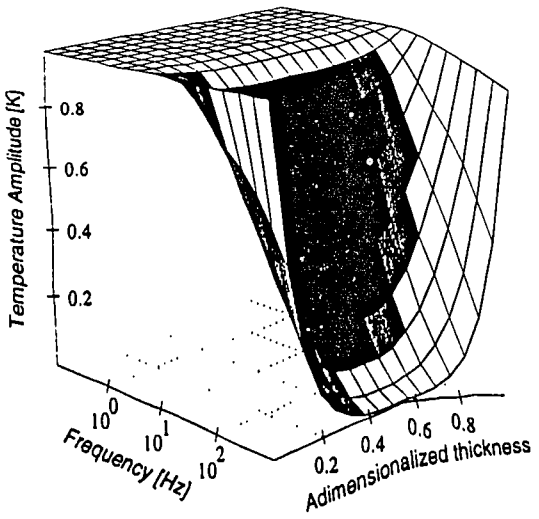

Figure 2. Simulation of the temperature oscillation inside the sample as a function frequency. It was assumed that the exciting temperature amplitude was $T_0 = 1$ K. The thickness, thermal diffusivity and area used in the simulation were, respectively, $L = 100$ μm, $K = 2.5 \times 10^{-7}$ m^2 s^{-1}, $A = 4.9 \times 10^{-4}$ m^2 and thus $2\alpha/2\pi$ is 7.95 Hz.

force which has been used before in the laser intensity modulation method (LIMM) to measure the spatial distribution of polarization in polymer electrets [10].

The short-circuit pyroelectric current I (A), measured for a sample subjected to a non-uniform distribution of temperature with a polarization and surface charge distribution $P(y)$ and $\sigma(y)$ respectively, has been deduced by Mospik [11], which after suitable manipulation is given by:

$$\frac{I}{A} = \alpha_P \int_0^1 P(y)\frac{\partial T}{\partial t}\,dy + (\alpha_\epsilon + \alpha_x)\int_0^1 [(P(y) - \overline{P}) - (\sigma(y) - \bar{\sigma})]\frac{\partial T}{\partial t}\,dy \quad (8)$$

where α_P, α_ϵ and α_x are the polarization, the dielectric constant and the linear temperature coefficients respectively and A (m^2) is the area of the sample. The surface charge $\sigma(y)$, is related to the volume space charge density by:

$$\sigma(y) = \int_0^y p(y)\,dy.$$

From equation (8) it may be observed that, when the temperature distribution is uniform across the sample, the second term of the current, due to the local spatial deviation from the mean of both the polarization and space charge, vanishes and thus does not contribute to the measured current. It should be emphasized that for all dynamic methods for the determination of the pyroelectric coefficient, including the step input of thermal radiation, the temperature distribution in the specimen will not be uniform unless the condition $\omega_0/2\alpha \ll 1$ is satisfied. The second term in equation (8) will make a contribution to the pyroelectric current if the above condition is not met.

Hence we can derive a constraint for the exciting thermal modulation frequency ω_0, which is $\omega_0 < 2\alpha$, in which case we obtain the usual expression for the pyroelectric current as:

$$I = A\alpha_P \int_0^1 P(y)\frac{\partial T}{\partial t}\,dy = \alpha_P \overline{P} A \frac{dT}{dt} = pA\frac{dT}{dt} \quad (9)$$

where p (C m^{-2} K^{-1}) $= \alpha_P \overline{P}$ is the pyroelectric coefficient.

We now assume that the polarization and space charge spatial distributions are uniform across the sample. The time derivative of equation (8) should then be taken from the average temperature of the sample. Substituting the expression for the temperature distribution (i.e. equation (7)) into equation (8) it may be shown that:

$$I = I_0 e^{i\omega_0 t} = pAT_0 2\alpha\omega \tanh\left(\frac{\omega}{2}\right) e^{i\omega_0 t}. \quad (10)$$

If the frequency of excitation is low enough, the phasor of the current I_0 will be given by:

$$I_0 = pAT_0 2\alpha\omega \tanh\left(\frac{\omega}{2}\right)^{\omega_0 < 2\alpha} \approx i\omega_0 pAT_0. \quad (11)$$

This equation describes the current phasor in terms of the pyroelectric coefficient, the sample area, the frequency of excitation and the temperature amplitude. It further shows that the current will be leading the temperature excitation by 90° provided that $\omega_0 < 2\alpha$.

As was pointed out by Garn and Sharp [6], when the depolarization current varies a great deal within the amplitude of the temperature oscillation there will be a significant current, in phase with temperature, which should be discarded from the total current by taking into account that in the case of a low frequency excitation the true pyroelectric current is 90° out of phase relative to the temperature.

3. Simulation, experimental results and discussion

An outline of the experimental method is shown schematically in figure 1 and is as follows. The sample is mounted in-between two sets of Peltier elements, whose temperature is kept oscillating with an amplitude T_0 (K) at a frequency ω_0 (rad s^{-1}). A good thermal contact between the Peltier elements and the sample was ensured whilst keeping the pressure on the sample to a minimum. In this work, we have not found a variation of the pyroelectric measurements within the pressure applied, due to the mounting. The output current is fed into a current-to-voltage converter and the voltage is monitored together with the driving voltage of the Peltier elements in an oscilloscope. The temperature amplitude and phase T_0 was measured and calibrated as a function of both frequency and the average (background) temperature of the sample, with the aid of a $LiTaO_3$ sample with documented properties. $LiTaO_3$ is used because it shows a truly pyroelectric response [6]. Within the frequency range 0.02–0.6 Hz, T_0

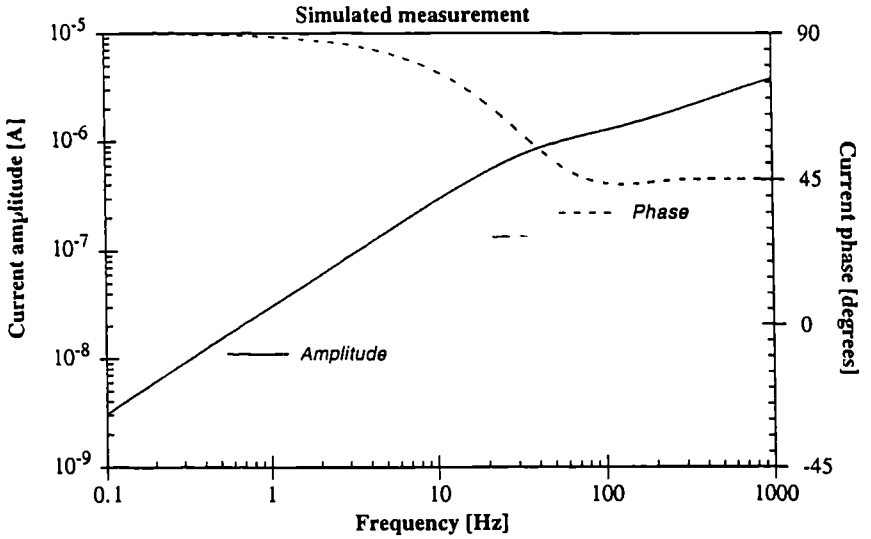

Figure 3. Simulation of the current amplitude and phase when heating the sample sinusoidally. In this simulation the following values were used: L = 100 μm, $K = 2.5 \times 10^{-7}$ m^2 s^{-1}, $A = 4.9 \times 10^{-4}$ m^2, $p = 1 \times 10^{-5}$ C m^{-2} K^{-1}, $T_0 = 1$ K.

varies proportionally to $1/f$ and we chose as a suitable measuring frequency 0.1 Hz, based on our estimation of the thermal cut-off frequency which is about 8 Hz. The driving voltage represents the power supplied to the Peltier elements, and at 0.1 Hz there is a 90° phase shift relative to the temperature wave. As the true pyroelectric current is also 90° phase shifted relative to the temperature wave, the two signals (i.e. the driving voltage and the pyroelectric current) have a phase shift of 0° or 180°, depending on the poling direction of the sample. Typical values for the temperature oscillation obtained in our experimental set-up and measured at 0.1 Hz are $T_0 = 1.51$ K and $T_0 = 1.67$ K when the background temperature is 14 °C and 40 °C respectively.

In figure 3 we have simulated the current which may be measured using typical values for the sample properties and assuming a constant temperature amplitude. The value used for the thermal diffusivity (i.e. 2.5×10^{-7} m^2 s^{-1}) is an estimate taking into account that the composite we are trying to emulate has a 60% ceramic volume fraction. Further, we have assumed a uniform polarization distribution such that the sample has a pyroelectric coefficient equal to 10^{-5} C m^{-2} K^{-1}. In this simulated case the thermal cut-off frequency (i.e. $2\alpha/2\pi$) is 7.95 Hz. From figure 3 we observe that in the low frequency range the current rises proportionally to the frequency while above the thermal cut-off it rises as the square root of the frequency. This can be explained by the fact that the current is proportional to the time derivative of the average temperature oscillation, which in turn is equal to the product of the frequency and the average temperature oscillation. At low frequency the temperature is uniform across the sample and so the current rises proportionally to the frequency, but as a thermal gradient starts to build inside the sample (i.e. for frequencies above 7.95 Hz), the average temperature oscillation begins to drop and the increase of the current will not be so steep. The phase plot shows that at low frequency the current leads by 90° and that this drops to 45° in the high frequency region.

We have checked the validity of the present technique for the composite of PT:P(VDF/TrFE) 60:40 vol.%, which was prepared in the following manner. The composite was obtained by mixing thoroughly the ceramic powder into the polymer melt at 175 °C after which a pressure of 1 kN m^{-2} was applied, also at 175 °C, to obtain an 80 μm thick film. After metallizing on both sides with Cr/Au electrodes ($A = 6.85$ cm^2) the film was DC poled for 2.6 h at $T = 102$ °C while applying a poling field of 30 kV mm^{-1}. In figure 4 we show the pyroelectric coefficient measured with the static and dynamic methods before and after poling.

Three runs were performed for the determination of the pyroelectric coefficient before we annealed the sample. The first run with the static set-up shows very large irreversible contributions as the measurement took place immediately after the poling process. The second run was performed with the dynamic set-up. During the amplitude measuring process we observed a high DC component yet the phase shift remained 0°. Therefore, we concluded that in this case the contribution of the depolarization current to the oscillating current is small enough to be neglected. The third run with the static set-up still displays a large depolarization current. After these measurements the sample was annealed at 55 °C for 17 h under short-circuit. Annealing is not only a time consuming step, there is also the risk of depoling the components with low T_c. The fourth and fifth runs show the static and dynamic measurements after the annealing, which agree very well. This ensures the fitness of the technique for the pyroelectric coefficient measurements in the present case. Nevertheless, should phase shifts between the two measuring signals be observed, a phase analysis would be necessary to

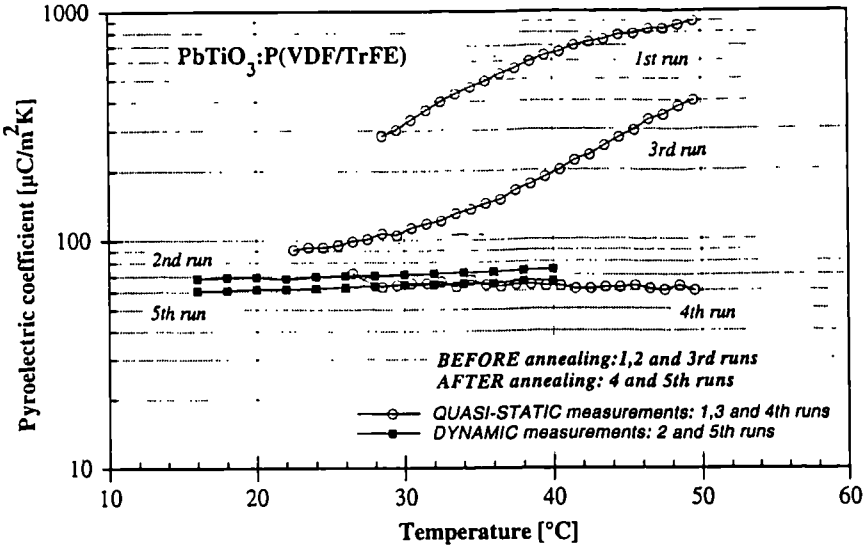

Figure 4. Pyroelectric coefficient of a poled composite sample of lead titanate: P(VDF/TrFE) [60 : 40 vol.%] measured before and after annealing by the dynamic temperature method and its comparison with measurements made by the direct method. The sample was poled with a field of 30 kV mm^{-1} at T = 102 °C for 2.6 h. The annealing procedure was performed at 55 °C under short-circuit for 17 h. The area and thickness of the sample were 6.85 cm^2 and 78 μm respectively.

determine the true pyroelectric current.

It is well established that an injection of charge carriers from the electrodes into the bulk of a dielectric becomes dominant when a sample is poled at high temperatures. These injected carriers may remain localized at grain boundaries, dislocation sites and other interfaces (namely crystalline–amorphous boundaries in semicrystalline polymers). For such a case a true reversible pyroelectric current may not be obtained, particularly at temperatures approaching that of the poling, unless an annealing process is undertaken to remove such trapped charges. However, at sufficiently high annealing temperatures not only the detrapping of charges but even the decaying of the frozen-in polarization can be promoted. The slight difference between the dynamic measurements, before and after annealing, can thus be due to a depoling or pre-ageing caused by the annealing process.

4. Summary and conclusions

In measuring pyroelectric coefficients a temperature change must always be induced in the sample to be measured. Methods which use a small temperature change of only one sign (e.g. only heating) cannot distinguish between the true pyroelectric currents and other thermally stimulated currents. One method to overcome this drawback is to use a sinusoidally modulated temperature wave. In this paper a theory is given to calculate an upper frequency below which the temperature distribution inside the sample is uniform, and it is shown how the cut-off frequency depends on the thickness and thermal properties of the sample (i.e. if a sample of the same material composition but thickness L = 500 μm is used the cut-off frequency will be as low as 0.3 Hz). An experimental set-up is described and a comparison between quasi-static and dynamic results given. The method proved to be suitable for measuring polymer–ceramic composites, which would otherwise need extensive annealing.

Acknowledgments

This work is financially supported by a BRITE EURAM research grant from the European Commission and one of the authors (CD) is grateful to the Commission for a maintenance grant.

References

[1] Yamaka E 1988 *The Applications of Ferroelectric Polymers* ed T T Wang (Glasgow: Blackie) p 329
[2] Das-Gupta D K and Abdullah M J 1988 *Ferroelectrics* **87** 213
[3] Newnham R E, Skinner D P and Cross L E 1978 *Mater. Res. Bull.* **13** 525
[4] Byer R L and Roundy C B 1972 *Ferroelectrics* **3** 333
[5] Hartley N P, Squire P T and Putley E H 1972 *J. Phys. E: Sci. Instrum.* **5** 787
[6] Garn L E and Sharp E J 1982 *J. Appl. Phys.* **53** 8974
[7] Porter S G 1981 *Ferroelectrics* **33** 193
[8] Carslaw H S and Jaeger J C 1959 *Conduction of Heat in Solids* 2nd edn (Oxford: Clarendon)
[9] Holeman B R 1972 *Infrared Phys.* **12** 125
[10] Lang S B and Das-Gupta D K 1986 *J. Appl. Phys.* **59** 2151
[11] Mopsik F I and De Reggi A S 1982 *J. Appl. Phys.* **53** 4333

Polymer/ceramic composites for piezoelectric sensors

C. Dias and D. K. Das-Gupta
University of Wales, School of Electronic Engineering Science, Dean Street, Bangor, Gwynedd LL57 1UT (UK)
Yolanda Hinton and R. J. Shuford
Materials Research Laboratory, US Laboratory Command, Watertown, MA 02172-0001 (USA)

Abstract

Polymer/ceramic composites with 0–3 connectivity have been produced by introducing fine-grain modified lead titanate powder in the matrix of a copolymer of vinylidene fluoride and trifluorethylene (VDF/TrFE). The electromechanical coupling factor k_t, the acoustic impedance Z_0 and the mechanical quality factor Q_m of these films are determined. k_t values in the range 30–35% have been achieved. Ultrasound transducers have been fabricated with these films. The impulse response of the transducer in the transmitting mode is determined. An attempt has been made to produce a theoretical model to match the experimental observations.

Introduction

Polymer/ceramic composites have recently been investigated with the objective of obtaining materials with improved piezoelectric, pyroelectric and mechanical properties. Here we report on the fabrication of composites made of calcium-modified $PbTiO_3$ with a copolymer of vinylidene fluoride (VDF) and trifluorethylene (TrFE).

Both PVDF and some of its copolymers, namely P(VDF/TrFE) [1], are known to be polar ferroelectric materials with significant pyro- and piezoelectric properties, whose main advantages over the ferroelectric ceramics are their low acoustic impedance (-4.5 MRayls) and low mechanical quality factor (≈ 20), which make them useful for underwater operation and/or for broadband applications [2]. On the other hand, ferroelectric ceramics have very high pyro- and piezoelectric coefficients with high acoustic impedance and quality factors. The idea underlying the composite fabrication is to make a material that would have a high piezoelectric activity whilst exhibiting low acoustic impedance and the quality factor of polymers.

An important consideration in view of the resulting composite properties is the concept of connectivity [3] of the constituent materials within the composite material. The composites fabricated were of 0–3 type connectivity, in which ceramic grains of calcium-modified lead titanate, 10–20 μm in size, were embedded in a polymer matrix of P(VDF/TrFE). The ceramic volume fraction used in the composite was in the 50–65% range. This type of connectivity, although not best suited for the purpose of getting the highest piezoelectric coefficients, has been chosen for our study because of its ease of manufacture. For instance, very good properties for the 1–3 composites have been reported in which rods of ceramic are embedded in a polymer matrix in what one might call a parallel connectivity pattern [4]. Thus in a 0–3 composite one has a mixture of a series and a parallel connectivity pattern, depending on the relative magnitudes of the ceramic grain size and the thickness of the sample. These should be of the same order of magnitude so as to get a higher parallel connectivity character in the composite.

Experimental

The composite material was obtained through the following procedure: the polymer matrix (i.e., P(VDF/TrFE) 75:25 mol%) is first melted in a hot rolling mill at 170 °C. The ceramic grains, with 20 μm average size, were then gradually added to the polymer melt while mixing, until all the ceramic is evenly distributed in the composite; a uniform colour and texture of the composite melt was then observed.

The material thus obtained was then pressed at high temperature and pressure to give films in the thickness range 50–100 μm. Aluminium electrodes of ≈ 1000 Å thickness were then evaporated on both sides of these films. The poling of these materials was performed inside silicone oil at 90 °C at a field of about 30 MV/m for 30 min.

The electromechanical coupling and the mechanical quality factor were obtained by measuring the electrical impedance of the sample over the frequency range in

0924-4247/93/$6.00

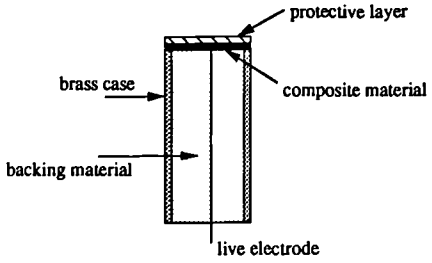

Fig. 1. Schematic diagram of an ultrasonic transducer.

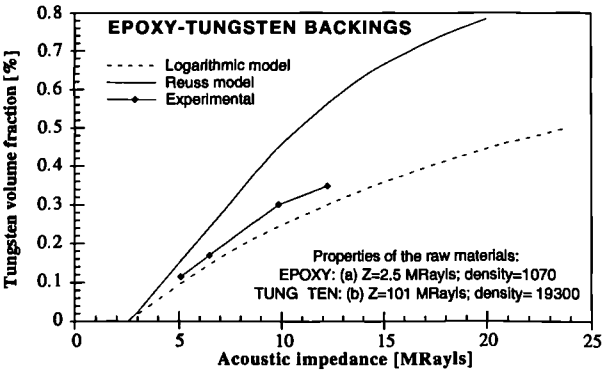

Fig. 2. Acoustic impedance of epoxy–tungsten mixtures.

which the composite film would resonate, which in the present case was around 20 MHz. A model HP 8702A network analyser was used to make the impedance measurements and the data were transferred to a computer in order to perform the mathematical computation of the piezoelectric properties.

The ultrasonic transducer fabricated with such a material is schematically shown in Fig. 1. The piezoelectric element, 10 mm in diameter, is cemented with a thin epoxy layer to a backing material whose function is to dampen the sound waves travelling to the back of the piezoelectric material. The backing is made of a tungsten/epoxy mixture of appropriate proportions.

Figure 2 shows the tungsten volume fraction needed in order to get a certain value for the acoustic impedance. We have plotted both the experimental points and two boundary models, namely the Reuss and the logarithmic models [5], between which the experimental values are believed to lie. We have used 35% (volume fraction) of tungsten in the transducer backings to get an acoustic impedance matched to the piezoelectric element impedance, which was 12.5 MRayls. The back of the film is connected to a wire where a voltage is applied or measured, depending upon whether the transducer is working as an emitter or a receiver. The other face of the film, electroded with gold, is connected to the case and grounded.

Theoretical model of the piezoelectric transducer

In contrast with inorganic piezoelectric materials, which have low mechanical losses and thus a high quality factor Q_m, for organic materials like PVDF, the familiar methods of analysing the frequency dependence of the electric impedance give rise to large errors in the determination of the piezoelectric constants [6]. However, following the analogy between the mechanical quantities, i.e., force and displacement velocity in an acoustic transmission line, and the electrical ones, i.e., voltage and current, the electrical network theory developed over the years to deal with electric transmission lines (including lossy ones) can be readily used for the study of acoustic transmission lines encountered in the design of the ultrasonic transducer. This scheme, which has been used before [7], allows the determination of the frequency response of an ultrasonic transducer together with its time response through a Fourier transformation. The key to this calculation is a matrix of impedances first derived by Bui and Shaw [8] for a lossy piezoelectric material relating the voltage and mechanical forces to the electric current and displacement velocity (see Fig. 3(a)):

$$\begin{bmatrix} F_1 \\ F_2 \\ V_c \end{bmatrix} = \begin{bmatrix} B\cot\left(\frac{\omega}{2\alpha f_0}\right) & B\csc\left(\frac{\omega}{2\alpha f_0}\right) & \frac{ih}{\omega} \\ B\csc\left(\frac{\omega}{2\alpha f_0}\right) & B\cot\left(\frac{\omega}{2\alpha f_0}\right) & \frac{ih}{\omega} \\ -\frac{ih}{\omega} & -\frac{ih}{\omega} & -\frac{i}{\omega C} \end{bmatrix} \begin{bmatrix} V_1 \\ V_2 \\ I_c \end{bmatrix} \quad \text{where} \quad \begin{aligned} B &= iAZ\alpha \\ \alpha &= \left(1+\frac{i\omega\psi}{2\pi f_0}\right)^{1/2} \\ C &= C_0[1+\tan(\delta_e)] \end{aligned} \tag{1}$$

where f_0 is the half-wave resonance, A the area of the sample, ψ the mechanical loss and h the piezoelectric voltage coefficient, which is related to the electromechanical coupling factor thus,

$$k_t^2 = \frac{h^2 \varepsilon_{33}^x}{c_{33}^D} \tag{2}$$

A knowledge of the backing acoustic impedance ($Z_b = 12.5$ MRayls) allows us to relate the force to the

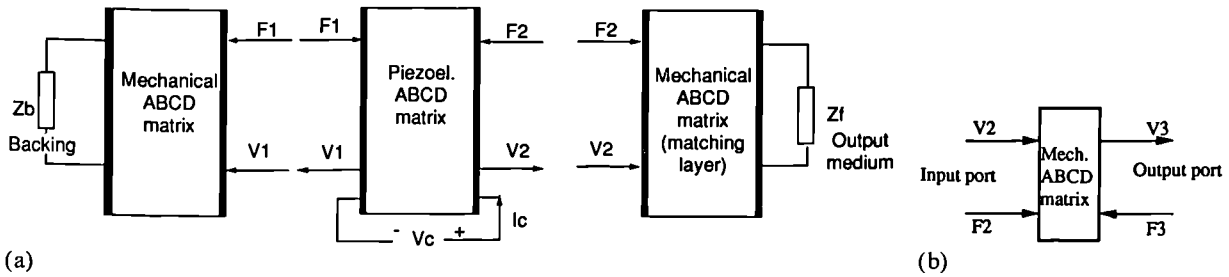

Fig. 3. (a) Network representation of an ultrasonic transducer. (b) ABCD network representation of a mechanical non-piezoelectric layer.

displacement velocity at the back of the transducer. This makes it possible to reduce the above matrix to a two-port network in which the input quantities (i.e., the voltage and current) are related to the output ones (i.e., the force and the displacement velocity at the front surface of the transducer) through a 2×2 matrix:

$$\begin{bmatrix} V_c \\ I_c \end{bmatrix} = \begin{bmatrix} A & B \\ C & D \end{bmatrix} \begin{bmatrix} F_2 \\ V_2 \end{bmatrix} \tag{3}$$

Furthermore, according to this formalism (so-called *ABCD* matrices) any non-piezoelectric mechanical layer also has a matrix which relates the input forces and displacement to the output force and displacement:

$$\begin{bmatrix} F_2 \\ V_2 \end{bmatrix} = \begin{bmatrix} \cos\left(\frac{\omega}{2\alpha f_0}\right) & B \sin\left(\frac{\omega}{2\alpha f_0}\right) \\ -\frac{1}{B} \sin\left(\frac{\omega}{2\alpha f_0}\right) & \cos\left(\frac{\omega}{2\alpha f_0}\right) \end{bmatrix} \begin{bmatrix} F_3 \\ V_3 \end{bmatrix} \tag{4}$$

Thus, to calculate the overall matrix relating the voltage/current to the force/displacement in the output medium, it is required to multiply all the matrices describing each of the elements composing the transducer. However, it is necessary to define both the mechanical and the electrical quantities appropriately so that Newton's third law, the continuity of displacement velocity and the electric Kirchhoff laws are obeyed while allowing for the chain rule of the *ABCD* matrices to apply (see Fig. 3(b)).

Finally, to calculate the frequency response we must know the acoustic impedance of the front output medium. The equation coupling the force and the velocity together with the matrix eqn. (3) relating the input to the output quantities in the transducer allow us to determine the ratio of the output force to the input voltage, which is the transfer function of the emitting transducer.

When the transducer works as a receiver unit the input quantities (i.e., voltage and current) will be the output quantities and vice versa for the case of force and velocity at the front surface of the transducer. In this case it turns out that the order of the elements in the matrix describing the receiver will be transformed to *DBCA*.

The determination of the piezoelectric properties of the composite has been achieved from the measurement of the electrical impedance of a sample vibrating as a free resonator. Thus $F_1 = F_2 = 0$ and it can be shown that

$$\frac{V_c}{I_c} = \frac{1}{i\omega C} - \frac{2}{iB}\left(\frac{h}{\omega}\right)^2 \tan\left(\frac{\omega}{2\alpha f_0}\right) \tag{5}$$

The experimentally determined electric impedance can thus be fitted by this equation upon optimizing the values of the electromechanical coupling factor (which relates to h, the piezoelectric voltage coefficient), the mechanical loss ψ and the resonance frequency f_0, allowing the determination of the piezoelectric properties of the material in hand even when its mechanical losses are not negligible.

Results and discussion

The piezoelectric properties of the composites produced were measured according to the procedure outlined in the previous Section. In Fig. 4 is shown a plot

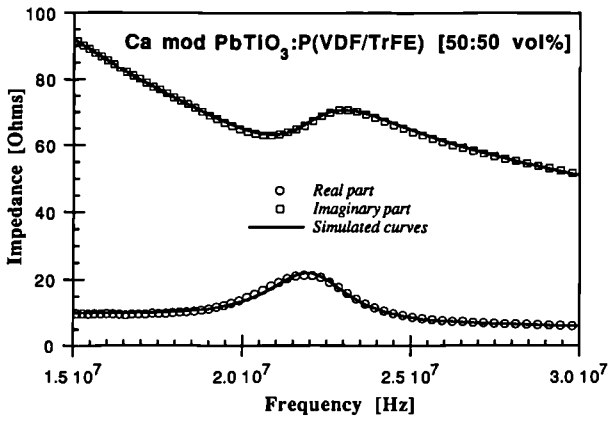

Fig. 4. Plot of the experimental and theoretical impedance curves around resonance for the calcium-modified lead titanate composite.

TABLE 1. Piezoelectric properties of composites together with a comparison with their constituent materials

Material	Density (kg/m^2)	v_s (m/s)	Z_0 (MRayls)	c_{33}^D (10^9 N/m^2)	$\|h_{33}\|$ (10^9 V/m)	Q_m	k_t (%)
PT(Ple):Cop [64:35]	5198	2647	13.7	36	3.7	6.8	0.36
PT(Ple):Cop [50:50]	4300	2833	12.2	34	3.7	7.7	0.32
P(VDF/TrFE)	1800	2400	4.51	11.3	4.7	20	0.30
PZT5A	7500	4350	33	147	21.5	75	0.49
$PbTiO_3$ calcium modified	6890	4200	29	183		80	0.6

of the impedance measured around resonance for a poled composite containing 50% calcium-modified lead titanate. A simulated curve obtained by eqn. (5) after adjusting the resonance frequency, the mechanical loss and the electromechanical coupling factor is also shown. It should be pointed out that the fitted parameters are found through a least-squares algorithm, which takes into account both the real and the imaginary parts of the impedance, thus leading to a more consistent estimation of these parameters.

In Table 1 a list of piezoelectric constants for the composites produced with various percentages of ceramic is shown. It may be observed that the electromechanical coupling factor is well over 30%, increasing for a higher volume fraction of the ceramic. The acoustic impedance, which ideally should be kept at a minimum, is about 12–13 MRayls, while the acoustic quality factor, which is the inverse of the mechanical losses, is quite low, especially when compared with the piezoelectric ceramics.

Figure 5 shows the time response of an ultrasonic transducer, work as an emitter. This transducer was made with a composite of calcium-modified lead titanate 50% in volume. The resonance frequency of this transducer is 16 MHz.

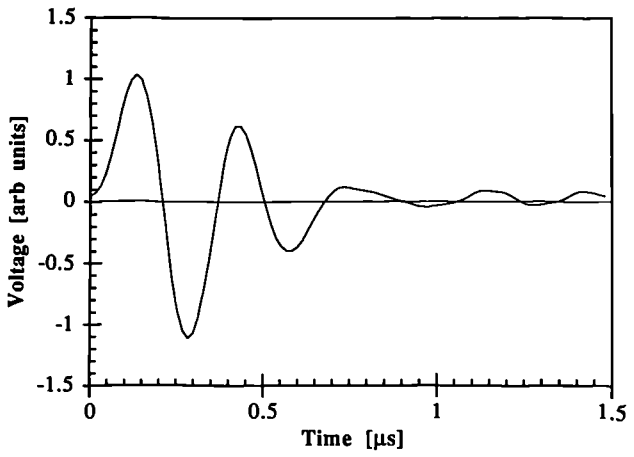

Fig. 5. Time response of an ultrasonic transducer made with a poled calcium-modified lead titanate composite 50% in volume fraction.

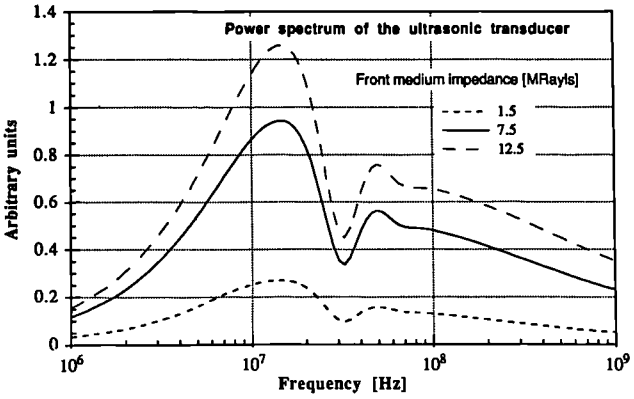

Fig. 6. Calculated frequency response of an ultrasonic transducer for various front-medium acoustic impedances.

A simulation of the magnitude of the frequency response of this transducer can be seen in Fig. 6 for various front-medium acoustic impedances. It can be observed that the magnitude of the output force at the front surface increases significantly when its acoustic impedance matches well with that of the composite, which is highly desirable.

By means of a Fourier transformation of the above calculated frequency spectrum, the time response was computed and is shown in Fig. 7. In this Figure is also plotted the time response of a transducer with an acoustic matching layer in the front surface whose acoustic impedance is the geometric mean of the acoustic

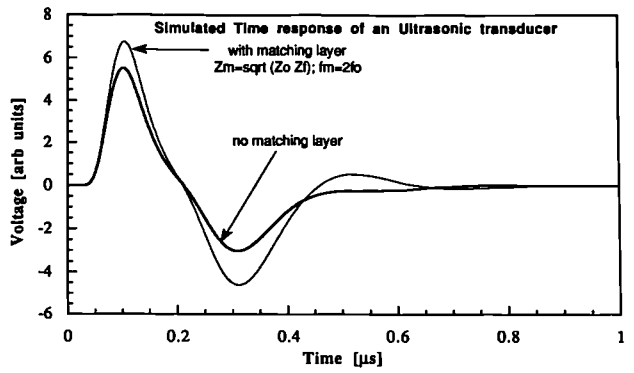

Fig. 7. Time response of an emitting ultrasonic transducer radiating into water with and without an acoustic matching layer.

impedances of the composite and water and whose thickness is $\lambda/4$ (i.e., its resonance frequency is twice that of the composite). Comparing the experimental curve with the simulation one without the matching layer, we can observe that the ringing of the simulated curves is not as great as the experimental one, which may be attributed to an imperfect bonding of the composite to the backing material. Comparing the simulated curves, we see that the voltage output is increased by 20% when a matching layer is present.

We conclude that a reasonable electromechanical coupling factor k_t, with a low mechanical quality factor (high losses) can be achieved in these composites. However, their acoustic impedance makes it difficult to couple the sound waves into the water without a front matching layer. Further work on the matching and simulation, together with a better way of bonding the various ultrasonic layers, is in progress.

Acknowledgements

This work is financially supported by a BRITE EURAM research grant from the European Commission and one of the authors (C. Dias) is grateful to the Commission for a maintenance grant. The authors are grateful to Messrs R. Twinney, G. M. Garner and Dr J. Chilton of GEC–Marconi for the generous supply of the modified lead titanate powder. It is a pleasure to thank P. Moreira and I. Darwazeh for valuable discussions during the course of this work.

References

1 T. Furukawa and K. Ishida, Piezoelectric properties in the composite systems of polymer and PZT ceramics, *J. Appl. Phys.*, *50* (1979) 4904–4912.
2 K. Kimura and H. Ohigashi, Generation of very high-frequency ultrasonic waves using thin films of vinylidene fluoride–trifluorethylene, *J. Appl. Phys.*, *61* (1987) 4749–4753.
3 R. E. Newnham, D. P. Skinner and L. E. Cross, Connectivity and piezoelectric–pyroelectric composites, *Mater Res. Bull.*, *13* (1978) 525–536.
4 T. R. Gururaja, W. A. Schulze, L. E. Cross, R. E. Newnham and B. A. Auldet, Piezoelectric composite materials for ultrasonic transducer applications. Part 1: Resonant modes of vibration of PZT rod–polymer composites, *IEEE Trans. Sonics Ultrasonics, SU-32* (1985) 481–498.
5 M. G. Grewe, T. R. Gururaja, T. R. Shrout and R. Newnham, Acoustic properties of particle/polymer composites for ultrasonic transducer backing applications, *IEEE Trans. Ultrasonics, Ferroelect. Freq. Contr., UFFC-37* (1990) 506–514.
6 H. Ohigashi, in T. T. Wang (ed.), *The Applications of Ferroelectric Polymers*, Blackie, Glasgow, 1988, pp. 237–273.
7 M. Platte, PVDF ultrasonic transducers for non-destructive testing, *Ferroelectrics*, *115* (1991) 229–246.
8 L. N. Bui and H. J. Shaw, Study of acoustic wave resonance in piezoelectric PVF2 film, *IEEE Trans. Sonics Ultrasonics, SU-24* (1977) 331–336.

iezoelectric Properties f 0-3 Ceramic/Polar olymer Composites

Dias and D.K. Das-Gupta

printed from Materials Research Society mposium Proceedings Volume 276, *Smart terials Fabrication and Materials for cro-Electro-Mechanical Systems*, A. Peter dine, George C. Johnson, Andrew Crowson and rk Allen, editors.

Piezoelectric properties of 0-3 ceramic/polar polymer composites

C. DIAS and D. K. DAS-GUPTA

School of Electronic Engineering Science, University College of North Wales, Dean Street, Bangor, Gwynedd LL57 1UT, UK

ABSTRACT

Ferroelectric ceramics such as PZT, while exhibiting strong piezoelectric effect, have the disadvantages of a high acoustic impedance, difficulty to miniaturize and not being suitable to broad band ultrasonic applications. Polar ferroelectric polymer such as PVDF and its copolymers which can be obtained in thin film form, have low mechanical Q and low acoustical impedance although their piezoelectric coefficients are significantly lower than those of the piezoelectric ceramics. Composites of piezoelectric ceramic powders, such as PZT and Calcium modified Lead Titanate (PT) in a matrix of P(VDF/TrFE) have been fabricated in our laboratory, in order to investigate whether these materials could have the low acoustic, broad band properties of the polymers whilst retaining the high piezoelectric coefficients of the ceramics. In the present paper the results of a study of the electromechanical coupling factor (kt), the quality factor (Qm) as well as the gh and dh piezoelectric coefficients of these 0-3 composites poled both by corona and by the conventional method are given.

I - INTRODUCTION

Composites made of ferroelectric ceramics in various forms (powders, fibers rods etc) dispersed or embedded in a polymer matrix have been previously investigated in order to get improved piezo- and pyroelectric properties [1-3] and quite a number of different approaches have been tested either in terms of the materials used or on their connectivity patterns. Here we report on the fabrication of 0-3 connectivity composites made of (i) PZT and (ii) Calcium modified $PbTiO_3$ ceramics with a copolymer of VDF and TrFE, together with measurements made of their piezoelectric properties i.e., the electromechanical coupling factor (k_t), the mechanical quality factor (Q_m) and the hydrostatic d_h and g_h coefficients.

Both PVDF and some of its copolymers namely P(VDF/TrFE) are known to be polar ferroelectric materials with significant pyro- and piezoelectric properties whose main advantages over the ferroelectrics ceramics are their low acoustic impedance (~4.5 MRayls) and low mechanical quality factor (~20) which make them useful for underwater operation and/or for broad band applications [4]. On the other hand both ferroelectric ceramics used have very high pyro- and piezoelectric coefficients with high acoustic impedance and quality factors. The main difference between the two being the much lower dielectric constant and larger hydrostatic piezo-properties of the Calcium modified $PbTiO_3$ ceramic in comparison with those of PZT. The idea underlying the composite fabrication is to make such a material which would have a high piezoelectric activity whilst exhibiting low acoustic impedance and quality factor of polymers.

II - EXPERIMENTAL AND ASSOCIATED THEORY

The PZT ceramic powder was milled to a grain size of about 1 μm, while the $PbTiO_3$ ceramic was first sintered and then quenched from a high temperature resulting thus in a coarser grain (~20 μm) with a much wider size distribution. The P(VDF/TrFE) in powder form from Solvay et Cie, had a 75:25 mol% ratio between the VDF and the TrFE polymers. The composites were fabricated as outlined in figure 1, and were made such that each of its constituents had a volume fraction of 50% on the resultant material. The mixing operation was done at high temperature by adding the ceramic powder into the melted polymer, while rolling the resulting composite for about one hour until its uniformity of colour and

Mat. Res. Soc. Symp. Proc. Vol. 276. ©1992 Materials Research Society

texture were found to be satisfactory. The 2 mm thick composites thus obtained were then pressed to a film thickness in the 50-100 μm range at high temperature and pressure.

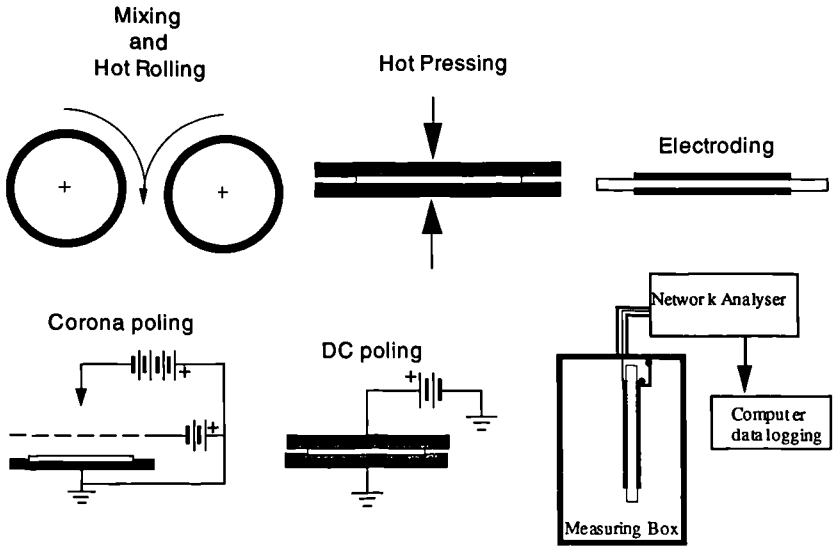

Figure 1 - Experimental procedure for obtaining 0-3 composites together with the electroding, poling and electromechanical coupling factor measurement schematics

Sample polarization either by the corona or by the conventional method, both at 100 °C was performed afterwards for about 15 minutes at various poling fields. The conventional poling method was always performed inside a silicone oil bath. Previous to any measurement and immediately after poling an annealing operation was performed at 90°C for 12 hours, in order to get rid of any space charge effects on the measured properties.

The electromechanical coupling and the mechanical quality factor were obtained by measuring the electric impedance over the frequency range in which the composite film would resonate, which in the present case, was around 20 MHz. A network analyser model HP 8702A was used to make the impedance measurements and the data were transferred to a computer in order to perform the mathematical computation of the piezo properties.

In contrast with inorganic piezo materials, which have a very high quality factor Q_m and thus low mechanical losses, for organic materials like PVDF, the familiar methods of analysing the frequency dependence of the electric impedance give rise to large errors in the determination of the piezoelectric constants. Various procedures have been proposed to analyse the impedance spectra of these lossy materials [5,6], one of them being the Ohigashi [7] method which has been used here with a minor modification. In this method, both the dielectric constant under constant strain (ε_3^x) and the elastic stiffness constant under constant displacement (c_3^D), for a lossy material, are considered to be complex quantities:

$$\varepsilon_3^{*x} = \varepsilon_3^x(1 - j\phi) \quad \text{and} \quad c_3^{*D} = c_3^D(1 + j\psi) \tag{1}$$

where $\phi=\tan\delta_e$ is the dielectric loss and $\psi=Q_m^{-1}=\tan(\delta_m)$ is the mechanical loss. The total measured impedance of a piezoelectric sample resonating in its transverse mode can be deduced to be a sum of two

terms i.e. (i) the electric impedance $Z_c(\omega)$ of the sample capacitance and (ii) an acoustic term $Z_a(\omega)$ [7]. The real and imaginary parts of the total impedance after being suitably modified are then given by:

$$\mathrm{Re}[Z(\omega)] = \frac{\phi}{(\phi+1)\omega C_o} + Max\cdot\left(\frac{\omega_o}{\omega}\right)^2 \frac{\tanh\left(\frac{\pi\psi}{4}\right)}{\sqrt{\psi^2+4}} \frac{\left(\psi\sin\left[\frac{\pi\omega}{\omega_o}\right]+2\sinh\left[\frac{\pi\psi\omega}{2\omega_o}\right]\right)}{\left(\cos\left[\frac{\pi\omega}{\omega_o}\right]+\cosh\left[\frac{\pi\psi\omega}{2\omega_o}\right]\right)} \quad (2)$$

$$\mathrm{Im}[Z(\omega)] = -\frac{1}{(\phi+1)\omega C_o} + Max\cdot\left(\frac{\omega_o}{\omega}\right)^2 \frac{\tanh\left(\frac{\pi\psi}{4}\right)}{\sqrt{\psi^2+4}} \frac{\left(2\sin\left[\frac{\pi\omega}{\omega_o}\right]-\psi\sinh\left[\frac{\pi\psi\omega}{2\omega_o}\right]\right)}{\left(\cos\left[\frac{\pi\omega}{\omega_o}\right]+\cosh\left[\frac{\pi\psi\omega}{2\omega_o}\right]\right)} \quad (3)$$

where ω_0 is the resonance frequency, C_0 is the sample capacitance, and *Max* denotes the real part of the acoustic impedance at resonance whose relationship with k_t is:

$$k_t^2 = \frac{\pi}{4}\omega_o C_o Max\sqrt{\psi^2+4}\tanh\left(\frac{\pi}{4}\psi\right) \quad (4)$$

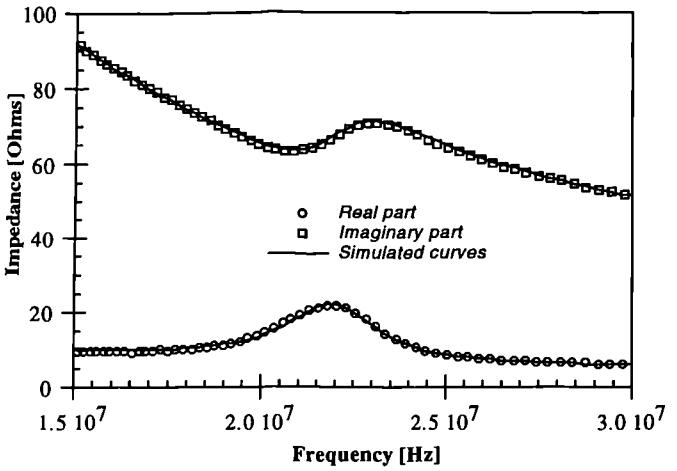

Figure 3- Comparison of actual impedance and Ohigashi's model results near resonance

The method requires the determination of the values of ω_0, *Max* and ψ which give the best fit to the total impedance once the capacitance and the dielectric losses are known to a reasonable approximation. This procedure is slightly different from the one used by Ohigashi [7] because the *Max* fitting parameter, which does not have any other significance apart from the one stated above, has been introduced in place of the k_t constant. This was done so that the fitting parameters would control specific features of the impedance curves. Thus ω_0 controls the position of the resonance frequency peak, *Max* controls the height of the real part of the impedance and ψ the width of the same peak. In this way the fitting variables are decoupled in relation to the features of the impedance curve they are trying to match. A computer program was then used to get the optimum parameters for each sample, although a very reasonable first guess was possible just by analysing the curves as measured. Once these parameters are found and the density is known, other material properties can also be computed i.e., the velocity of

sound v_s, the acoustic impedance Z_o, the stiffness constant c_{33} and the h_{33} piezoelectric voltage coefficient.

The g_h and d_h hydrostatic piezo-coefficients were measured using a low frequency acoustic method. The sample is placed in a box where a sound pressure is generated and the resulting output voltage compared with that of a calibrated microphone from which the voltage sensitivity g_h is then obtained. The d_h coefficient can be computed by multiplying the g_h constant by the permitivity at 1kHz. The hydrostatic figure of merit FOM=$d_h g_h$ has also been computed.

III - RESULTS AND DISCUSSION

Table I lists the composite materials, their poling conditions together with the obtained results from piezoelectric measurements. No results are reported on the PZT composite for the electromechanical factor and related properties as it was not possible to detect any resonance peak in the impedance spectra in any of its poled samples. This fact together with the low d_h and g_h coefficients leads us to suggest that this material has a low piezoelectric activity.

For the $PbTiO_3$ composite a reasonable electromechanical coupling factor was observed which increased with the poling field together with a very low quality factor. The latter can be related to dispersive nature of the embedded ceramic powder which act as scatterers of the sound waves. However it is possible that the mechanical quality factor is in excess of 7, as the thickness variation which was about 5%, could lead to a smoothing of the resonant impedance peak. The piezoelectric activity is difficult to predict as it depends on a number of factors like the volume fraction, size and morphology of the grains, the dielectric and resistivity mismatch between the phases to cite just a few of the factors. However the acoustic impedance of this composite roughly matches the Reuss model [8], which assumes a constant stress throughout the solid, giving for the case of the $PbTiO_3$ composite a value of 9.5 MRayls. This model has been used before with some success on the prediction of the acoustic impedance of other composites [9].

The values for the piezoelectric properties were in all cases performed at room temperature and pressure and for the electromechanical related properties they are strictly valid only around the resonant frequency range. However, we believe, from measurements performed in samples for an extended period of time, as well as, with samples annealed at 90°C for about 16 hours, that the polarization at least in the case of the $PbTiO_3$ composite does not decay with temperature as in the case of piezoelectric polymers.

The composites prepared, apart of being made of different ceramics, differ also in the grain size of the ceramic powder. This can be a significant factor in tailoring the properties of a particular composite.

The hydrostatic properties of these composites are directly related to the ceramic materials properties from which they are produced. In this respect the $PbTiO_3$ ceramic has a much higher g_h coefficient than the PZT ceramic and this is in agreement with the experimentally observed value of g_h for the $PbTiO_3$ composite which is greater than that of the PZT composite. In many applications g_h is the figure of merit and in relation to this constant the composite of Lead Titanate is better for hydrostatic applications than the pure ceramic. However hydrostatic piezoelectric properties of PVDF both with respect to g_h and FOM (Figure Of Merit =$d_h g_h$) coefficients are better than the composites produced.

In conclusion, the composites now made in our laboratories, have a potential in broad band application due to its low quality factor coupled to a reasonable electromechanical coupling factor. In addition, they have the advantages of ease of manufacturing and formability of polymers. In terms of hydrostatic properties we think that although the g_h coefficients of PVDF will not be achievable with the present approach its FOM can be improved with more research into the poling and volume fraction and grain size dependence of the piezo-activity of these composites.

Table I - Composites, poling conditions and piezoelectric properties together with a comparison with its constituents materials

Sample No.	Material	Density [kg/m^3]	Thickness [μm]	Poling method	Field [kV/mm]	ε @1kHz	tan δ_e
1	$PbTiO_3$:P(VDF/TrFE) [50:50 vol%]	4300	75	conv.	10	56	0.014
2	$PbTiO_3$:P(VDF/TrFE) [50:50 vol%]	4300	74	conv.	15	56	0.014
3	$PbTiO_3$:P(VDF/TrFE) [50:50 vol%]	4300	64	conv.	20	56	0.014
4	PZT:P(VDF/TrFE) [50:50 vol%]	4650	55	conv.	10	90	0.02
5	PZT:P(VDF/TrFE) [50:50 vol%]	4650	61	conv.	15	90	0.02
6	PZT:P(VDF/TrFE) [50:50 vol%]	4650	52	conv.	20	90	0.02
7	PZT:P(VDF/TrFE) [50:50 vol%]	4650	132	corona		90	0.02
8	P(VDF/TrFE)	1800				5.3	0.25
9	PZT5A	7500				830	0.02
10	$PbTiO_3$ Calcium modified	6890				207	0.006

Sample No.	v_s [m/s]	Z_o [MRayls]	c_{33}^D [10^9 N/m^2]	$\|h_{33}\|$ [10^9 V/m]	Q_m	k_t [%]	d_h [pC/N]	g_h [mV·m/N]	FOM [10^{-15}/Pa]
1	3080	13.2	40.8	3.1	6.9	0.26	6.4	12.9	82.5
2	2910	12.5	36.3	3.2	6.9	0.28	19.1	39	735
3	2833	12.1	34.5	3.8	7.7	0.33	19.8	40	790
4	no resonance peaks were found for this sample						4.2	5.3	22
5			"				7.5	9.5	71
6			"				10	12.5	124
7			"				2.1	2.8	5.6
8	2400	4.51	11.3	4.7	20	0.3	9	130	1170
9	4350	33	14.7	21.5	75	0.49	32	2	64
10	4200	29	183		80	0.6	62	33	2066

For the conventional poling method the temperature and poling time are 100°C and 15 minutes respectively

IV - ACKNOWLEDGEMENTS

This work is financially supported by a BRITE EURAM research grant from the European Commission and one of the authors (C. Dias), is grateful to the Commission for a maintenance grant. It is a pleasure to thank Messrs R. Twinney and G. M. Garner and Drs. J. Chilton (GEC Marconi - Plessey), R. Quad, J. Schieferdecker, M. Simon (Heiman GmbH) and K. Lubitz (Siemens) for valuable discussions.

V - REFERENCES

[1] Furukawa, T., K. Ishida, J. Appl. Phys., 50(7), 4904-4912, (1979)
[2] Gururaja, T. R., W. A. Schulze, IEEE Trans. Son. Ultrason., SU-32(4), 481-498, (1985)
[3] Garner, G. M., N. M. Shorrocks, Ferroelectrics, 93, 169-176, (1989)
[4] Kimura, K. and H. Ohigashi, J. Appl. Phys., 61(10), 4749-4753, (1987)
[5] Brown, L. and D. L. Carlson, IEEE Trans. UFFC, 36(3), 313-318, (1989)
[6] Bui, L. N., H. J. Shaw, IEEE Trans. Son. Ultrason., SU-24(5), 331-336, (1977)
[7] Ohigashi, H., in *The applications of ferroelectric polymers*, ed. by Wang (Blackie Glasgow 1988), p.237-273
[8] Pelmore, J. M., Acoust. Lett., 3(3), 65-68, (1979)
[9] Grewe, M. G., T. R. Gururaja, IEEE Trans. UFFC, 37(6), 506-514, (1990)